



24<sup>th</sup> DAE – BRNS Symposium  
on  
Thermal Analysis

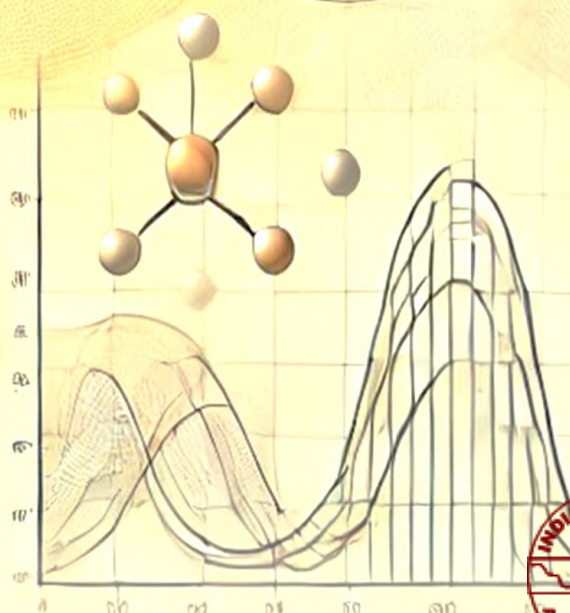
# THERMANS – 2024

January 16- January 18, 2025

[www.itasindia.org/thermans2024/](http://www.itasindia.org/thermans2024/)

Venue

Multi Purpose Hall, Training School Hostel, BARC  
Anushaktinagar, Mumbai, India

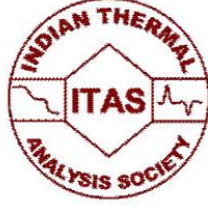


Organized by

**Indian Thermal Analysis Society (ITAS), Mumbai**



# थर्मलिस - 2024



## डी.ए.ई.-बी.आर.एन.एस. की ऊष्मीय विश्लेषण पर 24वीं संगोष्ठी की कार्यवाही

भा. प. अ. के. प्रशिक्षण विद्यालय छात्रावास एवं अतिथि गृह  
अणुशक्तिनगर, मुंबई

सम्पादक मंडल

दीपक त्यागी, के. ए. दुबे, एम. बसु, सलिल वर्मा

डी. चट्टराज, नैना राजे, वाई. के. भारद्वाज



# THERMANS -2024



## Proceedings of 24<sup>th</sup> DAE BRNS Symposium on Thermal Analysis

*BARC Training School Hostel and Guest House  
Anushaktinagar, Mumbai*

### Editorial board

Deepak Tyagi, K. A. Dubey, M. Basu, S. Varma

D. Chattaraj, Naina Raje, Y. K. Bharadwaj

## Preface

Indian Thermal Analysis Society (ITAS) has been organizing biennial Symposium on thermal analysis for last forty-five years in India. Thermal Analysis, Thermochemical & thermophysical property measurements, thermodynamic and phase diagram studies have contributed significantly to new technologically important materials. New developments in the field of instrumental thermal analysis play important role in characterization of almost all types of substances such as metals, alloys, ceramics, cermets, composites, polymers, glasses, electronic materials, food, pharmaceuticals, organic and inorganic compounds, even biological organisms. The 24th symposium on thermal analysis is being organized at the Bhabha Atomic Research Centre, Mumbai during January 16-18, 2025 with a theme "Thermal Analysis and Materials Characterization". It is heartening to find huge response from participants from national laboratories and academic institutions that symbolizes the wider applicability and popularity of thermo-analytical techniques among the scientific community. More than 125 abstracts covering the application of thermal analysis in the field of thermodynamics and phase equilibria, development of alloys and ceramics, thermal characterization of nuclear materials, soft materials, catalysts, organic compounds, polymers, kinetics of solid state reactions etc. have been received. About 150 delegates from different parts of the country and abroad will be participating in this three days event.

On behalf of Indian Thermal Analysis Society and the organizing committee of THERMANS-2024, we extend out hearty welcome to all the delegates and wish a fruitful scientific deliberation. We sincerely acknowledge Board of Research on Nuclear Sciences (BRNS) for the financial support towards THERMANS-2024.

We wish all our delegates a Happy and Prosperous New Year 2025.

Deepak Tyagi, K. A. Dubey

M. Basu, S. Varma



भारत सरकार  
Government of India

विवेक भसीन  
Vivek Bhasin

निदेशक, भाभा परमाणु अनुसंधान केंद्र  
Director, Bhabha Atomic Research Centre  
सदस्य, परमाणु ऊर्जा आयोग  
Member, Atomic Energy Commission



## MESSAGE

I am delighted to know that the 24th DAE-BRNS symposium on Thermal Analysis (THERMANS-2024), a platform designed to explore for sharing knowledge, fostering innovation, and advancing research in this critical field is being organised during 16-18th January, 2025 at Multipurpose Hall, TSH, Anushaktinagar, MUMBAI.

Thermal analysis is not merely a tool but a gateway to understanding the fundamental properties of materials, enabling breakthroughs across diverse applications. From developing advanced materials for next-generation technologies to addressing the unique challenges of the nuclear industry, the scope of this field is immense and transformative.

This symposium stands as a testament to DAE's commitment to fostering interdisciplinary collaboration and cutting-edge research. By bringing together experts and emerging talents, it aims to bridge gaps, ignite new ideas, and pave the way for solutions that benefit both science and society.

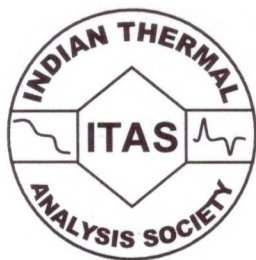
I extend my heartfelt gratitude to all participants for contributing to this endeavour and encourage all to make the most of this opportunity to explore, engage, and innovate.

Wishing you all a productive and inspiring THERMANS-2024.

02.01.2025

  
(Vivek Bhasin)





**Dr. Ratikanta Mishra**  
**President**  
**Indian Thermal Analysis Society**

---

### MESSAGE

Greetings to all the members of Indian Thermal Analysis Society and the participants of THERMANS - 2024.

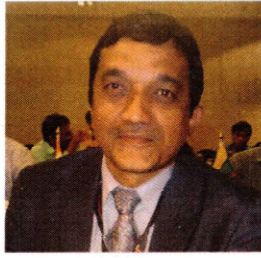
Thermal analysis is one of the oldest techniques used by the humans and was being employed long before the birth of modern science. It is an essential tool for material property evaluation at high temperature and provides invaluable information for its practical deployment. In the Department of Atomic Energy (DAE), thermal techniques are used to assess the material properties at every step of nuclear cycles. Considering significance of thermal analysis in the field of material characterisation, in general, and for Atomic Energy Program, in particular, Indian Thermal Analysis Society (ITAS) was formed in 1977, and since then has been actively engaged in promoting this branch of science and technology in India.

As a flagship scientific event, Indian Thermal Analysis Society (ITAS) is organizing its 24<sup>th</sup> biennial Symposium on Thermal Analysis (THERMANS-2024). I hope that THERMANS-2024 will provide a unique opportunity for the research community in material science to share their experience and discuss recent development in the field.

I extend my warm welcome to all the delegates and wish them a Happy, memorable and scientifically stimulating stay.

I wish THERMANS-2024 a grand success.

Ratikanta Mishra



**Dr. Y. K. Bhardwaj**  
**Chairman, THERMANS-2024 &**  
**Associate Director, Radiochemistry and Isotope Group,**  
**Bhabha Atomic Research Centre**

---

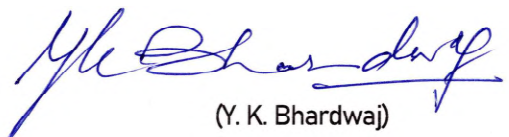
### **MESSAGE**

Greetings to all ITAS members and participants of THERMANS-2024. Thermal response of materials depends on their structure, state, composition and sample history. Thus, thermal analysis techniques, calorimetry, thermodynamic measurements, thermo-chemistry have proven to be immensely reliable characterisation techniques for selection of materials for desired applications. The forum of DAE-BRNS symposium on Thermal Analysis provides unique opportunity to review the progress of research and development in the subject domain, share knowledge and facilitate new collaborations among different laboratories.

It is heartening to know that Indian Thermal Analysis Society (ITAS) in association with Board of Research in Nuclear Science (BRNS) is organising 24<sup>th</sup> symposium on Thermal Analysis (THERMANS-2024) at Training School Hostel, Anushakti Nagar, MUMBAI during 16-18<sup>th</sup> January 2025. The symposium with theme as "Thermal Analysis and Materials Characterization" aims at deliberating on recent technological advancements in thermal analysis for development of new materials needed in the field of nuclear science which have direct relevance to ongoing, emerging and future programmes of DAE, glasses, polymers, hydrogen storage materials, biomaterials, nanomaterials, fuel cell materials etc.

I am sure THERMANS-2024 will be highly beneficial to scientists from DAE, academia, industry and other organizations. It will provide opportunity to young researchers to interact with eminent scientists and researchers working in the field of Thermal Analysis and allied areas. The knowledge shared by the experts will inspire the young scientists to take up new vistas in the field of thermal analysis and inspire the young minds to take up the new problems and challenges in this field.

On this occasion, I extend my sincere wishes to all delegates for interactive and scientifically enriching symposium and THERMANS-2024 a great success.

  
(Y. K. Bhardwaj)



**Dr. D. Chattaraj**  
Secretary, THERMANS-2024



**Dr. Naina Raje**  
Convener, THERMANS-2024

---

## Message

It is indeed a matter of privilege and a great pleasure to organize the prestigious event of the 24<sup>th</sup> DAE-BRNS Symposium on Thermal Analysis (THERMANS-2024). THERMANS-2024 is a pivotal scientific gathering for the thermal analysis community, serving a forum for taking stock of the current trends in thermal analysis research locally as well as globally. This symposium has been covering all the important and emerging areas on thermal analysis of several scientifically and industrially important materials like glass, metals and alloys, ceramics, food, biomaterials, medicines, polymers, nuclear materials, nanomaterials, hydrogen storage materials etc. This year we have received near about 110 contributory papers and nearly 20 invited presentations. The technical sessions include plenary talks, invited talks, evening lecture, contributory oral presentations, short lectures, award presentations and presentations from industry partners. We have no doubt that researchers from DAE, Universities, Research Institutions, and other Countries will be scientifically benefitted from this symposium and the discussion with leading scientists in the field of thermal analysis will spark innovative ideas among them.

We extend our warm greetings to all the delegates and wish for a great success in having a fruitful and beneficial scientific deliberations in the symposium.

*D Chattaraj*

*Naina Raje*



# **THERMANS – 2024**

## ***Patrons***

Vivek Bhasin, BARC, Mumbai  
U. Kamachi Mudali, HBNI, Mumbai

## ***National Advisory Committee***

C. G. Karhadkar, IGCAR, Kalpakkam  
Unmesh Malshe, RRCAT, Indore  
A. K. Tyagi, HBNI, Mumbai  
Awadhesh Kumar, BARC, Mumbai  
D. K. Aswal, BARC, Mumbai  
P. A. Hassan, BARC, Mumbai  
R. Tewari, BARC, Mumbai  
S. Adhikari, BARC, Mumbai  
S. M. Yusuf, BARC, Mumbai  
A. C. Bhasikuttan, BARC, Mumbai  
C. N. Patra, BARC, Mumbai  
N. Choudhury, BARC, Mumbai  
N. Kishore, IITB, Mumbai  
S. C. Parida, BARC, Mumbai

## *National Organising Committee*

R. Mishra	President, ITAS
Y. K. Bhardwaj,	Chairman, THERMANS-2024
Naina Raje,	Convener, THERMANS-2024
D. Chattaraj,	Secretary, THERMANS-2024
R. K. Mondal,	Treasurer, THERMANS-2024
A. Awasthi, BARC, Mumbai	
Abhishek Rai, BARC, Mumbai	
B. B. Kalekar, BARC, Mumbai	
Dheeraj Jain, BARC, Mumbai	
H. N. Jena, IGCAR, Kalpakkam	
K. A. Dubey, BARC, Mumbai	
M. K. Sapra, BRNS, Mumbai	
M. R. Pai, BARC, Mumbai	
Naved Malek, SVNIT, Surat	
Pradeep Samui, BARC, Mumbai	
P. Singh, IIT, BHU, Varanasi	
R. Ganeshan, IGCAR, Kalpakkam	
R. N. Singh, BARC, Mumbai	
Ram Avtar Jat, BARC, Mumbai	
Rajesh Pai, BARC, Mumbai	
Rimpi Dawar, BARC, Mumbai	
Rohan Phatak, BARC, Mumbai	
S. Kolay, BARC, Mumbai	
S. K. Rakshit, BARC, Mumbai	
S. N. Achary, BARC, Mumbai	
Salil Varma, BARC, Mumbai	
Sangita Pal, BRNS, Mumbai	
V. Sudarshan, BARC, Mumbai	
V. K. Aswal, BARC, Mumbai	
V. M. S. Verenkar, Goa Univ, Goa	

## ***Local Organizing Committee***

### ***Technical Committee***

Dr. Salil Varma,	ChD, BARC	Chairman
Dr. Manidipa Basu,	ChD, BARC	Co-Chairman
Dr. Siddhartha Kolay,	ChD, BARC	
Dr. Rimpi Dawar,	ChD, BARC	
Dr. Dheeraj Jain,	ChD, BARC	
Dr. Pradeep Samui,	PDD, BARC	
Dr. Rohan Phatak,	FCD, BARC	
Dr. Bal Govind Vats,	FCD, BARC	
Dr. Bhupesh Kalekar,	ACD, BARC	
Dr. Deepak Tyagi,	ChD, BARC	
Ms. Akanksha Samanta,	PIED, BARC	
Dr. A. M. Banerjee,	ChD, BARC	
Dr. P. Manikandan,	MCD, IGCAR	
Dr. S. Balakrishnan,	FChD, IGCAR	
Dr. Rumu Haldhar,	MSD, BARC	
Dr. Abhishek Mukherjee,	MP&CED, BARC	
Dr. Vinita G Gupta,	ChD, BARC	
Dr. Seemita Banerjee,	ChD, BARC	

### ***Publication & Souvenir Committee***

Dr. K.A. Dubey,	RTDD, BARC	Chairman
Dr. Deepak Tyagi,	ChD, BARC	Co-Chairman
Dr. Siddhartha Kolay,	ChD, BARC	
Dr. Gourab Karmakar,	ChD, BARC	
Mr. Shubham Narang,	ChD, BARC	
Mr. Pratik Das	PDD, BARC	
Mr. Sakshey Mittal,	RTDD, BARC	
Ms. Avanti Singh,	ACD, BARC	

### ***Catering Committee***

Dr. Harshala Parab,	ACD, BARC	Chairman
Dr. A.S. Ambolikar,	FCD, BARC	Co-Chairman
Mr. Lukman Ahmad,	FCD, BARC	
Mr. Amit Kulkarni,	RACD, BARC	
Dr. Manpreet Bassan,	ACD, BARC	
Mr. Prasenjit Saha,	ChD, BARC	

### ***Accommodation Committee***

Dr. A.M. Banerjee,	ChD, BARC	Chairman
Shri. K.B.Modi	PDD, BARC	Co-Chairman
Dr. Madhusudan Ghosh,	ACD, BARC	
Dr. Sunil Kumar,	RACD, BARC	
Mr. Shailesh Kumar,	PDD, BARC	

### ***Exhibition, Banner and Poster Committee***

Dr. Pradeep Samui,	PDD, BARC	Chairman
Dr. Rohan Phatak,	FCD, BARC	Co-Chairman
Mr. Suhas Phapale,	ChD, BARC	
Dr. Rakesh Shukla,	ChD, BARC	
Mr. B.M.Singh	PDD, BARC	
Ms.Manisha Venkatesh,	ACD, BARC	
Mr. Shafeeq P.P. Mohd,	FCD, BARC	
Mr. Arijit Ghoshal,	RTDD, BARC	
Mr. Raja Das,	PDD, BARC	

### ***Expenditure & Co-ordination Committee***

Dr. S. K. Rakshit,	PDD, BARC	Chairman
Dr. Prasad P. Phadnis,	ChD, BARC	Co-Chairman
Dr. Bhupesh Kalekar,	ACD, BARC	
Dr. Ruma Gupta,	FCD, BARC	
Dr. Nilanjal Mishra,	RTDD, BARC	

### ***Transport Committee***

Dr. N.K.Goel,	RTDD, BARC	Chairman
Dr. S.M.Bhojane,	PDD, BARC	Co-Chairman
Mr. Suresh Chopade,	ChD, BARC	
Dr. Srikant Sahoo,	ACD, BARC	
Mr. Swapnil A. Ramraje,	ChD, BARC	
Dr. A.N. Shrisat	ChD, BARC	
Mr. Sanjay Kumar Yadav,	PDD, BARC	
Mr. Sourav Majumdar,	ChD, BARC	
Mr. P. Ginishkumar,	PDD, BARC	
Mr. Nijith Sebastian,	PDD, BARC	

### ***Auditorium, Stage and Decoration Committee***

Dr. Dheeraj Jain,	ChD, BARC	Chairman
Dr. Ruma Gupta,	FCD, BARC	Co-Chairman
Mr. Ameya Wadawale,	ChD, BARC	
Dr. Rimpi Dawar,	ChD, BARC	
Mr. K. Venkatesh,	ACD, BARC	
Ms. Jyoti Pareek,	PDD, BARC	
Dr. Hirakendu Basu,	ACD, BARC	
Dr. Bal Govind Vats,	FCD, BARC	
Ms. Swarnima Rawat,	RTDD, BARC	

### ***Registration Committee***

Dr. Mrinal Pai,	ChD, BARC	Chairman
Dr. Sumana Paul,	FCD, BARC	Co-Chairman
Ms. Smita Sheelvantra,	ACD, BARC	
Ms. Darshana K. Ghonge,	ACD, BARC	
Ms. Hemlata Khadilkar,	PDD, BARC	
Ms. Annpurna Chandane,	RTDD, BARC	
Dr. V. G. Mishra,	RACD, BARC	
Dr. Rumu Halder Banerjee,	MSD, BARC	
Dr. Priyanka Ruz,	ChD, BARC	
Ms. Geeta R. Patkare,	FCD, BARC	

## Table of Content

Content	Title & Authors	Page No.
<i>Plenary Lecture</i>		
PL	New Approaches in Decarbonization of Metals Production <i>Prof. Ramana Reddy, University of Alabama, USA</i>	1
<i>Evening lecture</i>		
EL	Transforming solids into functional materials: Role of heat treatment <i>Dr. A. K. Tyagi, Homi Bhabha National Institute, Mumbai, India</i>	3
<i>Award Lecture</i>		
AL-1	Thermal Analysis in Chemical and Biological Systems: Mechanistic insights to Impactful Applications <i>Nand Kishore, Indian Institute of Technology Bombay, Powai, Mumbai, India</i>	5
AL-2	Calorimetry methods for the thermodynamic measurements <i>Rajesh Ganesan, Indira Gandhi Centre for Atomic Research, Kalpakkam, India</i>	6
<i>Invited Talk</i>		
IT-1	Reinforced Carbon-Carbon (RCC) Composite for high temperature applications in Rockets & missiles. <i>Dr. A. P. Dash, HEMRL, Pune, India</i>	7
IT-2	Applications of Thermal Analysis Techniques in the Development of CO <sub>2</sub> Removal Systems for Manned Space Missions <i>Dr. Rajeev Raghwan, Vikram Sarabhai Space Centre (VSSC), Thiruvananthapuram,</i>	8
IT-3	Air Processed Asymmetric Squaraine Dyes for Photovoltaic Application <i>Prof. Vilko Mandić, University of Zagreb, Croatia</i>	9
IT-4	Tailoring the Physico-Chemical Properties of Ionic Liquids and Deep Eutectic Solvents for Enhanced Sorption and Extraction Processes <i>Prof. Ramesh Gardas, IIT Madras, India</i>	10
IT-5	Thermal behavior and application of carbon nanostructures <i>Prof. Imre M. Szilagy, University of Miskolc, Hungary</i>	11
IT-6	Thermal Properties of Unsaturated Soils: Theory and Measurement <i>Prof. Rao Martand Singh, Norwegian University of Science &amp; Technology, Norway</i>	12
IT-7	Role of thermodynamics and Phase diagram in deciding the path of the transformation in Nb, Ti and Zr Based Systems <i>Dr. R. Tewari, Bhabha Atomic Research Centre (BARC), Mumbai, India</i>	13
IT-8	Nanoparticle assisted local hyperthermia in cancer therapy <i>Prof. Vesa-Pekka Lehto, University of Eastern Finland, Finland</i>	14
IT-9	Designing of inorganic compounds for chemical sensing applications - Insights	15

	from thermo-analytical techniques <i>Dr. Jayraman, Indira Gandhi Centre for Atomic Research, Kalpakkam, India</i>	
IT-10	Role of lattice degree of freedom in electronic transitions in solids <i>Dr. Bobby Joseph, Elettra-Sincrotrone Trieste, Italy</i>	16
IT-11	Study of Terminal Solid Solubility of Hydrogen and Deuterium in Zr-2.5Nb Alloy Pressure Tube Material <i>Dr. R. N. Singh, Bhabha Atomic Research Centre (BARC), Mumbai, India</i>	17
IT-12	Structure and Thermochemistry of Functional Metal Oxides <i>Prof. Pradha Saradhi M., SRM University, Amaravati, India</i>	18
IT-13	Impact of Calcination Conditions of the Catalyst on the Catalytic Performance <i>Dr. Suneet Kumar Yadav, Süd-Chemie India Pvt. Ltd., Vadodara, India</i>	19
IT-14	Thermal Behavior of MOF membranes: Morphology-Dependent Insights into Crystallization and Glass Transition <i>Prof. Prabhakar Singh, IIT BHU, Varanasi, India</i>	20
IT-15	Excitements of Thermal Analysis: Studying Thermo-oxidative Decomposition and Heat Quenching in Convenient Making of Useful Nanomaterials and in Understanding Use of Edible Oils <i>Prof. R. K. Verma, Magadh University, Bodhgaya, India</i>	21
IT-16	Metal Organic Framework Integrated Composite Patches as the Multifunctional Drug Delivery Platform for Enhanced Wound Healing and Anti-Inflammatory Applications in Freezing Conditions <i>Dr. Naved Malek, SVNIT, Surat, India</i>	22
<b>Short Lecture</b>		
SL-1	Controlled thermal conversion of molecule to nano-sized functional material <i>Dr. Adish Tyagi, Chemistry Division, BARC, Mumbai, India</i>	23
SL-2	Growth of single crystals at high temperature <i>Dr. Mohit Tyagi, Theoretical Physics Division, BARC, Mumbai, India</i>	24
SL-3	Radiolytically Functionalized Amine Dense Biodegradable Adsorbents for CO <sub>2</sub> capture: Thermo -gravimetric Characterization and Adsorption Analysis <i>Dr. Nilanjali Mishra, Radiation Technology Development Division, BARC, Mumbai, India</i>	25
SL-4	Hydrogen Ingress in Irradiated Coolant Channels: Role of DSC in In-Service Inspection and Monitoring <i>Ms. Akanksha Samanta, Post Irradiation Examination Division, BARC, Mumbai, India</i>	26
SL-5	High Temperature Processing of Materials for Steam Electrolysis <i>Dr. R. K. Lenka, Powder Metallurgy Division, BARC, Mumbai, India</i>	27
SL-6	Thermal Effects: An Essential Facet of Studies on Nuclear Materials <i>Dr. Dheeraj Jain, Chemistry Division, BARC, Mumbai, India</i>	28
SL-7	Spot technique - A tool for measuring the solidus and liquidus of refractory and	29

	radioactive alloys <i>Dr. S. Balakrishnan, MCMFCG, IGCAR, Kalpakkam, India</i>	
SL-8	Application of Thermodynamics in Solid State Transformations – Examples from Zirconium <i>Dr. Mani Krishna K. V., Mechanical Metallurgy Division, BARC, Mumbai, India</i>	30
SL-9	Thermal studies assisted evaluation of stability and polymorphism of potentially bioactive organo -selenium compounds <i>Dr. Prasad P. Phadnis, Chemistry Division, BARC, Mumbai, India</i>	31
<b>Abstracts</b>		
A1-121	Studies on Phase Equilibria in Na-Ti-O System <i>S. Pragadeeswari, A. S. Suneesh, Chinmay Routray, Rajesh Ganesan</i>	33
A1-122	Biophysical Analysis of Interactions of Copper (II) Complexes with Serum Albumin <i>Namrata Singh, Nand Kishore</i>	35
A1-123	Thermodynamic Studies on Li <sub>2</sub> NiO <sub>2</sub> Compound Employing KEQMS Sanjay Yadav, Hemlata Khadilkar, Raja Das, Pradeep Samui, Swarup Rakshit, Suresh Parida,	37
A1-124	Thermodynamic Studies on Calcium Fluoroapatite Employing KEQMS Raja Das, Hemlata Khadilkar, Pratik Das, Sanjay Yadav, Swarup Rakshit, Suresh Parida, Pradeep Samui,	39
A1-125	Structural and Thermodynamic Properties of ZrAl: A DFT Study Nijith S, D Chattaraj,	41
A1-126	Thermodynamic Properties of Li <sub>2</sub> BeF <sub>4</sub> near Melting Point: A DFT Study J Pareek, D Chattaraj,	43
A2-121	High temperature mass spectrometric studies on + NdAl <sub>3</sub> > of Nd-Al system Manikandan P, Neduraman S, Kumaresan, Hrudananda Jena	45
A2-122	Enthalpy increment of Na <sub>0.5</sub> Bi <sub>0.5</sub> TiO <sub>3</sub> by drop calorimetry Chinmay Routray, T. Muthu Ambika, Chita Patra, Sajal Ghosh, Rajesh Ganesan,	47
A2-123	Standard molar Gibbs energy of formation of Bi <sub>2</sub> Ti <sub>4</sub> O <sub>11</sub> (s) from EMF measurements Chita Patra, Chinmay Routray, T Ambika, Sajal Gosh, R Sudha, R Ganesan	48
A2-124	Heat capacity measurement of RE-Te compounds (La, Nd, Gd) Hriday Maji, Venkatesh M, Chita Ranjan Patra, Shyam Kumar S, Rajesh Ganesan,	49
A2-125	Sustainable Approaches for Immobilization of High-Level Nuclear Waste with Glass Matrix: A plant Experience kankan Patra, R Sah, V Mittal, Anoop Kelkar, Ashish Pandey, R. K. Malav, Chetan Baghra, G. Singh, D Sathe, R Bhatt,	51
A2-126	Exploring the Thermophysical & Structural Changes in Serpentine Induced by Mechanical Milling for Neutron Shielding Applications Mohit Rattanpal, Meenu Prasher, Pranesh Sengupta,	53

A2-127	Knudsen effusion mass spectrometric studies over liquid region of U-Zr-Mn alloy Manikandan P, Manivannan A, Balakrishnan S, Hrudananda Jena,	55
A2-128	Excess enthalpy associated with PRAN reactor, validation using TEG generator and application feasibility S Phapale, S Varma, R Mishra,	57
A2-129	Thermodynamic Investigations of Quaternary Compounds in Ni-Mn-Te-O System Rimpi Dawar, Shubham Narang, Ratikanta Mishra,	58
A2-130	Vapour pressure measurements in Nd-Te system S Shyam Kumar, Rajesh Ganesan,	60
A2-131	Studies on Thermophysical Properties of Simulated Waste Loaded Iron Phosphate Glass Matrix Logaraj P, Ravisankar P, Ashish Jain, Raja Madhavan R,	62
A2-132	Effect of isovalent substitution on the energetics of $Sr_x Ba_{(1-x)}CeO_3$ ( $0 \leq x \leq 1$ ) System Hemlata Khadilkar, Premanadana p, Pratik Das, Pradeep Samui, S Rakshit, S Parida,	64
A2-133	Electrochemical Kinetics of Reduction of $Mg^{2+}$ in Chloride and Fluoride molten salt electrolyte media Mohsin Jafar, S Gupta, A Satpati,	66
A2-134	Thermodynamic and Thermo-physical Properties of Frozen Fuel and Coolant Salts for Molten Salt Breeder Reactor Abhishek Rai, Manoj Sharma, Swarup Rakshit, Suresh Parida,	67
A3-122	Studies on effect of oxygen impurity on decomposition rate of sodium hydride in liquid sodium towards secondary cold trap regeneration Manikandan P, Faizal V A, Lavanya M, Karunakaran R, Murugesan, Hrudananda Jena, Rajesh Ganesan, Jayaraman V	69
A3-124	Thermal properties of Diglycine Perchlorate: IR, DSC, TGA and QMS study Harsha Kumawat, Shiv Vishwakarma, Babu Gonde, Naina Raje, Himal Bhatt,	71
A3-125	Mechanistic and Kinetic Aspects of Thermal Decomposition of $CuCl_2$ Under Different Flow Environments R. V. Singh, G. Patkare, A. Banerjee, M. Pai,	73
A3-126	Thermal Breakdown of Tin-selenolate Complex for Nanomaterial Synthesis Saibren Mandal, Atharva Kulkarni, Gourab Karmakar, G Kedarnath, Amey Wadawale, Balaji Mandal, Adish Tyagi,	75
A3-127	Thermolysis of Bismuth-Selenolate Complex through Molecular Precursor Approach Atharva Kulkarni, Rohit Chauhan, Balaji Mandal, Gourab Karmakar, Adish Tyagi,	77
A3-128	Thermolysis of copper thiolate complex for the preparation of digenite material and its lithium uptake property Suraj Yadav, Gourab Karmakar, G Kedarnath, Balaji Mandal, Adish Tyagi,	79



A3-129	Thermolysis of copper thiolate complexes for the preparation of photoresponsive binary copper sulphide and ternary copper indium sulphide materials Suraj Yadav, Rohit Chauhan, Gourab Karmakar, Adish Tyagi,	81
A3-130	Thermally Driven Synthesis of Bismuth Sulfide Nanoparticles through Single Source Precursor Approach Atharva Kulkarni, Rohit Chauhan, Gourab Karmakar, Adish Tyagi,	83
B1-121	Thermal Design and Simulation of the Radiator for High Power Space Travelling Wave Tube (TWT) Chirag Mistry, Amitavo Roy Choudhury, Sanjay Kumar Ghosh,	85
B1-122	Study of Temperature Dependent Corrosion of SS 304L in corrosive acidic medium using X-Ray Fluorescence K G Spoorthy, Sangita Dhara, Muhammed Shafeeq, Ruma Gupta	87
B1-123	Structural and Thermal Stability Studies on Irradiated Magnesium Potassium Phosphates for Back End Nuclear Fuel Cycle Applications Rumu Banerjee, Naina raje, Pranesh Sengupta	89
B1-124	Phase Evolution in Stainless Steel $\alpha$ -Zircaloy System upon Melt-solidification Sourav Majumder, Dheeraj Jain, V Sudarsan,	91
B1-125	Calorimetry and Dilatometry Studies of Tempering of a Cr-Mo-V Reactor Pressure Vessel Steel K Ravikanth, Amit Verma, J Singh,	93
B3-121	Thermal and Surface Area Analysis of Cesium and Strontium Sorbed Bentonite Clays Bhupesh Kalekar, Harshala Parab, Naina Raje,	95
B3-122	Studies on Natural Fluorapatite: Radiation and Thermal Effects Darshana Ghonge, Naina Raje, Rumu Banerjee, Pranesh Sengupta,	97
B3-123	Structural, Thermal and Thermodynamic Study of Rare Earth Containing Natural CaF <sub>2</sub> for Dosimetric Applications Athira raj, Rumu Banerjee, Uttam Jain, Abhishek Singh, Bhusan Dhabekar, Kulwant Singh, Pranesh Sengupta	99
B3-124	Thermal Stability Studies of Polyaniline -Halloysite Clay Composite Bhupesh Kalekar, Harshala Parab, Naina Raje, Remya Devi P.S., Sangita Kumar,	101
C2-121	Effect of B substitution on structure and hydrogen storage properties of Ti <sub>2</sub> CrV alloy Asheesh Kumar, Seemita Banerjee, P Ruz, V Sudarsan,	103
C2-122	Effect of Ni addition on dehydrogenation behaviour of MgH <sub>2</sub> Bhaskar Paul, Pankaj Shrivastava, Shubham Kumar, Jugal Kishor, Sanjay Kumar, Sanjib Majumdar,	105
C2-123	Hydrogen/Deuterium Desorption Kinetics of Pd-Ag Hydride/Deuteride S Sawant, Abhishek Sharma, Apurba Dutta, Ram JAt, S Parida,	106
C3-121	Pressure Composition Temperature Studies on Pd-Ag-Cu Hydride/Deuteride S Sawant, Abhishek Sharma, Apurba Dutta, Ram Jat, S Parida	108

C4-121	Catalytic Activity of CuFe <sub>2</sub> O <sub>4</sub> on the Thermal Decomposition of Ammonium Perchlorate Supriya N, Soumyamol PB, Vijayalakshmi KP, Deepa Devapal,	110
C4-122	Influence of Banana peel extract in the synthesis of ZrO <sub>2</sub> nano catalyst for removal of a potent Pesticide in visible light Namrat Kumari, Rohan Kunkalekar,	112
C5-121	Synthesis, Characterization and Thermal Expansion of Multilanthanides Incorporated at A site of High Entropy Pyrochlore Nitin Gumber, Muhammed Shafeeq, Swayam Kesari, S.N. Achary, Rajesh Pai,	113
C5-122	Order Evolution And Its Effect On The Hardness Property Of Ni-Cr-Mo-W Alloy Manoj Thota, A. Verma, J. Singh, M. Karri, K. Ravikanth,	114
C5-123	Effect of CaF <sub>2</sub> on NdF <sub>3</sub> Solubility in Indian Molten Salt Breeder Reactor Salt System Siddhartha Kolay, Ratikanta Mishra,	116
C5-124	Experimental and FEM Cooling Curve Simulations in End Quench Treatment and Hardness Profile Determination of Low Alloy Steel for Reactor Pressure Vessel Applications. Vaibhav Patel, Chiradeep Gupta,	117
C5-125	The phase relation and correlated thermal analysis of U-Y-O system Muhammed Shafeeq, Geeta Patkare, Rohan Phatak,	119
C5-126	Investigations Into Steady-State Comparative Techniques For Determining The Thermal Conductivity Of Irradiated Nuclear Fuel Farman Ali, Anil Bhandekar, Prerna Mishra, Dr. P. P. Nanekar,	121
C5-127	Investigations on alternate fuel salt of Indian Molten Salt Reactor Shubham Narang, Rimpi Dawar, Ratikanta Mishra,	123
C5-128	High Temperature Oxidation Behaviour of D9 Alloy Ashish Jain, Maharajan S, Dinu Shaji, Soja Vijay, Logaraj P,	125
C5-129	Thermal analysis of U-4Mo-4Pd Alloy Fuel Somesh Bhattacharya, Santu Kaity, Ashok Arya, Joydipta Banerjee, Amrit Prakash,	127
C5-130	High Temperature Oxidation of Zr-2.5(wt.%) Nb alloy in Heavy and Light Water Mixtures Akanksha Samanta, Y. Sunitha, Vijay Karki, Suparna Banerjee, A. Tyagi,	129
D1-121	Reaction pathway governing Ti <sub>2</sub> AlC MAX-phase formation: Insights from High-Temperature DSC Mohammad Yunus, Bikas Maji, R Singh,	131
D1-122	Examine the Structural, Magnetic, and Supercapacitance Characteristics of the Ni-Co Ferrite System after Zinc Substitution Vidhyadatta Verenkar, Sonam Kumari,	133
D1-123	Synthesis and characterization of the cobalt zinc ferrous fumarato-hydrazinate complex by precursor-combustion method and its decomposed product Sanjali Navelkar, V Verenkar	134

D1-124	Analysis of Thermal, Electrical and Magnetic properties of Al Doped Mn-Zn Ferrite synthesized by Auto-combustion Synthesis Manasi Ugvekar, V. Verenkar,	135
D1-125	Investigation of Reaction Kinetics Parameters for the Synthesis of Lithium Orthosilicate Shivdatsinh Ghariya, Aroh Shrivastava, Shital Amin, Swapnil Lonare, Paritosh Chaudhuri,	136
D1-126	Effect of Thermal Treatment on Structure of Reactively Sputtered NiO Thin Films Amrita Das, Debarati Bhattacharya, Swapan Jana, Sipra Choudhuri, Subir Ghosh, Surendra Singh,	138
D1-127	Thermal Analysis – An Important Tool for Preparation and Qualification of CuCrO <sub>2</sub> towards Hydrogen Sensing Applications Aleena Xavier, Dipankar Kundu, E Prabhu, Sajal Ghosh, S Muthuraja, V Jayaraman	140
D1-128	Structural and Thermal Investigation of Novel CaUW <sub>4</sub> O <sub>16</sub> Geeta Patkare, Shafeeq Muhammed, Rohan Phatak, Sangita Dhara, Meera Keskar,	142
D1-129	Thermodynamic Insights into the Design and Stability of High Entropy Oxides and their electrical behaviour Jyoti Chahal, Rimpi Dawar, Rakesh Shukla, Nitin Kumar, Vinita Gupta,	144
D1-130	Kinetics of HI decomposition and Activation Energy Calculation Ajit Shirsat, Suhas Phapale, Deepak Tyagi, Salil Varma, A Tyagi,	146
D1-131	Ti <sub>2</sub> AlC MAX-Phase: Synthesis and its Oxidation Rakesh Kumar, Mohammad Yunus, Bikas Maji,	147
D1-132	Solid-state synthesis, characterization and densification of aluminum borate ceramic Jyothi Sharma, Biranchi Tripathi, Pankaj Patro, Deep Prakash, Tarasankar Mahata,	149
D1-133	Understanding the Na <sub>x</sub> MnO <sub>2</sub> system: A Thermodynamics and XPS approach Shubham Narang, Rimpi Dawar, Kaustava Bhattacharyya, Padinhare Aiswarya, Ratikanta Mishra,	151
D1-134	Studies on Mg-Sb-Bi alloy towards development of uni-leg thermoelectric devices Swadesh Mohanty, Ajay Panthri, Ajay Singh, Ranita Basu,	153
D1-135	Phase characterization and oxidation of M <sub>2</sub> Zr <sub>2</sub> O <sub>7</sub> (M = Ce <sup>3+</sup> and Pu <sup>3+</sup> ) Chiranjit Nandi, Abhijeet Dadarya, K. Danny, Amrit Prakash,	154
D2-121	Tuning Thermal Properties of Zirconate Pyrochlore via Stoichiometric Alterations Santosh sahu, Rakesh Shukla, Rimpi Dawar, Vinita Gupta	155
D2-122	Investigating Thermal Expansion studies of Lithium Based $\hat{I}^3$ -LiAlO <sub>2</sub> compound Jeetendra Dhanuskar, K Modi, Shailesh Kumar, Sheetal Raut, Pratik Das, Pradeep Samui, Ram Jat, S Parida,	157

D2-123	Pebble Bed Thermal Expansion and Sintering Investigation of Lithium Titanate for Fusion Blanket Application Aroh Shrivastava, Swapnil Lonare, Paritosh Chaudhuri,	159
D2-124	Structural and Thermophysical Properties of Hf <sub>6</sub> Ta <sub>2</sub> O <sub>17</sub> Brij Singh, Suryakant Nagar, Pratik Das, Pradeep Samui, Swarup K Rakshit, Suresh C Parida	161
D2-125	Synthesis, Characterization and Properties of Nanosized Nickel Cobalt Ferrites Synthesized by the Thermolysis of an Hexahydrazine Nickel Cobalt Ferrous Succinate Precursor Daniel Coutinho, V Verenkar,	163
D3-121	Effect of Nb Substitution on the Thermal Stability and Glass-Forming Ability of Zr-Based Bulk Metallic Glasses Sanjay Saini, A. Srivastava, Suman Neogy,	165
D4-121	Thermolysis of Coordination Polymer of Copper(II) of 4,4'-dipyridyldiselenide and its Conversion to Copper Selenide Nanostructures Manoj Pal, Gourab Karmakar, Alpa Shah, Adish Tyagi, Nattamai Bhuvnesh, Sandip Dey	167
D4-122	Methyl Indium 4,6-dimethyl-2-pyrimidyl selenolate as molecular precursor for the synthesis of $\text{In}^{2+}\text{-In}_2\text{Se}_3$ and $\text{In}^{3+}\text{-In}_2\text{Se}_3$ nanoparticles Nisha Kushwah, Kedarnath G, A Wadawale, Gourab Karmakar, Sanjay Kumar, Amit Srivastava	168
D4-123	Air Processed Asymmetric Squaraine Dyes for Photovoltaic Application Vilko Mandic	169
D4-124	Water-Soluble Pd Metallacycles catalyst as a reservoir for Pd Nanoparticle in Suzuki Coupling Reaction Kamal Chaudhari, Amey Wadawale, Sandip Dey,	170
D4-125	Development of Biocompatible Ag <sub>2</sub> S Quantum Dots for Receptor-mediated Photothermal Therapy Sonali Gupta, Mansi Murkar, Bijaideep Dutta, Sandeep Shelar, Kanhu Charan Barick,	172
D4-126	Thermal Studies of highly monodispersed $\gamma\text{-Fe}_2\text{O}_3$ , ZnO, $\gamma\text{-Fe}_2\text{-}2\text{xZn}_2\text{xO}_3$ and $\gamma\text{-Fe}_2\text{O}_3\text{@ZnO}$ nanostructures Ruchi Agrawal, Ratikant Mishra, Raghmani Ningthoujam,	174
E1-121	Metal-Organic-Framework Based Aerogel: A Novel Thermally Stable Adsorbent for the Efficient Removal of Heavy Metal Ions from Aqueous Solution Hiral Ukani, Nildhara Parsana, Naved Malek,	175
E1-122	Sequential and Synergistic Ageing Assessment of XLPE used in I&C Cables of NPPs Rohit Ranjan, NB Shrestha, AK Ahirwar, TV Santhosh, PK Ramteke, KA Dubey, Gopika Vinod, J Chattopadhyay,	177
E1-123	Studies of the effect of high energy $\gamma$ -radiation on the extensional viscosity of Ethylene-Vinyl Acetate copolymer K Varshney, J Rana, T Shokeen, R Mondal, K Dubey, Y Bhardwaj,	179
E1-124	Studies of the thermal stability of radiation synthesised glycidyl methacrylate-	180

	based copolymer B Kaul, A Chandane, R Mondal, C Chaudhari, K Dubey, Y Bhardwaj,	
E1-125	Studies of thermal stability of radiation crosslinked polyolefin-multifunctional acrylate rubber blends Pratap Singh, Arijit Ghosal, R Mondal, K Dubey, Y Bhardwaj,	181
E1-126	Studies of the effect of high energy $\gamma$ -radiation on the oxidative stability of Ethylene-Vinyl Acetate copolymer Arijit Ghoshal, R. K. Mondal, K. A. Dubey, Y. K. Bhardwaj	182
E1-127	Studies on PBI Based Amperometric Hydrogen Sensor for Sodium Cleaning Application of Fast Reactor Components Sukumran V, Murugesan N, Manikandan P, Hrudananda Jena	183
E1-128	Development of Radiolytically Functionalized Amine Dense Biodegradable Adsorbent for CO <sub>2</sub> capture: Thermogravimetric Characterization and Adsorption Analysis Nilanjali Misra, Swarnima Rawat, Shubhangi Shelkar, Virendra Kumar	185
E1-129	Thermal analysis of radiation-synthesized super porous polymer using Thermogravimetric Analysis (TGA) and Differential Scanning Calorimetry (DSC) Sanju Francis, N Goel	187
E1-130	Synthesis and Characterization of Polymeric Composite for Fire Retardant Application Darshana Ghongea, Naina Raje, Meena Mahipal, C. Choudhary, K. Dubey	188
E2-121	Evaluation of thermal stability and polymorphism in dihydroxy selenolane: a pharmacological agent in cancer management Prasad Phadnis, Shubham Narang, Ratikant Mishra	189
E2-122	Exploring Potential of Pluronics Induced Protein Fibrils as Drug Delivery Agents: Mechanistic Understanding via Biophysical Approach Anu Jain, Nand Kishore	191
E2-123	Quantitative Calorimetric and Spectroscopic Analysis of Protein Interactions with Solid Lipid Nanoparticles (SLNs) Jyoti Rathee, Nand Kishore	192
E2-124	Temperature and Solvent Dependent Aggregation Characteristics of Biocompatible Ionic and Non-ionic Surfactants M Basu	193
E2-125	Evaluation polymorphism in a cytotoxic 2,2'-dipyridyl diselenide (Py <sub>2</sub> Se <sub>2</sub> ): a step A Step closer to development of anticancer drug Prasad Phadnis, Shubham Narang, Ratikant Mishra	195
E2-126	Thermal Study of Bombyx Mori Silk Fibroin Film obtained through Degumming Process for Biomaterial Applications Sanasam Yaiphabi, Sanjenbam Kabita, Sorokhaibam Singh, Shamjetshabam Chanu, Langlen Meinam, Thota Kumar, R Mishra, Senjam Singh, Laishram Singh, Sanjenbam Devi, Raghmani Ningthoujam	197
E3-121	Effect of Thermalization of Cobalt based Metal Organic Frameworks (MOFs) in supercapacitor application	199

	Srikant Sahoo, Ashish Satpati	
E3-122	Thermal Analysis of Zirconium loaded Iron Phosphate Glass Akhilesh Joshi, Raman Mishra, Dimple Dutta, S Achary	200
E4-121	Engineered Ionic Liquid based Hydrogel: A Multifunctional, Thermally Stable Platform for the Breast Cancer Treatment Raviraj Pansuriya , Tapas Patel, Sugam Kumar, Vinod Aswal, Naina Raje, Suresh Kailasa, Naved Malek	201
E4-122	Metal-Organic Framework-Integrated Polymeric Hydrogel : A promising drug delivery platform for breast cancer treatment Ishani Pandya, Sugam Kumar, Vinod K. Aswal, Naved Malek	203

## New Approaches in Decarbonization of Metals Production

Dr. Ramana G. Reddy

*FASM, TMS Fellow*

*ACIPCO Endowed Professor*

*Professor of Metallurgical and Materials Engineering*

*Department of Metallurgical and Materials Engineering*

*The University of Alabama, Tuscaloosa, Alabama, 35487, USA*

*Web Page: <https://rreddy.eng.ua.edu>*

*E-mail: [rreddy@eng.ua.edu](mailto:rreddy@eng.ua.edu)*

### Abstract

Decarbonization in the energy-intensive industries is essential to meet the new emission targets of net-zero emissions by 2050. The US energy related CO<sub>2</sub> emissions in 2020 are: transportation (35%), Industrial (30%), Residential (19%) and Commercial (17%). In the industrial sector accounted for 33% of the nation's primary energy and accounts for 30% of CO<sub>2</sub> emissions. Solutions that reduce the energy consumption and carbon footprint within the industry, new technologies are needed to help reinvigorate existing industries while supporting the growth and development of clean energy technologies. In this regard, new approaches in development of an innovative metal production concepts that associate with increase in the net energy productivity and lower carbon footprint such as *in-situ* production of lightweight composites and alloys are discussed. Also discussed a low temperature electrochemical intensified modular production of lightweight metals achieving energy-efficient processing by reducing process steps and developing alternate production pathways. A detailed TEA and LCA were conducted to learn the commercial and environmental viability of the technology.





## Transforming solids into functional materials: Role of heat treatment

A. K. Tyagi

*Homi Bhabha National Institute, Mumbai*

*(Email: aktyagi@barc.gov.in)*

Material science and engineering played a pivotal role in shaping the human civilizations. Such was the importance of materials that even the ages of civilizations are named after materials—with each new era being brought about by a new material. One of the first functional materials was activated carbon, which was prepared by a controlled heating of bio-mass. Several other materials such as luminescent ZnS, steel, cement, glasses, glass ceramics, new forms of carbon were also prepared by controlled heat treatment. Some of these interesting examples will be discussed. Based my own experience of about four decades in the field of materials chemistry, few notable functional materials prepared by employing controlled reaction conditions will also be discussed in the talk. The main emphasis will be on rational design of functional materials based on crystallographic concepts, use of optimum heat treatment and other reaction parameters. New functional materials can be designed by interplay of reaction parameters and crystallographic structure. Unconventional synthetic routes play an important role in this direction as many of these new materials are metastable and hence it is not possible to prepare them by conventional synthesis methods. Several examples will be discussed on strategies to isolate compounds beyond phase diagrams. The main emphasis would be on role of heat treatment and thermal technique in transforming ordinary solids into extraordinary functional materials.



## Thermal Analysis in Chemical and Biological Systems: Mechanistic insights to Impactful Applications

Nand Kishore

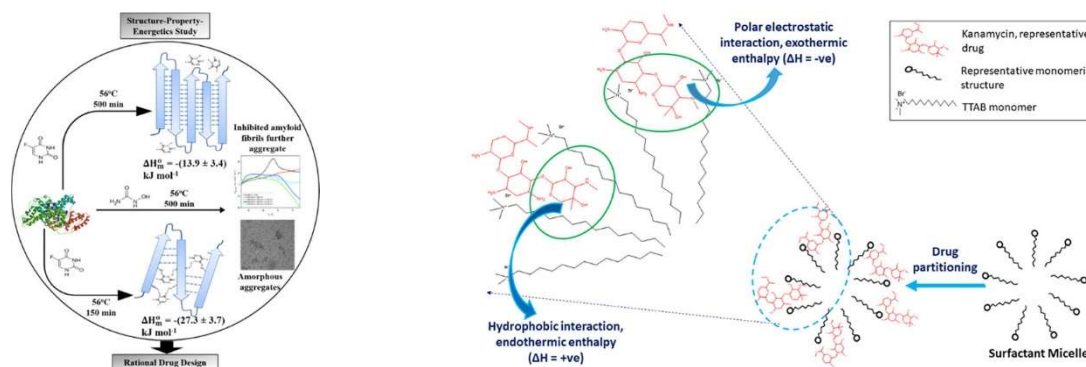
Department of Chemistry

Indian Institute of Technology Bombay, Powai, Mumbai, India

E-mail: [nandk@chem.iitb.ac.in](mailto:nandk@chem.iitb.ac.in)

Thermodynamic characterization of chemically and biologically important systems has contributed significantly from advancement in mechanistic understanding of the processes to impactful applications. Currently, direct determination of thermodynamic signatures has become a major part of research since it leads to quantitative mechanistic analysis. The emergence of thermodynamics in such systems has made tremendous progress over a period of several decades. Specifically, the structure, stability, and conformation of proteins and other biologically important macromolecules, along with their recognition abilities have been a major target of research. Technological developments in Isothermal Titration Calorimetry and Differential Scanning Calorimetry have made unquestionable contributions to quantitative understanding of such systems.

Misfolding of proteins can generate highly ordered soluble amyloid fibrils or amorphous aggregates depending upon the followed pathway. The misfolding process is driven by formation of transient intermediates, which promotes fibrillation/aggregation causing neurodegenerative diseases such as Alzheimer's, Parkinson's, Huntington's, diabetes, and Creutzfeldt-Jakob, amongst others. To revert amyloid fibrils to their native state is a challenge in finding a solution to prevent neurodegenerative diseases. We have adopted a structure–property–energetics correlation-based approach with molecular entities having diverse functionalities [1-3] to explore their potential towards prevention of fibrillation in proteins and obtain mechanistic insights. Our objective of identifying functionality on molecules that establishes effective intermolecular hydrogen bonding with  $\beta$ -strands



**J. Phys. Chem. B 124(2020) 8989-9008**

**Langmuir 37 (2021) 7203-7218**

of protein fibrils was achieved by combined isothermal titration calorimetric, differential scanning calorimetric, spectroscopic, and microscopic correlations. We have made efforts in exploring applications of thermodynamic principles in rational drug design and drug delivery systems based on the research carried out in our laboratory [4,5]. The approach adopted here highlights physical chemistry underlying such biologically important processes and hence has significance in deriving thermodynamic assessment-based guidelines for rational drug design.

- [1]. A. Jain, M. Lopus, N. Kishore, Langmuir, Articles ASAP (2025).
- [2]. R. Ghosh, N. Kishore, J. Phys. Chem. B 124 (2020) 8989-9008.
- [3]. A. Mukhija, N. Kishore, J. Phys. Chem. B 122 (2018) 9896-9906.
- [4]. E. Judy, N. Kishore, Langmuir 37 (2021) 7203-7218.
- [5]. E. Judy, D. Pagariya, N. Kishore, Langmuir 34 (2018) 3467-3484.

## Calorimetry methods for the thermodynamic measurements

Rajesh Ganesan  
*Materials Chemistry Division*  
*Materials Chemistry and Metal Fuel Cycle Group*  
*Indira Gandhi Centre for Atomic Research, Kalpakkam, INDIA*  
*rajesh@igcar.gov.in*

### **Abstract:**

The term "calorimetry" is derived from the Latin word *calor*, meaning heat, and the Greek word *metron*, meaning measure. Many chemical reactions and physical processes involve either the release or absorption of heat. Calorimetry methods are employed to measure heat, which typically causes a change in temperature in a substance or system. Various types of calorimeters exist, ranging from sophisticated commercial models to custom-built devices designed to meet specific requirements. In this presentation, we will explore thermodynamic measurements conducted on selected systems using an isoperibol calorimeter, a drop calorimeter, and a differential scanning calorimeter. Additionally, we will discuss the process of assembling calorimeters in the laboratory.

# Reinforced Carbon-Carbon (RCC) Composite for high temperature applications in Rockets & missiles.

Dr A P Dash  
OS & Director HEMRL, Pune

Reinforced Carbon-Carbon (RCC) composite is a high-performance material that has become a cornerstone in the aerospace industry, particularly for thermal insulation in rockets and spacecraft. Known for its exceptional heat resistance, lightweight properties, and structural strength, RCC is specifically designed to endure extreme temperatures while maintaining mechanical integrity. This article explores the properties, applications, and significance of RCC composites in rocket thermal insulation.

## What is Reinforced Carbon-Carbon?

Reinforced Carbon-Carbon is a composite material made from carbon fibers embedded in a carbon matrix. The process of manufacturing RCC involves impregnating carbon fibers with a resin or pitch, followed by high-temperature heat treatment in an inert atmosphere. This process creates a material that is not only lightweight but also capable of withstanding temperatures beyond 3,000°C (5,400°F), making it ideal for aerospace applications.

The reinforcement with carbon fibers enhances the structural integrity of the composite, while the carbon matrix provides excellent thermal resistance. Additionally, the material is highly resistant to thermal shock, a critical property for components exposed to rapid temperature changes during rocket launches and re-entry.

## Thermal Insulation in Rockets

Rockets are subjected to extreme thermal and aerodynamic stresses, particularly during ascent and atmospheric re-entry. RCC composites are widely used in thermal protection systems (TPS) to shield critical components from high heat fluxes. The material's ability to maintain strength at elevated temperatures makes it indispensable for thermal insulation in several key areas:

1. Nose Cones and Leading Edges: RCC is commonly used in nose cones and wing leading edges of spacecraft, where aerodynamic heating is most intense. For example, the Space Shuttle used RCC panels on its wing leading edges to endure temperatures exceeding 1,650°C (3,000°F) during re-entry.
2. Rocket Engine Nozzles: In rocket engines, nozzles and throat liners experience extreme temperatures due to the combustion of propellants. RCC composites are often used in these components to provide thermal insulation and structural support.
3. Heat Shields: RCC is also employed in heat shields for rockets and spacecraft. Its thermal resistance and durability make it a reliable material for protecting the vehicle's structure and payload from intense heat.

## Advantages of RCC Composites

The unique properties of RCC composites make them highly suitable for rocket thermal insulation:

High Thermal Resistance: RCC endures temperatures far beyond the limits of traditional materials like metals or ceramics.

Lightweight: The low density of RCC reduces the overall weight of the vehicle, enhancing fuel efficiency and payload capacity.

Thermal Shock Resistance: RCC can withstand rapid temperature fluctuations without cracking or degrading, ensuring reliability in dynamic environments.

Durability: The material resists oxidation and erosion, particularly when coated with protective layers like silicon carbide.

## Challenges and Innovations

Despite its advantages, RCC composites face challenges such as vulnerability to oxidation in oxygen-rich environments and the high cost of production. To address these issues, researchers are exploring advanced coatings, such as ceramic or silicon-based layers, to enhance oxidation resistance. Additionally, efforts are underway to optimize manufacturing processes to reduce costs and improve scalability.

## Future Prospects

As space exploration intensifies, the demand for robust and efficient thermal insulation materials like RCC continues to grow. Emerging technologies, including reusable rockets and hypersonic vehicles, rely heavily on the capabilities of RCC composites. Advancements in material science, such as the incorporation of nanomaterials and self-healing coatings may enhance the performance and versatility of RCC in the aerospace sector.

## Conclusion

Reinforced Carbon-Carbon composites are indispensable for rocket thermal insulation, offering unparalleled heat resistance, lightweight construction, and structural durability. As aerospace technology advances, RCC will remain a critical component in enabling the exploration of new frontiers while ensuring the safety and efficiency of spacecraft.

## Applications of Thermal Analysis Techniques in the Development of CO<sub>2</sub> Removal Systems for Manned Space Missions

R. Rajeev

*Former Head, Analytical and Spectroscopy Division  
Vikram Sarabhai Space Centre, Thiruvananthapuram, Kerala  
[arerajeev@gmail.com](mailto:arerajeev@gmail.com), Mob:944710755*

### Abstract

Manned space mission aims to send man to space for exploring the exhaustive space in detailed manner and to carry out purposeful scientific researches. The environment above the earth's atmosphere is not suitable for the existence of human life, as the environment is very harsh with very high / low temperatures, dangerous radiations, breathless vacuum, low gravitational force, etc. To provide a comfortable habitability for the crew inside the cabin, it must be provided with a breathable atmosphere. The main tasks of atmospheric management in the crew cabin involve the removal of carbon dioxide and maintenance of O<sub>2</sub> and N<sub>2</sub> partial pressure.

CO<sub>2</sub> is produced inside the crew cabin by humans as a by-product of metabolism. A normal human being inhales about 0.84kg of O<sub>2</sub> and exhales about 1kg of CO<sub>2</sub> per day. The allowable level of CO<sub>2</sub> during short term mission is about 1% and for long duration mission is 0.5% .

Most primary physico-chemical CO<sub>2</sub> removal systems for Life Support applications are sorption based. Molecular sieves are used to remove CO<sub>2</sub> by adsorption (physisorption) within the porous structure of Zeolites. Additionally, several systems have been developed for the removal of carbon dioxide by chemisorption. These include lithium hydroxide, silver oxide, alkali and alkaline metal oxides, solid phase amines, etc. Membrane technology and electrochemical methods are also explored. These methods are generally classified into regenerable and non-regenerable techniques. Based on their advantages and disadvantages for a space application, these methods are screened and used for various missions.

Thermal analysis techniques viz. TG and DSC are widely used for the development, evaluation and qualification of CO<sub>2</sub> removal systems. The mass and energy changes during the adsorption and desorption of CO<sub>2</sub> by the adsorbents are qualitatively and quantitatively estimated by these techniques. The recyclability of an adsorbent, a most crucial property is also evaluated by thermal methods.

# Air Processed Asymmetric Squaraine Dyes for Photovoltaic Application

Vilko Mandić <sup>a,\*</sup>

<sup>a</sup> University of Zagreb Faculty of Chemical Engineering and Technology, Trg Marka Marulića 19, 10000 Zagreb, Croatia

\* [vmandic@fkit.unizg.hr](mailto:vmandic@fkit.unizg.hr); Tel: +385 1 4597 226, Fax: +385 1 4597 260

## Abstract

Recently, organic photovoltaics (OPV) have been heavily researched as alternatives to silicon and significant progress in terms of power conversion efficiency (PCE) and stability has been made. The comparative advantages of OPV are mainly their low cost, flexibility, transparency, and bending durability. To obtain good performance, the electron donor absorbers are used in a bulk heterojunction (BHJ) configuration (maximizing the specific surface of the interface) with fullerene-based electron donors. One of the most promising ways to boost the PCE of the OPV was found through the incorporation of non-fullerene and small molecule donors and acceptors, which exhibit high absorption spectra, resulting in high photocurrents, with PCEs above 18% in state-of-the-art solar cells, bringing them closer to the market. The most important factors affecting OPV performance are traps and recombination, charge carrier mobility, charge carrier density, and parasitic resistances. Therefore, a few essential steps in the design of the improved SC devices are: the determination of appropriate processing and molecule design. In this work, we follow a structure modification strategy. We developed new small molecule photoabsorbers that are based on squaraines (SQ). Even though squaraines have been previously applied as xerographic photoreceptors, an optical recording medium, electro-light-emitting diodes, and nonlinear optical devices on behalf of their unique electronic structures and optical properties, their application in a group of organic photovoltaic devices (OPV) and related devices is still scarce in the literature. SQs advantages, when considering applications as donor materials in OPVs, are high absorption coefficients, where bandwidths can be adjusted in the visible and NIR range, as well as high photochemical and thermal stability. The seemingly straightforward synthetic pathways are also a nominal advantage. Namely, a variety of SQs can be prepared through the modification of the SQ structure. Replacement of the side groups allows for some adjusting of the physicochemical behaviour and optoelectrical properties, as well as the morphological and organizational properties of the SQs when processed into thin films, which can be used as a valuable tool to optimize the photovoltaic properties of squaraine based bulk heterojunction absorber layers. We assembled the solar cells on a laboratory scale and characterized them thoroughly (J/V, EQE, LID testing). Recombination mechanisms pointed out to differences in nanomorphology, which were later identified via structural methods (WAXS) and microscopy (FIB-SEM, AFM). The results gave new insight into the influence of processing parameters and molecule design on device performance and stability.

## Aim and Approach

The aim of the research is to explore air stable complex squaraine structures for photovoltaic application while retaining their ease of synthesis following the principles of green chemistry. We try to understand the structure-property relationship by utilizing an extensive set of characterization techniques. Through morphology and structure analysis, we hope to better understand the processes that govern charge carrier transfer whose behaviour is obtained through electrical measurements.

## Scientific Innovation and Relevance

Innovation in our work is best recognized when considering the easy synthesis and air stable conditions in which these solar cells can function application wise. However, during this research, a plethora of information has been collected which helps further understand energy losses in all organic photovoltaic systems.

## Results

The potential of the synthesized squaraines for photovoltaic application was tested through the most important property, UV-Vis absorption and bandgap.

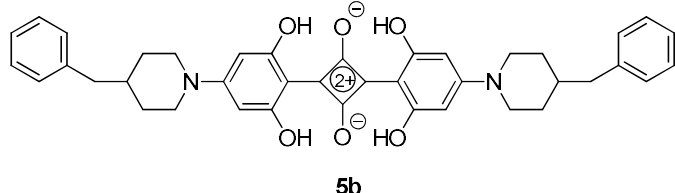


**Figure 1.** An example of the molecular structure of designed compounds.

The bandgap was estimated to be around 1.6 – 1.7 eV for all synthesized compounds (from the onset). The assembled devices are shown on Figure 3.

Where the device architecture can be observed: ITO (cathode)/ZnO (30 nm, electron transport layer)/BHJ (active layer, SQ:PC<sub>70</sub>BM)/MoO<sub>3</sub> (8 nm, hole transport layer)/Ag (100 nm, anode, current collector).

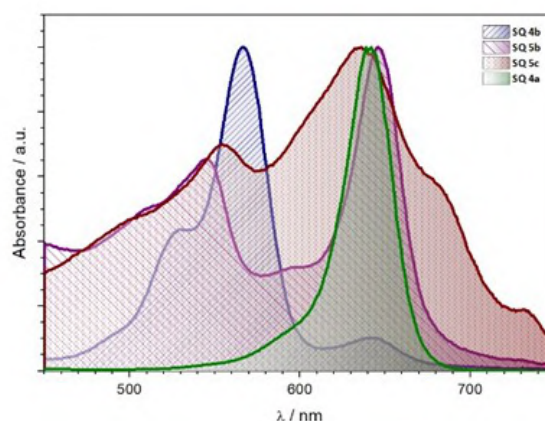


**Figure 2.** UV-Vis absorption spectra of the compounds in ethanol.

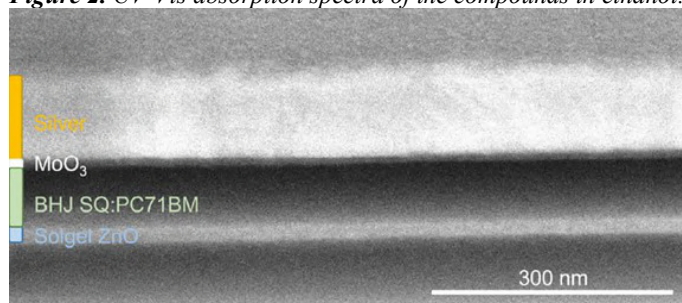


**Figure 3.** Cross-section of the assembled thin film device.

## Conclusion

Research results point out to good photovoltaic properties of the synthesized squaraines as well as a good interface during solar cell assembly, which implies that these compounds have good potential to be studied further.

## Acknowledgement

This work has been funded by the project UIP-2019-04-2367 SLIPPERY SLOPE by CS

## Tailoring the Physico-Chemical Properties of Ionic Liquids and Deep Eutectic Solvents for Enhanced Sorption and Extraction Processes

Ramesh L. Gardas

*Department of Chemistry, Indian Institute of Technology Madras, Chennai 600 036 INDIA.*

*Phone: +91 44 2257 4248; e-mail: [gardas@iitm.ac.in](mailto:gardas@iitm.ac.in) ; web: <http://chem.iitm.ac.in/faculty/gardas>*

### **Abstract**

Ionic liquids (ILs) and deep eutectic solvents (DESS) are promising solvents with tunable structures and unique properties, such as negligible vapor pressure, high ionic conductivity, and excellent solvating abilities. These features make them ideal for applications in pollutant extraction, CO<sub>2</sub> capture, metal ion extraction, and more. This talk will explore the thermophysical properties of ILs and DESS, their role in enhancing sorption and extraction processes, and their application in wastewater treatment. Additionally, it will highlight current research trends, focusing on sustainability, reusability, and the potential of these solvents in advancing green chemistry.



## Thermal behavior and application of carbon nanostructures

Imre Miklós Szilágyi

*Institute of Physical Metallurgy, Metal Forming and Nanotechnology, University of Miskolc, H-3515  
Miskolc, Hungary*

### **Abstract**

Based on our group's experience, this lecture present several examples about how to tune the properties of various carbon nanostructures by modifying their functional groups, composition or by coating them with atomic layer deposition (ALD) grown oxide ( $\text{TiO}_2$ ,  $\text{ZnO}$  and  $\text{Al}_2\text{O}_3$ ) nanofilms and nanoparticles. As substrates, fullerene ( $\text{C}_{60}$ ), carbon nanotubes (CNT), graphene oxide (GO), carbon nanospheres and carbon aerogels were used.

The preparation and functionalization reactions of carbon nanomaterials were thoroughly monitored by thermal analysis, and their thermal stability was also determined.

The as-prepared carbon nanomaterials and their various composites were investigated in photocatalysis, gas sensing, photonic crystal, electronic and nanofluid applications.

**Key Words:** Carbon nanostructure, Semiconductor oxide, Nanocomposite, Thermal behavior

## Thermal Properties of Unsaturated Soils: Theory and Measurement

Rao Martand Singh

*Department of Civil & Environmental Engineering, Norwegian University of Science & Technology (NTNU),  
Trondheim, Norway*

[rao.m.singh@ntnu.no](mailto:rao.m.singh@ntnu.no)

There are three mechanisms of heat flow in unsaturated soils; conduction, in which the excitation of an atom or molecule is transmitted to its neighbor by direct contact, oscillation-like in solids and liquids and by impact and exchange of momentum in gases; convection, in liquids and gases, where a portion of matter at a higher temperature is mechanically mixed with matter at a lower temperature; radiation by means of waves traversing space from one body to another without affecting the inter-lying space. Generally, heat flows through soils entirely by conduction, with radiation unimportant and convection important, only if there is a high flow rate of water or air (Mitchell, 1993). Johansen (1975) considered thermal radiation across soil air spaces and concluded that it is only significant for very coarse material at low moisture contents. Heat transfer is also found to occur due to chemical concentration gradients. This effect is commonly referred to as the Dufour effect but it has not been found to be of significance in soils. Therefore, this paper mainly focuses on heat transfer by conduction where thermal conductivity of a soil is the main governing thermal property. It presents various laboratory and field measurement methods including mathematical and empirical models to determine the thermal conductivity of soils.

Thermal conductivity is the property of a material that relates the heat flux (energy per unit area per unit time) to the temperature gradient (temperature difference per unit length) that exists over a material. Therefore, the laboratory measurement of thermal conductivity involves the measurement of the heat flux and temperature. The laboratory measurement methods can be divided mainly into two categories namely steady state and non-steady state (also known as transient state).

The steady state method is based on applying a constant heat flux and thermal gradient and uses Fourier's heat conduction law to evaluate thermal conductivity. There are various steady state methods described in literature such as divided bar, guarded-hot-plate apparatus (ASTM C 177-04), heat flow meter apparatus (ASTM C 518-04), guarded-comparative-longitudinal heat flow technique (ASTM E 1225-04), rhometer apparatus (Stolpe 1970) and Rapid k method (Mitchell & Kao 1978).

The non-steady state (transient state) method applies a heat pulse to soil and measures the transient temperature change with time. There are various transient state methods viz. thermal needle method, ring source method (Somerton & Mossahebi 1967), Shannon & Wells (1952) method and transient plane source (TPS) technique (Gustafsson 1991).

Thermal response testing (TRT) is a field test to determine the thermal conductivity of soils. The method involves heating the ground with a known constant heating power applied to a fluid that circulates in a pipe loop embedded in the ground. An analytical interpretation is undertaken on the measured average fluid temperature (average of inlet & outlet fluid temperature) with time based on infinite line heat source theory.

There are various theoretical (mathematical) and empirical models to calculate the thermal conductivity of soils in case laboratory and field measurements cannot be carried out. There are two types of theoretical models viz. two phases soil (solid + fluid) models and three phase soil (solid + water + air) models. Initially two phases soil models were proposed based on geometric mean, arithmetic mean and harmonic mean while three phase soil models were proposed later based on weighted average of the conductivities of the various soil constituent. Empirical models were introduced based on experimental results and type of soil, its state (dry or wet, dense or loose) and its mineralogy. Johansen (1975) empirical model for fine grained soil is the most popular method, however, a large number of empirical models are described in literature which can be employed to determine thermal conductivity of unsaturated soils.

This talk explains the concept of heat transfer in unsaturated soils, laboratory and field methods of measuring thermal conductivity, and theoretical and empirical models of calculating thermal conductivity.

## **Role of thermodynamics and Phase diagram in deciding the path of the transformation in Nb, Ti and Zr Based Systems**

R. Tewari\*, D. Harish B. Vishwanadh and S. Neogy  
*Materials Group, Bhabha Atomic Research Centre, Mumbai 400085*

Zirconium and titanium-based alloys depending upon the temperature of heat treatments and rate of cooling show variety of phase transformations. These transformations include diffusion as well as diffusionless transformations. In Zr-Nb alloys presence of large miscibility gap allows redistribution of Nb in various phases leading to the variety of morphologies of phase. In addition, in Nb alloys formation of various phases is determined by the relative stabilities of various precipitates and the choice of the final precipitates will depend upon the time and temperature of treatments. Active eutectoid phase transformations which are difficult to suppress by quenching even though the transformation involves diffusion of substitutional elements. In the present talk, these transformation in Ti-Cu, Zr-Cu, Zr-Ni will be discussed to explore the occurrence these transformation and possible mechanism of the active eutectoid decomposition of high temperature  $\beta$  phase into  $\alpha$  and an intermetallic phase. Combining various probing techniques results, it was shown that even under the fastest cooling rate employed (splat-quenching from the liquid phase) the eutectoid decomposition of the  $\beta$  phase could not be suppressed and the partitioning of the solutes into the two product phases, is nearly complete. Many such transformations where combination of thermodynamics and crystallography decides the morphologies of the products will also be discussed in the talk.

## Nanoparticle assisted local hyperthermia in cancer therapy

Vesa-Pekka Lehto

*Department of Applied Physics, University of Eastern Finland, Kuopio, Finland*

### Abstract

Nanoparticles capable of absorbing infrared (IR) radiation efficiently can generate localized hyperthermia *in vivo*, leveraging the tissue-penetrating properties of near-IR light. When targeted to cancerous tissues through the enhanced permeability and retention effect, these photothermal agents, or "nanoheaters," enable photothermal therapy (PTT) [1]. Porous nanoheaters further enhance this approach by allowing drug loading, enabling combination therapies of PTT and chemotherapy, with potential to elicit antitumoral immune responses effective against metastases.

This presentation explores the fundamentals of nanoparticle-assisted PTT, with a focus on black porous silicon (BPSi). BPSi demonstrates high photothermal conversion efficiency and robust drug-loading capacity [2]. When coated with temperature-responsive polymers, BPSi nanoparticles enable spatiotemporal drug release under IR irradiation [3], delivering local hyperthermia alongside controlled drug delivery [4]. Using a tailored therapeutic cocktail, this system has shown the ability to induce potent antitumoral immunity [5].

Further enhancing their functionality, BPSi nanoparticles can be cloaked in cancer cell membranes, achieving homologous targeting and improving *in vivo* specificity [6-7]. These biohybrid constructs, resembling "nanocyborgs," present an innovative pathway for advanced cancer treatment.

### References

- [1] Tamarov et al., Comparison between fluorescence imaging and elemental analysis to determine biodistribution of inorganic nanoparticles with strong light absorption. *ACS Appl. Mat. Inter.*, 13:40392-40400 (2021).
- [2] Xu et al., Scalable synthesis of biodegradable black mesoporous silicon nanoparticles for highly efficient photothermal therapy. *ACS Appl. Mater. Inter.* 10:23529-23538 (2018).
- [3] Tamarov et al., Temperature responsive porous silicon nanoparticles for cancer therapy – Spatiotemporal triggering through infrared and radiofrequency electromagnetic heating. *J. Control. Rel.* 241:220-228 (2016).
- [4] Happonen et al., Thermal dose as a universal tool to evaluate nanoparticle-induced photothermal therapy. *Int. J. Pharm.*, 587:119657 (2020).
- [5] Xu et al., Black porous silicon as a photothermal agent and immunoadjuvant for efficient antitumor immunotherapy. *Acta Biomater.* 151:473-483 (2022).
- [6] Liu et al., L., Cell membrane coating integrity affects the internalization mechanism of biomimetic nanoparticles. *Nature Comm.*, 12:5726 (2021).
- [7] Liu et al., Systematic design of cell membrane coating to improve tumor targeting of nanoparticles. *Nat. Comm.* 13:6181 (2022).

## Designing of inorganic compounds for chemical sensing applications - Insights from thermo-analytical techniques

V. Jayaraman

*Materials Chemistry and Metal Fuel Cycle Group*  
*Indira Gandhi Centre for Atomic Research, Kalpakkam 603 102*  
[vjram@igcar.gov.in](mailto:vjram@igcar.gov.in)

### Abstract

Inorganic compounds find immense applications in several domains of DAE. To name a few applications, membranes for separating or sorbing gaseous species, compounds for storage of hydrogen, electrolytes for batteries or fuel cells, pressure transducers, photovoltaic materials, opto-electronic materials, sensors, etc. In all the above mentioned applications, these compounds are required to be synthesized so that their chemical composition, phases responsible for the intended property, morphological features, surface properties, etc. either one or more of these characteristics is or are to be strictly satisfied. For tailoring these properties, strict heat treatment programmes / schedules are to be adhered or evolved in order to realize reproducible behavior in the intended end application of them. Thermo-analytical tools like, thermogravimetry, differential thermal analysis, calorimetry, etc. play vital roles in achieving the features desired. This presentation will deal with a few examples of synthesis and processing of inorganic compounds which find application in chemical sensing relevant to DAE.

## Role of lattice degree of freedom in electronic transitions in solids

Boby Joseph<sup>a</sup>

<sup>a</sup>*Elettra-Sincrotrone Trieste S. C. p. A., Basovizza, 34149, Trieste*

Several material systems host interesting collective quantum states which emerge below some typical critical temperatures. Such phenomena, though not strictly always connected to a symmetry changing the structural phase transition of the crystal lattice, leaves its signatures also in the lattice and can be captured through systematic experimental investigations. Our recent efforts in this direction will be discussed [1-4], particularly in connection with the charge density wave. Bringing the pressure, in addition to the temperature, can enable the exploration of the thermodynamic phase space thus providing further insights. Glimpses to such activities will be described [5,6]. These studies are conducted principally at the Indo-Italian beamline Xpress at the Elettra synchrotron radiation facility [7]. Present status of this facility will be presented. The status of the on-going synchrotron upgrade program at Elettra will also be touched upon.

### References

- [1] S. Lingannan, et al., *Phys. Rev. B* (2021); **103** 195126  
<http://dx.doi.org/10.1103/PhysRevB.103.195126>
- [2] S. Mathew, et al., *Condensed Matter* (2020); **5** 1  
<http://dx.doi.org/10.3390/condmat5040076>
- [3] R. Sokkalingam, et al., *Solid State Communications* (2023); **372** 115293  
<http://dx.doi.org/10.1016/j.ssc.2023.115293>
- [4] M. Sundaramoorthy, et al., *Chem. Phys. Chem.* (2024); **25** e20240286  
<http://dx.doi.org/10.1002/cphc.202400286>
- [5] M. Pelayo, et al., *J. Phys. Chem. Lett.* (2024); **16** 184  
<http://dx.doi.org/10.1021/acs.jpcclett.4c03336>
- [6] F. Alabarse, et al., *J. Phys. Chem. Lett.* (2022); **13** 9390  
<http://dx.doi.org/10.1021/acs.jpcclett.2c02718>
- [7] <https://www.elettra.eu/elettra-beamlines/xpress.html>

## Study of Terminal Solid Solubility of Hydrogen and Deuterium in Zr-2.5Nb Alloy Pressure Tube Material

A. N. Behera, A. Chatterjee, K. V. Ravikanth, R. N. Singh\*  
*Mechanical Metallurgy Division,  
Bhabha Atomic Research Centre, Trombay, Mumbai - 400085, India*  
\* [rnsingh@barc.gov.in](mailto:rnsingh@barc.gov.in)

Zr-2.5Nb alloy is used as structural material for reactor core components for their low neutron absorption cross-section, adequate aqueous corrosion resistance and good elevated temperature mechanical properties. The terminal solid solubility (TSS) of hydrogen in Zr-2.5Nb alloy, a critical parameter dictating hydride formation and delayed hydride cracking (DHC), is used for assessing the safety of zirconium alloy components in nuclear reactor environments. Terminal solid solubility of hydrogen or deuterium in Zr-2.5Nb alloy pressure tube material is the maximum amount of hydrogen or deuterium present in the Zr-2.5Nb alloy matrix without forming brittle hydride or deuteride precipitate. This study focuses on determining the TSS of hydrogen/ deuterium during both precipitation (TSSP) and dissolution (TSSD) processes over a temperature range of 100°C to 550°C. Using differential scanning calorimetry (DSC), dilatometry technique and resistivity method, the TSSP and TSSD values were experimentally determined and the hysteresis between these processes was analyzed. Zr-2.5Nb alloy pressure tube coupons were gaseously charged with different hydrogen and deuterium concentrations of 20 to 500 wppm, respectively. In dilatometry technique, TSSD and TSSP were determined from the change in slope of change in length vs. temperature plots. For DSC technique, the terminal solid solubility temperatures of dissolution were determined from the derivative of heat flow vs. time plots. In resistivity method, the TSS was determined from change in resistance of the sample with increasing temperature in the range of 50 to 550 °C. The TSSD and TSSP temperatures were found as 282, 325, 356, 354, 360, 388, 501°C and 216, 259, 288, 290, 298, 294, 420°C for the 35, 71, 79, 92, 107, 315, 500 wppm of hydrogen charged samples, respectively. The TSSD and TSSP temperatures were found as 250, 282, 352, 361, 380°C and 189, 214, 243, 298, 319°C for the 22, 46, 88, 123 and 126 wppm of hydrogen equivalents charged samples, respectively. The enthalpies of dissolution and precipitation of hydrides in Zr-2.5Nb pressure tube alloy were found as 40.5 and 30.7 kJ mol<sup>-1</sup>, respectively. For hydrogen equivalents charged samples the enthalpies of dissolution and precipitation of deuterides in Zr-2.5Nb pressure tube alloy were found as 37.6 and 29.8 kJ mol<sup>-1</sup>, respectively. These TSSD and TSSP values are comparable to the Slattery data from literature. These experimental results indicate that the TSS in Zr-2.5Nb follows a temperature-dependent solubility curve and exhibits a distinct hysteresis due to differences in nucleation and dissolution kinetics. This study enhances the understanding of hydrogen-induced degradation mechanisms, offering insights for optimizing material performance and safety in nuclear reactor components.

**Keywords:** *Zr-2.5Nb alloy, terminal solid solubility of hydrogen, dilatometry, differential scanning calorimetry, resistivity.*

## Structure and Thermochemistry of Functional Metal Oxides

Maram Pardha Saradhi

Department of Chemistry, SRM University – AP, Andhra Pradesh, Neerukonda, Mangalagiri Mandal – 522240, India  
e-mail: [pardha.m@sramp.edu.in](mailto:pardha.m@sramp.edu.in)

My talk centred on relating microscopic features of structure and bonding to macroscopic thermodynamic behaviour in mixed metal oxides and the general problem of structure-energy-property systematics. Determining the thermophysical properties of oxides requires special calorimeters, viz., high-temperature drop solution calorimeter, Calvet-type twin microcalorimeter, ultra-high temperature DTA, drop-catch calorimeter, etc. The principles and methodologies are presented, followed by examples of applications. The thermochemical data obtained are essential to understanding materials compatibility and reactivity in technological applications, but, more fundamentally, the energetics offer insight into chemical bonding, order-disorder reactions and phase transitions. Detailed examples will be presented.

**Keywords:** High-temperature drop solution calorimetry, Surface Enthalpy, Configurational Entropy

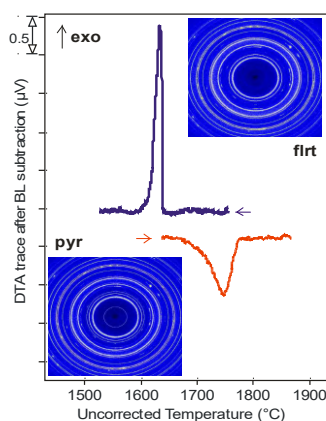


Fig: Ultra-high-temperature differential thermal analysis performed on  $\text{Sm}_2\text{Zr}_2\text{O}_7$ .

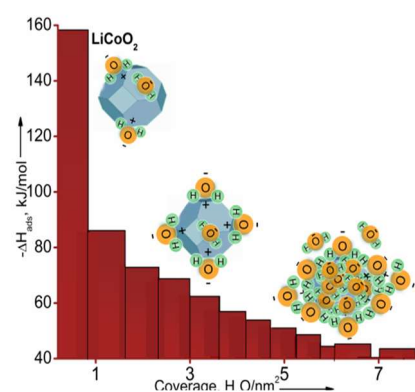


Fig. Differential  $\text{H}_2\text{O}$  adsorption on nanoscale  $\text{LiCoO}_2$  as a function of coverage

### References

- [1] Pardha S. Maram, Sergey V. Ushakov, Richard J.K. Weber, Chris J. Benmore, Alexandra Navrotsky, *Scientific Reports*, 8 (2018) 10658.
- [2] Sergey V. Ushakov, Pardha S. Maram et. al, *Adv. Appl. Ceram* 117 (2018) 582
- [3] Pardha S. Maram, Gustavo C. C. Costa and Alexandra Navrotsky, *Angew. Chem. Int. Ed.* 125 (2013) 12361



## Impact of Calcination Conditions of the Catalyst on the Catalytic Performance

Suneet Kumar Yadav

*Süd-Chemie India Pvt Ltd, Nandesari, Vadodara (Gujarat)*

### Abstract

Heterogeneous catalysts play an important role in the industrial applications and are used in many operational areas of Refineries, Petro-Chemicals, Fertilizers, Automotive and Chemical industries for achieving the desired conversions, removal of impurities, selectivity and productivity. Among the various processes in the catalytic synthesis, calcination is the final process for achieving desired physico-chemical characteristics by optimizing and standardizing conditions such as temperature, time, atmosphere and type of calciner etc. The suitable calcination temperature is required to remove the moisture and volatile matter to make it in the active form [1]. The calcination temperature, higher than optimum, affects the particle or metallic size of the active sites leading to sintering and it has impacts on the various physico-chemical properties of the catalyst like the metal dispersion, acidity and/or basicity, morphology, crystalline phase, surface area and pore size distribution. These changes directly affect the catalytic activity, stability and overall, the catalytic yield [1-2]. In addition to that the slow heating rate of the catalyst is always preferred for achieving better dispersion of the final catalyst [1]. Interestingly, in some cases, the higher calcination temperature is required for initiating the Metal Support Interaction (MSI) of the catalyst to improve the catalytic yield [3]. Moreover, the calcination condition not only has impact on the physico-chemical properties particularly porosity but also mechanical properties like Crush Strength of the catalyst. For instance, the changes in the calcination temperature and time, impacts the final crystalline phases of the catalyst leading to changes in the bulk density, crushing strength, final pellet/particle size and it invariably affects the quality of the final product. The present topic throws light on the relationship between Calcination temperatures and its impact on the Catalytic properties.

### References

1. Peter Munnik, Petra E. de Jongh, and Krijn P. De Jong Recent Developments in the Synthesis of Supported Catalysts *Chem. Rev.* 2015, 115, 6687–6718.
2. Lucie Smoláková, Martin Kout, Eva Koudelková, Libor Čapek Effect of Calcination Temperature on the Structure and Catalytic Performance of the Ni/Al<sub>2</sub>O<sub>3</sub> and Ni–Ce/Al<sub>2</sub>O<sub>3</sub> Catalysts in Oxidative Dehydrogenation of Ethane *Ind. Eng. Chem. Res.* 2015, 54, 51, 12730–12740.
3. Lulu He, Yuanhang Ren, Bin Yue, Shik Chi Edman T sang and Heyong He Tuning Metal–Support Interactions on Ni/Al<sub>2</sub>O<sub>3</sub> Catalysts to Improve Catalytic Activity and Stability for Dry Reforming of Methane *Processes* 2021, 9, 706

## Thermal Behavior of MOF membranes: Morphology-Dependent Insights into Crystallization and Glass Transition

Prabhakar Singh\*

*Department of Physics, Indian Institute of Technology (Banaras Hindu University) Varanasi, Varanasi (U.P)*

*\*Email: [psingh.app@iitbhu.ac.in](mailto:psingh.app@iitbhu.ac.in)*

The thermal behavior of materials plays a crucial role in determining their performance across various industries, from engineering and electronics to energy systems and advanced manufacturing. This talk delves into the thermal properties of materials particularly crystallization temperature and glass transition temperature with the variation of morphology and solvents. A significant focus will be placed on the insights provided by advanced thermal analysis techniques such as Differential Scanning Calorimetry (DSC) and Thermogravimetric Analysis (TGA).

The talk will explore how DSC is employed to analyze phase transitions, glass transitions, and crystallization behaviors, while TGA offers critical data on thermal stability, decomposition kinetics, and compositional analysis. In  $\text{Co}_3\text{O}_4$  dema samples, a cold crystallization peak at 84 °C is observed for the sample heat treated at 120 °C which reduces to 77 °C for the flower morphology obtained after double heat treatment of samples at 120 °C. Furthermore, it also appears at a lower value, 82 °C, with the increase in temperature for the sphere morphology sample. While, the glass transition temperature has not altered with the morphology. Furthermore, with the variation in transition metal from Co to Ti, crystallization temperature and glass transition temperature have reduced to a lower temperature in Ti as compared to Co. By bridging fundamental principles with practical applications, this talk aims to underscore the importance of thermal analysis in driving innovation in material science and engineering.

## Excitements of Thermal Analysis, Studying Thermooxidative Decomposition and Heat Quenching in Convenient Making of Useful Nanomaterials and in Understanding Use of Edible Oils

Ranjit K Verma,<sup>a,b,c</sup> \*

<sup>a</sup>University Department of Chemistry(s.a.), Magadh University, Bodh Gaya-824234

<sup>b</sup>Patna University (formerly,PVC), Patna-800005

<sup>c</sup>Munger University (founding VC), Munger-811201

\* profrkverma@gmail.com

The popularity and versatility of various Thermal Analysis (TA) techniques and particularly Differential Scanning Calorimetry can be gauged from the number of research papers published in the first eleven months of 2024. Out of about 180 thousand cites in TA, almost 24.5 thousand were on DSC! Despite complexities in qualitative interpretation and quantitative evaluation of the usually asymmetric shaped DSC peaks, this technique continues to be of immense significance on account of the versatility it is endowed with and the precise, convenient and fast options that it provides [1]. In this presentation, its use in understanding thermooxidative decomposition of edible oils and in optimization of annealing temperature through understanding of the curing in the making of nanoparticles of ferrites, aluminates, chromites, and yttrium aluminum bromate through citrate precursor route shall be discussed. The synthesis has been carried out under different local factors of sintering (temperature, sintering period, heat quenching technique). Cobalt ferrite nanoparticles having significant saturation magnetization (Ms), magneto crystallization anisotropy (K), coercivity (Hc), and retentivity values, barium hexaferrite nanoparticles having significant magnetic, PL properties (by varying the annealing time, 3h, 5h, 3h followed by quenching), monophasic magnesium ferrites with no detectable impurities (small crystalline size 13 nm at low annealing temperature 400°C) with super paramagnetic behavior are being reported. Samarium ferrites too, having wonderful optical and temperature dependent magnetization properties have been prepared after annealing at optimized temperature. Use of TA has also been made in understanding thermooxidative stability of mustard oil. Using N<sub>2</sub> /O<sub>2</sub> purging and different heating rates, the shelf life prediction has been made for pure oil and turmeric mixed oil (oxidation induction time). Marked changes have been observed in the pattern when the heating is done after mixing with ball milled turmeric powder (after undertaking XRD, spectrophotometric, PL, VSM studies for looking into changes with ball milling time).

### References

1. R. K. Verma, I. M. Szilagy, K. Pielichowska, *et al.* Good laboratory practice in thermal analysis and calorimetry. *J Therm Anal Calorim* **148**, 2211–2231

## **Metal Organic Framework Integrated Composite Patches as the Multifunctional Drug Delivery Platform for Enhanced Wound Healing and Anti-Inflammatory Applications in Freezing Conditions**

**Naved Malek**

*Ionic Liquids Research Laboratory, Department of Chemistry, Sardar Vallabhbhai National Institute of Technology, Surat-395007, Gujarat, India*

Metal-organic framework (MOF)-based polymeric patches represent an avant-garde drug delivery system, adeptly leveraging the synergistic integration of MOFs and polymers to enable precise, sustained, and site-specific therapeutic release, even in the most demanding environments. We, at Ionic Liquids Research Laboratory at SVNIT are engaged in designing various drug delivery platforms that encapsulate the drugs irrespective to their polarity and size and release them through biological stimuli at the target side in a controlled and sustained way. Herein, I will be discussing on engineering a skin-patch made through the crosslinking biocompatible polymer incorporating judiciously selected MOF to enhance drug loading capacity, mechanical resilience, swelling behaviour and antifreezing properties. The patch show distinct exothermic peak at -106 °C in DSC, underscoring its robustness in extreme temperatures. The patch demonstrated excellent hemocompatibility, with hemolysis levels below 2%, high biocompatibility with HaCaT cells at concentrations up to 20 mg/mL, and effective antimicrobial and antifungal activity. The patch also demonstrates remarkable adhesiveness, thermomechanical properties, flexibility, mechanical stability, biocompatibility, significant drug loading capacity, and efficient sustained drug release. Looking at the superior anti-freezing properties and versatility for modification, the patch was further utilized as the co-delivery platform for delivering the curcumin and diclofenac sodium for the Enhanced Wound Healing and Anti-Inflammatory Applications in Freezing Conditions. The studied patch emerges as a promising biomaterial for wound healing and anti-inflammatory applications, capable of performing efficiently under diverse environmental conditions.

## Controlled thermal conversion of molecule to nano-sized functional material

Adish Tyagi

*Chemistry Division*

*Bhabha Atomic research Centre, Mumbai – 400085*

*Homi Bhabha National Institute, Mumbai – 400094*

*(Email: [tyagia@barc.gov.in](mailto:tyagia@barc.gov.in))*

### Abstract

Nanomaterials have revolutionized modern science and technology, offering transformative solutions in energy, healthcare, and environmental applications. A critical aspect of their development lies in their synthesis, where soft chemical routes such as the single-source molecular precursor (SSP) method stand out for their precision and versatility. This talk focuses on the synthesis of nano-sized materials particularly metal chalcogenides via the SSP method, with a particular emphasis on the pivotal role of thermal studies. Thermal analysis is central to understanding the conversion pathways of precursors, enabling precise control over the composition and properties of the resulting nanomaterials. The discussion will highlight how thermal behaviour guides the selection of precursors and facilitates their low-temperature decomposition into well-defined nanostructures. Key factors such as solvent effects and growth temperature will be explored, showcasing their influence on the composition, morphology, and bandgap of the nanomaterials. The talk will also delve into the structural features of precursors that promote low temperature thermal conversion and discuss the challenges and opportunities inherent in SSP routes. Finally, select applications of the synthesized materials will be presented, highlighting their potential to address key challenges.

### Reference

1. G. Karmakar, A. Tyagi, A. Y. Shah, *Coord. Chem. Rev.* **2024**, 504, 215665.

## **Growth of single crystals at high temperature**

Mohit Tyagi

*Technical Physics Division, BARC, Mumbai, India*

Single crystals play a crucial role in the advancement of science and technology. Typically, large single crystals are grown using the melt growth method, with the Czochralski and Bridgman techniques being the most widely employed. However, growing single crystals at high temperatures presents significant challenges due to the differing thermophysical properties of the materials involved. Achieving high-quality, crack-free crystals requires careful optimization of growth parameters and heat flow patterns. Additionally, variations in the vapor pressure of constituent oxides can impact the stoichiometry of the material, which in turn influences its properties. This presentation will explore the growth of several oxide single crystals and examine how various factors affect their properties.

## Radiolytically Functionalized Amine Dense Biodegradable Adsorbents for CO<sub>2</sub> capture: Thermogravimetric Characterization and Adsorption Analysis

Nilanjali Misra<sup>a,b\*</sup>, Swarnima Rawat<sup>a,b</sup>, Shubhangi A. Shelkar<sup>a</sup> and Virendra Kumar<sup>a,b</sup>  
<sup>a</sup>*Radiation Technology Development Division, Bhabha Atomic Research Centre, Mumbai-400085*  
<sup>b</sup>*Homi Bhabha National Institute, Anushaktinagar, Mumbai-400085*  
\* Email ID: [nilanjali@barc.gov.in](mailto:nilanjali@barc.gov.in), Tel: 022-69295681

### Abstract

Direct Air Capture (DAC) is a sustainable and futuristic approach towards mitigating the adverse effects of a toxic air pollutant and greenhouse gas like CO<sub>2</sub>, by trapping the gas from the atmosphere in a suitable matrix and subsequently utilizing it as a resource for green fuel production. This work reports a facile radiation mediated two step fabrication of an amine dense, cellulose based biodegradable adsorbent for selective sequestration of CO<sub>2</sub>. <sup>60</sup>Co gamma radiation induced graft polymerization (C-RIGP) process was employed to introduce functional polyacrylonitrile groups onto the inert cellulose polymer backbone, followed by chemical incorporation of amine rich group tetraethylene pentaamine (TP5) onto the grafted matrix. Samples were characterized by FTIR and TGA analysis. The CO<sub>2</sub> adsorption behavior of the samples were isothermally analyzed by recording increase in weight of the samples in the presence of CO<sub>2</sub>. Parameters such as CO<sub>2</sub>/N<sub>2</sub> ratio and N<sub>2</sub> flow rate were varied. Preliminary investigations have revealed the samples to be capable of rapid CO<sub>2</sub> uptake with a maximum uptake capacity recorded at 31.5 mg/g adsorbent. This novel radiation processed material has potential applications in large scale Carbon Capture and Utilization (CCU), whereby CO<sub>2</sub> from the atmosphere can be judiciously removed and recovered for use as a raw material for catalytic production of methane.

## Hydrogen Ingress in Irradiated Coolant Channels: Role of DSC in In-Service Inspection and Monitoring

Akanksha Samanta

*Post Irradiation Examination Division, Bhabha Atomic Research Centre*

The core of a Pressurized Heavy Water Reactor comprises coolant channels arranged in a square array. These coolant channels are the heart of the reactor as their integrity is essential for the reactor operation. The pressure tubes in the coolant channel house fuel bundles and heavy water coolant at 300°C; 10 MPa flows through them, extracting heat from the bundles. The heat is thus used to generate steam on the secondary side for electricity generation. The pressure tubes have a long service life of 30 years and operate under extreme conditions of high pressure, high temperature, corrosive aqueous environment and high neutron flux. Constant corrosion reaction with High Temperature High Pressure (HTHP) heavy water coolant leads to the generation of hydrogen isotopes. A fraction of these isotopes is picked up by the tubes, resulting in hydrogen/deuterium build up in the tube. The solubility of hydrogen in the zirconium alloy matrices is limited to 60ppm at reactor operating temperatures. Hence, further pick-up can result in brittle hydride precipitation that can challenge the integrity of the tube. The mechanical integrity of the tubes is ensured by monitoring of hydrogen /deuterium isotopic pick-up at regular service life intervals. The presentation will highlight the role of Differential Scanning Calorimetry (DSC) in In-Service Inspection of operating pressure tubes of PHWRs in terms of hydrogen isotopic ingress. The sliver samples scraped from the inner surfaces of the operating tubes are analyzed for hydrogen pick up using DSC at the Post Irradiation Examination Division. The dissolution endotherm of the hydride phase is used to evaluate the hydrogen isotopic content in the samples. Since the technique is unable to differentiate between hydrogen and deuterium, the hydrogen isotopic content is expressed in terms of  $H_{eq}$ . The high sensitivity and non-destructive nature of analysis makes DSC an ideal technique for the analysis of  $H_{eq}$  in irradiated samples. The reproducibility of the heat flow curves is ensured by annealing the irradiated samples. To understand the hydride distribution, metallographic analysis is carried out.  $H_{eq}$  content, well below its solubility limit at reactor operating temperature, ensures safe operation of the coolant channels till the next In-Service Inspection Campaign.



## High temperature processing of materials for steam electrolysis

RK Lenka\*, and T Mahata

*Powder Metallurgy Division, BARC Vashi Complex, Mumbai – 400703, INDIA*

*\*Corresponding author, Email: rklenka@barc.gov.in*

### Abstract

Solid Oxide Cells (SOC) based on oxygen ion conducting electrolyte membrane are used in electrochemical devices to convert chemical energy of fuel directly to electrical energy in fuel cell mode (SOFC) and hydrogen production by high temperature steam electrolysis mode (HTSE). Two basic designs, namely, planar and tubular design have been adopted in making SOCs. In both the configurations, Ni-electrolyte cermet support is being deployed as cathode material in a solid oxide cell. Co-pressing and Co-sintering approach is adopted to prepare tubular cells and tape casting route to prepare planar cells. While going from materials to components through high temperature processing, there needs an understanding of the thermal stability and shrinkage behaviour of the components being integrated. During sintering of half cells (cathode-electrolyte), YSZ electrolyte need to be dense over a porous NiO-YSZ substrate. Based on the sintering data, sintering cycle is optimized to get an adherent electrode-electrolyte interface with desired porosity.

Gas diffusion through the Ni-YSZ electrode support plays an important role to minimise the concentration polarisation in an operating cell. The electrochemical reaction takes place at the triple phase boundaries formed by Ni phase, YSZ electrolyte and gas phase. Therefore, the anode structure needs to be essentially porous with maximum triple phase boundary. During the sintering process, decomposition behaviour of the pore formers tailors the microstructure of the triple phase boundary area. In this investigation, the effect of different pore formers on gas permeability and anode microstructure has been studied. Long term performance of high temperature electrolysis is carried out in tubular configurations. In a steam electrolysis experiment, a tubular solid oxide cell generates 7.2A current at an applied potential of 1.5V at 850 °C.

## **Thermal Effects: An Essential Facet of Studies on Nuclear Materials**

Dheeraj Jain

*Chemistry Division, Bhabha Atomic Research Centre, Trombay, Mumbai-400085, India.*

*jaind@barc.gov.in*

Globally, increasingly witnessed worrisome effects of climate change have made it inevitable to accelerate human efforts towards climate preservation. This needs to be done without slowing down the growth engines of fast developing nations like India. It thus calls for rapid enhancement of carbon-lean energy options like nuclear. Increasing nuclear energy capacity based on existing reactor technologies, and developing innovative nuclear energy options are imminent tasks ahead of nuclear fraternity. This also necessitates development of new/improved nuclear materials and, generation of reliable database on their physico-chemical properties over the thermal regime of their usage in nuclear technology. Consideration of thermal effects while assessing material behavior, and role of ‘thermal analyses techniques’ to decipher the same under reactor operation (normal and/or transient) conditions is very important. This short presentation would attempt to cover this aspect with the help of a few examples of studies on materials relevant to nuclear technologies in authors’ research group. These examples would cover (i) assessment of nuclear fuel properties, (ii) physico-chemical characterization of hull-immobilization alloys, (iii) optical behavior of actinide-based composites, etc. with special attention to thermal effects in such studies and the role of thermal analysis techniques in understanding them.

## Spot technique - A tool for measuring the solidus and liquidus of refractory and radioactive alloys

Dr S Balakrishnan

*Materials Chemistry & Metal Fuel Cycle Group, Indira Gandhi Centre for Atomic Research, Kalpakkam*

*Head Advanced Fuel Studies Section, FChD, MCMFCG*

*Ph: 044 27480500 Extn 24024, Email: [balakrish@igcar.gov.in](mailto:balakrish@igcar.gov.in)*

A variety of techniques are available for measuring the phase transformation temperatures of alloys and refractories. Some typical methods are based on cooling curves, differential thermal analysis, incipient melting, segregation and sampling, thermodynamic property measurements and change in emissivity / reflectivity. Choice of the method depends on the application, practical difficulties, temperature range and required accuracy. Experimental determination of solidus and liquidus in reactive systems at very high-temperatures requires special equipment and is rather complex. Spot-technique is a novel method to measure the solid to liquid phase transformation temperature, which is based on the change in reflectivity of the sample at the transformation. It is a convenient method, particularly for alloys containing refractory and/or radioactive materials, for it is amenable for glove box adaptation. Hence, an equipment based on the spot-technique has been built at our Centre for measuring the solid to liquid phase transformation temperature of radioactive alloys and refractories. The spot-technique is a relatively simple method devised by Ackermann and Raugh at Argonne National Laboratory and later by S P Garg at Bhabha Atomic Research Centre for determining the solidus and liquidus temperatures of refractories. This technique falls under the category of thermo-optometry, wherein the change in the optical reflectivity of the sample upon liquefaction during heating is monitored. Upon melting, the liquid formed on the surface of the sample acts as a mirror and reflects the image of the orifice of the container lid. The appearance of this image (as a single circular dark spot) corresponds to the melting point. In case of alloys, the first appearance of broken irregular dark tiny patches corresponds to the solidus. On further heating, several tiny irregular dark patches appear due to the formation of many droplets. These grow in size with the quantity of the liquid and finally coalesce into a single large dark circular spot at liquidus. This setup could be used to measure phase transformation temperatures involving liquids in refractory systems that comprise reactive and radioactive components, in the range of 1273 –2273 K. The equipment and the method were validated by measuring the melting points of high purity metals, namely, gold, copper, nickel, and zirconium. A measurement accuracy of  $\pm 2$  K could be realized at temperatures as high as 2128 K. Solidus and liquidus of several binary systems, Cu-Ni, U-Zr, U-Al, U-Sn, Ru-Sn, Fe-Zr, Zr-Al, Fe-Zr as well as metallic fuel (U-19Pu-6Zr) and FBTR Carbide fuels (Mark I & II) were measured.

# Application of Thermodynamics in Analysis of Solid State Phase Transformations: Examples from Zr

K V Mani Krishna

*Bhabha Atomic Research Centre, Trombay, Mumbai, 400 085*

## **Abstract**

Thermodynamics plays a pivotal role in understanding solid-state phase transformations, which govern the microstructure and, consequently, the mechanical properties of nuclear materials. These transformations determine precipitate size, shape, and distribution, critically influencing material behavior under operational conditions. By leveraging thermodynamic principles, it becomes possible to predict and control microstructural evolution to optimize performance in demanding environments.

The metastable transformations, including martensitic and omega transitions, as well as the evolution of bcc precipitates in an hcp matrix, are highly influenced by thermodynamic driving forces and competing strain energy effects. These factors govern the nucleation, growth, and stability of precipitates, with martensitic transformations observed beyond a critical size of the parent beta particles. Omega transformations, on the other hand, show less size sensitivity, owing to reduced strain energy contributions in comparison to thermodynamics factors, highlighting the complex interplay of thermodynamics and mechanical energy contributions in determining phase transformation behavior. This talk discusses these aspects through examples in the Zr system, illustrating the predictive power of thermodynamic principles in explaining microstructural evolution.

## Thermal studies assisted evaluation of stability and polymorphism of potentially bioactive organoselenium compounds

Prasad P. Phadnis<sup>a,b</sup>

<sup>a</sup>Chemistry Division, Bhabha Atomic Research Centre (BARC), Mumbai 400 085, India

<sup>b</sup>Homi Bhabha National Institute (HBNI), Anushaktinagar, Mumbai 400 094, India

\*Email: phadnisp@barc.gov.in

### Abstract

Thermal effects play a crucial role in biological domain pertaining to food chain, metabolic activities, in diseased conditions and treatments of diseases (like cancer) and in drug development process to evaluate thermal stability and existence of polymorphic forms in pharmacological agents. The thermal effects are detrimental also when ability of body to regulate its internal temperature is compromised. In our program of developing pharmacological agents for bio-medical applications like antioxidant, GPx mimics and anticancer, we have rationally designed and synthesized biocompatible heterocycles based organoselenium compounds. Some of them have exhibited potential bioactivity as anticancer agents and antioxidants. During their further pharmacological evaluations, we evaluated the compounds for their thermal behaviour for their thermal stability and existence of polymorphism which reflect in the shelf life and activities respectively. It is known, that most of drugs exist as the mixture of their polymorphic forms and individual polymorphous structures have been found to differ in their physicochemical and pharmacological properties. Hence, identification of polymorphic forms and their relative bioactivities is essential during drug development process, so that we can achieve a desired form through modulation of synthetic strategies and recrystallization solvent. In the present study, we have performed the TG-DTA as well as DSC analyses for the pyridyl-based organoselenium compounds as well as dihydroxy-selenolane. The DSC analysis of di-pyridinol-diselenide has exhibited two polymorphic structures evidenced with a very small change in heat flow. These polymorphic forms were obtained by their recrystallization in different solvents. Most of the active molecules existed in uniform crystalline forms *i.e.*, without any polymorphism. It revealed, that these compounds are stable in temperature window ~ 25 to 50 °C and retains the same stable crystal lattice arrangement and can therefore be used for further biological and pharmacological applications, without any further recrystallization with specific organic solvents. The results of thermal studies performed on some of the organoselenium compounds will be discussed.



## Studies on Phase Equilibria in Na-Ti-O System

S. Pragadeeswari,<sup>1,2\*</sup> A. S. Suneesh,<sup>1</sup> Chinmay Routray<sup>1</sup> and Rajesh Ganesan<sup>1,2</sup><sup>1</sup> Materials Chemistry and Metal Fuel Cycle Group, Indira Gandhi Centre for Atomic Research, Kalpakkam-603102, Tamil Nadu, India<sup>2</sup> Indira Gandhi Centre for Atomic Research, A CI of Homi Bhabha National Institute, Kalpakkam-603102, Tamil Nadu, India

\* pragathi@igcar.gov.in

**Abstract**

This paper outlines the experimental work on determining the coexistence of the Na-Ti-O ternary phase diagram along the pseudo-binary line of Na<sub>2</sub>O and TiO<sub>2</sub>. Different crystalline coexisting phases of sodium titanates, corresponding to the compositions Na<sub>2</sub>Ti<sub>6</sub>O<sub>13</sub>, Na<sub>2</sub>Ti<sub>3</sub>O<sub>7</sub>, Na<sub>4</sub>Ti<sub>5</sub>O<sub>12</sub>, Na<sub>8</sub>Ti<sub>5</sub>O<sub>14</sub>, Na<sub>2</sub>TiO<sub>3</sub> and Na<sub>4</sub>TiO<sub>4</sub> were identified by XRD analysis. A partial phase diagram of the Na-Ti-O ternary system valid for the temperature range 600 and 800°C will also be presented.

**Introduction**

Crystalline phases of sodium titanate (NTO) have emerged as promising materials for sodium-ion conducting applications, driven by the increasing demand for cost-effective and sustainable alternatives to lithium-based energy storage systems. This is due to their unique structure and electrochemical properties. Among the different NTOs, the Na<sub>2</sub>Ti<sub>3</sub>O<sub>7</sub> structure has been the most investigated as a promising anode with the lowest operating potential for sodium-ion batteries (SIBs)[1]. Other NTOs, such as Na<sub>2</sub>Ti<sub>6</sub>O<sub>13</sub> and Na<sub>4</sub>Ti<sub>5</sub>O<sub>12</sub>, have also been widely studied for similar applications.

These titanium oxides conductive and electrochemical properties are governed by their structure and the composition of different phases. Understanding the coexistence of phases at different mole ratios of Na, Ti, and O is crucial during the charging/discharging cycles of energy storage devices to gain a fundamental understanding of the possible phases. However, there is limited literature on the various phases that exist at different temperatures and compositions, and thus, the Na-Ti-O ternary phase diagram is yet to be fully established. This paper reports the coexistence of phases along a pseudo-binary line formed between Na<sub>2</sub>O and TiO<sub>2</sub> in an isothermal section at 600 and 800°C.

**Experimental**

The synthesis of NTOs such as Na<sub>2</sub>Ti<sub>6</sub>O<sub>13</sub>, Na<sub>2</sub>Ti<sub>3</sub>O<sub>7</sub>, Na<sub>4</sub>Ti<sub>5</sub>O<sub>12</sub>, Na<sub>8</sub>Ti<sub>5</sub>O<sub>14</sub>, Na<sub>2</sub>TiO<sub>3</sub> and Na<sub>4</sub>TiO<sub>4</sub>, which fall along a pseudo-binary line of Na<sub>2</sub>O-TiO<sub>2</sub> in the Na-Ti-O ternary phase diagram (shown in Fig. 1), was carried out using a solid-state reaction method. The appropriate molar ratios of Na<sub>2</sub>O and TiO<sub>2</sub> were mixed (shown in Table 1). Ground thoroughly, then made into pellets, were heated in alumina crucibles for 20 hrs in an air atmosphere from ambient temperature to 800°C, at a heating rate of 5°C/min, followed by a cooling procedure at a rate of 5°C/min. The heat-treated pellet was again ground and subjected to the second heat treatment, which was a similar heating-cum-cooling cycle, as mentioned above.

The pellets were powdered, and the XRD patterns of the samples were recorded using an X-ray diffractometer (Model: MPD 7501, Inel, France) with a Cu-K $\alpha$  (1.54184 Å) beam in Bragg-Brentano geometry, with 2 $\theta$  values ranging from 10° to

80°. The quantification of the different phases was carried out using the Rietveld method.

**Result and discussion**

XRD patterns of the different crystalline phases formed during the solid-state reaction between Na<sub>2</sub>O and TiO<sub>2</sub>, taken in various mole ratios (see Table 1), are shown in (Fig. 2.)

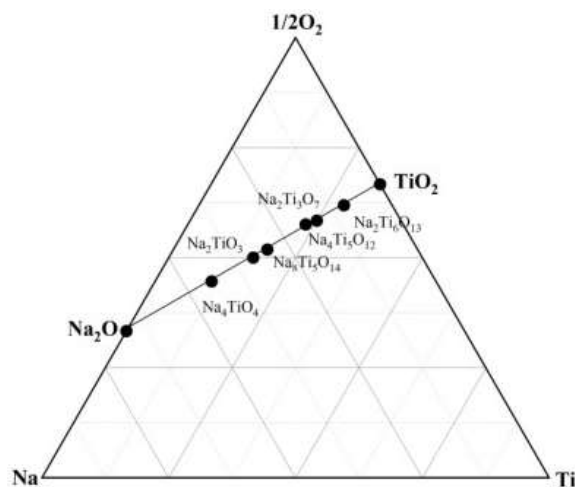


Fig.1. Compositional plot of Na-Ti-O system

Table.1. Experimental details for preparation of ternary compound and product phases obtained by XRD

Indented compound	Na <sub>2</sub> O:TiO <sub>2</sub>	Products phases obtained by XRD analysis
Na <sub>2</sub> Ti <sub>6</sub> O <sub>13</sub>	1:6	Na <sub>2</sub> Ti <sub>6</sub> O <sub>13</sub> , TiO <sub>2</sub>
Na <sub>2</sub> Ti <sub>3</sub> O <sub>7</sub>	1:3	Na <sub>2</sub> Ti <sub>3</sub> O <sub>7</sub> , Na <sub>2</sub> Ti <sub>6</sub> O <sub>13</sub>
Na <sub>4</sub> Ti <sub>5</sub> O <sub>12</sub>	2:5	Na <sub>2</sub> Ti <sub>3</sub> O <sub>7</sub> , Na <sub>8</sub> Ti <sub>5</sub> O <sub>14</sub>
Na <sub>8</sub> Ti <sub>5</sub> O <sub>14</sub>	4:5	Na <sub>8</sub> Ti <sub>5</sub> O <sub>14</sub>
Na <sub>2</sub> TiO <sub>3</sub>	1:1	Na <sub>2</sub> TiO <sub>3</sub> ,

		$\text{Na}_8\text{Ti}_5\text{O}_{14}$
$\text{Na}_4\text{TiO}_4$	2:1	$\text{Na}_8\text{Ti}_5\text{O}_{14}$ , $\text{Na}_2\text{TiO}_3$

The Na-Ti-O compositions considered for the ternary phases are also indicated in the ternary compositional plot in Fig. 1. Semi-quantification analysis using the Rietveld method, along with phase identification using Match software, revealed that a phase-pure crystalline form was obtained only for the compound  $\text{Na}_8\text{Ti}_5\text{O}_{14}$  (JCPDS File No. 01-084-8818) when  $\text{Na}_2\text{O}$  and  $\text{TiO}_2$  were mixed in a 4:5 ratio. In all other cases, mixtures of crystalline phases were formed (as shown in Table 1). The formation of a monophasic crystalline phase corresponding to  $\text{Na}_8\text{Ti}_5\text{O}_{14}$  for the  $\text{Na}_2\text{O}$  and  $\text{TiO}_2$  mole ratio of 4:5 could be due to the fact that this is the most stable crystalline phase. It can also be observed that at lower  $\text{Na}_2\text{O}$  compositions,  $\text{Na}_2\text{Ti}_3\text{O}_7$  or  $\text{Na}_2\text{Ti}_6\text{O}_{13}$  phases are formed[2], whereas, at higher  $\text{Na}_2\text{O}$  compositions, the  $\text{Na}_8\text{Ti}_5\text{O}_{14}$  phase is formed. At higher  $\text{TiO}_2$  compositions, the  $\text{Na}_2\text{Ti}_6\text{O}_{13}$  phase is more preferentially formed[3].

Several previously reported studies also agree that during prolonged heat treatment, some of the lower titanate compositions undergo phase transformation to higher titanium-bearing phases [4]. For example,  $\text{Na}_2\text{Ti}_3\text{O}_7$  undergoes a crystalline transformation to  $\text{Na}_2\text{Ti}_6\text{O}_{13}$ . Some of these transformations involve the loss of sodium oxide (referred to as soda loss). Equilibrium phase formation studies were also conducted to gain further insights.

The phase equilibrium studies were performed at two different temperatures, 600°C and 800°C. For this, seven different compositions with corresponding Stoichiometry amounts of  $\text{Na}_2\text{O}$  and  $\text{TiO}_2$  were selected. Additional compositions along the  $\text{Na}_2\text{O}$  and  $\text{TiO}_2$  pseudo-binary line were also chosen. These were thoroughly mixed, formed into pellets, placed in alumina crucibles, and equilibrated at 600°C and 800°C in air for two weeks and one week, respectively, followed by quenching in water. Analysis of coexisting phases enabled the partial phase diagram to be valid for the temperature range of 600–800°C.

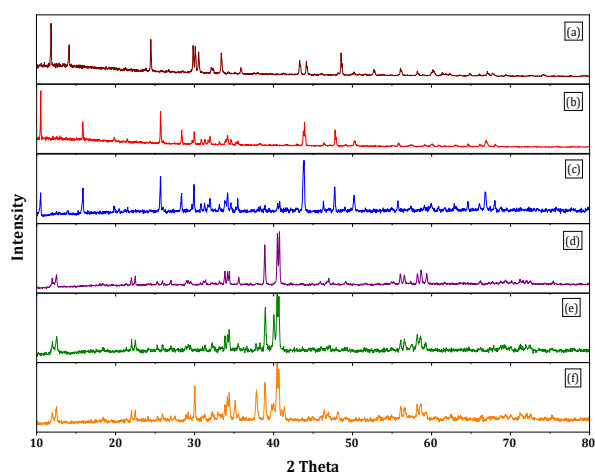


Fig. 2. XRD pattern of (a)  $\text{Na}_2\text{Ti}_6\text{O}_{13}$ , (b)  $\text{Na}_2\text{Ti}_3\text{O}_7$ , (c)  $\text{Na}_4\text{Ti}_5\text{O}_{12}$ , (d)  $\text{Na}_8\text{Ti}_5\text{O}_{14}$ , (e)  $\text{Na}_2\text{TiO}_3$  and (f)  $\text{Na}_4\text{TiO}_4$

## Conclusion

The studies revealed coexistence of phases along the  $\text{Na}_2\text{O}$  and  $\text{TiO}_2$  pseudo binary line and long term equilibration of samples resulted in establishing partial phase diagram of Na-Ti-O valid for the temperature range 600 – 800°C.

## Reference

1. Wang, Zhenghao, Rui Zhang, Liang Chen, Liping Cao, XiaodongGuo, Zhenguo Wu, Bin Liang, and DongmeiLuo. *Journal of Electroanalytical Chemistry* (2024): 118621.
2. Yakubovich OV, Kireev VV. *Crystallography Reports*. (2003) 48:24-8.
3. Kataoka, K., Awaka, J., Kijima, N., Hayakawa, H., Ohshima, K. I., & Akimoto, J. *Chemistry of Materials*, 23(9),(2011) 2344–2352.
4. Liu, H., Yang, D., Zheng, Z., Ke, X., Waclawik, E., Zhu, H. and Frost, R.L., *Journal of Raman Spectroscopy*, 41(2010), 1331-1337.



## Biophysical Analysis of Interactions of Copper (II) Complexes with Serum Albumin

Namrata Singh<sup>a</sup> and Nand Kishore<sup>b\*</sup>

<sup>a</sup>Ramrao Adik Institute of Technology, DY Patil University, Department of Engineering Sciences, Navi Mumbai, India

<sup>b</sup>Indian Institute of Technology, Department of Chemistry, Bombay, Maharashtra, India

\*Correspondence: nandk@chem.iitb.ac

### Abstract

We have selected three copper (II) metal complexes with promising anticancer properties and studied their binding interactions quantitatively with bovine serum albumin (BSA) by isothermal titration calorimetry, differential scanning calorimetry and fluorescence spectroscopy. The values of binding constant ( $K$ ), standard molar enthalpy ( $\Delta H^\circ$ ), standard molar entropy ( $\Delta S^\circ$ ) and stoichiometry of binding ( $N$ ) for the binding of complexes with BSA were determined using an isothermal titration calorimeter. Thermal stabilities of complexes were checked on a Differential Scanning Calorimeter in the temperature range of 298-423 K. All the interactions were observed to be endothermic and driven by entropic factors.

Understanding of drug binding with transport proteins is vital for various pharmaceutical, biological and clinical applications. Serum albumins being the most abundant proteins in blood plasma hold a special significance when it comes to binding of different therapeutic agents. Bovine serum albumin shares high sequence identity with human serum albumin, HSA (almost 76 %). One of the major difference is presence of two tryptophan residues (W131 and W214) in BSA and one in (W214) HSA [1]. Hence interaction study of drugs with BSA has been an area of major interests in recent years. Copper complexes have been extensively studied for development of anticancer drugs because of its oxidative nature and biocompatibility. We have therefore, selected three copper (II) metal complexes *viz.*  $[\text{Cu}(\text{L}^1)(\text{L}^2)\text{ClO}_4]$  (complex I),  $[\text{Cu}(\text{L}^2)(\text{L}^3)]\text{ClO}_4$  (complex II) and  $[\text{Cu}(\text{L}^4)_2(\text{H}_2\text{O})_2]$  (complex III) with promising anticancer properties and studied their binding interactions, binding sites and mode of action quantitatively with Bovine serum albumin (BSA) by isothermal titration calorimetry, differential scanning calorimetry and fluorescence spectroscopy. These copper complexes with nitrogen and oxygen donor ligands were synthesized and characterized by different physico-chemical methods and single crystal X-ray crystallography. These complexes been reported to possess promising anticancer and antitumor properties due to their biocompatible and oxidative nature (Chen et al., 2011). The values of binding constant ( $K$ ), standard molar enthalpy ( $\Delta H^\circ$ ), standard molar entropy ( $\Delta S^\circ$ ) and stoichiometry of binding ( $N$ ) for the binding of complexes with BSA were determined using an isothermal titration calorimeter. The analysis of dilutions corrected ITC profiles was done by fitting a non-linear least square regression binding model involving a single class of noninteracting binding sites to the experimental data points [3].

The representative ITC profiles accompanying the interaction of 1.4 mM CII with 0.07 mM BSA at pH 7.4 in the temperature range of 298.15 K to 313.15 K is shown in Fig.1. Each peak in this panel corresponds to heat absorbed when 10  $\mu\text{l}$  of CII is added in the cell of ITC containing BSA. The area under each peak in the form of integrated heat profile in terms of heat absorbed upon 25 sequential injection of CII into BSA. The analysis of dilutions corrected ITC profiles was done by fitting a non-linear least square regression binding model involving a single class of non-interacting binding sites to the experimental data points. Since phosphate has a very low ionization enthalpy,  $\Delta H_{\text{ion}} = 3.6 \text{ kJmol}^{-1}$ , the observed enthalpy of binding of CII with protein has practically very small error arising due to release or absorption of proton, if any. The binding of CII with BSA is strong with a binding constant of the order  $10^5$  in the studied range of temperature. The value of  $K$  is observed to increase slowly from  $(1.68 \pm 0.41) \times 10^5$  at  $T=298.15 \text{ K}$  to  $(2.08 \pm 0.37) \times 10^5$  at  $T=308.15 \text{ K}$ . The values of  $K$  suggest that beyond  $T=308.15 \text{ K}$  the value of binding constant does not change appreciably within the standard deviation. The enthalpy of binding varies

from  $14.4 \pm 1.5 \text{ kJmol}^{-1}$  at  $T=298.15 \text{ K}$  to  $21.4 \pm 1.2 \text{ kJmol}^{-1}$  at  $T=313.15 \text{ K}$ . The endothermic binding is driven by entropic factors, the value of which varies from  $\Delta S^\circ = (149 \pm 5) \text{ J K}^{-1} \text{ mol}^{-1}$  to  $(169 \pm 4.2) \text{ J K}^{-1} \text{ mol}^{-1}$ . The spontaneity of the binding process is clearly seen in sufficiently large negative values of Gibbs free energy of binding which vary from  $-(29.8 \pm 0.6) \text{ kJ mol}^{-1}$  at  $T=298.15 \text{ K}$  to  $-(31.5 \pm 0.5) \text{ kJ mol}^{-1}$  at  $T=313.15 \text{ K}$ .

The change in heat capacity upon binding is an important thermodynamic quantity associated with the strengthening or loosening of the protein conformation upon ligand binding. The value of  $\Delta C_p$  calculated from the plot of  $\Delta H^\circ$  against temperature is  $(0.49 \pm 0.08) \text{ kJ K}^{-1} \text{ mol}^{-1}$ . The change in heat capacity has generally been associated with burial or exposure of polar or non-polar residues of the protein upon binding with ligand. A very small value of  $\Delta C_p$  obtained in this case indicates some exposure of hydrophobic residues to solvent upon binding. Endothermic heats of interaction have generally been associated with hydrophobic association. The endothermic heat effects observed in the binding of CII with BSA suggest predominance of the interaction of hydrophobic phenanthrene group of CII with the binding site residues on the protein. The positive entropy change can be attributed to the release of water molecules as a result of desolvation of CII and of binding cavity in the protein. This forms the major driving force for the association process, even though the desolvation enthalpy of CII has led to significant penalty in association.

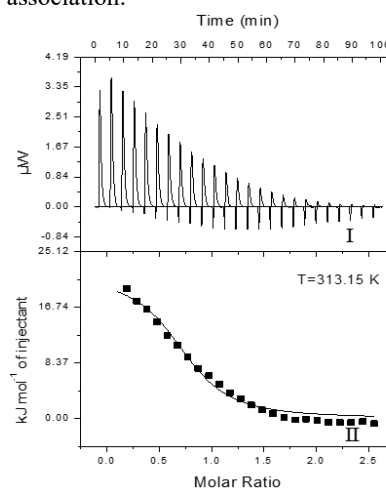


**Figure 1.** Raw data for the titration of 1.4 mM CII with 0.07 mM BSA at pH 7.4 at 313.15 K

### Steady state fluorescence measurements

In general, quenching of fluorescence is known to occur mainly by collision (dynamic quenching) or by the formation of complex between the quencher and the fluorophore (static quenching) [4].

**Table 2.** Values of binding constant ( $K_a$ ) and  $\Delta H^\circ$  determined from intrinsic fluorescence of BSA on complexation with CI, II and CIII at different temperatures.

Complexes	$K_a/(M^{-1})$		
	298.15 K	303.15 K	310.15 K
CI	$(1.05 \pm 0.06) \times 10^4$	$(1.30 \pm 0.05) \times 10^4$	$(2.11 \pm 0.09) \times 10^4$
CII	$(2.63 \pm 0.31) \times 10^4$	$(4.4 \pm 0.32) \times 10^4$	$(4.53 \pm 0.25) \times 10^4$
CIII	$(8.68 \pm 0.51) \times 10^5$	$(4.31 \pm 0.25) \times 10^5$	$(2.74 \pm 0.11) \times 10^5$

To understand the effect of copper complexes on tryptophan environment of the protein and to determine binding constant of the interaction, the intrinsic fluorescence of BSA in the presence of increasing concentration of the former was measured. Isothermal titration calorimetric experiments with CI and CIII could not be performed in aqueous buffer since these copper complexes were not soluble in water. Therefore fluorescence spectroscopy was used to determine thermodynamics of interaction of CI, CII and CIII with BSA. The interaction of CI, CII and CIII with BSA resulted in significant extent of fluorescence quenching. This indicates that CI, CII and CIII bind to BSA in the close vicinity of tryptophan residues which are located at positions 134 and 212 in sub domains IA and IIA, respectively. In the case of CI and CII, the emission maximum was shifted (red shift ~10nm) indicating that CI and CII bind to BSA by altering the local dielectric environment. The fluorescence quenching is described by the Stern-Volmer relation [2].

$$F_0/F = 1 + K_{sv}[Q]$$

Here,  $F_0$  and  $F$  represent the fluorescence intensities in the absence and presence of quencher,  $Q$  respectively.  $K_{sv}$  is Stern-Volmer quenching constant and  $[Q]$  is concentration of the quencher. It is known that the linear Stern-Volmer plots represent a single quenching mechanism, either static or dynamic. Since the lifetime experiments in the present investigation confirm that the interactions are mainly static in nature we have analyzed the intrinsic fluorescence data on the basis of static quenching mechanism. The values of the number of binding sites ( $n$ ) and association constant  $K_a$  can be calculated from the fluorescence titration data using the following equation.

$$\log \left[ \frac{F_0 - F}{F} \right] = \log K_a + n \log [Q]$$

Here,  $F_0$  and  $F$  are the fluorescence intensities of the tryptophan residues of the protein in the absence and presence of the investigated cu-complexes. Plots of  $\log F_0 - F/F$  against  $\log [Q]$  provided binding constant,  $K_a$  and number of binding sites,  $n$  values. CIII caused complete quenching of BSA which is well in agreement with the strong binding constant of CIII. On the contrary, CI and CII showed relatively weak binding profile therefore complete quenching was not manifested. The temperature dependence of binding constant reported in Table 2 was used to determine the value of enthalpy of interaction by using integrated form of the Van't Hoff equation mentioned below.

$$\left( \frac{\partial \ln K}{\partial T} \right)_p = \frac{\Delta H^0}{RT^2}$$

Since the variation in the value of  $K$  is very small with temperature, the enthalpy of interaction is also expected to be very small. The values of  $\Delta H^0$  calculated for the binding of complexes CI, CII, and CIII with BSA are respectively,  $45 \pm 3$  kJ mol<sup>-1</sup>,  $33 \pm 2$  kJ mol<sup>-1</sup> and  $-73 \pm 6$  kJ mol<sup>-1</sup>. Thus the binding of CI and CII is entropically driven whereas the binding of

CIII has a small enthalpic contribution. A comparison of thermodynamic parameters of binding of CII with BSA determined by Isothermal Titration Calorimetry (ITC) and fluorescence spectroscopy suggests that the data obtained by using these two techniques has a difference. The values of  $K$  differ by an order of ten whereas the enthalpies of interaction also have a sizeable difference. The discrepancies in the measured thermodynamic parameters can arise from different experimental conditions employed in the ITC and fluorescence experiments measurements, where the concentration of both the protein and copper complexes were largely different. We believe that ITC, being a direct technique provides more reliable values of the thermodynamic parameters accompanying protein ligand binding. On the other hand the thermodynamic parameters of interaction from the temperature dependence of  $K$  are determined indirectly from spectroscopic methods on the basis of Van't Hoff equation.

ing of CII with BSA is sufficiently high with binding constant of the order  $10^5$  in the studied range of temperature. The binding interactions are endothermic in nature driven by entropic factors. The spontaneity of the binding process is clearly manifested in sufficiently large negative values of Gibbs free energy of binding. Thermal stabilities of complexes [5] were checked on a Differential Scanning Calorimeter in the temperature range of 298-423 K as shown in Fig. 3.

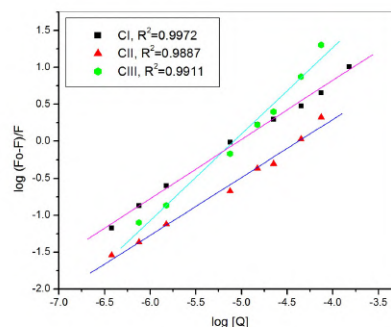


**Fig. 2.** Plots of  $\log \{[F_0 - F]/F\}$  against  $\log [Q]$  with copper complexes at pH 7.4 and 25°C;

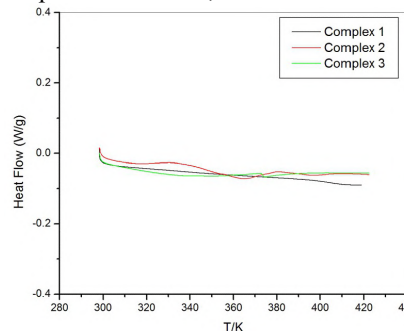


**Fig. 3.** Representative DSC profiles accompanying the heating of complexes CI, CII, and CIII in the temperature range of 298 K to 423 K

## References

1. Stezowski, J.J. *Journal of American Chemical Society*, 98 (1976) 6012.
2. Stern, O., & Volmer, M. *Zeitschrift für Physikalische Chemie*, 20 (1919) 183.
3. Sahoo, S., Shaikh, S.A., Priyadarsini, K.I. and Choudhary, S., *The Journal of Chemical Thermodynamics*, 193, (2024) 107273.
4. Chignell, C.F. In *Fluorescence techniques in cell biology* (1973) 345. Berlin, Heidelberg: Springer Berlin Heidelberg.
5. Weber, P.C. and Salemme, F.R., 2003. *Current opinion in structural biology*, 13 (2003) 115.

## Thermodynamic Studies on Li<sub>2</sub>NiO<sub>2</sub> Compound Employing KEQMS

Sanjay K. Yadav, Hemlata Khadilkar, Raja. Das, Pradeep Samui\*, Swarup K. Rakshit, Suresh C. Parida

Product Development Division, Bhabha Atomic Research Centre, Mumbai-400085,

\*Corresponding author, e-mail: psamui@barc.gov.in; phone:

### Abstract

Lithium-ion batteries (LIBs) are becoming used for storing energy and powering mobile electronics. Lithium-rich compound, Li<sub>2</sub>NiO<sub>2</sub>, in the Li-Ni-O system, is investigated as an alternative cathode additive to protect from overdischarge problem in Li-ion batteries. Understanding the thermodynamics of Li-Ni-O systems is crucial for assessing stability, durability and power of lithium-ion batteries. In this context, the Gibbs free energy formation of the compound has been determined using an in-house developed Knudsen effusion quadrupole mass spectrometry (KEQMS) based on Residual Gas Analyzer (RGA)

### Introduction

Lithium Nickel mixed oxide is a material of interest in the field of energy storage, particularly for lithium-ion batteries, supercapacitors, and other high-performance energy storage systems. Lithium nickel oxide typically has a layered or rock-salt structure having a space group R3m, in which alternate layers of Ni and Li ions are located at octahedral sites among the cubic close packed oxygen ions [1,2]. Lithium rich compound such as Li<sub>2</sub>NiO<sub>2</sub> in Li-Ni-O system has been deliberated to be act as an alternative cathode additive to protect from overdischarge safety issues in Li-ion batteries. Knowledge of thermodynamic properties of Li-Ni-O system is fundamental to study the stability and capacity of lithium ion batteries. The Gibbs energy functions of these phases are essential to predict the cell voltages and study the electrochemical properties of lithium ion batteries. Thus, the Gibbs free energy formation of the compound has been determined employing an in-house developed Knudsen effusion quadrupole mass spectrometry (KEQMS) based on Residual Gas Analyzer (RGA).

### Materials preparation

Powder samples of Li<sub>2</sub>CO<sub>3</sub>(s) from Aldrich Chemical Co., USA, (mass fraction purity 0.99) and NiO(s) from E. Merck, Germany (mass fraction purity 0.999) were used in this study. Stoichiometric ratios of preheated Li<sub>2</sub>CO<sub>3</sub>(s) and NiO(s) were mixed homogenously using an agate mortar-pestle and compacted into pellets at a pressure of 5 MPa using tungsten carbide lined steel die. The pellets were broke into pieces and loaded in a Knudsen cell.

### Knudsen effusion quadruples mass spectrometry (KEQMS)

In the present work, a Knudsen effusion mass spectrometer system was developed using a residual gas analyzer (RGA; model SRS RGA 100, USA) and in-house designed vacuum chamber attached to a turbo molecular pumping station. Residual gas analyzer is based on quadruple mass spectrometer and capable to measure quite accurately the partial pressures of permanent gases. The experimental setup has been described in detail by Rakshit et al. [3]. The temperature near the Knudsen cell was measured using a pre-calibrated (ITS-90) chromel-alumel thermocouple. The Knudsen cell used was made of CSZ with a knife edged orifice of diameter 0.8 mm at the centre of the upper lid. A Faraday cup detector is used to collect the ions generated which is proportional to ion intensity. The ion intensity of the *i*<sup>th</sup> ion is related to partial pressure and is represented as:

$$p_i = K_{inst} \cdot (I_i^+ \cdot T) / (\sigma_i \cdot a_i) \quad (1)$$

Where,  $K_{inst}$  is the instrumental constant,  $I_i^+$  is the measured ion current in ampere,  $T$  is the absolute

temperature,  $\sigma_i$  is the electron impact cross-section and  $a_i$  is the isotopic abundance of the specific ion. Taking natural logarithm on both sides, the Eq. (1) can be written as:

$$\ln p_i = \ln K_{inst} + \ln(I_i^+ T) - \ln \sigma_i - \ln a_i \quad (2)$$

For permanent gaseous species such as CO<sub>2</sub> at mass,  $m/e = 44$ , the isotopic abundance is 100% and  $\ln \sigma_i = -45.52$  at 30 eV [4] and Eq. (2) can be expressed as

$$\ln p_i = \ln K_{inst} + \ln(I_i^+ T) + 45.52 \quad (3)$$

### 3. Results and Discussions

Background mass spectrum is recorded from  $m = 1$  amu to  $m = 50$  amu using a blank Knudsen cell with the experimental setup at different temperatures. The background spectrum of the signal in ampere as a function of  $m/e$  (mass/charge) was recorded as a function of temperature and plotted in Figure 1. The background signal of CO<sub>2</sub><sup>+</sup> at  $m/e = 44$  is  $4 \times 10^{-13}$  Ampere at highest temperature of the measurement. This shows that the contribution of background value due to empty Knudsen cell and the quartz housing in actual measurement is very low and can be neglected.

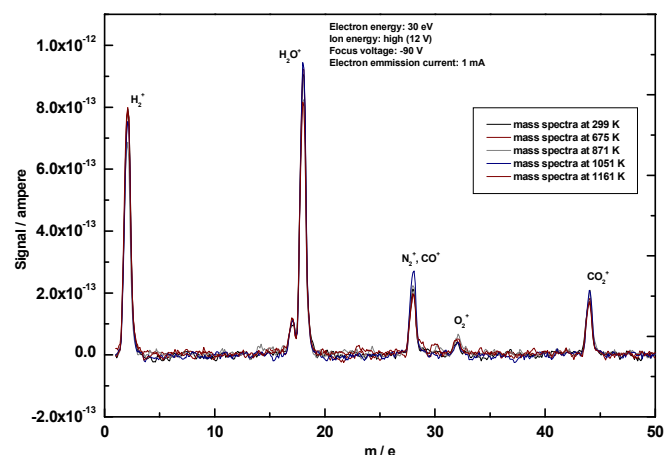


Figure 1: Background spectrum of KEQMS

### Calibration of the KEQMS experimental setup

The instrument was first calibrated to determine the instrument calibration constant using phase mixtures {Li<sub>2</sub>CO<sub>3</sub>(s) + Li<sub>2</sub>O(s)} at ionization energies 30 eV and keeping the other parameters such as emission current (1 mA), focus plate voltage (90 V) and ion energy constant for all sets of measurements. The ion intensities of CO<sub>2</sub><sup>+</sup> peak (ampere) were monitored in ampere as a function of  $m/e$  values using Faraday cup detector of RGA at various

temperatures. The instrument calibration constant was determined using literature values of  $\ln\{p(\text{CO}_2)/\text{atm}\}$  [ref],  $\ln\{\sigma(\text{CO}_2)\}$  value [5] and experimentally measured  $\ln\{I^+(\text{CO}_2) \times T\}$  values. The calculated values of  $\ln(K_{inst})$  as a function of temperature are represented in Eq.(4).

$$\ln(K_{inst}) = 3480 / (T / \text{K}) - 40.7 \quad (4)$$

Using this calibration constant, equilibrium  $p(\text{CO}_2)$  over the decomposition reaction of  $\text{CaCO}_3(\text{s})$  were calculated as a function of temperature and compared with literature values as shown in figure 2 and found to be they are in good agreement with each other.

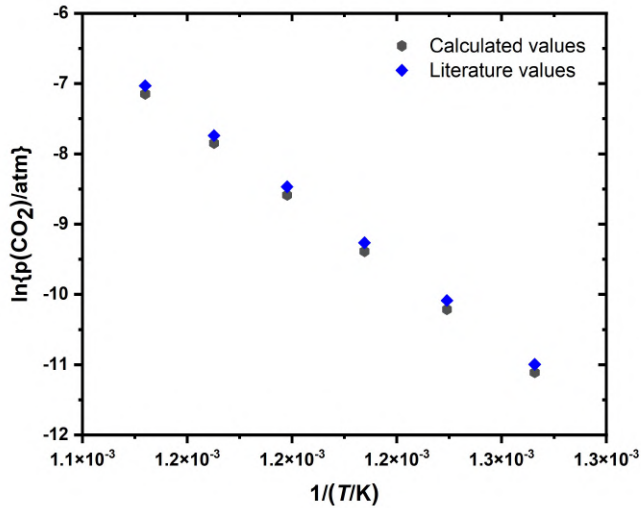


Figure 2: comparison of calculated  $p(\text{CO}_2)$  over the decomposition reaction of  $\text{CaCO}_3(\text{s})$  with literature values

### Partial pressure measurement of $\text{CO}_2(\text{g})$ over $\{\text{Li}_2\text{CO}_3(\text{s}) + \text{NiO}(\text{s})\}$

Partial pressures of  $\text{CO}_2(\text{g})$  over the above equilibrium phase mixture were determined by measuring the ion intensities of  $\text{CO}_2^+$  peak using KEQMS technique in the temperature range 830 K to 1000 K. Two such runs were carried out and the corresponding values were least square fitted as a function of temperature and is expressed as:

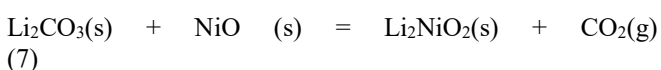
$$\ln\{I^+(\text{CO}_2)/\text{amp}\} \cdot (T/\text{K}) = -27185 (\pm 298) / (T / \text{K}) + 10.89 (\pm 0.62) \quad \{830 \leq T / \text{K} \leq 1000\} \quad (5)$$

The values in parentheses show the fitting error during least square analysis of individual data points.

Further, using the Eq.(3), (4) and (5) and  $\ln\sigma(\text{CO}_2)$  ( $= -45.52$  at 30 eV) from the literature [4],  $\ln\{p(\text{CO}_2)\}$  were calculated as a function of temperature and shown in Figure 3. Individual  $\ln\{p(\text{CO}_2)\}$  values were least square fitted against temperature for all these three runs and is expressed as:

$$\ln\{p(\text{CO}_2)/\text{atm}\} = -23705 (\pm 614) / (T / \text{K}) + 15.71 (\pm 0.78) \quad \{830 \leq T / \text{K} \leq 1000\} \quad (6)$$

The TG experiment followed by XRD analysis show that the following reaction takes place inside the Knudsen cell.



From the KEQMS experimental measurements of ion intensity of  $\text{CO}_2$ , the vapor pressure over the equilibrium phase mixture can be calculated. The Gibbs energy of the reaction for the Eq. (7) can be calculated using the Eq. (6) is expressed as:

$$\Delta_r G^\circ_m (\text{kJ} \cdot \text{mol}^{-1}) (\pm 5) = 197 - 0.131 \cdot (T / \text{K}) \quad \{830 \leq T / \text{K} \leq 1000\} \quad (8)$$

Further, Gibbs energy of the reaction from Eq. (7) can be represented as:

$$\Delta_r G^\circ = \Delta_f G^\circ_{\text{Li}_2\text{NiO}_2(\text{s})} + \Delta_f G^\circ_{\text{CO}_2(\text{g})} - \Delta_f G^\circ_{\text{Li}_2\text{CO}_3(\text{s})} - \Delta_f G^\circ_{\text{NiO}(\text{s})} \quad (9)$$

From Eq. (9), we can calculate the Gibbs energy of formation of  $\text{Li}_2\text{NiO}_2(\text{s})$  by using the Eq.(8). The Gibbs energy of formation of  $\text{CO}_2$ ,  $\text{Li}_2\text{CO}_3$  and  $\text{NiO}$  has been given in the Table 1.

Table 1: Gibbs Energy of formation of compound

Compounds	$\Delta_f G^\circ_m / \text{kJ} \cdot \text{mol}^{-1}$ (298-1100 K) [5]
NiO(s)	$-236.5 + 0.087 \cdot (T / \text{K})$
$\text{Li}_2\text{CO}_3(\text{s})$	$-1217.3 + 0.286 \cdot (T / \text{K})$
$\text{CO}_2(\text{g})$	$-393.8 + 0.002 \cdot (T / \text{K})$
$\text{Li}_2\text{O}$	$-567 + 0.173 \cdot (T / \text{K})$

The  $\Delta_f G^\circ$  of  $\text{Li}_2\text{NiO}_2(\text{s})$  as a function of temperature was found to be:

$$\Delta_f G^\circ_m(\text{Li}_2\text{NiO}_2, \text{s}, T) / \text{kJ} \cdot \text{mol}^{-1} (\pm 5) = -862.5 + 0.2445 \cdot (T / \text{K}) \quad \{830 \leq T / \text{K} \leq 1000\} \quad (10)$$

This value of Gibbs energy of formation of  $\text{Li}_2\text{NiO}_2(\text{s})$  was experimentally calculated for the first time.

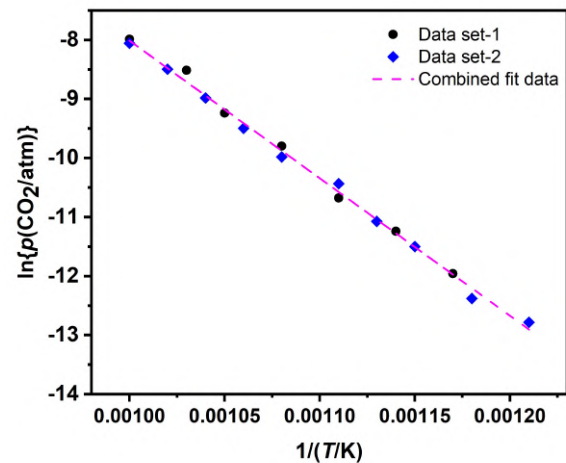


Figure 3: Partial pressure of  $\text{CO}_2(\text{g})$  as a function of temperature. The enthalpy of formation of  $\text{Li}_2\text{NiO}_2(\text{s})$  is calculated to be  $-862.5 \text{ kJ} \cdot \text{mol}^{-1}$  at the mean experimental temperature.

### Reference:

1. M.G. Kim, J. Cho, *J. Mat. Chem.* 18 (2008) 5880-5885.
2. Lee et al, *Chem. Mater.* 20 (2008), 5-7
3. Rakshit et al, *J. Sol. State Chem.*, 184. (2011) 1186-1194.
4. J.B. Mann, *J. Chem. Phys.* 46 (1967) 1646.
5. M.W. Chase, Jr. JANAF Thermochemical Tables, 4th ed., *J. Phys. Chem. Ref. Data*, Monograph No. 9 1995.

## Thermodynamic Studies on Calcium Fluorapatite Employing KEQMS

Raja Das<sup>a</sup>, Hemlata Khadilkar<sup>a</sup>, Pratik Das<sup>a,b,\*</sup>, Sanjay K. Yadav<sup>a</sup>, Swarup K. Rakshit<sup>a</sup>, Suresh C. Parida<sup>a,b</sup>, Pradeep Samui<sup>a,b,\*</sup>

<sup>a</sup>Product Development Division, Bhabha Atomic Research Centre, Mumbai-85,

<sup>b</sup>Homi Bhabha National Institute, Bhabha Atomic Research Centre, Mumbai-85,

\*pratikdas@barc.gov.in, \*psamui@barc.gov.in

### Abstract

Fluorapatite falls under the category of minerals containing phosphate and fluoride, serving as an alternative matrix for waste immobilization. They are currently considering as a potential matrix for nuclear waste immobilization of advance reactor system such as MSR application. The thermodynamic behavior of calcium fluorapatite,  $(Ca_{10}(PO_4)_6F_2)$ , particularly its thermal stability and resistance to radiation damage, is crucial for its application in this domain. Gibbs energy of formation of  $(Ca_{10}(PO_4)_6F_2)$  has been determined employing KEQMS in this study.

### Introduction

Radioactive waste consists of halides species is originated during pyrochemical reprocessing of spent nuclear fuel from advanced nuclear reactors such as molten salt reactors, metal fuel reactors, etc. Vitrification of halide waste in conventional alkali borosilicate glass is not suitable due to the low solubility of halide ions. Therefore, alternative waste form candidates is being investigated, such as fluorapatite, which can accommodate a wide variety of cations (mono-, bi- and trivalent) and anions due to its high structural flexibility. Calcium fluorapatite has attracted attention as a promising alternative to traditional borosilicate glass matrices for the immobilization of radioactive waste. The thermodynamic behavior of calcium fluorapatite, especially its thermal stability and resistance to radiation damage, is crucial for its application in this field.

Research has shown that calcium fluorapatite reveals favorable thermal expansion characteristics and maintains its structural durability under high temperatures, making it suitable for environments where thermal fluctuations are prevalent [1,2]. In this study, Gibbs energy of formation of calcium fluorapatite's  $(Ca_{10}(PO_4)_6F_2)$  has been determined to know thermal stability and its response to environmental stresses, such as temperature variations and radiation exposure. This is vital for optimizing its use in nuclear waste management and other advanced applications. The Knudsen effusion system coupled with QMS techniques has been employed for the present study.

### Materials preparation

The Calcium fluorapatite was prepared by solid state reaction at high temperature from stoichiometric mixtures of  $CaF_2$  (Merck-98%),  $CaCO_3$  (Merck-99%),  $Ca_2P_2O_7$  (Aldrich-99.9%). The homogenized mixture was gradually heated over 13 hours to a temperature of 1173 K to ensure the slow decomposition of the carbonate. Once cooled, the resulting products were finely ground using an agate mortar and subsequently sintered at 1473 K. Five cycles of grinding and sintering were performed to achieve a well crystallized apatite. Stoichiometric ratios of preheated  $CaF_2$  (Merck-98%),  $CaCO_3$  (Merck-99%),  $Ca_2P_2O_7$  (Aldrich-99.9%), and were mixed homogeneously using an agate mortar-pestle and compacted into pellets at a pressure of 5 MPa using tungsten carbide lined steel die. The pellets were broke into pieces and loaded in a Knudsen cell.

### Knudsen effusion quadruples mass spectrometry (KEQMS)

In the present work, a Knudsen effusion mass spectrometer system was developed using a residual gas analyzer (RGA; model SRS RGA 100, USA) and in-house designed vacuum chamber attached to a turbo molecular pumping station. Residual gas analyzer is based on quadruple mass spectrometer and capable to measure quite accurately the partial pressures of

permanent gases. The experimental setup has been described in detail by Rakshit et al. [3]. The temperature near the Knudsen cell was measured using a pre-calibrated (ITS-90) chromel–alumel thermocouple. The Knudsen cell used was made of CSZ with a knife edged orifice of diameter 0.8 mm at the centre of the upper lid. A Faraday cup detector is used to collect the ions generated which is proportional to ion intensity. The ion intensity of the  $i^{\text{th}}$  ion is related to partial pressure and is represented as:

$$p_i = K_{inst} \cdot (I_i^+ \cdot T) / (\sigma_i \cdot a_i) \quad (1)$$

Where,  $K_{inst}$  is the instrumental constant,  $I_i^+$  is the measured ion current in ampere,  $T$  is the absolute temperature,  $\sigma_i$  is the electron impact cross-section and  $a_i$  is the isotopic abundance of the specific ion. Taking natural logarithm on both sides, the Eq. (1) can be written as:

$$\ln p_i = \ln K_{inst} + \ln(I_i^+ T) - \ln \sigma_i - \ln a_i \quad (2)$$

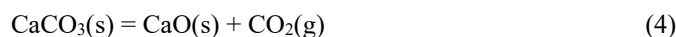
For permanent gaseous species such as  $CO_2$  at mass,  $m/e = 44$ , the isotopic abundance is 100% and  $\ln \sigma_i = -45.52$  at 30 eV [4] and Eq. (2) can be expressed as

$$\ln p_i = \ln K_{inst} + \ln(I_i^+ T) + 45.52 \quad (3)$$

### Results and Discussions

#### Calibration of KEQMS

The instrument was first calibrated using the phase mixture of  $\{CaCO_3(s) + CaO(s)\}$  at 30eV ionization energy and keeping the other ion optic parameters for RGA constant for all sets of measurements. The following equilibrium reaction was established inside the Knudsen cell.



The individual ion intensities of  $CO_2^+$  peak over the equilibrium phase mixture were recorded at different temperatures to determine the calibration constant of the instrument. The ion intensities of the two successive runs are least square fitted as a function of temperature and is expressed as:

$$\ln \{I^+(CO_2) \cdot T\} = -24752(\pm 494) / T + 1018 (\pm 0.54) \quad (760 \leq T / K \leq 900) \quad (5)$$

Thus, using the literature values of partial pressure of  $CO_2$  (g) for the above reaction (4) and the auxiliary data from literature [10], the instrument constant was determined as:

$$\ln(K_{inst}) = 1455 / T - 35.79 \quad (760 \leq T / K \leq 900) \quad (6)$$

Prior to calibration of the instrument, the background signals were also monitored by heating the Knudsen cell chamber with empty Knudsen cell at different temperatures from ambient to 1150 K at a pressure level of  $1 \times 10^{-5}$  Pa. The background signals as a function of temperature are shown in Fig. 2. It is evident from the figure that the background signals corresponding to  $H^+$ ,  $N^+$ ,  $CO^+$  and  $CO_2^+$  do not change appreciably with change in temperature. During experiments, the actual signals were obtained by subtracting the ion intensities due to background.

### Partial pressure measurement of $CO_2(g)$ over $\{3CaCO_3(s) + CaF_2(s) + 3Ca_2P_2O_7(s) + Ca_{10}(PO_4)_6F_2(s)\}$

Partial pressures of  $CO_2(g)$  over the above equilibrium phase mixture were determined by measuring the ion intensities of  $CO_2^+$  peak using KEQMS technique in the temperature range 710 K to 890 K. Two such runs were carried out and the corresponding values were least square fitted as a function of temperature and is expressed as:

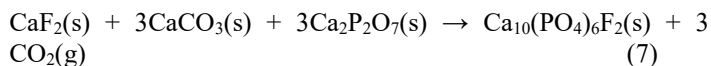
$$\ln\left[\frac{I^+(CO_2)}{\text{amp}}\right] \cdot (T/K) = -23519.5 (\pm 142) / (T / K) + 8.40 (\pm 0.15) \quad \{710 \leq T / K \leq 890\} \quad (5)$$

The values in parentheses show the fitting error during least square analysis of individual data points.

Further, using the Eq.(3), (4) and (5) and  $\ln\sigma(CO_2)$  ( $= -45.52$  at 30 eV) from the literature [4],  $\ln\{p(CO_2)\}$  were calculated as a function of temperature and shown in Figure 3. Individual  $\ln\{p(CO_2)\}$  values were least square fitted against temperature for all these three runs and is expressed as:

$$\ln\{p(CO_2)/\text{atm}\} = -21815 (\pm 247) / (T / K) + 17.85 (\pm 0.32) \quad \{710 \leq T / K \leq 890\} \quad (6)$$

The TG experiment followed by XRD analysis show that the following reaction takes place inside the Knudsen cell.



From the KEQMS experimental measurements of ion intensity of  $CO_2$ , the vapor pressure over the equilibrium phase mixture can be calculated. The Gibbs energy of the reaction for the Eq. (7) can be calculated using the Eq. (6) is expressed as:

$$\Delta_r G_m^\circ (\text{kJ}\cdot\text{mol}^{-1}) (\pm 7) = 545 - 0.445 \cdot (T/K) \quad \{710 \leq T / K \leq 890\} \quad (8)$$

Further, Gibbs energy of the reaction from Eq. (7) can be represented as:

$$\Delta_r G^\circ = \Delta_f G^\circ_{Ca_{10}(PO_4)_6F_2(s)} + 3\Delta_f G^\circ_{CO_2(g)} - 3\Delta_f G^\circ_{CaCO_3(s)} - \Delta_f G^\circ_{CaF_2(s)} - 3\Delta_f G^\circ_{Ca_2P_2O_7(s)} \quad (9)$$

From Eq. (9), we can calculate the Gibbs energy of formation of  $Li_2NiO_2(s)$  by using the Eq.(8). The Gibbs energy of formation of  $CaF_2(s)$ ,  $CO_2(g)$ ,  $CaCO_3(s)$  and  $Ca_2P_2O_7(s)$  has been given in the Table 1.

Table 1: Gibbs Energy of formation of compound

Compounds	$\Delta_f G_m^\circ / \text{kJ}\cdot\text{mol}^{-1}$ (298-1000 K) [5]
$CaF_2(s)$	$-1222.5 + 0.166 \cdot (T / K)$
$CaCO_3(s)$	$-1203.7 + 0.253 \cdot (T / K)$
$CO_2(g)$	$-393.8 + 0.002 \cdot (T / K)$
$Ca_2P_2O_7(s)$	$-3332.2 + 0.692 \cdot (T / K)$

The  $\Delta_f G^\circ$  of  $Ca_{10}(PO_4)_6F_2(s)$  as a function of temperature is expressed in Eq.(10).

$$\Delta_f G_m^\circ(Ca_{10}(PO_4)_6F_2, s, T) / \text{kJ}\cdot\text{mol}^{-1} (\pm 5) = -13101.5 + 3.451 \cdot (T / K) \quad \{710 \leq T / K \leq 890\} \quad (10)$$

This value of Gibbs energy of formation of  $Ca_{10}(PO_4)_6F_2$  was experimentally calculated for the first time.

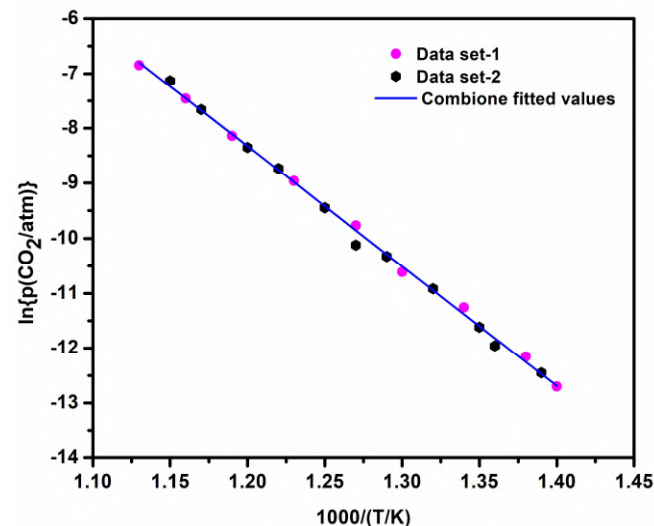


Figure 3: Partial pressure of  $CO_2(g)$  as a function of temperature over  $\{3CaCO_3(s) + CaF_2(s) + 3Ca_2P_2O_7(s) + Ca_{10}(PO_4)_6F_2(s)\}$

The enthalpy of formation of  $Ca_{10}(PO_4)_6F_2$  at the mean experimental temperature, i.e at 830 K is found to be  $-13101 \text{ kJ}\cdot\text{mol}^{-1}$ . The standard molar enthalpy of formation of  $Ca_{10}(PO_4)_6F_2$  at 298 K calculated to be  $-13695 \text{ kJ}\cdot\text{mol}^{-1}$ , which is in good agreement with the values of  $-13744 \text{ kJ}\cdot\text{mol}^{-1}$  reported in literature[1].

### Reference:

1. C. Drouet, *J. Chem. Thermodyn.*, 81(2015)143-159.
2. Pratik Das et al., *ChemistrySelect.* 6 (2021), 13817-13831
3. Rakshit et al., *J. Sol. State Chem.*, 184. (2011) 1186-1194.
4. J.B. Mann, *J. Chem. Phys.* 46 (1967) 1646.
5. M.W. Chase, Jr. JANAF Thermochemical Tables, 4th ed., *J. Phys. Chem. Ref. Data*, Monograph No. 9 1995.
6. Wagman, et al., *J. Phys. Chem. Ref. Data* 11 (1982). 1-&

## Structural and Thermodynamic Properties of ZrAl: A DFT Study

Nijith S<sup>a</sup>, D. Chattaraj<sup>b,\*</sup><sup>a,b</sup>Product Development Division, Bhabha Atomic Research Centre, Trombay, Mumbai-400085, India\* Corresponding author: [debchem@barc.gov.in](mailto:debchem@barc.gov.in), Ph-022 6929 6446**Abstract**

Zirconium-Aluminium alloys are considered to be potential structural materials for thermal nuclear reactors. Here, a comprehensive study on structural, elastic and thermodynamic properties of ZrAl has been reported using plane wave based density functional theory. The optimized lattice and internal parameters of ZrAl unit cell agree well within  $\pm 1$ -2% from the experimental values. The formation energy ( $\Delta fH$ ) of ZrAl at 0 K, after zero-point energy correction, has been estimated to be -44.93 kJ/mol. The temperature dependent thermodynamic functions of ZrAl have also been calculated from the Debye-Grüneisen quasi-harmonic approximation and reported here.

**1. Introduction**

In recent years, zirconium-aluminium (Zr-Al) alloys have drawn considerable attention as a structural material in thermal nuclear reactors due to their few favourable properties such as good mechanical strength, light weight, low absorption cross section for thermal neutrons and corrosion resistance at high temperature [1-2]. Zirconium alloys such as zircaloy-2 are in operations as clad material in the pressurized heavy water reactors (PHWRs). But, their properties at high temperature fails with longer run time of the reactors due to the embrittlement caused by hydrogen taken from coolant. Aluminium lining has been used inside the zircaloy tube to avoid such embrittlement [3]. Whether, the aluminium lining works and how long it can sustain depends on the interdiffusion of Al and Zr in the tube. In this aspect, ZrAl alloy may serve as an alternative for this purpose.

Properties of Zr-Al alloys have been studied in recent past. Murray *et al.* had done thermodynamic modeling of Zr-Al system and reported five phases in Zr-Al system i.e. Zr<sub>3</sub>Al, Zr<sub>2</sub>Al, ZrAl, ZrAl<sub>2</sub> and ZrAl<sub>3</sub> [4]. Yuan *et al.* have studied the pressure dependent thermodynamic properties of Zr<sub>2</sub>Al [2]. Recently, Kagdada *et al.* have investigated the structural, electronics and dynamical properties of binary alloy Zr-Al using density functional theory [5].

In order to understand the fundamental thermo-physical and thermo-chemical properties of ZrAl, a comprehensive computational study has been carried out using DFT formalism.

**2. Computational method**

All results reported here were calculated using Vienna ab initio simulation package (VASP), which implements Density Functional Theory (DFT) and PHONOPY code [6-7]. The quasi-harmonic Debye model was used to calculate the thermodynamic functions of the compounds. The details of Debye-Grüneisen quasi-harmonic method have already been discussed in our earlier publication [8].

**3. Results and discussion****3.1 Structural properties**

At room temperature, ZrAl posses' orthorhombic structure with space group Cmc<sub>2</sub>m (SG. 63). The experimental lattice parameters of ZrAl at 298 K and other computational data are shown in Table 1 [9, 10]. To obtain the equilibrium lattice and internal parameters, the atomic and electronic structure of ZrAl were optimized by varying the lattice parameters. The calculated lattice parameters of ZrAl, reported in Table 1, are found to differ within  $\pm 1$ -2% from the experimental and other theoretical data.

**Table 1** Experimental and calculated lattice parameters of ZrAl.

Compound	Present study	Experiment (at 298 K)	Theory (at 0 K)
ZrAl (Orthorhombic)	$a=3.36 \text{ \AA}$ , $b=10.94 \text{ \AA}$ , $c=4.29 \text{ \AA}$ , $V_0=158.06 \text{ \AA}^3$	$a=3.36 \text{ \AA}$ , $b=10.89 \text{ \AA}$ , $c=4.27 \text{ \AA}$ , $V_0=156.30 \text{ \AA}^3$ [9]	$a=3.36 \text{ \AA}$ , $b=10.96 \text{ \AA}$ , $c=4.29 \text{ \AA}$ , $V_0=157.98 \text{ \AA}^3$ [10]

**3.2 Thermodynamic Properties**

From the total energy calculations, the enthalpy of formation of ZrAl at 0 K is estimated to be -44.93 kJ/mol including zero-point energy. The calculated enthalpy of formation of zero-point energy (at 0 K) is good in agreement with the reported experimental values of  $-53 \pm 4$  kJ/mol [11] (at 298 K). The calculated value is also in good resemblance with others theoretical values [3].

The total DOS at Fermi level of a compound is an important parameter using which electronic contribution to the specific heat can be derived. The coefficient of the electronic specific heat ( $\gamma$ ) is calculated as

$$\gamma = \left(\frac{\pi^2}{3}\right) \cdot k_B^2 \cdot n(\epsilon_F)$$

(1)

where,  $k_B$  is the Boltzmann's constant and  $n(\epsilon_F)$  is the density of states at Fermi level. The calculated total DOS of ZrAl at the Fermi level is  $N(E_F) = 2.46$  states per eV-f.u. From this, the coefficient of electronic specific heat  $\gamma$  is estimated to be 5.78 mJ/ mol-K<sup>2</sup>.

In thermal reactors, a heat transfer phenomenon is associated between fuel and coolant through clad. The thermodynamic properties of the structural materials of thermal nuclear reactors are very important for their selection for various components as well as for the design of the thermal reactor. However, lack of comprehensive thermal data of such a structural material ZrAl has become the driving force of this study. The thermal properties of solids like thermal expansion, thermal conductivity, specific heat, thermal diffusion, electron-phonon interactions etc can be obtained from phonon calculations. In this study, the thermal properties are determined in the temperature range from 0 to 1000 K within GGA approximation, where the harmonic model remains fully valid. The thermal expansion coefficient ( $\alpha$ ) can be obtained from the temperature derivative of lattice constant. The variations of thermal expansion coefficient ( $\alpha$ ) with temperature at zero pressure for ZrAl have been calculated using the Debye-Grüneisen quasi-harmonic model and shown in Fig. 1(a). In the  $\alpha$ -T graph, it is seen that at zero pressure,  $\alpha$  increases exponentially with T at low temperatures and gradually attains a constant value at higher temperatures. In this study, calculated thermal expansion coefficient ( $\alpha$ ) of ZrAl is  $5.32 \times 10^{-6}$  (K<sup>-1</sup>) at 300 K and zero pressure. The temperature dependent thermodynamic functions of ZrAl, such as internal energy ( $E$ ),

Helmholtz free energy ( $F$ ), entropy ( $S$ ), enthalpy increments ( $H_T^0 - H_{298}^0$ ) and heat capacities ( $C_p$  and  $C_v$ ) are also calculated using the Debye-Grüneisen quasi-harmonic approximation. The variation of  $E$ ,  $F$ ,  $S$ , ( $H_T^0 - H_{298}^0$ ),  $C_v$  and  $C_p$  with temperature  $T$  are shown in Fig. 1(b-f) up to 1000 K, which is below the melting point of ZrAl (1548 K). Fig. 1(c) shows that the free energy ( $F$ ) of ZrAl decreases gradually with increase in temperature. In contrast, the internal energy  $E$  and entropy  $S$  increases with increase in temperature as shown in Fig. 1(b) and (d). The Helmholtz free energy (Fig. 1(c)) and entropy (Fig. 1(d)) graphs resembles well with those reported by Duan *et al.* [2].

We have also calculated the enthalpy increments and heat capacities of ZrAl which are interesting parameters to understand the thermodynamic stability and heat conduction of solids. The temperature dependence of enthalpy increments ( $H_T^0 - H_{298}^0$ ) and heat capacity ( $C_v$ ) of ZrAl are shown in Fig. 4(e) and 4(f), respectively. Fig. 4(e), shows almost linear dependency of enthalpy increments ( $H_T^0 - H_{298}^0$ ) with temperature within the range 298-1000 K. In Fig. 4(f) it is seen that at low temperature, upto 200 K, the heat capacity increases rapidly with increase in temperature and thereafter increases slowly up to 400 K, and attain the saturation value of  $\sim 50$  J/mol.K. This is the Dulong-Petit classical limit. For solids, the relation between  $C_p$  and  $C_v$  is

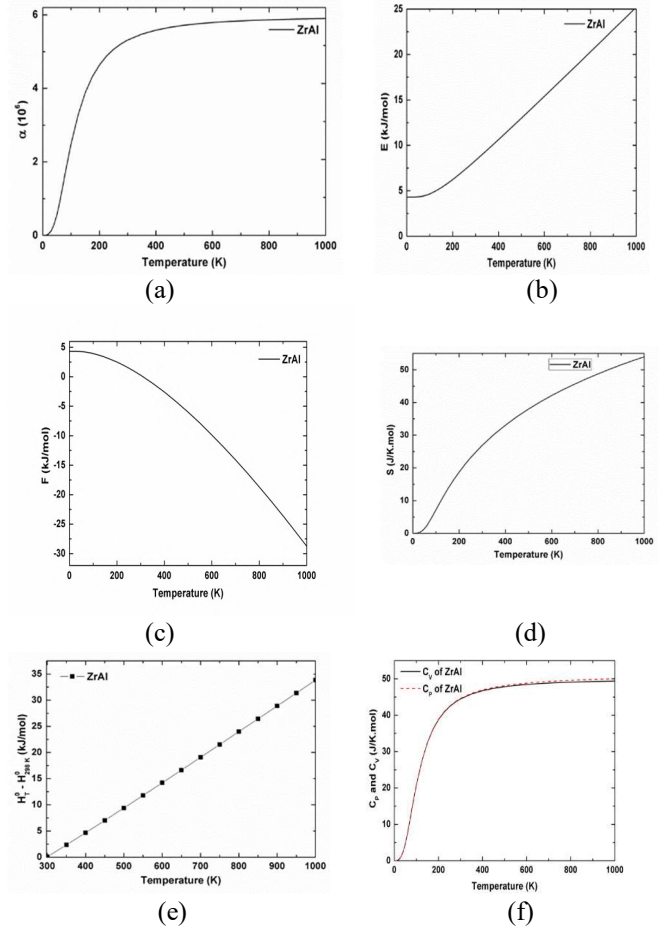
$$C_p - C_v = \alpha^2 TVB \quad (2)$$

where  $\alpha$  is the thermal expansion coefficient,  $T$  is temperature,  $V$  is the molar volume, and  $B$  is the bulk modulus of the system. Fig. 4(f) shows the heat capacities ( $C_v$  and  $C_p$ ) of ZrAl and depicts that  $C_v$  and  $C_p$  values are same up to 400 K and after that  $C_p$  values go away from the  $C_v$  values as temperature increases. This is because of the  $\alpha(T)^2$  term present in equation (2). It is reported that the difference between  $C_p$  and  $C_v$  is on the order of few percent of  $C_v$  [12]. The calculated enthalpy increment ( $H_T^0 - H_{298}^0$ ) and heat capacity ( $C_p$ ) of ZrAl as a function of temperature ( $T$ ) are given in table 2. The calculated values of heat capacity ( $C_v$ ) have been compared with the reported computational data [13] and found to be in good agreement with each other.

**Table 2** Calculated enthalpy of increment ( $H_T^0 - H_{298}^0$ ) and heat capacity ( $C_p$ ) values of ZrAl.

T (K)	( $H_T^0 - H_{298}^0$ ) (kJ/mol)	( $C_p$ ) (J/mol.K)
298	0	44.56
300	0.09	44.63
400	4.66	46.97
500	9.40	48.14
600	14.22	48.83
700	19.08	49.27
800	23.98	49.59
900	28.90	49.82
1000	33.83	50.01

**Fig.1** Temperature dependent thermodynamic functions of ZrAl. (a) linear thermal expansion coefficient ( $\alpha$ ) (b) internal energy ( $E$ ) (c) Helmholtz free energy ( $F$ ) (d) entropy ( $S$ ) (e) enthalpy increment ( $H_T^0 - H_{298}^0$ ) (f) heat capacities ( $C_p$  and  $C_v$ ) as function of  $T$ .



## 4. Conclusions

The structural and thermodynamic properties of ZrAl have been comprehensively studied using the first principles method. The calculated equilibrium structural parameters of the compound agree well with reported experimental values. The enthalpy of formation of ZrAl at 0K has been calculated with the zero-point energy contributions. The linear thermal expansion coefficient, internal energy, Helmholtz free energy, entropy, enthalpy increments and heat capacities ( $C_v$  and  $C_p$ ) of ZrAl are calculated as a function of temperature. The calculated values of ( $H_T^0 - H_{298}^0$ ) and  $C_p$  are found to be in good agreement with the previous experimental data. The thermodynamic data calculated in this study will be useful for screening of the structural material and designing of structural components in thermal nuclear reactors.

## References

1. X.L. Yuan, D.Q. Wei, Y. Cheng, J. At. Mol. Sci., 3 (2012) 160.
2. Y.H. Duan, B. Huang, Y. Sun, M.J. Peng, S.G. Zhou, J. Alloys Compd. 590 (2014) 50.
3. E.M. Schulson, M.J. Stewart, Metall. Trans. B, 7 (1976) 363.
4. J. Murray, A. Peruzzi, J.P. Abriata, J. Phase Equilibria 13 (1992) 277.
5. H.L. Kagdada, H. J. Trivedi, S.B. Pillai, N.N. Som, P.K. Jha, Advanced Materials Research, 1141 (2016) 204.
6. G. Kresse, J. Hafner, Phys. Rev. B, 49 (1994) 14251–14269.
7. A. Togo, F. Oba and I. Tanaka Phys. Rev. B 78 (2008) 134106.
8. D. Chattaraj, C. Majumder, Smruti Dash, J. Alloys Compd. 615 (2014) 234.
9. F.J. Spooner, C.G. Wilson, Acta Crystallogr. 15 (1962) 621.
10. A. Laik, K. Bhanumurthy, G.B. Kale, Intermetallics. 12 (2004) 69.
11. R.J. Kematic, H.F. Franzen, J. Solid State Chem. 54 (1984) 226.
12. X. Ke, I. Tanaka, Phys. Rev. B 71 (2005) 024117–024132.
13. L. Wang, S. Hou, D. Liang, Int. J. Mod. Phys. C. 26 (2015)1550143 (1-12).



# Thermodynamic Properties of $\text{Li}_2\text{BeF}_4$ near Melting Point: A DFT Study

J. Pareek<sup>a</sup>, D. Chattaraj<sup>b,\*</sup>

<sup>a,b</sup>Product Development Division, Bhabha Atomic Research Centre, Trombay, Mumbai-400085, India

\* Corresponding author: [debchem@barc.gov.in](mailto:debchem@barc.gov.in), Ph-022 6929 6446

## Abstract

The  $\text{LiF-BeF}_2$  system has attracted a potential application as heat transfer medium in molten salt reactors (MSRs) applications. Here we report an *ab-initio* study on structural, and thermodynamic properties of  $\text{LiF}$  and  $\text{Li}_2\text{BeF}_4$  using plane wave-based density functional theory. The optimized lattice parameters of  $\text{Li}_2\text{BeF}_4$  unit cell agree well within  $\pm 1\%$  from the experimental values. The formation energy ( $\Delta_f H$ ) of  $\text{Li}_2\text{BeF}_4$  at 0 K, after zero-point energy correction, has been estimated to be  $-992$  kJ/mol. The temperature dependent thermodynamic functions of  $\text{Li}_2\text{BeF}_4$  have also been calculated from the Debye-Grüneisen quasi-harmonic approximation.

## 1. Introduction

Now a days, next-generation nuclear reactors are drawing considerable attention worldwide. Among such reactors, one is molten salt reactor (MSR) where molten fluoride salts are being considered both as primary coolant and as solvent for nuclear fuel. Lithium tetrafluoroberyllate ( $\text{Li}_2\text{BeF}_4$ ) salt also known as FLiBe, with a mixture of  $\text{LiF}$  and  $\text{BeF}_2$  is one of the fluoride salts that have been extensively used in MSR experiments(s) as coolant and solvent for fissile material due to its advantageous thermophysical and thermochemical properties [1,2]. Few unique properties such as small thermal neutron absorption cross-section, high thermal efficiency, low spent fuel per unit energy, high degree of passive safety, high heat capacity, suitable atmospheric pressure operation, chemical stability at high temperature. low melting point and high boiling point makes  $\text{Li}_2\text{BeF}_4$  a primary candidate for application in MSR [3-4].

$\text{Li}_2\text{BeF}_4$  or FLiBe has a melting point of  $\sim 732$  K and boiling point of  $1703$  K [5]. The liquid salt is a good solvent for nuclear fuel and it can dissolve high concentration of (Th+U) fuel. Apart from that, FLiBe can also be used as a good tritium breeder material in fusion reactors because of its high chemical stability [6]. Thus, a comprehensive information regarding the structural and temperature-dependent thermodynamic properties of  $\text{Li}_2\text{BeF}_4$  is crucial for its application in MSR and other projects.

Here, in this paper, structural and thermodynamic properties of  $\text{Li}_2\text{BeF}_4$  along with its constituent fluoride compound  $\text{LiF}$  have been studied up to its melting point studied using Debye-Grüneisen quasi-harmonic approximation (QHA). The calculated properties of the compound provide comprehensive thermodynamic data which will be useful for experimental understanding.

## 2. Computational details

All results reported here were calculated using Vienna *ab initio* simulation package (VASP), which implements Density Functional Theory (DFT) and PHONON code [7-8]. The plane wave based pseudo-potential method has been used for the total energy calculations. The electron-ion interaction and the exchange correlation energy were described under the Projector-augmented wave (PAW) method and the generalized gradient approximation (GGA) of Perdew–Burke–Ernzerhof (PBE) scheme, respectively. All-electronic projector-augmented wave potentials were employed for the elements Li, Be and F. The energy cut off for the plane wave basis set was fixed at  $500$  eV. Total energies for each relaxed structure using the linear tetrahedron method with Blöchl corrections were subsequently calculated in order to eliminate any broadening-related uncertainty in the energies. Ground state atomic geometries were obtained by minimizing the Hellman-Feynman forces using the conjugate gradient method. The force on each ion was minimized upto  $5$  meV/Å. In order to verify the magnetic nature of the systems studied in this work, we have performed the total energy calculations using the spin polarized version of the DFT. The k-point meshes were constructed using

the Monkhorst-Pack scheme and the  $9 \times 9 \times 9$  k-point mesh was used for the primitive cell for Brillouin zone sampling. The quasi-harmonic Debye model was used to calculate the thermodynamic functions of the compound.

## 3. Results and discussion

### 3.1 Structural properties

At room temperature,  $\text{Li}_2\text{BeF}_4$  exhibits rhombohedral structure with space group R-3 (148). The unit cell crystal structure of  $\text{Li}_2\text{BeF}_4$  (s) is shown in Fig.1.

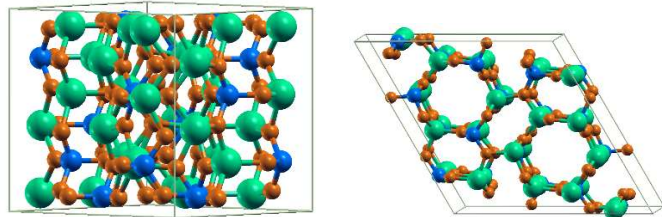


**Fig.1** Optimized unit cell of  $\text{Li}_2\text{BeF}_4$ (s) in two different orientations (Li = green, Be = blue, and F = orange).

The experimental lattice parameters of  $\text{LiF}$  and  $\text{Li}_2\text{BeF}_4$  are reported in Table 1 [9-10]. To obtain the equilibrium structural parameters, the atomic and electronic structure of  $\text{LiF}$  and  $\text{Li}_2\text{BeF}_4$  were optimized by varying the lattice parameters. The calculated lattice parameters listed in Table 1 are found to differ by less than  $\pm 1\%$  from the experimental data. A very good agreement between the calculated and experimental values of the structural parameters for  $\text{LiF}$  and  $\text{Li}_2\text{BeF}_4$  establishes the reliability and accuracy of the present computation method.

**TABLE 1.** Experimental and calculated lattice parameters of  $\text{Li}_2\text{BeF}_4$ .

Compound	Present study	Expt. [Ref]	Theory [Ref]
$\text{LiF}$	$a = b = c =$ $4.722 \text{ \AA},$	$a = b = c =$ $4.661 \text{ \AA},$	$a = b = c =$ $4.52 \text{ \AA},$
	$V_0 = 242.75 \text{ \AA}^3$	$V_0 = 236.32$ $\text{ \AA}^3$ [9]	$V_0 = 23.07 \text{ \AA}^3$ [10]
$\text{Li}_2\text{BeF}_4$	$a = 13.28 \text{ \AA},$ $b = 13.28 \text{ \AA},$ $c = 8.89 \text{ \AA},$ $V_0 = 1406.30 \text{ \AA}^3$ $\rho = 2.11$	$a = 13.28 \text{ \AA},$ $b = 13.28 \text{ \AA},$ $c = 8.89 \text{ \AA},$ $V_0 = 1357.70$ $\text{ \AA}^3$ $\rho = 2.18$ [9]	$a = 13.45 \text{ \AA},$ $b = 13.45 \text{ \AA},$ $c = 8.99 \text{ \AA},$ $V_0 = 408.73 \text{ \AA}^3$ $\rho = 2.14$ [10]

### 3.2 Thermodynamic properties

In molten salt reactor, a heat transfer phenomenon is associated between the fuel and coolant, containing the fluoride salts. The thermodynamic properties of the fluoride salts are very important for the selection as fuel and coolants as well as for the design of the fusion reactor. In this study, the thermal properties such as specific heat and entropy of  $\text{LiF}$  are determined in the temperature range from  $0$  to  $1000$  K within GGA approximation,

**Fig.2** Temperature dependent thermodynamic functions of (a) heat capacities ( $C_P$  and  $C_V$ ) as function of T (b) entropy ( $S$ ) of LiF.

#### 4. Conclusions

The structural and thermodynamic properties of  $\text{Li}_2\text{BeF}_4$  (s) have been studied using the first principles method. The calculated equilibrium lattice parameters of the compound LiF (s) and  $\text{Li}_2\text{BeF}_4$  (s) agree well with the experimental values. The enthalpy of formation of  $\text{Li}_2\text{BeF}_4$  (s) at 0 K has been calculated with the zero-point energy contributions. The entropy ( $S$ ), heat capacity ( $C_V$ ), internal energy ( $E$ ) and Helmholtz free energy ( $F$ ) of  $\text{Li}_2\text{BeF}_4$  (s) are calculated as a function of temperature. The thermodynamic data calculated in this study will be useful for screening of the fuel and coolant salt for MSR and designing of molten salt reactor.

#### Acknowledgments

The authors are thankful to Dr. S.C. Parida, Head, PDD, RC&IG, Bhabha Atomic Research Centre (BARC), Dr. S.K. Rakshit, Head, FDCS, BARC for their interest and helpful discussions during progress of this work. The authors are also thankful to the members of the Computer Division, BARC, for their kind cooperation during this work.

#### References

1. D.-K. Sze, M.E. Sawan, E.T. Cheng, Fusion Technol., 39 (2001) 789.
2. A. Suzuki, T. Terai, S. Tanaka, J. Nucl. Mater. 258–263 (1998) 519.
3. S. Delpech, C. Cabet, C. Slim, G.S. Picard, Mater. Today, 13 (2010) 13.
4. A. Suzuki, T. Terai, S. Tanaka, J. Nucl. Mater., 258 (1998) 519.
5. G. Zheng, L. He, D. Carpenter, K. Sridharan, J. Nucl. Mater., 482 (2016) 147–155.
6. A.L. Rollet, M. Salanne, Annu. Rep. Prog. Chem., Sect. C: Phys. Chem., 107 (2011) 88.
7. G. Kresse, J. Hafner, Phys. Rev. B, 49 (1994) 14251–14269.
8. A. Togo, F. Oba and I. Tanaka Phys. Rev. B 78 (2008) 134106.
9. P. Seiler, Acta Crystallogr., Sect. B: Struct. Sci., 49 (1993) 223.
10. K. Baral, S. San, R. Sakidja, A. Couet, K. Sridharan, W.Y. Ching, ACS Omega, 6 (2021) 19822.
11. X. Ke, I. Tanaka, Phys. Rev. B 71 (2005) 024117–024132.

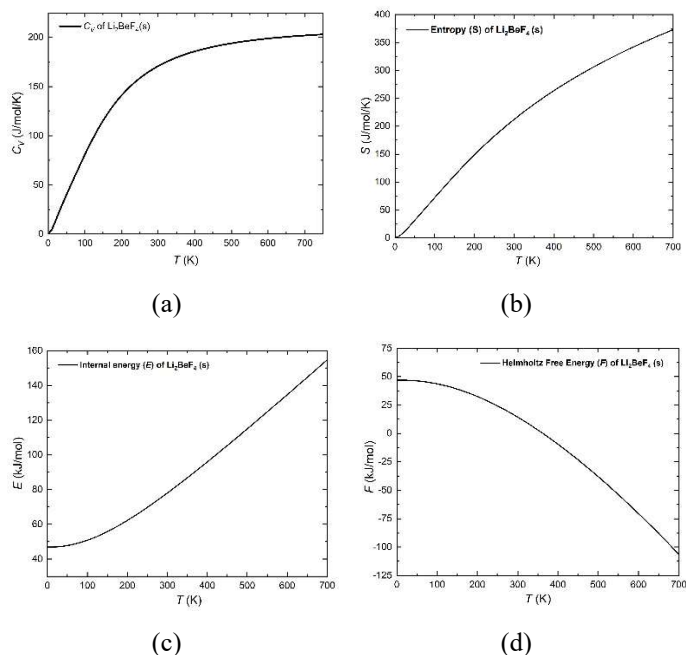
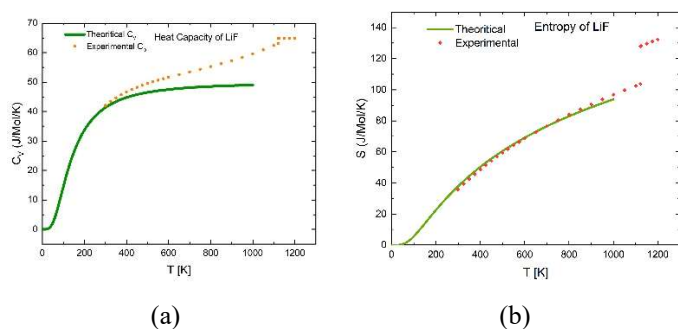


**Fig.3** Temperature dependent thermodynamic functions of  $\text{Li}_2\text{BeF}_4$ (s). (a) heat capacity ( $C_V$ ) (b) entropy ( $S$ ) (c) internal energy ( $E$ ) (d) Helmholtz free energy ( $F$ ) as function of T.

where the harmonic model remains fully valid (Fig. 2 (a-b)). A good agreement between the experimental  $C_P$  and calculated  $C_V$  upto 300 K and entropy( $S$ ) upto 1000 K for LiF provides accuracy of the calculation though at there is a difference between  $C_P$  and  $C_V$  above 300 K [11]. The enthalpy of formation of  $\text{Li}_2\text{BeF}_4$  (s) at 0 K has been calculated from the total energy and is found to be -992 kJ/mol.

In this study, the temperature dependent thermodynamic functions of  $\text{Li}_2\text{BeF}_4$ , such as heat capacities ( $C_V$ ), entropy ( $S$ ), internal energy ( $E$ ) and Helmholtz free energy ( $F$ ) are calculated using the Debye-Grüneisen quasi-harmonic approximation and shown in Fig. 3(a-d) up to 700 K, which is below the melting point of  $\text{Li}_2\text{BeF}_4$  (737 K). It is found that the entropy  $S$  increases with increase in temperature as shown in Fig. 3 (b).

We have also calculated the heat capacities of  $\text{Li}_2\text{BeF}_4$  which is an interesting parameter to understand the thermodynamic stability and heat conduction of solids. The temperature dependence of heat capacity ( $C_V$ ) of  $\text{Li}_2\text{BeF}_4$  is shown in Fig. 3(a). It is seen that at low temperature, upto 300 K, the heat capacity increases rapidly with increase in temperature and thereafter increases slowly up to 600 K, and attain the saturation value of ~200 J/mol.K after that. There will a difference between experimentally measured  $C_P$  and our calculated  $C_V$  specially at high temperature (above 300 K). This is because of the  $\alpha(T)^2$  term present in equation  $C_P - C_V = \alpha^2 T V B$ . It is reported that the difference between  $C_P$  and  $C_V$  is on the order of few percent of  $C_V$  [11].



High temperature mass spectrometric studies on <Nd<sub>3</sub>Al<sub>11</sub>> + NdAl<sub>3</sub>> of Nd-Al system

P. Manikandan\*, S. Nedumaran, R.Kumaresan, Hrudananda Jena

Materials Chemistry &amp; Metal Fuel Cycle Group, IGCAR.

\* Corresponding author: manikandan@igcar.gov.in

**Abstract:** In the present study, high temperature mass spectrometric studies on <Nd<sub>3</sub>Al<sub>11</sub> + NdAl<sub>3</sub>> two phase region of Nd-Al system were carried out in the temperature range 1198-1411 K using Knudsen Effusion Mass Spectrometer (KEMS). Al<sup>+</sup> was the only ionic species observed in the mass spectrum of the equilibrium vapour over the above two phase region. Al(g) was ascertained to be the corresponding neutral precursor of the ionic species. From the temperature dependence of partial pressures of Al(g) over the above two phase region, the mean enthalpy change of decomposition of Nd<sub>3</sub>Al<sub>11</sub> (Nd<sub>3</sub>Al<sub>11</sub>(s) = 3NdAl<sub>3</sub>(s) + 2Al(g)) was obtained to be 591.4±12.0 kJ. mol<sup>-1</sup> and the Gibbs energy change of the reaction was deduced to be  $\Delta_r G_T^\circ = (598.8 \pm 5.63) - (0.19 \pm 0.004) T$  kJ. mol<sup>-1</sup> (1198-1411 K)

Aluminum is considered as an alternative cathode material to cadmium in pyrochemical reprocessing of the metallic spent fuel and is effective in mutual separation of actinides from lanthanides [1]. In general, the knowledge of thermodynamic properties of intermetallic compounds of Ln and An with aluminum is considered a very useful tool since these data will allow modelling pyrochemical separation process envisaged [2]. In the present study, the high temperature vaporisation studies over <Nd<sub>3</sub>Al<sub>11</sub> + NdAl<sub>3</sub>> two phase region of Nd-Al system have been conducted to determine the thermodynamic properties of decomposition reaction involving Nd<sub>3</sub>Al<sub>11</sub>

Nd-Al samples with the compositions (78 and 77 at.% Al) and lying in <Nd<sub>3</sub>Al<sub>11</sub> + NdAl<sub>3</sub>> two phase region were prepared by arc melting appropriate amounts of Nd and Al required for each composition. About 1 g of sample was prepared for each composition. The samples were sealed in quartz tubes under vacuum and annealed at 1073 K for 7 days. They were characterized by XRD to ascertain the phases present.

High temperature vaporisation experiments over these samples were carried out by employing Knudsen effusion Mass spectrometer. The details of KEMS are described elsewhere [3]. Totally two lots of samples from two compositions were used. About 500 mg from each lot was loaded in a zirconia crucible (Knudsen cell) having a knife edged orifice of 0.5 mm in diameter located at the center of its lid. The Knudsen cell was placed into another tantalum outer cup having a black body hole provided at its bottom. The samples were heated by electron bombardment (EB) furnace located in the bottom chamber of the KEMS. The samples were heated to 1000 K in steps of 100 K and subsequently in steps of 25 K from there onwards. The temperatures were measured by sighting a disappearing filament pyrometer onto the black body hole. At each temperature above 1000 K, the sample was maintained for 30 min and the mass spectrum of the equilibrium vapour over the samples inside the Knudsen cell effusing to the ion source was recorded using Quadrupole Mass Spectrometer (QMS) housed in the chamber which is located above the chamber housing EB furnace. The vapour emanating out of the orifice is ionised in the ion source, mass analysed by QMS and detected by SEM operating in pulse counting mode. The first lot of the samples was used in identifying the ionic species generated from the equilibrium vapour, the corresponding neutral precursors and the temperature range over which meaningful vaporisation study can be performed. Al<sup>+</sup> was observed to be the ionic species in the mass spectrum of the equilibrium vapour. Subsequently, the ionisation efficiency curve was recorded at the mass number of 27 by measuring the ion intensity of <sup>27</sup>Al<sup>+</sup> as a function of electron energy. The

temperature dependence of intensity of <sup>27</sup>Al<sup>+</sup> was carried out in the temperature range 1198-1411 K using electrons of 13.8 eV with the emission current of 100 μA. The pressure calibration constant needed for converting intensity of partial pressure was obtained from the experiments carried out with pure Al loaded in the same crucible used over the samples.

XRD patterns of the freshly prepared and post KEMS samples revealed that they consist of Nd<sub>3</sub>Al<sub>11</sub> and NdAl<sub>3</sub>. Al(g) was found to be corresponding neutral precursor of Al<sup>+</sup> from the IE curve. The intensity (I) of <sup>27</sup>Al<sup>+</sup> was converted to p(Al) using the equation given below.

$$p_{Al} = k'_{Al} \cdot I \cdot T \quad (1)$$

where  $k'_{Al} = k/(\sigma n)_{Al}$ ;  $k'_{Al}$  = pressure calibration constant of Al(g); k = instrument constant; σ = ionisation cross section of Al(g); n = isotopic abundance of <sup>27</sup>Al (the only isotope); γ = multiplier yield of SEM which is equal to 1 for the KEMS employed in the present study since the detector is operated in pulse counting mode.

**Table 1: Partial pressure – Temperature relation for Al(g) over <Nd<sub>3</sub>Al<sub>11</sub>+ NdAl<sub>3</sub>> two phase region**

S.No	Run	T/K	log(p <sub>Al</sub> /Pa) =		*p <sub>Al</sub> /Pa x 10 <sup>3</sup>	
			A	B		
Nd-78at% Al	lot1	1	1203-1312	15485±152	9.83±0.12	9.21
		2	1203-1315	15508±225	9.84±0.18	9.05
		3	1222-1355	15457±247	9.75±0.20	8.05
	lot2	1	1220-1357	15346±276	9.68±0.21	8.33
		2	1198-1343	15303±274	9.63±0.21	8.01
		3	1248-1405	15577±361	9.90±0.27	9.20
Nd-77at% Al	lot 1	1	1256-1411	15547±269	9.94±0.20	10.6
		2	1294-1405	15434±507	9.76±0.37	8.57
		3	1224-1361	15326±239	9.72±0.18	9.46
	Overall		1198-1411	15638±147	9.94±0.11	9.08
	Pure Al [4]		m.p -1800	16211	10.92	31.2

\* middle temperature of the overall temperature range = 1305 K

n = isotopic abundance of <sup>27</sup>Al(g).

Overall, nine runs of temperature dependence of partial pressures of Al(g) over the samples were carried out in the temperature range 1198 -1411 K. p(Al) data from each run

were least squares fitted to the temperature to get the partial pressure temperature relation (p-T) for that run. The recommended p-T relation was obtained by using the data from all the nine runs employing least squares fitting. The plot of logarithmic values of p(Al) against the reciprocal of temperature is depicted in Fig. 1. The individual and recommended p-T relations are provided in Table 1. The above

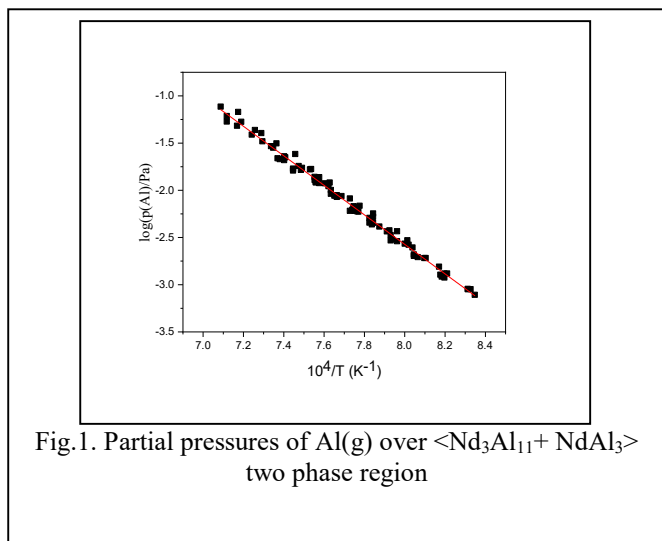
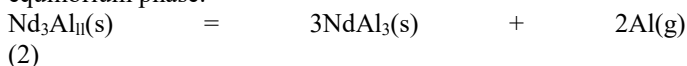


Fig.1. Partial pressures of Al(g) over <Nd<sub>3</sub>Al<sub>11</sub>+ NdAl<sub>3</sub>> two phase region

recommended relation was found to correspond to the reaction given below based on the phases present in the samples before and after KEMS studies and neutral species present in the equilibrium phase.



The p-T relation of each run was converted to the equilibrium constant temperature (K -T) relation using the relation given below.

$$K = p_{\text{Al}}^2 \text{ (atm}^2\text{)} \quad (3)$$

K-T relations thus obtained are shown in Table 2. In addition, the recommended K-T relation was deduced from the K values from all the runs.

The relation thus obtained is

$$\log(K) = -(31274 \pm 294)/T + (9.87 \pm 0.22) \quad (4)$$

**Table 2 Equilibrium constant (K) – Temperature relation for Al(g) over <Nd<sub>3</sub>Al<sub>11</sub>+ NdAl<sub>3</sub>> two phase region**

S.No	T/K	log(K/atm <sup>2</sup> ) = -A/T+ B Nd <sub>3</sub> Al <sub>11</sub> (s) = 3NdAl <sub>3</sub> (s) + 2Al(g)		$\Delta_r H_f^{\circ}$ (kJ. mol <sup>-1</sup> )
		A	B	
Nd-78at %Al	lot1			
	1203-1312	30970±30 4	9.65±0.24	593.0±5.8
	1203-1315	31016±45 0	9.67±0.36	593.9±8.6
	1222-1355	30914±49 4	9.49±0.40	591.9±9.5
lot2	1220-1357	30692±55 2	9.35±0.42	587.7±10.6
	1198-1343	30606±54 8	9.25±0.42	586.0±10.5
	1248-1405	31154±72 2	9.79±0.54	596.5±13.8

Nd-77at %Al				
lot 1	1256-1411	31094±53 8	9.87±0.40	595.3±10.3
	1294-1405	30868±10 14	9.51±0.36	591.0±19.4
	1224-1361	30652±47 8	9.43±0.36	586.9±9.2
Overall 1	1198-1411	31274±29 4	9.87±0.22	591.4±12.0

From the slope of the individual run, the enthalpy change of the above reaction was calculated. The mean enthalpy change of the reaction was calculated by averaging the individual enthalpy values and is 591.4±12.0 kJ. mol<sup>-1</sup> which corresponds to the middle temperature of the temperature range (1305 K).

In addition, the Gibbs energy change of the reaction was deduced from the overall pressure temperature of Al(g) by employing the equation given below:

$$\Delta_r G_T^{\circ} = -RT \ln(K) \quad (5)$$

The relation thus obtained is

$$\Delta_r G_T^{\circ} = (598.8 \pm 5.63) - (0.19 \pm 0.004) T \text{ kJ. mol}^{-1} \text{ (1198-1411 K)} \quad (6)$$

#### References:

1. O. Conocar, N. Douyere, J. Lacquement, J. Nucl. Mater. 344 (2005) 136
2. G. DeCórdob, A. Laplace, O. Conocar, J. Lacquement, C. Caravaca, Electrochimica Acta, 54 (2008) 280
3. D. Darwin Albert Raj, R. Viswanathan, P. Manikandan. ECS Trans. 46 (1) (2013)77.
4. C.B. Alcock, V.P. Itkin, M.K. Horrigan, Can. Metall. Q. 23 (1984) 309

Enthalpy increment of  $\text{Na}_{0.5}\text{Bi}_{0.5}\text{TiO}_3$  by drop calorimetryChinmay Routray<sup>a,\*</sup>, T. Muthu Ambika<sup>a</sup>, Chita Ranjan Patra<sup>a</sup>, Sajal Ghosh<sup>a</sup> and Rajesh Ganesan<sup>a,b</sup><sup>a</sup>Materials Chemistry and Metal Fuel Cycle Group, Indira Gandhi Centre for Atomic Research, Kalpakkam 603102, India<sup>b</sup>Homi Bhabha National Institute, Mumbai 400085, India

\* chinmay@igcar.gov.in

**Abstract**

The enthalpy increment of  $\text{Na}_{0.5}\text{Bi}_{0.5}\text{TiO}_3$  (NBT) was determined in the temperature range 473–973 K using drop calorimetry. NBT was synthesized via solid-state route, and its phase purity was confirmed by powder X-ray diffraction. Scanning electron microscopy coupled with energy dispersive spectroscopy indicated that the composition closely matched the expected stoichiometry. Thermogravimetric analysis up to 1573 K showed no mass loss before melting at 1523 K. The enthalpy increment was measured by drop calorimetry in the range 473–973 K and fitted with an in-house developed Python code. Thermodynamic properties, such as specific heat capacity, entropy, and Gibbs energy function, were also derived from the enthalpy increment data.

Sodium bismuth titanate ( $\text{Na}_{0.5}\text{Bi}_{0.5}\text{TiO}_3$ , NBT) is a promising lead-free ferroelectric perovskite material. It has garnered considerable interest as an environmentally friendly alternative to lead-based ceramics, particularly for capacitors, sensors, and actuators. It possesses a high remnant polarization and a Curie temperature of 320 °C [1].

Despite its potential, the thermodynamic properties of NBT, are not well characterized, which limits its broader application in high-temperature environments. This study aims to add essential thermodynamic data on NBT by measuring its enthalpy increment and calculating related properties such as heat capacity, entropy and Gibbs energy function.

NBT was prepared via a solid-state route using  $\text{Na}_2\text{CO}_3$ ,  $\text{Bi}_2\text{O}_3$ , and  $\text{TiO}_2$  in stoichiometric amounts. The mixture was ball-milled in tungsten carbide media with ethanol for 12 hours, dried, calcined at 700 °C for 2 hours, then milled for another 4 hours. Pellets (4.5 mm diameter, 3 mm height) were made using polyvinyl alcohol as a binder and sintered at 1150 °C for 2 hours. Enthalpy increments were measured using an MHTC-96 high-temperature drop calorimeter by alternately dropping five NBT and  $\alpha\text{-Al}_2\text{O}_3(\text{s})$  reference pellets (SRM 720) from room temperature to a crucible at high temperature. The enthalpy increments were then calculated based on the known values of the reference material.

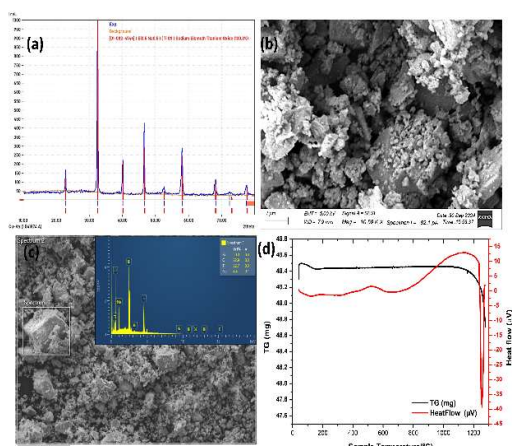


Figure 1. (a) XRD pattern (b) SEM micrograph (c) EDX spectrum showing elemental composition (d) TG-DTA curve of NBT

The X-ray diffraction pattern obtained for NBT matched with the ICDD card no. 0-083-4744 (Fig. 1a). The SEM micrograph is shown in Fig. 1b. The average grain size varies from 1 to 3  $\mu\text{m}$ . Elemental analysis via EDX confirms that the

local chemical composition closely matches the expected values (Fig. 1c). The DTA curve indicates NBT melting around 1250 °C, while mass loss beginning at approximately 1100 °C, likely due to  $\text{Bi}_2\text{O}_3$  volatilization (Fig. 1d).

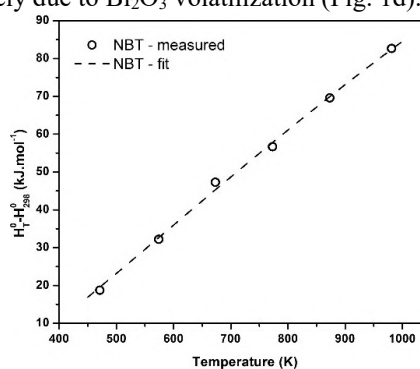


Figure 2. Enthalpy increment of NBT as a function of temperature

The enthalpy data collected at various temperatures were fitted to the following expression using a least-squares approach, implemented via Lagrange multiplier in a Python program (Fig. 2):

$$H_T^0 - H_{298}^0 <\text{Na}_{0.5}\text{Bi}_{0.5}\text{TiO}_3> \text{ (kJ.mol}^{-1}\text{)} = 0.1634 \times T - 2.1399 \times 10^{-5} \times T^2 + 4434.2509 \times T^{-1} - 61.6859 \text{ (T: 473 - 973 K)}.$$

The constraints used for fitting are: (a)  $H_T - H_{298} = 0$  at 298 K and (b) the derivative of the function at 298 K is equal to  $C_{p,298}^0$ .  $C_{p,298}^0$  was taken as 100.75  $\text{J.K}^{-1}\text{.mol}^{-1}$ , by applying the Neumann-Kopp's molar additivity rule on the constituent oxides. The  $S_{298}^0$  values needed for the computation of the entropy and Gibbs energy functions were also estimated in a similar method using Neumann Kopp's rule.

Other thermodynamic functions, namely, entropy and Gibbs energy functions were computed at various temperatures and are valid between the temperature range 298 K to 973 K (Table 1).

Table 1. Computed thermodynamic functions of NBT

T/K	$\text{J K}^{-1} \text{ mol}^{-1}$		
	$C_p^0$	$S_T^0$	$-(G_T^0 - H_{298}^0)/T$
298	100.74	110.46	110.46
373	115.57	134.89	112.95
573	125.36	187.28	130.28
773	122.88	224.58	150.11

**References**

1. M.V. Ramana, S.R. Kiran and N.R. Reddy, *Journal of Advanced Dielectrics*, 01 (2011).

## Standard molar Gibbs energy of formation of $\text{Bi}_2\text{Ti}_4\text{O}_{11}(\text{s})$ from EMF measurements

Chita Ranjan Patra<sup>a\*</sup>, Chinmay Routray<sup>a</sup>, T. Muthu Ambika<sup>a</sup>, Sajal Ghosh<sup>a</sup>, R Sudha<sup>a</sup>, and Rajesh Ganesan<sup>a, b</sup>,  
<sup>a</sup>Materials Chemistry and Metal Fuel Cycle Group, Indira Gandhi Centre for Atomic Research, Kalpakkam 603102, India

<sup>b</sup>Homi Bhabha National Institute, Mumbai 400085, India

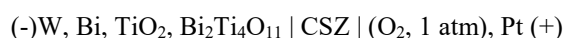
\* crpatra@igcar.gov.in

### Abstract

Electrochemical cell employing Calcia Stabilized Zirconia (CSZ) as solid-oxide electrolyte was used to determine the standard Gibbs energy of formation of  $\text{Bi}_2\text{Ti}_4\text{O}_{11}(\text{s})$ . The cell was validated by measuring the emf of  $\text{In}/\text{In}_2\text{O}_3(\text{s})$  against 1atm  $\text{O}_2(\text{g})$ .  $\text{Bi}_2\text{Ti}_4\text{O}_{11}(\text{s})$  was synthesized via a solid-state route. The standard Gibbs energy of formation of  $\text{Bi}_2\text{Ti}_4\text{O}_{11}(\text{s})$  was measured and is given by the expression:  $\Delta_f G_m^\circ < \text{Bi}_2\text{Ti}_4\text{O}_{11} > \text{kJ} = -4457.4 + 1.1(\text{T}/\text{K})$  (T: 818-1069K)

The  $\text{Bi}_2\text{Ti}_4\text{O}_{11}$  phase in the  $\text{Bi}_2\text{O}_3$ - $\text{TiO}_2$  system is notable for its unique structural and dielectric properties, relevant for applications in electro ceramics and high-temperature dielectrics. It exists as two polymorphs, with a low-temperature  $\alpha$ -phase and a high-temperature  $\beta$ -phase, transitioning near 240–250°C. Determining the Gibbs energy of formation for  $\text{Bi}_2\text{Ti}_4\text{O}_{11}$  is critical for understanding its thermodynamic stability and role within the Bi-Ti-O phase diagram, particularly due to its narrow formation window.

$\text{Bi}_2\text{Ti}_4\text{O}_{11}$  was synthesized via solid-state reaction from  $\text{Bi}_2\text{O}_3$  and  $\text{TiO}_2$  in a stoichiometric 1:4 molar ratio, with phase purity confirmed by powder X-ray diffraction and Rietveld refinement. The Gibbs energy of formation was determined using a solid-state galvanic cell with the configuration:



A Calcia Stabilized Zirconia (CSZ) tube served as the electrolyte. The sample electrode comprised a mixture of Bi,  $\text{TiO}_2$ , and  $\text{Bi}_2\text{Ti}_4\text{O}_{11}$ . During emf measurements, high purity argon and oxygen gases were passed through the sample and reference compartments, respectively. Consistent null-emf tests validated the cell's accuracy, and the Nernst equation:

$$E = (RT/4F)\ln(P_{\text{O}_2}^{\text{ref}}/P_{\text{O}_2}^{\text{sam}})$$

where E is emf, R is universal gas constant, F is Faraday,  $P_{\text{O}_2}^{\text{ref}}$  and  $P_{\text{O}_2}^{\text{sam}}$  are the partial pressures of reference and sample electrodes, respectively, was used to calculate Gibbs energy from the measured emf values. The oxygen potential at the sample electrode can be calculated from the above relation as  $\Delta \bar{G}_{\text{O}_2}^{\text{sam}} = 4FE$ , considering an oxygen partial pressure of 1 atm at the reference side. The results of the validation experiments in the  $\text{In}/\text{In}_2\text{O}_3$  system are given in Fig. 1 [1].

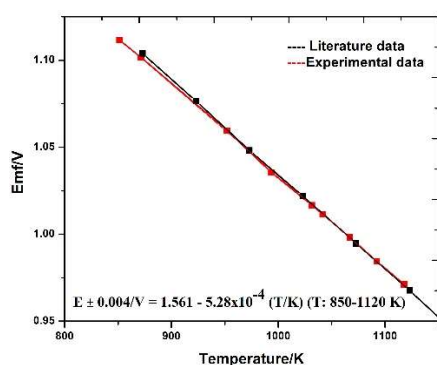


Fig 1. Variation of emf with temperature for  $\text{In}/\text{In}_2\text{O}_3$  system and it's comparison with literature values for validation of the cell

The XRD patterns of the sample electrode before and after the emf measurements confirmed the presence of the desired components namely Bi,  $\text{TiO}_2$  and  $\text{Bi}_2\text{Ti}_4\text{O}_{11}$ . The variation of emf with temperature is given in Fig. 2(a). The least square fitting of the emf data gives the following expression:

$$E \pm 8.77/\text{mV} = 1185.6 - 0.6 (\text{T}/\text{K}) \quad (\text{T}: 818\text{-}1069 \text{ K})$$

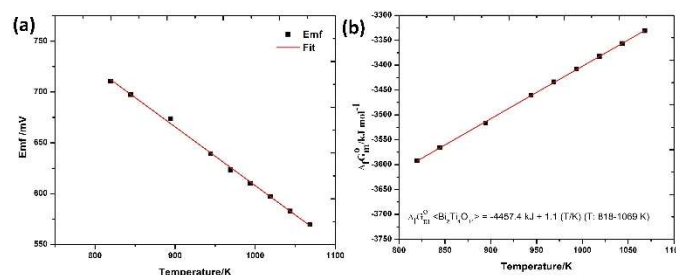
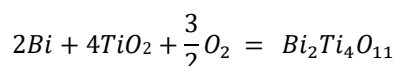


Fig 2. (a) Variation of emf with temperature for  $\text{Bi}_2\text{Ti}_4\text{O}_{11}$  system (b) Measured standard Gibbs energy of formation of  $\text{Bi}_2\text{Ti}_4\text{O}_{11}$

The Gibbs energy of formation of  $\text{Bi}_2\text{Ti}_4\text{O}_{11}$  was derived as follows



$$\Delta_f G_m^\circ < \text{Bi}_2\text{Ti}_4\text{O}_{11} > = 4\Delta_f G_m^\circ < \text{TiO}_2 > + \frac{3}{2}\Delta \bar{G}_{\text{O}_2}^{\text{sam}}$$

$$\Delta_f G_m^\circ < \text{Bi}_2\text{Ti}_4\text{O}_{11} > = 4\Delta_f G_m^\circ < \text{TiO}_2 > - 6FE$$

From literature [2],

$$\Delta_f G_m^\circ < \text{TiO}_2 > \text{kJ} = -942.8 + 0.2*(\text{T}/\text{K}) \quad (\text{T}: 300\text{-}1100\text{K})$$

Hence,

$$\Delta_f G_m^\circ < \text{Bi}_2\text{Ti}_4\text{O}_{11} > \text{kJ} = -4457.4 + 1.1(\text{T}/\text{K}) \quad (\text{T}: 818\text{-}1069\text{K})$$

### References

1. Klinedinst, K. A., and D. A. Stevenson. *The Journal of Chemical Thermodynamics* 5 (1973) 21-29
2. I. Barin, *Thermochemical data of pure substances*, 3<sup>rd</sup> ed., VCH publishes, 1995

## Heat capacity measurement of RE-Te compounds (La, Nd, Gd)

Hriday Maji<sup>a</sup>, M. Venkatesh<sup>b\*</sup>, Chita Ranjan Patra<sup>b</sup>, S Shyam Kumar<sup>b</sup> and Rajesh Ganesan<sup>b</sup><sup>a</sup>Process Development Division, Nuclear Recycle Group,  
Bhabha Atomic Research Centre, Trombay,  
Maharashtra – 400 094, India<sup>b</sup>Materials Chemistry Division, Materials Chemistry and Metal Fuel Cycle Group,  
Indira Gandhi Centre for Atomic Research, Kalpakkam,  
Tamil Nadu-603 102, India[\\*venk@igcar.gov.in](mailto:*venk@igcar.gov.in), mobile: +91 81898 83853**Abstract**

The phase pure compounds of LaTe<sub>2</sub>, NdTe<sub>2</sub>, and GdTe<sub>1.75</sub> have been prepared using the isopiestic method. Heat capacity measurements for these compounds have been carried out by Differential Scanning Calorimeter (DSC). The measured heat capacity for these compounds as a function of temperature was fitted to the standard equation and reported for the first time.

Rare earth fission products constitute 25% of the fission products [1]. Tellurium is a highly corrosive fission product; being volatile in nature, it tends to interact with constituent elements in the clad very aggressively [2]. It is reported in the literature that the interaction of rare earth elements with tellurium minimises clad corrosion. In this context, it is essential to study the thermodynamic properties of the RE-Te system.

LaTe<sub>2</sub>, NdTe<sub>2</sub> and GdTe<sub>1.75</sub> compounds were prepared using the isopiestic method [3]. Details of the construction and working of the isopiestic experimental setup can be found in the literature [4].

The starting metals used for the preparation of the compounds are La (>99.9 %, Alfa Aesar, USA), Nd (>99.5 %, Alfa Aesar, USA), Gd (>99.9 %, Alfa Aesar, USA) and Te (>99.9%, Nuclear Fuel Complex, India). These compounds were prepared by equilibrating for a period of 30 days in a temperature gradient double zone furnace using alumina crucibles. The sample and reservoir temperatures employed for the preparation of the compounds are given in Table 1. All initial starting metals and the compounds have been handled in an inert atmosphere glove box, as they are sensitive to air and moisture. All the temperature measurements were carried out by a K-type thermocouple.

The heat capacity of LaTe<sub>2</sub>, NdTe<sub>2</sub> and GdTe<sub>1.75</sub> was measured by taking the compound in the form of a 5 mm pellet under flowing UHP Ar at 50 ml.min<sup>-1</sup>. Heat capacity measurements were carried out using a heat-flux type of DSC of model no. DSC 3 STAR<sup>c</sup> system (M/s Mettler Toledo, Switzerland). The heat and temperature calibration of the instruments was calibrated by melting high-purity indium (99.999% Impag AG, Germany) and zinc metals (99.998% Impag AG, Germany). Heat capacity was measured using a three-step method where, sapphire (99.99% Industrie de Pierresscientifiques, France) was used as the internal standard. The details of the three-step procedure are available in the literature [3].

The samples were characterised by an X-ray diffractometer (M/s Inel, France) with Cu K<sub>α</sub> radiation and graphite monochromator. The XRD pattern of the prepared compounds are shown in Figure 1-3. Prior to characterising the samples, the diffractometer was calibrated with standard Si (Cat. No. 640 e). These air and moisture-sensitive samples were characterised by XRD by a specially fabricated brass sample holder. The samples were sandwiched in between two polyimide films (Kapton®

Film, Cat. No:446) smeared over Dow Corning® High Vacuum Grease. The films containing the samples are held in place by a suitable holder and a snugly fitting “O” ring pressing at the outer periphery of the film [3].

**Table 1:** Sample (T<sub>s</sub>) and reservoir (T<sub>R</sub>) temperatures employed for the preparation of the compounds.

Compounds	T <sub>s</sub> (K)	T <sub>R</sub> (K)
LaTe <sub>2</sub>	1203	941
NdTe <sub>2</sub>	1092	828
GdTe <sub>1.75</sub>	1130	828

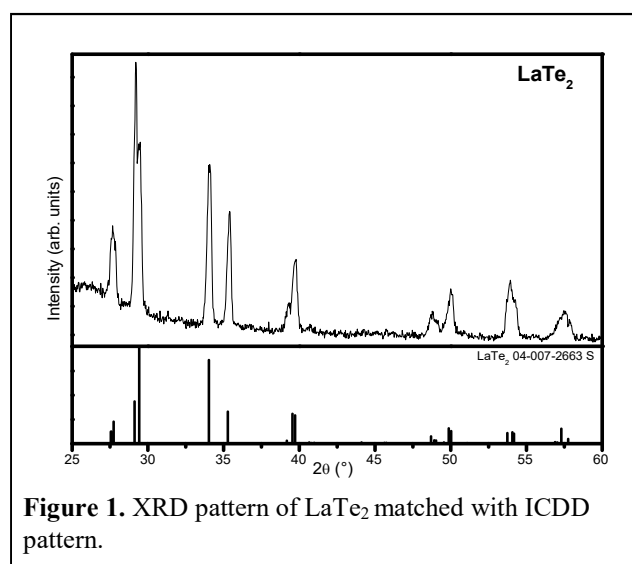
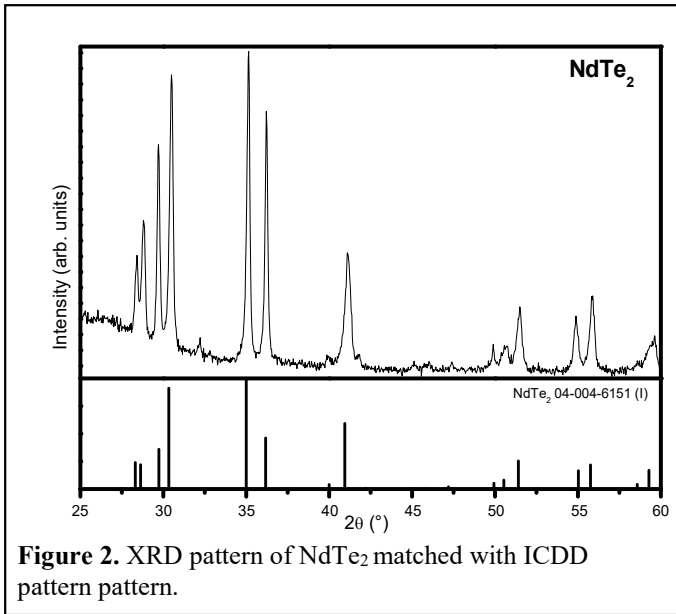
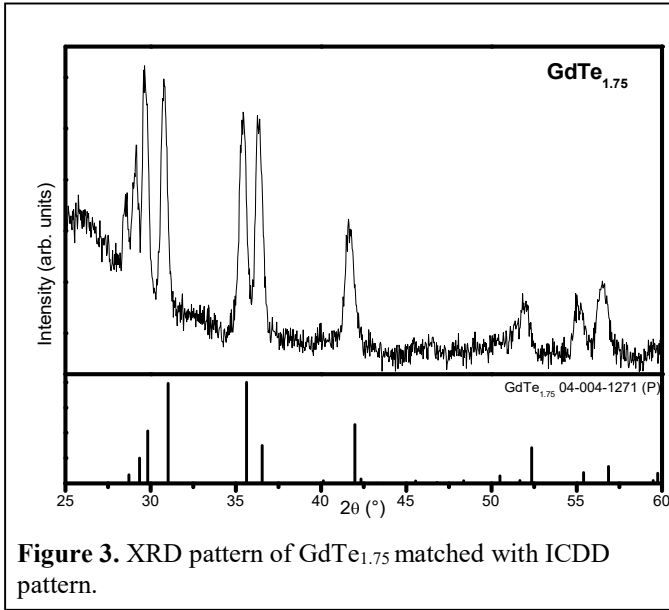


**Figure 1.** XRD pattern of LaTe<sub>2</sub> matched with ICDD pattern.

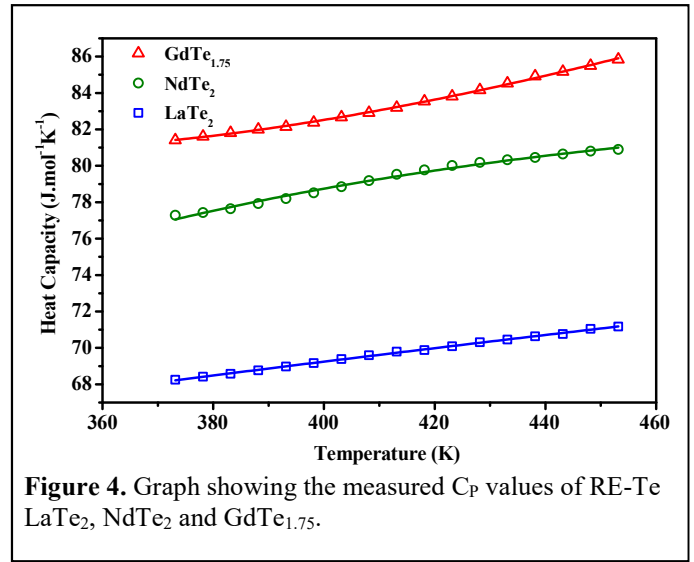


The graphical comparison of XRD patterns of the compounds with the corresponding ICDD database [5], 04-007-2663 for LaTe<sub>2</sub>, 04-004-6151 for NdTe<sub>2</sub>, and 04-004-1271 for GdTe<sub>1.75</sub> is shown in Figure 1-3.



Heat capacity measured for LaTe<sub>2</sub>, NdTe<sub>2</sub> and GdTe<sub>1.75</sub> is shown in Figure 4. The heat capacity curves shown in the figure are an average of ten measurements.

The measured heat capacity of these compounds as a function of temperature is given by the equations (1) to (3): GdTe<sub>1.75</sub> has the highest heat capacity and LaTe<sub>2</sub> has the lowest heat capacity among the three rare earth compounds, suggesting that the heat capacity of these intermetallic compounds are increasing as their atomic weights are increasing.



$$C_p < LaTe_2 > JK^{-1}mol^{-1} = 58.4 + 0.03T - 2.2 * 10^5 T^{-2} \quad (1)$$

$T: 373 - 453 \text{ K}$

$$C_p < NdTe_2 > JK^{-1}mol^{-1} = 101.1 - 0.019T - 2.4 * 10^6 T^{-2} \quad (2)$$

$T: 373 - 453 \text{ K}$

$$C_p < GdTe_{1.75} > JK^{-1}mol^{-1} = 13.9 + 0.131T + 2.6 * 10^6 T^{-2} \quad (3)$$

$T: 373 - 453 \text{ K}$

Phase pure compounds of LaTe<sub>2</sub>, NdTe<sub>2</sub> and GdTe<sub>1.75</sub> were prepared using the isopiestic method. Heat capacity measurements were carried out for the LaTe<sub>2</sub>, NdTe<sub>2</sub> and GdTe<sub>1.75</sub> in the temperature range 373-453 K using differential scanning calorimeter for the first time. GdTe<sub>1.75</sub> has recorded the highest heat capacity and LaTe<sub>2</sub> with the lowest heat capacity in the temperature range 373-453 K.

## References

- [1] E.A.C. Crouch, Academic Press Inc. (1977).
- [2] C.K. Mathews, J. Nucl. Mater. 201 (1993) 99–107.
- [3] S. Shyam Kumar, R, Ganesan, J. Chem. Thermodyn., 175 (2022) 10688
- [4] S. Shyam Kumar et al., Rev. Sci. Instrum. 93 (2022) 44105
- [5] PDF-5+ Database-2024. International Centre for Diffraction Data



## Sustainable Approaches for Immobilization of High-Level Nuclear Waste with Glass Matrix: A plant Experience

Kankan Patra<sup>1,2\*</sup>, R K Sah<sup>1</sup>, V.K. Mittal<sup>1\*</sup>, Anoop Kelkar<sup>1</sup>, Ashish Pandey<sup>1</sup>, R. K. Malav<sup>1</sup>, Chetan Baghra<sup>1</sup>, G. Singh<sup>1</sup>, D.B.Sathe<sup>1</sup>, R.B.Bhatt<sup>1</sup>.

<sup>1</sup>Nuclear Recycle Board, Bhabha Atomic Research Centre, Tarapur 401504, India

<sup>2</sup>Homi Bhabha National Institute, Anushaktinagar, Mumbai 400 094, India

\*Corresponding author's mail: vkmittal@barc.gov.in, 02525286203; kpatra@barc.gov.in, 02525286135

### Abstract

Nuclear energy has emerged as a clean and efficient power source, addressing the escalating global energy demand while mitigating the adverse effects of climate change. A major challenge for the sustainable use of nuclear power is the effective immobilization of hazardous nuclear waste, particularly high-level waste (HLW). A critical aspect of ensuring the sustainable and responsible use of nuclear energy is the effective management of nuclear waste. Borosilicate glass matrix have been considered as promising candidates for efficient management of high-level waste, which poses significant challenges due to its high radioactivity and extreme working condition. In this present study, we have immobilized simulated HLW (generated from reprocessing plant) with in borosilicate glass and characterized thoroughly the vitrified waste product (VWP). We have characterized the highly active HLW generated from the reprocessing plant. Following this characterization, we simulated the waste composition and formulate an appropriate chemical composition for glass with frit materials. We have obtained the fusion and pouring temperature of the glass product at 9000C and 950°C respectively. To investigate the properties of the VWP, we utilized Powder X-ray Diffraction (PXRD) to analyze its structural behaviour. Surface morphology and elemental composition were examined using Scanning Electron Microscopy (SEM) and Energy Dispersive X-ray Spectroscopy (EDS). These findings contribute to our understanding of HLW vitrification with glass matrix and the long-term storage of HLW.

### Introduction

Glass samples were prepared using analytical reagent (AR) grade chemicals. The raw materials used for the preparation are Ferric nitrate nonahydrate ( $\text{Fe}(\text{NO}_3)_3 \cdot 9\text{H}_2\text{O}$ ), Chromic Oxide ( $\text{CrO}_3$ ), Nickelous nitrate hexahydrate ( $\text{Ni}(\text{NO}_3)_2 \cdot 6\text{H}_2\text{O}$ ), Sodium nitrate ( $\text{NaNO}_3$ ), Manganese Nitrate six Hydrate ( $\text{Mn}(\text{NO}_3)_2 \cdot 6\text{H}_2\text{O}$ ), Strontium nitrate ( $\text{Sr}(\text{NO}_3)_2$ ), Barium nitrate ( $\text{Ba}(\text{NO}_3)_2$ ), Aluminium nitrate nonahydrate ( $\text{Al}(\text{NO}_3)_3 \cdot 9\text{H}_2\text{O}$ ), Cesium Nitrate ( $\text{CsNO}_3$ ), Potassium Nitrate ( $\text{KNO}_3$ ). Glass sample preparation was carried out in an Indfurr superheat furnace equipped with silicon carbide heating components. The produced samples were subjected to X-ray diffraction (XRD) investigation utilizing a Rigaku powder diffractometer equipped with Cu K $\alpha$  radiation ( $\lambda = 1.5406 \text{ \AA}$ ). [1] Semi-dynamic leaching analysis was performed on the glass samples to determine their chemical integrity. The glass sample was crushed and sieved through ASTM 40 and ASTM 16 sizes for this study. The average diameter of the resultant glass particles around 0.5 mm. This glass particle with a known weight of 0.5 g is precisely weighed and placed in a mesh packet made of stainless steel. This 0.5g glass materials and 10mL of distilled water were packed in a Teflon bottle. For a considerable amount of time, this setup was maintained in an oven at 70°C, but the leachate was periodically changed out for new, purified water. Leaching solution was collected with time to time. The amounts of each sodium element were measured using Flame-AES analysis. The density and the pouring temperature of the glass samples were noted. Fig.1.a represents the elemental composition of the waste. Fig 1.b. represents the pictorial presentation of glass formulation. Fig.1.c showed the composition of glass frit

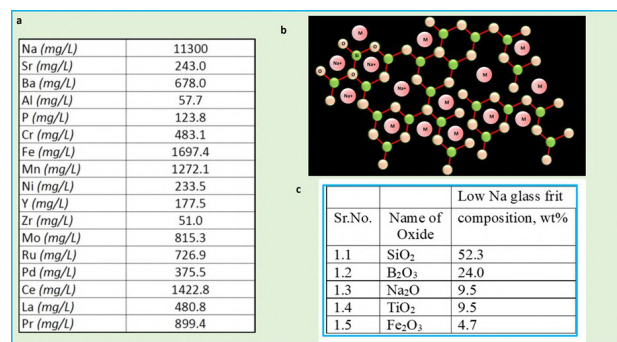


Fig. 1. (a) Represents the elemental composition of the HLW, (b) pictorial presentation of glass network formation, (c) chemical composition of frit.

Presences of crystalline phases within the glass samples are highly detrimental for immobilization of HLW. Crystalline phases present either on the surface or within the glass matrix leads to a number of undesirable properties. Hence XRD measurements of glass samples were carried out and presented in Fig 2.a. No sharp peaks were observed in the XRD patterns confirming that no crystalline phase separation has taken place in these samples. SEM study was carried out to examine the morphology and surface features of borosilicate glass and to Identify the distribution of key elements along with impurities that could affect glass properties. EDS experiments (Fig.2.e) was performed to obtain the elemental composition and the homogeneity, i.e evaluate the distribution of these elements throughout the sample, which is important for predicting leaching behaviour. Our SEM images (Fig.b-c) revealed that the glass product is homogeneous and hold the desired characteristic. The thermal characteristics show these structural changes. As a result, the glass samples' T<sub>g</sub> was

determined and shown in Fig.2.d, and observed  $T_g$  of around 516°C. In conclusion, we have conducted an important study on borosilicate base glasses. We have studied their structural, thermal, and chemical properties, which can provide valuable insights for the immobilization of high-level waste (HLW). We have analysed the glass structure using PXRD. We have highlighted thermal stability, including glass transition temperature. This information is crucial for processing and long-term storage. We measure the chemical Integrity of the VWP, evaluated the resistance of borosilicate glasses to leaching, ensuring long-term environmental conditions can demonstrate their suitability for HLW containment. By focusing on these areas, our findings could significantly inform the practical experience of effective strategies for HLW immobilization.

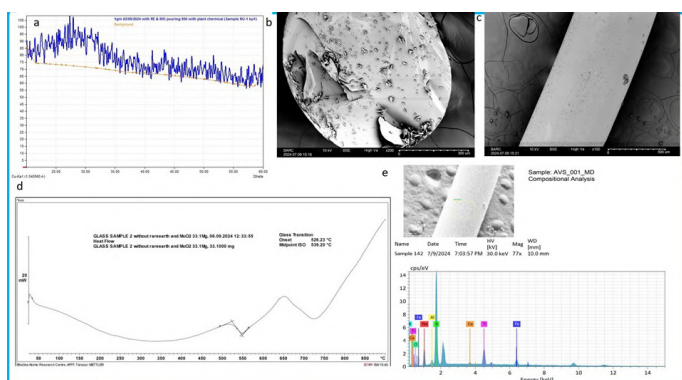


Fig.2. (a) PXRD of the VWP, (b-c) FE-SEM of the VWP, (d) TGA of the VWP, (e) EDS of the VWP.

**Acknowledgment:** Authors wish to acknowledge all lab staff, FF, NRB BARC.

**References.**1. Gianni Petrangeli, Chapter 23 - Radioactive waste, Nuclear Safety (2006) 221-223.

## Exploring the Thermophysical & Structural Changes in Serpentine Induced by Mechanical Milling for Neutron Shielding Applications

Mohit Rattanpal<sup>a</sup>, Meenu Prasher<sup>a</sup>, Pranesh Sengupta<sup>a,b</sup>

<sup>a</sup>Materials Science Division, BARC Mumbai-400085

<sup>b</sup>Homi Bhabha National Institute, Mumbai, 400094, India

\* Corresponding author, Email ID: [mohitr@barc.gov.in](mailto:mohitr@barc.gov.in), Telephone: +91-02225599216

### Abstract

Effective neutron shielding is critical in nuclear reactors to protect personnel, equipment, and the environment from harmful radiation. Traditional shielding materials include hydrogen-rich compounds, high atomic number elements (e.g., lead, steel), neutron absorbers (e.g., boron, cadmium, lithium), and specialized compounds such as heavy water and graphite. Serpentine, a magnesium silicate mineral with a significant hydrous content, has emerged as a promising candidate for neutron shielding due to its stability at temperatures up to 500°C. This study explores the potential of utilizing crushed serpentine powder in concrete to enhance biological shielding against neutrons.

In this work, the thermophysical properties of serpentine were tailored using mechanical milling to investigate its effects on the stability of the hydrous content, effect on dehydroxylation temperature, which are crucial for neutron attenuation. Serpentine powder was subjected to varying durations of milling in a planetary mill, revealing a decrease in the dehydroxylation temperature and an adverse impact on the stability of its hydrous content. These findings provide critical insights into optimizing serpentine-based shielding materials for nuclear applications.

### Introduction

Neutron shielding in nuclear reactors is essential for protecting personnel, equipment, and the environment from harmful radiation exposure. It involves materials and methods that attenuate neutron flux and mitigate secondary radiation generated during neutron interactions. Effective neutron shielding typically combines neutron moderation, where fast neutrons are slowed down by hydrogen-rich materials like water, or concrete, and neutron absorption, where materials like boron, cadmium, or gadolinium capture thermal neutrons. Multi-layer shielding, incorporating hydrogenous materials for moderation, absorbers for capture, and dense materials like lead or steel for gamma attenuation, is widely used. Reactor designs also utilize structural materials like reinforced concrete for inherent shielding, while advanced solutions, including borated polyethylene, heavy water, and neutron-reflecting materials like graphite or beryllium, enhance performance.

Among emerging materials, serpentine, a naturally occurring magnesium silicate mineral ( $\text{Mg}_3\text{Si}_2\text{O}_5(\text{OH})_4$ ), has gained attention as an effective neutron shielding material. Its high hydrogen content, combined with its ability to moderate and absorb neutrons, makes it a cost-effective and environmentally friendly alternative to synthetic shielding materials. Additionally, serpentine's thermal stability and radiation resistance allow it to perform well in harsh reactor environments, making it a versatile candidate for neutron shielding in modern reactor designs and waste management systems.

The present work investigates the impact of mechanical milling on serpentine's properties to optimize its performance as a neutron shielding material. Mechanical milling is known to alter a material's crystallinity, particle size, surface area, and defect density, all of which can influence its ability to moderate and absorb neutrons. This study examines these changes through detailed thermophysical analysis, structural characterization using XRD, and their correlation with neutron shielding efficiency. The findings aim to provide insights into the suitability of mechanically milled serpentine for practical applications in nuclear reactors and waste management systems, where high-performance and environmentally sustainable shielding materials are increasingly in demand.

### XRD of Mechanically Milled Serpentine

Serpentine exists in three polymorphic forms: Antigorite, Lizardite, and Chrysotile, which are distinguished by the specific space group associated with their crystal structure [1]. The serpentine sample used in this study was sourced from Bihar, India. To accurately determine the polymorph of the sample, Rietveld refinement of the XRD data from the powdered sample was performed, as recommended in prior studies [2]. The refinement was carried out using the Profex software, a freeware tool for XRD analysis, which confirmed the polymorph as Antigorite (**Fig. 1**). This identification provides a crucial basis for further analysis of the material's structural and thermophysical properties, particularly in the context of its potential neutron shielding applications.

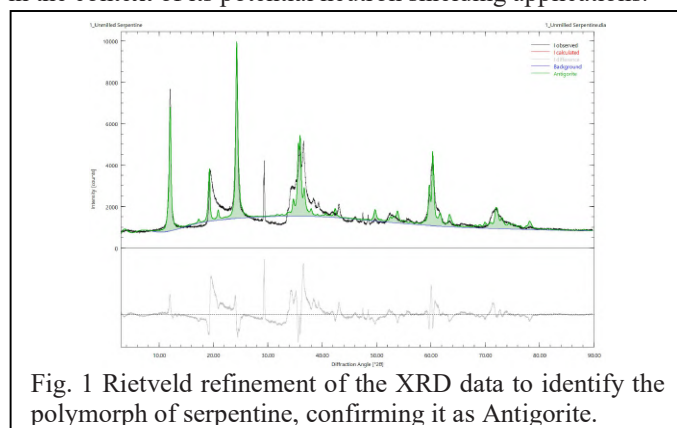


Fig. 1 Rietveld refinement of the XRD data to identify the polymorph of serpentine, confirming it as Antigorite.

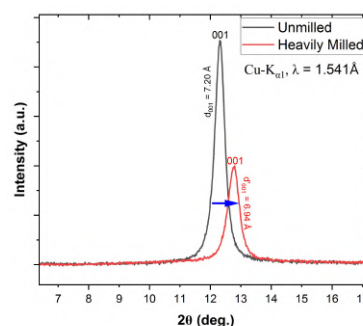


Fig. 2 XRD patterns of unmilled (black) and heavily milled (red) antigorite samples showing a shift in the 001 peak to higher  $2\theta$  values after milling. The interplanar spacing ( $d_{001}$ ) decreases from 7.20 Å to 6.94 Å, indicating a reduction of ~3.6% due to mechanical milling-induced structural compression.

The antigorite sample was subjected to intensive mechanical milling using a planetary ball mill for 3 hours at 180 RPM, employing aluminosilicate balls with a powder-to-ball weight ratio of 1:3. Post-milling, XRD analysis was performed under same conditions to investigate the changes in the crystal structure. The results (Fig. 2) revealed a systematic decrease in interplanar spacings caused by the mechanical milling process. This reduction was particularly pronounced along the 001 plane, corresponding to the c-axis, where the interplanar spacing decreased from 7.20 Å to 6.94 Å, representing a reduction of approximately 3.6%.

### Effect of milling on thermophysical Properties

The Differential Scanning Calorimetry (DSC) results (Fig. 3) for unmilled and mechanically milled (3 hrs at 180 RPM) antigorite samples reveal distinct thermal behaviors. For the unmilled sample, a broad endothermic peak centered at 725°C is observed, corresponding to the dehydroxylation of structurally bound water. This peak reflects the slower and more gradual breakdown of the serpentine structure due to its higher crystallinity.

In contrast, the mechanically milled sample shows the dehydroxylation endothermic peak shifted to a lower temperature of 670°C. This shift indicates that mechanical milling introduces lattice defects and reduces crystallinity, facilitating the earlier release of hydroxyl groups. Additionally, a sharp exothermic peak is observed in both samples around 820°C, which corresponds to the recrystallization of the dehydroxylated material into forsterite and enstatite. However, the exothermic peak is sharper and more intense in the unmilled sample, suggesting that milling disrupts the structural integrity, thereby limiting the extent of recrystallization.

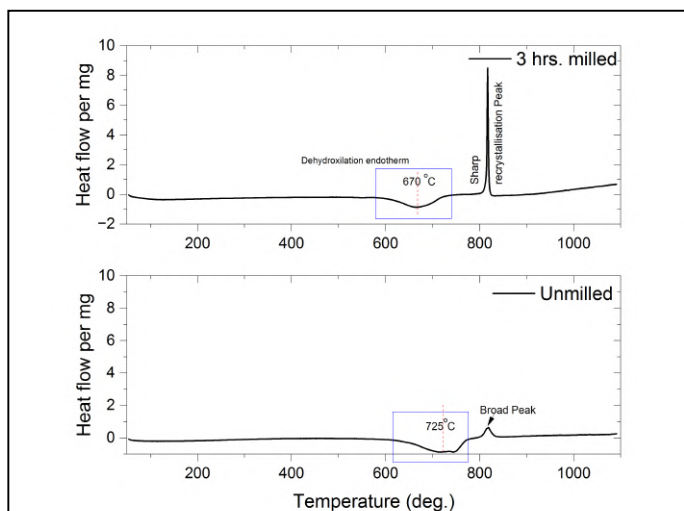


Fig. 3 Differential Scanning Calorimetry (DSC) curves of unmilled and mechanically milled antigorite samples. The unmilled sample shows a broad endothermic peak at 725°C (dehydroxylation) and a sharp exothermic peak at 820°C (recrystallization). For the milled sample, dehydroxylation occurs earlier at 670°C, with reduced intensity in the recrystallization peak, highlighting the effects of mechanical milling on structural stability.

The thermogravimetric analysis (TGA) of both unmilled and mechanically milled (3 hrs at 180 RPM) antigorite samples reveals significant differences in their thermal decomposition behavior (Fig. 4). The unmilled sample shows a gradual weight

loss starting at approximately 600°C, with a total weight loss of 11.8% by 900°C, corresponding to the dehydroxylation of the serpentine structure. In contrast, the milled sample exhibits an earlier onset of weight loss, beginning around 500°C, with a more pronounced and rapid decomposition, reaching a total weight loss of 14.1% by 800°C.

This shift in thermal behavior can be attributed to structural distortions and a higher defect density induced by mechanical milling, which reduces the crystallinity and weakens the hydroxyl bonds in the serpentine lattice. Consequently, the dehydroxylation process occurs at lower temperatures and progresses more rapidly in the milled sample. The increased weight loss in the milled sample suggests that mechanical milling enhances the material's reactivity, likely due to the increased surface area and introduction of lattice defects.

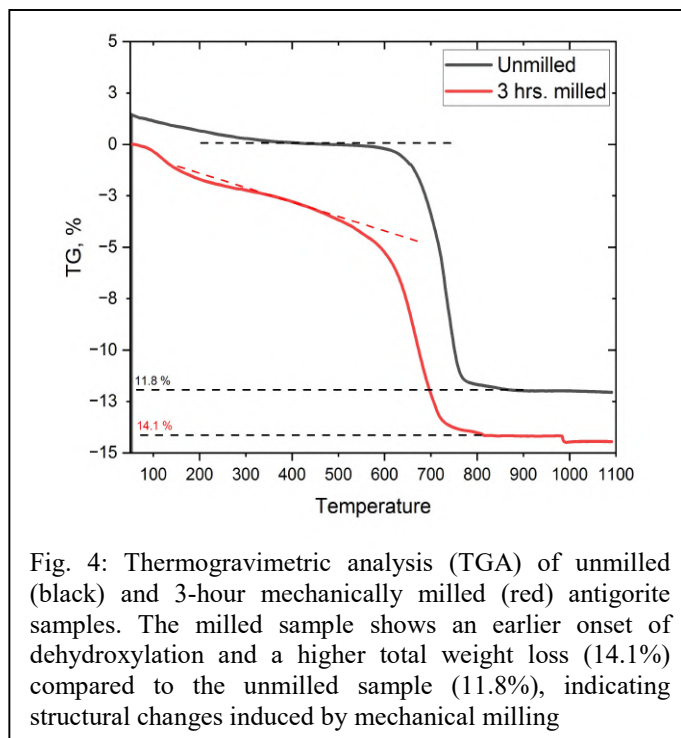


Fig. 4: Thermogravimetric analysis (TGA) of unmilled (black) and 3-hour mechanically milled (red) antigorite samples. The milled sample shows an earlier onset of dehydroxylation and a higher total weight loss (14.1%) compared to the unmilled sample (11.8%), indicating structural changes induced by mechanical milling

The TGA and DSC results demonstrate that the mechanically milled antigorite sample is more prone to dehydroxylation compared to the unmilled sample. Mechanical milling induces structural defects, reduces crystallinity, and increases surface area, resulting in an earlier onset of dehydroxylation (670°C for the milled sample vs. 725°C for the unmilled sample) and a higher overall weight loss (14.1% vs. 11.8%). Additionally, the sharp exothermic peak associated with recrystallization at 820°C is less intense in the milled sample, indicating that mechanical milling disrupts the structural integrity, limiting the extent of phase transformation to forsterite and enstatite.

### References

- [1] Bogdan Z. Dlugogorski, Reydick D. Balucan, Dehydroxylation of serpentine minerals: Implications for mineral carbonation, Renewable and Sustainable Energy Reviews (2014), 353-367
- [2] E. J. W. Whittaker and J. Zussman, The characterization of serpentine minerals by X-ray diffraction, Mineralogical magazine and journal of the Mineralogical Society (1956), 107-126.

## Knudsen effusion mass spectrometric studies over liquid region of U-Zr-Mn alloy

P. Manikandan\*, A. Manivannan, S. Balakrishnan, Hrudananda Jena

Materials Chemistry & Metal Fuel Cycle Group, IGCAR.

\* Corresponding author: manikandan@igcar.gov.in

**Abstract:** In the present study, high temperature mass spectrometric studies over liquid region of U-6Zr-5Mn (wt.%) alloy were carried out in the temperature range 1259-1345 K using Knudsen Effusion Mass Spectrometer (KEMS).  $Mn^+$  was the only ionic species observed in the mass spectrum of the equilibrium vapour over the above two phase region.  $Mn(g)$  was ascertained to be the corresponding neutral precursor of  $Mn^+$ . From the temperature dependence of partial pressures of  $Mn(g)$  over the liquid region of the alloy, the partial pressure – temperature relation for  $Mn(g)$  over the alloy was deduced by the second law method to be  $\log(p(Mn)/pa) = - (13251 \pm 218)/T + (10.36 \pm 0.17)$  and the mean enthalpy of vaporisation of  $Mn(g)$  over the alloy was obtained to be  $253.2 \pm 6.4$  kJ/mol

U-Pu-Zr alloy is envisaged to be attractive fuels for Fast Breeder Reactors in India [1]. Americium, which is formed in considerable quantities during the interim storage of plutonium, is of huge concern considering the radiological hazards. Hence, it is proposed to fabricate U-Pu-Zr-Am alloy using americium so formed during storage; subsequently Am could be transmuted to stable nuclide by irradiation of the alloy in fast reactor. This alloy is generally fabricated using injection casting. This process requires the knowledge of the vapour pressure data of all possible vapour species over this alloy to understand the loss of the components due to vaporisation during melting and to optimize the process parameters. Such data is largely required for americium since it is more volatile than other components of the alloy. It is found from the literature that manganese, which has similar vaporization behaviour to that of americium; hence, can be considered as the surrogate for americium [1]. In the preparation of the alloy employing injection casting, the alloy components are kept in the molten state (1723 K) for sufficient time to achieve their homogenization and during this time, there is a possibility of the loss of the most volatile component (americium) of the alloy due to vaporisation. Hence, the vapour pressure of americium especially over the liquid region of the alloy is needed to estimate the loss of americium due to vaporisation during melting. In the present study, the vapour pressure of  $Mn(g)$  over the liquid region of U-6Zr-5Mn (wt.%) alloy, one of the ternaries of U-Pu-Zr-Am system) has been measured. Earlier, we had reported the vapour pressure of  $Mn(g)$  over solid region of the alloy [2].

Homogeneous alloy of U-Zr-5Mn was prepared by arc melting appropriate amounts of U-6Zr alloy with pure Mn under inert atmosphere. Before melting the alloy components, zirconium was melted to remove the residual oxygen in the chamber environment. Subsequently, the alloy components were melted. The alloy ingot thus obtained was flipped and re-melted thrice to homogenize the components. The alloy was wrapped in tantalum sheet, vacuum sealed in a quartz tube under vacuum and subsequently annealed at 823 K for 72 hours. The alloy was subjected to Differential Scanning Calorimetric (DSC) studies to measure all possible phase transformations and the curve recorded is shown in Fig. 1. Two lots of sample were used in the KEMS experiments.

High temperature vaporisation experiments over this alloy were performed using Knudsen effusion Mass spectrometer. The detailed instrumentation of KEMS is given elsewhere [3]. For the experiments over each lot, about 500 mg of sample was used. The samples were taken in anytria crucible (Knudsen cell) having a knife edged orifice of 0.5 mm in diameter located at the center of its lid. The Knudsen cell was loaded into another tantalum outer cup with a black body hole provided at its bottom. The samples were heated by electron bombardment (EB) furnace present in the bottom chamber of the KEMS. The samples were

heated in steps of 100 K until 1000 K was reached and subsequently in steps of 25 K. The temperatures were measured by sighting a disappearing filament pyrometer onto the black body hole. At each temperature above 1000 K, the sample was maintained for 30 min so that thermodynamic equilibrium between the condensed phase and the vapour phase inside the Knudsen cell will be attained. The mass spectrum of the equilibrium vapour over the samples inside the Knudsen cell effusing to the ion source was recorded using Quadrupole Mass Spectrometer (QMS) housed in the chamber which is located above the chamber housing EB furnace. The vapour emanating out of the orifice is ionized in the ion source, mass analysed by QMS and detected by SEM operating in pulse counting mode. In the previous study over this alloy [2],  $Mn^+$  was observed to be the ionic species in the mass spectrum of the equilibrium vapour and  $Mn(g)$  was found to be its corresponding neutral precursor. The temperature dependence of intensity of  $^{55}Mn^+$  was carried out in the temperature range 1259-1345 K using electrons of 28.2 eV with the emission current of 100  $\mu A$ . The pressure calibration constant needed for converting intensity of  $^{55}Mn^+$  to partial pressure of  $Mn(g)$  [ $p(Mn)$ ] was obtained from the experiments carried out with pure Ag loaded in the same crucible used over the samples.

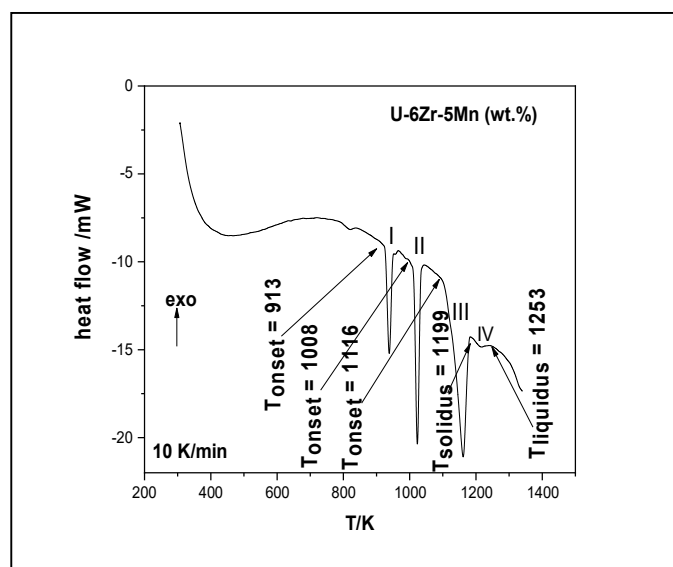


Fig.1. Differential scanning calorimetric curve of U-6Zr-5Mn (wt.%)

In DSC curve shown in Fig.1, the peak (I) corresponds to ( $\alpha - \beta$ ) transition of uranium while at 1008 K (peak II),  $\beta - \gamma$  transition of uranium takes place. It is worth nothing that the onset temperature of 1116 K corresponding to the peak (III) could not be attributed to any transition. But it is to be noted that the

sample heated up to 1199 K during the high temperature mass spectrometric (HTMS) experiments was found to be in solid state itself. It was also found that the same sample heated up to the 1253 K during HTMS studies was found to have completely liquified. The same observation was also inferred from the DSC curve that melting (solidus) of the alloy commences at 1199 K and ends at 1253 K (liquidus). In the present study, HTMS experiments were carried out at the temperatures above 1253 K.

Pressure calibration constant ( $k'_{Ag}$ ) was deduced using the equation given below:

$$p_{Ag} = k'_{Ag} \cdot I(Ag^+) \cdot T \quad (1)$$

$$k'_{Ag} = \frac{k}{(\sigma\gamma n)_{Ag}} \quad \text{where } p_{Ag} \text{ is the partial pressure of Ag over}$$

pure silver [4];  $k'_{Ag}$  is the pressure calibration constant of Ag;  $k$  is instrument or apparatus constant;  $\sigma(Ag)$  is the ionisation cross section of Ag(g) at the electron energy of 28.8 eV;  $\gamma(Ag)$  is the multiplier yield of  $^{107}Ag^+$ ;  $n(Ag)$  is the isotopic abundance of  $^{107}Ag$  (107 is the major isotope of silver).  $I(Ag^+)$  is the intensity of  $^{107}Ag^+$  and  $T$  is the temperature in Kelvin.

$k'_{Ag}$  thus obtained was used in the equation below to convert  $I(^{55}Mn^+)$  to  $p(Mn)$  by employing the equation below

$$p_{Mn} = \frac{k'_{Ag} \cdot (\sigma\gamma n)_{Ag}}{(\sigma\gamma n)_{Mn}} \cdot I(Mn^+) \cdot T \quad (2)$$

where  $\sigma(Mn)$ ,  $\gamma(Mn)$  and  $n(Mn)$  are the ionization cross section of Mn(g) at the electron energy of 28.8 eV, multiplier yield of  $^{55}Mn^+$  and the isotopic abundance of  $^{55}Mn$  (55 is the major isotope of Mn), respectively;  $I(Mn^+)$  is intensity of  $^{55}Mn^+$

It is assumed that  $\gamma$  of  $^{107}Ag^+$  and  $^{55}Mn^+$  is assumed to be unity since the secondary electron multiplier (SEM) present in the QMS is operated in pulsed counting mode.

One temperature dependence run alone could be conducted over each lot of the alloy since Mn in the alloy is highly volatile. There was a drastic decrease in the intensity of  $^{55}Mn^+$  at a given temperature during the second run compared to the first run on the same lot. Logarithmic values of  $p(Mn)$  values from each individual run were plotted against the reciprocal of temperature to get the pressure temperature relation for that run (second law method). The recommended p-T relation was obtained by plotting  $p(Mn)$  values from both runs against the temperature. Individual and recommended p-T relations are shown in Table 1. The plot between the  $p(Mn)$  values over the alloy and the temperatures is depicted in Fig 2.

**Table 1: Partial pressure – Temperature relation for Mn(g) over liquid region of U-6Zr-5Mn (wt.%)**

Lot	T/K	log(p(Mn)/Pa = -A/T+B		$P_{Mn}$ /Pa	$^* \Delta_v H_T$ (kJ./mol)
		A	B		
1	1259-1331	13242±342	10.36±0.26	1.55	253.6±6.5
2	1265-1345	13202±326	10.33±0.25	1.55	252.8±6.2
Overall 1	1259-1345	13251±218	10.36±0.17	1.52	253.2±6.4
Pure Mn [4]		14094	11.46	4.38	269.9

\* Middle temperature of the overall temperature range = 1302 K.

The enthalpy of vaporization of Mn(g) over the alloy for a particular run was obtained from the slope (A). The mean enthalpy of vaporization of Mn(g) was deduced by averaging the individual values to be 253.2±6.4 kJ/mol. It is seen from the table that the pressure of Mn(g) over the alloy is about three time lower than that over pure Mn. The activity of Mn in the alloy was calculated using the pressure data over the alloy and pure Mn to be 0.35. That the activity co-efficient of Mn ( $\gamma_{Mn}$ ) 56

computed for this composition ( $x_{Mn} = 0.17$ ) is greater than one shows that a repulsive interaction exists among the alloy components in the liquid.

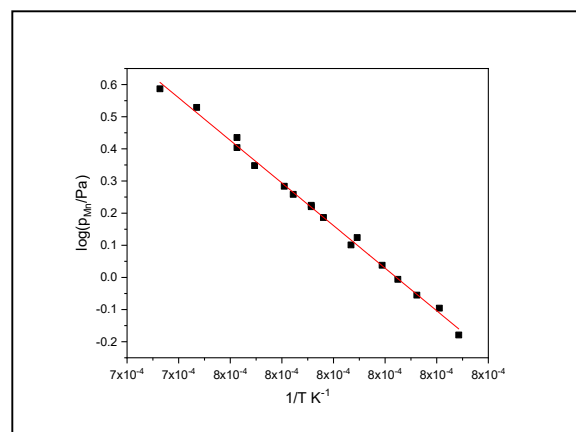


**Fig.2. Partial pressures of Mn(g) over liquid region of U-6Zr-5Mn (wt.%)**

#### References:

1. Jong-Hwan Kim, Ki-Hwan Kim, and Chan-Bock Lee. Advances in Materials Science and Engineering, 2015, <http://dx.doi.org/10.1155/2015/131704>.
2. P. Manikandan, A. Manivanna, C.V.S. Brahmanandha Rao, Kitheri Joseph, presented at 16<sup>th</sup> biennial DAE BRNS Symposium held during 01-05,2023.
3. D. Darwin Albert Raj, R. Viswanathan, P. Manikandan, ECS Trans. 46 (1) (2013) 77
4. Alcock, C. B., Itkin, V. P., and Horrigan, M. K., Canadian Metallurgical Quarterly, 23 (1984) 309

## Excess enthalpy associated with PRAN reactor, validation using TEG generator and application feasibility.

\*S.Phapale<sup>a</sup>, S.Varma<sup>b</sup>, R.Mishra<sup>c</sup>

<sup>a, b, c</sup>Chemistry Division, Bhabha Atomic Research Centre, Trombay, Mumbai,

\* Corresponding author: phapale@barc.gov.in, (022)25592282

### Abstract

The transmutation model proposed to account for excess heat associated with PRAN reactor was supported by both theoretical simulations and experimental data. This model corroborates excess enthalpy, so in that point of view experiment has been planned to look for said excess enthalpy generation, so in this aspect apart from Pd electrode other electrodes like Ni also has been tried. In view of this, the excess enthalpy i.e. using simply water, deuterated water, in combination with said electrodes has been determined by solution calorimetry as a function of applied DC potential at varying time scale.

### Introduction:

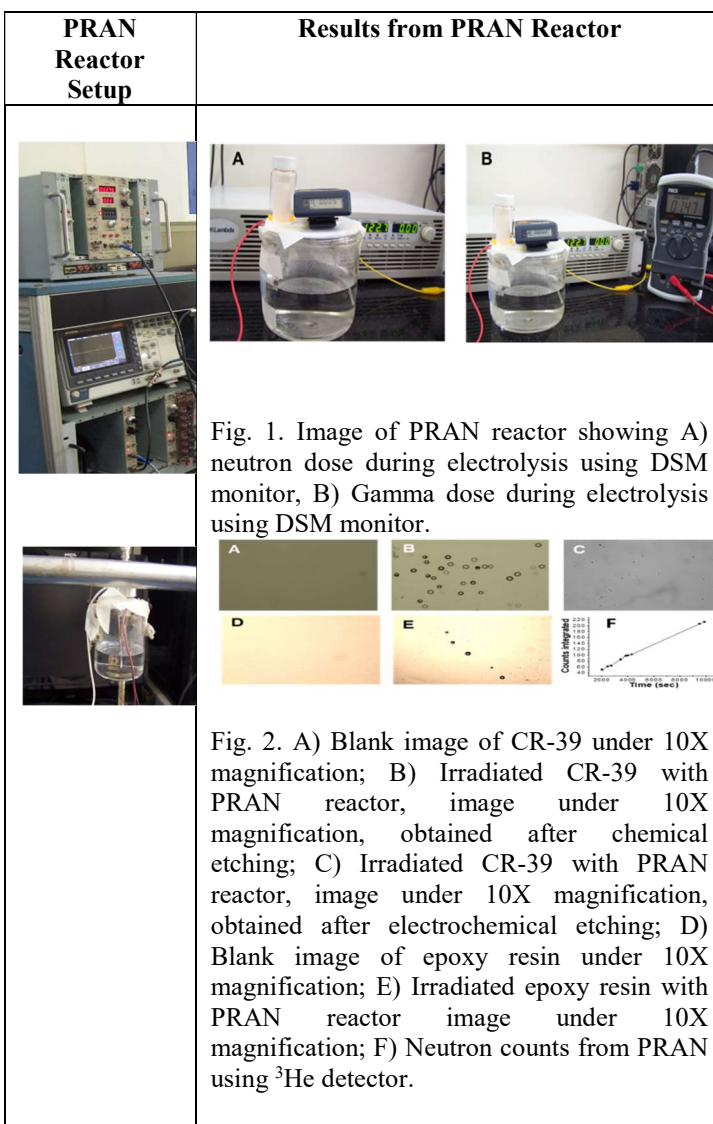
Energy creation is critical for progress, so our electrolysis reactor has been activated to produce extra enthalpy with Pt as an anode and either Pd or Ni as cathode. The idea is to test the generated excess heat using a TEG Generator and quantify it in order to determine its application. Our D<sub>2</sub>O electrolysis with a Pd electrode will be used as a thermoelectric device to efficiently extract heat for many applications. The thermoelectric device transforms heat into electricity by utilizing the material's thermoelectric power. The temperature differential in such a device encourages charge carrier diffusion to the colder end of the sample, whereas charge accumulation at the end generates a net electric field, which controls thermoelectric power. To test this thermoelectric power generation Peltier device, we loaded it into our setup and monitored the temperature gradient from bottom to top surface to ensure that the device met the temperature gradient criterion and could be used as a thermoelectric material.

### Experimental Details:

Solution calorimetry is commonly used to calculate the enthalpy of formation/heat of a system. This approach requires electrolysis of the corresponding electrodes in a solution calorimeter dewar flask. An isoperibol solution calorimeter is just a glass Dewar filled with D<sub>2</sub>O. The vessel is immersed in a constant-temperature bath. During electrolysis, the temperature of the calorimeter changes while the temperature of the surroundings remains constant due to a thermostatic setup. The temperature difference between the calorimeter and the constant temperature bath causes heat leakage, either from or to the calorimeter. The rate of heat leaking can be expressed using Newton's law of cooling. The true temperature rise due to the reaction is calculated by applying adequate correction to the apparent temperature rise due to heat leakage and stirring. The absolute temperature and water equivalent of the calorimeter are not directly monitored when the enthalpy is calculated. Instead, the heat effect perceived in terms of mV output in the computer is recorded. The heat effect can be produced by either flowing current or starting an electrolysis.

### Result and Discussion:

We also investigated temperature rise as a function of applied potential, which is expressed in terms of joule quantities of heat. The excess enthalpy for D<sub>2</sub>O electrolysis using Ni as cathode and Pt as anode at 298.15 K was determined to be 1254J as a function of variable voltage, as compared to electrical calibration of the order of 63J. So, by computing the mv signal rise from the plots, we can determine the surplus energy at each applied voltage. As calibration factor (1 mv= 155940.59J), so we can calculate mv rise from the each applied voltage plot, converting each signal to joules energy. We can simply calculate the amount of heat rise for each mv increase.



**Conclusion:** This setup produces excess heat, which is validated by an isoperibol solution calorimeter. Finally, the mv signal must be converted directly into temperature rise in order to determine the amount of input heat, i.e. without electrolysis, and the net heat rise from electrolysis. A program has been developed to directly quantify the rise in voltage signal to the corresponding temperature rise. Electrolysis of D<sub>2</sub>O can be used as a portable neutron source with numerous applications, such as heat source, without the complexity of large reactor operations.

**References:** [1] Fleischmann, M., Pons, S. & Hawkins, M. Electrochemically induced nuclear fusion of deuterium. *J. Electroanal. Chem.* **261**, 301 (1989)

## Thermodynamic Investigations of Quaternary Compounds in Ni-Mn-Te-O System

\*Rimpi Dawar<sup>a,b</sup>, Shubham Narang<sup>a,b</sup> and Ratikanta Mishra<sup>a,b</sup><sup>a</sup>Chemistry Division, Bhabha Atomic Research Centre, Trombay, Mumbai-400085<sup>b</sup>Homi Bhabha National Institute, Anushaktinagar, Mumbai- 400094

\*Email id: rimpid@barc.gov.in

**Abstract**

In the present study, we have investigated thermodynamic stability of quaternary tellurate compounds  $Ni_{0.5}Mn_{2.5}TeO_6(s)$  and  $Ni_{2.5}Mn_{0.5}TeO_6(s)$  in Ni-Mn-Te-O system. Calorimetric investigations have been performed on these compounds to determine their Standard molar enthalpy of formation and isobaric heat capacity employing calvet calorimeter and differential scanning calorimeter, respectively.

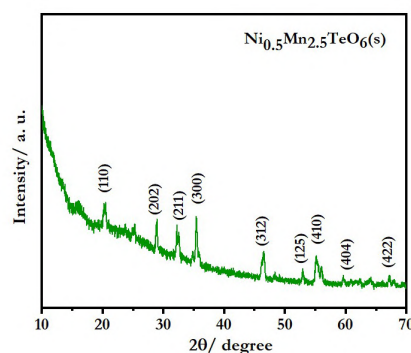
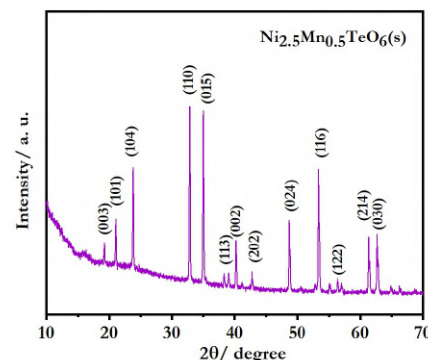
In order to evaluate the performance of (U, Pu) mixed oxides (MOX) as fuels for fast breeder reactors, thermodynamic characterization of the compounds that could be formed due to the possible interactions among fuel, fission products and the constituents of the clad and coolant are required. Tellurium is one among the reactive fission products which gets formed during the burn up of MOX fuel and is major reason behind embrittlement in stainless steel [1]. Therefore, data on thermodynamic stability of compounds containing Te and clad constituents i.e., Fe, Cr, Mn, Ni etc. are required in order to predict the integrity of the fuel pins and hence, lifetime of fuel pins inside the reactor. Also, compounds containing tellurium oxoanions have shown increasing interest in recent past because they show non-linear optical behavior [2].

Investigations on syntheses, crystal structures and optical absorption were carried out by Kim et al. [3]. For Ni-Mn-Te-O system, evolution of magnetic state with the substitution of the  $Ni^{2+}$  spins by isotropic  $Mn^{2+}$  spins, namely  $(Ni,Mn)_3TeO_6$  (NMTO) were also investigated in detail by Kim et al. [3]. Despite all of the attention paid to these compounds due to their applicability in various fields, many of the thermochemical properties of these compounds remain poorly investigated. Understanding their thermochemical characteristics is essential to predict their stability and effectiveness in reactive environments. Knowledge on different thermochemical properties of these compounds also enables one to do calculations to optimize the conditions of their synthesis as well as to fine-tune the phase equilibria in this system. In this regard, we have carried out a detailed investigation on the thermodynamic stability of  $Ni_{0.5}Mn_{2.5}TeO_6(s)$  and  $Ni_{2.5}Mn_{0.5}TeO_6(s)$  tellurate compounds.

The tellurate compounds investigated in the present study i.e.  $Ni_{0.5}Mn_{2.5}TeO_6(s)$  and  $Ni_{2.5}Mn_{0.5}TeO_6(s)$  were prepared by conventional solid-state reaction route. Towards this synthesis binary oxide  $NiO(s)$ ,  $Mn_3O_4(s)$  and  $TeO_2(s)$  were subjected to prior heating at 473K for 2 h to remove any adsorbed moisture. The intimate mixture of the components was subjected to compaction into pellets and heated in a furnace at 1023 K for 48 h under static air. Intermediate grinding was provided to ensure the completeness of the reaction.

The composition and phase purity of the prepared samples were analysed by the X-ray diffraction method (XRD) using a diffractometer (M/s Rigaku, Japan) equipped with Cu  $K\alpha$  radiation ( $\lambda = 1.541 \text{ \AA}$ ). The experimentally obtained XRD patterns of the synthesized  $Ni_{0.5}Mn_{2.5}TeO_6(s)$  and  $Ni_{2.5}Mn_{0.5}TeO_6(s)$  compounds are depicted in Figures 1, 2. The XRD patterns of  $Ni_{0.5}Mn_{2.5}TeO_6(s)$  and  $Ni_{2.5}Mn_{0.5}TeO_6(s)$  compounds were matched with standard patterns (collection codes #230205 and #230206), respectively of ICDD-PDF-2 database. The patterns clearly show the absence of any secondary or impurity phases in the prepared samples.

The temperature dependence of molar heat capacity of the synthesized compounds were performed employing a heat flux differential scanning calorimeter (DSC1) supplied by Mettler Toledo, Switzerland. The calibration of the DSC instrument for its temperature and heat flow was performed by measuring the temperatures and heat of fusion of high purity indium (99.995%) and zinc (99.999%) metals.

Figure 1. XRD pattern of  $Ni_{0.5}Mn_{2.5}TeO_6(s)$ Figure 2. XRD pattern of  $Ni_{2.5}Mn_{0.5}TeO_6(s)$ 

The temperature dependence of molar heat capacity of  $Ni_{0.5}Mn_{2.5}TeO_6(s)$  and  $Ni_{2.5}Mn_{0.5}TeO_6(s)$  compounds obtained by DSC measurements are given in Figures 3,4 respectively. The DSC plot reveals that within the temperature range of measurement, the compounds do not undergo any structural or phase transformation. The average heat capacity values were fitted by the least squares method in the form of Maier-Kelley equation and are provided by the following equations (1) and (2).

$$C_p < Ni_{2.5}Mn_{0.5}TeO_6 > / JK^{-1}mol^{-1} = 289.53 - 0.0557T - 6.0253 \times 10^6 T^{-2} \quad (300 < T/K < 600) \quad (1)$$

$$C_p < Ni_{0.5}Mn_{2.5}TeO_6 > / JK^{-1}mol^{-1} = 278.27 - 0.0171T - 6.7199 \times 10^6 T^{-2} \quad (300 < T/K < 600) \quad (2)$$



The standard molar enthalpy of formation of the synthesized compounds  $Ni_{0.5}Mn_{2.5}TeO_6(s)$  and  $Ni_{2.5}Mn_{0.5}TeO_6(s)$  was measured employing a HT-1000 Calvet calorimeter supplied by M/s Setaram, France. The principle and instrumental details of the calorimeter employed in the present study are described in Ref. [4]. The dissolution experiments were performed using  $3Na_2O.4MoO_3$  as the calorimetric solvent. The temperature of the calorimeter was set to be 986 K and the solvent was allowed to attain thermal equilibrium with the calorimeter. The attainment of thermal equilibrium was indicated by the appearance of a steady state heat flow signal.

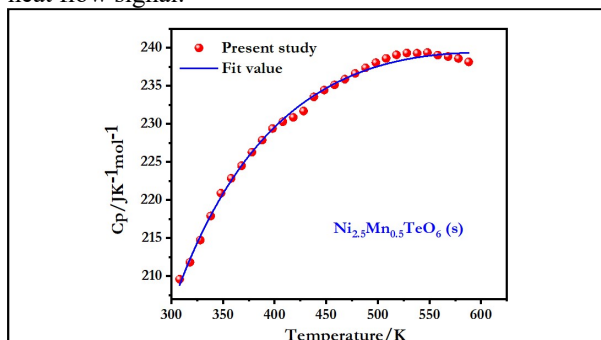


**Fig. 3** Variation of molar heat capacity of  $Ni_{0.5}Mn_{2.5}TeO_6(s)$

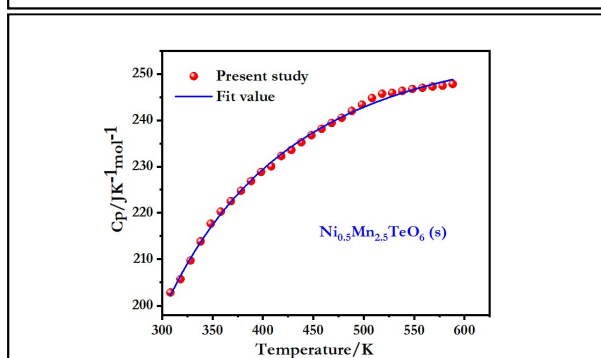


**Fig. 4** Variation of molar heat capacity of  $Ni_{2.5}Mn_{0.5}TeO_6(s)$

Small pellets of synthesized compounds  $Ni_{0.5}Mn_{2.5}TeO_6(s)$  and  $Ni_{2.5}Mn_{0.5}TeO_6(s)$  and their respective component oxides such as  $TeO_2(s)$ ,  $NiO(s)$  and  $Mn_3O_4(s)$ , weighing about 5 to 7 mg were dropped from room temperature (298.15 K) to the molten solvent at 986 K. In order to determine the enthalpy of dissolution, the heat flow signals as a function of time was integrated using the SETSOFT software and the obtained values are given in Table 1.

**Table 1** The molar enthalpies of dissolution in  $3Na_2O.4MoO_3$  solvent at  $T = 986$  K;  $\Delta_{sol}H_m$  is the molar enthalpy of solution

Sample	$\Delta_{sol}H_m$ (kJ mol <sup>-1</sup> )
$TeO_2(s)$	$74.35 \pm 1.00$
$NiO(s)$	$26.03 \pm 5.57$
$Mn_3O_4(s)$	$236.3 \pm 1.56$
$Ni_{0.5}Mn_{2.5}TeO_6(s)$	$324.9 \pm 2.07$
$Ni_{2.5}Mn_{0.5}TeO_6(s)$	$377.84 \pm 5.67$

The standard molar enthalpy of formation of quaternary tellurates at 298.15 K from their constituent elements can be determined by applying a suitable thermochemical cycle as described in Table 2.

**Table 2** Thermo chemical cycles for derivation of standard molar enthalpies of formation of  $Ni_xMn_{3-x}TeO_6$  compounds

Reaction	$\Delta H$ (kJ mol <sup>-1</sup> )
$Ni_xMn_{3-x}TeO_6(s, 298.15K) +$ $(sln, 986K) = xN(sln, 986K) +$ $\frac{3-x}{3}Mn_3O_4(sln, 986K) + TeO_2(sln, 986K) +$ $\frac{x}{6}O_2(g, 986K)$	$\Delta H_1 = \Delta H_{ds}$
$NiO(s, 298.15K) + (sln, 986K)$ $= NiO(sln, 986K)$	$\Delta H_2 = 26.03 \pm 5.57$
$Mn_3O_4(s, 298K) + (sln, 986K) =$ $Mn_3O_4(sln, 986K)$	$\Delta H_3 = 236.3 \pm 1.56$
$TeO_2(s, 298.15K) + (sln, 986K)$ $= TeO_2(sln, 986K)$	$\Delta H_4 = 74.35 \pm 1.00$
$O_2(g, 298K) = O_2(g, 986K)$	$\Delta H_5 = 22.32 \pm$ $0.33$ [5]
$Ni(s, 298.15K) + \frac{1}{2}O_2(g, 298.15K) =$ $NiO(s, 298.15K)$	$\Delta H_6 = -239.70 \pm 3.6$ [5]
$3Mn(s, 298.15K) + 2O_2(g, 298.15K)$ $= Mn_3O_4(s, 298.15K)$	$\Delta H_7$ $= -1387.8 \pm 20.8$ [5]
$Te(s, 298.15K) + O_2(g, 298.15K)$ $= TeO_2(s, 298.15K)$	$\Delta H_8 = -323.42 \pm$ $4.8$ [5]
$xNi(s, 298.15K) + (3 -$ $x)Mn(s, 298.15K) + Te(s, 298.15K) +$ $3O_2(g, 298.15K) =$ $Ni_xMn_{3-x}TeO_6(s, 298.15K)$	$\Delta H_{f,298.15}^o =$ $-\Delta H_1 + x\Delta H_2 +$ $\frac{3-x}{3}\Delta H_3 + \Delta H_4 +$ $\frac{x}{6}x\Delta H_5 + x\Delta H_6 +$ $\frac{3-x}{3}\Delta H_7 + \Delta H_8$

The calculated values of standard molar enthalpy of formation ( $\Delta H_{f,298.15}^o$ ) of  $Ni_{0.5}Mn_{2.5}TeO_6(s)$  and  $Ni_{2.5}Mn_{0.5}TeO_6(s)$  compounds are  $-2209 \pm 25.1$  and  $-1733 \pm 22.8$  kJ mol<sup>-1</sup>, respectively.

Both the compounds have showed exothermic enthalpies of formation indicating their thermodynamic stability. The thermodynamic functions of these compounds can be derived using the measured data on molar heat capacity and enthalpy of formation.

## References

- H. Kleykamp, *J Nucl Mater*, 131 (1985) 131.
- D. Wang, Zhang, Y. Zhang, Q. Liu, B. Zhang, D. Yang and Y. Wang, *Dalton Trans*, 51 (2022) 8955.
- A. Bhim, J. Gopalakrishnan and S. Natarajan, *Eur J Inorg Chem*, 20 (2018) 2277.
- S. Narang, P. M. Aiswarya, Rimpi Dawar, C. Nandi, R. Phatak, P. D. Babu and R. Mishra, *J Alloys Compd*, 968 (2023) 171973.
- O. Kubaschewski, C.B. Alcock and P. J. Spencer, *Metallurgical Thermochemistry (6th Ed.)*, Pergamon, Oxford (1993).

## Vapour pressure measurements in Nd-Te system

S Shyam Kumar<sup>a,b\*</sup> and Rajesh Ganesan<sup>a,b</sup><sup>a</sup>Materials Chemistry Division, Materials Chemistry and Metal Fuel Cycle Group,  
Indira Gandhi Centre for Atomic Research, Kalpakkam<sup>b</sup>Homi Bhabha National Institute, Mumbai[\\*shyam@igcar.gov.in](mailto:shyam@igcar.gov.in), mobile: +91 91765 37015**Abstract**

Isopiestic measurements have been carried out in Nd-Te system for the first time. Four sets of isopiestic experiments have been carried. The temperature range of measurement spans from 821 to 1257 K in the composition range 64.4 to 74.4 at% Te and thermodynamic activities of tellurium were determined. Non-stoichiometry was determined in both NdTe<sub>2</sub> and NdTe<sub>3</sub> phases. Partial enthalpy of mixing of tellurium has been determined for the homogeneity range of NdTe<sub>2</sub>, which lies from 64.37 to 65.27 at% Te. The Gibbs energy of the reactions for selected reactions have been calculated from the experimental data obtained in the two-phase regions.

Rare earth fission products constitute 25% of the fission products [1]. Neodymium has high fission yield of around 16.4% in Pu<sup>238</sup> fission [1]. Tellurium is a highly corrosive fission product; being volatile in nature, it tends to interact with constituent elements in the clad very aggressively [2]. It is reported in the literature that the interaction of rare earth elements with tellurium minimises clad corrosion. In this context, the thermodynamic study on Nd-Te system was carried out.

Experimental investigation on the Nd-Te binary system remains largely untouched. Based on the experimental data reported in the literature, Villars et al. [3] reported the phase diagram of the Nd-Te system.

The starting metals used for study are Nd (>99.5 %, Alfa Aesar, USA), and Te (>99.9%, Nuclear Fuel Complex, India). Details of the construction and working of the isopiestic experimental setup can be found in the literature [4]. Isopiestic experiments have been carried out with reservoir temperatures of 731, 785, 828 and 911 K. The tellurium vapour pressure ranges from ~ 0.3 to 14.7 mbar from lowest to highest reservoir temperatures. A representative X-ray diffraction data for selected samples equilibrated at a reservoir temperature of 785 K, indicating the phases present are shown in Fig 1. The equilibrium sample temperatures and compositions (the so-called equilibrium curves) for each isopiestic run are shown in Fig. 2 superimposed over the phase diagram reported by Villars et al. [3]. The compound Nd<sub>2</sub>Te<sub>5</sub> is shown as a vertical line and NdTe<sub>2</sub> & NdTe<sub>3</sub> solid solutions are also shown. The uncertainty in the composition is estimated to be less than 0.1 at% for the samples and the temperatures are accurate within ± 2 K. The uncertainties for the Te at% include the uncertainty from the chemical analysis as well as an assessment for the assumption that no neodymium is sublimed during the experiments. The temperature range of the samples spans from 821 to 1257 K and the composition ranges from 64.37 to 74.40 at% Te.

Partial enthalpy of mixing of Te was calculated in the homogeneity range of NdTe<sub>2</sub>. The sample temperatures for the entire homogeneous range were obtained by interpolation and extrapolation of the equilibrium curves constructed based on the experimental data points, as shown in Fig 2. For these hypothetical sample compositions, Te activities were calculated according to the eq 1. Natural logarithms of these activities were plotted as a function of the reciprocal temperatures for the selected compositions (referred to as iso-compositional plots), as shown in Fig. 3.

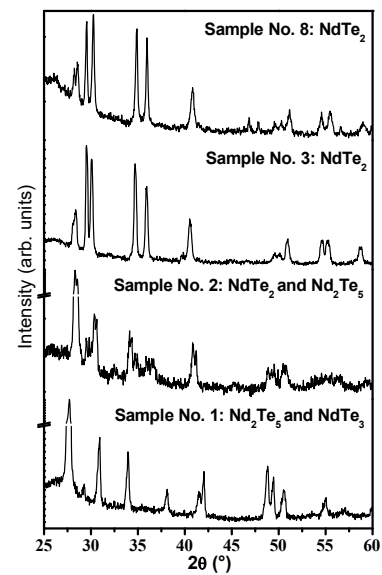


**Figure 1.** XRD plot of equilibrated samples in the isopiestic run with reservoir temperature 785 K.

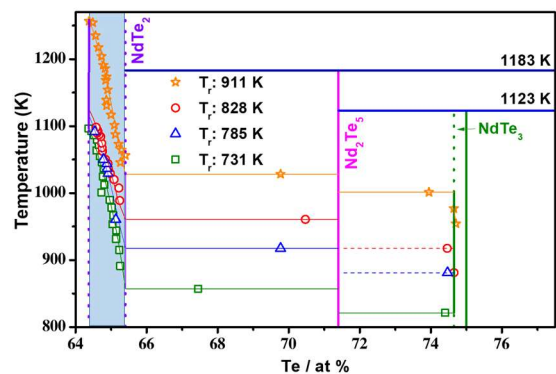


**Figure 2.** Sample temperature against composition superimposed on the partial Nd-Te phase diagram [3].

$$a_{Te} = \sqrt{\frac{P_{Te_2}^o(T_R)}{P_{Te_2}^o(T_S)}} \quad (1)$$

The experimental data of selected compositions were least square fitted to derive the partial enthalpy of mixing of tellurium. The slopes of these plots give the partial enthalpy of mixing according to the adapted Gibbs – Helmholtz equation. The partial enthalpy of mixing of tellurium derived from the slopes of the iso-compositional plots is used for constructing the

enthalpy versus composition plot shown in Fig 4. The obtained least squares fitted expression was used to derive the partial enthalpy value for each composition for the NdTe<sub>2</sub> phase. The partial enthalpy values were spread from -77.59 kJ.mol<sup>-1</sup> on the Nd-rich side to - 57.53 kJ.mol<sup>-1</sup> on the Te-rich side of the homogeneity range.

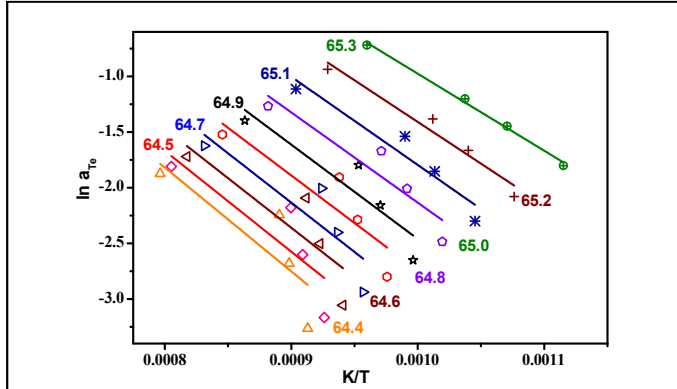


**Figure 3.** Natural logarithm of the Te activity against reciprocal sample temperature for selected compositions in the homogeneity range of NdTe<sub>2</sub>.

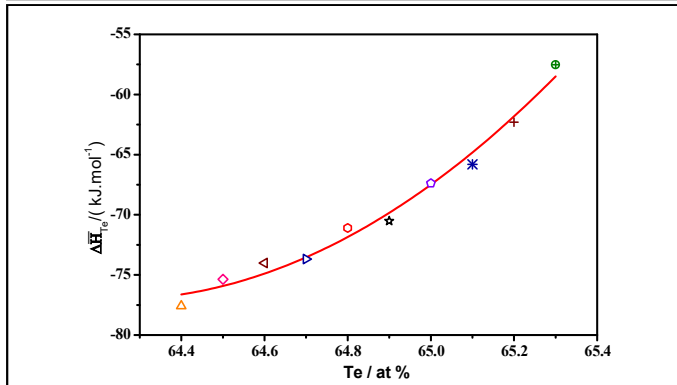


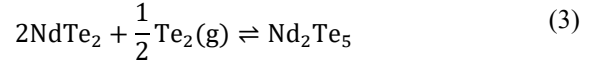
**Figure 4.** Partial molar enthalpy of Te in the homogeneity range of NdTe<sub>2</sub>.

The thermodynamic activity of tellurium was computed at 1050 K, which is an approximate mid-temperature of all the experimental data, using an integrated form of the adapted Gibbs- Helmholtz equation as given below in eq. 2.

$$\ln a_{\text{Te}}(1050 \text{ K}) = \ln a_{\text{Te}}(T_s) + \frac{\Delta \bar{H}_{\text{Te}}}{R} \left( \frac{1}{1050} - \frac{1}{T_s} \right) \quad (2)$$

where,  $T_s$  is the sample temperature in K,  $R$  is 8.314 J.K<sup>-1</sup>.mol<sup>-1</sup> and  $\Delta \bar{H}_{\text{Te}}$  is the partial enthalpy of tellurium in J.mol<sup>-1</sup>. The statistical error arises from the temperature measurements, viz., the reservoir and sample temperatures. The temperature error of  $\pm 2$  K results in a relative extended (0.95 confidence interval) error of  $\pm 0.15$  at the most in the value of the  $a_{\text{Te}}$  after conversion to one common temperature using these enthalpy values. A detailed discussion on error analysis has been presented by Ipser et al. [5]. The natural logarithm of the activity of tellurium for all the samples from various experimental runs for the compound NdTe<sub>2</sub> is plotted versus composition at a common temperature of 1050 K is presented in Fig. 5. All the calculated data lie within the phase boundaries as expected. The convergence of the experimental data from various runs indicates the consistency of the measured data.

The plot of the logarithm of partial pressure of tellurium versus reciprocal temperature for a two-phase field is shown Fig. 6. Vapour pressures measured in the two-phase regions of the NdTe<sub>2</sub> – Nd<sub>2</sub>Te<sub>5</sub> region allowed the determination of Gibbs energy of reaction for the following reaction.



Gibbs energy for the above reaction is

$$\Delta_f G_m^0(\text{Nd}_2\text{Te}_5, \text{s}) = 2\Delta_f G_m^0(\text{NdTe}_2, \text{s}) + \frac{1}{2} RT \ln p_{\text{Te}_2} \quad (4)$$

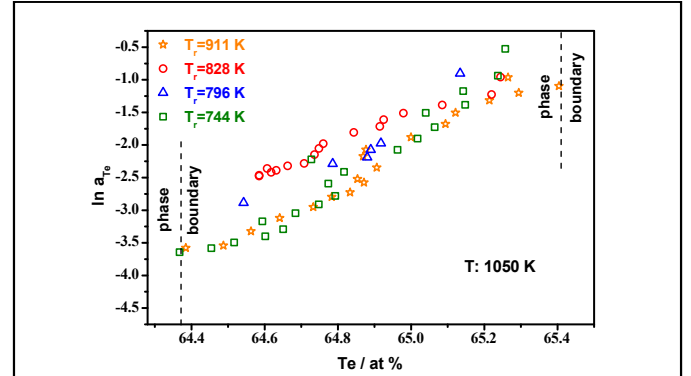


**Figure 5.** Natural logarithm of the Te activity for NdTe<sub>2</sub> at 1050 K.

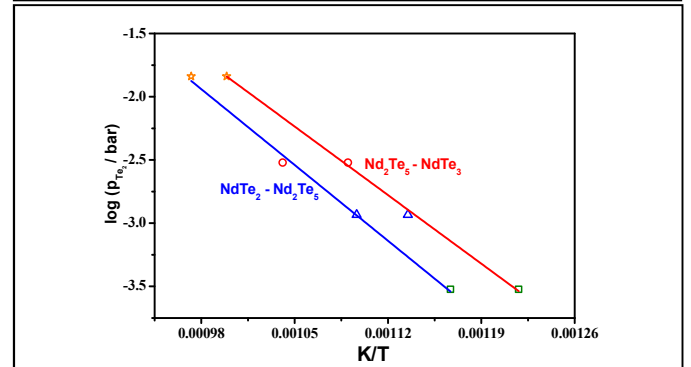


**Figure 6.** Logarithm of the Te<sub>2</sub> pressure against reciprocal sample temperature for NdTe<sub>2</sub> - Nd<sub>2</sub>Te<sub>5</sub> and Nd<sub>2</sub>Te<sub>5</sub>-NdTe<sub>3</sub> phase fields.

The expression for partial pressure as a function of temperature is given as,

$$\log(p_{\text{Te}_2}/\text{bar}) \pm 0.47 = 6.45 - \frac{8566}{T} \quad (T: 857 - 1028 \text{ K}) \quad (5)$$

The Gibbs energy of the reaction ( $\Delta G_r^0$ ) is given by,

$$\Delta G_r^0 = \Delta_f G_m^0(\text{Nd}_2\text{Te}_5, \text{s}) - 2\Delta_f G_m^0(\text{NdTe}_2, \text{s}) = \frac{1}{2} RT \ln p_{\text{Te}_2} \quad (6)$$

$$\Delta G_r^0(\text{kJ.mol}^{-1}) \pm 3.02 = -82.0 + 0.062 T \quad (T: 857 - 1028 \text{ K}) \quad (7)$$

Similarly, Gibbs energy of reaction for phase field Nd<sub>2</sub>Te<sub>5</sub> – NdTe<sub>3</sub> can be obtained as

$$\Delta G_r^0(\text{kJ.mol}^{-1}) \pm 3.02 = -74.2 + 0.056 T \quad (T: 821 - 1001 \text{ K}) \quad (9)$$

The errors given in the above expressions are expanded uncertainties with a 0.95 confidence level. The experimental thermodynamic data based on vapour pressure measurements are reported for the first time.

## References

- [1] E.A.C. Crouch, Academic Press Inc. (1977).
- [2] C.K. Mathews, J. Nucl. Mater. 201 (1993) 99–107.
- [3] P. Villars, H. Okamoto, K. Cenzual, eds., Binary Alloy Phase Diagram Database, ASM International, ASM International, 2018.
- [4] S. Shyam Kumar et al., Rev. Sci. Instrum. 93 (2022) 44105.
- [5] H. Ipser, R. Krachler, K.L. Komarek, The Isopiestic Method and its Application to a Thermodynamic Study of the Au-Zn System, in: H. Brodowsky, H.J. Schaller (Eds.), Thermochem. Alloy., Kluwer Academic Publishers, 1989: pp. 293–206.

## Studies on Thermophysical Properties of Simulated Waste Loaded Iron Phosphate Glass Matrix

P. Logaraj<sup>a</sup>, P. Ravisankar<sup>a</sup>, Ashish Jain<sup>a</sup> and R. Raja Madhavan<sup>a\*</sup>

<sup>1</sup>Materials Chemistry & Metal Fuel Cycle Group, Indira Gandhi Centre for Atomic Research, Kalpakkam, 603 102, India [\\*email \(rajam@igcar.gov.in\)](mailto:rajam@igcar.gov.in)

**Abstract:** Simulated high level waste in the form of stainless steel T91 was loaded in iron phosphate glass (IPG). The effect of waste loading on thermal expansion behavior of IPG was studied by push-rod dilatometry and compared with pristine IPG. Glass transition temperature of the glass was measured by DSC and the glass stability was assessed by measuring the characteristic temperatures of the glass by DTA.

Iron phosphate glass (IPG) is a potential alternate matrix for the immobilization of high level radioactive waste (HLW) [1,2]. During pyrochemical reprocessing of spent fuel discharged from fast breeder nuclear reactor, stainless steel (SS) cladding hull, noble metal fission products and zirconium from alloy fuel remains in the anode basket. These metal waste constituents are melted together at 1873 K to get a SS-zirconium metal waste alloy. The metal waste primarily (approx. 75 wt.%) consists of T91 steel clad [3]. As an alternate way to immobilize and store this metal waste, vitrification in IPG was studied. Radioactive decay heat of the fission product constituents of HLW results in an increase in temperature of the waste matrix. This will influence the thermophysical properties, which have a significant bearing on the long-term stability of the glass matrix. Thermophysical properties like thermal expansion and glass transition temperature ( $T_g$ ) measurements on the IPG samples were carried out.

T91 in the form of turnings was dissolved in 10 %  $FeCl_3$  solution under reflux conditions at 353 K. To this solution stoichiometric amounts of glass constituents were added as  $Fe_2O_3$  and ammonium dihydrogen phosphate. The reaction mixture in the form of slurry was heated to dryness on a hot plate (~393 K). The dried mass was melted and quenched in air at 1423 K. Up to 13 wt. % T91 steel loaded IPG was prepared (referred as T91IPG hereafter). Thermal expansion of 13 wt. % T91 steel loaded IPG was measured by dilatometry using a home-built push rod dilatometer up to 723 K in air at a heating rate of 2 K/min. High density thoria pellet was used as standard. Glass transition temperature  $T_g$  of these glass samples was determined using a heat flux type differential scanning calorimeter (Model : DSC 3 M/s. Mettler Toledo GmbH, Switzerland) in the temperature range of 320-723 K at a heating rate of 5 K/min in high pure argon atmosphere.

13 wt. % T91 steel loaded IPG found to be X-ray amorphous (Figure.1).  $Fe^{2+}$  content in T91 loaded IPG determined by redox titrimetry was found to be 14 % compared to 7 % in pristine IPG. The percentage thermal expansion of T91IPG and

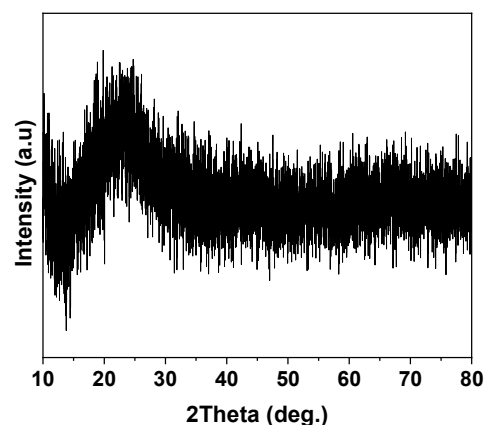


**Figure.1** XRD pattern of 13 wt. % T91 steel loaded IPG

pristine IPG as a function of temperature is depicted in figure.2. The expansion behaviors of both the glass samples were found to be linear up to 700 K. The coefficient of thermal expansion (CTE) (average)  $\alpha_{av}$  was calculated in the temperature range 300-700 K. CTE of T91IPG and pristine IPG were found to be  $8.9 \times 10^{-6} K^{-1}$  and  $6.7 \times 10^{-6} K^{-1}$  respectively. The small increase in expansion as a result of T91 steel loading is attributed to the increase in  $Fe^{2+}$  content.  $Fe^{2+}$  acts as a network modifier compared to  $Fe^{3+}$  as a network former, resulting in the depolymerization of the glass network and increase in non-bridging oxygen and weakening the network bonds. Weakening of the

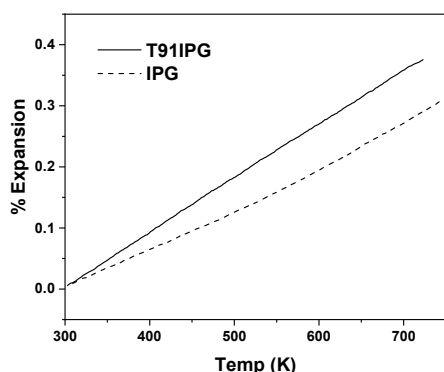


**Figure.2 Linear thermal expansion of 13 wt. % T91 steel loaded IPG and pristine IPG as a function of temperature.**

glass network is also reflected in change in glass transition temperature.  $T_g$  of T91IPG was found to be 777 K, lower than pristine IPG (783 K).

Glass stability (GS) which is characteristic of resistance to crystallization while heating can be assessed based on the characteristic temperatures viz.  $T_g$ , onset temperature of crystallization ( $T_x$ ) and liquidus temperature ( $T_L$ ). These characteristic temperatures of T91IPG was determined from DTA (Figure 3) and are listed in table 1.

**Table 1.** Characteristic temperatures determined by DTA

Sample	$T_g$ (K)	$T_x$ (K)	$T_L$ (K)
T91IPG3	777	1029	1228
IPG [4]	783	968	1198

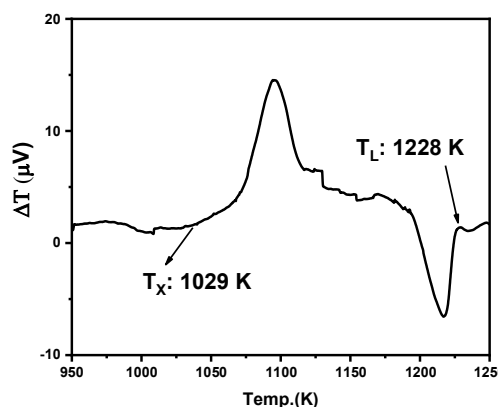


**Figure.3 DTA curve of T91IPG showing the characteristic temperature**

Higher  $T_x$ ,  $T_g$  and lower  $T_L$ .  $T_x$  in the case of T91IPG compared to pristine IPG shows better glass stability.

The effect on thermal expansion and  $T_g$  due to the loading of T91 steel constituents in IPG matrix was

studied and it was found that there was an increase in expansion behavior and decrease in  $T_g$  due to increase in  $Fe^{2+}$  content. Glass stability was found to be better than pristine IPG.

#### References:

- [1] R.K. Brow, C. W. Kim, S. T. Reis, International Journal of Applied Glass Science, 11 (2019), 4.
- [2] H. Li, J. Yi, Z. Qin, Z. Sun, Y. Xu, C. Wang, F.Zhao, Y. Hao, X. Liang, Journal of Non-crystalline Solids, 522 (2019), 119602.
- [3] S. G. Johnson, presented at WM'01 Conference, February 25-March 1, 2001, Tucson, AZ.
- [4] K. Joseph, Sajal Ghosh, K.V.G. Kutty, P.R.V.Rao, J. Nucl. Mat., 426 (2012) 233.

Effect of isovalent substitution on the energetics of  $\text{Sr}_x\text{Ba}_{(1-x)}\text{CeO}_3$  ( $0 \leq x \leq 1$ ) System

Hemlata Khadilkar, Premanadana P., Pratik Das, Pradeep Samui\*, S.K. Rakshit, S.C. Parida

Product Development Division,

Bhabha Atomic Research Centre, Mumbai - 400085

\*Corresponding author: psamui@barc.gov.in; phone: 022-25596464

**Abstract**

Proton conducting ceramic electrolyser cells are gaining attention worldwide for overriding greenhouse gases and to produce fuel for syngas. For this purpose, perovskite-type proton conducting ceramic oxides such as  $\text{SrCeO}_3(\text{s})$  and  $\text{BaCeO}_3(\text{s})$  have been studied and their combination being considered as the best candidates to be used as electrolytes for such SOFCs. Compounds in the  $\text{Sr}_x\text{Ba}_{(1-x)}\text{CeO}_3$  ( $0.2 \leq x \leq 0.8$ ) have been synthesized. The standard molar enthalpy of formation of these compounds have been determined by measuring the enthalpies of solution in lead borate solvent using high temperature solution calorimetry. The aim of this study is to optimize composition of Ba to Sr ratio for chemical stability by measuring thermal stability of different composition.

**Introduction**

Proton conducting ceramic electrolyser cells are gaining interest worldwide for devouring greenhouse gas  $\text{CO}_2$  and to produce fuel (syngas)[1-3]. For this purpose, perovskite-type proton conducting ceramic oxides such as  $\text{SrCeO}_3(\text{s})$  and  $\text{BaCeO}_3(\text{s})$  have been studied and being considered as the best candidates to be used as electrolytes for such SOFCs[1-5]. These ceramics have high proton conductivities in moist environment with low activation energy [3]. However,  $\text{BaCeO}_3$  exhibit high proton conductivity and less chemical stability against  $\text{CO}_2$ -containing gas. On the other hand,  $\text{SrCeO}_3(\text{s})$  shows relatively high chemical stability but low proton conductivity. The aim of this study is to optimize both proton conductivity and chemical stability by using a combination of the  $\text{BaCeO}_3$  (exhibiting high proton conductivity),  $\text{SrCeO}_3$  (exhibiting high chemical stability). Strontium doped barium cerate having composition  $\text{Sr}_x\text{Ba}_{(1-x)}\text{CeO}_3$  ( $0 \leq x \leq 1$ ) has been synthesized and the heat capacity of the compound was determined employing DSC. In this paper, the enthalpy of formation of compound was determined using high temperature oxide melt solution calorimeter using lead borate solvent.

**Experimental**

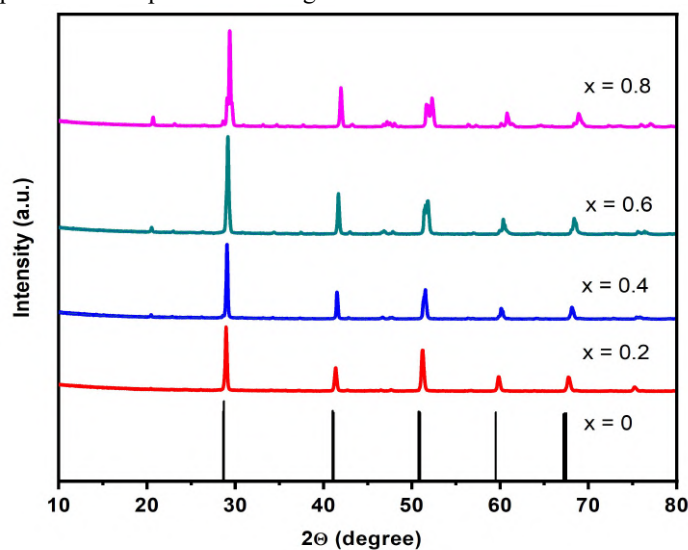
$\text{Sr}_x\text{Ba}_{(1-x)}\text{CeO}_3$  ( $0.2 \leq x \leq 0.8$ ) was prepared using solid state reaction method by heating a homogenous mixture of stoichiometric amounts of  $\text{BaCO}_3$  (99.9%, Sigma Aldrich),  $\text{CeO}_2$  (99.95%, Sigma Aldrich),  $\text{SrCO}_3$  (99.9%, Sigma Aldrich) in pellet form. Pellets were heated at 1073 K for 120 h in air atmosphere. Formation of compounds were confirmed by XRD analysis.

The enthalpies of formation of  $\text{Sr}_x\text{Ba}_{(1-x)}\text{CeO}_3$  ( $0.2 \leq x \leq 0.8$ ) compounds were determined by measuring the enthalpy change for the  $\text{Sr}_x\text{Ba}_{(1-x)}\text{CeO}_3$  ( $0.2 \leq x \leq 0.8$ ) and its reactants  $\text{BaCO}_3(\text{s})$ ,  $\text{SrCO}_3(\text{s})$  and  $\text{CeO}_2(\text{s})$  in liquid lead borate solvent ( $2\text{PbO} \cdot \text{B}_2\text{O}_3$ ) at 966 K using Alexsys high temperature calorimeter (Setaram, France). The details of the experimental measurements have been described elsewhere [6]. The lead borate solvent ( $2\text{PbO} \cdot \text{B}_2\text{O}_3$ ) was initially prepared by heating mixture of perfectly dried  $\text{PbO}$  (BDH, reagent grade) and  $\text{H}_3\text{BO}_3$  (BDH, reagent grade) in appropriate molar ratio and slowly heated in a platinum crucible inside the furnace. The melt was held at 966 K for 3 hours for homogenization. The solution calorimetry were performed at 966 K in air atmosphere with the provision of  $\text{Ar}(\text{g})$  bubbling for better mixing. The calibration of the calorimeter was carried out with small pieces of a synthetic sapphire [SRM-

720] from ambient into platinum crucible, maintained at 966 K [7].

**Result and Discussion**

The XRD patterns of  $\text{Sr}_x\text{Ba}_{(1-x)}\text{CeO}_3$  ( $0 \leq x \leq 1$ ) were shown in Fig. 1. When  $\text{Ba}^{2+}$  was doped with  $\text{Sr}^{2+}$  ions, the main peak shifted to a larger diffraction angle due to a decrease in lattice parameters as presented in Fig. 1.

Figure 1. XRD pattern of  $\text{Sr}_x\text{Ba}_{(1-x)}\text{CeO}_3$  compound

Enthalpy of dissolution values of  $\text{SrO}$  and  $\text{BaO}$  was calculated indirectly as both are highly hygroscopic and reactive materials under ambient condition. Their dissolution values are determined from the enthalpy of dissolution of  $\text{SrCO}_3$  and  $\text{BaCO}_3$  using a thermochemical cycle given in Tables 1. Standard molar enthalpy of formation of each composition was determined using the enthalpy of dissolution data of the  $\text{Sr}_x\text{Ba}_{(1-x)}\text{CeO}_3$  ( $0.2 \leq x \leq 0.8$ ) compounds and their component oxides viz.,  $\text{BaO}$ ,  $\text{SrO}$  and  $\text{CeO}_2$  in molten  $\text{PbO} + \text{B}_2\text{O}_3$  (2:1M ratio) solvent maintained at 966 K. The experimental details have been described in our previous work [6].

Table 1: Thermo-chemical cycle for determination of molar enthalpy of dissolution ( $\Delta H_{\text{ds}}^{\text{a}}$ ) of  $\text{MO}$  ( $\text{M}=\text{Ba}/\text{Sr}$ ) from 298 K ( $\text{Tr}$ ) to the solvent at 966K ( $\text{Ts}$ ) at  $P = 101325 \text{ Pa}^{\text{b}}$ .  $\Delta H_{\text{ds}}(\text{MO}) = \Delta H_1 - \Delta H_2 - \Delta H_3$ .

Reactions	$\Delta H_i$	$\Delta H / \text{kJ} \cdot \text{mol}^{-1}$	
		Sr	Ba
$\text{MCO}_3(\text{s}, 298\text{K}) = \text{MO}(\text{sln}, 966\text{K}) + \text{CO}_2(\text{sln}, 966\text{K})$	$\Delta H_1$	$206.6 \pm 4.6^c$	$207.9 \pm 4.7^c$
$\text{MCO}_3(\text{s}, 298\text{K}) = \text{MO}(\text{s}, 298\text{K}) + \text{CO}_2(\text{g}, 298\text{K})$	$\Delta H_2$	$234.3 \pm 1.8^d$	$269.2 \pm 2.1^d$
$\text{CO}_2(\text{g}, 298\text{K}) = \text{CO}_2(\text{sln}, 966\text{K})$	$\Delta H_3$	32.2	32.2
$\text{MO}(\text{s}, 298\text{K}) = \text{MO}(\text{sln}, 966\text{K})$	$\Delta H_{\text{ds}}$	$-59.5 \pm 4.9^c$	$-93.5 \pm 5.1^c$

<sup>a</sup> The heat effect associated to dissolution of solid at 298 K in 8 g of PbO+B<sub>2</sub>O<sub>3</sub> (2:1) at 966 K.

<sup>b</sup> Standard uncertainties u are u(p)=5000 Pa, u(T<sub>r</sub>)=0.5 K, u(T<sub>s</sub>)=0.05 K.; <sup>c</sup> Expanded uncertainties for  $\Delta H$  with 0.95 level of confidence (k ≈ 2); <sup>d</sup> Ref.[7]; <sup>e</sup> Uncertainty of the combined reaction is estimated as the square root of the sum of the squares of uncertainty of each individual reaction

The values of enthalpy of dissolution of Sr<sub>x</sub>Ba<sub>(1-x)</sub>CeO<sub>3</sub> (0.2 ≤ x ≤ 0.8) compounds and their component oxides viz., BaO, SrO and CeO<sub>2</sub> are given in Table 2. The values for molar enthalpy of dissolution ( $\Delta H_{\text{ds}}$ ) of Sr<sub>x</sub>Ba<sub>(1-x)</sub>CeO<sub>3</sub> (0.2 ≤ x ≤ 0.8), BaO, SrO and CeO<sub>2</sub> were combined with other auxiliary data such as standard molar enthalpy of formation of BaO, SrO, CeO<sub>2</sub> from the literature [7] to determine the standard molar enthalpy of formation of Sr<sub>x</sub>Ba<sub>(1-x)</sub>CeO<sub>3</sub> (0.2 ≤ x ≤ 0.8) at 298 K. Table 2 shows the thermo-chemical cycle devised to determine standard molar enthalpy of formation of Sr<sub>x</sub>Ba<sub>(1-x)</sub>CeO<sub>3</sub> (0.2 ≤ x ≤ 0.8) as a function of isovalent substitution of Ba<sup>2+</sup>. The quantitative variation of standard molar enthalpy of formation of Sr<sub>x</sub>Ba<sub>(1-x)</sub>CeO<sub>3</sub> (0.2 ≤ x ≤ 0.8) as function of composition is given in the Fig. 2. From Fig. 2, it could be observed that the  $\Delta_f H_{298}^\circ$  of Sr<sub>x</sub>Ba<sub>(1-x)</sub>CeO<sub>3</sub> becomes progressively more negative with increase in the substitution of SrCeO<sub>3</sub>.

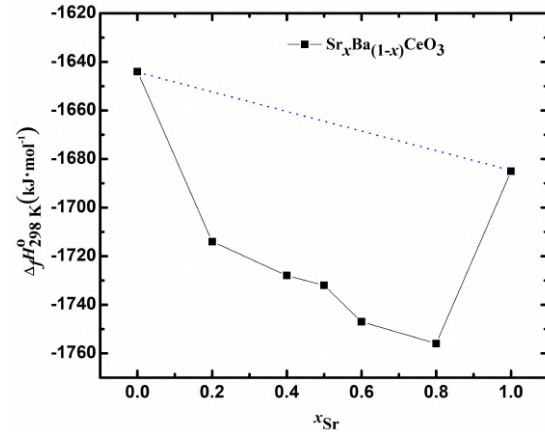


Figure 2. Variation of standard molar enthalpy of formation of Sr<sub>x</sub>Ba<sub>(1-x)</sub>CeO<sub>3</sub> (0 ≤ x ≤ 1) as a function of extent of Sr<sup>2+</sup> substitution.

This variation in excess molar enthalpy of formation could be due to the incorporation of multiple ions and the higher average charge to radius ratio of Sr<sup>2+</sup> than the Ba<sup>2+</sup> ion that increases the columbic force of attraction between metal ions and the oxide ions.

#### References

1. N. Kumar, J.J. Spivey. *Encycl Sustain Technol* (2017) 605-610.
2. E. H. P. Cordfunke et al., *J. Chem. Thermodynamics* 30(1998) 437-447.
3. J. Sarabut et al., *Int J Hydrogen Energy* 44 (2019) 20634–20640
4. N. I. Matskevich et al., *J. Therm. Anal. Calorim.* 130 (2017)1125–1131.
5. M.J. Scholten et al. *Thermochimi. Acta* 268 (1995) 161-168.
6. Navrotsky A., *Phys. Chem. Miner.* 2 (1977) 89.
7. Chase Jr. MW., *JANAF Thermochemical Tables*, 4th ed., J. Phys. Chem. Ref. Data 1995; Monograph No.9.
8. Rakshit et al., *J. Alloys Compd.* 505 (2010) 302–308.

Table 2: Thermo-chemical cycles for derivation of standard molar enthalpies of formation of Sr<sub>x</sub>Ba<sub>(1-x)</sub>CeO<sub>3</sub> (0.2 ≤ x ≤ 0.8) compounds at 298 K (T<sub>r</sub>)<sup>b</sup> using enthalpy of dissolution<sup>a</sup> data at temperature of solvent<sup>b</sup> 1089 K (T<sub>s</sub>)<sup>b</sup> and pressure P=101.325 kPa<sup>b</sup>.

Reactions	$\Delta H_i$	$\Delta H / \text{kJ} \cdot \text{mol}^{-1}$	Ref.
$\text{Sr}_x\text{Ba}_{(1-x)}\text{CeO}_3(\text{s}, 298\text{K}) \rightarrow x \cdot \text{SrO}(\text{sln}, 966\text{K}) + (1-x) \cdot \text{BaO}(\text{sln}, 966\text{K}) + \text{CeO}_2(\text{sln}, 966\text{K})$	$\Delta H_{1i}$		This Work
x = 0.2	i=1	30.2±3.0 <sup>d</sup>	
x = 0.4	i=2	43.8±2.7 <sup>d</sup>	
x = 0.5	i=3	47.8±2.5 <sup>d</sup>	
x = 0.6	i=4	62.2±2.2 <sup>d</sup>	
x = 0.8	i=5	70.1±2.1 <sup>d</sup>	
$\text{SrO}(\text{s}, 298\text{K}) \rightarrow x \cdot \text{SrO}(\text{sln}, 966\text{K})$	$\Delta H_2$	-59.5 ± 4.9 <sup>d</sup>	
$\text{BaO}(\text{s}, 298\text{K}) \rightarrow (1-x) \cdot \text{BaO}(\text{sln}, 966\text{K})$	$\Delta H_3$	-93.5 ± 5.1 <sup>d</sup>	
$\text{CeO}_2(\text{s}, 298\text{K}) \rightarrow \text{CeO}_2(\text{sln}, 966\text{K})$	$\Delta H_4$	50.5 ± 4.0 <sup>d</sup>	
$\text{Sr}(\text{s}, 298\text{K}) + 0.5\text{O}_2(\text{g}, 298\text{K}) \rightarrow \text{SrO}(\text{s}, 298\text{K})$	$\Delta H_5$	-592	[7]
$\text{Ba}(\text{s}, 298\text{K}) + 0.5\text{O}_2(\text{g}, 298\text{K}) \rightarrow \text{BaO}(\text{s}, 298\text{K})$	$\Delta H_6$	-553	[7]
$\text{Ce}(\text{s}, 298\text{K}) + \text{O}_2(\text{g}, 298\text{K}) \rightarrow \text{CeO}_2(\text{s}, 298\text{K})$	$\Delta H_7$	-1086	[7]
$x \cdot \text{Sr}(\text{s}, 298\text{K}) + (1-x) \cdot \text{Ba}(\text{s}, 298\text{K}) + \text{Ce}(\text{s}, 298\text{K}) + 1.5\text{O}_2(\text{g}, 298\text{K}) \rightarrow \text{Sr}_x\text{Ba}_{(1-x)}\text{CeO}_3(\text{s}, 298\text{K})$	$\Delta_f H_{298}^\circ$		This Work
	K		
x = 0.2	i=1	-1714±4 <sup>e</sup>	
x = 0.4	i=2	-1728±5 <sup>e</sup>	
x = 0.5	i=3	-1732±5 <sup>e</sup>	
x = 0.6	i=4	-1747±5 <sup>e</sup>	
x = 0.8	i=5	-1756±6 <sup>e</sup>	

$$\Delta_f H_{298}^\circ[\text{Sr}_x\text{Ba}_{(1-x)}\text{CeO}_3(\text{s}, 298\text{K})] = -\Delta H_{1i} + x \cdot \Delta H_2 + (1-x) \cdot \Delta H_3 + \Delta H_4 + x \cdot \Delta H_5 + (1-x) \cdot \Delta H_6 + \Delta H_7$$

<sup>a</sup> The heat effect associated to dissolution of solid at T<sub>r</sub> in 10 g of PbO+B<sub>2</sub>O<sub>3</sub> (2:1M ratio) at T<sub>s</sub>; <sup>b</sup> Standard uncertainties u are u(p)=5000 Pa, u(T<sub>r</sub>)=0.5 K, u(T<sub>s</sub>)=0.05 K; <sup>d</sup>Expanded uncertainties for  $\Delta H$  with 0.95 level of confidence (k ≈ 2); <sup>e</sup>Uncertainty of the combined reaction is estimated as the square root of the sum of the squares of uncertainty of each individual reaction.

## Electrochemical Kinetics of Reduction of $Mg^{2+}$ in Chloride and Fluoride molten salt electrolyte media

Mohsin Jafar<sup>1,3</sup>, S. K. Gupta<sup>2</sup> and A. K. Satpati<sup>1,3\*</sup>

<sup>1</sup> Analytical Chemistry Division

<sup>2</sup> Uranium Extraction Division

Bhabha Atomic Research Centre

Trombay, Mumbai 400085

<sup>3</sup>Homi Bhabha National Institute, Anushaktinagar, Mumbai 400094

\*Email: asatpati@barc.gov.in

### Abstract

Electrochemical method of deposition and purification of magnesium has been carried out in the present work using fluoride and chloride based molten salt media. Process optimization of electrochemical parameters were done to ascertain the conditions of electrochemical depositions. Cyclic voltammetry studies were carried out to find out the nature of the oxidation and reduction peaks both in blank molten salt and analyte dissolved molten salt respectively. Selective deposition of magnesium metal from molten salt media was confirmed by optimizing chronoamperometry measurements.

Purification of metal for the industry especially in the electronic industry has been a challenge. Vacuum distillation method has been reported to have purified magnesium, electrochemical method of recovery of magnesium in molten salt media is an interesting alternative to recover and purify magnesium as it produces efficient and clutter free method of recovery and purification. However, being a reactive metal, it is important to have a suitable electrolyte media to recover and recycle magnesium. In the present work electrochemical investigations are carried out to obtain the conditions for efficient recovery of magnesium from molten chloride and fluoride baths. Prior to the optimization of the parameters for the electrolysis some of the basic electrochemical investigations are carried out to ascertain the deposition and recovery conditions of Mg. Eutectic electrolyte bath containing the mixture of chloride and fluoride is used for the experiments [1].

Cyclic voltammetry scans are recorded at different scan rates and also with repeated scans the temperature of the experiments is kept at 600 °C. The results are shown in Fig.1. In blank supporting electrolyte the reduction current in the cathodic scan and the corresponding oxidation peaks during the reverse scans are related to the reduction of the molten metal ions ( $Li^+$  and  $Na^+$ ) in the forward scan and oxidation of the corresponding metals in the backward scan (Fig.1 A).

With increase in the scan rate of the measurements the peak current is increased without any significant shift in the peak potential during the reduction process. After establishing the electrochemical processes of the bare molten electrolyte solution, the electrochemical measurements were carried out by loading the electrolyte with  $MgF_2$  and the cyclic voltammetry scan were recorded at different scan rates and also with repetitive scans, corresponding results of the repetitive cyclic voltammetry scans are placed in Fig.1B.

The Reduction peak due to  $Mg^{2+}$  is clearly observed, with repetitive scans the reduction peak remained either stable or marginally enhanced. The corresponding peaks are increased from initial scans and there-after the peaks remained almost stable, indicating the deposition of Mg metal due to the reduction in the cathodic scans. The feasibility of selective deposition of Mg metal has been

ascertained from the cyclic voltammetry and chronoamperometry investigations.

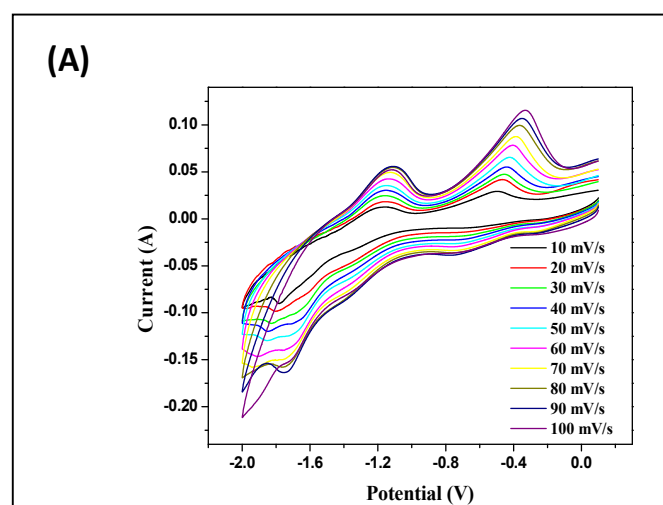


Figure 1A. Cyclic voltammetry of LiCl/KCl molten mixture at different scan rates

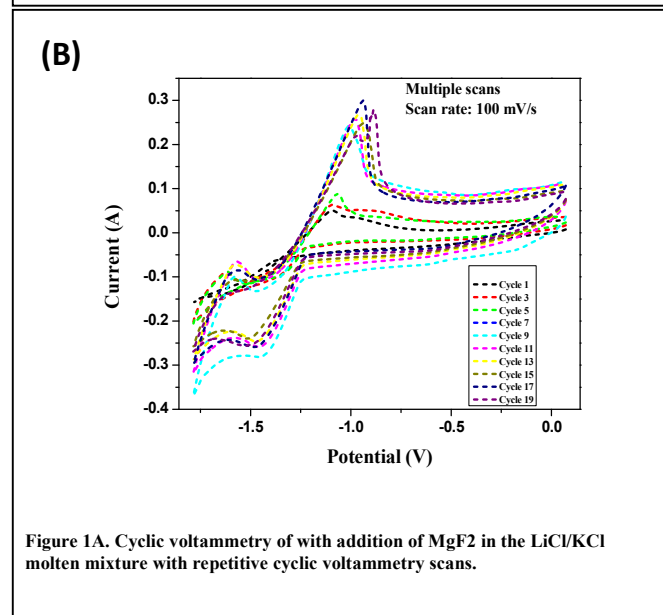


Figure 1A. Cyclic voltammetry of with addition of  $MgF_2$  in the LiCl/KCl molten mixture with repetitive cyclic voltammetry scans.

### References

[1] Satpati et al, RSC advances, 2015,5, 33163-33170.



## Thermodynamic and Thermo-physical Properties of Frozen Fuel and Coolant Salts for Molten Salt Breeder Reactor

Abhishek Kumar Rai<sup>a,c,\*</sup>, Manoj Kumar Sharma<sup>b,c</sup>, S. K. Rakshit<sup>a</sup> and S. C. Parida<sup>a,c</sup>

<sup>a</sup>Product Development Division, Radiochemistry & Isotope Group, Bhabha Atomic Research Centre, Mumbai, 400085

<sup>b</sup>Fuel Chemistry Division, Radiochemistry & Isotope Group, Bhabha Atomic Research Centre, Mumbai, 400085

<sup>c</sup>Homi Bhabha National Institute, Anushaktinagar, Mumbai, 400094

\* [abhirai@barc.gov.in](mailto:abhirai@barc.gov.in) Tel: 022 25594593

### Abstract

Alkali / alkaline earth fluorides and actinide fluorides are key components of the fuel in a molten salt reactor (MSR). In the present work, thermodynamic and thermo-physical parameters (melting/liquidus points, isobaric specific heat capacities, thermal diffusivities and thermal conductivities) of two frozen candidate fuel salts (0.70LiF-0.08CaF<sub>2</sub>-0.22UF<sub>4</sub>) and 0.70LiF-0.08CaF<sub>2</sub>-0.206ThF<sub>4</sub>-0.014UF<sub>4</sub>) and one frozen secondary coolant salt (LiF-NaF-KF eutectic) have been determined.

### Introduction:

Molten salt reactor (MSR) is one of the six reactor concepts proposed by Gen IV International Forum [1]. According to the Indian molten salt breeder reactor (IMSBR) concept, ThF<sub>4</sub> and UF<sub>4</sub> (or PuF<sub>3</sub>) dissolved in a carrier salt consisting of alkali and/or alkaline earth fluorides will be the fuel salt which will also serve the purpose of primary coolant. For secondary coolant channel, LiF-NaF-KF eutectic (FLiNaK) is being considered as a typical candidate coolant.

The transfer of the heat produced in the reactor core will be primarily governed by the thermal properties of the fuel and coolant salts. For this reason, it becomes very important for smooth and successful operation of an MSR, to have the knowledge of thermodynamic and thermo-physical properties of fuel and coolant salts. These thermodynamic and thermo-physical properties are heat capacity, enthalpy increments, enthalpy of fusion, thermal conductivity, viscosity, thermal expansion etc. These properties (for molten as well as solid salts) are also essential for understanding the energetics of the fuel during heating/cooling cycles. Enthalpies of transition, heat capacities and thermal conductivities are the parameters helpful in estimation of the time required and heat dissipated during cooling of the salt mixture at the time of reactor shut down.

Two candidate fuel salt mixtures consisting of LiF and CaF<sub>2</sub> as carrier salts have been taken in this work. Chemical composition of the fuel and the coolant salt mixtures are as follows:

**Fuel Salt 1:** 70 mol% LiF - 8 mol% CaF<sub>2</sub> - 22 mol% UF<sub>4</sub>

**Fuel Salt 2:** 70 mol% LiF - 8 mol% CaF<sub>2</sub> - 20.6 mol% ThF<sub>4</sub> - 1.4 mol% UF<sub>4</sub>

**Coolant Salt:** 46.5 mol% LiF - 11.5 mol% NaF - 42 mol% KF  
Thermodynamic and thermo-physical properties of the above frozen salt mixtures like melting/liquidus points, isobaric specific heat capacities, thermal diffusivities and thermal conductivities have been determined in the present work.

### Experimental:

LiF, NaF, KF and CaF<sub>2</sub> used in this work are of 99.9 % purity. However, they were vacuum dried at 723 K for 8 hrs. UF<sub>4</sub> was obtained from UED, BARC. It was treated with NH<sub>4</sub>HF<sub>2</sub> to avoid the presence of any oxide or oxyfluoride impurity. ThF<sub>4</sub> was prepared by solid state hydro-fluorination of ThO<sub>2</sub> by ammonium bifluoride [2].

For preparation of the fuel and coolant salt mixtures, requisite stoichiometric amount of the constituent salts were mixed physically in mortar and loaded in graphite crucibles. The mixtures were then heated at 423 K under rotary vacuum of 10 Pa (to remove any moisture absorbed during mixing) followed by heating at 1150 K (above the melting point of LiF) under flowing HP-Ar gas passed through various oxygen and

moisture getters. The salts were cooled under HP-Ar atmosphere.

Melting points of the coolant salt and liquidus temperatures of the fuel salt mixtures were measured using indigenously designed differential thermal analyzer (DTA) at heating/cooling rate of 5 K.min<sup>-1</sup>. Heat capacity measurements were carried out using Setaram DSC-131 by standard three step method in continuous mode with a heating rate of 5 K.min<sup>-1</sup> in the temperature range well below their melting points using  $\alpha$ -Al<sub>2</sub>O<sub>3</sub> (SRM 720) as reference material. Thermal diffusivities were measured by laser flash analysis technique using Linseis LFA-1000. All the measurements were done under HP-Ar atmosphere. The samples (disc shape) were coated with graphite spray to enhance the emission/absorption properties of the sample, optimizing the signal-to-noise ratio.

### Results and Discussion:

Melting points of the frozen fuel salts (Li<sub>0.7</sub>Ca<sub>0.08</sub>U<sub>0.22</sub>F<sub>1.74</sub> and Li<sub>0.7</sub>Ca<sub>0.08</sub>Th<sub>0.206</sub>U<sub>0.014</sub>F<sub>1.74</sub>) and coolant salt (Li<sub>0.465</sub>Na<sub>0.115</sub>K<sub>0.42</sub>F), determined by differential thermal analysis is tabulated in Table 1. Temperature calibration of the indigenously designed DTA was carried out by melting of NIST standard samples Bi ( $T_m=271.4$  °C), Pb ( $T_m=327.5$  °C), Zn ( $T_m=419.5$  °C) and Sb ( $T_m=630.6$  °C). The DTA thermograms obtained in the heating as well as cooling cycles are shown in Fig. 1.

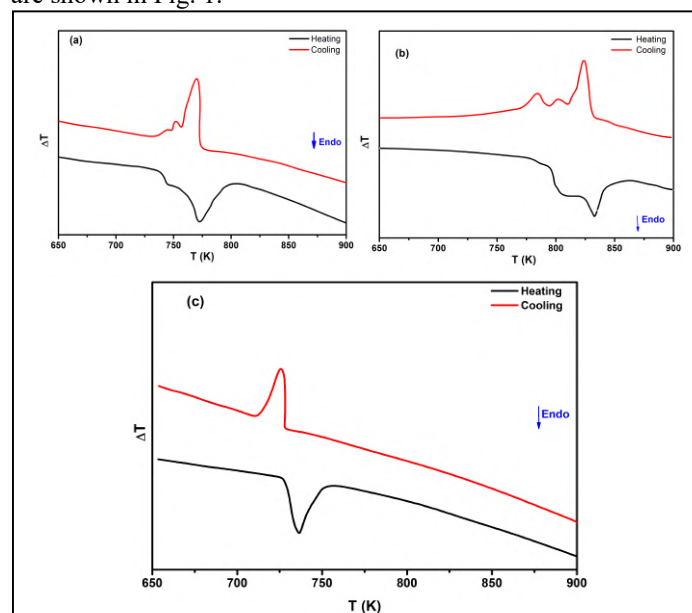


Figure 1. DTA thermograms obtained in heating and cooling cycles for (a) Fuel Salt 1, (b) Fuel Salt 2 and (c) Coolant Salt

**Table 1.** Melting /liquidus temperatures and densities of fuel salts and coolant salt mixtures (frozen)

	Composition	Melting / liquidus point	Density (g/cm <sup>3</sup> )
<b>Fuel Salt 1</b>	0.70LiF-0.08CaF <sub>2</sub> -0.22UF <sub>4</sub>	773 K	6.10
<b>Fuel Salt 2</b>	0.70LiF-0.08CaF <sub>2</sub> -0.206ThF <sub>4</sub> -0.014UF <sub>4</sub>	833 K	6.01
<b>Coolant Salt</b>	0.465LiF-0.115NaF-0.42KF	728 K	2.51

Isobaric specific heat capacities of the frozen salt mixtures, measured by heat flux differential calorimetry in the temperature ranges well below their melting/liquidus temperatures, are plotted in Fig. 2. Fig. 2 also shows the comparison of the measured values with the values estimated by Neumann Kopp's additivity rule. The measured values show reasonable agreement with the Neumann Kopp values. The measured heat capacity values are fitted into non-linear equations as following:

**Fuel Salt 1 (300-725K):**

$$C_p (\pm 0.003) (\text{Jg}^{-1}\text{K}^{-1}) = 0.662 + 1.671 \times 10^{-4} \times T - 7394.039 / T^2 \dots(1)$$

**Fuel Salt 2 (300-775K):**

$$C_p (\pm 0.003) (\text{Jg}^{-1}\text{K}^{-1}) = 0.696 + 1.541 \times 10^{-4} \times T - 7404.012 / T^2 \dots(2)$$

**Coolant Salt (300-675K):**

$$C_p (\pm 0.004) (\text{Jg}^{-1}\text{K}^{-1}) = 1.045 + 4.237 \times 10^{-4} \times T - 6875.623 / T^2 \dots(3)$$

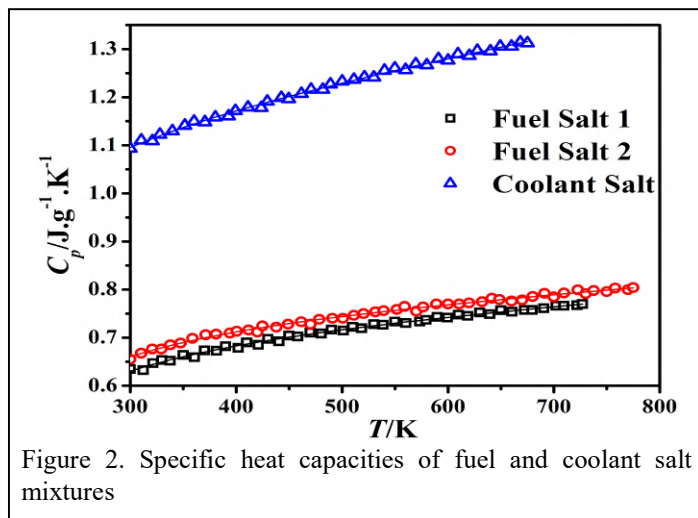


Figure 2. Specific heat capacities of fuel and coolant salt mixtures

Thermal diffusivities of the frozen fuel and coolant salts, measured by laser flash method in the temperature ranges well below their melting/liquidus temperatures, are shown in Fig. 3. Thermal diffusivity ( $\alpha$ ) is related to the thickness of sample ( $l$ ) and time required for attaining the maximum temperature rise at the other surface of sample ( $t_{1/2}$ ) as follows [3]:

$$\alpha = 0.13879 \times l^2 / t_{1/2} \dots(4)$$

The measured thermal diffusivity values are fitted into following equations:

**Fuel Salt 1 (300-725K):**  
 $\alpha (\pm 0.00008) (\text{cm}^2\text{s}^{-1}) = 0.00389 + 1.336 / T \dots(5)$

**Fuel Salt 2 (300-775K):**  
 $\alpha (\pm 0.00007) (\text{cm}^2\text{s}^{-1}) = 0.00482 + 1.484 / T \dots(6)$

**Coolant Salt (300-675K):**  
 $\alpha (\pm 0.00003) (\text{cm}^2\text{s}^{-1}) = 0.00371 + 1.098 / T \dots(7)$

Thermal conductivity ( $\lambda$ ) is related to thermal diffusivity ( $\alpha$ ), specific heat capacity ( $C_p$ ) and density ( $\rho$ ) of the sample as follows:

$$\lambda = \alpha \times C_p \times \rho \dots(8)$$

Geometrically determined densities of the samples are given in Table 1. Using these densities and the measured thermal diffusivities and specific heat capacities, thermal conductivities of the salt mixtures were calculated. The values are plotted in Fig. (4), and are fitted into following expressions:

**Fuel Salt 1 (300-725K):**

$$\lambda (\pm 0.04) (\text{Wm}^{-1}\text{K}^{-1}) = 2.32 + 271.77 / T \dots(9)$$

**Fuel Salt 2 (300-775K):**

$$\lambda (\pm 0.03) (\text{Wm}^{-1}\text{K}^{-1}) = 2.84 + 314.68 / T \dots(10)$$

**Coolant Salt (300-675K):**

$$\lambda (\pm 0.01) (\text{Wm}^{-1}\text{K}^{-1}) = 1.54 + 144.81 / T \dots(11)$$

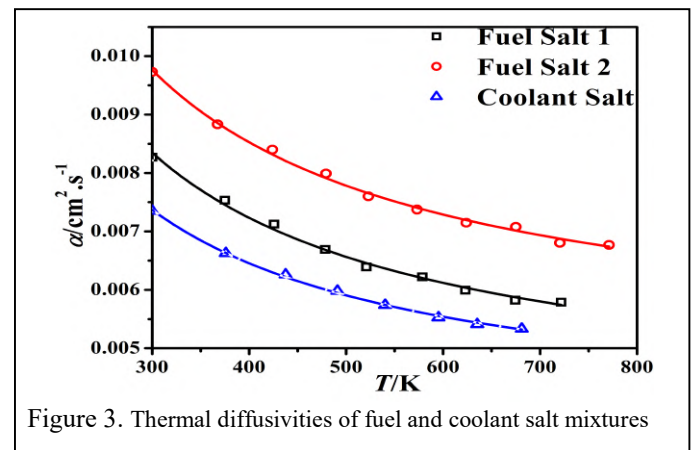


Figure 3. Thermal diffusivities of fuel and coolant salt mixtures

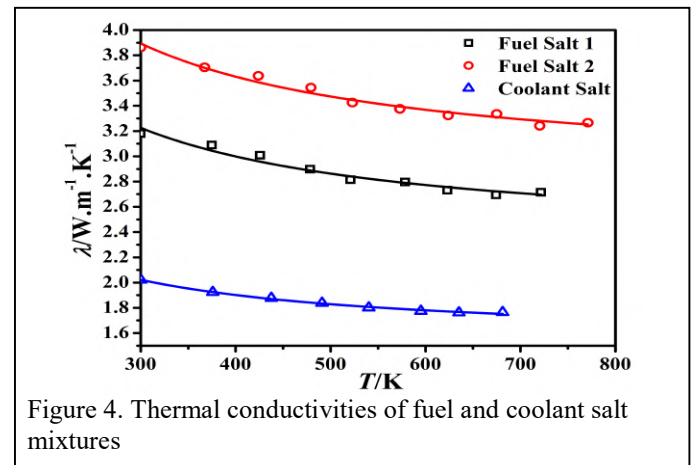


Figure 4. Thermal conductivities of fuel and coolant salt mixtures

Decrease in thermal diffusivity and thermal conductivity with increase in temperature may be explained on the basis of the fact that there is more scattering of phonons at higher temperatures making the phononic conduction difficult.

**References:**

1. A Technology Roadmap for Generation IV Nuclear Energy Systems, US DOE Nuclear Energy Research Advisory Committee and the Generation IV International Forum, December 2002, GIF-002-00.
2. B.N. Wani, S.J. Patwe, U.R.K. Rao, K.S. Venkateswarlu, Journal of Fluorine Chemistry, 44 (1989) 177-185.
3. W.J. Parker, R.J. Jenkins, C.P. Butler, and G.L. Abbott, J. Appl. Phys., 32 (1961) 1679-1684.

## Studies on effect of oxygen impurity on decomposition rate of sodium hydride in liquid sodium towards secondary cold trap regeneration

P. Manikandan\*, V.A. Faizal, M. Lavanya, R. Karunakaran, N. Murugesan, Hrudananda Jena, Rajesh Ganesan, V. Jayaraman

*Materials Chemistry & Metal Fuel Cycle, IGCAR, Kalpakkam*

\* Corresponding author: manikandan@igcar.gov.in

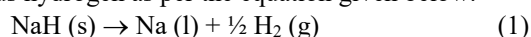
### Abstract

Cold traps in primary and secondary sodium circuits of FBRs play a vital role in maintaining the hydrogen and oxygen levels in liquid sodium below the permissible limits so that, steam leak in secondary sodium circuit could be detected at the incipient stage itself. They are maintained at 393 K and trap hydrogen and oxygen as NaH and Na<sub>2</sub>O when liquid sodium containing larger amounts of dissolved hydrogen and oxygen is passed through them. When they are saturated with these impurities, they need to be regenerated to reduce the down time of reactor. It is known that NaH dissociates completely on heating to 673 K. In the present study, the effect of oxygen in liquid sodium on the decomposition behavior of NaH was investigated.

Typically Fast Breeder Reactors (FBR) two liquid sodium coolant circuits, namely, primary and secondary [1]. Sodium in the secondary circuit passes through steam generators (SG), transfers heat to water and produces steam at high temperature and pressure. Replacement of Fuel Sub-Assemblies (FSA) and reusable components in the core of the reactor and impurities in argon cover gas elevate the levels of oxygen and hydrogen in the primary sodium. The inner wall of SG, which is in contact with high temperature steam, corrodes continuously and releases hydrogen. Hydrogen thus liberated diffuses through the steel wall to the secondary sodium and increases hydrogen concentration in sodium. The presence of oxygen even in ppm levels and high hydrogen concentration in liquid sodium leads to the corrosion and embrittlement of structural materials, respectively. To resolve this problem, cold traps (CT), which are held at 393 K, are installed in primary and secondary sodium circuits of FBR to maintain the concentrations of hydrogen and oxygen in liquid sodium below the permissible limits. During the reactor operation, SS mesh of these CTs acts as nucleation centres and NaH and Na<sub>2</sub>O get precipitated on it when the sodium containing higher concentrations of dissolved hydrogen and oxygen is circulated through them. At this temperature, the saturation solubility of hydrogen and oxygen in liquid sodium are 50 ppb and 2 ppm, respectively. Sodium flow reduction is observed in CTs when they get saturated on operation for long duration. Hence regeneration is necessitated to restore their trapping efficiency so that impurity levels in liquid sodium can be kept within the acceptable limits. Maintaining hydrogen impurity below the limits is vital to detect the steam leak into secondary sodium at the incipient stage.

As per the design, the primary sodium cold trap of FBR can remain in the sodium circuit for the entire lifespan of the reactor, typically ~40 years. However, the secondary cold trap (SCT) of FBR needs to be regenerated regularly once in 4.5 years. The quantity of hydrogen released during every regeneration is estimated to be about 93 kg [2].

For regeneration of cold trap of FBR, a well-known technique called Thermo Vacuum Process (TVP) is to be adopted [3]. In this process, as NaH deposited on the SS mesh is heated to 673 K under the vacuum of 10 mbar, it decomposes to Na and gaseous hydrogen as per the equation given below.



H<sub>2</sub> evolved during the process needs to be accounted for accurately and mitigated effectively so that the concentration of hydrogen discharged into the atmosphere never exceeds 2% (50% of LEL of H<sub>2</sub> in air). The Hexamini cold trap was recently regenerated successfully by TVP using in-house developed hydrogen sensors [4].

### Experimental

The photograph given in Fig 1 shows the experimental facility used in the present experiment. This facility has a knife-edge flanged stainless steel reaction vessel (RV) equipped with a gas purging unit, a pressure transducer, a vacuum pump, a pirani gauge, a furnace with a PID controller and hydrogen sensors, namely, Proton Exchange Membrane Hydrogen Sensor (PEMHS) and Nucon Hydrogen Sensor (NHS). The gas purging lines, which are made of stainless steel tubes, are used for passing UHP argon to the RV and for flowing commercial argon to dilute the released hydrogen due to decomposition of NaH. Oil free dry vacuum pump is used to generate the vacuum in RV and the vacuum is read by the pirani gauge. PID controller along with the furnace is used for heating RV containing the sample to the required temperature.

NaH, Na and Na<sub>2</sub>O were weighed in appropriate amounts and loaded in RV. SS flange with knife edge provided with inlet and outlet valves was used to seal the vessel with an annealed copper gasket. Masses of these three chemicals used in different experiments are given in Table 1. Masses of sodium and NaH were kept constant at ~70 g and ~1.5 g, respectively whereas the mass of sodium oxide in the mixture was varied in multiples of 5% in the range 0 to 20%. The RV loaded with the sample was placed in the furnace of the experimental set-up and it was heated to 673 K. The RV outlet was connected to hydrogen sensors via a vapour trap, a condenser and a vacuum pump. The experiments were conducted in two stages. In stage 1, UHP Argon was passed through the RV while heating from room temperature to 673 K to sweep the hydrogen gas formed in the process. In stage 2, the vessel was evacuated to the pressure of 10 mbar and hydrogen produced during the decomposition was pumped out, diluted with commercial argon and passed through the hydrogen sensors. The hydrogen concentration as a function of time was measured by PEMHS and NHS and data was logged. Utmost care was taken to ensure that the concentration of H<sub>2</sub> in mixture released to the atmosphere was below 2%.

### Results and discussion

PEMHS and NHS were calibrated using 8% H<sub>2</sub>/Ar mixture and the commercial argon as the diluting gas in the hydrogen concentration range 0 – 4%. The concentration of hydrogen in the gas mixture measured in TVP is related to hydrogen release rate by the equation (2).

$$C_{\text{H}_2} = \left( \frac{R_{\text{H}_2}}{R_{\text{H}_2} + F} \right) \times 100 = \left( \frac{R_{\text{H}_2}}{F} \right) \times 100 \quad (2)$$

Where, R<sub>H<sub>2</sub></sub> is the rate at which hydrogen is released in SCCM, F is the flow rate of argon in SCCM and C<sub>H<sub>2</sub></sub> is the measured concentration of hydrogen in argon in percentage at a given

NaH (g)	Na <sub>2</sub> O (g)	Na <sub>2</sub> O in NaH (wt%)	H <sub>2</sub> measured (SCC)	Decomposition Efficiency (%)
1.5030	0.000	0.0	676.39	96.4
1.4794	0.067	4.5	532.4	77.1
1.5012	0.156	10.4	521.4	74.4
1.5104	0.218	14.4	509.3	72.3
1.5598	0.328	21.0	431.97	59.3

instant of time. Since the flow rate of argon was very high compared to that of hydrogen flow rate,  $R_{H_2} + F \approx F$ .

$$R_{H_2} = C_{H_2} \times F \times 100 \quad (3)$$

The hydrogen release profiles in SCCM obtained as per the equation 2, for pure NaH and the mixtures of Na, NaH and Na<sub>2</sub>O containing the fixed amounts of Na and NaH and the varied quantities of Na<sub>2</sub>O are depicted in Fig. 2. In all the experiments the temperature of the RV was increased under argon purging subsequently argon flow to the RV was stopped and pumping out of hydrogen was continued under vacuum until hydrogen



**Fig. 1. Photograph of the experimental facility used in the present study**

concentration became zero. The peak hydrogen release rates were observed at different times as the evacuation was started at different times. The total quantity of hydrogen released  $m_{EH_2}$  in SCC was obtained from hydrogen release profiles using the equation 4.

$$m_{EH_2} = \int R_{H_2} dt \quad (4)$$

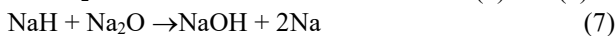
$m_{EH_2}$  is mass of hydrogen released in SCC during the time interval of integration. Quantity of theoretical H<sub>2</sub> release ( $m_{TH_2}$ ) from NaH decomposition (two moles of NaH release one mole of H<sub>2</sub>) can be calculated using equation 5.

$$m_{TH_2} = (1.5 \times 22400)/(2 \times 24) \quad (5)$$

NaH decomposition efficiency as a function of Na<sub>2</sub>O content was calculated using the equation 6.

$$\text{NaH decomposition Efficiency (\%)} = \left( \frac{m_{EH_2}}{m_{TH_2}} \right) \times 100 \quad (6)$$

The data obtained for all the experiments are shown in Table 1. It can be seen from Table 1 that pure NaH in liquid sodium decomposed up to ~96% and as the amount of Na<sub>2</sub>O in the mixture increases, the volume of H<sub>2</sub> released due to NaH decomposition decreases. This trend can be understood by considering the reactions of a fraction of H<sub>2</sub> released and NaH itself with Na<sub>2</sub>O as can be seen from the reactions (7) and (8).



The decrease in the efficiency may be attributed to the reduced chemical activity of NaH by incorporation of oxygen into NaH phase as OH [5]. According to Mcpheeters et al. [6], the presence of Na<sub>2</sub>O appears to inhibit the hydrogen evolution rate

by as much as one order of magnitude [6]. This reduction of evolution rate is probably due to interaction of the hydrogen and oxygen species either in solution, or at interfaces between the phases. These results will be useful in the regeneration of the cold trap of FBR loaded with oxide impurities along with NaH.

**Table.1 NaH decomposition efficiency as a function of Na<sub>2</sub>O content in liquid sodium.**

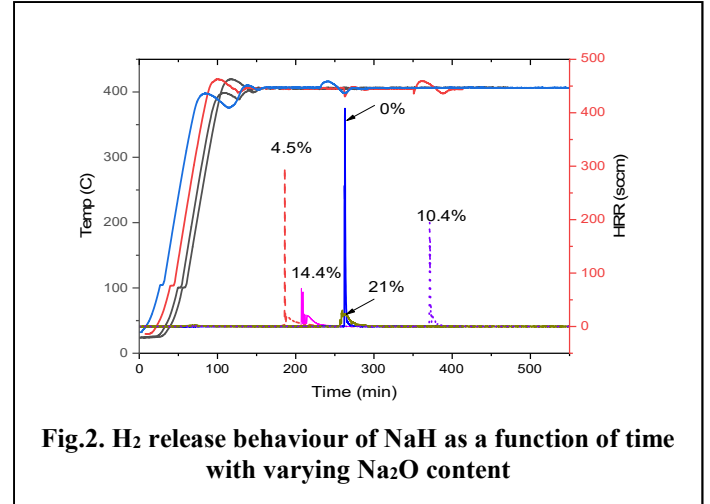


**Fig.2. H<sub>2</sub> release behaviour of NaH as a function of time with varying Na<sub>2</sub>O content**

#### References

1. S.C Chetal, SB. Bhoje, R.D. Kale, A.S.L.K. Rao, T.K. Mitra, A. Selvaraj, V.K. Sethi, T.R. Sundaramoorthy, V. Balasubramaniyan, G. Vaidyanathan, Conceptual design of heat transport systems and components of FBR-NSSS, IAEA Techdoc-XA9643093.
2. M.G.Hemanath, C. Meikandamurthy, A. Ashok kumar, S. Chandramouli, K.K. Rajan, M. Rajan, G. Vaidyanathan, G. Padmakumar, P. Kalyanasundaram, Baldev Raj, Nucl. Engg.Des. 240 (2010) 2737-2744.
3. P. Kalyanasundaram, B. Baldev Raj, M.G. Hemanatha,, S. Chandramouli, B. Venkatraman, Regeneration qualification of cold trap using modeling validated by radiography and image processing, Nucl. Engg.Des. 255 (2013) 368-375.
4. N. Murugesan, V.A. Faizal, E. Prabhu, S. Shyam Kumar, SajalGhosh, A. Sree Rama Murthy, R. Sudha, Hrudananda Jena, Rajesh Ganesan, V. Jayaraman, Studies on In-situ regeneration of cold trap of a Bench-Top sodium loop, ", Nucl. Engg.Des., 403 (2023)112156.
5. C.F. Knights, A.C. Wittingham, in: Proceedings of the Conference on Material Behaviour and Physical Chemistry in Liquid Metal Systems, Karlsruhe, Germany, March 24-26, 1981, Plenum, New York, 1982, p. 287.
6. C. C. McPheeters, S. B. Skladzien, D. J. Raue, Experiments on Cold-Trap Regeneration by NaH Decomposition, ANL-79-100 (1980) 1-14.

## Thermal properties of Diglycine Perchlorate: IR, DSC, QMS and TGA Study

Harsha Kumawat,<sup>a,b</sup> S.R. Vishwakarma,<sup>a</sup> B. R. Gonde,<sup>c</sup> N. Rajee,<sup>d</sup> and Himlal Bhatt,<sup>a,b,\*</sup>

<sup>a</sup>High Pressure & Synchrotron Radiation Physics Division, Bhabha Atomic Research Centre, Trombay, Mumbai, India 400085

<sup>b</sup>Homi Bhabha National Institute, Anushaktinagar, Mumbai, India 400094

<sup>c</sup>Electromagnetic Applications & Instrumentation Division, Bhabha Atomic Research Centre, Trombay, Mumbai, India 400085

<sup>d</sup>Analytical Chemistry Division, Bhabha Atomic Research Centre, Trombay, Mumbai, India 400085

\*hbhatt@barc.gov.in, 20331

### Abstract

Diglycine perchlorate (DGPCl) is an organic perchlorate with promising applications in optoelectronics and high-power laser systems. Understanding the thermal properties and dissociation mechanism of such perchlorates is crucial, as these materials exhibit potential as high-energy density materials. The current investigation focuses on identifying the gaseous products released during the high-temperature phase transition of DGPCl, which occurs at  $\sim 240^\circ\text{C}$ . The study reveals the evolution of a variety of gaseous products, including hydrogen cyanide (HCN), carbon monoxide (CO), carbon dioxide (CO<sub>2</sub>), water vapor (H<sub>2</sub>O), methane (CH<sub>4</sub>), nitrous oxide (N<sub>2</sub>O), nitric oxide (NO), and hydrogen chloride (HCl). These decomposition products were analysed using *in-situ* ro-vibrational infrared spectroscopy and quadrupole mass spectrometry equipped with an externally controlled heating stage. Also, the exothermic energy release was estimated from differential scanning calorimetry measurements (which comes out to be  $\sim 400\text{kJ/mol}$ ); whereas the transitions were confirmed by thermogravimetric – Infrared technique. The combination of these techniques provided a comprehensive understanding of the dissociation process of DGPCl.

Perchlorates hold special interest for their potential applications in munitions, rocket propellants, food packaging industries, non-linear optics, etc. Diglycine perchlorate (DGPCl) is an underexplored organic perchlorate [1]. It is a potential candidate for optoelectronics and high-power laser applications due to its wide band gap and high laser induced damage threshold [2]. At high pressures, it shows phase transition near 9GPa [3]. Its asymmetric unit cell (triclinic - crystal structure) is formed by 5 perchlorate anions (ClO<sub>4</sub><sup>-</sup>) and two types of glycine moieties – zwitterionic (NH<sub>3</sub><sup>+</sup>CH<sub>2</sub>COO<sup>-</sup>) and cationic (NH<sub>3</sub><sup>+</sup>CH<sub>2</sub>COOH), forming 5 glycine dimeric units. These dimers are interconnected by O-H---O hydrogen bonds and connected with perchlorate units by N-H---O hydrogen bonds.

DGPCl shows melting transitions at 103.5°C, 123°C and  $\sim 216^\circ\text{C}$ , decomposes at 262.6°C as shown by DSC studies [1]. The evolution of gaseous products during the thermal decomposition plays an important role in determining the new phase and/or the residuals after certain phase transformations, mechanism of decomposition. In this work we are presenting the *in-situ* infrared (IR) analysis of gases evolved during heat treatment of DGPCl in temperature range from 27 to 350°C. DGPCl crystals were placed in a glass tube which was then heated by Nichrome wire and gases were allowed to pass in to a gas cell sealed with IR transparent (KBr) windows. The IR spectra of trapped gases were recorded by high-resolution Bruker make FTIR. A total of 200 scans were coadded during each measurement, conducted at temperatures of  $\sim 100^\circ\text{C}$ , 250°C, and 350°C. The temperature was monitored and controlled with an accuracy of  $\pm 5^\circ\text{C}$ . We also used an Ex-torr make RGA XT-200M Quadrupole Mass Spectrometer (QMS) coupled to the Linkham LTS350 heating stage in Electron Multiplier detector mode, in order to examine gaseous products released from heat treatment of DGPCl crystals from room temperature to 300°C. The RGA is housed in vacuum chamber maintained at  $1 \times 10^{-7}$  mbar or lower pressure. The flow of the sample was adjusted to get sample pressure of the order of  $10^{-6}$  mbar in the chamber. Differential Scanning Calorimetric (DSC) measurements were also conducted to estimate the energy released from heating 4 mg DGPCl at 5°C/min in the temperature range of 0 to 500°C. For this we used a Mettler Toledo DSC 822 instrument, with an empty aluminum pan serving as the reference. The instrument calibration was done using cyclohexane and indium for temperature and enthalpy.  $\pm 0.1^\circ\text{C}$  and  $\pm 5\%$  were the expected experimental errors in calculated temperature and energy values respectively.

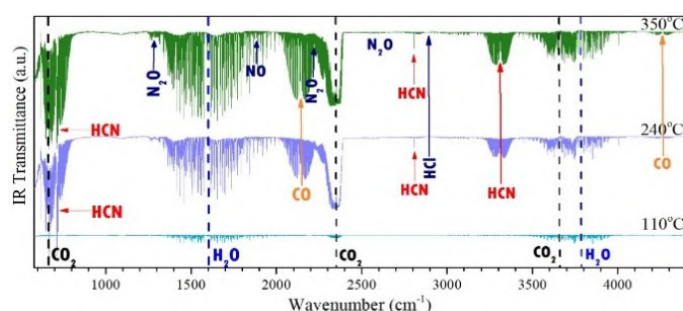
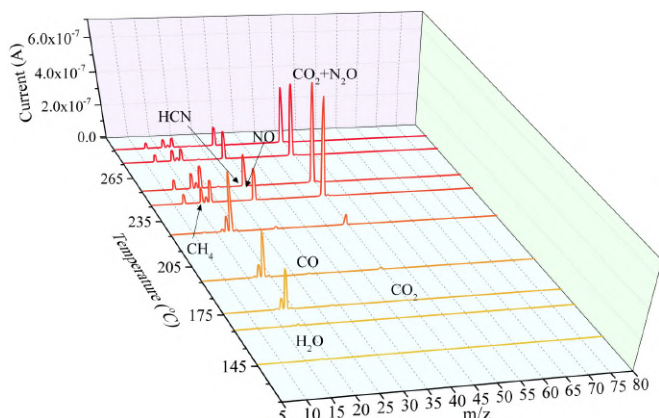


Figure 1. High resolution IR spectra of gases released during the heat treatment of DGPCl at different temperatures, recorded at resolution of  $1\text{ cm}^{-1}$ .

The IR spectra of the trapped gases recorded at  $1\text{ cm}^{-1}$  resolution, are shown in the Figure 1. The gas spectra reveal the absence of any gases other than H<sub>2</sub>O and CO<sub>2</sub> upon heating DGPCl up to  $\sim 100^\circ\text{C}$ . Above  $240^\circ\text{C}$ , the vibrational spectral features of other gasses were also observed, which are assigned by calculating and comparing the values of rotational constant ( $2B$ ) and characteristic vibrational frequencies. For this, the data were recorded at several high resolutions ( $2\text{cm}^{-1}$ ,  $1\text{cm}^{-1}$ ,  $0.5\text{cm}^{-1}$ ,  $0.2\text{cm}^{-1}$ ,  $0.1\text{cm}^{-1}$ ). The evolution of CO gas above  $250^\circ\text{C}$  could be confirmed by the emergence of its fundamental and overtone bands at  $\sim 2143\text{ cm}^{-1}$  and  $\sim 4260\text{ cm}^{-1}$  respectively. Presence of HCN was confirmed by its three IR fundamental modes at  $\sim 3311\text{ cm}^{-1}$  (stretching mode) and doubly degenerate bending mode at  $\sim 712\text{ cm}^{-1}$ . The prominent presence of these gasses was confirmed by recording spectra at further high temperatures, where we found rotational bands of N<sub>2</sub>O, NO, CH<sub>4</sub> and HCl at  $350^\circ\text{C}$  [3-9]. All these observations are well supported by the QMS measurements as shown in figure 2.



These results are significant in view of the fact that the decomposition mechanism involving release of gaseous products from diglycine linkages is substantially different from that observed in the case of glycine [10, 11]. In particular, no traces of  $\text{NH}_3$  were observed in the present study.

In addition, perchlorate group shows remarkable resilience to heating. During the presentation, complete details of decomposition mechanism, including the properties of gaseous as well as solid residual products will be discussed, to claim DGPCl as a new potential energetic material.

## References

1. L. Panicker, P. Mathur, S.M. Mobin, Crystal Structure and Phase Transition of Diglycine Perchlorate, *Journal of Chemical Crystallography*, 41 (2011) 147-154.
2. C. Muthuselvi, R. Natarajan, K. Selvalakshmi, Vibrational, Optical and Antimicrobial Activity Studies on Diglycine Perchlorate Single Crystal, *Journal of Applied Sciences*, 19 (2019) 848-856.
3. I.E. Gordon, L.S. Rothman, R.J. Hargreaves, R. Hashemi, E.V. Karlovets, F.M. Skinner, E.K. Conway, C. Hill, R.V. Kochanov, Y. Tan, P. Wcisło, A.A. Finenko, K. Nelson, P.F. Bernath, M. Birk, V. Boudon, A. Campargue, K.V. Chance, A. Coustenis, B.J. Drouin, J.M. Flaud, R.R. Gamache, J.T. Hodges, D. Jacquemart, E.J. Mlawer, A.V. Nikitin, V.I. Perevalov, M. Rotger, J. Tennyson, G.C. Toon, H. Tran, V.G. Tyuterev, E.M. Adkins, A. Baker, A. Barbe, E. Canè, A.G. Császár, A. Dudaryonok, O. Egorov, A.J. Fleisher, H. Fleurbaey, A. Foltynowicz, T. Furtenbacher, J.J. Harrison, J.M. Hartmann, V.M. Horneman, X. Huang, T. Karman, J. Karns, S. Kass, I. Kleiner, V. Kofman, F. Kwabia-Tchana, N.N. Lavrentieva, T.J. Lee, D.A. Long, A.A. Lukashchinskaya, O.M. Lyulin, V.Y. Makhnev, W. Matt, S.T. Massie, M. Melosso, S.N. Mikhailenko, D. Mondelain, H.S.P. Müller, O.V. Naumenko, A. Perrin, O.L. Polyansky, E. Raddaoui, P.L. Raston, Z.D. Reed, M. Rey, C. Richard, R. Tóbiás, I. Sadiek, D.W. Schwenke, E. Starikova, K. Sung, F. Tamassia, S.A. Tashkun, J. Vander Auwera, I.A. Vasilenko, A.A. Vígasin, G.L. Villanueva, B. Vispoel, G. Wagner, A. Yachmenev, S.N. Yurchenko, The HITRAN2020 molecular spectroscopic database, *Journal of Quantitative Spectroscopy and Radiative Transfer*, 277 (2022) 107949.
4. E.K. Plyler, E.F. Barker, *Physical Review*, 38 (1931) 1827-1836.
5. H.C. Allen, Jr., E.D. Tidwell, E.K. Plyler, Infrared Spectra of Hydrogen Cyanide and Deuterium Cyanide, *The Journal of Chemical Physics*, 25 (1956) 302-307.
6. K.N. Choi, E.F. Barker, Infrared Absorption Spectrum of Hydrogen Cyanide, *Physical Review*, 42 (1932) 777-785.
7. C.R. Keedy, The rotational-vibrational spectra of HCN and DCN: A physical chemistry experiment, *Journal of Chemical Education*, 69 (1992) A296.

8. G. Herzberg, *Molecular spectra and molecular structure*, D. van Nostrand, 1945.

9. R.J. Barber, J.K. Strange, C. Hill, O.L. Polyansky, G.C. Mellau, S.N. Yurchenko, J. Tennyson, ExoMol line lists – III. An improved hot rotation-vibration line list for HCN and HNC, *Monthly Notices of the Royal Astronomical Society*, 437 (2014) 1828-1835.

10. J. Li, Z. Wang, X. Yang, L. Hu, Y. Liu, C. Wang, Evaluate the pyrolysis pathway of glycine and glycyglycine by TG-FTIR, *Journal of Analytical and Applied Pyrolysis - J ANAL APPL PYROL*, 80 (2007) 247-253.

11. I.M. Weiss, C. Muth, R. Drumm, H.O.K. Kirchner, Thermal decomposition of the amino acids glycine, cysteine, aspartic acid, asparagine, glutamic acid, glutamine, arginine and histidine, *BMC Biophysics*, 11 (2018) 2.

## Mechanistic and Kinetic Aspects of Thermal Decomposition of CuCl<sub>2</sub> Under Different Flow Environments

R. V. Singh<sup>a, #</sup>, G. R. Patkare<sup>b</sup>, A. M. Banerjee<sup>a, #</sup>, M. R. Pai<sup>a, #, \*</sup>

<sup>a</sup>Chemistry Division, Bhabha Atomic Research Centre, Mumbai – 400085, India.

<sup>b</sup>Fuel Chemistry Division, Bhabha Atomic Research Centre, Mumbai – 400085, India.

<sup>#</sup>Homi Bhabha National Institute, Training School Complex, Anushaktinagar, Mumbai 400085, India

\*Corresponding author: [mrinalr@barc.gov.in](mailto:mrinalr@barc.gov.in)

### Abstract

The Cu–Cl thermochemical cycle offers a promising approach for large-scale H<sub>2</sub> production. This study examines the thermal decomposition of CuCl<sub>2</sub> under N<sub>2</sub>, zero air & moist Ar flows at 325°C for 12 h using ex-situ HT-XRD. Rietveld refinement showed low conversion, with Cu(OH)Cl as the main product (2.5%, 7.3%, and 25.2% in N<sub>2</sub>, zero air & moist Ar, resp). Cu<sub>2</sub>OCl<sub>2</sub> (1.34 wt%) was seen only in moist Ar. Activation energy (E<sub>a</sub>) & rate constants(k) for thermolysis and oxidation were higher than for hydrolysis with the thermolysis rate constant at 400°C being 1.35 h<sup>-1</sup>, compared to 0.70 h<sup>-1</sup> for oxidation.

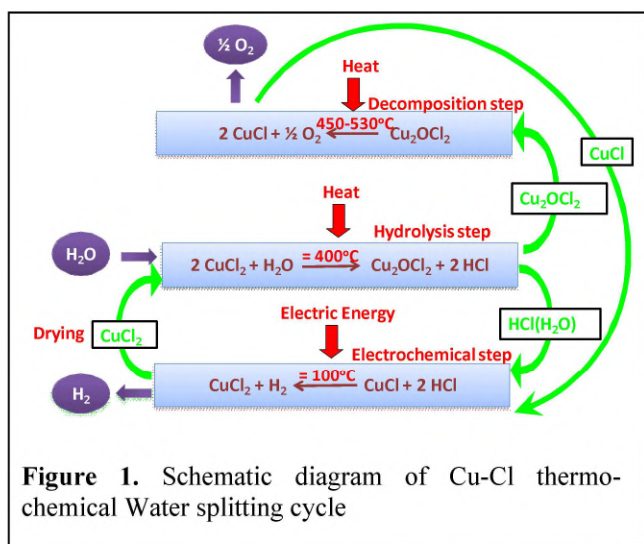
Given the growing global energy demands and the negative environmental impacts of fossil fuels, such as global warming, there is an urgent need to explore alternative energy sources. Hydrogen, as a green, renewable, and promising energy carrier, presents a viable solution [1]. Thermochemical water splitting processes hold significant potential for large-scale hydrogen production. Among these, the Cu–Cl cycle (Figure 1) stands out as a highly promising thermochemical cycle, offering the advantage of a relatively low operating temperature of 530°C compared to other cycles.

Thermal steps, such as the CuCl<sub>2</sub> hydrolysis and decomposition (O<sub>2</sub> evolution) step, present significant challenges that impact the overall cost and efficiency of the cycle. During the decomposition step, Cu<sub>2</sub>OCl<sub>2</sub>, a product of the hydrolysis, decomposes to produce molten CuCl and O<sub>2</sub>. The purity of Cu<sub>2</sub>OCl<sub>2</sub> plays a crucial role in the progression and kinetics of this step. Impurities such as CuCl and CuO are naturally present in the hydrolysis product, arising from side reactions of thermolysis of CuCl<sub>2</sub> to CuCl and oxidation processes that occur within the same temperature range [2-4].

present. Further, Rietveld refinement of XRD data was performed to quantify the phases present. In order to study mechanism of CuCl<sub>2</sub> decomposition in air isothermal TG experiments were carried out at temperatures 350, 370 and 400°C under zero air flow at rate of 40 ml/min. For recording isothermal TG anhydrous CuCl<sub>2</sub> was first heated to requisite temperatures at fast rate within 30 min then kept on that temperature for 6 hours.

Results from Rietveld refinement of powder XRD patterns of decomposition mixture after 12 h time are compiled in Table-1. In case of heating under N<sub>2</sub> and Zero air flow low conversions were obtained with more than 90 wt% of unreacted Eriochoalcite (CuCl<sub>2</sub>•2H<sub>2</sub>O) phase present in mixture while under moist Ar flow 73 wt% CuCl<sub>2</sub>•2H<sub>2</sub>O was obtained. Along with this, Belloite (Cu(OH)Cl) was the major phase: 2.5, 7.3 and 25.2 wt% under N<sub>2</sub>, Zero air and Moist Ar flow respectively. CuCl and CuO were the minor phases (<1%) under N<sub>2</sub> and Zero air flow respectively. 1.34 wt% Melanothallite (Cu<sub>2</sub>OCl<sub>2</sub>) was obtained under Moist Ar flow only.

**Table 1:** Composition from Rietveld refinement for CuCl<sub>2</sub> decomposition under different gas flows at 325°C



In this work, thermal decomposition of CuCl<sub>2</sub> was carried out under different environmental flow conditions viz. N<sub>2</sub>, Zero Air and moist Ar. For this ~3.0 g of anhydrous CuCl<sub>2</sub> was kept in a platinum crucible and heated at a rate of ~10°C/min to desired temperature of 325°C and then kept at that temperature over a period of 12 hours. Samples were taken out from the reaction mixture at different intermittent times and characterized using powder XRD to get idea about phases

S. No.	Heating Condition	Phase from PXRD	Amount (Wt%) from refinement
1	Moist Ar	CuCl <sub>2</sub> •2H <sub>2</sub> O	73.2
		Cu(OH)Cl	25.2
		Cu <sub>2</sub> OCl <sub>2</sub>	1.34
2	N <sub>2</sub> -	CuCl <sub>2</sub> •2H <sub>2</sub> O	94.5
		Cu(OH)Cl	2.51
		CuO	1.1
		CuCl <sub>2</sub>	1.2
3	Zero Air-	CuCl <sub>2</sub> •2H <sub>2</sub> O	91.63
		Cu(OH)Cl	7.39
		CuCl+CuO	<1

Isothermal TG curves were obtained during decomposition of CuCl<sub>2</sub> under different gas flow conditions. Using

gravimetric data from isothermal TG, conversion factor  $\alpha$  is defined by equation 1 below:

$$\alpha = \frac{m_0 - m_t}{m_0 - m_\infty}$$

where,  $m_0$  is initial weight,  $m_t$  is weight at time  $t$ , and  $m_\infty$  is final weight. The general rate equations for solid state reaction is expressed in terms of conversion factor  $\alpha$  as below:

$$d\alpha/dt = k(T) f(\alpha)$$

where  $k(T)$  is rate constant given by Arrhenius equation as:  $k(T) = A \exp(-E_a/RT)$  and  $f(\alpha)$  is the reaction model. Uniform reaction model was applied to  $\text{CuCl}_2$  thermolysis and geometrical contraction model were applied to  $\text{CuCl}_2$  hydrolysis and oxidation reactions to obtain rate constant  $k(T)$  as given below in **Table-2**.

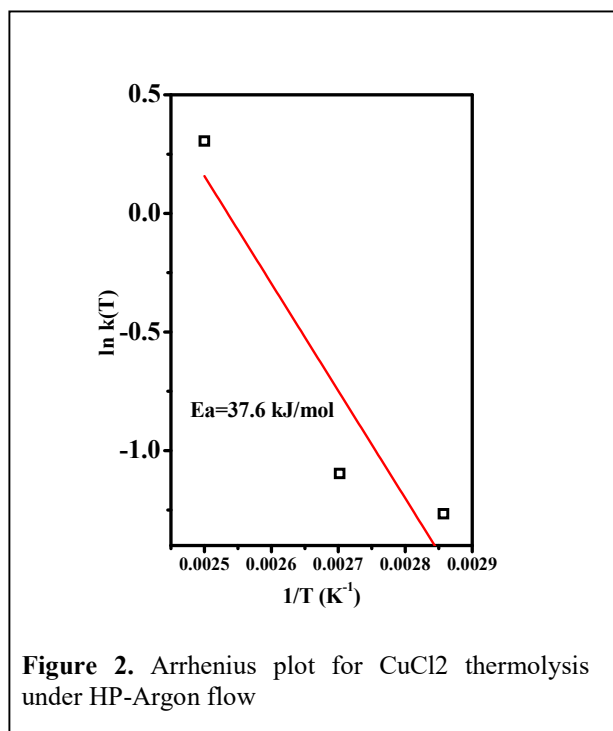


**Figure 2.** Arrhenius plot for  $\text{CuCl}_2$  thermolysis under HP-Argon flow

Temperature /°C	HP-Argon ( $\text{CuCl}_2$ thermolysis)		Zero Air ( $\text{Cu(OH)Cl}$ formation)	
	$k(T)$ / $\text{h}^{-1}$	$E_a$ (kJ/mol)	$k(T)$ / $\text{h}^{-1}$	$E_a$ (kJ/mol)
350	0.2817	37.6	0.2756	67.03
370	0.3338		0.3561	
400	1.3566		0.7089	

**Table 2:** rate constant ( $k$ ) and activation energy derived from isothermal TG

Using rate constant values at different temperatures Arrhenius plots were obtained. From this activation energy was obtained (**Table-2**). It was observed that activation energy of  $\text{CuCl}_2$  thermolysis (37.6 kJ/mol) <  $\text{CuCl}_2$  oxidation (67.03 kJ/mol) <  $\text{CuCl}_2$  hydrolysis (106 kJ/mol). Thus, thermolysis and oxidation both are competing reaction for  $\text{CuCl}_2$  hydrolysis. Formation of  $\text{CuO}$  and  $\text{CuCl}$  (does not utilize water) are very likely to be formed along with the main product  $\text{Cu}_2\text{OCl}_2$  in hydrolysis step. Further, residue obtained after isothermal TG experiment under zero air flow (oxidation) were characterized by powder XRD

and Rietveld refinement of patterns was performed to obtain the phase composition in the residue. Maximum conversion was observed at 400°C.  $\text{Cu(OH)Cl}$ , (63.5 wt%) was obtained as main phase with 11.8 % of  $\text{CuO}$  and 3.91 %  $\text{Cu}_2\text{OCl}_2$  at 350°C. Decrease in  $\text{Cu(OH)Cl}$  quantity and corresponding increase in oxidized products  $\text{CuO}$  (12% at 370°C and 30.5% at 400°C) and  $\text{Cu}_2\text{OCl}_2$  (8.2% at 370°C and 15.4 % at 400°C) was observed with increasing temperature. This confirms that  $\text{Cu(OH)Cl}$  is an intermediate phase and it gets converted to  $\text{Cu}_2\text{OCl}_2$  at very slow rate.

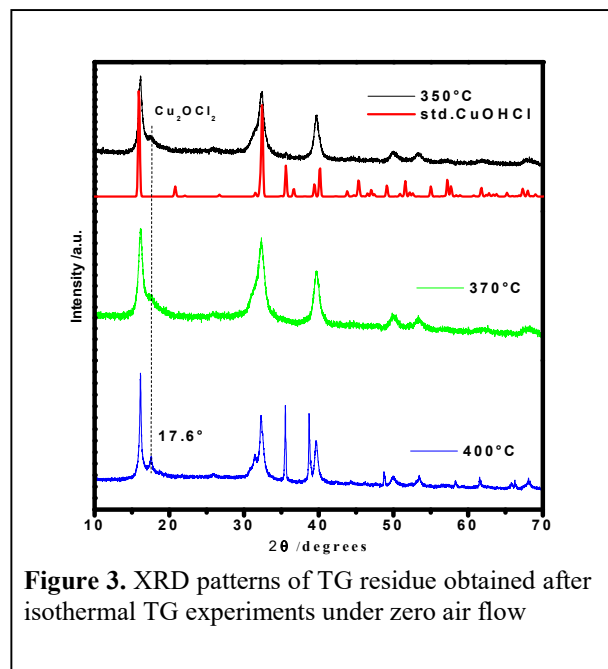


**Figure 3.** XRD patterns of TG residue obtained after isothermal TG experiments under zero air flow

The main conclusions derived from the above studies are as follows: (i) The decomposition and hydrolysis of  $\text{CuCl}_2$  proceed at a very slow rate at 325°C, while it improved at higher temperatures. The highest conversion was achieved when  $\text{CuCl}_2$  was subjected to a moist Argon atmosphere. (ii) Kinetic analysis revealed that the activation energy for the thermolysis of  $\text{CuCl}_2$  is lower than that for its oxidation, and both processes have a lower activation energy compared to its hydrolysis. This suggests that thermolysis and oxidation are competing reactions in the hydrolysis of  $\text{CuCl}_2$ , (iii) During the hydrolysis process,  $\text{CuO}$  and  $\text{CuCl}$  (which do not require water for formation) are likely to be produced along with the primary product  $\text{Cu}_2\text{OCl}_2$ .

## References

1. R. V. Singh, M. R. Pai, A. M. Banerjee, Anshu Shrivastava, Uttam Kumar, Indrajit Sinha, B. Dutta, P. A. Hassan, R. S. Ningthoujam, Rajib Ghosh, S. Nath, R. K. Sharma, Jagannath and R. D. Bapat, *ACS Omega*, 38 (2024) 40182–40203.
2. R. V. Singh, M. R. Pai, A. M. Banerjee, G. Patkare, R. V. Pai, A. Kumar, A. K. Yadav, S. Phaphale, A. K. Tripathi, *International Journal of Energy Research*, 44 (2020) 2845–2863.
3. R. V. Singh, M. R. Pai, A. M. Banerjee, C. Nayak, S. Phapale, D. Bhattacharyya, A. K. Tripathi, *Journal of Thermal Analysis and Calorimetry*, 147 (2022) 7063–7076.
4. R. V. Singh, M. R. Pai, A. M. Banerjee, D. Thomas, G. Patkare, S. Phapale, C. Nayak, V. Bhasin, A. K. Tripathi, *ACS Energy & Fuels*, 37 (2023) 15206–15221.



## Thermal Breakdown of Tin-selenolate Complex for Nanomaterial Synthesis

Saibren Mandal<sup>a</sup>, Atharva Kulkarni<sup>b</sup>, Gourab Karmakar<sup>c,d</sup>, G. Kedarnath<sup>c,d</sup>, Amey Wadawale,<sup>c</sup> Balaji P. Mandal<sup>c,d\*</sup> and Adish Tyagi<sup>c,d\*</sup>

<sup>a</sup>UM-DAE Centre for Excellence in Basic Sciences, Mumbai - 400098, India

<sup>b</sup>Department of Chemistry, K. J. Somaiya College of Science and Commerce, Vidyavihar, Mumbai 400077, India.

<sup>c</sup> Chemistry Division, Bhabha Atomic Research Centre, Mumbai 400085, Homi Bhabha National Institute, Mumbai 400094, India

<sup>d</sup> Homi Bhabha National Institute, Anushaktinagar, Mumbai- 400094, India.

**Email:** [tyagia@barc.gov.in](mailto:tyagia@barc.gov.in)

### Abstract

The study focuses on synthesis of phase pure nanostructures of SnSe using 2-pyridylselenolate complexes of di-organotin as the single-source molecular precursor. TGA of complexes indicates that these complexes can be used as precursors for preparing SnSe nanostructures. The nanostructures derived from high boiling solvents were characterized using PXRD, EDS, and electron microscopy.

### Introduction:

Group IV-VI metal chalcogenide semiconductor nanomaterials have received significant attention due to their interesting desirable electronic and optical properties. Among them, tin selenides are emerging members of this family due to their earth abundant, low cost and environmentally benign characteristics. Tin selenide exists in two stable phases orthorhombic SnSe and hexagonal SnSe<sub>2</sub>, which make them promising candidates in energy storage applications. Among them, SnSe have the special recognition as they exhibit optical bulk band gap of 1.3 eV (direct) and 0.9 eV (indirect). The unique combination of anisotropy and optical properties including slow carrier relaxation rate render SnSe as a suitable candidate for thermoelectric, photovoltaic and infrared optoelectronic devices [1]. It has been observed that the performance of SnSe in energy application greatly depends upon its morphology which in turn relies on the synthetic strategy adopted.

Over the period, tin selenide nanostructures have been prepared either by solution-based methods or deposited in the form of thin films. Solution-based methods can be broadly categorized as multiple sources and single-source precursor (SSP) approach. However, materials through thermal breakdown of single-source precursor (SSP) is considered to be advantageous due to the presence of preformed bonds between the constituent elements which lead to better stoichiometry and control over morphology [2]. Till date only few SSP's have been developed for the preparation of tin selenide.

In this view, novel organotin pyridyl selenolate complex have been synthesized and explored for the preparation of SnSe nanostructures.

**Scheme. 1** Schematic illustration for the Synthesis of [Ph<sub>2</sub>Sn(5-MeSePy)<sub>2</sub>](1) molecular precursor and its facile conversion into Bi<sub>2</sub>Se<sub>3</sub> nanostructures.

### Experimental:

#### Preparation of molecular precursor

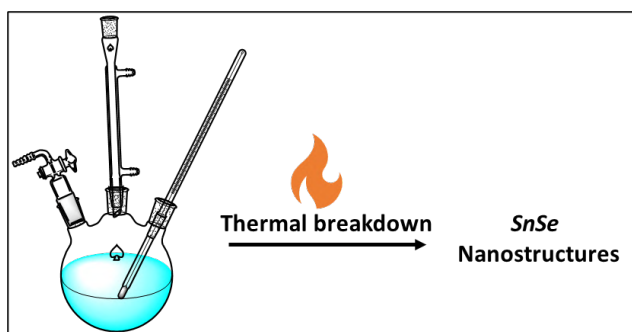
To a freshly prepared methanolic solution, 5-methyl-2-pyridyl selenolate [obtained by the reduction of (5-MeSePy)<sub>2</sub> (0.91 mmol) [with methanolic solution of NaBH<sub>4</sub> (1.82 mmol)] was added solid Ph<sub>2</sub>SnCl<sub>2</sub> (0.91 mmol). The reaction mixture was stirred vigorously at room temperature for 3 h and the solvents were evaporated under vacuum. The residue was dissolved in methanol and passed through a G-3 filtration assembly. The filtrate was dried under reduced pressure and the residue was recrystallized from methanol to yield off-white crystals.

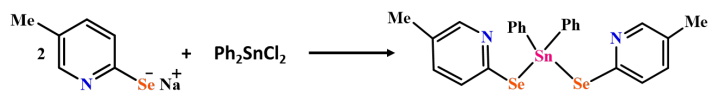
#### Preparation of tin selenide nanostructures

The organotin complex with 5-methyl-2-pyridyl selenolate was exploited as molecular precursor for the preparation of tin selenide nanostructure. In a different set of reactions, the 150 mg of the precursor was taken in three neck round flask having 10 ml of high boiling solvent (oleyl amine or octadecene which differ in the capping ability and reducing power at elevated temperature). The reaction temperature was gradually raised to 200 °C and kept there for 10 minutes. The dark solution formed was cooled rapidly to 70 °C where excess methanol was added into the flask. The resulting nanocrystals were separated by centrifugation and purified by washing several times with 2:1 mixture of methanol and toluene solution.

### Result and discussion:

The reaction of sodium 2-pyridyl selenolate with diphenyl tin dichloride afforded diorganotin selenolate complex (Scheme 2). Elemental analysis of the complexes matches well theoretically predicted values. The purity of the complexes was assessed using NMR spectroscopy. The <sup>1</sup>H and <sup>13</sup>C{<sup>1</sup>H} NMR spectra showed expected resonances and peak multiplicities. The molecular structure of the complex, determined from single crystal X-ray diffraction technique revealed that the geometry around the tin complex is distorted tetrahedral (Fig. 1) and exists in a triclinic crystal system.





**Scheme 2.** Synthesis of  $[\text{Ph}_2\text{Sn}(5\text{-MeSePy})_2]$

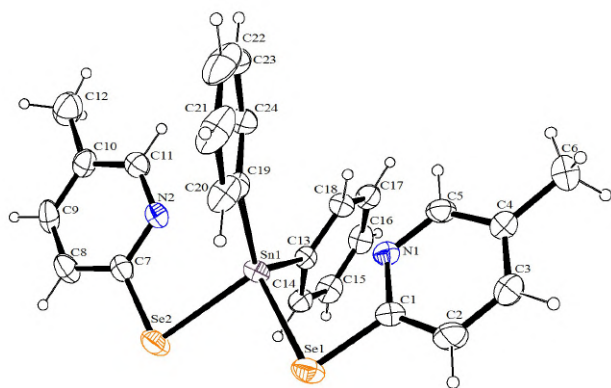


**Figure. 1** ORTEP diagram of complex  $[\text{Ph}_2\text{Sn}(5\text{-MeSePy})_2]$

The thermogravimetric analysis showed that the titled complex is stable up to 280 °C beyond which it undergoes single step thermal decomposition. From the weight loss calculation it is inferred that the complex yielded SnSe residue upon the thermal decomposition. The TG analysis also indicated that the complex can act as a suitable precursor for the preparation of nano-sized tin selenide nanostructures.

Consequently, the known amount of the complex was thermal disintegrated in different solvent to investigate the solvent assisted decomposition product. Further, the effect of temperature and reaction solvent on the final product has been systematically investigated. The complex was thermolyzed in different high boiling solvent to assess their utility as SSP for SnSe. The phase purity and crystal structure of the resulting material have been determined from PXRD which reveals the formation orthorhombic SnSe while the morphology, homogeneity and band gap of the resulting products were characterized by powder X-ray diffraction (PXRD), energy dispersive X-ray analysis (EDX), SEM, TEM and SAED.

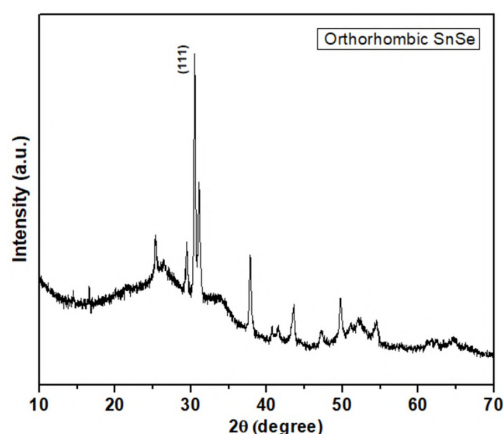


**Figure. 2.** XRD pattern of SnSe obtained by decomposition of  $[\text{Ph}_2\text{Sn}(5\text{-MeSePy})_2]$ .

The band gap of the nanomaterial was investigated using diffuse reflectance spectroscopy (DRS-UV). The band gap of the nanocrystalline SnSe was found to be ~1.7 eV which indicates that the material possesses good electronic conductivity which is useful for the application in lithium ion battery applications, electrocatalysis and photodetector

application. In view of this, the as prepared material is used as anode materials in lithium ion battery and its performance was investigated.

### Conclusion:

Air-stable diorganotin selenolate complexes have been synthesized and characterized through multinuclear NMR and Single-crystal X-ray diffraction techniques. The complex  $[\text{Ph}_2\text{Sn}(5\text{-MeSePy})_2]$  has been utilized for the preparation of SnSe nanostructures which finds potential applications in energy conversion and energy storage devices.

### References:

- [1] M. Kumar, S. Rani, Y. Singh, K. S. Gour and V. N. Singh, *RSC Adv.*, 11 (2021) 6503.
- [2] G. Karmakar, A. Tyagi and A. Y. Shah, *Coord. Chem. Rev.*, 504 (2024) 215665.

## Thermolysis of Bismuth-Selenolate Complex through Molecular Precursor Approach

Atharva Kulkarni<sup>a</sup>, Rohit Singh Chauhan<sup>a</sup>, Balaji P. Mandal,<sup>b,c</sup> Gourab Karmakar<sup>b,c\*</sup>, Adish Tyagi<sup>b, c\*</sup>

<sup>a</sup>Department of Chemistry, K. J. Somaiya College of Science and Commerce, Vidyavihar, Mumbai 400077, India.

<sup>b</sup>Chemistry Division, Bhabha Atomic Research Centre, Mumbai 400085, Homi Bhabha National Institute, Mumbai 400094, India

<sup>c</sup>Homi Bhabha National Institute, Anushaktinagar, Mumbai- 400094, India.

Email: [tyagia@barc.gov.in](mailto:tyagia@barc.gov.in), [gourabk@barc.gov.in](mailto:gourabk@barc.gov.in)

### Abstract

A moisture-stable bismuth-selenolate complex have been prepared and characterized. The molecular structures of the complex were established through single crystal X-ray diffraction and heteronuclear NMR technique. Thermogravimetric analysis of the complex indicate that complex can utilized as single source precursors for the preparation of Bi<sub>2</sub>Se<sub>3</sub> nanostructures. Thermolysis of complexes in different high boiling solvents afforded 2D nanostructure which were further characterized by XRD, SEM and TEM techniques.

Binary layered metal chalcogenide semiconducting materials hold significant attention in their nano-regime due to their promising applications in energy storage devices and thermoelectrics. Among metal chalcogenides, particularly (Bi<sub>2</sub>Se<sub>3</sub>) which belong to class of V–VI materials have emerged as promising materials due to their interesting physical properties. Also, it possesses several key attributes such as a narrow band gap, high absorption coefficient and good carrier mobility, which make them promising candidates for energy conversion applications [1]. Bi<sub>2</sub>Se<sub>3</sub> belongs to a class of topological insulators and crystallizes in a rhombohedral crystal structure with R3m space group. Due to high electrical conductivity and optical properties, Bi<sub>2</sub>Se<sub>3</sub> is suitable for energy storage devices.

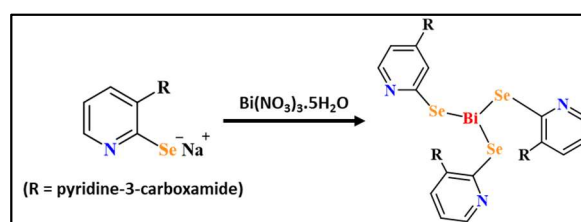
Various solution-assisted and solventless synthetic routes have been explored for the synthesis of Bi<sub>2</sub>Se<sub>3</sub> nanostructures. Most of these methods employ a dual precursor route. On the other hand, single-source precursor (SSP) has gained significant attraction as it contains preformed bonds between desired elements. This approach ensures a low decomposition temperature, phase purity of the final product resulting high reproducibility of experimental results [2, 3]. Moreover, molecular precursors offer several distinct advantages in terms of lower defect concentrations and better control over their morphology and electronic properties. In this view, novel bismuth-selenolate complex have been synthesized and explored for the preparation of Bi<sub>2</sub>Se<sub>3</sub> nanostructures.

### Experimental

To a methanolic solution of [2NaSepy(R-3)] (R = pyridine-3-carboximide) (freshly prepared in an situ from [2-Sepy(R-3)]<sub>2</sub> (0.75 mmol), methanol (10 ml) and NaBH<sub>4</sub> (1.5 mmol)] was added [Bi(NO<sub>3</sub>)<sub>3</sub>·5H<sub>2</sub>O] (0.50 mmol). The reaction mixture was stirred for 4h at room temperature. The resultant green precipitate was filtered and dried. The residue obtained was further washed with hexane to remove the impurities and the complex was collected as faint yellow powder

### Results and Discussion

Treatment of Bi(NO<sub>3</sub>)<sub>3</sub>·5H<sub>2</sub>O with the corresponding sodium salt of selenolate ligand in an appropriate molar ratio resulted in the title complex (Scheme 1). The <sup>77</sup>Se{<sup>1</sup>H} NMR spectra displayed a single resonance confirming the existence of only one bismuth containing stable species in solution. Molecular structure of the complex determined from single crystal X-ray diffraction technique revealed that geometry around bismuth is distorted octahedral (Fig. 1).



Scheme. 1 Synthesis of [Bi(Sepy(R-3))<sub>3</sub>]

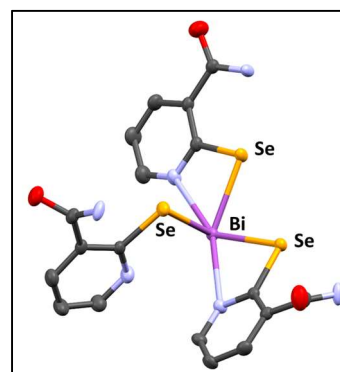


Figure. 1. Molecular structure of [Bi(3-RSepy)<sub>3</sub>]

Thermogravimetric analyses (TGA) were carried out to evaluate the thermal decomposition behaviour of the complexes under flowing argon atmosphere. TG curve for the complexes showed a decomposition at ~26.3% which corresponds to the formation of Bi<sub>2</sub>Se<sub>3</sub> (calculated ~26.1%) (Fig. 2).

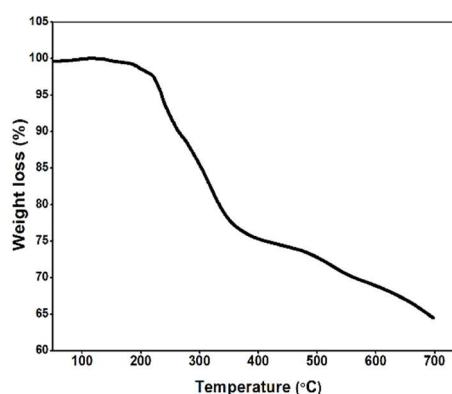
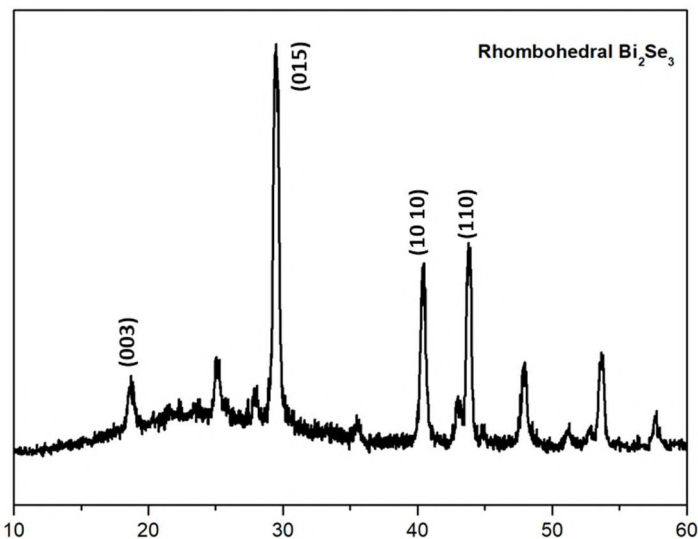
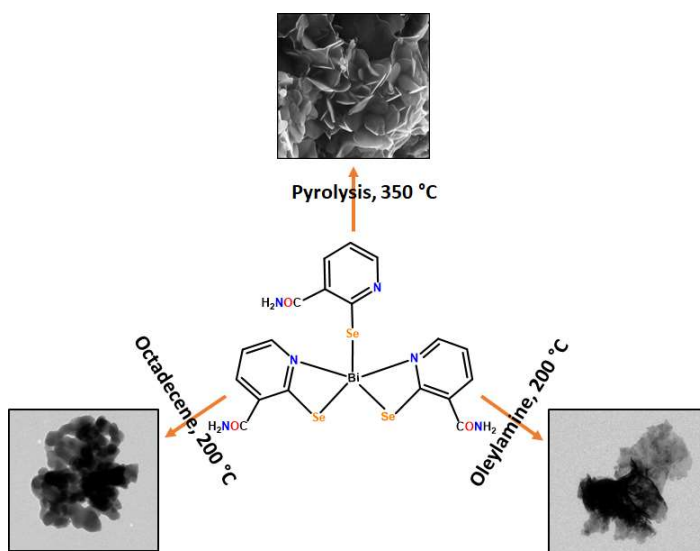


Figure 2: Thermogravimetric data analysis for [Bi(3-RSepy)<sub>3</sub>]



**Figure 3:** XRD pattern of  $\text{Bi}_2\text{Se}_3$  obtained by the decomposition of  $[\text{Bi}(3\text{-RSePy})_3]$

The TG data indicates that this complex underwent decomposition to yield bismuth selenide. Hence, this complex was thermolyzed in different conditions to assess their utility as molecular precursor for the preparation of pre phase  $\text{Bi}_2\text{Se}_3$  nanostructures. The complex was thermolyzed in both solvent less and solvent assisted conditions. In solvent less condition the thermolysis of complex produces nanoplatelets, whereas in solvent assisted conditions the thermal disintegration of complex afforded the formation of mixture of nanomaterials and nanosheets (in case of ODE) and nanoflakes (in case of OAm) as shown in Fig. 2. The phase purity and crystal structure of the resulting material have been determined from PXRD which reveals the formation of two-dimensional rhombohedral phase  $\text{Bi}_2\text{Se}_3$  while the morphology, homogeneity, band gap of the resulting products were characterized by PXRD, energy dispersive X-ray analysis (EDX), SEM, TEM, SAED and solid state diffuse reflectance spectroscopy (DRS), respectively.



**Figure 2:** Schematic representation of thermal decomposition reaction conditions on the morphology of  $\text{Bi}_2\text{Se}_3$  nanostructures.

### Conclusion:

Novel, bismuth-selenolate complex have been synthesized and characterized through multinuclear NMR and Single crystal X-ray diffraction technique. This complex provides a facile

pathway for the synthesis of 2D bismuth selenide nanostructures.

### References

1. F. Wang, L. Li, W. Huang, L. Li, B. Jin, H. Li, T. Zhai, *Adv. Funct. Mater.*, 28 (2018), 1802707.
2. A. Y. Kulkarni, G. Karmakar, A. Y. Shah, S. Nigam, G. Kumbhare, A. Tyagi, R. J. Butcher, R. S. Chauhan, N. Naveen Kumar, *Dalton Trans.*, 52 (2023) 16224.
3. A. Thomas, G. Karmakar, A. Y. Shah, S. V. Lokhande, A. Y. Kulkarni, A. Tyagi, R. S. Chauhan, N. N. Kumar, A. P. Singh, *Dalton Trans.*, 51 (2022) 121

## Thermolysis of copper thiolate complex for the preparation of digenite material and its lithium uptake property

S. P. Yadav,<sup>a</sup> G. Karmakar,<sup>b, c</sup> G. Kedarnath,<sup>b, c</sup> B. P. Mandal,<sup>b, c\*</sup> Adish Tyagi<sup>b, c\*</sup>

<sup>a</sup>Chemistry Department, K. J. Somaiya College of Science and Commerce, Mumbai 400077, India

<sup>b</sup>Chemistry Division, Bhabha Atomic Research Centre, Mumbai 400085, India

<sup>c</sup>Homi Bhabha National Institute, Anushakti Nagar, Mumbai 400094, India

Email: [bpmandal@barc.gov.in](mailto:bpmandal@barc.gov.in), [tyagia@barc.gov.in](mailto:tyagia@barc.gov.in)

### Abstract

This study present a facile synthetic route involving thermal disintegration of molecular complex for the preparation of copper sulfide nanostructures. Towards this endeavour, an air-stable copper complex containing pyrimidyl thiolates has been synthesized and studied using elemental analysis and NMR spectroscopy. The molecular structures of the complexes were determined using single crystal X-ray diffraction techniques. TGA analysis shows that these compounds are effective precursors to generate digenite ( $\text{Cu}_{1.8}\text{S}$ ) nanostructures. Thermolysis of complexes in high boiling solvents produced  $\text{Cu}_{1.8}\text{S}$  nanoparticles, which were studied using XRD, SEM, and TEM techniques.

### Introduction:

The development of high-performance energy storage systems has attracted a lot of attention due to the world's growing energy consumption and growing environmental concerns [1]. Lithium-ion battery is one of the best energy storage devices due to its capability for rapidly store and release electricity. Numerous transition metal sulfides have been thoroughly investigated as negative electrode materials for rechargeable batteries due to their advantages, which include a high theoretical capacity, reasonable cost, and an appropriate discharge voltage. Although many metal sulfides have been examined as LIB anode materials, copper sulfides have received little attention, despite the abundance and affordability of the component elements.

Copper sulphide ( $\text{Cu}_x\text{S}$ ) was prepared by various chemicals method using multisource. Solution phase synthetic pathways have significant advantages in terms of low production costs, ease of processing, phase purity, size and shape controllability, but gas phase methods have greater reaction control due to convenient reactant supply and mixing, as well as pace of reaction. Reaction can simply be controlled by the temperature of the substrate and reacting gases/vapor. In terms of phase purity, reproducibility, and low defect concentration because of preformed bonds, the single-source molecular precursor approach (SSP), in which the desired constituent elements are present in the same molecule in the bonded state, offers numerous significant advantages over the dual source route. Furthermore, the synthesis of nanocrystals via SSP is straightforward, quick, scalable, and appropriate for thin-film deposition [2].

We have examined a number of metal complexes with internally functionalized hemilabile pyridyl/ pyrimidyl/ pyrazinyl chalcogenolate ligands in ongoing search for possible single source molecular precursors for the synthesis of technologically significant metal chalcogenides in order to produce high-quality nanocrystals and thin films. In continuation of our endeavour, this study present a pyrimidyl thiolate based copper complex  $[(\text{PPh}_3)_2\text{CuCl}(\text{SpymMe}_2)]$  which has been used as a SSP for the synthesis of  $\text{Cu}_{1.8}\text{S}$  and study its performance as an anode material in lithium ion battery.

### Experimental:

#### Synthesis of $[(\text{PPh}_3)_2\text{CuCl}(\text{SpymMe}_2)]$ (1)

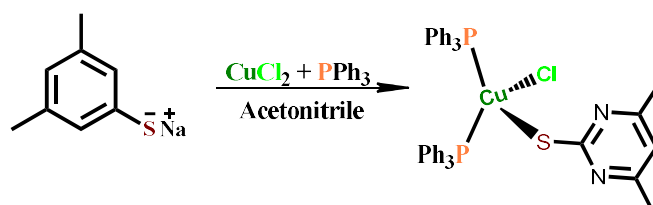
To a freshly prepared methanolic solution of  $\text{NaSpymMe}_2$  [from methanolic solutions of 2-HSpymMe<sub>2</sub> (0.64 mmol) and  $\text{NaOCH}_3$  [(0.64 mmol)], solid  $\text{CuCl}_2 \cdot 2\text{H}_2\text{O}$  (0.64 mmol) was added with vigorous stirring and add  $\text{PPh}_3$  (1.28mmol) in acetonitrile solution. The reaction mixture was stirred at room temperature for 5 h and the solvents were evaporated under vacuum. The residue was dissolved in methanol and passed through a G-3 filtration assembly. The filtrate was dried under reduced pressure and the residue was recrystallized from methanol to yield pale yellow crystals of the product.

#### Synthesis of copper sulfide nanostructures

Copper sulfide nanostructures were synthesized via solvent assisted thermolysis of  $[(\text{PPh}_3)_2\text{CuCl}(\text{SpymMe}_2)]$ . The complex has been thermally disintegrated in high boiling solvents which differ in the nature of capping ability and reducing nature at elevated temperature.

### Results and Discussion:

The reaction of sodium pyrimidyl thiolate ( $\text{NaSpymMe}_2$ ) with  $\text{CuCl}_2$  and  $\text{PPh}_3$  in the requisite stoichiometric ratio produced the air-stable copper (I) complex (**Scheme 1**). Elemental analysis of the complexes confirms the theoretically anticipated values. The solution state stability of the complexes was evaluated using NMR spectroscopy. The  $^1\text{H}$  and  $^{13}\text{C}\{^1\text{H}\}$  NMR spectra revealed predicted resonances and peak multiplicity. Molecular structure of the complexes as determined from single crystal x ray diffraction technique revealed that geometry around copper is distorted tetrahedral surrounded by chlorine,  $\text{PPh}_3$  and ligand environment. (**Fig. 1**).



Scheme 1: Synthesis of  $[(\text{PPh}_3)_2\text{CuCl}(\text{SpymMe}_2)]$  (1)

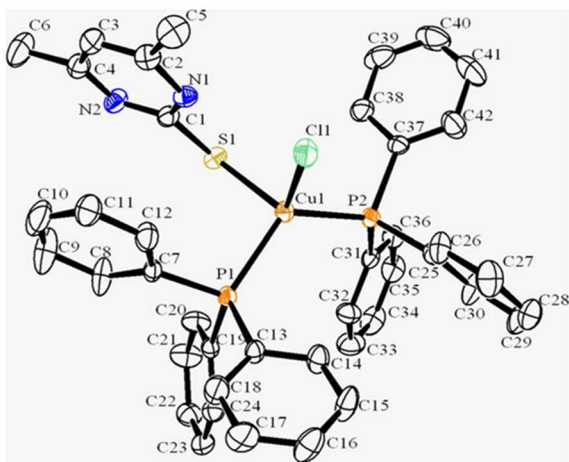


Fig. 1: Molecular structure of the  $[(PPh_3)_2CuCl(SpymMe_2)]$  (1). Redrawn from CCDC no. 2157596.

Thermogravimetric analyses (TGA) were carried out to evaluate the thermal decomposition behaviour of the complexes under flowing argon atmosphere. TG curve for the complexes showed two step decomposition at 300 and 440 °C before the weight loss ceases and the plateau is reached a weight of residue corresponding to the formation of  $Cu_1.8S$  (88% weight loss) (Fig. 2) also confirmed from the pXRD pattern of the residue.

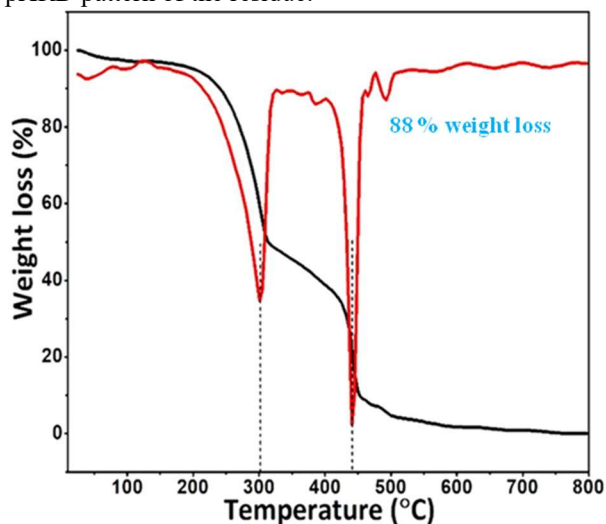


Figure 2: Thermogravimetric data for the  $[(PPh_3)_2CuCl(SpymMe_2)]$  (1)

The data obtained from thermogravimetric analysis based on the results, complex under thermal decomposition using three different solvents ODE (Octadecene), OAm (Oleyamine) and TOPO (Trioctylphosphineoxide) at 250 °C for 20 min. The phase purity and crystal structure of the resulting material have been determined from pXRD which reveals the formation rhombohedral  $Cu_{1.8}S$  material. while the morphology, homogeneity and band gap of the resulting products were characterized by powder X-ray diffraction (PXRD), Raman spectroscopy, energy dispersive X-ray analysis (EDX), SEM, TEM, respectively.

Morphology of  $Cu_{1.8}S$  nanoparticles was revealed that morphology of  $Cu_{1.8}S$  has change with solvents (Fig. 3). The nanoparticle synthesized in TOPO has smaller particle size and well-defined morphology among the three materials.

This material has been evaluated as anode material in LIB. The material possesses multisized polyhedral which

enable sustainable Li uptake and also provide cushioning during intercalation and de-intercalation of lithium. This results into high Li uptake capacity by the material with high cyclability.

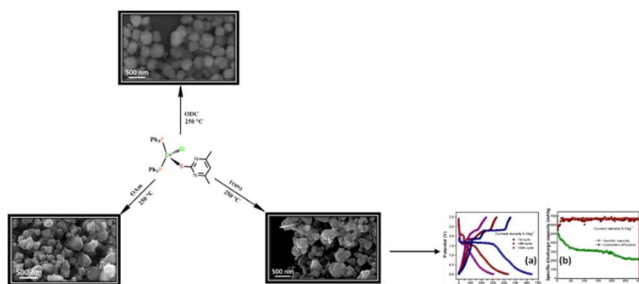


Fig. 3: Synthesis of digenite ( $Cu_{1.8}S$ ) and morphology in ODE, OAm and TOPO.

### Conclusion:

Novel, air stable copper thiolate complexes have been synthesized and characterized through multinuclear NMR and Single crystal X-ray diffraction technique. The complexes have been used for preparation of  $Cu_{1.8}S$  nanoparticle and display promising application in lithium ion battery.

### References:

1. Y. Zhang, L. Zhang, T. Lv, P. K. Chu and K. Huo, *ChemSusChem*, 2020, 13, 1–42A.
2. G. Karmakar, A. Tyagi, A. P. Wadawale, A. Y. Shah, G. Kedarnath, A. P. Srivastava and V. Singh, *J. Mater. Sci.*, 2020, 55, 15439–15453.

## Thermolysis of copper thiolate complexes for the preparation of photoresponsive binary copper sulphide and ternary copper indium sulphide materials

Suraj Peerappa Yadav,<sup>a</sup> Rohit Singh Chauhan,<sup>a</sup> Gourab Karmakar,<sup>b,c,\*</sup> Adish Tyagi<sup>b,c,\*</sup>  
<sup>a</sup>Chemistry Department, K. J. College of Science and Commerce, Mumbai 400077, India  
<sup>b</sup>Chemistry Division, Bhabha Atomic Research Centre, Mumbai 400085, India  
<sup>c</sup>Homi Bhabha National Institute, Anushakti Nagar, Mumbai 400094, India  
 Email: [gourabk@barc.gov.in](mailto:gourabk@barc.gov.in), [tyagia@barc.gov.in](mailto:tyagia@barc.gov.in)

### Abstract

Binary and ternary copper-based sulfide materials have gained significant attention due to their excellent photophysical properties and nontoxic nature. This study describes a direct, scalable synthetic route for synthesis of binary and ternary Cu-based sulfide nanoparticles using molecular precursor method. Three precursors;  $\text{CuX}(\text{PPh}_3)_2(2\text{-SC}_4\text{H}_2\text{N}_2(4,6\text{-Me})_2)$  (where  $X = \text{Cl, I}$ ) and hexagonal Cu-pyrimidylthiolate cluster complex were synthesized and thermolyzed in appropriate condition to afford the nanostructures. Furthermore, combining the hexagonal Cu-pyrimidylthiolate precursor with an appropriate indium source resulted in a simple one-pot route to  $\text{CuInS}_2$  nanocrystals. Phase purity and composition analysis of the nanostructure suggested the formation of pure  $\text{Cu}_{1.8}\text{S}$  and  $\text{Cu}_{31}\text{S}_{16}$  nanostructures from the  $-\text{Cl}$  and  $-\text{I}$  substituted complexes. Phase pure  $\text{Cu}_{1.8}\text{S}$  was isolated from hexagonal Cu-pyrimidylthiolate complex. The morphology of the synthesized nanomaterials was investigated by SEM and TEM. DRS investigations on the pure materials revealed a blue-shifted optical band gap. A prototype PEC cell constructed from pristine nanostructures exhibits stable photo-switching properties, making it a viable choice for cost-effective materials for optoelectronic and photodetector devices.

### Introduction:

Research on metal sulphide nanomaterial has drawn significant attention due to their promising applications in diverse fronts such as batteries, solar cells, photocatalyst and sensors [1]. Copper sulfide, especially in nano-domain, has found multiple applications in a variety of industries, including clean energy and healthcare [2].

Copper sulphide has a variety of semiconducting phases with distinct compositions and crystal arrangements. They are p-type semiconductors with narrow band gaps (1.2-2.5 eV). Beyond copper sulphide binary compounds, there is a fascinating category of Cu-based ternary materials that are of great scientific interest. These materials have outstanding physical and electrical properties and possess more degrees of freedom, allowing for substantial customizing in morphology and band gap engineering.

Single source molecular precursors (SSP) pathway for nanomaterials synthesis is a soft chemical route, which have proved to be instrumental for scalable and low-cost production of these materials.

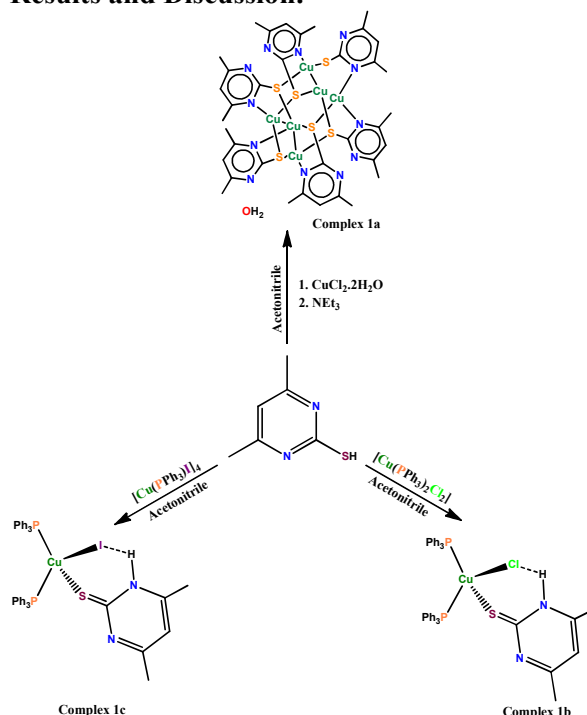
In present study, we have identified three potential copper thiolate complexes namely,  $\text{CuX}(\text{PPh}_3)_2(2\text{-SC}_4\text{H}_2\text{N}_2(4,6\text{-Me})_2)$  ( $X = \text{Cl, I}$ ), which have been explored for the preparation phase pure  $\text{Cu}_{1.8}\text{S}$  and  $\text{Cu}_{31}\text{S}_{16}$  nanoparticles and  $[\text{Cu}(2\text{-SC}_4\text{H}_2\text{N}_2(4,6\text{-Me})_2)]_6$ , which have been used for preparation of Phase pure  $\text{Cu}_{1.8}\text{S}$  nanocrystals and  $\text{CuInS}_2$  nanosheets.

### Experimental:

**Synthesis of  $[\text{Cu}(2\text{-SC}_4\text{H}_2\text{N}_2(4,6\text{-Me})_2)]_6$  (1a):** The complex was prepared in acetonitrile (10 ml) with addition of  $\text{CuCl}_2 \cdot 2\text{H}_2\text{O}$  (0.6 mmol) in 4,6-dimethyl pyrimidine-2-thiolate. Crystal of complex 1a was obtained in acetonitrile solution by slow evaporation method.

**Synthesis of  $\text{CuX}(\text{PPh}_3)_2(2\text{-SC}_4\text{H}_2\text{N}_2(4,6\text{-Me})_2)$  ( $X = \text{Cl, I}$ ) (1b and 1c):** These complexes were prepared in acetonitrile solution with addition of  $[\text{Cu}(\text{PPh}_3)_2\text{Cl}_2]$  (0.40 mmol) for complex 1b and  $[\text{Cu}(\text{PPh}_3)_4\text{I}]$  (0.143 mmol) for 1c in 4,6-dimethyl pyrimidine-2-thiolate ligand (0.58 mmol). Yellow-coloured title compounds were crystallized in acetonitrile solution by slow evaporation method.

### Results and Discussion:



Scheme 1: Synthesis of copper thiolate complexes

The complex 1a was obtained by treating one equivalent of the thiolate ligand with  $\text{CuCl}_2 \cdot 2\text{H}_2\text{O}$  in acetonitrile. However, the same reaction with the Cu-PPh<sub>3</sub> complex,  $[\text{CuCl}_2(\text{PPh}_3)_2]$  in acetonitrile, produced the complex 1b. The complex 1c was produced by reacting four equivalents of the same ligand with the tetranuclear mono-iodo  $[\text{Cu}(\text{PPh}_3)_4\text{I}]$ . Scheme 1 summarizes this reaction.

NMR spectroscopy has been used to evaluate the complexes' purity in the solution state. The  $^1\text{H}$  and  $^{13}\text{C}\{^1\text{H}\}$  NMR spectra displayed anticipated peak multiplicities and resonances.

Thermogravimetric analyses (TGA) were carried out to evaluate the thermal decomposition behaviour of the complexes under flowing Ar atmosphere. According to the TGA curve and

corresponding DTG analysis, the complex **1a** is stable up to about 200°C. After that, it undergoes a two-step clean decomposition that is completed at about 400°C. The 92% weight loss calculation during decomposition indicates that CuS is formed from the title complex (**Fig. 1**).

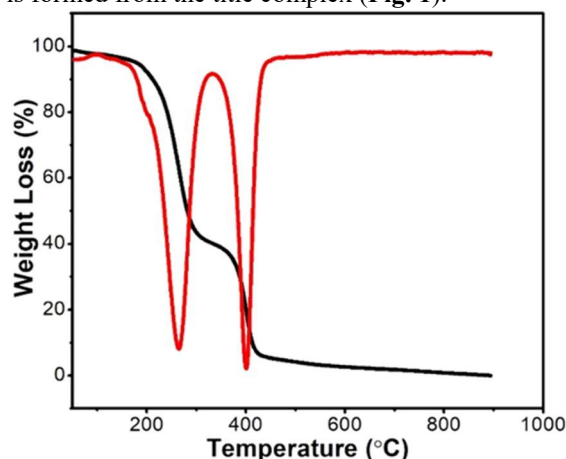


Fig. 1: Thermogravimetric data for the  $[\text{Cu}(2\text{-SC}_4\text{H}_2\text{N}_2(4,6\text{-Me})_2)_6]$ .

These complexes were thermolyzed in high boiling solvents at appropriate temperature to afford copper sulfide materials. It was found that Complex **1a** thermolyzes to yield  $\text{Cu}_{1.8}\text{S}$  nanostructures. The complex **1b** also resulted in  $\text{Cu}_{1.8}\text{S}$  at 220°C, whereas complex **1c** gave  $\text{Cu}_{31}\text{S}_{16}$  at 95°C. Complex **1a**, when co-thermolyzed with  $\text{InCl}_3$  in appropriate molar ratio in OAm at  $\sim 250^\circ\text{C}$ , resulted into  $\text{CuInS}_2$ . The phase purity and crystal structure of these materials were evident from the PXRD patterns (Fig. 2) SEM analysis reveals that nanoflake morphology for  $\text{Cu}_{1.8}\text{S}$  prepared from **1b** and spherical morphology for  $\text{Cu}_{31}\text{S}_{16}$  prepared from **1c**. Polygonal  $\text{Cu}_{1.8}\text{S}$  nanocrystals were isolated from **1a**, while  $\text{CuInS}_2$  was mostly made up of hexagonal sheets and blocks with a wide size distribution.

Additionally, prototype liquid junction PEC cells fabricated from the as-prepared copper sulfide and copper indium sulphide nanostructure, demonstrated good photo-stability and promising photoresponsivity. Following numerous cycles of on-off trials, the amperometric current vs. time ( $I-t$ ) curve at a bias voltage of -1.5 V indicates that these materials can be excellent choice for next-generation photo-detector and photovoltaic systems.

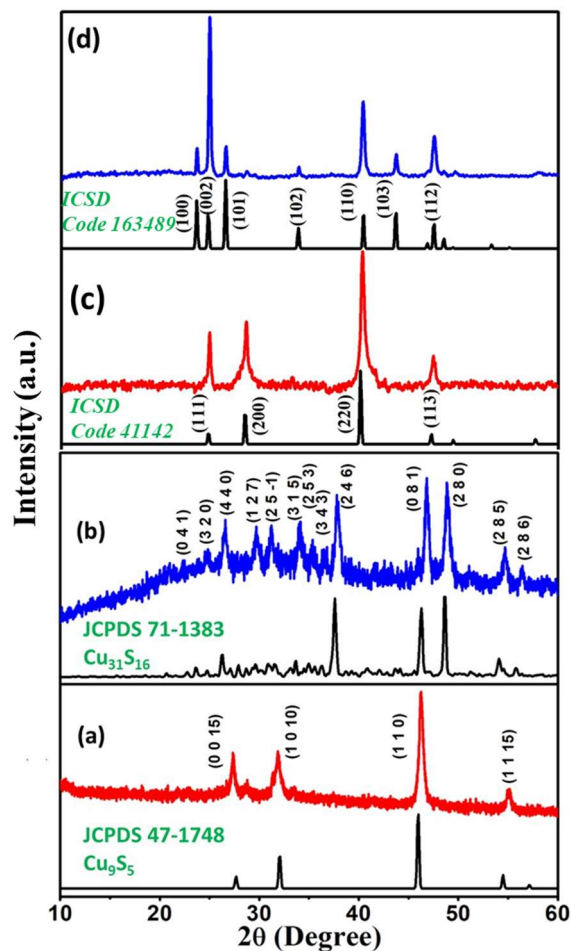


Fig. 2: PXRD pattern of (a)  $\text{Cu}_{1.8}\text{S}$  (b)  $\text{Cu}_{31}\text{S}_{16}$  prepared from **1b** and **1c** and (c)  $\text{Cu}_{1.8}\text{S}$  and  $\text{CuInS}_2$  respectively prepared from **1a**.

### Conclusion:

To summarize the work, three copper (I) pyrimidylthiolate complexes have been synthesized and characterized through multinuclear NMR and Single crystal X-ray diffraction technique. The thermal signature of the complexes intrigued us to utilize the same as molecular precursors for the preparation of technologically important  $\text{Cu}_{1.8}\text{S}$ ,  $\text{Cu}_{31}\text{S}_{16}$  and ternary  $\text{CuInS}_2$  nanostructures. Under alternating light and dark circumstances, the PEC devices based on immaculate nanostructures show stable photo-switching and strong photocurrent production.

### References:

1. Z. Shao, J. Chen, Q. Xie, L. Mi, Coordination Chem. Rev., 2023, **486**, 215118.
2. C. Coughlan, M. Ibanez, O. Dobrozhan, A. Singh, A. Cabot and K. Ryan, Chem. Rev. 2017, **117**, 5865-6109.



## Thermally Driven Synthesis of Bismuth Sulfide Nanoparticles through Single Source Precursor Approach

Atharva Kulkarni<sup>a</sup>, Rohit Singh Chauhan<sup>a</sup>, Gourab Karmakar<sup>b,c,\*</sup>, Adish Tyagi<sup>b,c,\*</sup>

<sup>a</sup>Department of Chemistry, K. J. Somaiya College of Science and Commerce, Vidyavihar, Mumbai 400077, India.

<sup>b</sup>Chemistry Division, Bhabha Atomic Research Centre, Mumbai 400085

<sup>c</sup>Homi Bhabha National Institute, Mumbai 400094, India

<sup>e</sup>Homi Bhabha National Institute, Anushaktinagar, Mumbai- 400094, India.

**Email:** tyagia@barc.gov.in, gourabk@barc.gov.in

### Abstract

An air-stable bismuth-pyrimidyl thiolate complex has been prepared and characterized by elemental analysis. The molecular structure of the complex was established through single crystal X-ray diffraction technique. TGA of the complex indicates that it can be utilized as single source precursors for the preparation of Bi<sub>2</sub>S<sub>3</sub> nanostructures. This study also revealed the profound effects of temperature and growth duration of the nanostructures in OAm.

Research on group V-VI semiconducting materials has drawn significant attention both in their nano-regime and bulk state due to their promising applications in optoelectronics and energy storage devices. Among group V metal chalcogenides (V–VI materials), Bi<sub>2</sub>S<sub>3</sub> have emerged as promising photon absorber materials due to their enticing electrical and optical properties. It benefits from several key attributes such as a narrow band gap, high absorption coefficient which make them promising candidates for energy conversion applications [1]. Bi<sub>2</sub>S<sub>3</sub> is stibnite-structured and crystallizes in the orthorhombic *Pnma* space group and can be described as a layered structure with a band gap ranging from 1.3 to 1.9 eV. Moreover, having advantages of relatively abundant resources, non-toxicity, high stability, etc., Bi<sub>2</sub>S<sub>3</sub> is projected as a fine candidate for low-cost sustainable solar cells.

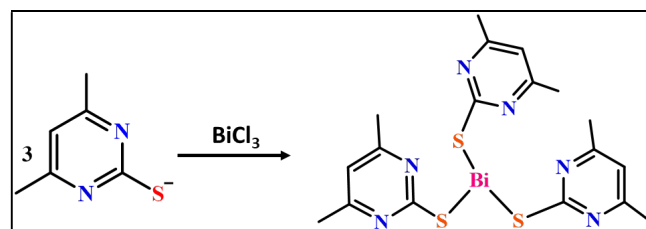
Various solution-assisted and solventless synthetic routes including solvothermal, hydrothermal, microwave-assisted, green synthesis etc., have been explored for the synthesis of Bi<sub>2</sub>S<sub>3</sub> nanostructures. Most of these methods employ a dual precursor route wherein a bismuth source (e.g., BiCl<sub>3</sub> etc) combines with a suitable sulfur source (elemental S, thiourea etc). On the other hand, single-source precursor (SSP) constitute a class of soft chemical route to exotic materials, which houses the desired elements in a single small molecule with physical bond between them. This strategy has gained significant attraction due to its simplicity and versatility. It ensures a low decomposition temperature, phase purity of the final product and high reproducibility of experimental results due to preformed bonds between the desired constituent elements [2, 3]. Moreover, molecular precursors offer several distinct advantages in terms of lower defect concentrations and better control over their morphology which in turn affect their electronic properties. In this view, a new bismuth-pyrimidyl thiolate complex, namely [Bi(2-SC<sub>4</sub>H<sub>2</sub>N<sub>2</sub>(4,6-Me)<sub>2</sub>)<sub>3</sub>], have been synthesized, thoroughly characterized and explored for the preparation of Bi<sub>2</sub>S<sub>3</sub> nanostructures by tuning the thermal conditions.

### Experimental

To a methanolic solution of (2-SHC<sub>4</sub>H<sub>2</sub>N<sub>2</sub>(4,6-Me)<sub>2</sub>) (0.62 mmol) and NEt<sub>3</sub> (1.24 mmol), solid Bi(NO<sub>3</sub>)<sub>3</sub>·5H<sub>2</sub>O (0.21 mmol) was added. The reaction mixture was stirred for 3 hrs at room temperature. The resulting turbid solution was dried under reduced pressure. A resulting solid was washed thoroughly with methanol and extracted in hot toluene mixture. The ensuing solution was kept at low temperature to afford pale yellow crystals.

### Results and Discussion

Treatment of Bi(NO<sub>3</sub>)<sub>3</sub>·5H<sub>2</sub>O with the thiolate ligand in an appropriate molar ratio resulted in the title complex (Scheme 1). Molecular structure of the complexes determined from single crystal X-ray diffraction technique revealed that geometry around the bismuth is distorted square pyramidal (Fig. 1).



**Scheme. 1** Synthesis of [Bi(2-SC<sub>4</sub>H<sub>2</sub>N<sub>2</sub>(4,6-Me)<sub>2</sub>)<sub>3</sub>].

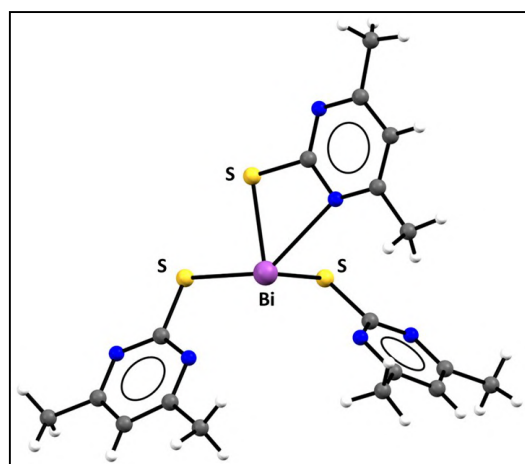


**Fig. 1.** Molecular structure of [Bi(2-SC<sub>4</sub>H<sub>2</sub>N<sub>2</sub>(4,6-Me)<sub>2</sub>)<sub>3</sub>].

Thermogravimetric analyses (TGA) were carried out to evaluate the thermal decomposition behaviour of the complexes under flowing argon atmosphere. TG curve for the complexes showed a decomposition at ~18.1% which corresponds to the formation of Bi<sub>2</sub>S<sub>3</sub> (calculated ~18.2%) (Fig. 2).

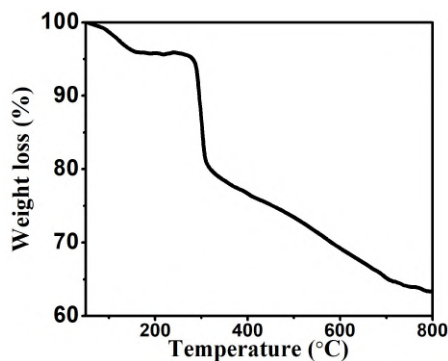


**Fig. 2:** Thermogravimetric data analysis for  $[\text{Bi}(\text{2-SC}_4\text{H}_2\text{N}_2(4,6\text{-Me})_2)_3]$ .

The thermal signature of the title complex clarifies that the complex undergoes single-step decomposition to bismuth sulfide. To ascertain this point, thermolysis of the precursor was performed using a heat-up approach. Oleylamine (OAm) was primarily used as a high-boiling solvent. The morphological modulation of the nanostructures was studied by thermolyzing the precursor at different thermal parameters as a function of time. Further, the phase purity  $\text{Bi}_2\text{S}_3$  was determined using PXRD which revealed the formation of amorphous nanoparticles at low temperatures (Fig. 3b and c) and highly crystalline nanostructures at relatively high temperature (Fig.3d).

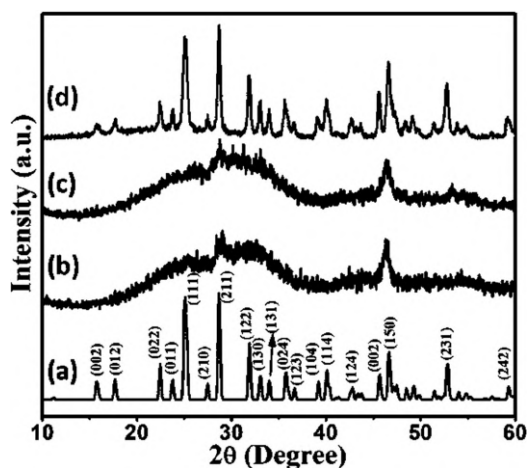


**Fig. 3.** (a) Simulated powder X-ray pattern (PXRD) of orthorhombic  $\text{Bi}_2\text{S}_3$  (ICSD Coll. Code 30775). PXRD patterns of  $\text{Bi}_2\text{S}_3$  synthesized at (b)  $130^\circ\text{C}$ , 10 min, (c)  $130^\circ\text{C}$ , 30 min and (d)  $150^\circ\text{C}$ , 10 min.

To gain the better insight into the morphology, electron microscopic techniques were used. The bright field TEM images revealed the formation of nano-sized  $\text{Bi}_2\text{S}_3$  of different crystallinity where, bismuth sulfide synthesized relatively at a higher temperature revealed the presence of 1-D nanorods.

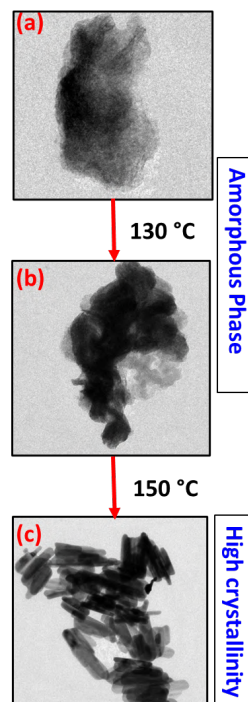


**Figure. 4.** Shape evolution of (a, b) amorphous and (c) crystalline 1-D  $\text{Bi}_2\text{S}_3$  nanostructures by regulating temperature as a function of time.

The optical properties of these materials were studied using diffuse reflectance spectroscopy (DRS) which ranged between 2.15 to 1.93 eV. These bandgaps fall within the range, suitable for photovoltaic and solar cell applications.

#### Conclusion:

This study focuses on the synthesis and structural elucidation of a bismuth complex coordinated to internally functionalized pyrimidyl thiolate ligand. The complex was utilized as a single source molecular precursor for the preparation of  $\text{Bi}_2\text{S}_3$  nanostructures. Significant influence of temperature as a function of time on phase formation, morphology was studied. Further, the bandgap of these materials, as evaluated by DRS studies, were found to be in optimum range, suitable for energy conversion and storage applications. This strategy of bismuth sulfide nanomaterials synthesis is versatile and economic and holds great promise for future energy and environmental technologies.

#### References

1. A. A. Tahir, M. A. Ehsan, M. Mazhar, K. G. U. Wijayantha, M. Zeller and A. D. Hunter, *Chem. Mater.*, 22 (2010) 5092.
2. G. Karmakar, A. Tyagi, A. Y. Shah, S. Nigam, A. P. Wadawale, G. Kedarnath, B. G. Vats, N. N. Kumar, V. Singh, *Dalton Trans.*, 51 (2022) 12670.
3. G. Karmakar, A. Tyagi, A. Y. Shah, *Coord. Chem. Rev.*, 504 (2024) 215665.

## Thermal Design and Simulation of the Radiator for High Power Space Travelling Wave Tube (TWT)

Chirag Mistry\*, Amitavo Roy Choudhury, Sanjay Kumar Ghosh  
 Vacuum Electron Devices Group, CSIR-Central Electronics Engineering Research Institute, Pilani-333031,  
 Jhunjhunu, Rajasthan, India

\*Corresponding author email ID-cpmistry@ceeri.res.in, M-9723665881

### Abstract

Radiation cooled Space TWT is most commonly used as a power amplifier for satellite communication. In general, the radiator is mounted on the Multistage Depressed Collector (MDC) and the objective of the radiator is to dissipate waste heat into the space environment. In this paper, the author has presented the design and thermal simulation of the radiator to dissipate heat up to 140W. Further, the topology optimization of the radiator for room temperature and space temperature has been carried out to keep the maximum radiator temperature below the allowable temperature limits. The radiator is simulated in the ANSYS tool.

### Introduction

Radiation cooled Helix TWT is commonly used for satellite communication due to its high efficiency. The function of the radiator of the space TWT is to dissipate waste heat into the environment. The radiator has to mount on the Multistage Depressed Collector (MDC) of the space TWT as shown in the figure 1. High energy beams incident on the inner surface of the electrodes of MDC. Some energy has recovered from the electrodes and the remaining produced heat at MDC. In general, TWT has to operate under RF and DC operating conditions. In addition, space TWT has to operate in an environment temperature ranging from  $-40^{\circ}\text{C}$  to  $85^{\circ}\text{C}$  in a thermo-vacuum chamber for space qualification [1, 2]. Therefore, in this paper thermal simulation of the radiator assembly has been carried out for the RF, DC and at different environment temperatures ( $-40^{\circ}\text{C}$  &  $85^{\circ}\text{C}$ ) under RF case. The temperature profile of the radiator assembly has been estimated using ANSYS tool under different operating cases at different environment temperatures. The simulation results i.e. maximum temperature were validated with the allowable temperature limit criteria of the material. Further, the geometry of the radiator has been optimized to keep the maximum temperature below the allowable temperature limit of the material. A cross section view of the initial design of the radiator is as shown in the figure 2. The initial design of the radiator (D1) has four fins of fin thickness ( $t$ ) and fin length ( $L$ ). The heat dissipation capacity of the radiator can be increased by introducing fin structure to increase surface area for heat dissipation. Therefore, to keep the maximum temperature below the allowable limit, the geometry of the radiator is optimized as listed in Table 1. The design iterations from D1 to D4 each has been simulated in the ANSYS for the temperature profile. The thermal simulation presented here is for the final optimized geometry of the radiator (D4). The non-functional space between the fins no 2 to 4 of initial

radiator design is utilized to add more fins for the final design of the radiator.

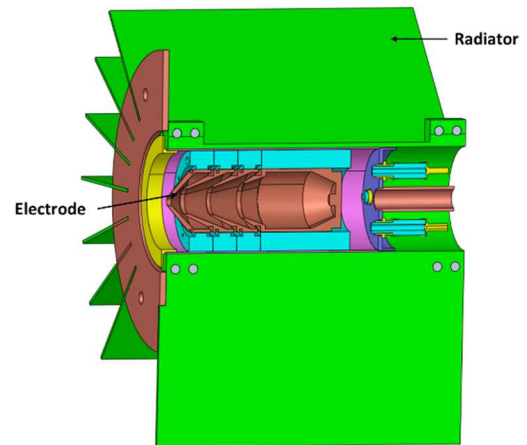


Figure 1. The radiator mounted on Multistage Depressed Collector (MDC)

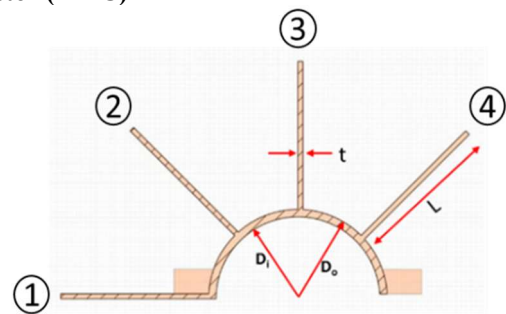


Figure 2. A cross section view of initial design of the radiator

Table 1. Thermal design optimization iterations

Sr. No	Parameters	D1	D2	D3	D4
1	Inner diameter ( $D_i$ )	$D_i$	$D_i$	$D_i$	$D_i$
2	Outer diameter ( $D_o$ )	$D_o$	$D_o$	$D_o$	$D_o$
3	Fins length ( $L$ )	$L$	$2L$	$L$	$2L$
4	Thickness ( $t$ )	$t$	$t$	$t$	$t$
5	No of fins	4	4	8	8
6	Weight (g)	58	91	91	157

### Thermal Simulation and Results

The geometry of the radiator assembly has been model in the Solid Works [3] and thermal simulation have been carried out in the ANSYS tool [4]. The heat load on the

different electrodes of the MDC are as listed in the Table 2. The heat dissipate through the environment is by means of the natural convection and radiation. Accordingly, thermal boundary condition are applied for the thermal simulation in ANSYS. The final optimized geometry of the radiator (D4) has eight no of fins of double length (2L) compared to initial design as shown in Figure 3. The weight of the final optimized geometry of the radiator is 157g. There is always tread off between the weight and thermal performance of the radiator when, it was used for the space application. Therefore, based on the thermal performance D4 design of the radiator is best choice. The radiator is made of Al-6061.

**Table 2. The heat load on the different electrodes of the MDC**

Sr. No	Electrode	RF	DC
1	Electrode 1	19	5
2	Electrode 2	27	5
3	Electrode 3	20	5
4	Electrode 4	74	125

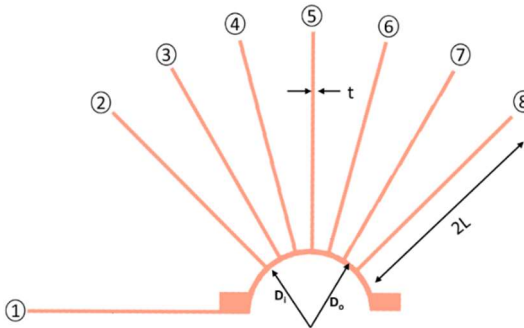


**Figure 3. A cross section view of the final optimized design (D4) of the radiator**

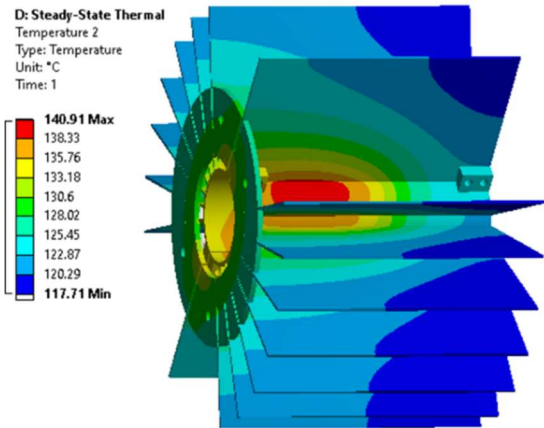


**Figure 4. Temperature profile of the radiator for RF case under 85°C**

The temperature profile of the radiator for RF case at 85°C environment temperature is as shown in Figure 4. The estimated maximum temperature through the simulation is ~141 °C, which is well below the allowable temperature limit of the material of 200 °C. Therefore, the radiator assembly is safe to operate under extreme environmental temperature of 85°C. The maximum radiator temperature plots for different operating conditions for each design iterations are as shown in Figure 5. It can be observe from the Figure 5 that, D4 version of the radiator design has least temperature compared

to all other cases. While radiator design, D2 and D3 are also most same for both thermal and weight aspects.

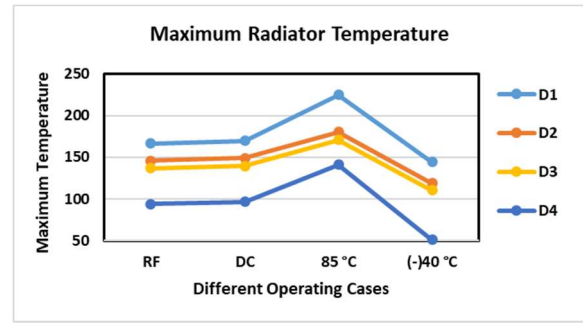


**Figure 5. The maximum radiator temperature plots for different operating cases**

### Conclusion

The thermal design and simulation of the radiator have been carried out to dissipate heat up to 140W to the environment. The design of the radiator have been optimized to keep the maximum temperature below the allowable limit of the material under extreme environment temperature. Therefore, the proposed design of the radiator is safe to operate under different operating conditions at extreme environmental conditions.

### Acknowledgment

The authors would like to thank the Director of the Council of Scientific and Industrial Research–Central Electronics Engineering Research Institute (CSIR–CEERI), for his kind permission to publish this paper.

### Reference

- [1] C. Mistry and S. K. Ghosh, "Thermal Design and Analysis of Radiation Shield Cooling Assembly for Efficient Heat Dissipation of Space Traveling-Wave Tube," in IEEE Transactions on Electron Devices, vol. 71, no. 1, pp. 374-380, Jan. 2024, doi: 10.1109/TED.2023.3338591.
- [2] P. Chen et al., "Development of Ka-band 100W Radiation-cooled Space TWT," 2023 24th International Vacuum Electronics Conference (IVEC), Chengdu, China, 2023, pp. 1-2, doi: 10.1109/IVEC56627.2023.10157339.
- [3] SolidWorks Manual, Canonsburg, PA, USA, 2011.
- [4] ANSYS® Academic Research Mechanical, release 19.0, Help System, Static Analysis Guide, ANSYS Inc. 2019.

## Study of Temperature Dependent Corrosion of SS 304L in corrosive acidic medium using X-Ray Fluorescence

K.G. Spoorthy<sup>a</sup>, Sangita Dhara<sup>b,c\*</sup>, Muhammed Shafeeq<sup>b</sup>, Ruma Gupta<sup>b,c</sup>

<sup>a</sup> Raja Ramanna Center for Advanced Technology, Indore, 452013, India

<sup>b</sup> Fuel Chemistry Division, Bhabha Atomic Research Centre, Trombay, Mumbai 400085, India

<sup>c</sup> Homi Bhabha National Institute, Anushaktinagar, Mumbai, 400094, India

\* Corresponding author: sdhara@barc.gov.in, 02225594567

### Abstract

The temperature dependent corrosion studies were carried for SS 304L coupons immersed in three different acidic mediums: Conc. HNO<sub>3</sub>, 1M HCl in Conc. HNO<sub>3</sub> and 2M HCl in Conc. HNO<sub>3</sub> at various temperatures from 25 °C to 90°C. The Corrosion Rates (CRs) were calculated using the weight loss calculated by the leaching of metals into the medium and its determination by EDXRF. The corrosion rates followed the order: Conc. HNO<sub>3</sub> < 1M HCl in Conc. HNO<sub>3</sub> < 2M HCl in Conc. HNO<sub>3</sub>. Further studies on the corrosion kinetics have revealed that the rate of reaction of the alloy corrosion increases with increase in chloride concentration, while the half life decreases with increase in chloride concentration.

Stainless steel (SS) is one of the most widely used Fe alloys. It finds applications as structural material in a variety of industries including Nuclear. In fact, SS 304L is the workhorse material of the reprocessing plant which faces the hostile conditions of acid, temperature as well as high radiation dose. One of the main reasons for deterioration of the structural materials is corrosion. This degradation process is due to the interaction of the alloy with air, water, acids, or salts, leading to the formation of corrosion products (like rust for iron) and weakening of the structural material. The concentration, temperature and radiation dose are the factors which enhance or inhibits the corrosion rates. Corrosion rate (CR) refers to the rate at which a material deteriorates due to chemical reactions with its environment. The corrosion in materials is estimated in terms of corrosion rates. In fact, corrosion rate is a critical parameter for understanding the longevity and durability of the material in various environments. The traditional way to measure the corrosion rates is the weight loss method wherein the material is weighed before and after exposure to the corrosive environment. The difference in weight (due to the loss of material) is used to calculate the corrosion rate using the given formula [1]:

$$CR = \frac{\text{Weight loss (g)} * 87500}{\text{Alloy Density} \left(\frac{\text{g}}{\text{cc}}\right) * \text{Area (cm}^2\text{)} * \text{Time (H)}}$$

HCl is a very corrosive acid and useful to study from the standpoint of corrosion and material damage. Further HCl is also used for pickling of steel. The aim of this work is to investigate the corrosion behavior and mechanism for stainless steel 304L (SS304L) in Conc. HNO<sub>3</sub>, 1M HCl in Conc. HNO<sub>3</sub> and 2M HCl in Conc. HNO<sub>3</sub> at various temperatures from 25 °C to 90°C using EDXRF.

### Experimental:

For corrosion studies stainless steel 304L coupons having 0.5 X 0.5 cm<sup>2</sup> area and 2 mm thickness were taken. These coupons were first polished using emery paper to remove any oxide formed over the SS surfaces. Then, it was dipped in 5% HCl solution to further remove any impurities or oxides from the surface. Then these coupons were cleaned with high purity ethanol followed by Milli-Q water. After complete drying, these cleaned coupons were finally dipped in 2 mL solution of three different acid mediums: a) Conc. HNO<sub>3</sub>, b) 1M HCl in Conc. HNO<sub>3</sub> and c) 2M HCl in Conc. HNO<sub>3</sub>. A known volume of Ga internal standard was added to all the samples. For

studying the effect of temperature, the SS coupons were also subjected to different temperatures by heating them in a water bath of 40°C, 50 °C, 60°C and 90 °C.

The concentrations of Fe, Cr, Ni, Mn, Mo in the acid solutions were determined using EDXRF. The EDXRF spectrometer, model Xenometrix Genius IF used for the elemental analysis consists of Rh target and operated at 45 kV and 1000 µA. Prior to EDXRF analysis, all the samples were kept in ultrasonic bath for a few minutes so that the elements released from the stainless steel surface will be uniformly distributed in the whole solution. Then, 20 µL of the sample solution is deposited on mylar film, dried and measured.

### Results and discussions:

It has been observed from the previous studies that as the nitric acid concentration increases passivation of SS also increases [2]. Passivation of steel using nitric acid is a chemical process that creates a protective oxide layer on the surface of steel to prevent it from further corrosion. Nitric acid dissolves the Fe compounds and other trace elements and activates the formation of Cr<sub>2</sub>O<sub>3</sub> protective layer. However, hydrochloric acid can attack the protective layer and cause pitting corrosion. Fig. 1 shows the SEM images of the SS 304L coupons immersed in Conc. HNO<sub>3</sub> and 2M HCl in Conc. HNO<sub>3</sub>. From the figure it can be clearly seen that the pitting corrosion is more enhanced in the sample immersed in Conc. HNO<sub>3</sub> with 2M HCl.

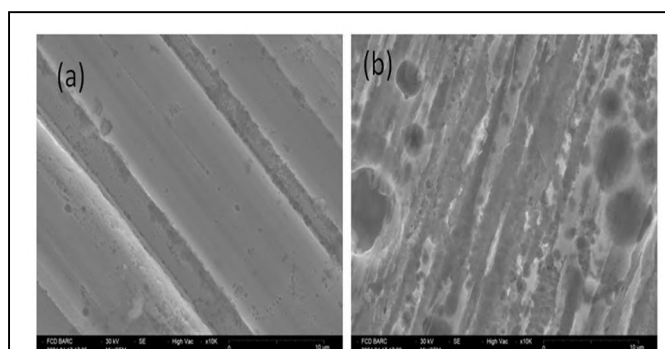
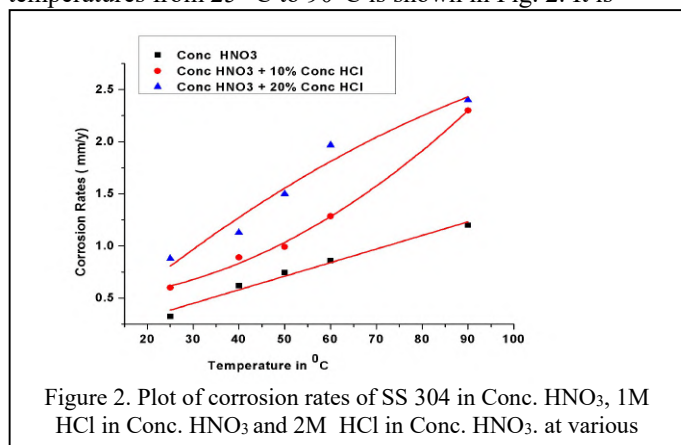


Figure 1. SEM images of SS304L coupons immersed in (a) Conc. HNO<sub>3</sub> and (b) 2M HCl in Conc. HNO<sub>3</sub>

In a solution containing both HNO<sub>3</sub> and HCl, the passivation and pitting corrosion will occur simultaneously and the corrosion rates will depend on the acid medium,

concentration, time as well as temperature. The Corrosion rates (CRs) of SS 304L were evaluated in different medium using the given formula. The weight loss was calculated by determining the concentration of the trace elements that has leached into the acid medium during corrosion using the EDXRF. The CRs in different mediums at various temperatures from 25 °C to 90°C is shown in Fig. 2. It is



observed from the figure that the CRs are least in HNO<sub>3</sub> medium and it increases as the chloride concentration increases in the solution. In case of nitric acid medium the CR increases linearly which clearly suggests that the corrosion follows a uniform rate with increasing temperature. However, the non-linear relationship in case of the other two mediums containing Cl<sup>-</sup> ion suggests more complex corrosion mechanism such as pitting or localized corrosion.

The steel surface spontaneously, when in contact with air, forms an oxide layer consisting of complex composition of Fe and Cr oxides. In HNO<sub>3</sub> medium SS forms a passive layer of Cr<sub>2</sub>O<sub>3</sub> which prevents the further corrosion of SS. This was further corroborated with the XRD analysis. The XRD data of these coupons were recorded directly by placing the coupons in the XRD sample holder such that the surface was analysed. The XRD patterns are shown in Fig. 3. In this figure multiple peaks of SS are seen at 29°, 44°, 52° and 75° (2θ). Some additional peaks are seen in the unreacted and Conc. HNO<sub>3</sub> immersed coupons. These peaks at 29.5°, 46°, 47° and the peaks between, 55° to 70°, corresponds to the complex oxides of Cr and Fe formed in contact with air and oxidizing medium. These peaks are completely absent in the coupons that were immersed in 1M and 2M HCl in Conc. HNO<sub>3</sub>. The increased corrosion rate in coupons is due to attack of chloride ions on the passive layer that is formed on the surface.

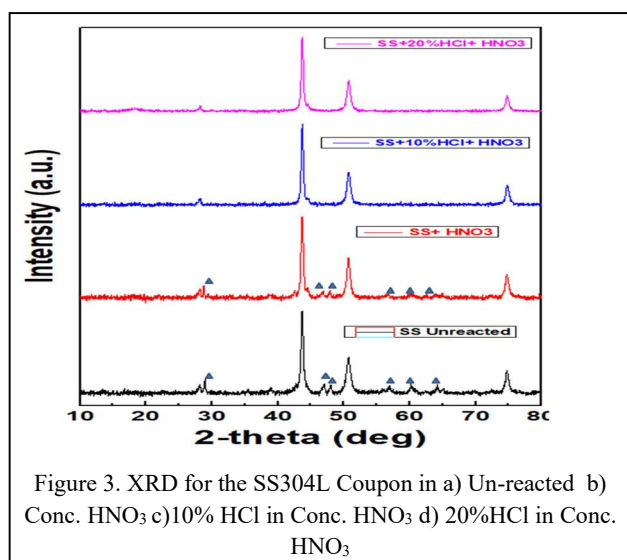


Figure 3. XRD for the SS304L Coupon in a) Un-reacted b) Conc. HNO<sub>3</sub> c)10% HCl in Conc. HNO<sub>3</sub> d) 20%HCl in Conc. HNO<sub>3</sub>

Corrosion kinetics is another important study that helps in understanding the factors influencing the rate of corrosion. At 90°C the CRs for three different acid solutions were measured at a time interval of 10 min for 60 mins. A plot of CRs Vs the time at 90 °C is shown in Figure 4. The corrosion rate decrease with time in all the cases due to depletion of corrosive ions as it may be consumed during the corrosion process and due to the formation of protective layer.

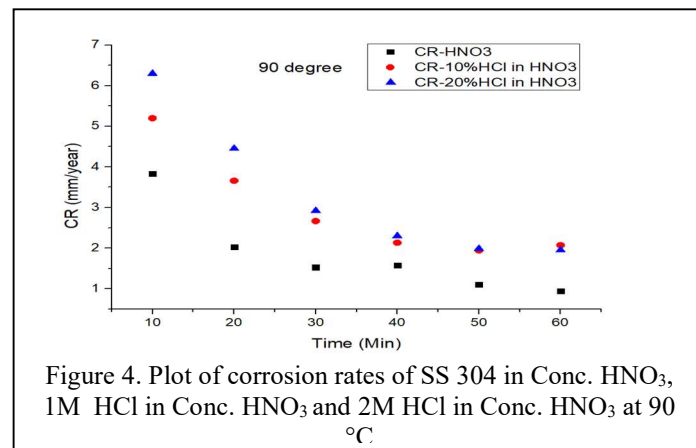


Figure 4. Plot of corrosion rates of SS 304 in Conc. HNO<sub>3</sub>, 1M HCl in Conc. HNO<sub>3</sub> and 2M HCl in Conc. HNO<sub>3</sub> at 90 °C

At higher temperatures 60 °C and 90 °C the mass loss is proportional to Cl<sup>-</sup> concentration. Hence a first order corrosion reaction was modeled. Table 1 gives the values of the specific corrosion rates calculated using first order rate expression:

$$k = \frac{2.303}{t} \text{Log} \frac{\text{initial weight of coupon}}{\text{weight of coupon at time, } t}$$

The half live time were then calculated using the formula  $t_{1/2} = 0.693/k$  [3].

**Table 1.** The specific corrosion rates and  $t_{1/2}$  values of SS304L in different acid mediums and temperature

Medium	K x 10 <sup>-7</sup> ( min <sup>-1</sup> )	t <sub>1/2</sub> x10 <sup>+6</sup> (min)	Temp 90°C	
			K x 10 <sup>-7</sup> ( min <sup>-1</sup> )	T <sub>1/2</sub> x10 <sup>+5</sup> (min)
HNO <sub>3</sub>	2.98	2.33	4.67	14.8
1M HCl + HNO <sub>3</sub>	4.00	1.73	8.27	8.38
2M HCl + HNO <sub>3</sub>	4.95	1.40	11.1	6.24

### Conclusions:

The feasibility of using XRF as an analytical tool for determination of Corrosion Rates of SS 304L was explored in this study. The CRs were determined by the weight loss calculated by determining the concentration of the trace elements that has leached into the acid medium during corrosion using the EDXRF. The studies have revealed that as Cl<sup>-</sup> ion concentration increase the CRs also increase. Further, the specific corrosion rates of the reaction (k) and the  $t_{1/2}$  were also determined in this study.

### References

- [1] F. Malaret, *Experimental Results*, 3 (2022) e13, 1-12.
- [2] J. Chachal, S. Dhara, *Spectrochim. Acta Part B*, 221 (2024) 10705
- [3] A. D. Usman, F. V. Adams, L. Okoro, *Journal of Advances in chemistry*, 11 (2015) 3434-3440. <https://doi.org/10.24297/jac.v11i2.2211>

## Structural and Thermal Stability Studies on Irradiated Magnesium Potassium Phosphates for Back End Nuclear Fuel Cycle Applications

Rumu Halder Banerjee<sup>a,\*</sup>, Naina Rajee<sup>b</sup> and Pranesh Sengupta<sup>a,c</sup>

<sup>a</sup>Materials Science Division, Bhabha Atomic Research Centre, Mumbai - 400085, INDIA

<sup>b</sup>Analytical Chemistry Division, Bhabha Atomic Research Centre, Mumbai - 400085, INDIA

<sup>c</sup>Homi Bhabha National Institute, Anushaktinagar, Mumbai - 400094, INDIA

\* Corresponding author's email: [rumu@barc.gov.in](mailto:rumu@barc.gov.in) ; Tel:022-25592186

### Abstract

Magnesium potassium phosphate (MKP) cement has emerged as a potential eco-friendly alternative to Portland cement for nuclear waste encapsulation. Its superior resistance to sulfate attack, low permeability, and mechanical strength makes it a promising material. This study investigates the thermal and radiation stability of MKP specimens prepared by gel crystallization, followed by heat treatment at 120°C, 400°C, 800°C, and 1000°C. Specimens were irradiated with a 10 MeV electron beam to a dose of 20 MGy. Analytical techniques, including XRD, TGA, EGA, and DTA, revealed that MKP heat-treated at 1000°C exhibited exceptional structural stability, minimal weight loss, and negligible gas evolution under thermal and radiation conditions, making it suitable for encapsulating beta-emitting radionuclides.

### Introduction

Magnesium potassium phosphate cement ( $\text{MgKPO}_4 \cdot 6\text{H}_2\text{O}$ , MKP) is gaining traction as a sustainable and high-performance alternative to Portland cement, addressing critical challenges in nuclear waste immobilization [1]. Synthesized through an acid-base reaction between magnesium oxide and potassium dihydrogen phosphate, MKP exhibits superior mechanical strength, high resistance to sulfate attack and compatibility across a broad pH range. These characteristics, along with low leachability and permeability, render MKP particularly suitable for encapsulating beta-emitting radionuclides such as  $^{137}\text{Cs}$  and  $^{90}\text{Sr}$  which are major contributors to radioactive waste activity [1-3]. In contrast to Portland cement, which is prone to structural degradation from radiolytic gas generation, chemical instability and poor performance in high-salt environments, MKP demonstrates improved chemical resilience and long-term durability [1].

The application of MKP in nuclear waste management necessitates a detailed understanding of its behavior under combined thermal and radiation stresses. Ionizing radiation, particularly from beta-emitting isotopes, can induce significant structural modifications, including defect generation, amorphization and radiolysis of bonded water molecules. These effects, compounded by thermal stresses from decay heat, may lead to dehydration and phase transformations, potentially compromising matrix integrity. This study systematically investigates the thermal and radiation stability of MKP, with a focus on the role of heat treatment in enhancing its structural and chemical stability.

### Experimental Study

#### Sample Synthesis

MKP specimens were synthesized by reacting magnesium oxide ( $\text{MgO}$ ) with potassium dihydrogen phosphate ( $\text{KH}_2\text{PO}_4$ ) in stoichiometric proportions. The resulting gel was cured at ambient conditions to form  $\text{MgKPO}_4 \cdot 6\text{H}_2\text{O}$ . Heat treatments at 120°C, 400°C, 800°C, and 1000°C were performed for 2 hours to study the effects of thermal annealing.

#### Electron Irradiation

The irradiation experiments were performed using a 10 MeV electron beam operated in pulsed mode at the indigenously developed Linear Accelerator (LINAC) facility at the Electron Beam Centre, Khraghar [2,3]. The beam pulses were directed through a 1 m long titanium exit window and scanned uniformly over the MKP powder kept in nickel

crucibles, which were placed at room temperature under normal light conditions and an ambient atmosphere. The specimens were irradiated with a 10 MeV electron beam to a total dose of 20 MGy at a dose rate of 1 MGy/h.

#### Structural and Spectroscopic Characterization

The pre- and post-irradiation characteristics of the MKP samples were analyzed using X-ray diffraction (XRD). Simultaneous thermogravimetric analysis (TGA) and differential thermal analysis (DTA) were performed using a Netzsch STA 409 PC Luxx system to evaluate the thermal behavior of MKP specimens. Platinum versus platinum-rhodium (Pt vs. Pt-10% Rh) thermocouples were employed for precise measurements of temperature and thermal effects. The experiments were conducted under both air and inert nitrogen atmospheres, with a heating rate set to 10°C/min to ensure controlled and consistent thermal conditions. Nitrogen was used as the purge gas to maintain an inert environment, minimizing potential oxidative reactions during the analysis. Each specimen was accurately weighed to ensure repeatability and reliability of the results.

Evolved gas analysis (EGA) was conducted alongside TGA-DTA to monitor and identify gases released during heating. A Fourier transform infrared (FTIR) spectroscopy system was employed for this purpose, featuring a liquid nitrogen-cooled MCT detector and a gas cell with a small internal volume and a long optical path length. The gas transfer line, sample cell, and adapter head were heated to 200°C to prevent condensation of volatile compounds. Infrared spectra were recorded in the mid-IR range (400–4000  $\text{cm}^{-1}$ ) to analyze gaseous products, with the data processed using specialized software for detailed interpretation.

### Results and Discussion

#### Characterization of as-prepared specimens

The X-ray diffraction patterns recorded for MKP synthesized at room temperature (MKP-RT) is presented in Fig. 1.  $\text{KMgPO}_4 \cdot 6\text{H}_2\text{O}$  phase having orthorhombic crystal structure was observed to be the main phase in MKP-RT along with a minor amount of unreacted  $\text{MgO}$ . Upon annealing at different temperatures, MKP-RT undergoes a phase transformation owing to dehydration to form  $\text{MgKPO}_4$  having a monoclinic structure. This is further supported by TGA-DTA-EGA results. DTA results indicated an endothermic peak between 100°C and 150°C for as-prepared MKP (MKP-RT), consistent with the dehydration of structural water. The

absence of any thermal events in MKP-1000°C confirmed its resistance to thermal degradation. TGA curves revealed a progressive reduction in weight as MKP specimens were subjected to increasing temperatures. For as-prepared MKP, the weight loss of ~26.4% was associated with the loss of six structural water molecules between 100°C and 200°C, consistent with the dehydration of  $\text{MgKPO}_4 \cdot 6\text{H}_2\text{O}$ . Heat-treated samples displayed significantly lower weight losses: MKP-120 (17%), MKP-400 (7.6%), and MKP-800 (5.6%), culminating in MKP-1000 with the lowest weight loss of only 1.9%. The stability of MKP-1000 is attributed to the complete removal of loosely bound water during annealing, leaving a highly crystalline and thermally stable structure.

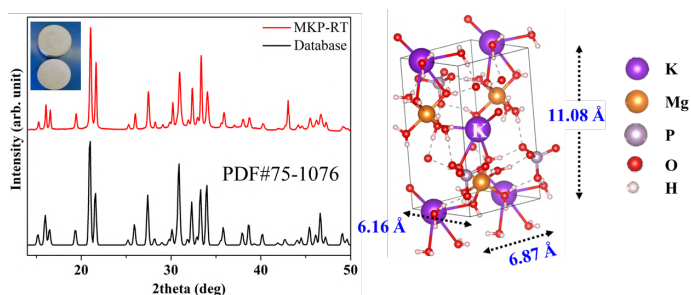


Figure 1. XRD pattern for MKP-RT specimen with the image of the synthesized pellet provided in the inset and schematic of the crystal structure of MKP-RT.

### Characterization of irradiated specimens

The stopping power for electrons in MKP-RT matrix with incident energy in the range 0-1000 MeV was derived using data from the NIST ESTAR program [4] and is presented in figure 2, which provides reliable values for electron interactions in various materials. The stopping power quantifies the energy loss experienced by electrons as they traverse the material. For MKP-RT, the collision stopping power for 10 MeV incident electrons was determined to be  $1786 \text{ KeVcm}^{-2}\text{g}^{-1}$ , accounting for energy loss due to inelastic collisions with atomic electrons. The radiative stopping power, representing energy loss from Bremsstrahlung radiation production, was calculated as  $243 \text{ KeVcm}^{-2}\text{g}^{-1}$ . The nuclear stopping power was calculated using NIEL program and was evaluated to be  $0.2799 \text{ KeVcm}^{-2}\text{g}^{-1}$  indicating that electrons mainly lose energy through collisions.

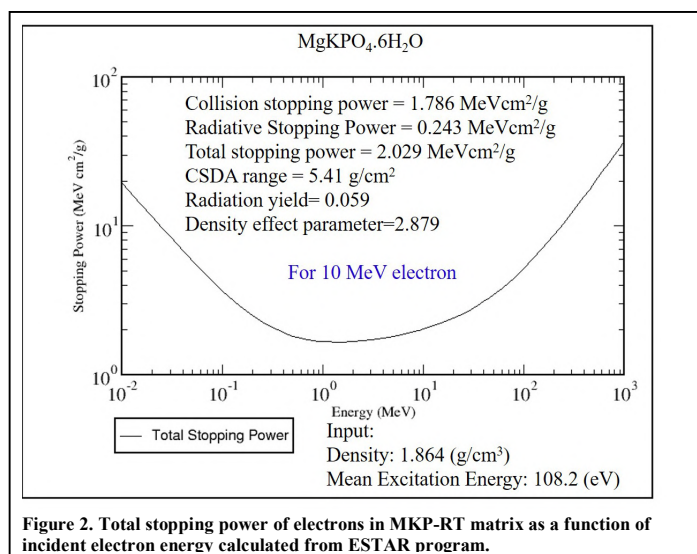


Figure 2. Total stopping power of electrons in MKP-RT matrix as a function of incident electron energy calculated from ESTAR program.

After irradiation, XRD patterns did not reveal any significant changes for samples annealed at 400, 800 and 1000 °C. However, formation of  $\text{MgKPO}_4$  and an unidentified amorphous phase in irradiated MKP-RT specimen was noted.

Post-irradiation TGA confirmed that irradiation did not induce significant changes in thermal stability for MKP-400, MKP-800, and MKP-1000 (Fig. 3). However, as-prepared MKP exhibited a reduction in weight loss post-irradiation (Fig. 3), indicating partial removal of structural water by the electron beam. EGA measurements complemented TGA by identifying the gases released during thermal treatment. For as-prepared MKP, two distinct peaks corresponding to the evolution of water (~150°C) and  $\text{CO}_2$  (~343°C) were observed, with the latter attributed to trace carbon impurities in the matrix. In contrast, MKP-1000 showed negligible gas evolution, highlighting its suitability for high-temperature applications. The absence of significant gas release during post-irradiation heating further validates the thermal stability of annealed MKP. Post-irradiation DTA curves showed no significant deviations for heat-treated samples, reaffirming their stability under combined thermal and radiation stresses.

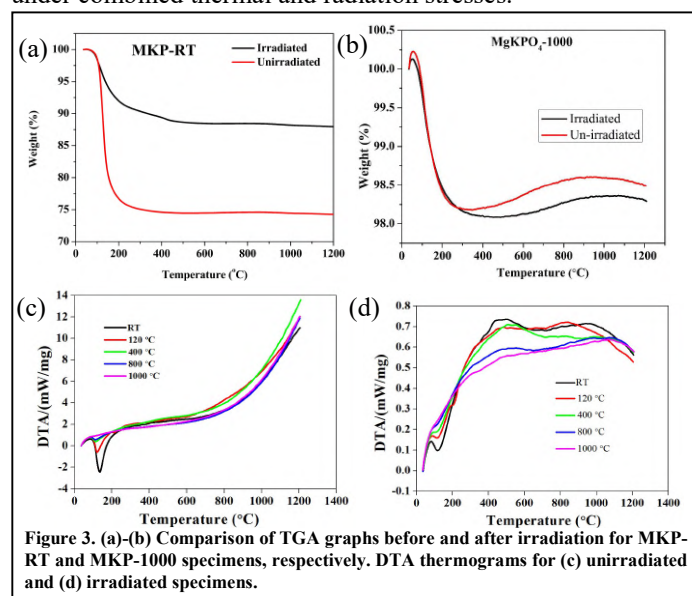


Figure 3. (a)-(b) Comparison of TGA graphs before and after irradiation for MKP-RT and MKP-1000 specimens, respectively. DTA thermograms for (c) unirradiated and (d) irradiated specimens.

### Summary

Magnesium potassium phosphates (MKP), proposed as eco-friendly substitutes for ordinary Portland cement, exhibit promising radiation stability under electron irradiation. Irradiation upto 20 MGy dose reveal minimal structural degradation in annealed specimens.

### Acknowledgements

The samples were received as a part of the INWARD coordinated research project (Ion Beam Irradiation for High Level Nuclear Waste Form Development, 2020-2023) supported by the IAEA on "Radiation testing of hydrated and dehydrated magnesium potassium phosphate cement" Doc. No. NWR-RADCRP-PRP-21001. The authors thank Dr. Nishant Chaudhary, EBC, Kharghar for electron beam irradiation and Dr. R. Tewari, Director, Materials Group for his constant encouragement and support.

### References

1. Wagh, A., 2016. Chemically Bonded Phosphate Ceramics; Twenty-first Century Materials with Diverse Applications. second ed. USA: Elsevier.
2. Rumu H Banerjee, N. Chaudhary, N. Raje et al. Bull Mater Sci 47, (2024) 209. <https://doi.org/10.1007/s12034-024-03281-6>
3. Rumu H. Banerjee, Swikisani M.M. Nelwamondo, Naina Raje, Harshala Parab, Nishant Chaudhary, P. Mathi, Jacoba Badenhorst, Amelia Goede, Pranesh Sengupta, Ceramics International, 50 (2024) 2405-2414.
4. Rumu H. Banerjee, R. Alexander, N. Chaudhary, S. Sanyal, P. Sengupta, Journal of Nuclear Materials, 599 (2024) 55199.



## Phase Evolution in Stainless Steel – Zircaloy System upon Melt-solidification

Sourav Majumder<sup>a,b</sup>, Dheeraj Jain<sup>a</sup> and V. Sudarsan<sup>a,b,\*</sup>

<sup>a</sup>Chemistry Division, Bhabha Atomic Research Centre, Trombay, Mumbai, India – 400 085.

<sup>b</sup>Homi Bhabha National Institute, Anushaktinagar, Mumbai – 400 094.

\* vsudar@barc.gov.in; Telephone: +91 22 2559 5355; Fax: +91 22 2550 5151

### Abstract:

Zircaloy-based clad, which remains undissolved during the head-end process of UO<sub>2</sub>-based spent nuclear fuel reprocessing (PUREX process) is classified as high level metallic solid nuclear waste (also known as hull). Immobilization of hull into a physico-chemically stable metallic matrix is one of the strategies being contemplated for Long-term safe management for hull. With this application in mind, different alloys comprising of stainless steel (SS 316) and nuclear-grade virgin clad (Zircaloy 4) were prepared via DC arc-melting technique. As prepared (melt-solidified) alloys were characterized using weight change, powder X-ray diffraction (PXRD), Scanning Electron Microscope (SEM) and Energy Dispersive X-ray Spectroscopy (EDS). Transformation of the austenite (face centered cubic; FCC) phase of as-received SS 316 to Martensite (body centered tetragonal; BCT) has been observed upon zircaloy addition. Zircaloy-induced stabilization of martensite phase has been explained in terms of rapid cooling of molten alloy facilitated by zircaloy incorporation and has been evidenced by microstructural data. These results provide important structural and phase behavior details to develop steel-based matrices for hull management.

### Introduction:

Zirconium-based alloys are used as cladding and structural materials in most of the light / heavy water nuclear reactors. These alloys offer low capture cross-section for thermal neutrons as well as good corrosion resistance in aqueous media under LWR / HWR operating conditions [1,2]. Zircaloy-4 is used as clad material in UO<sub>2</sub> (comprising natural uranium) fueled Indian PHWRs. Spent nuclear fuel from PHWRs is chemically reprocessed to retrieve fissile material and depleted uranium and, separate valuable fission product radioisotopes from the minuscule amount of high level liquid waste [3]. Zircaloy-4 remains undissolved during the head-end of PUREX process and is classified as high level metallic solid nuclear waste (known as hull). Immobilization of hull into a physico-chemically stable metallic matrix is one of the strategies being contemplated for its long-term safe management [4]. Towards this strategy, stainless steel-zircaloy system is being investigated in our research group with primary focus to evaluate their phase behavior, microstructure and thermophysical properties. Stainless Steel is chosen as for its excellent corrosion resistance (both, in air and aqueous medium) and well known physico-chemical properties as a function of temperature. Present study highlights the phase behavior of melt-solidified alloys wherein martensite phase of steel evolves upon zircaloy addition.

### Experimental Section:

Commercially available stainless steel (SS-316; > 99.9% purity) and nuclear grade Zircaloy-4 were used as starting materials. Binary alloys with nominal composition {Zircaloy<sub>(1-x)</sub>-SS316<sub>(x)</sub>; x = weight fraction} were prepared by DC arc-melting technique. Melting was performed under Argon gas flow (~200 mL/min.). Each alloy (typically ~10 g scale) was melted three times to maximize compositional homogeneity. Weight change upon melt-casting process was recorded using 5-digit precision analytical balance (XP-205, Mettler-Toledo). A portion of each as-cast alloy was powdered by abrasion and phase characterized by powder XRD (Smart Lab, Rigaku) using Cu-K $\alpha$  (1.5418 Å) radiation. Flat surface of as-cast alloys was polished (successively over SiC paper and Al<sub>2</sub>O<sub>3</sub> paste), ultrasonicated (in methanol) and imaged using scanning electron microscope (AIS2100, Seron Technologies) in both secondary electron (SE) and back scattered electron

(BSE) image mode. Elemental analyses over imaged alloy surfaces were performed using Energy Dispersive X-ray Spectrometer (EDS, Oxford Instruments).

### Results and Discussions:

Fig. 1 shows weight change (%) observed upon melt-solidification of zircaloy-steel alloys prepared by DC arc-melting. SS316-rich compositions ( $x \geq 0.5$ ) showed systematic weight loss (up to ~1%). In contrast, zircaloy-rich ( $x \leq 0.5$ ) alloys showed systematic weight gain (up to ~0.6%). Systematic weight loss in SS-rich alloys is attributed to predominated vaporization-induced losses arising from lower melting temperature (~1400°C) of SS316 as compared to that of Zircaloy-4 (~1850°C). This was supported by observation of dark color powder residue deposited over the surface of arc-melting crucible (Cu). The residue was characterized by EDS technique to contain Manganese (Mn) and Chromium (Cr); arising from their preferential segregation in vapor phase during melt-solidification process.

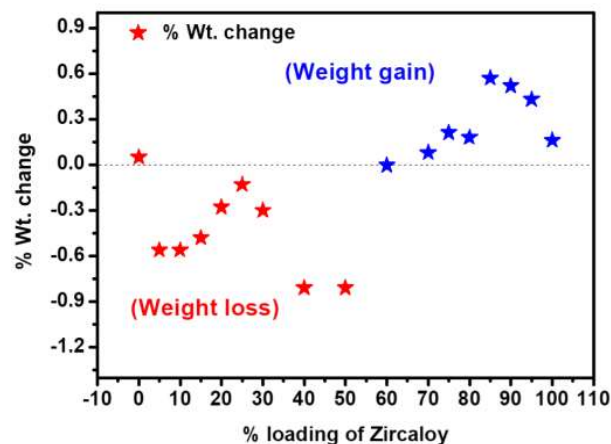


Figure 1: Weight change in melt-solidified SS 316-Zircaloy 4 alloys upon arc-melting

In contrast to SS-rich alloys, systematic weight gain (albeit to a lower extent) in melt-solidified zircaloy-rich compositions ( $x \leq 0.5$ ) is attributed to oxidation (uptake of oxygen impurity present in Argon cover gas) at high temperatures attained during arc-melting.

Fig. 2 (a) and 2(b) show XRD patterns recorded on both as-received and melt-solidified powdered SS-316 and zircaloy-4, respectively. Diffraction patterns of melt-solidified end members, namely SS-316 (austenite; FCC) and zircaloy-4 (HCP) grossly match with those of as-received starting materials, confirming overall phase retention even after melt-solidification (up to three cycles). For SS-316, appearance of martensite (body centered tetragonal; BCT) phase in melt-solidified product can be seen (Fig. 2a), which is attributed to hardening due to rapid cooling of arc-melted steel where fast solidification prevents carbon atoms to diffuse from the crystal lattice and BCT structure emerges. In case of zircaloy-4, melt-solidification cycles cause broadening of diffraction peaks, thereby indicating increased structural disorder / strain.

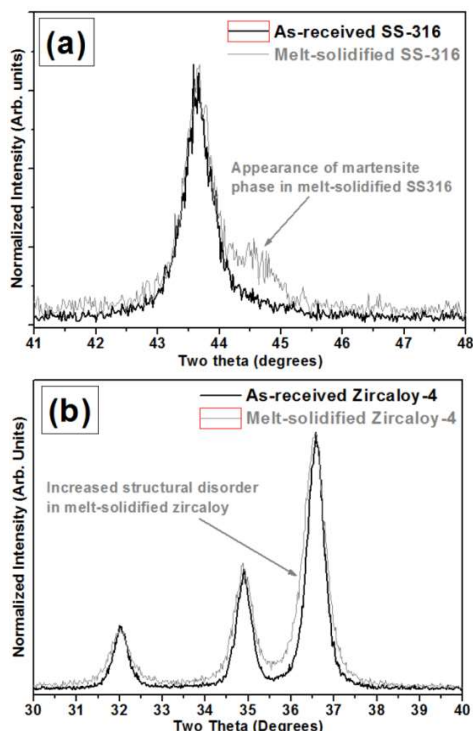


Figure 2: RT XRD patterns of (a) SS-316 and (b) zircaloy-4, both before and after melt-solidification

Fig. 3 shows powder XRD patterns of alloys prepared with varying fractions of Zircaloy-4 & SS-316. While melt-solidification of SS-316 causes appearance of martensite phase (minor fraction), incorporation of zircaloy-4 (~5 wt.%) causes near-complete transformation to martensite phase, which is an interesting result. Further addition of zircaloy-4 (up to 20 wt.%) fully stabilizes martensite phase of steel (Fig. 3).

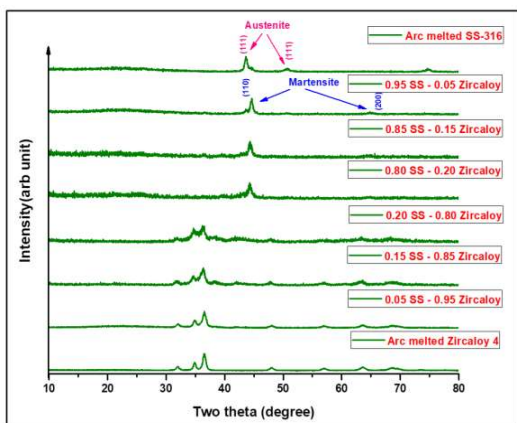


Figure 3. XRD patterns of melt-solidified Zircaloy-SS316 alloys

On the other side, upon gradual incorporation of SS-316 (up to 20 wt.%), zircaloy-rich alloys retained major matrix phase (HCP) along with systematically increasing structural disorder/strain.

Zr-Fe binary phase diagram shows that Zr has very little solubility in Fe and addition of zirconium facilitates the formation of Laves phases such as  $ZrFe_2$ . XRD results obtained by us using lab X-ray source didn't show signature of Laves phase. We therefore attribute the martensite phase stabilization (upon zircaloy incorporation) to accelerated cooling of molten alloys as zircaloy (melting point ~ 1850°C) solidifies prior to steel (melting point ~1400°C) and facilitates overall cooling due to higher thermal conductivity of zircaloy as compared to steel. Further investigations are underway to deeply probe the genesis of martensite phase stabilization.

Fig. 4 shows SEM micrographs (both SE & BSE mode) and EDS spectra recorded on distinct phases observed on polished surface of zircaloy-rich alloy (30% SS 316 – 70% Zircaloy 4). Composite morphology with randomly distributed dark phase confirmed segregation of steel-rich region in Zr-rich matrix. Further studies are aimed at identification of exact lattice form of these dispersed phases in zircaloy-rich alloys.

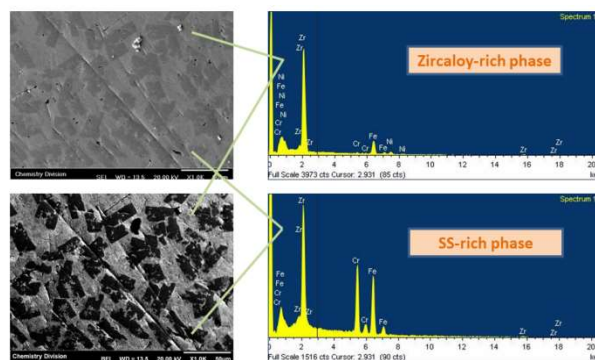


Figure 4. SE & BSE images of zircaloy-steel alloy (30% SS 316-70% Zircaloy) by SEM and elemental analysis

### Conclusion:

Incorporation of zircaloy-4 into stainless steel facilitates stabilization of martensite (BCT) phase of steel in melt-solidified alloys. No such phase transformation is observed when steel is gradually added in zircaloy matrix. Zircaloy-induced acceleration in solidification process is attributed to be the reason for martensite phase stabilization. Zircaloy-rich alloys (candidate compositions for hull management) show composite phase morphology with randomly dispersed steel-rich phases in zirconium-rich matrix. These results provide important data on phase behavior of melt-solidified alloys, which would be useful for development of suitable matrices for hull management application.

### References:

1. R. Krishnan, M. K. Asundi, *Proc. Indian Acad. Sci. (Engg. Sci.)*, 4 (1981) 41-56.
2. G. Sanyal, M. K. Samal, *Int. J. Fracture*, 173 (2012) 175-188.
3. J. E. Birkett, M.J. Carrott, O.D. Fox, C.J. Jones, C.J. Maher, C.V. Roubé, R.J. Taylor, D.A. Woodhead, *CHIMIA Int. J. Chem.*, 59 (2005) 898-904.
4. N. Das, P. Sengupta, S. Roychowdhury, G. Sharma, P.S. Gawde, A. Arya, V. Kain, U.D. Kulkarni, J.K. Chakravarty, G.K. Dey, *J. Nucl. Mater.*, 420 (2012) 559-574.

## Calorimetry and Dilatometry Studies of Tempering of a Cr-Mo-V Reactor Pressure Vessel Steel

K.V. Ravikanth<sup>a,b,\*</sup>, Amit Verma<sup>a,b</sup> and J. B. Singh<sup>a,b</sup>

<sup>a</sup>Mechanical Metallurgy Division, Materials Group, BARC

<sup>b</sup>Homi Bhabha National Institute, Mumbai.

\* Email: kanthkvr@barc.gov.in, Phone no: 022-25592358

### Abstract

Tempering behaviour of a Cr-Mo-V reactor pressure vessel steel, in two different microstructural conditions (Q1-martensite & Q2-bainite), was compared and analysed using calorimetry and dilatometry. Isochronal tempering up to 400 °C in a DSC in both normal mode and temperature modulated mode revealed presence of an exothermic peak in both Q1 and Q2 samples in the 250-380 °C temperature range. The normalized enthalpy was found to be much higher in the Q2 sample than in the Q1 sample. The exothermic peak in the Q1 sample corresponded to precipitation of cementite, whereas decomposition of retained austenite and cementite precipitation together contributed to higher heat release in the Q2 sample. Activation energies of the reactions were in the range of 170-190 kJ/mol.

**Introduction:** Low alloy Cr-Mo-V steels, due to their excellent mechanical properties and superior weldability, are one of the main candidate materials for thick structures such as reactor pressure vessels. Conventional heat treatment of these steels involves austenitization, quenching and tempering. Microstructure of the steel is sensitive to rate of cooling to room temperature post austenitization. Within the practically observed cooling rates, the microstructure after quenching can vary from fully bainitic (at low rates) to fully martensitic (at high rates). Bainite differs from martensite in that the former may contain significant fraction of retained austenite ( $\gamma_R$ ), which is stabilized by solute partitioning during the austenite to bainite transformation [1].

Tempering process of Cr-Mo-V steels can be divided in to six stages: stage 1 and 2 consists of segregation of carbon atoms to lattice defects and formation of clusters of carbon atoms below 80 °C; stage 3 involves precipitation of a transition carbide ( $\epsilon$ ,  $\eta$ ) between 80-180 °C; stage 4 is transformation of retained austenite to ferrite ( $\alpha$ ) and cementite ( $\theta$ ) between 200-350 °C; stage 5 convert transition carbide into cementite between 250-500 °C; stage 6 dissolves cementite particles and forms more stable alloy carbides between 450-700 °C. Though, stages 1 and 2 may not be apparent in low carbon steels, stages 4 and 5 are difficult to delineate using Differential Scanning Calorimeter (DSC) because of exothermic nature of both reactions and significant overlapping temperature range of both reactions. On the other side, dilatometry appears more suitable technique to delineate stages 4 from 5 owing to sample expansion in the former and contraction in the latter case [2].

In this study, a low alloy Cr-Mo-V steel in two different microstructural conditions (with and without retained austenite) was subjected to isochronal tempering in a dilatometer and a DSC, in an attempt to delineate the tempering stages corresponding to the decomposition of retained austenite and the precipitation of cementite and assess their kinetic parameters.

**Experimental:** The chemical composition of the steel investigated in this study is given in the Table 1. The steel was cooled after austenitization at 950 °C for 1h at two different rates namely, water quenching (Q1) and 10 °C/min (Q2) to room temperature. The details of heat treatment cycles and the equipment used can be found elsewhere [3]. One set of Q2

samples were subsequently quenched in liquid nitrogen to convert retained austenite ( $\gamma_R$ ) to martensite. These samples are designated as Q2-LNQ. Cylindrical specimens (10 mm in length and 4 mm in diameter) of Q1, Q2 and Q2-LNQ were isochronally tempered in a BHR DIL805A dilatometer up to 500 °C at 5 °C/min under a vacuum of  $5 \times 10^{-4}$  mbar. For the tempering treatments in DSC (Mettler Toledo), discs (1mm thick and 4 mm dia) were cut from dilatometer specimens. Isochronal tempering treatments of Q1, Q2 and Q2-LNQ specimens were carried out up to 400 °C at heating rates of 5, 10, 20 and 30 °C/min under dynamic argon atmosphere (flow rate of 30 ml/min). The reference crucible was left empty. After the first run, the system was cooled to room temperature with a cooling rate of -30 °C/min and a second cycle was carried out. Temperature modulated DSC (TOPEM<sup>®</sup>) of the samples was also carried out up to 400 °C at a heating rate of 2 °C/min.

**Results and discussion:** The cooling rates in the present study were chosen to ensure formation of martensite in Q1 and bainite in Q2, as per the experimental continuous cooling transformation (CCT) diagram of the studied steel [3]. XRD spectra of the two samples, shown in Fig.1, confirmed that the microstructure is fully martensitic in Q1, whereas Q2 contained

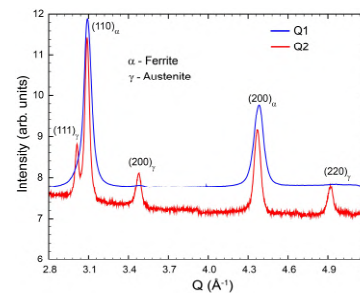


Fig. 1. Plot compares XRD spectra of samples corresponding to Q1 state (i.e. water quenched) with Q2 state (i.e. 10 °C/min)

bainite along with a significant amount of retained austenite (~10 %). Compared to martensite, bainite forms at higher temperatures, which facilitate partitioning of carbon to the parent austenite during the transformation, thereby stabilizing the austenite phase

down to room temperature. Though retained austenite is also reported to be present along with martensite, its fraction is insignificant in low alloy low carbon steels. Retained austenite is a metastable phase and transforms to a mixture of ferrite and carbide phases during tempering. Such a transformation can be unambiguously identified using a dilatometer, as the sample undergoes an expansion due to higher molar volume of ferrite than austenite. On the other hand, tempering of martensite essentially involves precipitation of carbides, leading to a contraction of the sample. Fig.2 shows the length change

Table 1. Chemical composition of the steel (wt.%)

Fe	Cr	Mn	Mo	Nb	Ni	Ti	V	C
Bal.	2.75	0.42	0.61	0.02	0.67	0.02	0.24	0.17

curves and their slopes as a function of temperature for the Q1 and Q2 samples during isochronal tempering at 5 °C/min up to 500 °C. It is evident that Q1 exhibited contraction in 225-325 °C range that corresponded to the precipitation of cementite, while Q2 exhibited expansion in 250-375 °C range, corresponding to the two overlapping reactions, namely, decomposition of retained austenite and precipitation of cementite. Fig. 2 also shows dilatation data of the Q2 sample after liquid nitrogen quenching (Q2-LNQ). This sample also exhibited expansion during heating similar to the Q2 sample.

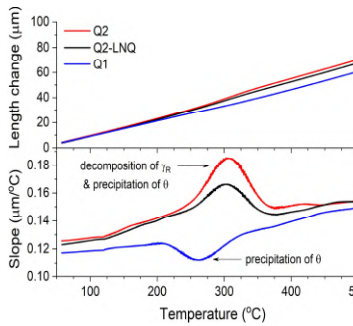


Fig. 2. Length change and its derivative during isochronal tempering of the samples

However, the degree of expansion is lesser, implying that the amount of retained austenite in the Q2 sample reduced after the liquid nitrogen quenching. Previously, many studies have reported the conversion of retained austenite to martensite following a liquid nitrogen quench [2,4]. Many of those studies claim almost complete conversion of retained austenite to martensite by liquid nitrogen quenching, however, only partial conversion was observed in the present study. Higher stability of retained austenite in the present study could be attributed to its high carbon content, fine size and microstructural constraints.

Tempering reactions studied using a DSC can provide valuable information of the thermal effects like enthalpy and specific heat changes during tempering. However, in order to ascertain the underlying reactions responsible for observed thermal effects, comparing the DSC data with dilatometer data would be very helpful.

Fig. 3 shows the DSC and dilatometer data of the Q2 sample during isochronal tempering at 5 °C/min up to 400 °C. The DSC curve shows an exothermic peak at 310 °C and the slope of the dilatation curve shows a positive deviation at the same temperature. Both the data together confirm that the exothermic peak is due to the two overlapping reactions: (i) decomposition of retained austenite (stage-4) and (ii) precipitation of cementite (stage-5), which could not be completely delineated using either of the techniques.

The non-reversible heat flow during isochronal tempering of the Q1, Q2 and Q2-LNQ samples up to 400 °C, measured using temperature-modulated (TOPEM) DSC measurements, is shown in Fig.4. The area under the peak of the DSC curve of each sample in the 250-400 °C range denotes the enthalpy of the underlying stage-4 and stage-5 reactions. Among the three samples, highest normalized enthalpy (2.81 J/g) was observed

in the Q2 sample as it contained the highest amount of retained austenite. Q2-LNQ sample showed slightly lower enthalpy (2.14 J/g), as its retained austenite fraction was reduced due to liquid nitrogen quenching. The lowest enthalpy (1.13 J/g) was exhibited by the Q1 sample, which did not contain any detectable amount of retained austenite. Therefore, the measure enthalpy in the case of Q1 sample corresponds to precipitation of cementite alone. Therefore, it can be inferred that the enthalpy of cementite precipitation in this steel is ~1.2 J/g, whereas the enthalpy of combined stage-4 and stage-5 is higher (~2.8 J/g) for a retained austenite volume fraction of 10%.

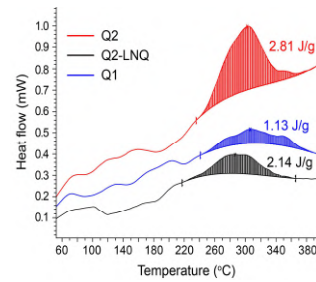


Fig. 4. Non-reversible heat flow during isochronal tempering, measured using TOPEM analysis

The activation energies of the tempering reactions observed in Q1 and Q2 samples were calculated using Kissinger analysis of the DSC data obtained at different heating rates using the peak transformation temperatures ( $T_p$ ). The activation energy of the cementite precipitation reaction in Q1 sample was found to be ~188 kJ/mol, which lies between pipe diffusion of iron (152 kJ/mol) and the volume diffusion of iron (251 kJ/mol) [2]. This suggests that the pipe diffusion of iron possibly controls the cementite precipitation in the studied steel. The activation energy of the overlapping reactions in Q2 sample was ~175 kJ/mol, which agrees well with the activation energy of carbon diffusion in austenite, suggesting that carbon diffusion in austenite is the rate-determining step for the decomposition of retained austenite.

**Conclusions:** It was concluded that a combined approach of DSC and dilatometer analysis is necessary for thermo-kinetics analysis of the tempering of a RPV in order to establish heat of reactions with overlapping thermal events. For instance, exothermic peak corresponds to cementite formation in the fully martensitic microstructure, while it includes heat effect due to simultaneous decomposition of retained austenite and cementite formation in a bainitic microstructure. The enthalpy of the cementite precipitation in Q1 is around 1.13 J/g, whereas the combined enthalpy due to decomposition of retained austenite and cementite formation in Q2 is around 2.81 J/g. Kissinger analysis of the DSC data showed that the activation energies of cementite precipitation and retained austenite decomposition are 188 kJ/mol and 177 kJ/mol respectively.

**References**

1. H.K.D.H. Bhadeshia, R.W.K. Honeycombe, *Steels: Microstructure and Properties*, 3rd edition, **2006**.
2. Morra, P. & Bottger, AJ & Mittemeijer, E, *Journal of Thermal Analysis and Calorimetry*, 64 (2001) 905.
3. K.V. Ravikanth, Amit Verma, J.B. Singh, B. Vishwanadh, S.K. Rai, Malvika Karri, *Journal of Nuclear Materials*, 602 (2024).
4. S. Primig, H. Leitner, *Thermochimica Acta*, 526 (2011).

## Thermal and Surface Area Analysis of Cesium and Strontium Sorbed Bentonite Clays

Bhupesh Kalekar\*, Harshala Parab and Naina Rajee

Analytical Chemistry Division, Bhabha Atomic Research Centre, Trombay, Mumbai – 400085, India

\* Corresponding author: e-mail - [bhupkal@barc.gov.in](mailto:bhupkal@barc.gov.in); contact no.: 25597031**Abstract**

Simultaneous Thermogravimetry (TG) - Evolved Gas Analysis (EGA) as well as Surface Area Analysis was performed for metal ions ( $\text{Cs}^+$  and  $\text{Sr}^{2+}$ ) sorbed bentonite clays. The results of thermal analysis indicate higher accumulation of physisorbed water on strontium sorbed clay than cesium sorbed clay. Magnesium and calcium carbonates are observed in both the clays. Higher surface area for cesium surface modified clay than strontium surface modified clay is attributed to low surface charge and low polarisation coefficient of cesium compared to strontium in the diffused ionic atmosphere during the sorption process.

High surface area, porous structure, high ion exchange capacities and swelling abilities are the key features of bentonite clays. These clays are widely used in many industrial processes such as the suspending medium in paints and pharmaceuticals; absorbents in oil sorption industries and cosmetic sector. Bentonite clay contains montmorillonite as the principal component with smaller quantities of kaolinite and quartz. Bentonite clays are considered potential barriers for radioactive waste disposal. The ability of bentonites to absorb radionuclides depends on their mineralogical composition, surface area, and pore structure. The radionuclide sorption on bentonites is also affected by the chemical composition and properties of solutions in contact with bentonite. Bentonite clay contains calcium, and sodium and majorly magnesium aluminosilicate with a chemical composition of  $(\text{Ca},\text{Na})_{0.3}(\text{Al},\text{Mg})_2\text{Si}_4\text{O}_{10}(\text{OH})_2 \cdot n\text{H}_2\text{O}$ . Herein, the thermal and surface area analysis of cesium and strontium ions ( $\text{Cs}^+$  and  $\text{Sr}^{2+}$ ) sorbed bentonite clays have been performed.

Bentonite clay was accurately weighed (1gram) and equilibrated with solutions (20 mL of 10000 ppm) of cesium and strontium ions for three days. Experiments were performed in triplicates by adopting batch mode strategy. The metal ions sorbed clays were then phase separated and air dried for thermal characterisation at high temperatures. The residual solution was collected and analysed for remaining contents of cesium and strontium. The residues were analysed qualitatively by EDXRF. The residues ensured sorption of cesium and strontium ions from solutions. Simultaneous TG-EGA measurements were carried out on cesium and strontium ions sorbed clays using Netzsch thermal analyser (Model No.: STA 409 PC Luxx) coupled to Bruker FTIR system (Model No.: Tensor 27) via a heated Teflon capillary (1 m long, 2 mm i.d.) in high purity nitrogen atmosphere with a flow rate of  $120 \text{ mL min}^{-1}$ . Specimen holders were made up of recrystallized alumina. Heating rate of  $10^\circ\text{C min}$  was maintained in all the measurements in the temperature range of 30 to  $1000^\circ\text{C}$ . Surface area analysis initiated with pre-treatment of bentonite, cesium sorbed and strontium sorbed bentonite clays. These specimens were independently heated at  $150^\circ\text{C}$  for four hours in the mixture of nitrogen and helium gases. Single point BET method was carried out at relative pressure ratio of 0.3 of

mixture of nitrogen and helium gases. Adsorption and desorption peaks of nitrogen were recorded at liquid nitrogen temperature and room temperatures, respectively, using thermal conductivity detector. Volume of nitrogen gas was utilized for the surface area calculation using modified single point BET equation.

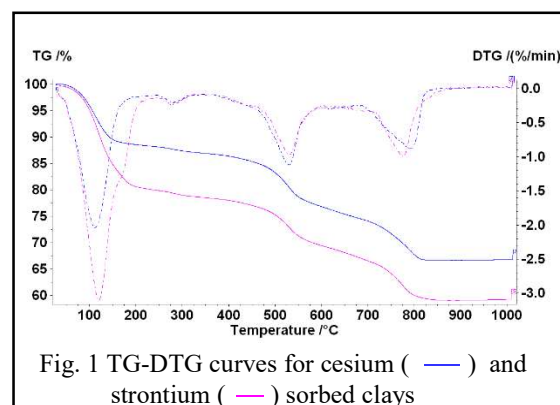


Fig. 1 TG-DTG curves for cesium ( — ) and strontium ( — ) sorbed clays

TG - DTG (Derivative TG) curves for cesium sorbed and strontium sorbed clays given in Fig. 1 indicate that water molecules are removed sequentially according to its binding strength with the clay surface. The entire physisorbed water adhered to the surface as well condensed in the pores of clay particles is removed above the room temperature. Fig. 2 shows evolution of water above room temperature from cesium sorbed clay. The water molecules get organized with interlayer cations, upon removal of bulk interlayer water. The hydration enthalpy of each cation plays a crucial role during dehydration of well organised water molecules. The higher the absolute value of the cation hydration enthalpy, the stronger the interaction between water molecules and the interlayer cation. It means, the greater the energy is required to remove any remaining strongly bound water. The polyvalent cations possess higher hydration enthalpy [1], hence, DTG curve show a main dehydration peak with additional shoulder extended up to  $220^\circ\text{C}$  for strontium sorbed clay, whereas, single DTG peak for cesium sorbed clay is completed by  $180^\circ\text{C}$ . The lower mass

loss of 8% is noticed for cesium ions sorbed clay than higher mass loss of 20% for strontium ions sorbed clay. These observations suggest more accumulation of adsorbed water on strontium loaded clay than cesium loaded clay.

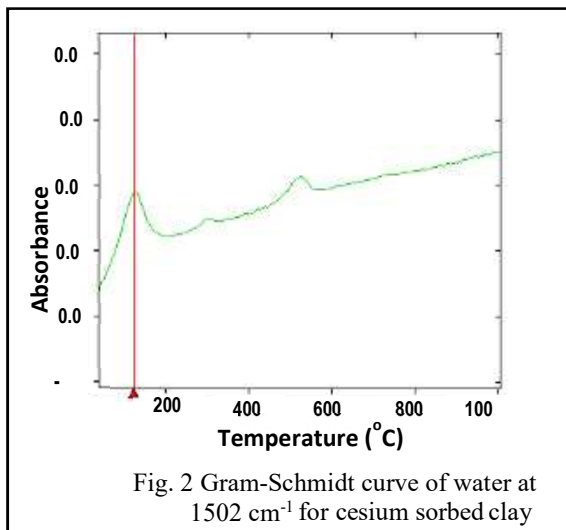


Fig. 2 Gram-Schmidt curve of water at 1502 cm<sup>-1</sup> for cesium sorbed clay

The dehydration of samples is continued from 220 up to 420°C. The accumulation of water vapours can occur during dehydration of clay around sample in the furnace chamber. The water vapours recombine with sample and can cause further hydroxylation of  $(Ca,Na)_{0.3}(Al,Mg)_2Si_4O_{10}(OH)_2$ . The mass loss for both metal ions sorbed clays can occur due to dehydroxylation of in-situ formed hydroxyl groups in the temperature range of 220 - 420°C. Additionally, the small evolution of CO<sub>2</sub> evidenced from EGA curve probably due to decomposition of organic carbon present in the clay. The major mass loss and the corresponding evolution of water in the Figs. 1 and 2 associated with temperature range of 420 - 580°C are mainly attributed to removal of structural water from cesium / strontium loaded clays. The evolution of water in very minute quantities is noticed from Fig. 2 corresponding to relatively higher mass loss in the temperature range of 580-825°C on TG-DTG curves. Additional mass loss is contributed by CO<sub>2</sub> gas evolution in the temperature ranges of 630-740 and 740-825°C. The temperature ranges confirm the presence of magnesium and calcium carbonates in the clays [2]. Both, cesium/strontium loaded clays exhibit identical thermal behaviour above 220°C. The only difference lies in the extent of physiosorbed water which is more in the case of strontium sorbed clay.

**Table 1. Surface area analysis of bentonite clay obtained by single point BET method**

Matrix	Surface area (m <sup>2</sup> g <sup>-1</sup> )
Raw bentonite clay	24
Cs sorbed clay	48
Sr sorbed clay	32

Table 1 shows that surface area of bentonite clay increases with loading of alkali (Cs<sup>+</sup>) or alkaline earth (Sr<sup>++</sup>) metal ions on the surface of bentonite clay. Cesium and strontium sorbed clays show surface area of 48 and 32 m<sup>2</sup>g<sup>-1</sup>, respectively, indicating high adsorption capacity of cesium than strontium. During sorption, equivalent exchange between

cations from the solutions of diffuse ionic atmosphere and the cations of hydrated clay particles takes place. The sorption happens mainly at outer shell of the double electric layer. The enhanced adsorption of cesium by clays in comparison with strontium is attributed to the high probability of the fixation of cesium ions in a diffuse ion atmosphere of clay particles. The probability is decided by ratio of charge of ion to the area of outer ion surface. High adsorption of cesium over strontium lies in its low surface charge and low polarisation coefficient of cesium than strontium in the diffused ionic atmosphere [3].

**Acknowledgements:**

The authors thanks Dr. C. N. Patra, Head, ACD, BARC for constant encouragement during the work.

**References:**

[1] Smith D. W., J. Chem. Educ. 54 (1977)540.  
 [2] S. Gunasekaran and G. Anbalagan, Bull. Mater. Sci., 30(2007)339.  
 [3] Y. Zabulonov V. Kadoshnikov H. Zadvernyuk T. Melnychenk and V Molochk, Adsorption, 27 (2021) 41.

## Studies on Natural Fluorapatite: Radiation and Thermal Effects

Darshana K. Ghonge<sup>a</sup>, Naina Raje<sup>\*a</sup>, Rumu Halder Banerjee<sup>b</sup> and Pranesh Sengupta<sup>b</sup>

<sup>a</sup>Analytical Chemistry Division, Bhabha Atomic Research Centre, Mumbai – 400094, India

<sup>b</sup>Material Science Division, Bhabha Atomic Research Centre, Mumbai – 400094, India

\* Email: [nraje@barc.gov.in](mailto:nraje@barc.gov.in), Ph. No. :022 69293291

### Abstract

Fluorapatites are potential candidates for hosting nuclear waste from molten salt reactors. To evaluate their radiation and thermal stability for long-term performance, a natural analogue study was conducted. Naturally occurring fluorapatites with carbonate substitutions were irradiated with 10 MeV electron beam radiation at doses of 1MGy and 20 MGy. Analyses using TG-DTA-EGA, ATR-FTIR, X-ray diffraction, SEM and EDS showed no signs of structural degradation upto 700 °C. Overall, the study confirmed that fluorapatite exhibits strong structural stability against electron beam irradiation up to 20 MGy.

Fluorapatite materials ( $M_{10}(PO_4)_6X_2$ , where M = Ca, Sr, Ba, etc., and X = OH, Cl, F, etc.) have emerged as promising alternatives for immobilizing high-level radioactive waste from MSR. The apatite matrix is advantageous due to its ability to accommodate multiple cationic and anionic substitutions, resulting in high chemical durability and radiation stability. Furthermore, apatite is the thermodynamically stable form of calcium phosphate and hence, the mineral is found abundantly on the earth's crust. Fluorapatite ( $[Ca_5(PO_4)_3F;FAp]$ ) is preferred over chloro- or hydroxyapatite due to its lower water solubility, greater strength, and improved thermal stability [1].

In deep geological repositories, the conditions surrounding waste-forms are vital for their long-term stability and safety. To evaluate the suitability of materials for nuclear waste management, it is crucial to establish their structure-property correlations under various types of ionizing and non-ionizing radiation, as well as their performance over geological timescales. Natural analogues are an established research avenue in radioactive waste management, offering valuable insights into the long-term performance of nuclear waste-forms.

A review of the literature indicates that most research tends to focus on radiation effects in synthetic fluorapatite compounds [2] or gem-quality natural fluorapatite crystals but owing to the benefits of using natural analogues, we have carried out the studies on natural fluorapatite samples. Present work have been carried out to understand the effect of radiation and temperature on the stability of natural fluorapatite, received from Beldih, West Bengal. Different techniques, like TG-DTA-EGA, ATR - FTIR, X-Ray diffraction, SEM - EDS were applied to characterize the fluorapatite. In order to understand the radiation behaviour, the fluorapatite samples were irradiated with 10 MeV electron beam (EB) at the dose rate of 1MGy per hour in ambient condition. Fluorapatite samples with 1 MGy and 20 MGy dose were analyzed using above said techniques, for radiation and temperature effect studies on their structural stability, surface morphology etc. and results are being discussed here.

**Experimental Details:** These are as below-

**Sample Collection:** In the present investigation, naturally occurring fluorapatites were collected from Beldih, West Bengal. One variety of the fluorapatites were collected. The specimens were then powdered for further characterization.

**Compositional and Phase Analyses:** Compositional and phase analyses have been carried out using XRD, SEM-EDS and EDXRF measurement techniques. X - ray diffraction (XRD) measurements were performed on powdered specimens on 600W Rigaku MiniFlex Benchtop Powder XRD instrument diffractometer employing Cu  $K_\alpha$  (1.5406 Å) radiation under ambient conditions in the scattering angle range ( $2\theta$ ) 20–60 deg, keeping a scan rate of 1 deg/min.

The microstructure of the fluorapatites was examined using a 5–20 keV focused electron beam in a Field Emission - Scanning Electron Microscope (FE-SEM; Carl Zeiss Auriga Cross Beam). Energy dispersive X-ray spectroscopy (EDS) was used for the qualitative elemental analyses. Energy dispersive X-ray fluorescence (EDXRF) of the fluorapatite samples were done in Bruker EDXRF instrument under both air and vacuum environment keeping voltages as 30 kV and 5 kV, respectively.

**Electron Irradiation:** The powdered specimens were placed in nickel crucibles and were irradiated with 10 MeV electron beam (EB) in ambient conditions for 20 MGy dose at the dose rate of 1 MGy/h at electron beam centre Kharghar.

**ATR – FTIR measurements:** FTIR spectrometer (Model No.: Bruker Tensor 27), equipped with PIKE MIRacle attenuated total reflection (ATR) accessory having a single reflection diamond ATR crystal, KBr beam splitter and DLaTGS (deuterated L-alanine-doped triglycene sulfate) detector was used to record FTIR spectra of all the samples. Powder samples were spread over the ATR crystal in the form of thin film, and maximum pressure was applied using the slip-clutch mechanism. All spectra were collected at 4  $cm^{-1}$  spectral resolution over the range of 400–4000  $cm^{-1}$ , using 1minute collection time for sample and background each. FTIR data analysis was done using Opus (version 6.0) software from Bruker.

**TG – DTA – EGA measurements:** Simultaneous TG – DTA measurements have been carried out using Netzsch Thermo-balance (Model No.: STA 409 PC Luxx system. Pt vs. Pt-10% Rh thermocouples were used as temperature and differential temperature sensors for all the experiments involving TG – DTA analysis. Accurately weighed samples were heated in air/inert atmosphere to the desired temperature at the heating rate of 10°C  $min^{-1}$ . High purity nitrogen was used as purge gas.

EGA measurements have been carried out using FTIR system for the identification of IR absorbance in the mid IR region (400 - 4000  $cm^{-1}$ ). It is equipped with liquid nitrogen cooled MCT detector and low-volume gas cell (8.7 mL) with a 123 mm path length and KBr windows. The adapter head of thermo-balance, transferline and sample cell were heated to a constant temperature of 200°C to avoid condensation of low volatile compounds. FTIR data analysis was done using Opus (version 6.0) software from Bruker.

**Results and Discussion:** It can be seen from Figs 1A, 1B and 1C that unirradiated and irradiated fluorapatite decomposes endothermically in two steps with an overall mass loss of around 45 – 48% in air/inert atmosphere, in the temperature region of RT – 900°C. The first step often involves the loss of fluoride ions ( $F^-$ ) and water, if present, and in the second step, the remaining structure/associated minerals break down, depending on the measurement temperature.

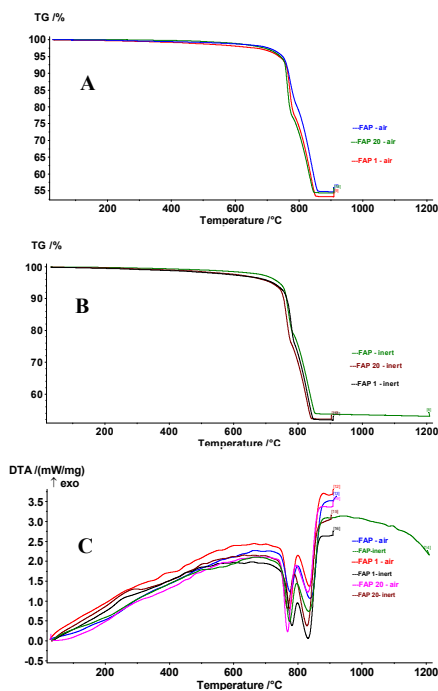


Fig. 1: A-TG-air; B-TG-inert; C-DTA – air / inert

shape of TG curves that radiation dose affects the decomposition behavior and at higher dose (20MGy), the decomposition reaction gets preponed to 686°C and rate of decomposition becomes faster which is in concurrence with DTA results too. It should be noted that mass loss is around 1-2% higher in inert atmosphere than that of in air which suggests that the presence of oxygen can affect the thermal stability of the mineral phases due to probable oxidation reaction, leading to stable oxides in air.

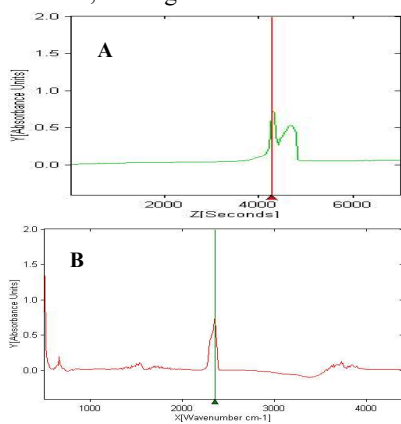


Fig. 2: EGA - unirradiated /irradiated natural fluorapatite in air/inert atmosphere; A - Gram Schmidt Curve B - Extracted IR Spectra

evolution through H-O-H bending and stretching vibrations at 1220 - 2095 and 3375 - 4000  $\text{cm}^{-1}$ , respectively [3]. Also, the presence of  $\text{CO}_2$  evolution was seen through O-C-O bending vibrations at 660  $\text{cm}^{-1}$  and asymmetric stretching vibrations at 2361  $\text{cm}^{-1}$ . This suggests that natural fluorapatite should have some carbonate bearing minerals which are decomposing to give  $\text{CO}_2$  evolution during second step observed at TG/DTA curves. SEM analysis showed the presence of crater like indentations as the radiation dose was increased to 20MGy, which is in concurrence to the report available in literature stating that 20MGy is the initiation dose to start the radiation damage in fluorapatite matrix [4]. EDS spectra of natural fluorapatite chunk clearly showed the presence of Fe, Ca, Mg and traces of Mn. Being the natural material, it is not homogeneous and so at some location, it is Ca and Mg rich while at some location it is Fe rich.

It can be seen from Figs 1A & B that fluorapatite matrix is quite rugged matrix as even after getting 20MGy radiation dose, its stability is not affected and remains stable at least upto 700°C in air/inert environment. In the present case, the experiments have been performed to 900°C, hence the probability of calcium phosphate decomposition is least expected, and so, the second step may be corresponding to the decomposition of associated minerals with natural fluorapatite. Also, it can be seen from the

In order to understand the comprehensive picture, simultaneously evolved gas analysis was carried out, where traces of water evolution at lower temperature and  $\text{CO}_2$  evolution above 715°C was observed in all the cases, irrespective of the measurement environment. Fig. 2 shows the representative of the EGA curves where Gram Schmidt curve shows the evolution of gases and the extracted IR spectra shows the water

This observation explains the anomaly of having more mass loss in inert atmosphere as compared to that in air atmosphere during TG measurements. It is possible siderite ( $\text{FeCO}_3$ ) is entrapped in fluorapatite matrix and decomposes at higher temperature of 716°C and the resultant FeO in the presence of oxygen provides stable oxides, leading to less mass loss in air. Presence of dolomite ( $\text{Ca,Mg}(\text{CO}_3)_2$ ) mineral is also being predicted on the basis of EDS and TG-DTA-EGA results. It has been reported that dolomites are composed of dolomite and variable amounts of calcite. Naturally occurring dolomite is a double carbonate of calcium and magnesium with chemical composition as  $\text{CaMg}(\text{CO}_3)_2$  which is typically sedimentary rock associated with calcite, widely scattered in nature. In geological formations where fluorapatite is found, it is common for various minerals, including carbonates like dolomite, to coexist. Also, it has been reported [8] that depending on the experimental conditions, the thermal decomposition can proceed in one endothermic step in air/nitrogen atmosphere between 973 and 1,023 K through  $\text{CO}_2$  evolution. In the present studies, we can see the second  $\text{CO}_2$  evolution at 1059K, at a higher temperature than the reported value. This may be due to the dolomite entrapped inside the natural fluorapatite sample. FTIR analysis was carried out for unirradiated and irradiated natural fluorapatite samples to understand the effect of radiation. FAP is having peaks at 1024 and 667  $\text{cm}^{-1}$ , corresponding to ( $\text{PO}_4^{3-}$ ) and (F) group respectively which are missing in the irradiated FAP samples. It is possible to have defect formations during irradiation which may reduce the intensity of respective vibrations. The shift in the XRD peak positions of 20MGy irradiated fluorapatite sample has been attributed to the lattice expansion caused by irradiation track volume increase. This may be due to the possibility of change in material orientation after the defect formation. These results are in accordance with FTIR results. However, unlike in the case of ion irradiation, no amorphous fraction was observed in the present study. The observed XRD results suggest that the fluorapatites exhibit good structural stability under electron irradiation.

**Conclusion:** Thermal studies along with EDS studies, suggested that the collected fluorapatite samples are associated with siderite and dolomite. It should be noted that in the case of natural material applications, sampling is a crucial component and its homogeneity testing is must before being put for any industrial application, especially for nuclear industry. SEM analysis showed the presence of crater like indentations as the radiation dose was increased to 20MGy. Thermal stability was found to be upto 700 °C for unirradiated and irradiated fluorapatite samples (1MGy) which does not reduce much (686 °C) at higher irradiation dose (20MGy). FTIR and XRD studies suggests some defect formations in the matrix at 20MGy dose. Overall, present studies suggest that the fluorapatites exhibit good structural stability under electron irradiation upto 20MGy.

#### References:

1. P. Das, N. Pathak, P. Modak, B. Modak, J. Hazard. Mater. 411 (2021) 125025.
2. P. Das, B.G. Vats, P. Samui, S. Kesari, M. Shafeeq, S.C. Parida, S. Dash, Chem. Select 6 (2021) e202103990.
3. Naina Raje, Bhupesh B. Kalekar and Darshana Ghonge, Journal of Analytical and Applied Pyrolysis, DOI: 10.1016/j.jaap.2017.12.012
4. Rumu H. Banerjee, Rajath Alexander, Nishant Chaudhary, Sanjoy Sanyal and Pranesh Sengupta, Journal of Nuclear Materials 599 (2024) 155199.

**Acknowledgements:** Authors sincerely thanks to Dr. C. N. Patra, Head Analytical Chemistry Division and Dr. R. Tewari, Director, MSG for their continuous support.



## Structural, Thermal and Thermodynamic Study of Rare Earth Containing Natural CaF<sub>2</sub> for Dosimetric Applications

Athira KV Raj<sup>a,\*</sup>, Rumu H Banerjee<sup>a</sup>, Uttam Jain<sup>a</sup>, Abhishek Singh<sup>b</sup>, Bhusan Dhabekar<sup>b</sup>, Kulwant Singh<sup>a</sup> and Pranesh Sengupta<sup>a</sup>

<sup>a</sup>Materials Science Division, Bhabha Atomic Research Centre, Mumbai, India-400 085

<sup>b</sup>Radiation Protection and Advisory Division, Bhabha Atomic Research Centre, Mumbai-85

\*[athirakvr@barc.gov.in](mailto:athirakvr@barc.gov.in), Tel: 022-25592186

### Abstract

Natural calcium fluoride (CaF<sub>2</sub>) exhibits strong radiation-induced thermoluminescence (TL), making it a promising material for applications in environmental monitoring, thermoluminescent dosimetry and accidental dosimetry. Investigating radiation-induced defects in these crystals is crucial for understanding and enhancing their functional properties. In this study, a comprehensive analysis of the structural, thermal and thermodynamic properties of natural CaF<sub>2</sub> was conducted using spectroscopic techniques, including X-ray diffraction (XRD), X-ray Photoelectron Spectroscopy (XPS), Raman Spectroscopy and photoluminescence (PL). The enthalpy of sublimation was estimated to evaluate the thermodynamic stability of the material. Thermal analyses indicated that natural CaF<sub>2</sub> possesses high thermal stability, both before and after irradiation. TL measurements were employed to correlate the radiation response of CaF<sub>2</sub> with its luminescence properties. The findings demonstrate that natural CaF<sub>2</sub> exhibits significant potential for use in dosimetric applications due to its favorable thermal and luminescent characteristics.

### Introduction

Fluorite-based structures, particularly calcium fluoride (CaF<sub>2</sub>), are widely studied due to their relevance in applications such as ultraviolet (UV) windows, lasers, and dosimeters. CaF<sub>2</sub>, in both synthetic and natural forms, exhibits high optical transmittance across UV, visible, and infrared spectral ranges, making it suitable for optical and photonic applications. It is also employed in environmental monitoring and radiation detection due to its thermoluminescent properties [1-2]. Natural CaF<sub>2</sub> demonstrates significant radiation-induced thermoluminescence, indicating its potential as a UV-transparent dosimetric material. However, its use in optical systems is affected by the formation of radiation-induced defects, which influence material performance [3].

This study focuses on the characterization of naturally occurring yellow CaF<sub>2</sub> crystals collected from Ambadongar, Gujarat, utilizing multiple analytical techniques to evaluate their structural, thermal, thermodynamic and dosimetric properties for technological applications.

### Experimental Study

In this study, naturally occurring yellow CaF<sub>2</sub> crystals were collected from Ambadongar, Gujarat, and characterized using various techniques. Characterization of fluorites. The concentrations of various rare-earth elements in the coloured fluorites were determined by inductively coupled plasma optical emission spectrometry (ICP-OES) method. About 1 g of the specimen in powdered form was dissolved in a solution of HF and HNO<sub>3</sub> in a platinum crucible and analysed in ICP-OES along with the calibration standards (REEs, Ca and F). The procedure is in concordance with the optimised process as outlined by Rao et al [1]. The specimens were characterized using various techniques. XRD of samples was carried out in the two-theta range 10-80 deg at a scan speed of 1 deg/min. The vaporization behaviour of CaF<sub>2</sub> was investigated in the temperature range 1540-1640 K by Knudsen effusion mass spectrometry (KEMS). The measurements were carried out with an indigenously made Knudsen effusion mass spectrometer system (KEMS). The KEMS system consists of two chambers, one containing the Knudsen cell furnace assembly and the other compartment having the quadrupole mass spectrometer (QMS) chamber. The Knudsen cells made of molybdenum were used to hold the samples. The cell was provided with a lid having knife edged effusion orifices. In the QMS, the ions were generated by electron impact with energy of 20 eV. As mentioned above, a

metallic valve separated the ion source of QMS from the Knudsen cell chamber.

The measured ion intensities in QMS were converted into partial pressures by means of the standard mass spectrometric relation:

$$p_i = \frac{kT}{\sigma_i A_b^i} \sum_j I_{ij} \quad (1)$$

where  $T$  is the temperature;  $k$  is the general pressure calibration

constant;  $p_i$ ,  $\sigma_i$  and  $A_b^i$  are the partial pressure, the ionization cross section and isotopic abundance of species  $i$  respectively; and  $I_{ij}$  is the ion intensity of ion  $j$  originating from species  $i$ .

The partial pressures and thermodynamic activities of CaF<sub>2</sub> were evaluated directly from the measured ion intensities formed from the equilibrium vapor over the specimen surface.

In addition, the radiation response of the powder was investigated and correlated with the luminescence properties using thermoluminescence technique. Thermoluminescence measurements were recorded in the temperature range 50-450 deg at dose of 1700 mGy.

### Results and Discussions

XRD studies confirmed the cubic crystal structure of the fluorites, and the lattice parameter was determined using the Nelson Riley function. XRD patterns, presented in Fig. 1 show that the Bragg peak positions match well with those reported for CaF<sub>2</sub> and no additional peaks corresponding to any secondary phase were recorded. This confirms that the specimens of fluorites have cubic structure (space group:  $Fm\bar{3}m$ ) in concordance with the reported literature. However, depending on the mineral chemistry, the peak positions shift off the Bragg peak maxima to either higher or lower angles, including asymmetric nature of the peaks. The lattice constants were estimated from the extrapolation of the Nelson-Riley equation,  $F(\theta)$  defined as

$$F(\theta) = \frac{1}{2} \left( \frac{\cos^2 \theta}{\sin \theta} + \frac{\cos^2 \theta}{\theta} \right) \quad (2)$$

where  $\theta$  is the Bragg angle. The intercept of the plot between  $F(\theta)$  versus lattice parameter ( $a$ ) gives the lattice constant of the specimen. The phase stability however was maintained under natural radiation exposure and elemental substitutions. Mass spectrometric analyses reveal that the yellow fluorites contained higher Sr (~1000-1500 ppm) and higher Y contents (~700 ppm) in concordance with the available literature. The calculated lattice parameters for all the natural fluorites were found to be closer to the synthetic CaF<sub>2</sub> crystal 5.4575 Å (ICSD:

60-368). A comparison of ionic radii of  $\text{Ca}^{2+}$  (1.26 Å) in eightfold coordination with relevant cations in present case (as discussed later), e.g.,  $\text{Er}^{3+} = 1.14$  Å,  $\text{Y}^{3+} = 1.04$  Å suggests that the lattices get contracted after  $\text{Ca}^{2+}$  is substituted by smaller cations and subsequently there is a shift of the Bragg peak maxima to higher angles. On the other hand, substitution of a bivalent cation by a trivalent one, occasionally results in fluorine occupying interstitial positions. This results in the relaxation of the  $\text{CaF}_2$  lattice by  $\sim 7\%$  around the interstitial fluorine ions at the first nearest neighbour distances leading to an increase in the lattice parameter and volume. In addition, accommodation of  $\text{Sr}^{2+}$  (1.40 Å) in fluorite lattice increases its parameter. Photoluminescence emission spectra, recorded at a 230 nm excitation wavelength, showed a broad emission spectrum from 400 to 500 nm with peaks centered around 420, 440, and 485 nm, corresponding to F-centres bound to rare earth elements like  $\text{Er}^{3+}$ .

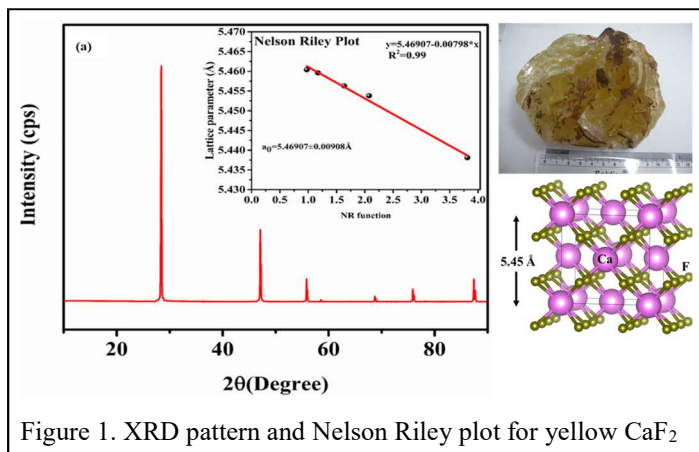


Figure 1. XRD pattern and Nelson Riley plot for yellow  $\text{CaF}_2$

The detected ions in mass spectrometer included *majorly*  $\text{Ca}^+$ . Vapour pressure of  $\text{CaF}_2$  in yellow sample was evaluated from ion intensity data and was found to be  $1.5 \times 10^{-5}$  atm at mean temperature of 1600 °C and activity of  $\text{CaF}_2$  was calculated and found to be 0.88 at 1600 °C temperature. Thermogravimetric studies carried out upto 700 °C shows the samples have good thermal stability before and after irradiation.

Additionally, the radiation response of the powder was investigated and correlated with its luminescence properties using the thermoluminescence technique. Natural yellow  $\text{CaF}_2$  showed promising results for dosimetric applications.

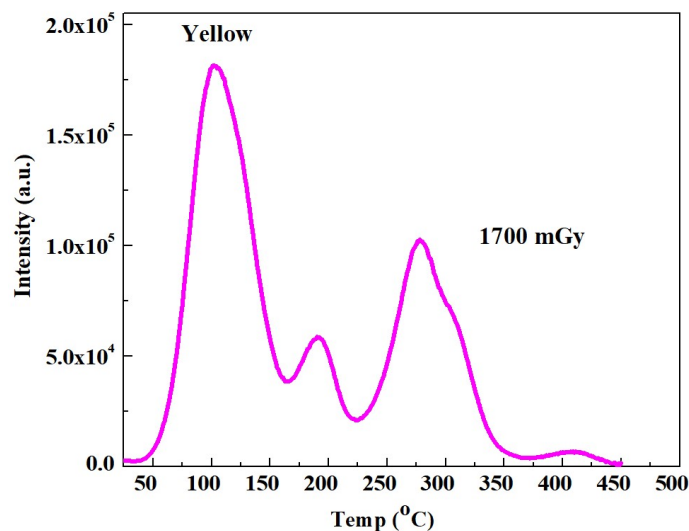


Figure 2. TL Glow curve

## Summary

Natural calcium fluoride ( $\text{CaF}_2$ ) demonstrates strong thermoluminescence (TL) under radiation, making it suitable for environmental monitoring and dosimetry. This study analyzes its structural, thermal, and thermodynamic properties using XRD, XPS, Raman spectroscopy, and photoluminescence. High thermal stability, both pre- and post-irradiation, was confirmed through thermal analysis. The enthalpy of sublimation highlights its thermodynamic stability, while TL measurements link its radiation response to luminescence properties, showcasing its potential for dosimetric applications.

## Acknowledgements

The study was carried out under the ongoing Department of Atomic Energy Project ‘Irradiation Induced Phase Transformations in Nuclear Materials’. The authors thankfully acknowledge the help provided by Ms. Shaniya in sample preparation and Dr. A. K. Debnath in XPS measurements. The authors are grateful to Dr. R. Tewari, Director, Materials Group, Dr. B.K. Sapra, Head, RP&AD for their keen interest in this study.

## References

1. Rumu H. B, Nimai P, Nandi P, Debnath A. K, Viladkar S, Sengupta P, Journal of Luminescence, 254 (2023) 119540.
2. Martina S, Andreas H, Joachim H, Christian R, Optical Materials, 62 (2016) 424.
3. Rumu H. B, Alexander R, Chaudhary N, Srivastava A. P, Debnath A. K, Sudarsan V, Sengupta P, Ceramics International, 49 (2023) 21324

## Thermal Stability Studies of Polyaniline -Halloysite Clay Composite

Bhupesh Kalekar\*, Harshala Parab, Naina Raje, Remya Devi P.S. and Sangita D. Kumar  
Analytical Chemistry Division, Bhabha Atomic Research Centre, Trombay, Mumbai – 400085, India

\* Corresponding author: e-mail - [bhupkal@barc.gov.in](mailto:bhupkal@barc.gov.in); contact no.: 25597031.

### Abstract

Polyaniline - Halloysite (Pani - HC) composite is synthesized and characterized. Thermal characteristics of Pani - HC composite is studied along with native halloysite clay. The results indicate independent decomposition of the constituents (Pani and halloysite clay) of the composite at elevated temperatures. Thermal behaviour of Pani - HC composite in nitrogen environment is found to vary from air environment owing to the leftover unburnt carbon.

Halloysite is a naturally occurring, biocompatible, nanosized clay mineral. It is aluminosilicate clay with 1:1 layered structure consisting of a tetrahedral silica layer and an octahedral alumina layer with a structural composition  $\text{Al}_2\text{Si}_2\text{O}_5(\text{OH})_4 \cdot n\text{H}_2\text{O}$  (containing 0 to 2 water molecules). Owing to its structural properties halloysite clay can be used in the form of different composites for various applications such as advanced ceramic material, fillers, sorbent, catalyst, coatings, tissue engineering drug delivery etc. Herein, a polymeric nanocomposite of halloysite clay with polyaniline has been synthesized by oxidative polymerization of aniline in acidic medium in presence of halloysite clay in a one pot reaction [1]. The successful synthesis of Pani on the surface of clay has been confirmed by FTIR characterization. The Pani - HC composite has been studied for its thermal stability at high temperatures.

Thermal measurements have been carried out using Netzsch Thermo-balance (Model No.: STA 409 PC Luxx) coupled to Bruker FTIR system (Model No.: Tensor 27) via a heated Teflon capillary (1 m long, 2 mm i.d.). Pt vs. Pt-10% Rh thermocouples were used as temperature and differential temperature sensors during all the thermo-analytical measurements. The mass loss in the temperature range of 30 - 200°C is attributed to the release of adsorbed water adhered on the surface of clay particles. The major mass loss event is observed in the temperature region of 450-730°C. The experimental mass loss of 13.3 % observed on TG curve is in

set temperature of 978°C. It indicates conversion of metahalloysite to a distinct alumina-rich phase and amorphous  $\text{SiO}_2$  [2].

Fig.2 shows the TG-DTA curves for Pani - HC composite in air as well as nitrogen atmospheres. Fig. 3 indicates IR spectra extracted from Gram Schmidt curve at 1502 and 2354  $\text{cm}^{-1}$  that are assigned for  $\text{H}_2\text{O}$  and  $\text{CO}_2$ , respectively, in the air atmosphere. The initial mass loss upon heating up to 150°C on TG curve in the air atmosphere is supported by the evolution of water in Fig. 3A1. It is associated with the loss of adsorbed water from the surface of Pani - HC composite. A very small mass loss observed in the temperature range of 150-250°C may be due to loss of HCl used for preparation of Pani - HC composite. The major mass loss for Pani - HC composite is indicated in the temperature region of 250 to 550°C.

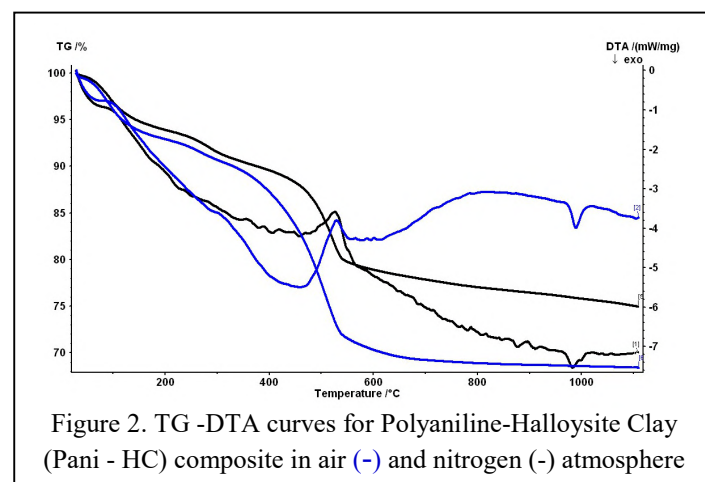


Figure 2. TG -DTA curves for Polyaniline-Halloysite Clay (Pani - HC) composite in air (-) and nitrogen (-) atmosphere

The  $\text{CO}_2$  gas evolution is seen from EGA curve indicating initiation of decomposition of Pani (Fig. 3B1). The second peak for water evolution is also noticed from Fig. 3A1 in the temperature range of the 450-650°C. The data suggest a mass loss step is combination of Pani decomposition and dehydroxylation of halloysite clay in the composite. Pani decomposition in the air atmosphere is exothermic in nature which can be seen on DTA curve of Pani-HC composite. DTA exhibits sum total of heat effects depending on the nature of decomposition reactions. It may be either exothermic / endothermic or sum total of both effects in the case of simultaneously occurring reactions. Herein, dehydroxylation of clay is endothermic in nature while decomposition of Pani is exothermic in nature in air environment. Once dehydroxylation of clay is initiated, prominence of endothermicity is accelerated in decomposition of Pani-HC composite, the overall heat effect changes to endothermic side above 460°C as seen from Fig. 2.

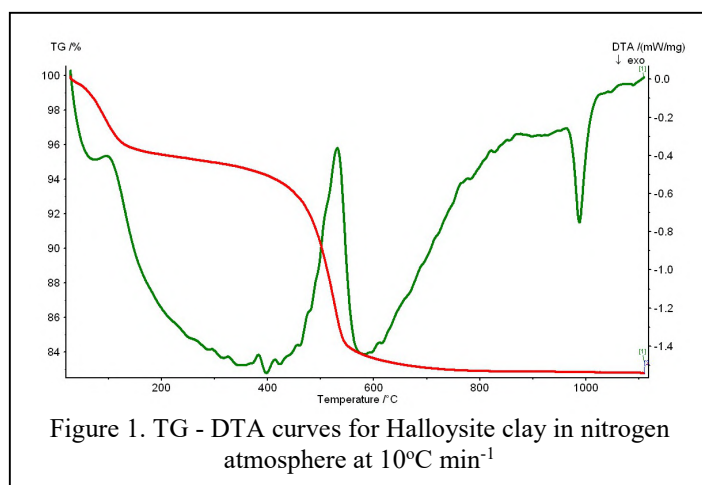
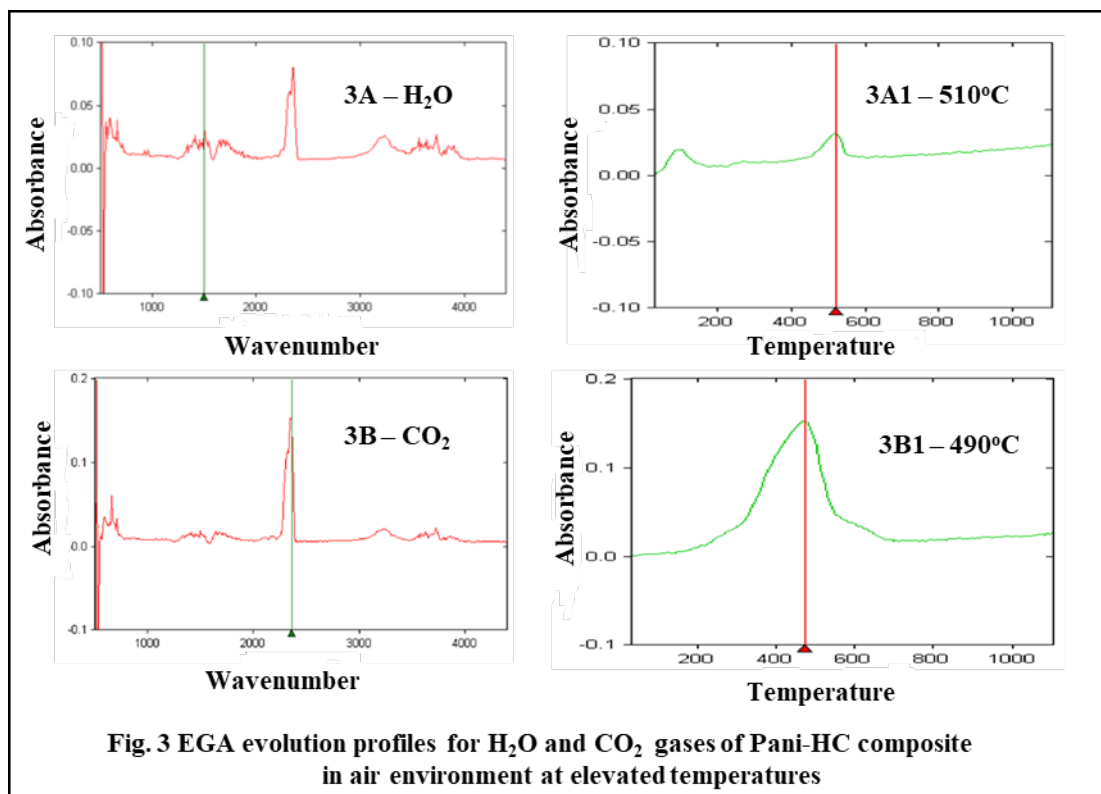


Figure 1. TG - DTA curves for Halloysite clay in nitrogen atmosphere at  $10^\circ\text{C min}^{-1}$

good agreement with theoretical mass loss for thermal decomposition of  $\text{Al}_2(\text{OH})_4\text{Si}_2\text{O}_5$  to  $\text{Al}_2\text{O}_3 \cdot 2\text{SiO}_2$  (metahalloysite). It exhibits the dehydroxylation of halloysite clay. An extrapolated on-set temperature for DTA peak is considered closer to equilibrium temperature of any thermal event. The sharp exotherm is observed at the extrapolated on-



Carbon accumulates during the decomposition of Pani for the composite material, a small and comparatively higher mass losses on TG curve above 450 and 600°C, respectively, are ascribed to carbon burning. The exothermic peak observed at 978°C precisely replicates the exothermic peak for halloysite clay (corresponding to the conversion of metahalloysite to alumina and amorphous SiO<sub>2</sub>). This also indicates the independent decomposition of halloysite in Pani-Halloysite composite.

Total mass loss for Pani - HC composite is 31.5% in the air and 25% in the nitrogen atmosphere in the temperature region of 31- 1100°C (Fig.2). The amount of mass loss owing to the removal of HCl gas and decomposition of Pani is lower in nitrogen atmosphere in comparison to air atmosphere in the temperature range of 150 to 400°C due to absence of combustion reaction. The results indicate 6.5% of carbon is left in the residue of Pani - HC composite at 1100°C in nitrogen atmosphere. The exotherm is completely absent during decomposition of Pani on the DTA in the temperature range of 150 to 400°C. The final exotherm is noticed for the conversion of metahalloysite to alumina and amorphous SiO<sub>2</sub>.

**Acknowledgements:** The authors thank Dr. C. N. Patra, Head, ACD, BARC for constant encouragement during the work.

#### References:

1. H. Parab, et. al., Int. J. Environ. Anal. Chem., 102 (2020)1.
2. A. Raghdi, et. al., J. Ind. Chem. Soc., 101(2024)101413.

Effect of B substitution on structure and hydrogen storage properties of Ti<sub>2</sub>CrV alloy

Asheesh Kumar, Seemita Banerjee, P. Ruz and V Sudarsan  
 Chemistry Division Bhabha Atomic Research Center Trombay Mumbai-400085 India.  
[asheeshk@barc.gov.in](mailto:asheeshk@barc.gov.in) Ph. No.-022-25595093

**Abstract**

The influence of B addition on structure and hydrogen absorption-desorption properties of Ti<sub>2</sub>CrV alloy has been investigated. B substitution in place of Ti in this alloy leads to decrease in lattice parameter and reduction in hydrogen storage capacity. The plateau pressure of the alloys increases with increase in B substitution in place of Ti. It is observed that Ti<sub>1.9</sub>CrVB<sub>0.1</sub> alloy shows better cyclic stability with marginal decrease in hydrogen storage capacity.

In the search of perfect hydrogen storage materials, rigorous material research is going on throughout the world with various sorption mechanisms to improve the storage properties [1-2]. Among different hydrogen storage materials, alloys and intermetallic based hydrides continue to be the most interesting materials for practical applications. The Ti-Cr-V based alloys with body centered cubic (bcc) structure are being studied extensively due to their high hydrogen absorption capacity of ~ 3 wt% which is almost twice as that of AB<sub>5</sub> type alloys [2]. Among Ti-Cr-V series the alloys Ti<sub>0.32</sub>Cr<sub>0.43</sub>V<sub>0.25</sub> and Ti<sub>2</sub>CrV having bcc structure are of great interest because of its good cyclic life and high hydrogen absorption capacity at room temperature [3-4].

In our previous study we reported that the Ti<sub>2</sub>CrV alloy shows maximum 4.00 wt% hydrogen storage capacity at room temperature. Though this alloy has high hydrogen absorption capacities among reported alloys, it need activation and it's desorption temperature is high. In order to improve hydrogen desorption and activation requirement we have explored the substitution of Fe, Co and Ni in place of Ti in Ti<sub>2</sub>CrV alloy [4]. It is inferred from this study that the substitution of Co and Ni in place of Ti in the alloy has decreased the hydrogen desorption temperature considerably with marginal decrease in hydrogen absorption capacity. The effect of Zr substitution on hydrogen storage properties of Ti<sub>2</sub>CrV alloy was explored in detail. Zr substitution improves the hydrogen desorption behaviour of Ti<sub>2</sub>CrV alloy with better cyclic stability. Composites of Ti<sub>2</sub>CrV and Zr-Fe-V alloy with different composition has been evaluated in details and desorption temperature is also found to reduced [5]

Even though substitution of late transition metal decreased the hydrogen desorption temperature, tuning of several other properties is essential for practical applications. In order to improve the hydrogen storage properties of Ti<sub>2</sub>CrV alloy, B substitution in place of Ti has been tried.

In the present work Ti<sub>2-x</sub>CrVB<sub>x</sub> (x =0.1&0.2) alloys have been synthesised and the structure, morphology and compositional analysis has been done. Kinetics of absorption-desorption hydrogen storage capacities, and the desorption profile have been evaluated for the studied alloys.

Both boron substituted Ti<sub>2</sub>CrV alloys have been made by arc melting the constituent elements under Ar flow. The high purity (99.99%) metals are taken in the required fraction. The alloy has been re-melted 3-4 times to insure homogeneity.

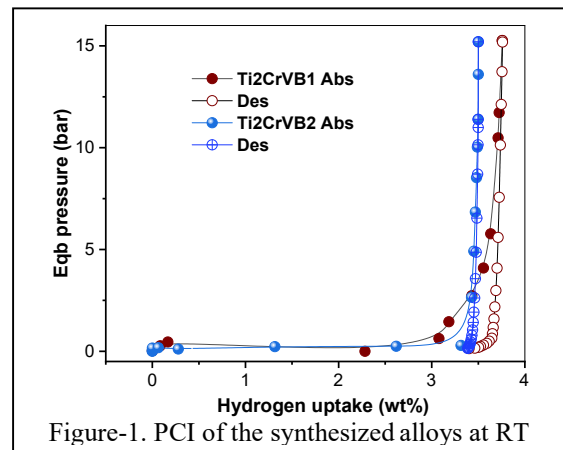


Figure-1. PCI of the synthesized alloys at RT

The characterization has been done by using XRD, EDX and SEM techniques. The hydrogen storage property measurement has been done by using automated gas sorption analyzer (HTP-1).

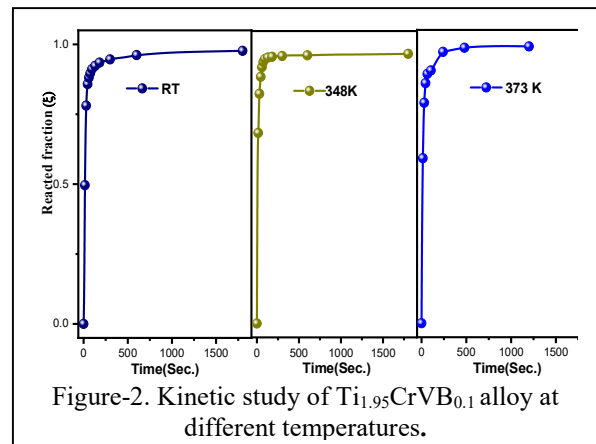


Figure-2. Kinetic study of Ti<sub>1.95</sub>CrVB<sub>0.1</sub> alloy at different temperatures.

The XRD analysis of B substituted alloys confirms the formation of pure body centered cubic (bcc) structure. It is observed in the studied alloy that diffraction peaks shift toward right, suggesting that lattice parameter decreases with B incorporation.

EDX study revealed that the elemental compositions of synthesized alloys well match with the amount of constituent's elements initially taken. The studied alloys undergo structural change from bcc to fcc structure after hydrogenation. In this case, however, the increase in the boron content (the value of X) results in the decrease in the total titanium content of the final Ti-Cr-V-B alloy.

Hydrogen absorption-desorption property of the alloys at different temperature and cyclic study have been studied by Gas sorption analyzer (HTP-1) after activation. For activation, the alloy samples were heated at 673K for 2 hrs under high vacuum ( $10^{-6}$  mbar). The Fig.1 shows the pressure composition isotherm of both the alloy studied at room temperature. The  $Ti_{1.9}CrVB_{0.1}$  alloy shows a maximum of 3.8 wt% hydrogen absorption capacity at room temperature. The pressure composition isotherm of both boron substituted alloy has been measured at 303K, 348K, 373K and 423K respectively. The absorption isotherm of studied alloy indicates decrease in hydrogen uptake with increase in temperature. The  $II^{nd}$  alloy found to absorb maximum 3.5 wt% of hydrogen at room temperature. The plateau pressure of both the alloys increases with increase in hydrogen absorption temperature.

Fig. 2 shows the hydrogen absorption kinetics of  $Ti_{1.95}CrVB_{0.1}$  alloy measured at room temperature, 348K, and 373K upto 20atm hydrogen pressure after one PCT measurement. The  $Ti_{1.9}CrVB_{0.1}$  alloy absorbs maximum 94% of total hydrogen absorption capacity at room temperature within 5 min. Within the same time the studied alloy absorbs maximum 96% and 97.5% of total absorbed hydrogen at 348K, and 373K respectively. The absorption kinetics of substituted alloy increases with elevation in temperature.

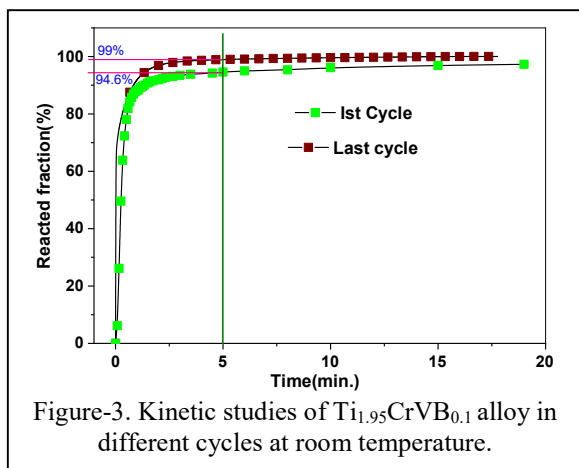


Figure-3. Kinetic studies of  $Ti_{1.95}CrVB_{0.1}$  alloy in different cycles at room temperature.

To understand long term applicability of studied alloys, cyclic stability was evaluated. Using the same set up cycling studies of  $Ti_{1.9}CrVB_{0.1}$  alloy was carried out upto 16 cycles. The sample was heated at 673K under vacuum for 2 hrs before each cycle. Hydrogen storage capacity in each cycle was measured at room temperature and upto 15 bar hydrogen pressure. Hydrogen storage capacity of  $Ti_{1.9}CrVB_{0.1}$  alloy decreases with increase in number of cycles. The hydrogen absorption kinetics of this alloy in  $I^{st}$  and last cycle at room temperature are shown in Fig.3. As clear from the figure, the kinetics of the alloy enhances with the subsequent cycles. The studied alloy shows absorption of 94.6 and 99% of total hydrogen uptake in  $I^{st}$  and last cycle respectively.

The desorption study of alloys have been done by Differential Scanning Calorimeter (DSC). The saturated hydrides of the alloys were heated under Ar flow with heating rate  $10^{\circ}C/min$ . Two desorption peak was observed in the desorption profile of hydrogenated B substituted  $Ti_2CrV$  alloys. The studied alloys show hydrogen desorption at higher temperature than parent  $Ti_2CrV$  alloy. Fig.4 shows the dsc profile of both the studied alloy deuterides. The

deuteride of both the alloys also show two peaks similar to hydrides.

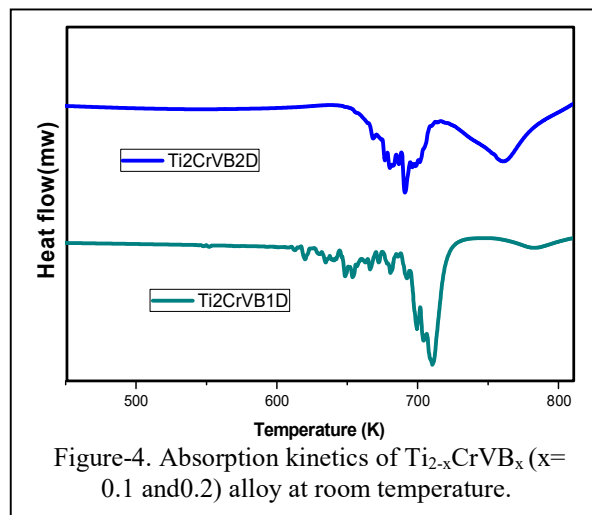


Figure-4. Absorption kinetics of  $Ti_{2-x}CrVB_x$  ( $x=0.1$  and  $0.2$ ) alloy at room temperature.

To make stable deuterated alloy Boron has been doped in the sample. Around 5% B doped sample showed an additional deuteride desorption peak around 770K along with main peak at 695 K. With more amount of B doping, phase separation occurs and along with the main desorption peak a high temperature desorption peak is also clearly observed.

The influence of of B substitution on hydrogen storage properties of  $Ti_2CrV$  alloy was studied. The  $Ti_{2-x}CrVB_x$  ( $x=0.1$  and  $0.2$ ) alloys shows marginal decrease in hydrogen storage capacity with boron substitution in place of Ti. Both substituted alloy shows enhancement in hydrogen absorption kinetics with increase in temperature.

## References

1. B. Sakintuna, L. D. Farida and H. Michael, *Int. J. Hydrogen Energy*, 32 (2007) 1121-40.
2. H. Iba and E. Akiba, *J Alloys Compd*, 231 (1995) 508-512.
3. J. H. Yoo, G. Shim, S. W. Cho, C. N. Park, *Int. J. Hydrogen Energy*, 32 (2007) 2977-81.
4. A. Kumar, S. Banerjee, C.G.S. Pillai, S.R. Bharadwaj, *Int. J. of Hydrogen Energy* 38, (2013) 13335-42.
5. S. Banerjee, A. Kumar, P. Ruz and P. Sengupta, *Int. J. Hydrog. Energy* 41-40, (2017) 18130

## Effect of Ni addition on dehydrogenation behaviour of MgH<sub>2</sub>

Bhaskar Paul, Pankaj Shrivastava, Shubham Kumar, Jugal Kishor, Sanjay Kumar, Sanjib Majumdar  
 MP&CED, Bhabha Atomic Research Centre, Mumbai-400 085, India  
 Email: bpaul@barc.gov.in

### Abstract

Magnesium hydride is an attractive and widely researched hydrogen storage material because of its high hydrogen capacity and lower cost of production. The present study deals with the optimization of the process parameters for the conversion of magnesium powder to magnesium hydride (MgH<sub>2</sub>) in bulk quantity and characterization of MgH<sub>2</sub>. Ni is used to reduce the dehydrogenation temperature of as synthesized MgH<sub>2</sub>. Thermal analysis tools such as TG, DTA, DSC, pressure-composition isotherms were used extensively to understand the dehydrogenation behavior of as prepared MgH<sub>2</sub> and catalyzed MgH<sub>2</sub>.

A large number of materials have been investigated for solid state hydrogen storage, including physical adsorbents (carbon, MOF, etc.), complex hydrides (LiBH<sub>4</sub>, LiNH<sub>4</sub>, NaAlH<sub>4</sub>, etc.), alloys hydrides (Mg<sub>2</sub>NiH<sub>4</sub>, Ti<sub>2</sub>VCrH<sub>2</sub>, TiFeH<sub>2</sub>, NaMgH<sub>3</sub> etc.), and metal hydrides (MgH<sub>2</sub>). Among them magnesium hydride (MgH<sub>2</sub>), catalyzed MgH<sub>2</sub>, MgH<sub>2</sub> alloy/composite are widely acknowledged as an encouraging solid-state hydrogen storage material because of their higher gravimetric capacity, good reversibility, low cost, abundance of Mg in earth crust and their non-toxic nature [1]. However, its practical utility is still limited due to the technical challenges of synthesis of producing magnesium hydride (MgH<sub>2</sub>) in bulk quantity and its high de-hydrogenation temperature. The present investigation deals with the process optimization of hydrogenation of Mg powder to produce MgH<sub>2</sub> in bulk quantity, characterization with respect to morphological changes during hydrogenation, hydrogen storage capacity, and dehydrogenation temperature. Magnesium (purity >99.9%, 200 mesh size) was placed in a reaction vessel of indigenously developed hydrogenation setup and hydrogenated at 350 °C with a hydrogen pressure of 2.5MPa after activation. The samples were removed in different intervals and characterized for knowing the progress of hydrogenation. The prepared MgH<sub>2</sub> was characterized with respect to the morphology, phase, purity, particle size, hydrogen content, and dehydrogenation temperature. Thermal analysis tools such as TG, DTA, DSC, pressure-composition isotherms were used for characterizing the samples with respect to dehydrogenation temperature and plateau pressure.

As prepared MgH<sub>2</sub> was catalyzed using Ni to address the limitation of high de-hydrogenation temperature. For this, MgH<sub>2</sub> powder was mechanically milled with Ni powder (stoichiometric quantity for formation of Mg<sub>2</sub>Ni phase) in a planetary ball mill under argon atmosphere. The milling was carried out using hardened steel balls of 5 mm and 10 mm in diameter. The ball-to-powder weight ratio was kept at about 40:1. The milled powders were characterized with respect to their size, phase, microstructure and dehydrogenation temperature by powder XRD and SEM, TG-DTA and DSC.

Fig.1 shows XRD patterns of MgH<sub>2</sub>-Ni revealing the progress of phase formation during the ball milling. The Mg<sub>2</sub>Ni phase was formed after 4 hours of milling. With time, the phase fraction of Mg<sub>2</sub>Ni was found to increase slightly, whereas the free Ni and MgH<sub>2</sub> fraction was found to be decreased. However, because of the diffusion-controlled mechanism, the complete conversion of Mg<sub>2</sub>Ni was not possible, even after 50 hours of milling. The peak of MgH<sub>2</sub> was found to be broadened significantly suggesting substantial size reduction which was confirmed through SEM imaging.

Fig.2 shows the DSC curves of (a) as synthesized MgH<sub>2</sub> and (b) MgH<sub>2</sub>-33 at.% Ni samples with a heating rate of

10°C/min. The dehydrogenation of MgH<sub>2</sub>-33 at.% Ni was found to be completed in two steps. In the first step, the dehydrogenation of Mg<sub>2</sub>NiH<sub>4</sub> was completed and the onset of dehydrogenation was found to be 270°C. It is noteworthy to mention here that the onset of dehydrogenation is reported as 250-300°C for single phase Mg<sub>2</sub>NiH<sub>4</sub> [2]. In the second step, partially catalyzed finer MgH<sub>2</sub> was dehydrogenated, which started releasing hydrogen at 330°C. The dehydrogenation of fine and partially catalyzed MgH<sub>2</sub> was found to be substantially lowered as compared to the as prepared MgH<sub>2</sub> which starts de-hydrogenating at 425°C (Fig.2b).

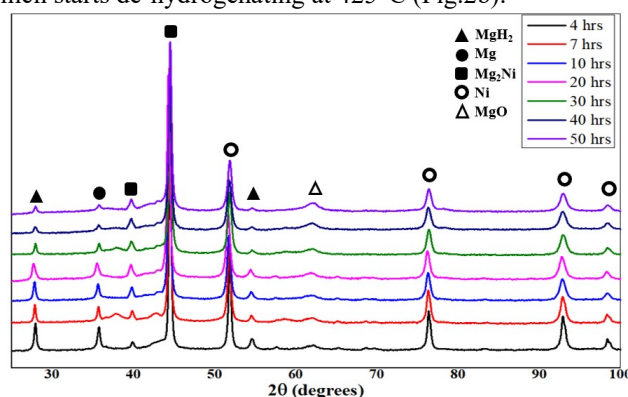


Fig. 1: XRD pattern of MgH<sub>2</sub>-Ni

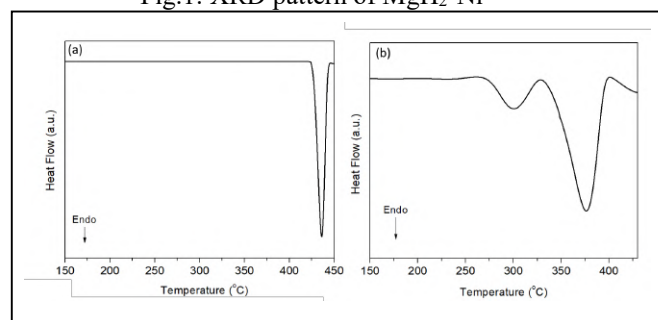


Fig. 2: DSC curves of (a) as synthesized MgH<sub>2</sub> and (b) MgH<sub>2</sub>-33 at.% Ni (10hr milling) samples with a heating rate of 10°C/min.

Thus, magnesium powder could be hydrogenated completely at 350°C in bulk quantity to form magnesium hydride. The dehydrogenation temperature of as prepared MgH<sub>2</sub> was found to be 425°C. Ni was found to be effective in reducing the dehydrogenation temperature of MgH<sub>2</sub>. MgH<sub>2</sub>-33 at.% Ni could start releasing hydrogen at 270°C.

### References

- Bhaskar Paul, Sanjay Kumar, Sanjib Majumdar, International Journal of Hydrogen Energy 96 (2024) 494–501
- B. Sakintuna, F. Lamari-Darkrim, M. Hirscher; Int J Hydrogen Energy, 32 (2007), pp. 1121-1140

## Hydrogen/Deuterium Desorption Kinetics of Pd-Ag Hydride/Deuteride

Abhishek Sharma<sup>a</sup>, S.G. Sawant<sup>a</sup>, Ram Avtar Jat<sup>a,\*</sup>, S.C. Parida<sup>a,b</sup>

<sup>a</sup>Product Development Division, Bhabha Atomic Research Centre, Trombay, Mumbai-400 085, India

<sup>b</sup>Homi Bhabha National Institute, Mumbai-400 094, India

\*E-mail: avtar@barc.gov.in, Tel. No.: +91 22 2559 6448/4592, Fax No.: +91 22 2550 5151

### Abstract

Palladium and its alloys have favourable hydrogen isotope effect which can be used for hydrogen isotope separation. In this study, we have prepared Pd<sub>0.89</sub>Ag<sub>0.11</sub> alloy and investigated its hydrogen isotope effect on the desorption kinetics using Differential scanning calorimetry (DSC) at four different heating rates. The apparent activation energies for desorption of hydrogen/deuterium from the alloy hydride/deuteride was determined using Kissinger's method. It is observed that the desorption of deuterium has lower activation energy than the corresponding hydride which makes the alloy suitable for the separation of hydrogen isotopes.

Palladium and its alloys are most promising materials for purification and separation of hydrogen isotopes. These alloys can be used as column bed materials in self-displacement gas chromatography (SDGC) technique for hydrogen isotope separation [1]. Such type of processes are useful for separation of exhaust gases from International Thermonuclear Experimental Reactor (ITER).

Several studies are reported on the thermodynamic properties of different Pd based binary and ternary alloys [2,3]. Alloying of palladium with Ag, Au and Cu etc. significantly affects the hydrogen/deuterium equilibrium pressure of the system [2,3]. In order to use metal hydride (MH) as hydrogen isotope storage, separation etc. alloy's kinetic behavior must be studied along with the thermodynamic parameters. Because, kinetic parameters play an important role in metal hydride absorption/desorption characteristics. Some MH's possess favorable thermodynamic properties but lack in kinetic properties. Such type of MHs can't be useful for hydrogen isotope separation [3].

In the present study, we have reported the hydrogen isotope effect on the hydrogen/deuterium desorption kinetics of Pd<sub>0.89</sub>Ag<sub>0.11</sub> alloy-hydride/deuteride using non-isothermal technique employing differential scanning calorimeter (DSC). Arc-melting method was used for the preparation of binary alloy-Pd<sub>0.89</sub>Ag<sub>0.11</sub>. The alloy was re-melted properly for 4-5 times in arc melter under helium atmosphere, followed by annealing at 1073 K in a vacuum sealed quartz ampoule for 150 h. The alloy was powdered and characterized using powder XRD. The XRD pattern had shown the formation of a single FCC phase. After activation, the alloy was loaded in DSC instrument (Make: M/s. SETARAM Instrumentation, France, Model: Sensys-Evo) and leak tested.

The alloy was activated in situ by hydrogen/deuterium absorption/desorption. DSC measurements were performed under an argon atmosphere in the temperature range of 303 – 473 K at four different heating rates viz. 8, 12, 16 and 20 K/min. From the peak temperature of DSC curves, Kissinger plots were constructed [4].

Hydrogen/deuterium desorption DSC curves for the alloy-hydride/deuteride are shown in Fig. 1. It is observed that the DSC curves had shown a downward movement in heat flow from the beginning which is due to a finite desorption pressure of hydrogen/deuterium over alloy-hydride/deuteride at all experimental temperatures. The peak temperature of DSC curves signifies the maximum hydrogen/deuterium desorption rate. It is also worth noting that, an increase in heating rate leads to higher peak maxima. To calculate activation energy for the desorption process, Kissinger method was used. According to H.E. Kissinger [4], the activation energy ( $E_a$ ) for

the desorption process in a solid-gas reaction depends on the heating rate and the peak temperature as:

$$\ln(\beta / T_{max}^2) = -\frac{E_a}{RT_{max}} + \ln(k_o) \quad (1)$$

where,  $T_{max}$  is the temperature corresponding to the peak maxima in DSC curve,  $\beta$  the heating rate,  $R$  is the gas constant, and  $k_o$  is a constant.

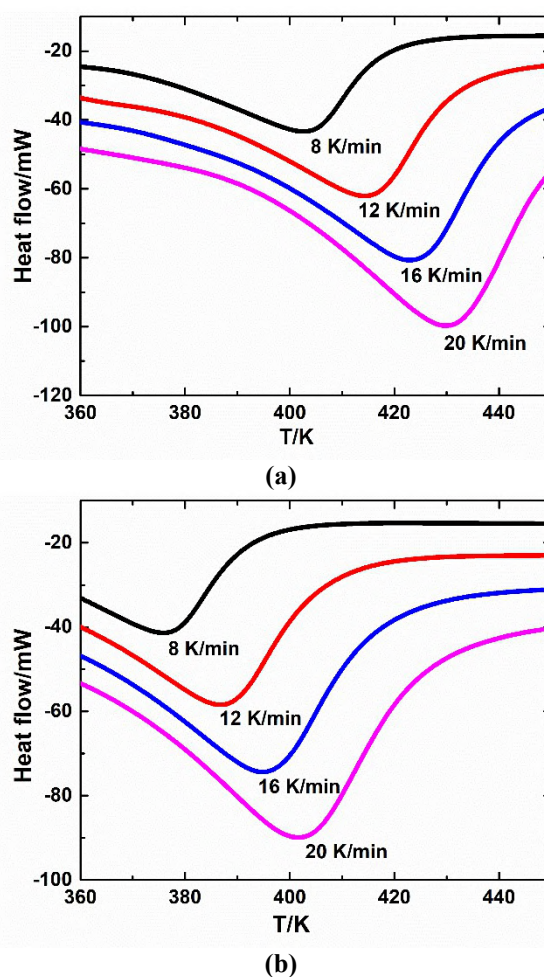
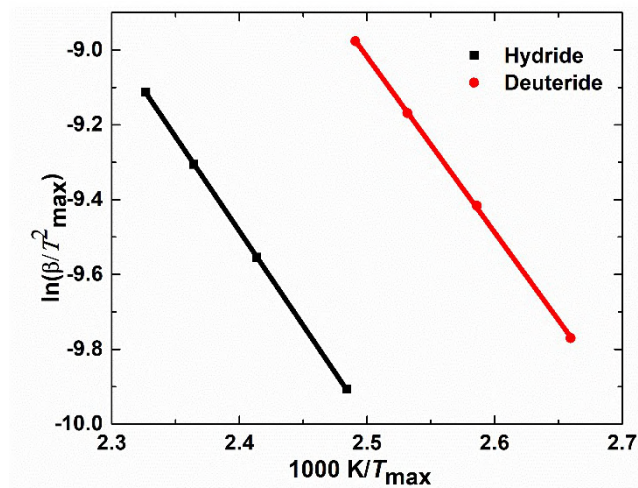


Fig 1. DSC curves for (a) Pd<sub>0.89</sub>Ag<sub>0.11</sub>-Hydride, (b) Pd<sub>0.89</sub>Ag<sub>0.11</sub>-Deuteride, respectively.

The temperature of maximum desorption or peak temperature ( $T_{max}$ ) obtained from the DSC curves, shown in Fig.1. were plotted according to eq.(1) to generate the Kissinger plots and are shown in Fig. 2. Kissinger plot for hydride and deuteride is linearly best fitted.





**Fig 2.** Kissinger plot for hydrogen/deuterium desorption reactions in Pd<sub>0.89</sub>Ag<sub>0.11</sub>-H<sub>2</sub>/D<sub>2</sub> systems.

The activation energies for the desorption of hydrogen/deuterium from the hydride/deuteride of Pd<sub>0.89</sub>Ag<sub>0.11</sub> were determined using slope of the Kissinger plots. The

apparent activation energy for desorption of hydrogen from Pd<sub>0.89</sub>Ag<sub>0.11</sub> hydride is  $41.9 \pm 0.2$  kJ/mol and for desorption of Pd<sub>0.89</sub>Ag<sub>0.11</sub> deuteride is  $39.0 \pm 0.3$  kJ/mol. From these activation energies it is clear that the activation energy for desorption of deuterium is found to be lower than that of hydrogen desorption. This observation makes Pd<sub>0.89</sub>Ag<sub>0.11</sub> alloy a material of interest for its application in the separation of hydrogen isotopes using SDGC.

#### References

1. Fukada S., Fujiwara H., Comparison of chromatographic methods for hydrogen isotope separation by Pd beds. *J. Chromatogr. A*, 898 (2000), 125-31.
2. Anand N.S., Pati S, Jat R.A., Parida S.C., Mukerjee S.K.. Hydrogen isotope effect on thermodynamic properties of Pd<sub>0.9</sub>X<sub>0.1</sub>(X = Cu, Ag and Au) alloys. *Int. J. Hydrogen Energy*, 42 (2017) 3136-41.
3. Sharma A., Rawat D., Raut S.K., Jat R.A., Parida S.C., Study of isotope effect on dehydrogenation kinetics of Pd based alloys using differential scanning calorimetry. *Int. J. Hydrogen Energy*, 47 (2022), 20546-55.
4. Kissinger H.E., Reaction kinetics in differential thermal analysis. *Anal Chem* 29 (1957) 1702-6

## Pressure Composition Temperature Studies on Pd-Ag-Cu Hydride/Deuteride

S.G. Sawant<sup>a</sup>, Abhishek Sharma<sup>a,b</sup>, Apurba Dutta<sup>a</sup>, Ram Avtar Jat<sup>a,\*</sup>, S.C. Parida<sup>a,b</sup>

<sup>a</sup>Product Development Division, Bhabha Atomic Research Centre, Trombay, Mumbai-400 085, India

<sup>b</sup>Homi Bhabha National Institute, Mumbai-400 094, India

\*E-mail: avtar@barc.gov.in, Tel. No.: +91 22 2559 6448/4592, Fax No.: +91 22 2550 5151

### Abstract

Investigation of thermo-physical properties by hydrogen/deuterium desorption reaction in ternary alloy  $Pd_{0.89}Ag_{0.05}Cu_{0.06}$  was studied using Sieverts' instrument. Pressure composition isotherms (PCIs) was generated. Enthalpy and entropy for the desorption processes were calculated from the Van't Hoff plots and are found to be  $39.3 \pm 1.0$  kJ/mol and  $106.4 \pm 3.0$  J/K.mol for hydrides and  $34.9 \pm 0.3$  kJ/mol and  $105.0 \pm 1.0$  J/K.mol for deuterides, respectively. Observed trends in equilibrium plateau pressure,  $Peq(D_2) > Peq(H_2)$ , is favorable for use as hydrogen isotope separation.

Generation of high purity hydrogen isotopes is a difficult task. High purity (HP) hydrogen isotopes have importance due to various applications in thermonuclear fusion reactors, fuel cells, chemical reactions etc. In International Thermonuclear Experimental Reactor (ITER), deuterium and tritium are to be used as fuel [1]. Palladium based alloys are extensively used for separation and purification of these isotopes from the exhaust gases of ITER. Self-displacement chromatography is one of the promising method used for hydrogen isotope separation. Palladium based alloys having Ag, Cu, Au etc are being explored as a column material [2,3].

Efforts are being made to make the column material cost effective by replacing the palladium with other metals. For the hydrogen isotope separation, the material of interest should have large isotope effect. In the present study, we have studied the hydrogen isotope effect of  $Pd_{0.89}Ag_{0.05}Cu_{0.06}$  alloy. Arc melting method was used for the preparation of  $Pd_{0.89}Ag_{0.05}Cu_{0.06}$  ternary alloy. The alloy was annealed for 150 h at 1073 K and characterized using powder XRD. It was activated by passing (Ar + 4%  $H_2$ ) gas mixture at 673 K before carrying out pressure-composition-temperature (PCT) studies. Sieverts' type volumetric apparatus (M/s. SETARAM Instrumentation, France, model no. PCT-Pro 2000) was used for generating pressure-composition isotherms (PCI) in the temperature range of 303 – 353 K at a step of 10 K.

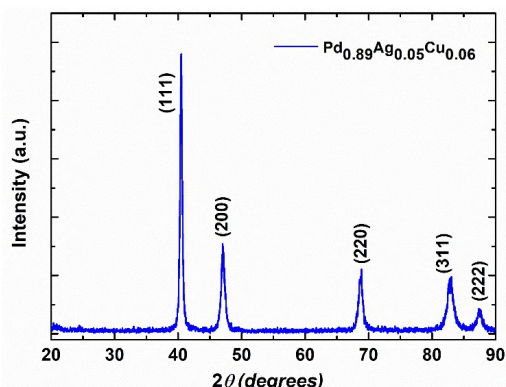
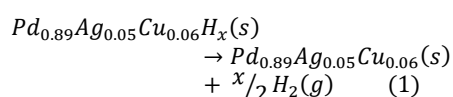


Fig. 1 Powder XRD pattern of  $Pd_{0.89}Ag_{0.05}Cu_{0.06}$  alloy

The XRD pattern of the alloy is shown in Fig. 1 which confirmed the formation of a single-phase FCC alloy. PCIs for desorption of hydrogen/deuterium from  $Pd_{0.89}Ag_{0.05}Cu_{0.06}$ -hydride/deuteride at four different temperatures were generated and are shown in Fig. 2.

The  $Pd_{0.89}Ag_{0.05}Cu_{0.06}$  - hydride equilibrium reaction for the plateau of PCI can be written as:



It can be observed from Fig. 2 that on increasing the temperature, equilibrium pressure also increases. It was also observed that, at a particular temperature, the equilibrium pressure for deuteride is higher than that of corresponding hydride thus confirming the presence of normal hydrogen isotope effect.

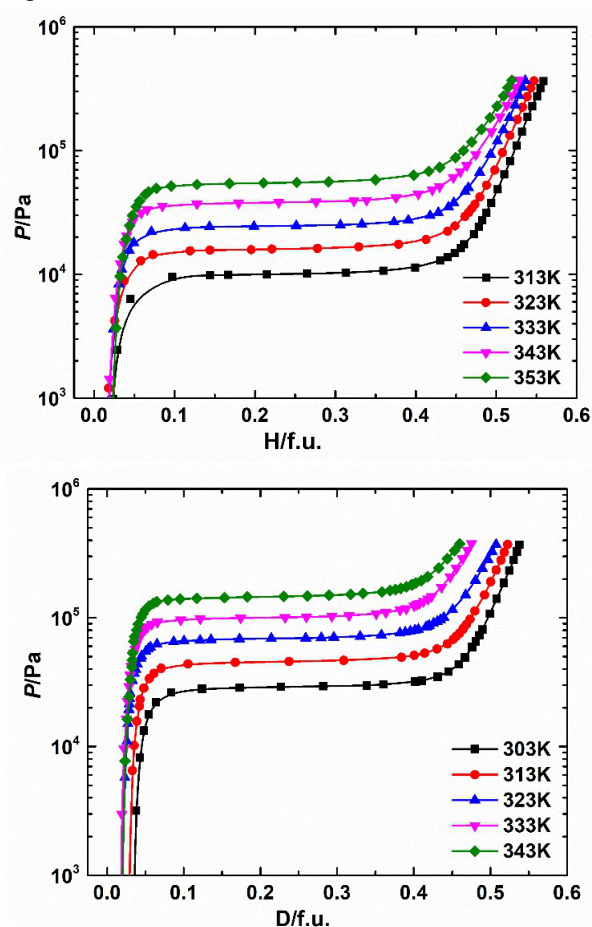


Fig. 2 Pressure-composition isotherms (PCIs) of (a) hydrogen desorption and (b) deuterium desorption from  $Pd_{0.89}Ag_{0.05}Cu_{0.06}$ -hydride/deuteride

Thermodynamic parameters for the hydrogen/deuterium desorption from alloy-hydride/deuteride were derived from equilibrium plateau pressures at the midpoint of corresponding PCIs and van't Hoff plots were constructed and shown in Fig. 3. The enthalpy and entropy for desorption reactions were calculated from slope of the van't Hoff plots and are found to be  $39.3 \pm 1.0$  kJ/mol and  $106.4 \pm 3.0$  J/K.mol for hydrides and  $34.9 \pm 0.3$  kJ/mol and  $105.1 \pm 1.0$  J/K.mol for deuterides, respectively.

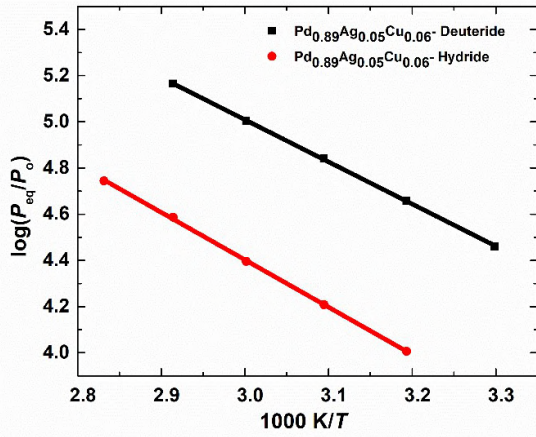


Fig 3. Vant' Hoff plot for desorption reaction of Pd<sub>0.89</sub>Ag<sub>0.05</sub>Cu<sub>0.06</sub> alloy-hydride/deuteride

## References

1. A. Wilson J., Becnel J., Demange D., Rogers B., The ITER tokamak exhaust processing system design and substantiation. Fusion Sci. Technol., 2019, 1-8.
2. Pati S., Jat R. A., Mukerjee S. K., Parida S. C., Hydrogen isotope effect on thermodynamic and kinetics of hydrogen/deuterium absorption-desorption in Pd<sub>0.77</sub>Ag<sub>0.10</sub>Cu<sub>0.13</sub> alloy. J. Phys. Chem. C, 119 (2015), 10314–20.
3. Anand N. S., Pati S., Jat R. A., Parida S. C., Mukerjee S. K., Hydrogen isotope effect on thermodynamic properties of Pd<sub>0.9</sub>X<sub>0.1</sub>(X = Cu, Ag and Au) alloys. Int. J. Hydrogen Energy, 42 (2017) 3136-41.

Catalytic Activity of  $\text{CuFe}_2\text{O}_4$  on the Thermal Decomposition of Ammonium Perchlorate

Supriya N\*, Soumyamol PB, Vijayalakshmi KP and Deepa Devapal

Analytical and Spectroscopy Division, Analytical, Spectroscopy and Ceramics Group,  
Propellants, Polymers, Chemicals and Materials Entity, Vikram Sarabhai Space Centre, Thiruvananthapuram-  
695022, India

e-mail: supriya.vssc@gmail.com, n\_supriya@vssc.gov.in

**Abstract**

Mixed metal oxides (MMO) of the type  $\text{AB}_2\text{O}_4$  are receiving much attention because of their better catalytic activity compared to single metal oxides for AP decomposition.  $\text{CuFe}_2\text{O}_4$ , a MMO of Cu and Fe, was synthesized using co-precipitation method and its catalytic activity towards thermal decomposition of ammonium perchlorate (AP) was evaluated using Thermogravimetry. The catalyst lowered the high temperature decomposition temperature of AP by 19 °C when added in 0.5%, also increasing the enthalpy of decomposition by 340 J/g.

Ammonium perchlorate (AP) is the workhorse oxidizer for composite solid propellants used for the propulsion of launch vehicles. The thermal decomposition of AP has been extensively studied as it alters the burn rate of composite solid propellant. Transition metal oxides like ferric oxide, copper oxide, cobalt oxide, manganese oxide, zinc oxide etc. are reported to enhance the thermal decomposition of AP [1,2]. The physical characteristics of these metal oxides like particle size, surface area, defects in the crystalline structure and chemical characteristics like oxidation state, chemical composition etc., affects its catalytic activity for the thermal decomposition of AP, thereby affecting the burning behavior of AP based propellants [3,4]. Mixed metal oxides (MMO) are spinel oxides of the type  $\text{AB}_2\text{O}_4$  like metal chromites, ferrites and cobaltites are receiving much attention because of their better catalytic activity compared to single metal oxides for AP decomposition. The improved activity of mixed metal oxides is due to their active phases and synergic interactions between the two different metal ions offering rapid mass transfer processes during AP decomposition. The catalytic properties of the MMOs is also dependent on the synthesis method, chemical composition, nature of substituted ions, charges and their distribution among the octahedral (Oh) and the tetrahedral (Td) sites in their spinel structure [5-7]. In this work,  $\text{CuFe}_2\text{O}_4$ ; a mixed metal oxide of Cu and Fe was synthesized using co-precipitation method, followed by calcination at 900°C.

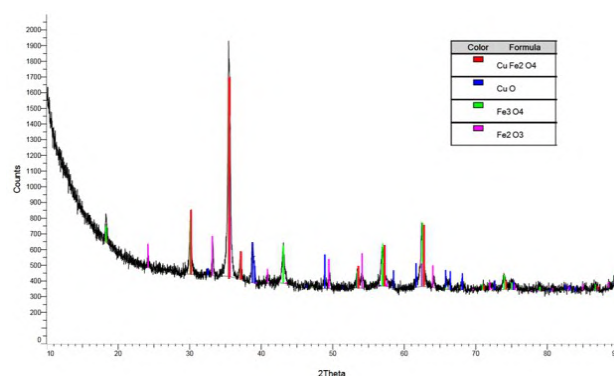
All the chemicals used for the study were of analytical grade and was used as such, without further purification. Ammonium perchlorate manufactured in VSSC was used as such for the catalytic activity evaluation.  $\text{Cu}(\text{NO}_3)_2 \cdot 3\text{H}_2\text{O}$ , 98.0%, was procured from Ottochemie Pvt. Ltd., India.  $\text{Fe}(\text{NO}_3)_3 \cdot 9\text{H}_2\text{O}$ , 98.0%, was procured from Merck Lifescience Pvt. Ltd., India. For the synthesis of  $\text{CuFe}_2\text{O}_4$  catalyst, stoichiometric quantities of  $\text{Cu}(\text{NO}_3)_2$  and  $\text{Fe}(\text{NO}_3)_2$  were dissolved initially in distilled water and mixed under constant stirring. To this solution, NaOH solution was added drop wise until pH reached 10. The stirring was continued for 1 hour and the solution was filtered to collect the precipitate. The precipitate was washed thoroughly and then dried at 110°C for 3 hrs to obtain the copper ferrite precursor. The precursor was then heated in a muffle furnace at 900 °C for 4 hrs in an alumina crucible to obtain the  $\text{CuFe}_2\text{O}_4$  catalyst.

The synthesized  $\text{CuFe}_2\text{O}_4$  catalyst was characterized using different analytical techniques. X-ray powder diffraction analysis was carried out using Bruker D8 Discover

diffractometer from 10 to 80° with Cu-K $\alpha$  radiation ( $\lambda = 1.5406 \text{ \AA}$ ) at a scanning rate of 4° min<sup>-1</sup>. Surface area was measured using Quantachrome NOVA touch LX2 surface area analyser. Particle size was assessed using Malvern Mastersizer 2000 particle size analyser using laser diffraction. Surface morphology was captured using a Bruker Nano GmbH Gemini SEM 500 Field emission scanning electron microscope and the elemental identification was done using Bruker Quantax X-Flash energy dispersive X-ray spectrometer at 10 keV.

The TG-DSC analysis of the copper ferrite precursor, fine AP and AP with  $\text{CuFe}_2\text{O}_4$  catalyst was evaluated using TA Instruments Q-600 simultaneous Thermogravimetric analyser-Differential scanning calorimeter (TG-DSC). The catalytic effect of 0.5%  $\text{CuFe}_2\text{O}_4$  on AP decomposition was studied. For this, fine AP and the synthesised  $\text{CuFe}_2\text{O}_4$  catalyst was taken in mass ratio of 99.5:0.5 and was blended thoroughly using an agate mortar and pestle. Approximately 5 mg of this mixture was subjected to TG-DSC analysis. The analysis was performed by heating the sample mix from room temperature to 400°C at a heating rate of 5 °C min<sup>-1</sup> in platinum pan under ultra pure argon atmosphere at flow rate of 100 mL min<sup>-1</sup>.

The XRD curve of the synthesized MMO is given in Fig.1, which showed  $\text{CuFe}_2\text{O}_4$  as the major peak, with traces of CuO,  $\text{Fe}_2\text{O}_3$  and  $\text{Fe}_3\text{O}_4$ . Characteristic peaks of  $\text{CuFe}_2\text{O}_4$  at 2 $\theta$  of 29.9°, 34.7°, 35.8°, 43.7°, 57.8° and 63.6° corresponding to the diffraction from the (112), (103), (211), (220), (321) and (400) lattice planes were identified. The sharp peaks confirm the crystalline nature of  $\text{CuFe}_2\text{O}_4$  synthesized at the high temperature.

Figure 1. XRD curve of  $\text{CuFe}_2\text{O}_4$

The average particle size of the synthesized  $\text{CuFe}_2\text{O}_4$  was around  $103 \mu\text{m}$ , with very low surface area of  $0.3\text{m}^2/\text{g}$ . The low surface area of the MMO is due to the sintering of the particles during the high temperature calcination process. SEM image (Fig.2a) shows that the synthesised  $\text{CuFe}_2\text{O}_4$  is having a polygonal morphology, with particles of smooth and homogeneous texture. EDS spectra shown in Fig.2b confirmed the presence of copper, iron and oxygen in the sample.

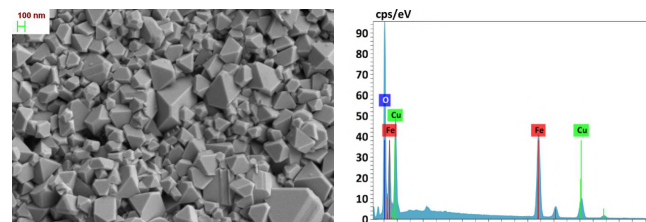


Fig.2a. FESEM image of  $\text{CuFe}_2\text{O}_4$

Fig.2b. EDS spectra of  $\text{CuFe}_2\text{O}_4$

The overlaid TG-DTG curves of AP and AP with 0.5%  $\text{CuFe}_2\text{O}_4$  is shown in Fig.3 and the corresponding DSC curve is shown in Fig.4. The TG-DTG results corresponding to the decomposition is tabulated in Table 1.

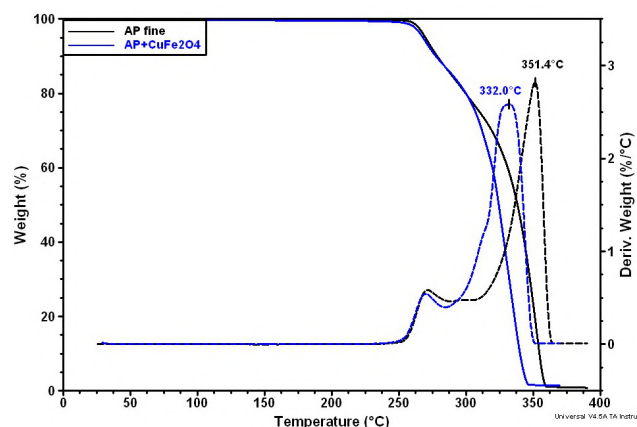


Figure 3. Catalytic effect of 0.5 %  $\text{CuFe}_2\text{O}_4$  on AP decomposition

Pure AP decomposes in two distinct stages, with low temperature decomposition (LTD), accounting for around 30% mass loss and peak decomposition at  $271^\circ\text{C}$  and high temperature decomposition (HTD), accounting for around 70% mass loss and peak decomposition at  $351^\circ\text{C}$ .

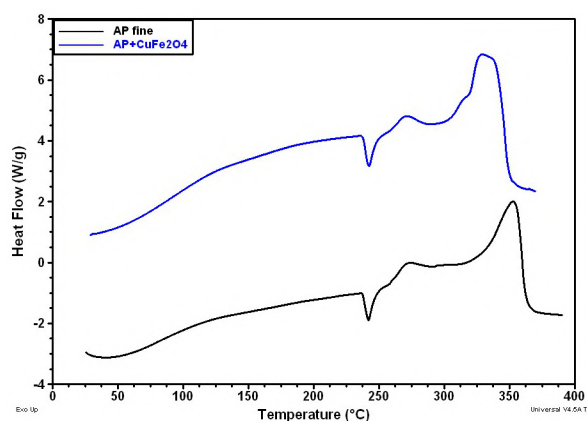


Figure 4. Overlaid DSC curves of AP and AP with 0.5%  $\text{CuFe}_2\text{O}_4$

Table 1. Catalytic effect of 0.5 %  $\text{CuFe}_2\text{O}_4$  on AP decomposition

Sample	LTD (Ts) °C	HTD (Ts) °C
AP fine	271	351
AP + $\text{CuFe}_2\text{O}_4$	270	332

The thermal decomposition of AP proceeds with the most accepted electron transfer and proton transfer mechanisms, with the formation of  $\text{HCl}$ ,  $\text{NH}_3$ ,  $\text{H}_2\text{O}$ ,  $\text{O}_2$ ,  $\text{NO}$ ,  $\text{Cl}_2$ ,  $\text{N}_2$ ,  $\text{NO}_2$  etc., as the major decomposition products. In presence of MMO catalysts, the decomposition of AP becomes faster with increase in reaction exothermicity. The TG-DTG analysis clearly shows the catalytic effect of  $\text{CuFe}_2\text{O}_4$  towards AP decomposition. The mixed metal oxide alters the electron transfer process from  $\text{Cl}_4^-$  to  $\text{NH}_4^+$  at low temperature and decomposition of  $\text{HClO}_4$  by controlling the transformation of  $\text{O}_2$  to superoxide ion,  $\text{O}_2^-$  at high temperature which can further react with  $\text{NH}_3$  to form  $\text{N}_2$ ,  $\text{NO}$  and  $\text{H}_2\text{O}$ . The synthesized  $\text{CuFe}_2\text{O}_4$  catalyst is a spinel oxide with the divalent  $\text{Cu}^{2+}$  and trivalent  $\text{Fe}^{3+}$  cations occupying the octahedral and tetrahedral sites within the crystal lattice and offering more active sites for rapid mass transfer processes during the decomposition reaction. The addition of 0.5% catalyst could lower the high decomposition temperature of AP by  $19^\circ\text{C}$ .

The DSC curves of AP and AP with  $\text{CuFe}_2\text{O}_4$  shows an endothermic peak and two exothermic peaks. The endotherm around  $242^\circ\text{C}$  is due to the phase transition of AP from orthorhombic to cubic phase. The exotherms corresponds to the two stage decomposition of AP. Presence of 0.5%  $\text{CuFe}_2\text{O}_4$  enhances the exothermicity of the decomposition reaction by increasing the enthalpy ( $\Delta\text{H}$ ) of decomposition from  $920 \text{ J/g}$  to  $1260 \text{ J/g}$ .

The study concludes that  $\text{CuFe}_2\text{O}_4$  synthesized using the present method, catalysed AP decomposition by lowering the high temperature decomposition peak by  $19^\circ\text{C}$ , suggesting  $\text{CuFe}_2\text{O}_4$  as a good catalyst for AP decomposition.

#### Acknowledgement

The authors acknowledge Director, VSSC, Deputy Director VSSC (PCM), Group Director, Analytical, Spectroscopy and Ceramics Group for their permission to present the work and colleagues in Analytical and Spectroscopy Division, VSSC for their analytical support.

#### References

- [1] D. Zhang, Q. Li, R. Li, H. Li, H. Gao, F. Zhao, L. Xiao, G. Zhang, G. Hao W. Jiang. *ACS Omega*, 6 (2021) 16110.
- [2] P.N. Dave, R. Sirach. *J Therm Anal Calorim.* 147 (2022) 10999.
- [3] T.Chen, Y. Hu, C. Zhang, Z.Gao, *Defence Techn.*17 (2021) 1471.
- [4] I.P.Kapoor, P.Srivastava, G. Singh, *Propellants Explos. Pyrotech.* 34 (2009) 351
- [5] E.Alizadeh-Gheshlaghi, B. Shaabani, A.Khodayari, Y. Azizian-Kalandaragh, R. Rahimi. *Powder Tech.* 217 (2012) 330.
- [6] N.M. Juibari, A. Eslami, *J Therm Anal Calorim.*128 (2017) 115.
- [7] X.Xiao, B. Peng, L. Cai, X. Zhang, S. Liu, Y. Wang, *Scientific Reports*, (2018).
- [8] C.Parvathy, B.Sreeja, T.Deepthi, T.Jayalatha, S.Vishnu, R.Rajeev. *J Therm Anal Calorim.*, 2023.

## Influence of Banana peel extract in the synthesis of ZrO<sub>2</sub> nano catalyst for removal of a potent Pesticide in visible light

Namrata Kumari., Rohan K. Kunkalekar\*

<sup>a</sup>School of Chemical Sciences, Goa University, Taleigao Plateau, Goa. 403206

\* [rohankunkalekar@unigoa.ac.in](mailto:rohankunkalekar@unigoa.ac.in)

### Abstract

ZrO<sub>2</sub> is a flourishing photocatalyst with a high band-gap (5.2-5.5 eV) which is deemed ineffective for photodegradation of pollutants. However, its high stability as a material and biocompatibility has influenced its utilization to synthesise ZrO<sub>2</sub> with a better surface area and optical properties proved to be effective for efficient photocatalysis. In the current research work, banana peel extract has been first used to synthesise a ZrO<sub>2</sub>-banana peel extract based composite followed by calcination at appropriate temperature to gauge its effectiveness as a photocatalyst in terms of its optical and surface properties.

ZrO<sub>2</sub> has a high band-gap which is deemed ineffective for photocatalysis at visible light.[1] However, as a material with high mechanical strength, great photostability, good oxygen carrier and diverse examples of effective tuned materials (doped and composite) material, it is a potential good photocatalyst.[2]

Banana peel extract is a bio-waste which is used as a capping agent to reduce the problem of agglomeration for a better surface property useful for an effective adsorption of pesticides on the catalyst's surface for photodegradation.[3]

The composites were prepared by hydrothermal method followed by calcination to eliminate organic pollutants. The material at each temperature was characterized by IR, and CHNS analysis to identify the functional group and total organic content. XRD pattern and Raman spectra were done to study the characteristic phase of ZrO<sub>2</sub>. The formed catalyst was further characterized for its specific surface area and SEM for its surface properties. Band-gap and photoluminescence studies were additionally done to know its optical suitability for photodegradation.

Resultant material's band-gap was reduced to 4.7 eV as compared to a 5.2eV band-gap of ZrO<sub>2</sub> prepared with banana peel. Formed material was rich in defects and oxygen vacancies which was studied through PL spectra.

ZrO<sub>2</sub> calcined to 400°C was used for photocatalysis of 2,4-dichlorophenoxyacetic acid in the visible light. 2,4-dichlorophenoxyacetic acid is a well-known pesticide widely used worldwide and is known to be a persistent organic pollutant. Prolonged usage has been known to impact the reproductive system in humans and some animals.[4]

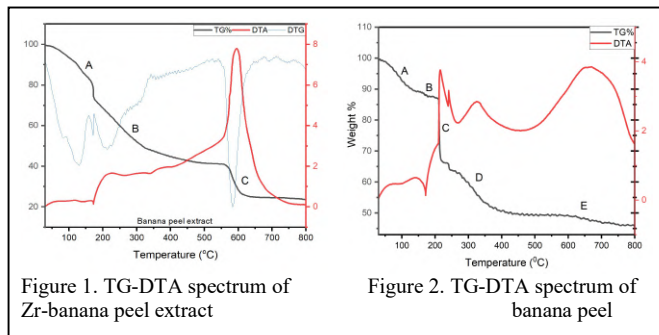


Figure 1. TG-DTA spectrum of Zr-banana peel extract

Figure 2. TG-DTA spectrum of banana peel

Table 1. Comments on weight loss% in the TGA plot

Weight loss %		Comments	
Banana peel extract	ZrO <sub>2</sub> -banana peel extract	Banana-peel extract	ZrO <sub>2</sub> -banana peel extract
A.28%	A-B. 14%	Removal of adsorbed and trapped water molecules and low-volatile organic compounds	
B-C. 43%	B-D. 36%	Removal of other volatile organic compounds	Removal of volatile organic compounds
E.-	-	-	Point of crystallization of ZrO <sub>2</sub>

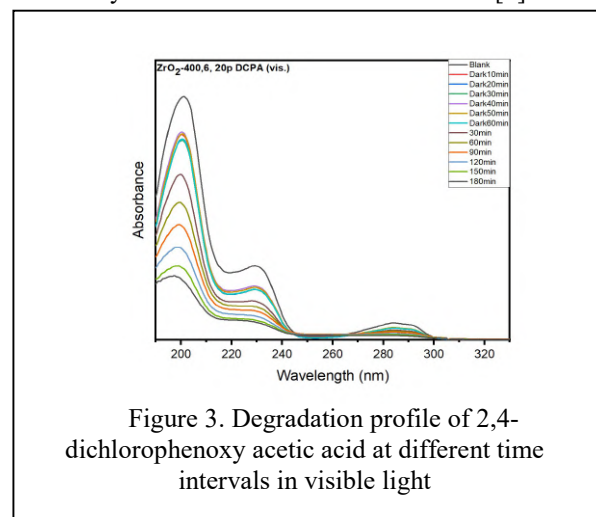


Figure 3. Degradation profile of 2,4-dichlorophenoxy acetic acid at different time intervals in visible light

From fig. 3, pesticide was 74.8% degraded in presence of ZrO<sub>2</sub> calcined at 400°C, as compared to no degradation when uncalcined material was used as a precursor. Degraded products were further confirmed by HPLC to analyse the percentage loss in carbon content from the pesticide.

### References

- [1] D.G. Lamas, A.M. Rosso, *Scr. Mater.* **2006**, *55*, 553-556.
- [2] X. Dong, F. Li, N. Zhao, *Appl. Catal. B.* **2016**, *191*, 8-17
- [3] A. Selvarajoo, D. Muhammed, *MESE.* **2020**, *6*, 115-128
- [4] K. Parashar, N. Ballav, *J. Colloid. Interface Sci.* **2017**, *508*, 342-358.

## Synthesis, Characterization and Thermal Expansion of Multilanthanides Incorporated at A site of High Entropy Pyrochlore

Nitin Gumber<sup>a,b</sup>, Muhammed Shafeeq<sup>a</sup>, Swayam Kesari<sup>c</sup>, S.N. Achary<sup>d</sup> and Rajesh V. Pai<sup>a,b,\*</sup>

<sup>a</sup>Fuel Chemistry Division, Bhabha Atomic Research Centre, Mumbai – 400085

<sup>b</sup>Homi Bhabha National Institute Anushakti Nagar, Mumbai - 400094

<sup>c</sup>Solid State Physics Division, Bhabha Atomic Research Centre, Mumbai – 400085

<sup>d</sup>Chemistry Division, Bhabha Atomic Research Centre, Mumbai – 400085

\* Corresponding author: rajeshvp@barc.gov.in, 022-25596183

### Abstract

The high-entropy pyrochlores have gathered increasing attention of researchers due to their ability to immobilize multiple nuclides simultaneously, as compared to normal pyrochlores. Simultaneous incorporation of multi lanthanide ions was carried out at A site of pyrochlore with compositions viz.,  $Nd_2(ZrTi)O_7$ ,  $(Nd_{1/3}Eu_{1/3}Gd_{1/3})_2(ZrTi)O_7$ ,  $(Nd_{1/4}Eu_{1/4}Gd_{1/4}Tb_{1/4})_2(ZrTi)O_7$ ,  $(Nd_{1/5}Eu_{1/5}Gd_{1/5}Tb_{1/5}Dy_{1/5})_2(ZrTi)O_7$  and  $(La_{1/6}Nd_{1/6}Eu_{1/6}Gd_{1/6}Tb_{1/6}Dy_{1/6})_2(ZrTi)O_7$ . The phase purity and atomic positions were established through Rietveld Refinement using XRD data. The absence of fluorite phase was confirmed using Raman spectra. Finally, the thermal expansion, both axial and volume expansion coefficients were evaluated using HTXRD from RT to 1273 K.

**Introduction:** Large amounts of radioactive nuclear waste have been generated in nuclear power industry, among which high-level radioactive waste (HLW) is the most challenging to treat and dispose.[1] Different matrices like borosilicate glass, pyrochlores, perovskites and glass-ceramics have been proposed literature for disposal of waste.[2] Among these, pyrochlores ( $A_2B_2O_7$ ) stand out best due to their ability to incorporate radionuclides at both A and B site, high thermal and irradiation stability. A and B sites are usually occupied by trivalent and tetravalent cations having coordination number 8 and 6 respectively. In recent times, the concept of high entropy ceramics is being explored which consists of 5 or more cations with different ionic radii and mass.[3] Following the above footsteps, we have synthesized high entropy pyrochlores with simultaneous incorporation of lanthanides at A site without phase segregation.

**Experimental:** Samples with compositions  $Nd_2(ZrTi)O_7$ ,  $Nd_{1/3}Eu_{1/3}Gd_{1/3})_2(ZrTi)O_7$ ,  $(Nd_{1/4}Eu_{1/4}Gd_{1/4}Tb_{1/4})_2(ZrTi)O_7$ ,  $(Nd_{1/5}Eu_{1/5}Gd_{1/5}Tb_{1/5}Dy_{1/5})_2(ZrTi)O_7$  and  $(La_{1/6}Nd_{1/6}Eu_{1/6}Gd_{1/6}Tb_{1/6}Dy_{1/6})_2(ZrTi)O_7$  were synthesized using Gel-combustion method and are termed as HEP-1, HEP-2, HEP-3, HEP-4 and HEP-5 respectively in the subsequent sections. For synthesis, stoichiometric amounts of respective metal nitrate solutions were added to a beaker and citric acid in the ratio 1:1 was added and heated at ~ 423 K to form a gel which leads to auto combustion forming ash like material. It was further heated at 1073 K to remove carbonaceous material. Pellets of dia 5 mm were made out of them and sintered at 1673 K in air for 4 h to yield final compounds. The above synthesized compounds were used for characterization and other property determinations.

**Results & Discussion:** The formation of stable pyrochlore is governed by the radius ratio ( $r_A/r_B$ ) and should be within 1.46-1.74. The base composition HEP-1, has radius ratio of 1.67 and hence a pyrochlore structure was expected and confirmed by observing the superlattice peak around 15 °. All the compounds crystallized as pyrochlore and no extra peak was observed as shown in Fig. 1(a). The atomic positions and lattice parameter of all the composition were optimized using Rietveld refinement and the corresponding lattice parameters are shown in Table 1. As a representative result, Rietveld refinement of HEP-4 is shown in Fig 1 (b). To know the local structure, Raman spectra were recorded and the signature peaks corresponding to fluorite phase were absent and presence of pure pyrochlore corroborating our XRD results.

Due to the emission of different types of characteristic radiation from respective radionuclides, the self heating would occur and hence lead to thermal expansion. Thus, we have evaluated the thermal expansion of all the above mentioned compositions from RT up to 1273 K using High Temperature XRD (HTXRD). As the temperature was increased the peaks were shifted to lower  $2\theta$  angle thus revealing positive thermal expansion coefficient. The matrices were thermally stable as no extra peak was observed in the XRD at high temperatures. Average axial and volume expansion coefficients were evaluated using the following expressions

$$\alpha_a = (\Delta a_T / a_{298}) \times (1/\Delta T)$$

$$\alpha_v = (\Delta v_T / v_{298}) \times (1/\Delta T)$$

Where  $\Delta a_T$  and  $\Delta v_T$  represents the difference in lattice parameter and volume at temperature 'T' and RT. The corresponding values are tabulated in Table 1.

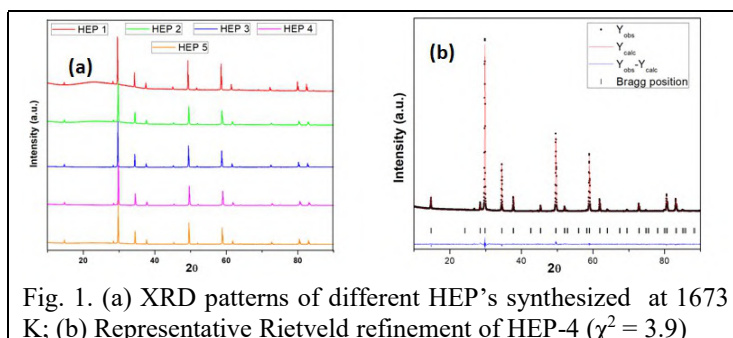


Fig. 1. (a) XRD patterns of different HEP's synthesized at 1673 K; (b) Representative Rietveld refinement of HEP-4 ( $\chi^2 = 3.9$ )

**Table 1. Average axial and volume expansion coefficients of HEPs with their lattice parameters at 298 K.**

Sample	Lattice Parameter at 298 K	Thermal Expansion Coefficient * $10^{-5} K^{-1}$	
		Axial	Volume
HEP-1	$10.4608 \pm 0.0001$	1.00	3.03
HEP-2	$10.4158 \pm 0.0001$	1.01	3.06
HEP-3	$10.4299 \pm 0.0001$	1.03	3.14
HEP-4	$10.3862 \pm 0.0001$	1.04	3.18
HEP-5	$10.4029 \pm 0.0001$	0.99	3.02

### References

1. R.C. Ewing, *Nat. Mater.*, 14 (3) (2015). 252
2. N. Gumber *et al.*, *Dalton Transactions*, 52 (2023) 14170
3. Z. Wang *et al.*, *J. Nuclear Materials*, 574 (2023) 15421

## Order Evolution And Its Effect On The Hardness Property Of Ni-Cr-Mo-W Alloy

Manoj K. Thota<sup>a</sup>, A. Verma<sup>a,\*</sup>, J.B. Singh<sup>a</sup>, M. Karri<sup>a</sup>, and K V Ravikanth<sup>a</sup>

<sup>a</sup>Mechanical Metallurgy Division, Materials Group, BARC

\* Email: [averma@barc.gov.in](mailto:averma@barc.gov.in), Phone no: 022-6929-0383

### Abstract

Commercial precipitate hardened Ni-Cr-Mo-based alloys have been developed by exploiting strengthening property of coherent precipitates of a Ni<sub>2</sub>(Cr,Mo) phase. This strengthening phase forms by disorder-order transformation by chemical ordering of constituent's species. Present work reports the effect of W on phase transformation behavior of Ni-Cr-Mo- alloys to delineate the role of different solutes on the pathway of the order evolution addition. Thermal analysis using differential scanning calorimetry and resistivity measurements in conjunction with microscopic evidences confirmed that order evolution in Ni-Cr-Mo-W alloys choose path identical to that of Ni-Cr-Mo alloys involving short-range order.

**Introduction:** Addition of different solutes in Ni-base alloys has resulted in the development of many Ni-base alloys for applications requiring good mechanical strength at elevated temperatures with excellent corrosion and oxidation resistance properties [1]. Particularly, precipitate hardened Ni-Cr-Mo-base alloys majorly derive their strength by fine precipitates of Ni<sub>2</sub>(Cr,Mo) phase that forms during ageing at temperatures less than 750°C [2]. This phase has been reported to form via disorder to order transformation mechanism involving either continuous ordering path or nucleation and growth mode depending upon ageing temperatures [2, 3]. Recently it has been reported that the increase of Mo in the alloy increases the precipitation kinetics and also raises the thermal stability of the Ni<sub>2</sub>(Cr,Mo) phase by increasing its solvus temperature [1]. However, the opposite effect of accelerated coarsening kinetics of the Ni<sub>2</sub>(Cr,Mo) affect the desired property for a stable microstructure. Tawancy et al. [4] has reported that addition of tungsten in Ni-Cr-Mo alloy, e.g. Hastelloy C and 276, improves the thermal stability of the microstructure by reducing the ordering kinetics. This effect has been attributed to different factors like sluggish diffusivity of W atoms and destabilization of Ni<sub>2</sub>(Cr,Mo) phase in presence of tungsten [4]. Recent study has also suggested that the presence of W in Ni-Cr-W alloy favor the formation of D0<sub>22</sub> structure over the Ni<sub>2</sub>(Cr,Mo) phase [5]. Thus, the aim of present manuscript is to investigate the role of W in ternary Ni-Cr-Mo alloy on the phase stability and precipitation kinetics and the investigation of the possibility of the multiple phase precipitation at different ageing temperatures.

**Experimental:** Ni-17.3Cr-12.9Mo-4.5W (in at%) alloy prepared by using an induction skull melting has been used in the present work. The bulk composition of the alloy was analyzed by using XRF analysis and found close to the desired composition of the alloy. The alloy was homogenized at 1300 °C for 36 h under flowing high purity argon gas and water quenched to solutionize the alloy in a single  $\gamma$ -phase. Subsequently, Alloy samples were aged at 665 °C and 720 °C for time periods upto 100 h for hardness studies and microstructural characterization. Hardness values of both solution treated samples as well as aged samples were measured using Vicker's microhardness tester using a constant load of 1 kgf to obtain average hardness of each sample on the basis of hardness measurement at 20 independent locations. The microstructural investigations of different samples were carried out using scanning electron microscope (SEM) and transmission electron microscope (TEM). Microstructural characterization was carried out on a Carl Zeiss make Field Emission Scanning Electron Microscope (FESEM) equipped with Energy Dispersive Spectrometer (EDS). Samples for

TEM analysis were prepared by electrolytic jet thinning in a solution of 20% perchloric acid and 80% ethanol maintained at -40 °C. TEM experiments were carried out using a Jeol 2000FX microscope operating at 160 kV. Standard TEM techniques such as bright-field (BF) and dark-field (DF) imaging and selected area electron diffraction (SAED) were employed. Order evolution path in the solutionized alloy samples was studied employing isochronal heating experiments at a heating rate of 5 °C/min using differential scanning calorimetry (DSC) and high temperature resistivity measurements. The thermal stability of the ordered phase in the aged samples was also studied using high temperature resistivity measurement. Details of sample preparation for resistivity measurement and other details of resistivity instrument are given elsewhere [3]. A heat flux differential scanning calorimeter from Mettler Toledo was used for phase transformations studies on about 0.5 mm thick sample slices.

**Results and discussion:** Fig. 1 shows SEM micrograph of the solutionized sample exhibiting formation of 2<sup>nd</sup> phase particles which appeared in the bright and light gray contrast in the backscattered electron image. These particles were mostly

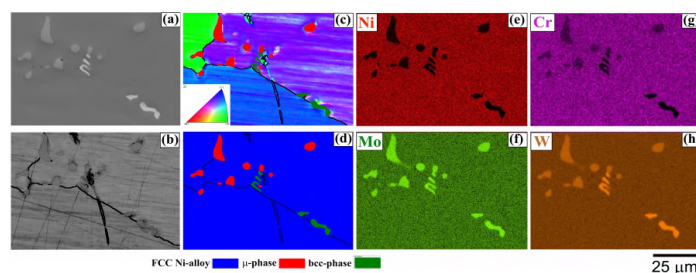


Fig. 1 (a) BSE image of the solutionized sample showing formation of bright and gray color precipitates at the grain boundaries of the austenite matrix. Figs. (b), (c) and (d) shows band contrast image, IPF map and phase map obtained from EBSD analysis of same region. Figs. (e) – (h) shows EDS elemental map revealing predominant enrichment of Mo and W solutes in two particles.

observed at the grain boundaries of the austenite  $\gamma$ -matrix. The elemental map obtained using EDS analysis revealed them enriched with Mo-W solutes and depleted from Ni and Cr solutes (Figs. 1e - 1h). The composition of bright particles was found to Mo-36.9at%W-6.4at%Cr-6.3at%Ni while light gray particles were having Ni-30.4at%Mo-16.7at%Cr-12.3at%W composition. EBSD analysis revealed bright and light gray particles corresponded to bcc phase of solid solution of W and Mo solutes and  $\mu$ -phase as shown in Fig. 1d showing phase map. Formation of mu-phase has been well known in alloys containing high concentration of refractory elements. Fig. 2



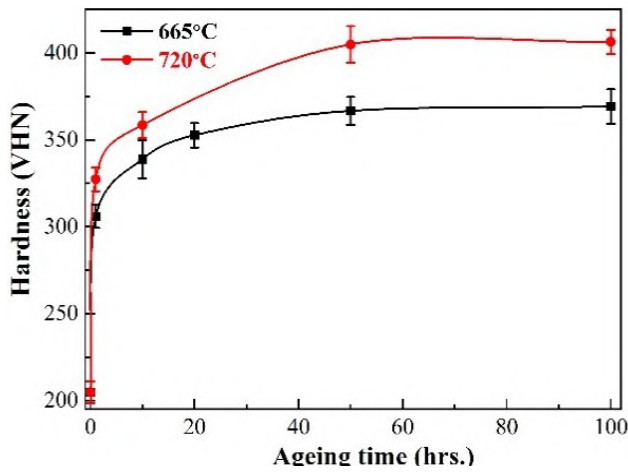


Fig.2 Plot showing variation of hardness as a function of time during ageing at two different temperatures.

shows the hardness plot of the alloy obtained from samples aged at 665 °C and 720 °C as a function of ageing time. It was clear from Fig. 2 that hardness increased sharply within few hours at both at both temperatures and then increased gradually to attain hardness plateau at 369 VHN and 406 VHN, respectively, within 100 h. Samples aged at 720 °C always exhibited higher hardness value than at 665 °C. Previous studies reports about 360 VHN peak hardness in Ni-16.7Cr-16.7Mo during ageing at 680 °C, which was attributed to the precipitation of the Ni<sub>2</sub>(Cr,Mo) phase particles. Likewise,

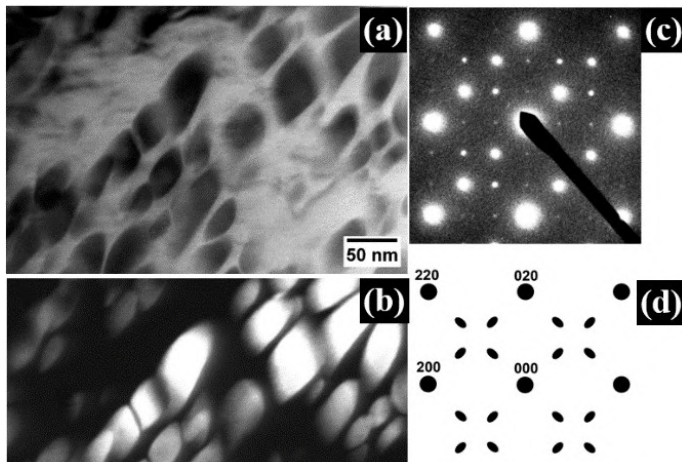


Fig. 3 (a) and (b) shows BF- and DF-TEM images of the nano-sized domains of the Ni<sub>2</sub>(Cr,Mo) phase particles. Fig. c shows SAED pattern in the <001> zone axis of the FCC crystal and (d) shows key to the diffraction pattern.

precipitates of same phase were attributed to similar hardness change in Ni-Cr-Mo-W- alloys, however, higher hardness of the alloy at 720 °C suggested the possibility of additional hardening phase at 720 °C. The nature of hardening phases in the sample therefore was investigated using TEM studies. Fig. 3a and 3b shows, respectively, a BF- and a DF- TEM micrographs of alloy sample aged at 720 °C for 100 h. SAED pattern corresponding to this sampling volume in the <001> orientation of the FCC crystal is shown in Fig. 3c. It was clear from the SAED pattern that g-vector connecting direct beam with {220} reflection of the FCC phase was trisected by superlattice reflections at 1/3{220} and equivalent positions. A key to diffraction pattern is given in Fig. 3d. A comparison of Fig.3c and Fig. 3d confirms the presence of superlattice reflections corresponding to Ni<sub>2</sub>(Cr,Mo) type phase. Fig. 3a

and 3b shows nano-sized precipitates of the Ni<sub>2</sub>(Cr,Mo) type phase in the black contrast and white contrast in the BF and DF TEM images, respectively. Surprisingly, no other hardening phase was identified in the TEM analysis. This has suggested the possibility of higher misfit strain contribution on the hardness property of the alloy possibly due to increase in the difference of lattice parameters of the matrix phase and the precipitate phases. The path of order evolution was mapped on the basis of calorimetry and resistivity studies on the solutionized samples. Fig. 4 shows a thermogram and resistivity plots during heating of samples at a controlled heating rate of 5 °C/min. The evolution of heat as well as of resistivity of the samples during heating appeared closely similar to that reported earlier on Ni-Cr-Mo alloys [2, 3]. The initial rise of resistivity in the temperature range from 500-550°C corresponded to the evolution of short-range-order that appeared as weak exothermic peak in the thermograph of DSC scan, while a sharp decrease of resistivity in conjunction with strong exothermic peak in the temperature range from 550-700°C represented the evolution of the long-range ordered precipitates of the Ni<sub>2</sub>(Cr,Mo) phase, in agreement with earlier work [2, 3]. This confirmed that the alloy undergoes similar order evolution path involving short-range-order to long-range-order to SRO and then to disorder, an ordering mechanism similar to that reported for Ni-Cr-Mo alloys.

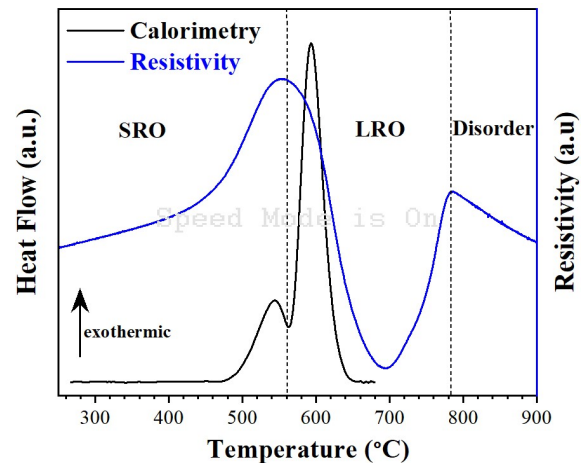


Fig. 4 shows a plot of differential scanning calorimeter thermogram superimposed with resistivity plot obtained during heating of samples at a rate of 5C/min on solutionized sample. Different regimes of the order evolution are marked in the plot.

#### References:

1. C.T. Sims, N.S. Stoloff, and W.C. Hagel: Superalloys II. Wiley, New York, 1987.
2. A. Verma, J. B. Singh, N. Wanderka, J K Chakravarty, Acta Materialia, Volume 96, 2015, 366-377.
3. A. Verma, Jung B. Singh, M. Sundararaman, Nelia Wanderka, Metallurgical and Materials Transactions A, 2012, No. 9, 3078-3085.
4. H. M. Tawancy, R.B. Herchenroeder & A. I. Asphahani, JOM, volume 35, 1983, 37-43.
5. A. Verma, J. B. Singh, Metallurgical and Materials Transactions A, Volume 52, 2021, 4317-4323.

Effect of CaF<sub>2</sub> on NdF<sub>3</sub> Solubility in Indian Molten Salt Breeder Reactor Salt SystemS. Kolay<sup>a</sup> and R. Mishra<sup>a\*</sup><sup>a</sup>Chemistry Division, Bhabha Atomic Research Centre, Mumbai-400 085, India..E-mail id: [mishrar@barc.gov.in](mailto:mishrar@barc.gov.in); Phone: +91-22-25592460; Fax: +91-22-25505151**Abstract**

The salt mixture containing 78 mol % LiF, 20 mol % ThF<sub>4</sub> and 2 mol % UF<sub>4</sub> is being considered as a potential fuel for the Indian Molten Salt Breeder Reactor (IMSBR). It is proposed to add 8 mol % CaF<sub>2</sub> to lower its melting point and also to reduce the <sup>7</sup>LiF loading. Here, we report the effect of CaF<sub>2</sub> on the solubility of NdF<sub>3</sub> which is one of the major fission products in IMSBR salt system employing XRD, DTA and quenching experiments. Significant decrease in NdF<sub>3</sub> solubility has been observed upon CaF<sub>2</sub> addition.

**Introduction**

Molten Salt Reactors (MSBRs) have attracted lot of attention in recent years due to their inherent safety features [1]. In these reactors, the molten fuel serves as the primary coolant and enables online reprocessing of spent fuel, achieve self sustainability <sup>233</sup>U/Th cycle, and makes the process proliferation resistant. Thermo-physical properties of molten salt like heat capacity, thermal conductivity and viscosity are among the most important parameters affecting the heat transfer properties and efficiency of these reactors. With increase in burn-up, these properties are expected to change due to presence of several fission and corrosion products which may react with the salt components resulting some high melting insoluble phase. Hence the solubility limits of major fission products and corrosion products in FS need to be investigated thoroughly. Rare earth metals are major fission products accounting for about 27 % of fission yield. Determination of the solubility limits of the REF<sub>3</sub> are, therefore, required to predict thermo-physical property and heat transport efficiency as a function of burn up. Here, we report the effect of CaF<sub>2</sub> on the solubility of NdF<sub>3</sub> as a representative of rare earth fluoride in 78 mol % LiF, 20 mol % ThF<sub>4</sub> and 2 mol % UF<sub>4</sub> at 700 °C employing XRD, DTA and quenching experiments.

**Experiments**

Salt mixture (78 mol% LiF, 20 mol% ThF<sub>4</sub> & 2 mol% UF<sub>4</sub>) and (70 mol% LiF, 8 mol% CaF<sub>2</sub>, 20 mol% ThF<sub>4</sub> & 2 mol% UF<sub>4</sub>) were prepared by melting the physical mixtures at 973 K under flowing Ar + HF(g) mixture. DTA experiments were carried out by taking 75 mg of the salt mixtures in Pt-crucible and heating/cooling under purified argon flow. For quenching experiments, 200 mg salt mixtures were heated at 973 K for 3 hours and then quenched at 77 K (liq. N<sub>2</sub>). PXRD were recorded using Ni filtered Cu-K $\alpha$  radiation.

**Results & Discussions**

Negligible mass change was observed during the synthesis of FS and modified FS indicating that no vaporization loss or any chemical reaction due to moisture or oxygen has taken place during the synthesis of salt mixture. DTA plots of fuel salt without CaF<sub>2</sub> with gradual addition of NdF<sub>3</sub> are shown in figure 1A. The gradual shifting in peak temperature for FS, FS + 3 mole % NdF<sub>3</sub> and FS + 7.5 mol % NdF<sub>3</sub> followed by no change in DTA pattern for FS + 10 mol % NdF<sub>3</sub> indicates that there is no change in nature of chemical interaction between NdF<sub>3</sub> and the components of FS beyond 7.5 mol % of NdF<sub>3</sub> addition. Hence from the DTA data it may be assumed that the solubility of NdF<sub>3</sub> in FS is less than 10 mol %. DTA plots of fuel salt containing 8 mol% CaF<sub>2</sub> is shown in figure 1B. Here, unlike previous case, specific area of the main

melting peak gradually decreases upon NdF<sub>3</sub> addition indicating the formation of compound whose formation energy counter balance the melting enthalpy.

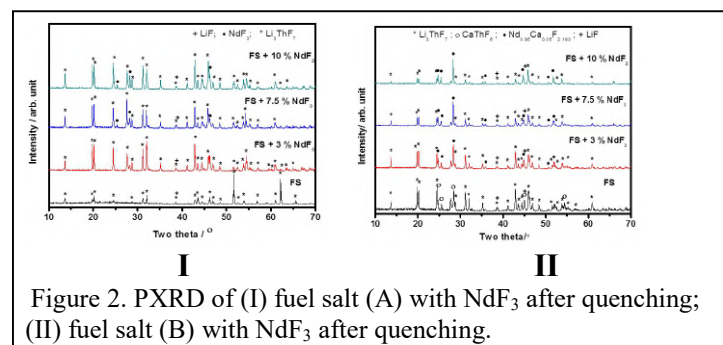
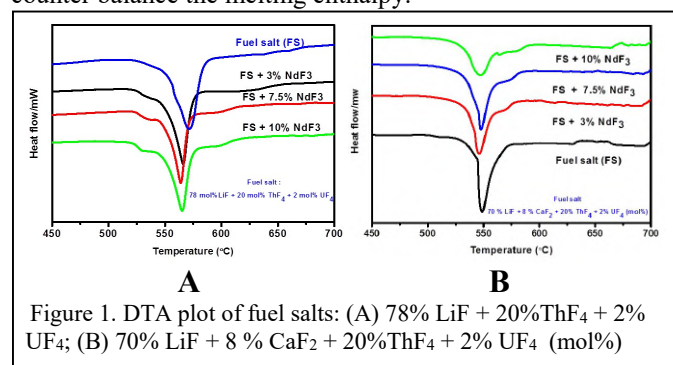


Figure 2 shows the PXRD patterns of the mixture after quenching from 973 K to 77 K. From the analysis, It has been observed that fuel salt (A) consists of Li<sub>3</sub>ThF<sub>7</sub> and LiF. Below 7.5 mol% NdF<sub>3</sub>, no extra peak due to free NdF<sub>3</sub> was observed. From 7.5 mol % and above in addition of Li<sub>3</sub>ThF<sub>7</sub> & LiF, additional extra peaks due to NdF<sub>3</sub> was observed. So, from DTA and XRD of quenched samples, it can be conclude that for salt system without CaF<sub>2</sub>, NdF<sub>3</sub> solubility limit is below 7.5 mol%. PXRD of salt mixture with 8 mol% CaF<sub>2</sub> indicates the presence of Li<sub>3</sub>ThF<sub>7</sub>, CaThF<sub>6</sub> and LiF. Upon NdF<sub>3</sub> addition, starting from from 3 mol% NdF<sub>3</sub>, CaThF<sub>6</sub> phase gradually disappear with the formation a high melting new phase Nd<sub>0.95</sub>Ca<sub>0.05</sub>F<sub>2.183</sub>.

**Conclusion:**

Presence of CaF<sub>2</sub> leads to a significant decrease in NdF<sub>3</sub> solubility with the formation of a high melting Nd<sub>0.95</sub>Ca<sub>0.05</sub>F<sub>2.18</sub> secondary phase.

**References**

- Serp. J. et. al.; "The molten salt reactor in generation IV: Overview and perspective", Progress in Nuclear Energy, 77 (2014)308.

## Experimental and FEM Cooling Curve Simulations in End Quench Treatment and Hardness Profile Determination of Low Alloy Steel for Reactor Pressure Vessel Applications.

Vaibhav Patel <sup>a,b</sup>, Chiradeep Gupta <sup>a,b</sup>

<sup>a</sup> Mechanical Metallurgy Division, Bhabha Atomic Research Centre, Mumbai – 400085, India.

<sup>b</sup> Homi Bhabha National Institute, Anushaktinagar, Mumbai- 400094, India.

### Abstract

A combined experimental and computational thermal analysis of the end quench treatment is undertaken to determine the cooling curve and hardness prevailing in a cylindrical sample of 1045 from literature and low alloy steel from the end quench experiments conducted. The hardness profile across the end quench sample shows that the presence of alumina filled internal hole appreciably reduces the cooling rate across the sample cross-section.

### 1. Introduction

The end quenching experiment is a convenient method to generate thermal conditions for investigating mechanical properties developed in components under cooling rate gradients. This is an important consideration to understand the variation of tensile and fracture properties commonly observed in large thick section components such as nuclear reactor pressure vessel. In this work end quench experiment has been carried out on an eastern grade RPV steel with simultaneous monitoring of the temperature profile at a single section. Hardness variation as a function of distance from the quenched end was carried out along with finite element modelling of the experimentally measured cooling temperature – time profile using transient heat transfer equation. The work validates the FEM simulation of thermal analysis of the end quench sample and determines the hardness profile developed in the low alloy steel after end quench treatment.

### 2. Experimental and Analytical Methods.

The End quench test sample used for the study is adopted from the sample design for Jominy test given in ASTM A255 – 20. An internal hole is drilled at the centre of cylindrical sample of diameter 6 mm and length 63 mm from the top surface upto a distance of 55mm away from the quench end. The thermocouple at one end is spot welded and inserted inside the sample and for ensuring its contact with the sample material the remaining space is filled with alumina wool and alumina cement. Radiography of the sample has been done to ensure that the thermocouple remains in contact with the material. The sample is heated upto a temperature of 1010°C and held for 50 mins for homogeneous austenization. The sample is then placed in Jominy Apparatus such that quenching at the bottom surface of the sample occurs by continuous flow of water as shown in fig.

The temperature data was recorded in Data Logger with sampling rate of 8 Hz and the cooling curve is

plotted. The samples of approximately 1.2 - 2.5mm in length were cut and hardness values at different locations were measured by making indents with load 5Kg and dwell time of 10 secs.

#### Analytical Methods

FEM Simulations for cooling curves were carried out in ABAQUS. The specimen experiences all 3 modes of heat transfer

- 1) Conduction within the specimen
- 2) Convection between the surface of specimen and air in the environment except the bottom surface which is subjected to convective heat transfer by fountain of water.
- 3) Radiative heat transfer also takes place through all surfaces.

The Fourier's Equation of Heat Transfer through Conduction is given by,

$$Q = -k. A. \nabla T$$

$Q$  = Heat Flux.

$k$  = Conductivity of material.

$\nabla T$  = spatial Temperature Gradient.

The Newton's Law of Cooling is given by,

$$Q = -h. A. \Delta T$$

$h$  = Convective heat transfer Coefficient.

$A$  = Surface area through which Convection takes place.

$\Delta T$  = Temperature difference between the material and ambient temperature.

Heat Transfer through Radiation

$$Q = \sigma. e. A. (T^4)$$

$\sigma$  = Stefan - Boltzmann Constant.

$e$  = Emissivity of the Material.

$T$  = Absolute Temperature.

Initial and Boundary Conditions

The temperature of heated sample from which quenching will take place at time (t) = 0secs is the initial condition.

The values of  $h_{air}$ ,  $h_{water}$ ,  $k_{material}$ ,  $\sigma$ ,  $e$  and ambient Temperature are the boundary conditions.

Latent heat was not considered during simulation.

### 3. Results and Conclusion

The FEM simulation based on 3D axi-symmetric model of one-half of the sample to simulate a cooling curve of AISI 1045 steel reported in literature [2,3] was carried out with the values of thermal conductivity of the material, and air, and heat transfer coefficient of water as .....The Fig.1 shows the experimental cooling rate from research paper and simulated by our model. There is good match between the experimental and simulated cooling curve values.

The Fig.2 shows the cooling curves obtained from end quench experiment and simulated by FEM model used for the 1045 steel sample. In the simulation the HTC of air was made temperature dependent to account for the oxide formation of steels during cooling from elevated temperature.

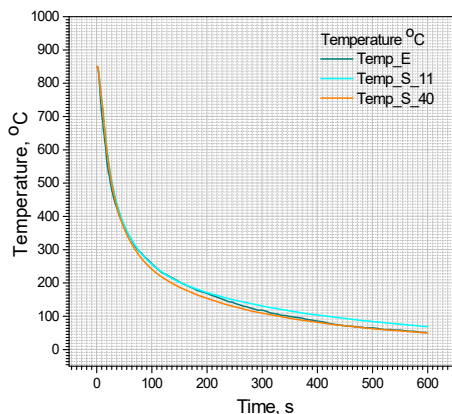


**Fig.1 Experimented and Simulated Cooling Curves of AISI 1045 Steel.**

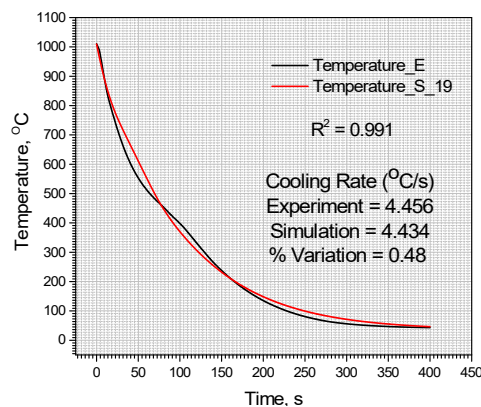


**Fig.2 Experimented and Simulated Cooling Curves of CrMoV steel**

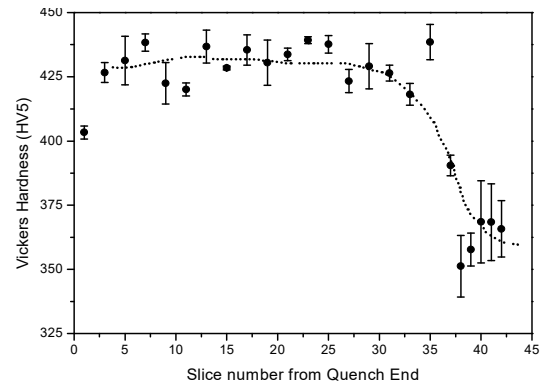


**Fig.3 Hardness Variation along the length of the specimen.**

The hardness profile along the length has been shown in Fig.3. The higher cooling rate corresponds to high hardness region and comparatively lower cooling rate corresponds to lower hardness. The cooling rate decreases as we move away from the quench end. Lowering the cooling rate below  $\sim 4.5$  C/min to the hardness drops in the vicinity of internal hole. Hence it can be concluded that the alumina filled hole retards the cooling rate developed in the low alloy steel.

### 4. References.

- 1) Huiping, L., Guoqun, Z., Shanting, N. and Chuanzhen, H., 2007. FEM simulation of quenching process and experimental verification of simulation results. *Materials Science and Engineering: A*, 452, pp.705-714.
- 2) Esfahani, A.K., Babaei, M. and Sarrami-Foroushani, S., 2021. A numerical model coupling phase transformation to predict microstructure evolution and residual stress during quenching of 1045 steel. *Mathematics and Computers in Simulation*, 179, pp.1-22.
- 3) Nunura, C.R., dos Santos, C.A. and Spim, J.A., 2015. Numerical-Experimental correlation of microstructures, cooling rates and mechanical properties of AISI 1045 steel during the Jominy end-quench test. *Materials & Design*, 76, pp.230-243.
- 4) Elmaryami, A.S. and Omar, B.B., 2013. Transient Computer Simulation of Industrial Quenched Steel Bar to Determine the Lowest Hardness Point of Molybdenum and Boron Steel at 850 C as Austenitizing Temperature Quenched in Different Medium. *International Journal of Materials Science*, 8(1), pp.13-28.
- 5) Liu, L., Liao, B., Li, D., Li, Q., Wang, Y. and Yang, Q., 2011. Thermal-elastic-plastic simulation of internal stress fields of quenched steel 40Cr cylindrical specimens by FEM. *Materials and Manufacturing Processes*, 26(5), pp.732-739.

## The phase relation and correlated thermal analysis of U-Y-O system

Muhammed Shafeeq<sup>a</sup>, Geeta Patkare<sup>a</sup> and Rohan Phatak<sup>a\*</sup>

<sup>a</sup>Fuel Chemistry Division, Bhabha Atomic Research Centre, Mumbai

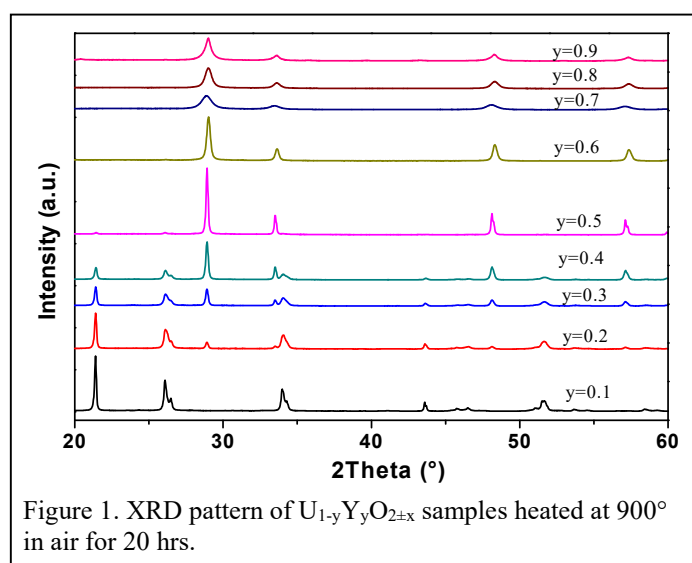
\* Rohan Phatak, [raphatak@barc.gov.in](mailto:raphatak@barc.gov.in), 022-25594593

### Abstract

To study the phase relation, various compositions of  $U_{1-y}Y_yO_{2+x}$  (where  $y = 0.1, 0.2, 0.3, 0.4, 0.5, 0.6, 0.7, 0.8$  and  $0.9$ ) were synthesized using citrate nitrate gel combustion method. Phase relation study was carried out under oxidized and reduced conditions. Correlated study of thermogravimetric and high temperature X-ray diffraction data analysis was used to investigate the oxidation of representative reduced sample  $U_{0.6}Y_{0.4}O_{2+x}$ .

Thermal analysis and thermo-physical studies of U-RE-O (RE: Rare Earth) system are critical for understanding its behavior under high-temperature conditions relevant to nuclear fuel applications and ceramic materials design [1]. Studies on uranium oxides have demonstrated their complex temperature dependent phase transitions, which are pivotal in fuel performance under reactor conditions [2]. It is well known that aliovalent doping with  $RE^{3+}$  cation inhibits the formation of  $U_3O_8$  phase, restricting it to fluorite structure [3], yet the detailed phase relation with smaller 3+ cations are not well studied. The current study investigates U-Y-O system where yttrium is chosen considering as smallest +3 substitutional cations.

$U_{1-y}Y_yO_{2+x}$  (where  $y = 0.1, 0.2, 0.3, 0.4, 0.5, 0.6, 0.7, 0.8$  and  $0.9$ ) were prepared by citrate nitrate gel combustion method followed by heating at  $700^\circ\text{C}$  in air atmosphere to remove residual carbon. The samples were further heated up to  $900^\circ\text{C}$  for 20 hrs in air atmosphere. XRD pattern of samples were recorded using X-ray diffractometer with Cu target in  $2\theta$  range  $10-100^\circ$ . A part of the sample was reduced at  $900^\circ\text{C}$  in Ar-8%  $H_2$  atmosphere. Thermo gravimetric (TG) and high temperature XRD (HTXRD) data of representative reduced sample,  $U_{0.6}Y_{0.4}O_{2+x}$  was recorded up to  $900^\circ\text{C}$  in air atmosphere. Considering the TG curve, XRD data was recorded at selected temperatures in  $2\theta$  range  $18-65^\circ$  with fast recording speed to attain the same conditions of TG curve. Phase quantification in the biphasic region and the lattice parameters were obtained by Rietveld refinement of XRD data.



from  $y=0.2$  to  $y=0.5$  biphasic ( $M_3O_8$ +fluorite phase) is observed with amount of fluorite increasing with yttrium concentration. For compositions  $y=0.6$  to  $y=0.8$ , pure fluorite phase is observed. Above which at composition  $y=0.9$ , residual  $Y_2O_3$  phase is visible.

For the samples heated in reducing atmosphere up to  $900^\circ\text{C}$ , for the composition  $y=0.1$  shows single fluorite phase. From compositions  $y=0.2$  to  $y=0.5$  XRD pattern shows mixture of two fluorite phases. For compositions  $y=0.6$  to  $y=0.8$ , again presence of single fluorite phase is observed. This observation indicates that under the current reducing conditions  $M_3O_8$  phase and fluorite phase present in the oxidized samples get reduced to two separate fluorite phases FCC1 and FCC2, respectively. FCC1 formed from  $M_3O_8$  ( $M = U_{0.9}Y_{0.1}$ ) shows higher lattice parameters compared to FCC2 which is formed from oxidized fluorite phase having tentative composition  $U_{0.5}Y_{0.5}O_{2+x}$ .

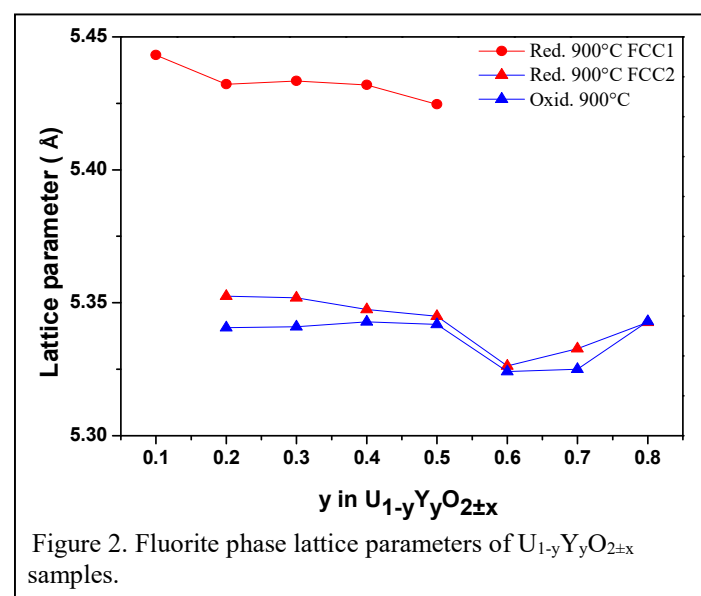


Figure 2. Fluorite phase lattice parameters of  $U_{1-y}Y_yO_{2+x}$  samples.

Figure 2 shows lattice parameter (LP) of fluorite phases for the samples heated in air and reducing atmospheres at  $900^\circ\text{C}$ . FCC2 which is formed from the oxidized fluorite phase shows similar lattice parameter with reduced lattice parameter slightly greater than the oxidized due to conversion of  $U^{6+}$  to  $U^{4+}$  during the reduction. At composition  $y=0.6$ , there is sudden dip in the LP which may be due to change over from hyper-stoichiometric composition to hypo-stoichiometric composition but need to be verified by O/U analysis.

Figure 1 shows the XRD pattern of the samples heated up to  $900^\circ\text{C}$  in air atmosphere for 20hr. For the composition  $y = 0.1$ , single  $U_3O_8$  type phase was observed above which at composition  $y = 0.2$  minor quantity of fluorite phase is visible indicating solubility of yttrium is up to 10 atom % in  $U_3O_8$  phase (hence forth called as  $M_3O_8$  phase). For all the compositions

To understand the oxidation reaction for the series, TG and HTXRD of reduced sample with composition  $y=0.4$  was recorded as a representative sample of the series. TG curve of  $U_{0.6}Y_{0.4}O_{2+x}$  shows two step weight gains up to  $900^\circ\text{C}$ , similar to  $UO_2$  oxidation curve. As the reduced sample,  $y=0.4$  shows mixture of two fluorite phases FCC1 and FCC2, the gain in the oxidation will be contributed by both the phases and cannot be

estimated individually. To decipher this HT-XRD of the same sample was recorded in the similar condition as TG experiment.

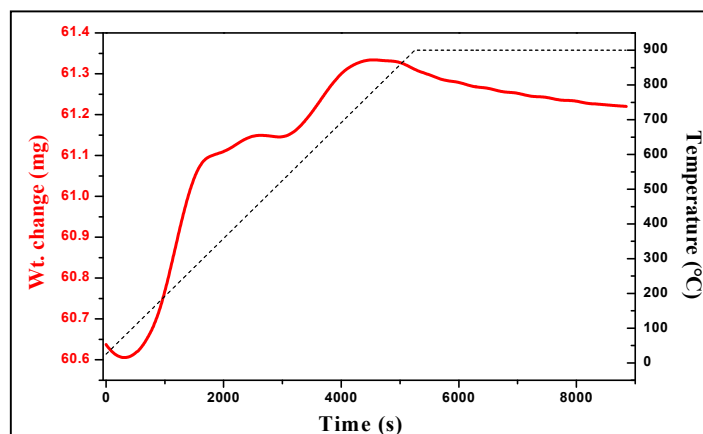


Figure 3. Thermogravimetric curve of reduced sample with composition  $y=0.4$  heated up to  $900^{\circ}\text{C}$  in air atmosphere.

Considering TG curve, various temperatures were selected to record the HT-XRD data during oxidation of reduced sample with composition  $y=0.4$ . The recorded HT-XRD data at few specific temperatures are shown in the figure 4. The HT-XRD data shows presence of two fluorite phases, FCC1 and FCC2 below  $560^{\circ}\text{C}$ . Above this temperature,  $\text{M}_3\text{O}_8$  lines appear in the HT-XRD and this temperature match with the plateau region of first step in TG curve. This correlation shows that the first step in the oxidation is due to oxidation of fluorite phases without formation of  $\text{M}_3\text{O}_8$  phase. The second step in the oxidation corresponds to formation of  $\text{M}_3\text{O}_8$  phase from FCC1 phase. This is clearly observed in the HT-XRD data where intensity of FCC1 decreases and  $\text{M}_3\text{O}_8$  phase increases with increase in temperature above  $560^{\circ}\text{C}$ .

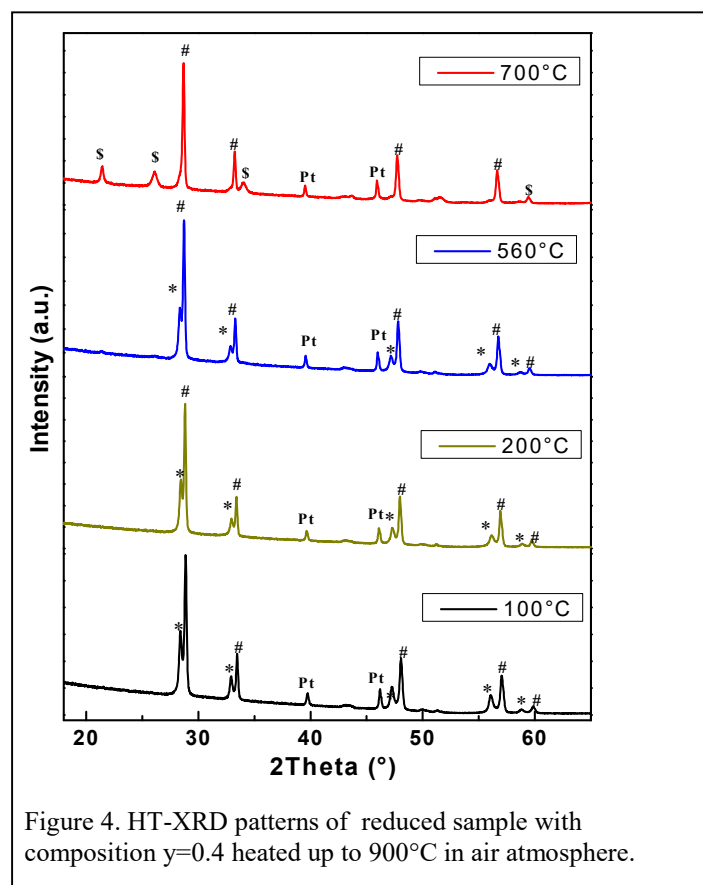


Figure 4. HT-XRD patterns of reduced sample with composition  $y=0.4$  heated up to  $900^{\circ}\text{C}$  in air atmosphere.

The lattice parameters of fluorite phases were refined using HT-XRD data and are shown in the figure 5. As seen in the figure, LP of FCC2 does not have much variation except linear increase due to normal thermal expansion, whereas FCC1 phase shows no linear trend. The LP of FCC1 increases linearly up to  $150^{\circ}\text{C}$  and above which there is decrease in the LP which is due to oxidation. This indicates that FCC1 is responsible for the weight gain in the first step of TG curve. Above  $250^{\circ}\text{C}$ , the LP again shows linear trend up to  $560^{\circ}\text{C}$  which indicates that oxidation of FCC1 is complete at  $250^{\circ}\text{C}$  and later linearly increase due to thermal expansion. Above  $560^{\circ}\text{C}$ , the FCC1 phase decomposes to form  $\text{M}_3\text{O}_8$  which also corresponds to second step in TG curve.

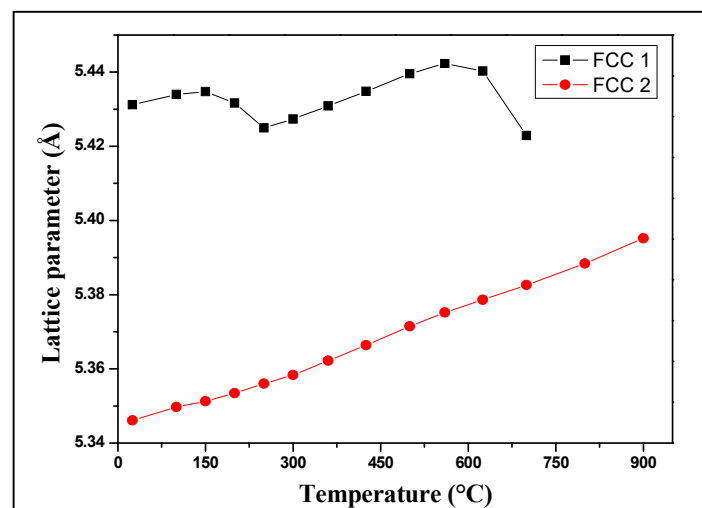


Figure 5. Lattice parameters of two FCC phases obtained from HTXRD analysis of reduced sample with composition  $y=0.4$

## Summary

U-Y-O phase relation was studied in oxidized and reduced atmospheres up to  $900^{\circ}\text{C}$ . In oxidized samples  $\text{U}_3\text{O}_8$  phase shows solubility of yttrium up to 10 atom %. At composition 60 atom % of yttrium pure fluorite phase is formed. The solubility breaks at 90 atom % of yttrium with formation of  $\text{Y}_2\text{O}_3$  as additional phase.

In reduced condition with low synthesis temperature, there is formation of two separate reduced fluorite phases formed from  $\text{M}_3\text{O}_8$  and oxidized fluorite phase.

Thermogravimetry and HT-XRD studies were correlated to decipher the oxidation reaction. It is observed from the correlated analysis that, FCC1 phase which is formed from  $\text{M}_3\text{O}_8$  undergoes oxidation in two steps while FCC2 phase almost remains the same with minor oxidation.

## References

1. Fujino T, Miyake C, in; Handbook on the physics and chemistry of actinides, Vol. 6, (Ed) A.J. Freeman, C. Keller, Elsevier, Amsterdam (1991) 155.
2. McEachern RJ, Taylor P. A review of the oxidation of uranium dioxide at temperatures below  $400^{\circ}\text{C}$ , J Nucl Mater., 254 (1998) 87.
3. W.B. Wilson; Stabilization of  $\text{UO}_2$ , J. Inorg. Nucl. Chem., 20 (1961) 242.

## Investigations Into Steady-State Comparative Techniques For Determining The Thermal Conductivity Of Irradiated Nuclear Fuel

Farman Ali<sup>a,\*</sup>, A. Bhandekar<sup>b</sup>, P. Mishra<sup>b</sup> and P.P. Nanekar<sup>b</sup>

<sup>a</sup>Radio Metallurgy Division, BARC, Mumbai, India

<sup>b</sup>Post-Irradiation Examination Division, BARC, Mumbai, India.

\* [farman@barc.gov.in](mailto:farman@barc.gov.in), 022-25596109

### Abstract

Thermal conductivity is essential for optimizing thermal systems, particularly in nuclear power, as it affects heat transfer and fuel safety. Understanding how irradiation impacts fuel conductivity is key to improving fuel design. This work proposes a new method to estimate the thermal conductivity of irradiated fuel in hot cell conditions. An experimental setup using fins, based on the modified Jaeger and Disselhorst method, heats one end of the specimen while the other is exposed to ambient conditions. Applying fin heat transfer theory, the temperature profile along the specimen allows for a qualitative estimate of thermal conductivity through comparative analysis.

Thermal conductivity, a key property for heat transfer, is crucial in reactor design and safety. While various methods like Guarded Hot Plate Method [1], Direct Heating Method [2], Jaeger and Disselhorst method [3] etc are used for measuring thermal conductivity, irradiated fuel poses challenges due to radiation interference with electronic and optical systems [4]. Measurements must be conducted in shielded environments like hot cells to avoid gamma radiation.

Methods like Guarded hot plate, Laser flash and hot wire are unsuitable due to refabrication issues and electronic complexity. The direct heating method, though simpler, involves complex components, making it difficult for hot cell operation. In this work, a modified Jaeger and Disselhorst method is proposed using half of the symmetric setup with one furnace-heated end and the other exposed to ambient conditions. Applying fin heat transfer theory, a temperature profile can be measured to estimate thermal conductivity qualitatively. The finite element simulations used for design and validation of test setup and final experimental test setup is discussed in the subsequent section.

The experimental test setup features a copper block with an outer diameter (OD) of 50 mm and a length of 150 mm, surrounded by a furnace with a 65 mm OD. The entire setup is insulated with glass wool, having an OD of 90 mm. Inside the copper block, three circular fins are arranged in a triangular pitch, with each fin having an outer diameter of 14.5 mm and a pitch circle diameter of 28.9 mm. The fins extend 300 mm in length, with 52 mm embedded in the copper block for secure placement. Experimental test setup is shown in Figure 1.

The copper block serves as the base material, offering strength, while the furnace is made of stainless steel for durability and heat resistance. The fins are made from stainless steel (SS), mild steel (MS), and aluminum (Al). These straight cylindrical fins are fixed within the copper block using melted lead shots to ensure stability and optimal thermal contact. Temperature measurements are taken with thermocouples that have a resolution of 1°C, allowing precise monitoring of thermal gradients and fluctuations within the system.

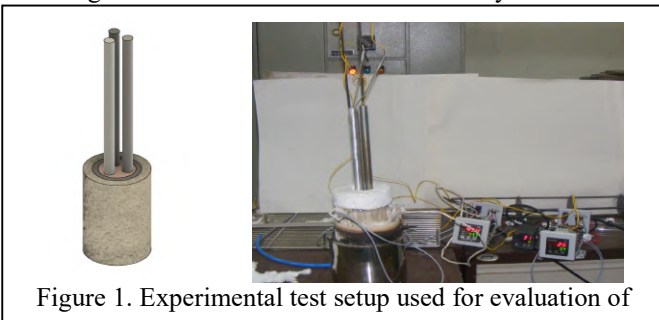


Figure 1. Experimental test setup used for evaluation of

To determine the optimal location for temperature measurement along the fin, a finite element analysis was performed to identify where the temperature difference between the two bars is maximized, ensuring accurate thermocouple measurements. A finite element model of a solid lead rod (with thermal conductivity,  $K = 35 \text{ W/mK}$ ) was created, with one end heated to  $350^\circ\text{C}$  and the other exposed to ambient conditions.

A steady-state thermal analysis was conducted, and the resulting temperature contour is shown in Figure 2(a). The temperature decreases continuously along the rod's length. The same analysis was repeated for a mild steel (MS) rod ( $K = 45 \text{ W/mK}$ ), with the temperature contour comparison shown in Figure 2(b). It is evident that the temperature drops more rapidly in mild steel than in lead, due to the higher conductivity of mild steel. The maximum temperature difference was found to occur approximately 75 mm (Figure 2(c)) from the heated end of the rod, which is the location used for temperature measurements in the experiments.

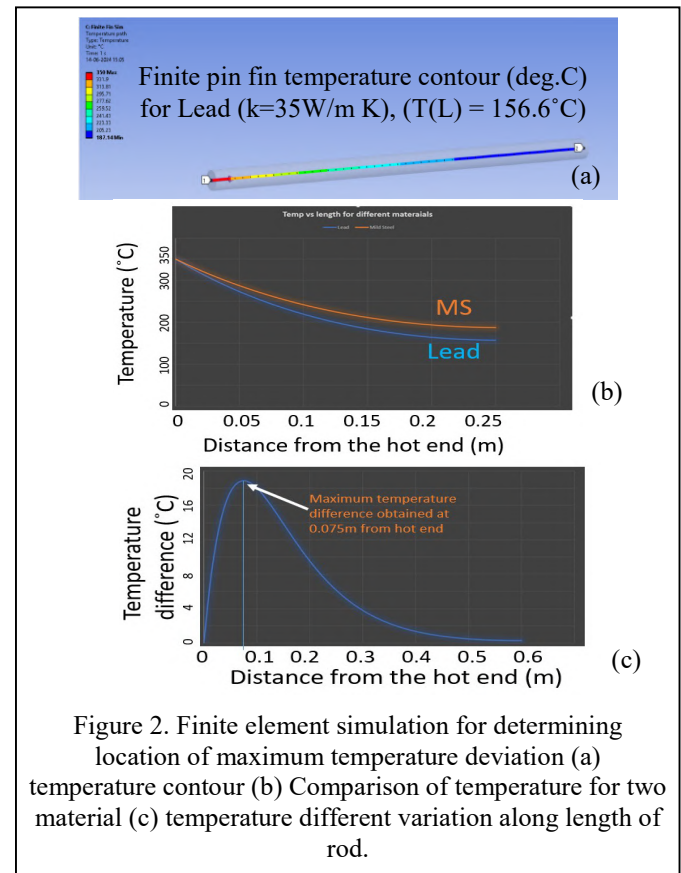
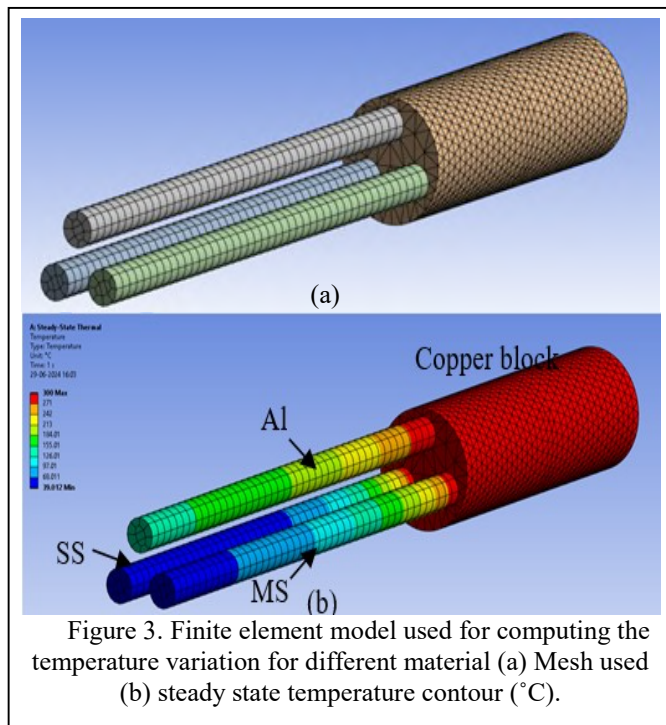


Figure 2. Finite element simulation for determining location of maximum temperature deviation (a) temperature contour (b) Comparison of temperature for two material (c) temperature different variation along length of rod.

Once the experimental setup is ready, the furnace is turned on to heat the copper block to 300°C. The ambient temperature is recorded, and the heat transfer coefficient for natural convection is obtained from the literature. Thermocouples are attached at 75 mm away from the hot ends, and temperature data is collected from these points. The measured temperature of Al, Mild Steel and SS is around 210, 131 and 97 °C respectively. This indicates the temperature at the ends are proportional to the thermal conductivity of the material since  $K_{Al} > K_{MS} > K_{SS}$ .

The entire test setup, as described earlier, was modeled using finite element analysis to assess the temperature variation along the length of the fins. This analysis also predicts the temperatures at both the ends and at the 75 mm point from the hot ends of the fins, helping to evaluate whether the setup is suitable for determining the thermal conductivity of an unknown sample. The copper block was maintained at 300°C, with an ambient temperature of 35°C and a convective heat transfer coefficient of 23 W/m<sup>2</sup>·K as the boundary conditions.

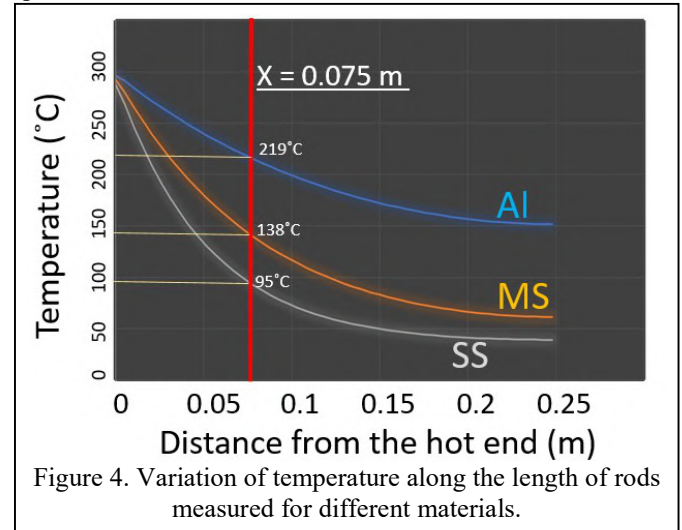
A mesh convergence study was performed, and the final mesh used is shown in Figure 3(a). The steady-state temperature contour plot is presented in Figure 3(b). It is evident that the temperature decreases continuously along the length of the rods. The copper block maintains a temperature close to 300°C throughout the simulation. A larger temperature drop is observed for SS material compared to Al and MS, owing to its lower thermal conductivity.



The temperature variation along the length of the rod was evaluated for all materials. From Figure 4, it was observed that the temperature continuously decreases along the rod from the hot end. The temperature drop is more pronounced for materials with lower thermal conductivity, such as SS, compared to others. This is attributed to the rapid heat transfer from the copper block to the opposite end exposed to the ambient environment, resulting in a higher temperature at the cold end. A similar trend was observed in the experimental results.

A comparison between the simulation and experimental temperature data at the 75 mm location from the hot end is presented in Table 1. The results show excellent agreement between the experimental and simulated temperatures. Any

slight deviation in temperature may be due to factors such as imperfect contact between the copper block and the fins, errors in measuring the thermal conductivities of the three specimens



using the laser flash method, limitations in the thermocouple's least count and resolution, the angle at which the thermocouple contacts the fin tips, insulation losses, fluctuations in furnace temperature causing disturbances in the steady state, etc. However, the errors remain within a 5% margin, confirming that the test setup is suitable for the qualitative evaluation of the thermal conductivity of an unknown sample.

**Table 1.** Comparison of temperature of different material measured at 75 mm distance from the hot end.

Material	Measured temperature (°C)	Simulated temperature (°C)	Absolute error (%)
Aluminum 6061 (k = 190 W/mK)	210	219	4.2
Mild Steel (k = 45 W/mK)	131	138	5.1
Stainless Steel (k = 17 W/mK)	97	95	2.2

To determine the thermal conductivity of an unknown sample or nuclear fuel rods inside the hot cell, the following simple and reliable procedure will be used. Two rods with known thermal conductivities are placed inside a solid copper block, which has blind holes for rod placement. These rods should be chosen so that the thermal conductivity of the unknown sample falls between the thermal conductivities of the two known rods. The unknown rod or irradiated fuel pins are placed in a third blind hole in the copper block. The copper block is then heated to a specific temperature (300°C in our case), and the entire setup is maintained at this temperature until a steady state is achieved. The temperature at a specific location or at the ends of the rods is then recorded, which is related to their thermal conductivity. The temperature of the unknown sample will provide a qualitative estimate of its thermal conductivity range.

#### References

1. S. Dubois and F. Lebeau. *Materials and Structures*, 48 (2013) 407-421.
2. Y. Tomo, H. Koga, T. Fukunaga, K. Kurata, H. Matsuno, K. Tanaka and H. Takamatsu. *International Journal of Heat and Mass Transfer*, 176, (2021) 121501.
3. R.D. Patel, C.J. Patel and P.R. Patel. *International Journal of Emerging Technologies and Innovative Research*, 3(2) (2016) 51-58.
4. T.R. Pavlov, S.C. Middlemas, B.D. Miller, F. Cappia, J.I. Cole and J.J. Giglio. *Journal of Nuclear Materials*, 557(15) (2021) 153280.



## Investigations on alternate fuel salt of Indian Molten Salt Reactor

Shubham Narang<sup>a,b</sup>, \*Rimpi Dawar<sup>a,b</sup> and \*Ratikanta Mishra<sup>a,b</sup>

<sup>a</sup>Chemistry Division, Bhabha Atomic Research Centre, Trombay, Mumbai-400085

<sup>b</sup>Homi Bhabha National Institute, Anushaktinagar, Mumbai- 400094

\*Email id: [rimpid@barc.gov.in](mailto:rimpid@barc.gov.in), [mishrar@barc.gov.in](mailto:mishrar@barc.gov.in)

### Abstract

In this work, the vaporization behavior of molten salt reactor fuel having composition 53.5 mol % NaF, 40 mol % ZrF<sub>4</sub> and 6.5 mol % UF<sub>4</sub> was carried out. The vapour pressure of the above fuel salt was compared with the fuel salt of composition 53.5 mol % NaF, 30 mol % ZrF<sub>4</sub>, 10 CaF<sub>2</sub> and 6.5 mol % UF<sub>4</sub>. Significant reduction in vapour pressure and having other favourable properties of this composition makes it one among the promising fuel salt composition which does not require <sup>7</sup>LiF and BeF<sub>2</sub>.

Molten Salt Reactors (MSRs) are Gen-IV fluid fuel reactors having potential to achieve self-sufficiency in Th-<sup>233</sup>U fuel cycle that makes them a viable alternative for large scale thorium utilization. Many flagship projects for the development of the MSRs and related technologies have been initiated worldwide to meet the long-term energy needs. These reactors have gained increased attention due to their better safety characteristics, outstanding heat transport properties, higher thermodynamic efficiency, and resistance to proliferation etc. [1, 2].

Presently, salt mixtures containing LiF, BeF<sub>2</sub>, ThF<sub>4</sub> and UF<sub>4</sub>, is being considered as possible fuel salts for Indian molten salt reactor. However, these salt mixtures require huge amount of 99.99% <sup>7</sup>Li-enriched LiF, which is quite challenging. In addition, handling of toxic BeF<sub>2</sub> in laboratory is also problematic due to chemical toxicity associated with it [3]. In view of this, research on finding out a new salt composition has been initiated in our group. Salt containing 53.5 mol % NaF, 40 mol % ZrF<sub>4</sub> and 6.5 mol % UF<sub>4</sub> was used in ARE (Aircraft reactor experiment by ORNL in 1954) due to its favourable thermal properties and high solubility for fission products [4]. The eutectic composition of this system NaF-ZrF<sub>4</sub>-UF<sub>4</sub> is shown in Fig. 1. This composition is promising in terms of low melting point (540 °C) and does not require <sup>7</sup>LiF and BeF<sub>2</sub>. However, due to high vapor pressure of ZrF<sub>4</sub>, the composition of this salt mixture continuously changes, which alters the thermo-physical properties of the fuel salt (FS). In order to reduce the vaporization loss of ZrF<sub>4</sub>, additional component such as CaF<sub>2</sub> in various mole ratios were mixed with the above fuel salt and their melting & vaporization behavior were determined.

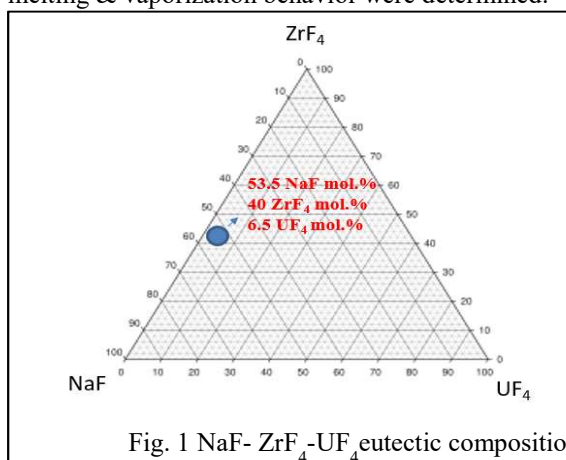


Fig. 1 NaF- ZrF<sub>4</sub>-UF<sub>4</sub> eutectic composition

As fluorides are hygroscopic in nature, all the chemicals were dried by heating at 323 K for 8 h under dynamic vacuum of the order 10<sup>-6</sup> mbar to eliminate any traces of moisture. These dried chemicals were characterized for their phase purity using powder X-ray diffraction technique prior to their use in the current study.

Thermal analysis for the salt mixture containing 53.5 mol % NaF, (40-x) mol % ZrF<sub>4</sub>, x mol% CaF<sub>2</sub> (x = 0 and 10) and 6.5 mol % UF<sub>4</sub> was carried out employing a TG-DTA instrument (SETSYS Evolution, M/s Setaram, France). The mass sensitivity of this instrument is 0.1 µg. The temperature calibration of this instrument was carried out by determining the melting points of pure metals viz., Au, Pd, and Al which was found to be within ±1 K. The temperature was measured using Pt-Rh10% / Pt thermocouple (S type) which was kept in close proximity to the sample holder. The carrier gas flow over the sample was controlled and measured by means of using a mass flow controller. The sample was heated in platinum crucible (capacity~100 µl) with lid under the continuous flow of argon gas maintained at 0.020 dm<sup>3</sup> min<sup>-1</sup> during each experiment.

The TG plot of the salt mixture containing of 53.5 mol % NaF, (40-x) mol % ZrF<sub>4</sub>, x mol% CaF<sub>2</sub> (x = 0 and 10) and 6.5 mol % UF<sub>4</sub> heated at a rate of 10 K/min is shown in In Fig. 2. From the TG curve it can be observed that on addition of 10% CaF<sub>2</sub> the rate of mass loss reduced by a factor 5.

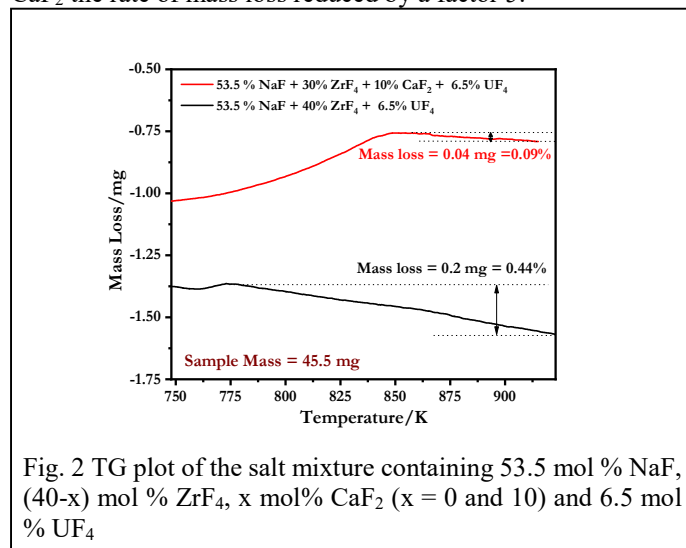


Fig. 2 TG plot of the salt mixture containing 53.5 mol % NaF, (40-x) mol % ZrF<sub>4</sub>, x mol% CaF<sub>2</sub> (x = 0 and 10) and 6.5 mol % UF<sub>4</sub>

Fig. 3 shows the DTA plot of 53.5 mol % NaF, (40-x) mol % ZrF<sub>4</sub>, x mol% CaF<sub>2</sub> (x = 0 and 10) and 6.5 mol % UF<sub>4</sub>. From Figure 2 it is clear that the salt mixture without containing CaF<sub>2</sub> completely melts (liquidus temperature) at about 813 K when heated for the first run, while its liquidus temperature drastically increases to 905 K in the second run. This increase is attributed to the loss of ZrF<sub>4</sub> which changes the composition. On the other hand, the salt mixture containing 10 mol % CaF<sub>2</sub> melts at 848 K in the first run and at 854 K in the second run which suggests that in the second sample on addition of CaF<sub>2</sub> the compositional variation is reduced drastically. It was further observed that at given temperature the rate of mass loss decreases with time

suggesting that the bonding of unreacted  $\text{CaF}_2$  increases as time progresses.

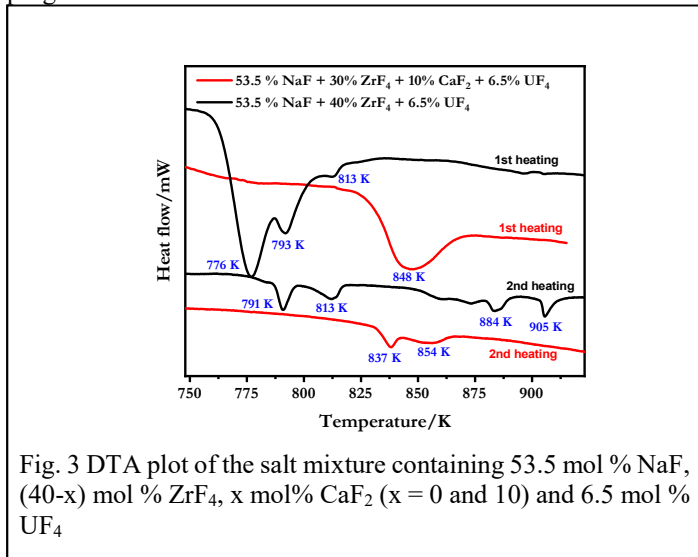


Fig. 3 DTA plot of the salt mixture containing 53.5 mol % NaF, (40-x) mol %  $\text{ZrF}_4$ , x mol%  $\text{CaF}_2$  (x = 0 and 10) and 6.5 mol %  $\text{UF}_4$

The vapor pressure of  $\text{ZrF}_4$  over molten (53.5 mol % NaF, 40 mol %  $\text{ZrF}_4$  and 6.5 mol %  $\text{UF}_4$ ) and (53.5 mol % NaF, 10 mol %  $\text{CaF}_2$ , 30 mol %  $\text{ZrF}_4$  and 6.5 mol %  $\text{UF}_4$ ) salt mixtures were measured employing Knudsen effusion mass loss technique. It is a dynamic gravimetric technique based on the rate of escape of vapor molecules through an orifice of a Knudsen cell into the vacuum at a known temperature. The rate of mass loss through the orifice is measured by micro thermo balance (SETARAM, Model B-24) having mass sensitivity of 0.1  $\mu\text{g}$ . Sample temperature was measured using closely located (~2 mm) calibrated ‘S’ type thermocouple (Pt-10%Rh, Pt). Pure metals viz., Al, Ag, Sn were used for temperature calibration of the instrument by determining their melting points.

In typical experiment, the sample is sealed in a Knudsen cell made of graphite containing an orifice of known area. The Knudsen cell with the sample is then heated to a desired temperature and kept at this temperature for equilibrium to reach. The rate of mass loss at temperature T and time t is related to vapor pressure of condensed phase, P, derived from Knudsen equation (1), where  $dm/dt$  is the rate of mass loss with time t, M sample molar mass, R universal gas constant,  $K_c$  is Clausing factor and A is the orifice area.

$$P = \frac{1}{A} \frac{dm}{dt} \frac{1}{K_c} \sqrt{\frac{2\pi RT}{M}} \quad (1)$$

Vapor pressure calibration was done by measuring the vapor pressure of  $\text{ZrF}_4$ . The temperature dependent vapor pressure of  $\text{ZrF}_4$  over pure  $\text{ZrF}_4(\text{s})$  is determined and is given as

$$\ln p(\text{ZrF}_4)/\text{Pa} = -\frac{28471.6}{T} + 36.17 \quad (773 < T/\text{K} < 860) \quad (2)$$

It found to be in good agreement with the literature data as shown in Fig. 4. Temperature dependent vapour pressure of  $\text{ZrF}_4$  over 53.5 mol % NaF, 40 mol %  $\text{ZrF}_4$  and 6.5 mol %  $\text{UF}_4$  salt mixture is

$$\ln p(\text{ZrF}_4)/\text{Pa} = -\frac{10102.0}{T} + 12.98 \quad (900 < T/\text{K} < 1000) \quad (3)$$

and over 53.5 mol % NaF, 30 mol %  $\text{ZrF}_4$ , 10 mol %  $\text{CaF}_2$  and 6.5 mol %  $\text{UF}_4$  salt mixture is

$$\ln p(\text{ZrF}_4)/\text{Pa} = -\frac{10009.0}{T} + 11.37 \quad (900 < T/\text{K} < 1000) \quad (4)$$

**Table 1** Comparison of vapour pressures of  $\text{ZrF}_4$ , salt mixture containing 53.5 mol % NaF, (40-x) mol %  $\text{ZrF}_4$ , x mol%  $\text{CaF}_2$  (x = 0 and 10) and 6.5 mol %  $\text{UF}_4$  at reactor operating temperature

	T=873 K	T=973 K
$p(\text{ZrF}_4)/\text{Pa-ZrF}_4$	35.0	1000.6
$p(\text{ZrF}_4)/\text{Pa-FS without CaF}_2$	4.1	13.4
$p(\text{ZrF}_4)/\text{Pa-FS with 10% CaF}_2$	0.8	2.7

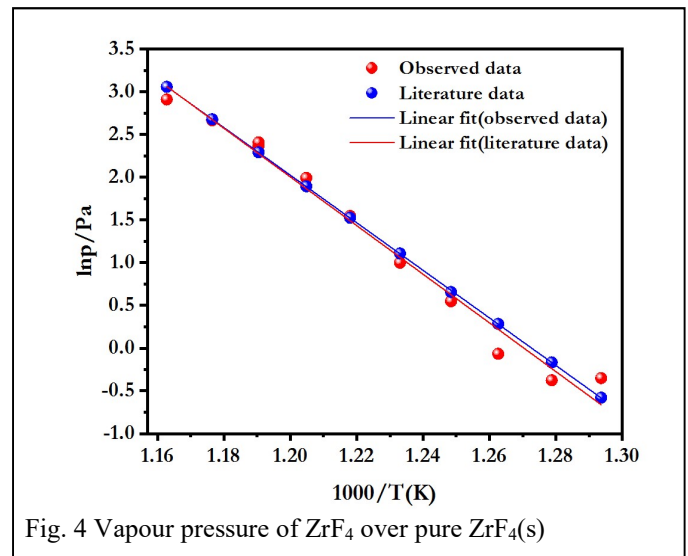


Fig. 4 Vapour pressure of  $\text{ZrF}_4$  over pure  $\text{ZrF}_4(\text{s})$

The comparison of the vapour pressure of pure  $\text{ZrF}_4$ , salt mixture containing 53.5 mol % NaF, 40 mol %  $\text{ZrF}_4$  and 6.5 mol %  $\text{UF}_4$  and 53.5 mol % NaF, 30 mol %  $\text{ZrF}_4$ , 10 mol%  $\text{CaF}_2$  and 6.5 mol %  $\text{UF}_4$  is shown in Fig. 5 and their values at temperatures 873 K and 973 K are tabulated in Table 1.

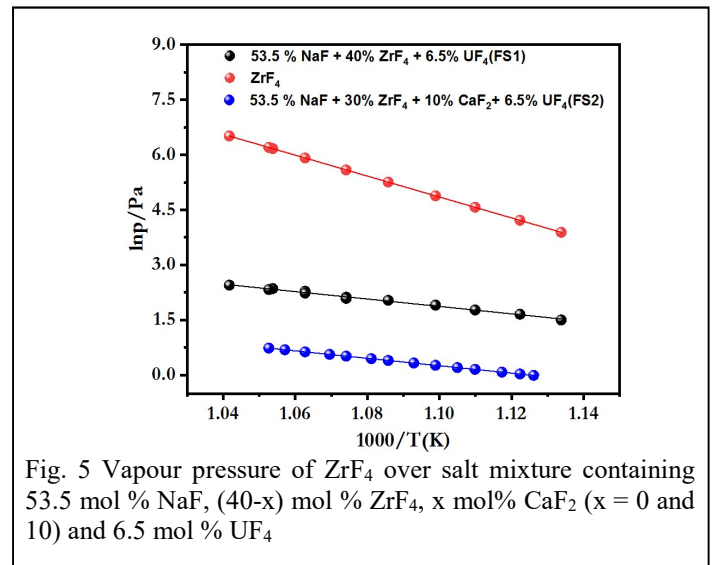


Fig. 5 Vapour pressure of  $\text{ZrF}_4$  over salt mixture containing 53.5 mol % NaF, (40-x) mol %  $\text{ZrF}_4$ , x mol%  $\text{CaF}_2$  (x = 0 and 10) and 6.5 mol %  $\text{UF}_4$

From the TG-DTA and vapor pressure measurement studies it may be assumed that addition of  $\text{CaF}_2$  to the salt mixture 53.5 mol % NaF, 40 mol %  $\text{ZrF}_4$  and 6.5 mol %  $\text{UF}_4$  decreases the vaporization of  $\text{ZrF}_4$  over the mixture. This may be due to short range bonding between  $\text{CaF}_2$  with  $\text{ZrF}_4$  resulting in the formation of dispersed  $\text{CaZrF}_6$  phases in the liquid state which leads to reduction in the vaporization loss.

Hence the salt mixture containing 53.5 mol % NaF, 30 mol %  $\text{ZrF}_4$ , 10 mol%  $\text{CaF}_2$  and 6.5 mol %  $\text{UF}_4$  may be considered as potential fuel salt for MSR application.

#### References

- O. Ashraf, A.D. Smirnov and G.V. Tikhomirov, *J. Phys. Conf. Ser.*, 1189 (2019) 012007
- S. Delpech, E. Merle-Lucotte, D. Heuer, M. Allibert, V. Ghetta, Le-Brun, X. Doligez and G. Picard, *J. Fluor. Chem.*, 130 (2009) 11
- M.W. Rosenthal, P.R. Kasten and R.B. Briggs, *J. Nucl. Appl. Technol.*, 8 (1970) 107
- J. Elguero and I. Alkorta, *Struct. Chem.*, 34 (2023)

## High Temperature Oxidation Behaviour of D9 Alloy

Ashish Jain<sup>\*a</sup>, S. Maharajan<sup>a</sup>, Dinu Shaji<sup>a</sup>, Soja K. Vijay<sup>a</sup>, P. Logaraj<sup>a</sup>

<sup>a</sup>Materials Chemistry and Metal Fuel Cycle Group, Indira Gandhi Centre for Atomic Research, Kalpakkam – 603102, TamilNadu, India

<sup>\*</sup>ashish@igcar.gov.in, +91 44 27480500 24268 (extn.) and +91 44 27480065.

### Abstract

The oxidation of D9 alloy (clad material for India's first prototype fast breeder reactor) was studied in the temperature interval (1273 - 1773 K). Oxidation was carried out in the stream of oxygen under dynamic and isothermal conditions. Product of oxidation were analyzed by x-ray diffraction technique. Multi step oxidation reaction with ignition at high temperature was observed. Completion of oxidation reaction was found to be independent of heating rate and ~38 mass% gain in mass was observed at the end. Extent of oxidation was found to be a function of time, temperature and partial pressure of oxygen.

**1. Introduction:** Austenitic stainless steel alloy D9 (15Cr-15Ni-Mo-Ti-C) with specifically tailored composition (w.r.t. Ti, Si), in 20% cold worked condition has been chosen for the fuel subassembly for the Prototype Fast Breeder Reactor (PFBR) [1]. Minor elements such as silicon (Si), titanium (Ti) and phosphorous (P) are known to have a major influence on the void swelling behaviour of alloy D9 [2]. Higher Si and Ti concentrations lead to enhanced radiation tolerance and high temperature creep strength. The possibility of oxidation of this alloy under the influence of high temperature and exposure time cannot be ruled out. The formation of oxide scale may increase the surface temperature and may lead to failure of tubes due to corrosion and creep. The study on the high temperature oxidation of this steel is useful in understanding the underlying mechanism of oxidation and for further improvement in the oxidation resistance of this alloy.

**2. Experimental:** The D9 alloy was characterized by chemical analysis (ICP-OES, Spectro Arcos, M/S. Ametek GmbH) and X-ray diffraction technique (M/S. G N R Italy). The typical chemical composition of the D9 alloy is given in Table 1 and XRD pattern is shown in Fig. 1a.

The high temperature oxidation of D9 alloy was studied using thermogravimetry and differential thermal analyses technique in a TGA / DSC 3+ thermogravimetric analyzer procured from M/S. Mettler Toledo, Switzerland. The equipment had a mass sensitivity of 0.1  $\mu\text{g}$  and a temperature sensitivity of 0.01 K. It was calibrated using ICTAC recommended standards (In, Al, Au & Pd). To study high temperature oxidation of D9 alloy, oxidizing atmosphere was maintained by a constant supply of oxygen (50 ml  $\text{min}^{-1}$ ) the flow of which was controlled by mass flow controller in close vicinity of the sample. For a typical experiment ~ 5 mg of D9 alloy of 1 x 1 mm size was heated from 1273 to 1773 K, maintaining controlled heating rate (5, 10, 15 K  $\text{min}^{-1}$ ) in an alumina crucible of 70  $\mu\text{l}$  capacity.

**3. Results and discussion:** The thermogravimetry and differential thermal analysis curves obtained for oxidation of D9 alloy is shown in Fig. 2. No significant mass change was observed up to 1450 K. Beyond this temperature gradual increase in mass was observed up to 1700 K. Rapid increase in mass was observed after this temperature and reaction completed at 1750 K. The total mass gain during oxidation reaction was found to be ~38 mass %. Gain in mass in temperature interval (1450 – 1700 K) showed the simultaneous oxidation of individual constituents of alloy D9. The change in slope of the curve is due to difference in the tendency of constituent elements to form oxides, which is governed by the standard Gibbs energy of formation of respective oxide and kinetics of the reaction. A slight loss in mass was observed in temperature interval (1725 - 1775 K) which is the indication of

loss of volatile oxides of Mo and other constituent elements. It is observed that the oxidation reaction involved ignition also as shown in DTA plot as two sharp exothermic events in Fig. 2b.

The x-ray diffraction pattern of product of oxidation is shown in Fig. 1b. Most of the peaks correspond to the oxides of major constituents of the alloy D9 (Fe, Cr, Ni, Mo). Peaks pertaining to constituent elements were not observed in the oxidized product which indicates the complete oxidation of D9 alloy. After completion of the oxidation reaction, alloy loose its metallic luster and surface becomes dark grey. Expansion in the volume of the specimen was observed which could be due to formation of oxides. Most of the cases specimen crumbled and converted into powder.

**Table 1: Chemical composition of D9 alloy**

Element	Fe	Cr	Ni	Mo	Mn	Ti	Al	P
Wt. (%)	65.9	14.5	15.4	2.1	1.6	0.23	0.10	0.17

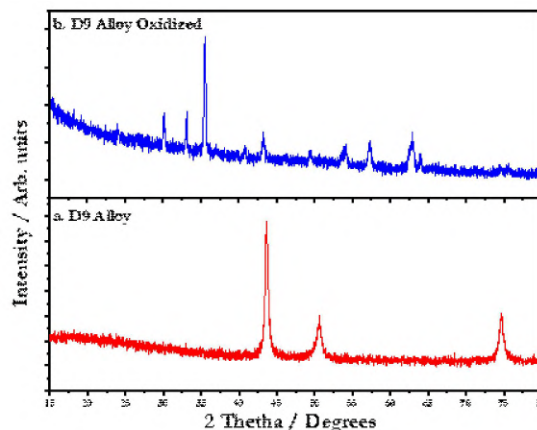


Figure 1. a) X-ray diffraction pattern of D9 alloy b) Product of oxidation reaction

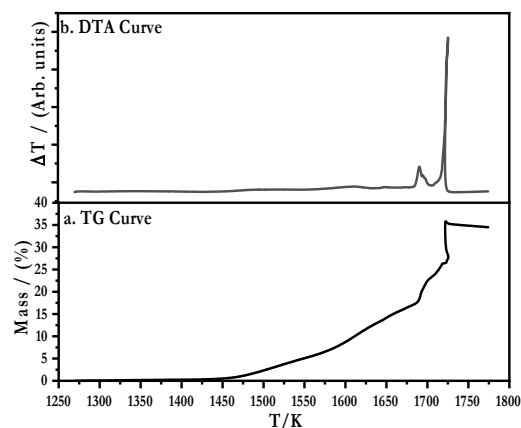


Figure 2 a) TG b) DTA curves for the oxidation of D9 alloy

Non-isothermal experiments were performed at three different heating rates viz. 5, 10 and 15 K min<sup>-1</sup>. The extent of oxidation was evaluated for non-isothermal experiments by the

$$\text{following relation [3]: } \alpha = \frac{W_T - W_i}{W_f - W_i}$$

(1a)

where  $w_i$ ,  $w_f$  and  $w_T$  correspond to initial, final and intermediate masses at temperature 'T' respectively. The change in extent of oxidation ( $\alpha$ ) with respect to temperature at various heating rates is shown in Fig. 3. It is inferred from the figure that at a constant temperature extent of oxidation is high for low heating rate. This could be due to better equilibration of the sample temperature with furnace temperature. After reaching ' $\alpha$ ' = 1, a decreasing trend in ' $\alpha$ ' with respect to temperature was observed which indicated the reverse reaction (mass loss in place of mass gain).

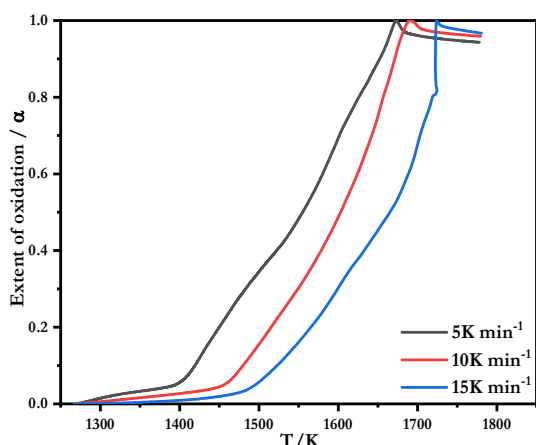


Figure 3. A plot of extent of oxidation ( $\alpha$ ) with temperature (Non-isothermal experiment)

Model free isoconversional method [4] was applied to study the kinetics and mechanism of the reaction. A continuous change (increase) in effective activation energy ' $E_\alpha$ ' vs. temperature showed the multiple steps / mechanisms involved in the oxidation reaction. Higher values of ' $E_\alpha$ ' beyond ' $\alpha$ ' greater than 0.5 shows the hindrance provided by the oxide film formed on the surface of specimen for the diffusion of oxygen into the unreacted D9 alloy. The film is not protective in nature, it got removed from the sample surface and exposes the fresh sample surface to oxygen.

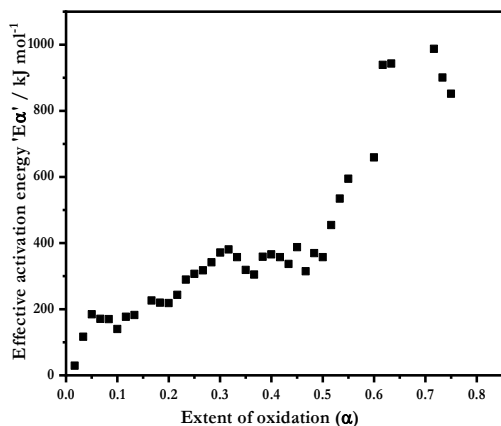


Figure 4. A plot of ' $E_\alpha$ ' as a function of ' $\alpha$ ' for D9 alloy (Non isothermal experiments)

Isothermal experiments were performed at four different temperatures for a period of 6 h (Figure 5). The percent gain in mass during the isothermal experiment is given in Table 2.

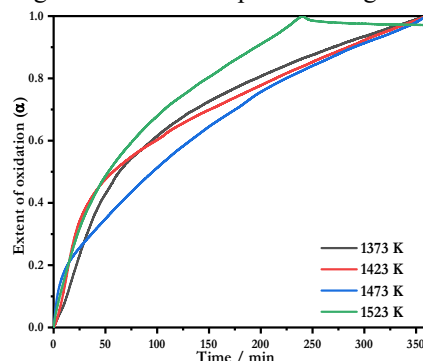


Figure 5: A plot of ' $\alpha$ ' with 't' at various 'T' for D9 alloy (Isothermal experiments)

The increase in mass with respect to temperature showed that the extent of oxidation is a function of temperature and time of exposure. A rapid loss in mass was observed in isothermal experiment carried out at 1573 K which could be due to loss of volatile oxides formed during oxidation.

Table 2: Mass (%) gain during isothermal experiments

T / K	1373 K	1423 K	1473 K	1523 K
Mass (%)	12.7	21.6	33.8	34.0

Effect of partial pressure of oxygen ( $p_{O_2}$ ) on the oxidation of D9 alloy was studied by carrying out the experiments using three different reactive gases viz. oxygen, air and UHP argon (2 ppm of  $O_2$ ). The thermogravimetric curves obtained are shown in Fig. 6. It was observed that mass gain / extent of oxidation was a function of partial pressure of oxygen. Rate of oxidation could be controlled even at high temperature by suitably controlling the  $p_{O_2}$ .

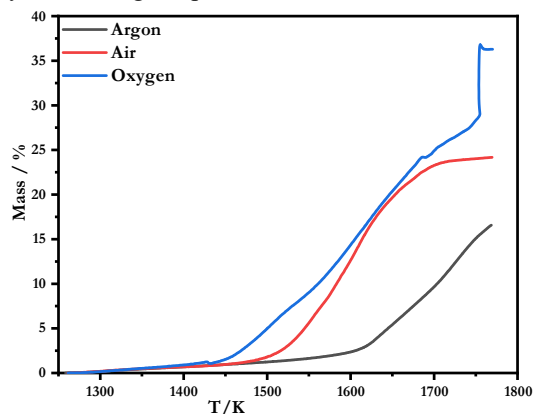


Figure 6. Plot of percent increase in mass with temperature under varying atmosphere.

**4. Conclusions:** Oxidation of D9 alloy was studied under isothermal and non-isothermal conditions. The oxide film formed was non protective in nature. Extent of oxidation was dependent on time, temperature and  $p_{O_2}$ .

#### References

1. T. Jayakumar, M.D. Mathew, K. Laha, R. Sandhya, Nuclear Engineering and Design, 265 (2013) 1175.
2. S. Latha, M.D. Mathew, P. Parameswaran, M. Nandagopal, S. L. Mannan, J. Nucl. Mater., 409 (2011) 214.
3. M. E. Brown, D. Dollimore, A. K. Galwey, Comprehensive chemical kinetics. vol. 22. Amsterdam Elsevier; 1988.
4. Ortega A. A simple and precise linear integral method for isoconversional data. Thermochim. Acta. 474 (2008) 81.

## Thermal analysis of U–4Mo–4Pd Alloy Fuel

Somesh Bhattacharya<sup>a,b,\*</sup>, Santu Kaity<sup>a</sup>, A. Arya<sup>b</sup>, Joydipta Banerjee<sup>a</sup>, Amrit Prakash<sup>a</sup>

<sup>a</sup>Radiometallurgy Division, Bhabha Atomic Research Center, Mumbai

<sup>b</sup>Homi Bhabha National Institute, Mumbai

Email i.d. someshb@barc.gov.in, Telephone Number: 022-2559-7005

**Abstract** Formation enthalpy of probable phases in U–Mo–Pd ternary system was calculated using density functional theory.  $\Delta H_f$  of  $UPd_3$  is found to be most negative indicating Pd will bind with U. This observation is experimentally validated by recording and indexing the XRD pattern. Solidus and liquidus temperature and other high temperature phase transitions of the alloy were determined using differential thermal analysis.

The U–Mo alloy has been extensively studied as a potential material for dispersion or monolithic fuels in thermal reactors. However, literature available on U–Mo system in context of fast reactor fuel development is limited. The most attractive feature of this alloy system is its linear thermal expansion behavior over wide temperature range when the concentration of Mo is greater or equal to eight weight percent [1]. This occurs because of metastability of high temperature body centered cubic phase at room temperature. In addition to its favourable thermal expansion properties, the U–Mo system also exhibits better corrosion resistance, making it easier to fabricate and handle. However, lanthanide migration and fuel-clad chemical interaction (FCCI) present significant challenges in the development of metallic fuels. One approach to mitigate lanthanide migration is to trap lanthanide fission products within the fuel matrix using an alloying element. Palladium has been shown to be particularly effective in this role, as it can form stable intermetallic compounds with lanthanide fission products, preventing their migration [2]. Furthermore, Pd has a higher melting point than uranium. Given these advantages, it has been decided to add Pd to the U–Mo alloy system. This addition could enhance the alloy's ability to trap fission products, improve its thermal stability, and potentially mitigate issues like lanthanide migration and FCCI in the context of fast reactor fuels.

U–4wt.%Mo–wt.%4Pd alloy was prepared by arc melting. Remelting was done multiple time to ensure similar composition throughout the melted mass. As cast alloy was homogenized at 900°C for 100 hours and then slowly cooled down to room temperature inside the furnace. Then it was used for thermal analysis and recording x-ray diffraction pattern (XRD). All calculations were performed using density functional theory (DFT) implemented in Vienna Ab initio Simulation Package (VASP). The exchange correlation functional was approximated with Generalized Gradient Approximation of Perdew, Burke and Ernzerhof (PBE) [3]. Atomic orbitals were represented by Projector Augmented Wave method with an energy cut-off of 400 eV. The configurational randomness in disordered phases were accounted by constructing unit cells with Special Quasirandom Structure method [4]. The unit cells contain 54 atoms and their Brillouin zones were sampled with a uniform 4x4x4  $\gamma$  centered Monkhorst Pack grid [5]. No significant improvement in the values of formation enthalpies was observed when coulomb correlation and relativistic effects of 5f electrons in uranium atoms were taken into consideration. Except  $UPd_3$ , all other systems are non-magnetic. Therefore, spin polarized calculations were done for  $UPd_3$  and the computation for remaining phases mentioned here were non spin polarized.

Literature available on U–Mo–Pd ternary system is limited. Therefore, possible phases in the ternary alloy are assessed from associated binary phase diagrams. The formation enthalpies of these phases are calculated using density functional theory. The results are given in Table 1. The ternary alloy can be generated by substitution of Mo in U–8Mo binary alloy by Pd. The formation enthalpy decreases on substitution which indicates that palladium helps in stabilization of  $\gamma$  phase. But this effect is outweighed by large negative formation enthalpy of  $UPd_3$  intermetallic phase. Therefore, palladium will separate out with uranium forming intermetallic compound. Remaining uranium and molybdenum may behave like U–Mo binary phase and give rise to a mixture of  $\alpha$  uranium and  $\gamma$  phase [6, 7]. This prediction is purely based on thermodynamic stability of different phases. The phases that are experimentally observed is also influenced by the kinetics of phase transformation.

**Table 1.** Formation energies of different phases calculated using density functional theory

Phases	$\Delta H_f$ (kJ/mol)
Pure metallic phases ( $\alpha$ -U, Mo, Pd)	0
$\gamma$ (U–8Mo)	+14.50
$\gamma$ (U–4Mo–4Pd)	+2.89
$MoPd_2$	-8.64
$UPd_3$	-50.49
Pd–28Mo	-1.41

The powder diffraction pattern of the furnace cooled alloy is shown in Figure 1. All the peaks are identified and indexed. The peaks in the diffraction pattern correspond to  $\alpha$  U, U–Mo  $\gamma$

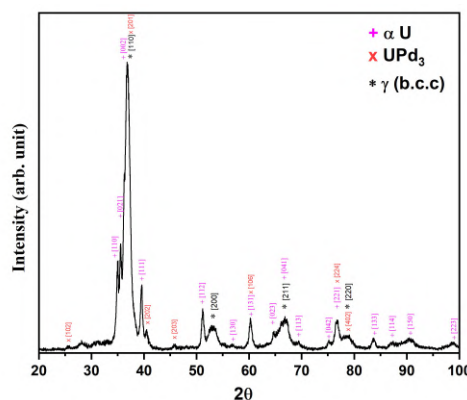


Figure 1. Powder X-ray diffraction pattern of the alloy after homogenization.

and  $UPd_3$  intermetallic phases which is consistent with the theoretical prediction. Therefore, thermodynamics plays

dominant role in the phase separation due to palladium addition in U–Mo system.

Phases that appear above room temperature is determined using differential thermal analysis (DTA). The results of DTA run during heating cycle is given in Figure 2. The solidus and liquidus temperature of the alloy is 1368 K and 1418 K

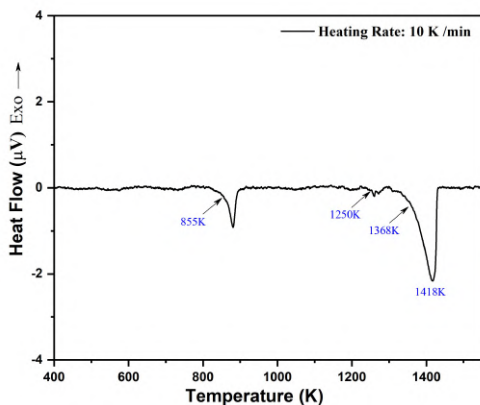


Figure 2. Differential thermal analysis of the homogenized alloy. Phase transition temperatures are highlighted in the plot with arrows.

respectively. Apart from these two transitions, two more phase

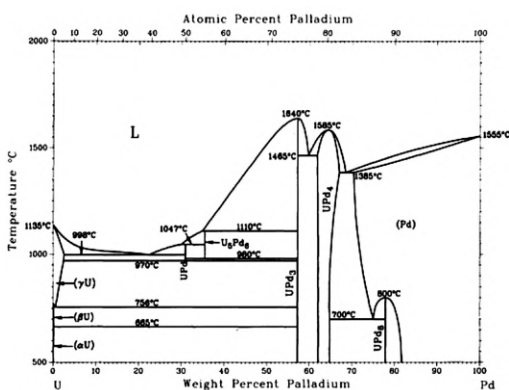


Figure 3. Uranium-Palladium phase diagram.

transitions are observed. The temperature of transition and the transformation reaction is given in Table 2. The binary phase diagram of uranium and palladium is shown in Figure 3. Below 1243K temperature, the uranium rich side of the phase diagram is a biphasic region containing phases of U and UPd<sub>3</sub>. Above this temperature, UPd<sub>3</sub> decomposes into a high temperature intermetallic phase UPd and the peak at 1250 K is due to the decomposition reaction [8].

**Table 2.** Phase transition temperatures and associated phases involved in the transitions

Temperature	Phase transition
855 K	$\alpha + \text{UPd}_3 + \gamma \rightarrow \text{UPd}_3 + \gamma$
1250 K	$\text{UPd}_3 + \gamma \rightarrow \text{UPd} + \gamma$
1368 K	Solidus
1418 K	Liquidus

Addition of Pd in U–Mo system leads to phase separation and formation of intermetallic phase which is governed by thermodynamic stability of phases. At room temperature, the furnace cooled alloy is a mixture of  $\alpha$  U,  $\gamma$  U–Mo and UPd<sub>3</sub> phase. At higher temperature, UPd<sub>3</sub> decomposes into UPd and then liquid phase appears.

## References

1. V. Sinha, P. Hegde, G. Prashad, G. Dey, H. Kamath, *J. Alloy. Compd.*, 491 (2010) 753-760.
2. F. G. Di Lemma, T. M. Trowbridge, L. Capriotti, J. M. Harp, M. T. Benson, R. D. Mariani, *J. Nucl. Mater.*, 558 (2022) 153403.
3. J. P. Perdew, K. Burke, and M. Ernzerhof, *Phys. Rev. Lett.*, 77 (1996) 3865–3868.
4. A. Zunger, S.-H. Wei, L. G. Ferreira, and J. E. Bernard, *Phys. Rev. Lett.*, 65 (1990) 353–356.
5. H. J. Monkhorst and J. D. Pack, “Special points for brillouin-zone integrations,” *Phys. Rev. B*, 13 (1976) 5188–5192.
6. R. Rakesh, V. Sinha, K.V. Manikrishna, N Kesar, R Tiwari, *J. Nucl. Mater.*, 573 (2023) 154113.
7. S. Kaity, J. Banerjee, S. C. Parida, P. G. Behere, V. Bhasin, *J. Nucl. Mater.*, 532 (2020) 152046.
8. S. C. Middlemas, M. C. Marshall, C. A. Adkins, F. D. Lemma, K. R. Tolman, M. T. Benson, C. Hin, *J. Alloy. Compd.*, 850 (2021) 156664.

## High Temperature Oxidation of Zr-2.5(wt.%) Nb alloy in Heavy and Light Water Mixtures

Akanksha Samanta<sup>\*a,b</sup>, Y. Sunitha<sup>c</sup>, Vijay Karki<sup>d</sup>, Suparna Banerjee<sup>a</sup> and A.K. Tyagi<sup>b</sup>

<sup>a</sup>Post Irradiation Examination Division, Bhabha Atomic Research Centre, Trombay, Mumbai-400085

<sup>b</sup>Homi Bhabha National Institute, Anushaktinagar, Mumbai-400094

<sup>c</sup>National Centre for Composition and Characterization of Materials, Bhabha Atomic Research Centre, Hyderabad-500 062

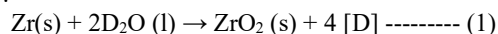
<sup>d</sup>Fuel Chemistry Division, Bhabha Atomic Research Centre, Trombay, Mumbai-400085.

\* e-mail id: [akanksha@barc.gov.in](mailto:akanksha@barc.gov.in); Phone No: 0222559-4028.

### Abstract

The impact of light water impurities on the oxidation behavior of Zr-2.5 (wt. %)Nb alloy in high-temperature, high-pressure heavy water environments is discussed. The alloy coupons were exposed to mixtures of heavy and light water, with light water concentrations ranging from 5% to 95% by volume. The oxide layer was characterized by its thickness and composition using p-EBS and SIMS techniques. The results indicated that the presence of light water impurities increases the oxidation rate of the alloy in high-temperature heavy water environments. ERDA analysis of H and D in the oxide indicated preferential H pick-up in the alloy.

Pressure tube is the most critical component in the core of a Pressurized Heavy Water Reactor (PHWR). These tubes operate under demanding conditions of high temperature, pressure, corrosive aqueous environment and neutron flux. The inner surface of the tube undergoes corrosion reaction with High Temperature High Pressure (HTHP) heavy water coolant as per the equation 1.



The corrosion reaction generates oxide scale on the surface of the tube leading to reduction in metal thickness. A fraction of Deuterium released in the reaction is absorbed by the pressure material. With time the D concentration builds up in the alloy and often affects the service life of the tube adversely. In fact, corrosion and subsequent hydriding is one of the major degradation mechanisms seen by these tubes [1]. Zr-2.5 (wt. %)Nb alloy is presently the pressure tube material in PHWRs [2]. Due to its technological importance, the mechanism of corrosion of Zr-2.5 (wt. %)Nb alloy is studied world over exploring different reactor simulated environments to predict its in-service behavior. In the present study, the effect of decrease in isotopic purity of the heavy water coolant on corrosion and hydriding of Zr-2.5 (wt. %)Nb is reported.

20mmX30mmX4.5mm coupons extracted from Zr-2.5 (wt. %)Nb pressure tube spool piece were subjected to oxidation in heavy water and light water mixtures at 673K, 100bar for 72 hours. It is well known that the isotopic purity of heavy water can vary from 95-99% during operation. Hence, the tests were carried out in three light water concentrations in D<sub>2</sub>O: (i) 5% by volume (ii) 50% by volume and (iii) 95% by volume. The oxide layer formed on the coupons as a result of oxidation was characterized in terms of thickness and composition by SIMS (Secondary Ion Mass Spectrometry) and p-EBS (Proton Elastic Backscattering Spectrometry) techniques. The oxide thickness estimated from the techniques was further validated by cross-sectional analysis by SEM (Scanning Electron Microscopy).

Fig. 1 shows the SEM micrograph of the oxide film formed on the one of the coupons exposed to environment having 5%H<sub>2</sub>O and 95% D<sub>2</sub>O. The morphology of the oxide was observed to be adherent with negligible cracks and pores.

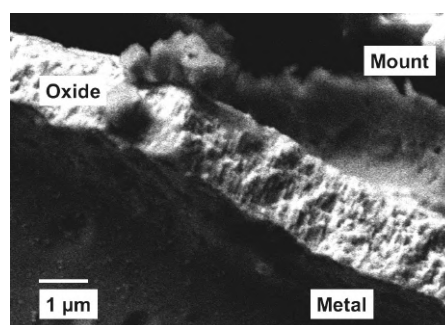


Fig. 1: The oxide layer morphology on coupon exposed to 5% H<sub>2</sub>O and 95% D<sub>2</sub>O as observed in SEM

The SIMS analysis of oxide films formed on the coupons is shown in Fig. 2. The variation in the oxide thickness as a function of light water concentration in the corrosive environment is shown. Intensity of O<sup>16</sup> is plotted as a function of thickness of the sample probed by Cs<sup>+</sup> ion beam to follow the oxide profile. The profile of the oxide is typical of the protective oxides formed on metals with significant interface consisting of sub-oxides of zirconium [3]. The middle of the interface is taken as the metal-oxide interface as shown by coloured arrows. The left of the interface shows the oxide and right of the interface shows the metal rich region.

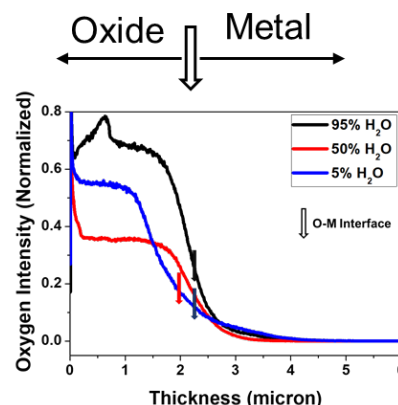


Fig. 2: Oxide layer measurement by SIMS

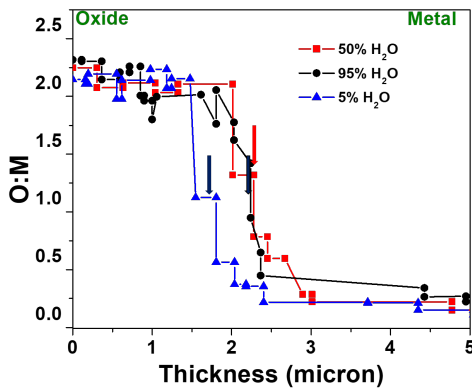
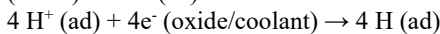
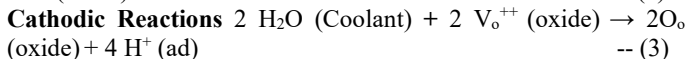
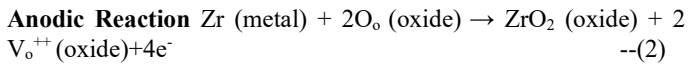


Fig.3: Composition of the oxide across the oxide thickness as analysed by p-EBS

The chemical composition of the oxide layer formed on the specimens was analysed in terms of their O/M ratio by p-EBS technique as shown in Fig.3. The technique is capable of measuring oxide thickness also. The oxide was observed to be nearly stoichiometric near the surface with an O/M of  $2 \pm 0.3$ . Hence, the effect of presence of light water was insignificant on the oxide composition. However, significant effect was observed on the oxide thickness. The oxide thickness was observed to be higher in the case of light water rich environment as shown in Figs. 2 and 3. This indicates significant isotopic effect of light water on oxidation of Zr-2.5 (wt. %) Nb alloy in high temperature light and heavy water mixtures. The hydrogen pick-up in the base alloy matrix was studied by Differential Scanning Calorimetry. The hydrogen/deuterium pick-up was observed to be  $< 5\%$ . The pick-up is typical of that shown by Zr-Nb alloys in pure water and steam environments.

The oxidation reaction of zirconium in water/steam environments is a complex electrochemical phenomenon. Equation 1 can be further divided into anodic and cathodic partial reactions as shown below:



The anodic half of the corrosion reaction takes place at the O-M interface whereas the oxygen ions are generated on the oxide-water/coolant interface by reduction of water molecules. The overall reaction has been postulated to be limited by either (i) oxygen ion diffusion across the oxide as per equation 2 or (ii) reduction of hydrogen ions at the oxide-water interface as shown in the equation 3. The oxygen ion diffusion has been shown to take place through grain boundaries of the oxide and thus is mainly expected to depend upon the morphological and chemical characteristics of the oxide [4]. From the present study, it was clearly seen that the morphology as well as composition of the oxide layer was unaffected by presence of light water concentration. Hence, it can be inferred that the oxide growth is mainly controlled by cathodic half of the corrosion reaction. It is also supported by the very low hydrogen pick-up observed in the base matrix.

Quantitative H and D profiling along the thickness of the oxide was carried out by ERDA (Elastic Recoil Detection Analysis) technique. The main advantage of this technique is very low hydrogen background beyond few nm. The H and D profiles in the oxide layers on coupons exposed to 5% and 50% H<sub>2</sub>O concentrations are shown in Figs. 4 and 5 respectively.

The H and D concentration in the oxide layer in terms of atom fraction as shown as a function of oxide layer thickness. The left extreme of the figure shows the oxide surface or the oxide-water interface. The peaking of hydrogen on the surface may be due to

surface contamination or background hydrogen effects. The D profile on the other hand shows a peak at  $400 \times 10^{15}$  atoms/cm<sup>2</sup>. Multiplying the thickness with bulk density of ZrO<sub>2</sub> gives an oxide thickness of 0.3 μm. Hence, the concentration of hydrogen isotopes first increases till this depth and then follow a diffusion-controlled profile till the O-M interface. This is attributed to the presence of double-layer microstructure of the oxide [5]. The outer oxide is rich in micro-pores due to which there is high solubility of hydrogen isotopes in this region. As the O-M interface is approached, the porosity in the oxide becomes negligible and the transport of hydrogen isotopes is showing characteristics of diffusion-based phenomenon. It was interesting to see preferential hydrogen migration towards the O-M interface. Similar observations were seen in the oxide formed in 50% H<sub>2</sub>O. The preferential diffusion of H indicates significant isotopic effect on hydriding behavior of Zr-Nb alloys. This also supports the hypothesis that cathodic reaction is the rate controlling step in the corrosion of the alloy.

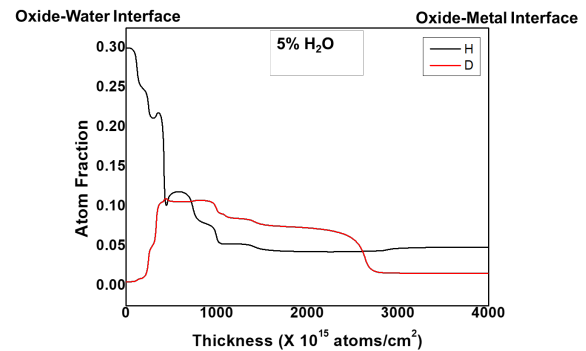


Fig.4: H and D profiles in the oxide layer formed in 5% H<sub>2</sub>O

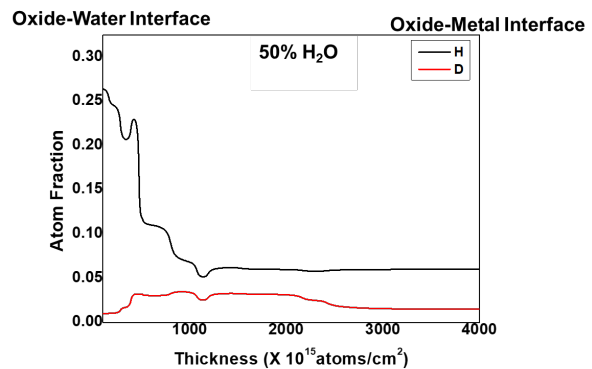


Fig. 5: H and D profile across the oxide layer formed in 50% H<sub>2</sub>O

The studies on isotopic effect of light water on corrosion of zirconium alloys in high temperature heavy and light water mixtures are limited. Sieteinks and co-workers in their study on zircaloy-2 observed minimal isotopic effect on oxidation rate of the alloy. However, the authors reported significant isotopic effect on H and D pick up in the alloy. The authors attributed the observations to anodic half controlled oxide growth. Cathodic half controlled growth in Zr-2.5 (wt. %) Nb alloy can be related to the Nb doping in the oxide phase which results in better electronic conduction across the oxide.

#### References

1. R. K. Sinha, S. K. Sinha, K. Madhusoodanan, *Journal of Nuclear Materials* 383 (2008) 14-21.
2. S.S. Bajaj, A.R. Gore, The Indian PHWR, *Nuclear Engineering and Design*, 236 (2006) 701-722.
3. Marc Tupin, Frantz Martin, Caroline Bisor, Romain Verlet, Philippe Bossis, Jacques Chene, Francois Jomard, Pascal Berger, Serge Pascal, Nicolas Nuns, *Corrosion Science*, 116 (2017) 1-13.
4. B. Cox, *Journal of Nuclear Materials*, 336 (2005), 331-368.
5. I. Takagi, K. Une, S. Miyamura, T. Kobayashi, *Journal of Nuclear Materials*, 419 (2011), 339-346.



## Reaction pathway governing Ti<sub>2</sub>AlC MAX-phase formation: Insights from High-Temperature DSC

Mohammad Yunus<sup>1,a</sup>, Bikas C. Maji<sup>1</sup> and R. N. Singh<sup>1</sup>

<sup>1</sup>Mechanical Metallurgy Division, Bhabha Atomic Research Centre, Trombay, Mumbai, INDIA-400094

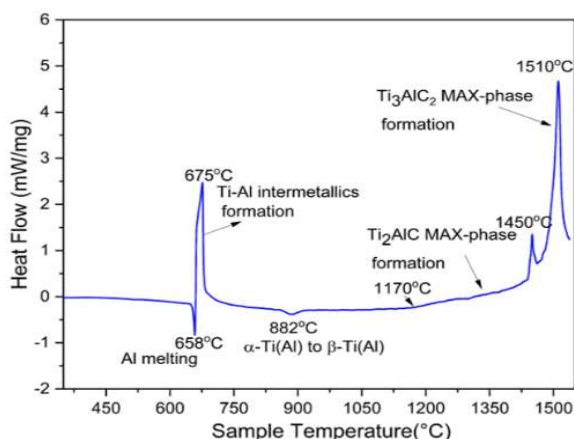
a) Corresponding author email: [myunus@barc.gov.in](mailto:myunus@barc.gov.in), 02225590922

**Abstract.** In this study, we aimed to interpret the high-temperature differential scanning calorimetric (DSC) thermogram obtained from a 2Ti:1Al:1C (molar ratio) elemental powder mixture, heated up to 1500°C. Various endothermic and exothermic reactions observed in the thermogram, corresponding to phase transformations occurring within the powder mixture during heating, were analyzed using phase and microstructural examinations conducted at different stages of heating. The enthalpies associated with the phase transformations, as derived from the DSC thermogram, were further interpreted through first-principles energy calculations. A comparison between experimental DSC and theoretical predictions reveals significant insights into the reaction pathways governing the phase evolution of the 2Ti:1Al:1C powder mixture.

Ti<sub>2</sub>AlC MAX-phase is a proposed coating material for Zr-based accident-tolerant fuel (ATF) clad [1]. However, the synthesis of this material often involves complex phase transformations at high-temperature, which can be studied in great detail through a combinatorial approach of DSC thermal analysis, characterization through XRD, SEM-EDS-EBSD and first principle calculations.

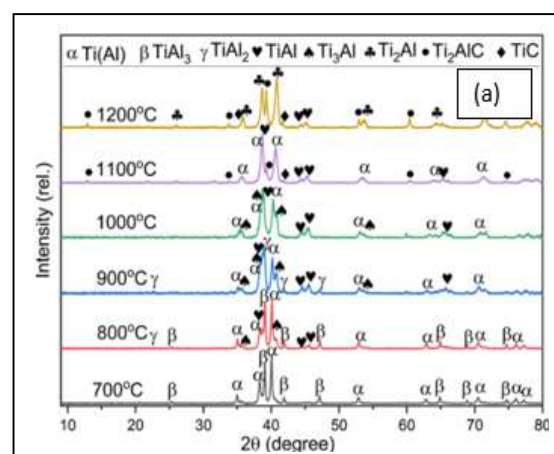
High-temperature DSC experiment was conducted on ball milled 2Ti:1Al:1C powder mixture up to 1500°C at heating rate of 10°C/min under flowing Argon. Figure 1, displays HTDSC thermogram, revealed a sharp endothermic peak at 658°C followed by high enthalpy exothermic peak. A small endothermic peak was also observed at 882°C temperature. Further at a still higher temperature, a broad exothermic peak started emerging at around 1170°C onwards, succeeded by two sharp exothermic peaks at 1450°C and 1510°C. Various phase transformations associated to these exothermic and

Based on the DSC observations, the powder mixture was incrementally heated from 700°C to 1500°C, at 100°C intervals, for identifying the phase transformations at various temperatures using XRD and SEM-EDS-EBSD techniques. Figure 2(a) and (b) show XRD patterns summarizing the phase evolution during heating from 700°C to 1500°C. Although, a qualitative correlation between the XRD analyses and DSC thermogram could be established such as exothermic peak at 675°C occur possibly due to various Ti-Al intermetallic formation and exothermic peaks at 1450°C and 1510°C could be associated with Ti<sub>2</sub>AlC and Ti<sub>3</sub>AlC<sub>2</sub> formation, however, further insights could only be revealed by microstructural analysis and first principle calculations. SEM-EDS-EBSD analysis of these specimens further revealed that the endothermic peak at 658°C essentially occurs due to melting of Al in powder mixture; Al-rich TiAl<sub>3</sub> formation is kinetically faster due to liquid phase formation when compared to other Ti-rich TiAl and Ti<sub>3</sub>Al intermetallic which forms via solid state diffusion; and Ti<sub>2</sub>AlC MAX-phase formation occurs via two different reactions.



**FIGURE 1.** HTDSC thermogram of 2Ti:1Al:1C

endothermic peaks are indicated in Fig. 1, which will be elucidated in the succeeding paragraphs.



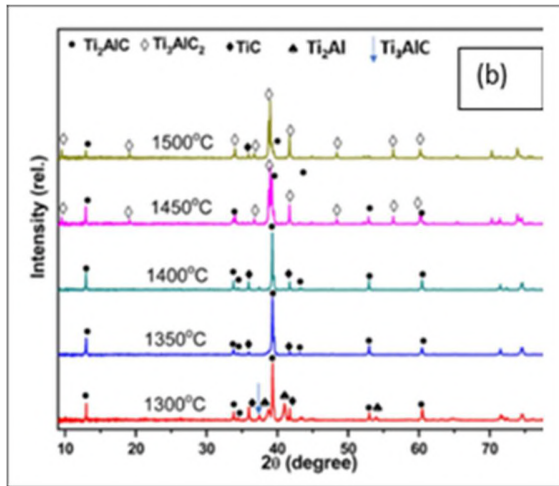


**FIGURE 2.** XRD patterns of powder mixture after SPS heating in the temperature range of 700-1500°C.

Table 1. Reaction Mechanism

Reaction	Temperature (°C)
$12\text{Al (s)} = 12\text{Al (l)}$	658
$4\text{Ti} + 12\text{Al(l)} = 4\text{TiAl}_3$	660-700
$2\text{Ti} + 4\text{TiAl}_3 = 6\text{TiAl}_2$ $5\text{Ti} + \text{TiAl}_2 = 2\text{Ti}_3\text{Al}$	800-900°C
$\text{Ti}_3\text{Al} + 2\text{TiAl}_2 = 5\text{TiAl}_2$	900°C
$4\text{Ti} + \text{Ti}_3\text{Al} + 4\text{TiAl}_2 = 3\text{Ti}_2\text{Al} + 6\text{TiAl}_2$	1000-1200°C
$9\text{Ti} + 9\text{C} = 9\text{TiC}$	1100-1200
$9\text{TiAl} + 9\text{TiC} = 9\text{Ti}_2\text{AlC}$ (outer periphery)	1200-1300°C
$3\text{Ti}_2\text{Al} + 3\text{C} = 12\text{Ti}_2\text{AlC}$ (inner core)	1200-1350°C

The results summarize that the major enthalpy contribution in exothermic peak at 675°C is essentially due to the rapid formation of  $\text{TiAl}_3$  phase from liquid

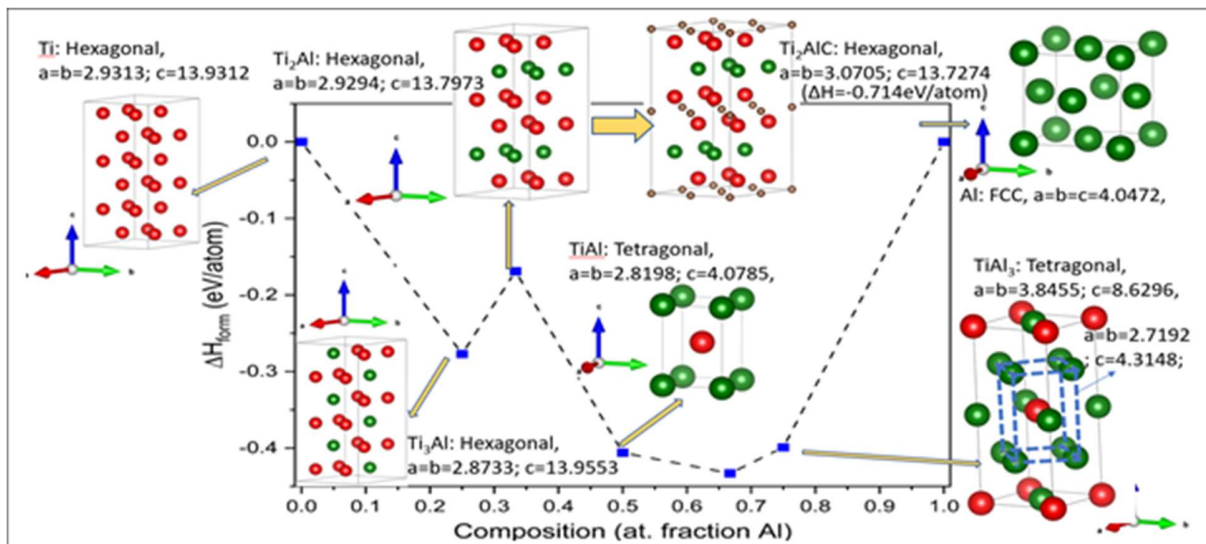


**FIGURE 3.** shows calculated enthalpy of formation (in eV/atom) of various phases along with their structures.

The structural information and enthalpy of formation of various phases were computed through first principle calculations, and is shown in Fig. 3. From this data, the enthalpy of various possible reactions was calculated for their thermodynamic feasibility assessment.

Al whereas the Ti-rich  $\text{TiAl}$  and  $\text{Ti}_3\text{Al}$  occurs via solid state diffusion with much lesser enthalpy. In addition, the high temperature exothermic reactions occur essentially due to i) formation of  $\text{Ti}_2\text{AlC}$  MAX-phase due to carbon diffusion into  $\text{Ti}_2\text{Al}$  and ii) formation of  $\text{Ti}_3\text{AlC}_2$  MAX-phase from  $\text{Ti}_2\text{AlC}$  and  $\text{TiC}$ , which are in well agreement to our experimental observations. Finally, a reaction mechanism for  $\text{Ti}_2\text{AlC}$  MAX-phase formation was proposed, mentioned in Table 1.

#### Reference

1. K. Terrani, J. Nucl. Mater., 501 (2018) 13.

## Examine the Structural, Magnetic, and Supercapacitance Characteristics of the Ni-Co Ferrite System after Zinc Substitution

Sonam Kumari and V.M.S. Verenkar\*

School of Chemical Sciences, Goa University, India

\*E-mail: [vmsv@uni.goa.ac.in](mailto:vmsv@uni.goa.ac.in) ; Contact no. : +91- 9822980123

### Abstract

Zinc substituted Ni-Co ferrites were synthesised by combustion method using Succinic acid as a fuel and characterised by XRD, IR spectroscopy, Raman spectroscopy and XPS studies. Thermal analysis of the melt was done by TG-DTA studies. SEM and HR-TEM images was examined to study its morphology. These 'as prepared' ferrites were further studied for its magnetic and electrochemical properties.

Nanoparticles of  $\text{Ni}_{0.5-x}\text{Zn}_x\text{Co}_{0.5}\text{Fe}_2\text{O}_4$  ( $x=0.0-0.5$ ) are prepared by combustion method using succinic acid as fuel. The structural, magnetic and supercapacitance properties were studied for the synthesised 'as prepared' zinc substituted Ni-Co ferrites. The TG/DTA analysis of the redox melt was done in order to determine the decomposition temperature and to confirm the complete formation of Ni-Zn-Co ferrite (Fig.1b). The thermogram shows an initial marginal weight loss of water molecules from the nitrates, followed by a loss due to the decomposition of the melt indicated by a sharp exothermic DTA peak observed at  $360^\circ\text{C}$ , which shows the combustion of nitrates with fuel. Once the synthesis temperature was fixed, the ferrite synthesis was carried out at  $400^\circ\text{C}$  [Table 1].

Table 1. TG-DTA of in the temperature range (RT- $800^\circ\text{C}$ )

TG Temp ( $^\circ\text{C}$ )	DTA Peak ( $^\circ\text{C}$ )	Remarks
RT-110	100 (Endo)	Loss of $\text{H}_2\text{O}$
110-360	360 (Exo)	Combustion of nitrates with fuel
360-800	-	Metal Oxide formed

The XRD pattern of the 'as prepared' ferrites showed formation of monophasic cubic spinel structure (Fig.1a). There is an increase in the lattice parameter with an increase in zinc concentration [1]. The IR spectra depict two characteristic absorption peaks of spinel at around  $600\text{ cm}^{-1}$  and  $400\text{ cm}^{-1}$  [2].

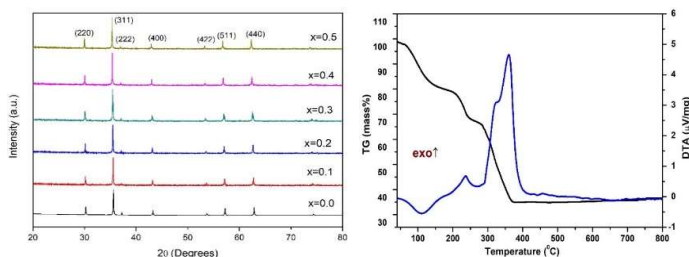


Figure 1. a) X-Ray diffraction pattern of 'as prepared'  $\text{Ni}_{0.5-x}\text{Zn}_x\text{Co}_{0.5}\text{Fe}_2\text{O}_4$  ( $x=0.0-0.5$ ) and b) The TG-DTA curves of the melt to form 'as prepared'  $\text{Ni}_{0.5-x}\text{Zn}_x\text{Co}_{0.5}\text{Fe}_2\text{O}_4$  ( $x=0.0-0.5$ ).

The Curie temperature determined from A.C. susceptibility measurements found to decrease with increase in zinc content [1]. The VSM plots of all the ferrites indicate ferromagnetic nature and shows a random trend in saturation magnetisation ( $M_s$ ) with increase in the zinc content in Ni-Co ferrites may be due to variation in particle size of the end products [3]. From the SEM images shows the agglomeration of particles and the EDS spectra confirms that all the constituent metal ions of the synthesised ferrite are present. [Fig.2]

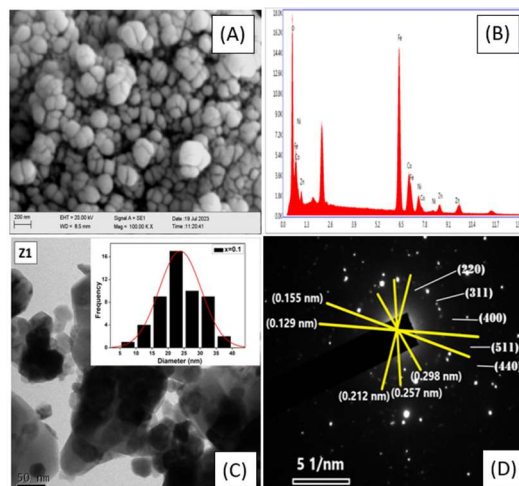


Figure 2. (A) SEM micrographs, (B) EDAX spectra, (C) HR-TEM images, Inset: Histogram of particle size distribution (D) SAED pattern of  $\text{Ni}_{0.5-x}\text{Zn}_x\text{Co}_{0.5}\text{Fe}_2\text{O}_4$  ferrite.

HR-TEM images shows the agglomeration of irregular cuboidal-shaped particles [Fig.2]. The histograms confirm that the average particle size falls within 10-45nm range [4]. The Raman spectra shows the five Raman active optical modes  $A_{1g}$ ,  $E_g$ ,  $2T_{2g}$  as seen in ferrites. The XPS studies verified the expected oxidation states of all the corresponding elements in ferrites. The electrochemical analysis exhibited the highest capacitance ( $C_{sp}$ ) of  $35.46\text{ F/g}$  for the composition  $x=0.1$  at the lowest scan rate [4].

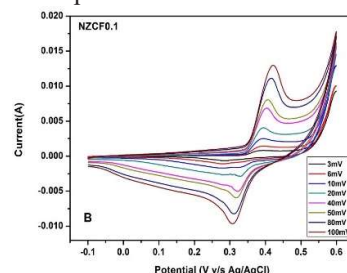


Figure 3. Cyclic voltammograms of 'as prepared'  $\text{Ni}_{0.5-x}\text{Zn}_x\text{Co}_{0.5}\text{Fe}_2\text{O}_4$  ferrites at potential window of  $-0.1-0.6\text{ V}$  with scan rates varying from 3 to  $100\text{ mV/s}$ .

### References:

1. M. Mozaffari, J. Amighian and E. Darsheshdar, *J. Magn. Mater.*, 350 (2014) 19.
2. A. Baykal, N. Kasapoglu, Y. Koseoglu, A.C. Basaran, H. Kavas and M. S. Toprak, *Cent. Eur. J. Chem.*, 6 (2008) 125.
3. R. C. Kambale, P. A. Shaikh, S. S. Kamble and Y. D. Kolekar, *J. Alloys Comp.*, 478 (2009) 599.
4. P. P. G. Dessai, S. S. Meena and V.M.S. Verenkar, *J. Alloys Compd.*, 842 (2020) 155855.

## Synthesis and characterization of the cobalt zinc ferrous fumarato-hydrazinate complex by precursor-combustion method and its decomposed product

Sanjali Navelkar and V. M. S. Verenkar\*  
 School of Chemical Sciences, Goa University, Taleigao  
 Plateau, Goa, 403206, India  
 \* [ymsv@unigoa.ac.in](mailto:ymsv@unigoa.ac.in)

### Abstract

The mixed metal fumarate hydrazine complex was synthesized by the precursor combustion method. Infrared spectral studies carried out a thorough characterization of the precursor. The thermal decomposition studies were carried out using isothermal mass loss, where a mass loss at set temperatures was noted. IR and hydrazine estimation were also conducted simultaneously at each set temperature, and all the data supported the decomposition of the precursor,  $Ni_{0.1}Co_{0.4}Zn_{0.5}Fe_2(C_4H_2O_4)_3 \cdot 6N_2H_4$ . TG-DTA data revealed decomposition in two steps, finally giving  $Ni_{0.1}Co_{0.4}Zn_{0.5}Fe_2O_4$ . The formation of ferrite was confirmed by X-ray diffraction. The saturation magnetization was found to be 57 emu/g

Ferrites are an important class of compounds with vast applications in the electronic industry, such as radio, television, satellite communication, permanent magnets, etc. Apart from this, they can be used as catalysts in organic reactions from which the ferrite can be easily retrieved due to their magnetic properties. Also, ferrites as sensor materials are gaining wide importance these days. Preparing ferrites is simple and easy, and various synthesis methods are available. One of the methods is the precursor combustion method, which yields stoichiometric pure and single-phase nanomaterials. In this study, we are reporting the synthesis and characterization of cobalt zinc ferrous fumarate hydrazine complex as a precursor for forming  $Ni_{0.1}Co_{0.4}Zn_{0.5}Fe_2O_4$  by the precursor combustion method [1,2]. The infrared spectrum of the complex shows absorption peaks at around  $3353-3144\text{ cm}^{-1}$ , corresponding to N-H stretching in the complex. The frequencies of  $1595\text{ cm}^{-1}$  and  $1383\text{ cm}^{-1}$  correspond to the carboxylate ion's asymmetric and symmetric stretching. The peak observed at  $967\text{ cm}^{-1}$  is due to N-N stretching, which confirms the presence of bidentate bridging hydrazine ligand in the complex [3,4]. The peak at  $1122\text{ cm}^{-1}$  is due to  $NH_2$  wagging, whereas the peak at  $667\text{ cm}^{-1}$  and  $581\text{ cm}^{-1}$  is due to  $NH_2$  rocking motion. The decomposition of the precursor complex towards the formation of the ferrite was closely monitored using IR spectroscopy. It was observed that the hydrazine loss started

around  $100-120\text{ }^\circ\text{C}$ , which can be easily noticed from IR data, and the intensity of N-H stretching and N-N stretching peaks decreased with an increase in temperature. The peaks completely disappear above  $140^\circ\text{C}$ ; no peak is observed for the IR plot at  $180^\circ\text{C}$ . Further decomposition of the fumarate group begins. Finally, at  $450^\circ\text{C}$ , the two peaks of spinel ferrite are formed. The total mass loss after pyrolysis of the complex in the air (66.35%) during the isothermal mass loss study agrees with the calculated weight loss (66.17%). The decrease in hydrazine percentages during isothermal mass loss studies matches closely with the TG-DTA and IR data. TG-DTA-DTG plot of  $x=0.5$  where at RT-  $100^\circ\text{C}$  a mass loss of 3.43 %, which is equivalent to little less than 1 hydrazine molecule, which is followed by a DTA peak at  $163^\circ\text{C}$  with exothermic nature and DTG peak  $161^\circ\text{C}$  is observed with a mass loss of 24.86%. A total mass loss of 28% is seen from RT- $230^\circ\text{C}$ , which indicates the total loss of all six hydrazine molecules and the start of decarboxylation. In the final step, 36.97% mass loss is obtained with a DTG peak at  $296^\circ\text{C}$  and DTA peak at  $331^\circ\text{C}$  due to the decarboxylation of the fumarate group. X-ray studies of the as-prepared sample revealed the formation of single-phase spinel ferrite, and the crystallite size was calculated using Scherrer's formula. The saturation magnetization at room temperature was found to

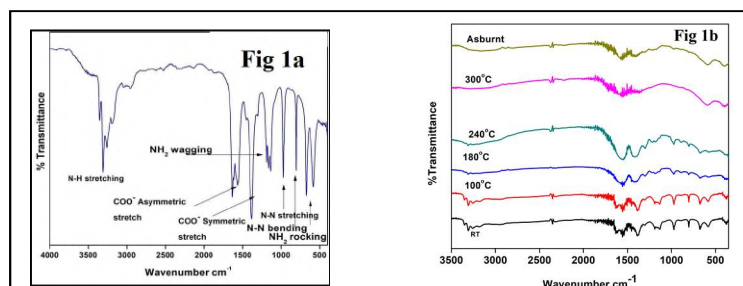


Fig.1: IR spectrum of  $Ni_{0.1}Co_{0.4}Zn_{0.5}Fe(C_4H_2O_4)_3 \cdot 6N_2H_4$ : 1a) at Room temperature and 1b) at various set temperatures

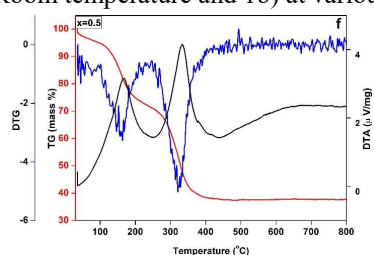


Fig.2: Thermogram of  $Ni_{0.1}Co_{0.4}Zn_{0.5}Fe_2(C_4H_2O_4)_3 \cdot 6N_2H_4$ .

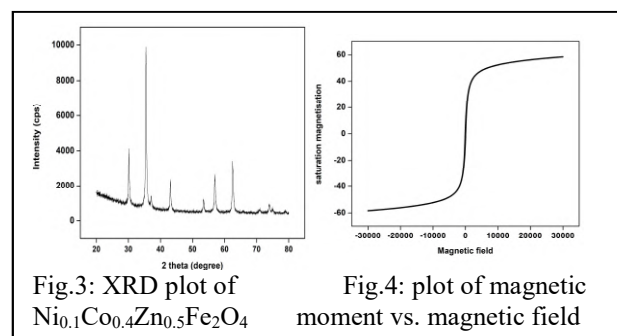


Fig.3: XRD plot of  $Ni_{0.1}Co_{0.4}Zn_{0.5}Fe_2O_4$  Fig.4: plot of magnetic moment vs. magnetic field

be 57 emu/g, and the particles are superparamagnetic.

### References

1. S.G. Gawas, V.M.S. Verenkar, *Thermochimica Acta*, 605 (2015) 16.
2. P.P.G. Dessai, V.M.S. Verenkar, *Journal of Thermal Analysis and Calorimetry*, 142 (2020) 1399.
3. T. Premkumar, S. Govindarajan, *Thermochimica Acta*, 386 (2002) 35.
4. S. Vairan, T. Premkumar, S. Govindarajan, *Journal of Thermal Analysis and Calorimetry*, 101 (2010) 97.

## Analysis of Thermal, Electrical and Magnetic properties of Al Doped Mn-Zn Ferrite synthesized by Auto-combustion Synthesis

Manasi A. Ugvekar and V.M.S. Verenkar\*

School of Chemical Sciences, Goa University, India

\*E-mail: [vmsv@unigoa.ac.in](mailto:vmsv@unigoa.ac.in); Contact no.: +91-9822980123

### Abstract

In this study, nanoparticles of Al-doped Mn-Zn ferrites were synthesized via the autocombustion method, using iminodiacetic acid as a novel fuel. Prior to synthesis, an optimization study was conducted to determine the appropriate metal nitrate-to-fuel ratio. Thermogravimetric analysis of the redox melt was performed to ascertain the decomposition temperature and ensure the complete formation of the nano-ferrites. Structural, electrical and magnetic properties were analyzed using powder XRD, IR spectroscopy, Raman spectroscopy, SEM, VSM, and AC magnetic susceptibility.

In this work, nanoparticles with Al-doped Mn-Zn ferrites of the general formula  $Mn_{0.4}Zn_{0.6}Fe_{2-x}Al_xO_4$  ( $x = 0.1-0.6$ ) were synthesized via an autocombustion method using iminodiacetic acid as a novel fuel. Before synthesis, optimization studies were conducted with  $x = 0.5$ , determining a metal nitrates-to-fuel ratio of (1:0.87) as optimal for further synthesis [1]. Thermogravimetric analysis of the redox melt of the selected (oxidiser: fuel) ratio confirmed the complete formation of the desired nano-ferrite. The thermogram (Fig. 1a) shows three distinct stages. Table 1 summarizes the TG results in the temperature range RT-800°C.

TG Temp (°C)	Remarks
RT- 130	Loss of H <sub>2</sub> O
130-170	Combustion redox reaction of nitrates with fuel
170-800	Metal oxide formed

**Table 1.** TG OF REDOX melt in the temperature range of RT-800°C

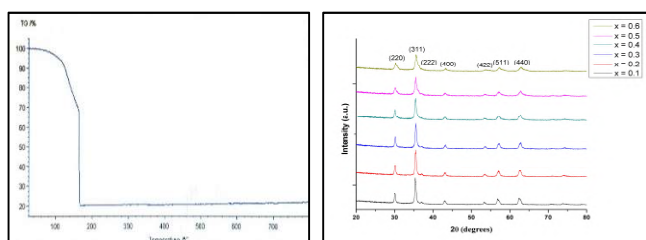


Figure 1. a) TG Curve of redox melt to form 'as-prepared'  $Mn_{0.4}Zn_{0.6}Fe_{1.5}Al_{0.5}O_4$  and b) X-Ray diffraction pattern of 'as-prepared'  $Mn_{0.4}Zn_{0.6}Fe_{2-x}Al_xO_4$  ( $x = 0.1 - 0.6$ ).

Powder XRD analysis (Fig. 1b) revealed the presence of characteristic peaks at (220), (311), (222), (400), (422), (511), and (440), confirming the cubic spinel ferrite structure. The absence of additional peaks indicates the purity and

monophasic nature of the samples. Aluminium incorporation broadened the diffraction peaks and reduced their intensity, demonstrating the successful substitution of  $Al^{3+}$  ions into the spinel structure [2]. The IR spectra reveal two distinct absorption bands around  $400\text{ cm}^{-1}$  and  $550\text{ cm}^{-1}$  range, aligning with the characteristic of spinel ferrites, while Raman spectra revealed five active optical modes ( $A_{1g}$ ,  $T_{2g}(1)$ ,  $T_{2g}(2)$ ,  $T_{2g}(3)$  and  $E_g$ ), confirming cubic spinel ferrite formation. VSM plots confirmed ferrimagnetic behaviour. The AC magnetic susceptibility indicated a decrease in curie temperature ( $T_c$ ) with increasing  $Al^{3+}$  content. This reduction is attributed to weakened superexchange interactions between metal ions at the A and B sites [3]. A decrease in electrical resistivity with increasing temperature was observed, suggesting semiconductor behaviour in the synthesized ferrites [4]. SEM images displayed agglomerated nanoparticles, consistent with nanocrystalline characteristics.

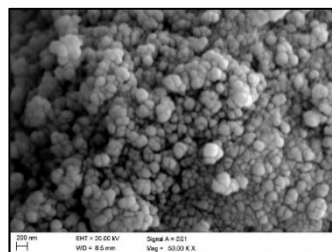


Figure 2. SEM image of 'as-prepared'  $Mn_{0.4}Zn_{0.6}Fe_{1.5}Al_{0.5}O_4$ .

### References:

- P.P.G. Dessai, S.S. Meena, V.M.S. Verenkar, *J. Alloys Compd.*, 842 (2020) 155855.
- R.L. Dhiman, S.P. Taneja, V.R. Reddy, *Adv. Condens. Matter Phys.*, 2008 (2009) 839536.
- M.B. Mohamed, A.M. Wahba, *Ceram. Int.*, 40 (2014) 11773 – 1178.
- A.K. Singh, A. Verma, O.P. Thakur, C. Prakash, T.C. Goel, R.G. Mendiratta, *Jpn. J. Appl. Phys.*, 41 (2002) 51.

## Investigation of Reaction Kinetics Parameters for the Synthesis of Lithium Orthosilicate

Shivdatsinh Ghariya<sup>a\*</sup>, Aroh Shrivastava<sup>b,c</sup>, Shital Amin<sup>a</sup>, Swapnil S. Lonare<sup>b</sup> and Paritosh Chaudhuri<sup>b,c</sup>

<sup>a</sup>L.D. College of Engineering, Ahmedabad

<sup>b</sup>Institute for Plasma Research, Gandhinagar, Gujarat

<sup>c</sup>Homi Bhabha National Institute, Training School Complex, Anushakti Nagar, Mumbai

[shivdatsinhghariya@gmail.com](mailto:shivdatsinhghariya@gmail.com)

### Abstract

Thermo-gravimetric analyzer is employed to investigate the reaction kinetic parameter for the formation of Lithium orthosilicate ( $\text{Li}_4\text{SiO}_4$ ). The experiments are conducted in temperature ranging from 300 K to 1173 K under argon atmosphere in three different heating rates of 5, 10 and 20 K/min. The non-isothermal kinetic data is compared with different model-free techniques such as iso-conversional method of Flynn–Wall–Ozawa (FWO), Kissinger–Akahira–Sunose (KAS). Activation energy for lithium orthosilicate synthesis is estimated as 294 kJ/mol and 296 kJ/mol by FWO and KAS methods.

### 1. Introduction

In fusion reactors, lithium orthosilicate ( $\text{Li}_4\text{SiO}_4$ ) has drawn attention as a tritium breeder material. Because it can create tritium when exposed to neutron irradiation, it is a good candidate for this use.  $\text{Li}_4\text{SiO}_4$  exhibits good tritium release properties, robust thermal stability, and outstanding chemical compatibility with other reactor materials. Additionally, the high lithium density of  $\text{Li}_4\text{SiO}_4$  increases the efficiency of tritium breeding. Because of these characteristics, it is a vital part of the blanket of fusion reactors, where it helps to guarantee a steady supply of tritium for reactor operation. The synthesis and development of lithium ortho-silicate is challenging. To initiate the development of this materials, the step is to identify the reaction mechanism of the lithium ortho-silicate formation. Earlier researchers [1] have worked on the reaction kinetics of this synthesis however much details could not be extracted. The identification of the reaction kinetics parameters is highly dependent of raw materials, its particle size, and its purities. In this work, we tried our initial attempts to synthesize the lithium ortho-silicate by solid state reaction by using a silicon dioxide and lithium carbonate as raw materials. The study examines the reaction kinetics of lithium ortho-silicate synthesis its activation energy and reaction mechanism.

### 2. Materials & Experiments

$\text{Li}_2\text{CO}_3$  and  $\text{SiO}_2$  (Analytical reagent (A.R) grade) were taken in 2:1 molar stoichiometric ratio. Wet milling and mixing were carried out inside pot mill. Grinding was carried out for 24 hours with ball to powder ratio 10:1. The milled mixture was dried in vacuum oven at 100 °C for 4 h. These grinded raw materials were used for thermo-gravimetric measurement. Thermo-gravimetric analysis (TGA) experiments were performed by using simultaneous thermal analyzer (Linseis STA PT 1600). In each experiment ~15 mg. sample was placed inside the alumina crucible. Samples were heated from 300 K to the maximum temperature of 1173 K with three different heating rates of 5, 10 & 20 K/min. under argon atmosphere with 20 ml/min flow rate.

### 3. Kinetics Analysis

The general expression for the rate of reaction is

$$\frac{d\alpha}{dt} = k(T) \cdot f(\alpha) \quad (1)$$

$\alpha$  = degree of conversion,  $\frac{d\alpha}{dt}$  is rate of reaction. The amount of the sample at time 't' is defined in terms of the change of the mass of sample:

$$\alpha = \frac{\Delta W}{\Delta W_\infty} = \frac{W_0 - W}{W_0 - W_\infty} \quad (2)$$

Where  $W_0$ ,  $W$  and  $W_\infty$  are the initial weight, weight at any arbitrary time t, final weight of sample.  $f(\alpha)$  is the function of  $\alpha$  depending on the reaction mechanism,  $k(T)$  is the rate constant at temperature T,

$$k(T) = Ae^{-E_a/RT} \quad (3)$$

Where, A is pre-exponential factor ( $\text{min}^{-1}$ ),  $E_a$  is the activation energy (kJ/mol), R is the universal gas constant ( $\text{J K}^{-1} \text{mol}^{-1}$ ) and T is the absolute temperature (K). Substituting of (3) into (1) gives the expression to calculate the kinetic parameters:

$$\frac{d\alpha}{dt} = f(\alpha)Ae^{-E_a/RT} \quad (4)$$

Activation energy of the reaction is determined by using FWO, KAS method.[2]

Table 1: Model free methods for the kinetic

Method name	Equation	Eq. No
Flynn–Wall–Ozawa Method	$\ln(\beta) = \ln \frac{AE}{Rg(\alpha)} - 5.331 - 1.052 \frac{E}{RT}$	(5)
Kissinger–Akahira–Sunose Method	$\ln \left( \frac{\beta}{T^2} \right) = \ln \frac{AR}{E} + \ln \left( \frac{df(\alpha)}{d\alpha} \right) - \frac{E}{RT}$	(6)

### 4. Results & Discussion

The TG and DTG curve of the formation of  $\text{Li}_4\text{SiO}_4$  under argon atmosphere is obtained at three different heating rates of 5, 10 and 20K/min are shown in figure 1. The TG curve shows the percentage mass loss of sample over the range of temperature 590 K to 1173 K. The weight loss started from 590 K. There is minimal mass loss below 590 K for all heating rates. This implies that the material is thermally stable in this range and no decomposition or reaction has started yet.

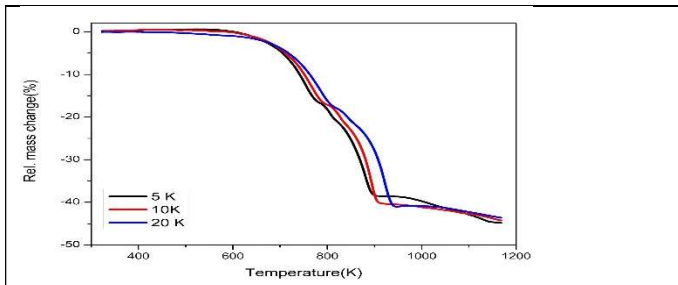


Figure 1 effect of heating rate on relative mass change of lithium carbonate and silicone dioxide

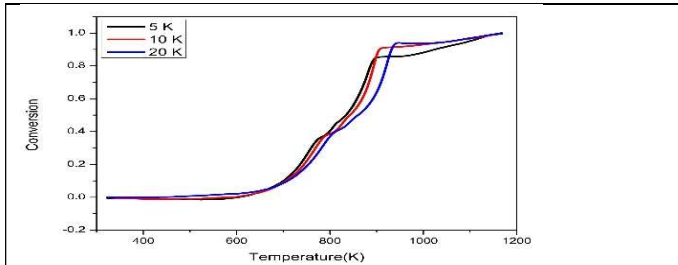


Figure 2 Conversion of lithium carbonate and silicone dioxide to lithium orthosilicate as a function of temperature

Major mass loss begins around 633 K, accelerating through 633-1139 K for 5 K/min heating rate, 648-1163 K for 10 K/min and, 678-1168 K. The total mass loss observed as 45.3%, 44.5% and 43.3 % for 5, 10, and 20 K respectively. Figure 2 shows the effect of temperature on the conversion to lithium orthosilicate at different heating rate. It is observed that there is a shift in the temperature due to the change in the heating rate. The higher heating rate shows the higher temperature for the same degree of conversion. The DSC signal of the same experiments is shown in figure 3 and support the TGA data. The DSC signal confirms that this reaction is a multi-step reaction. There are multiple endothermic peaks are shown in the initial stage of the reaction followed by an exothermic reaction between 923-1173 K.

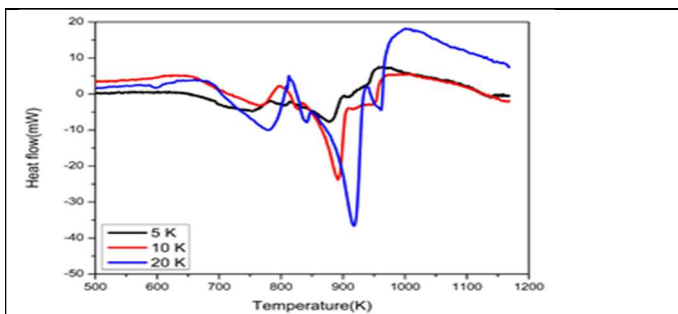


Figure 3 Mass loss derivative curves as a function of temperature

#### 4.1 Determination of activation energy

The TG/DTG experimental data are used for the reaction kinetics analysis. Two iso-conversional methods i.e. Flynn–Wall–Ozawa (FWO) and, Kissinger–Akahira–Sunose (KAS) are used to calculate the activation energy of the reaction. The iso-conversional plots of these methods are shown in Figures 4 and 5, respectively. In this analysis, conversion from 0.2 to 0.8 is considered for calculating the kinetic parameters based on iso-conversional method. Curves are plotted  $\ln(\beta)$  versus  $(1000/T)$  in FWO method,  $\ln(\beta/T^2)$  versus  $(1000/T)$  in KAS method. The activation energies are calculated from the slope obtained from the curve.

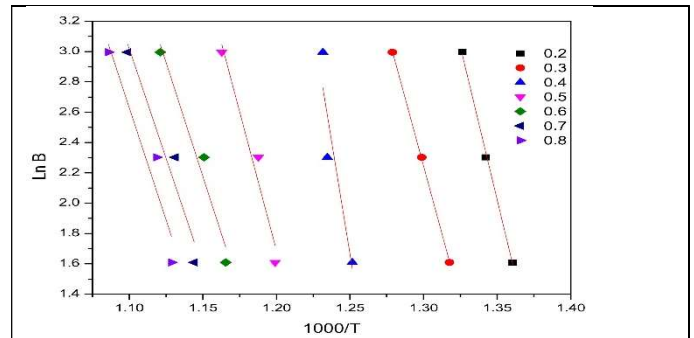


Figure 4  $\ln\beta$  versus  $1000/T$  (FWO Plot)

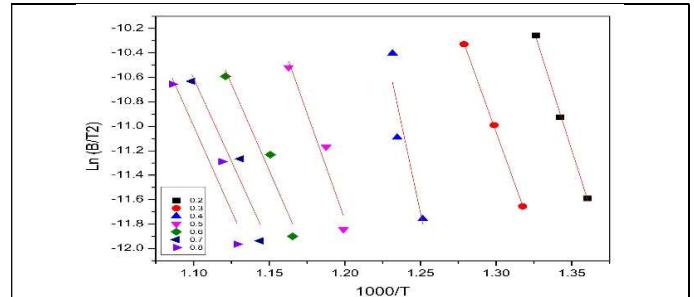


Figure 5  $\ln(\beta/T^2)$  Vs.  $1000/T$  KAS Plot

#### 5. Conclusion

The activation energy ( $E_a$ ) in this work was determined using the iso-conversional methods of KAS and FWO, which produced mean values of 294 and 296 kJ/mol, respectively, showing good agreement. The reaction mechanism is calculated and will be presented in this paper.

#### References

- [1] Ghuge, N. S., Mandal, D., Jadeja, M. C., & Chougule, B. K. (2022). Kinetics Analysis of Solid-State Reaction for the Synthesis of Lithium Orthosilicate. *Environmental Science and Engineering*, 379–391.
- [2] Flynn JH, Wall LA (1966) A quick direct method for determination of activation energy from thermogravimetric data. *J Poly Science B, Poly Lett* 4:323–3.

## Effect of Thermal Treatment on Structure of Reactively Sputtered NiO Thin Films

Amrita Das<sup>a\*</sup>, Debarati Bhattacharya<sup>a,b</sup>, Swapan Jana<sup>a</sup>, Sipra Choudhury<sup>c</sup>, S K Ghosh<sup>d</sup> and Surendra Singh<sup>a,b</sup>

<sup>a</sup>Solid State Physics Division, B.A.R.C, Mumbai 400085

<sup>b</sup>Homi Bhabha National Institute, Anushaktinagar, Mumbai 400094

<sup>c</sup>Radiation and Photochemistry Division, B.A.R.C, Mumbai 400085

<sup>d</sup>Materials Processing And Corrosion Engineering Division, B.A.R.C, Mumbai 400085

\* amritad@barc.gov.in

### Abstract

NiO thin films were prepared using reactive sputtering with different oxygen gas flow rate. The obtained films were annealed in vacuum as well as in air at 400°C for 1hour. As deposited and annealed films were investigated with GIXRD and UV-Visible spectroscopy for structural and optical changes due to annealing.

**Introduction:** NiO is a *p*-type semiconductor with wide band gap energy of 3.6eV to 4.0eV with high hole concentration. Due to its wide band gap semiconducting properties it has been thoroughly investigated for possible application in toxic gas sensing[1], electro-catalysis[2] and optoelectronic devices[3]. NiO thin films are prepared using various techniques. We have prepared NiO films using reactive dc magnetron sputtering in which two oxygen argon flow ratios were used[4]. The obtained films were annealed at 400°C for 1hr both in vacuum and ambient atmosphere. All the films were analyzed using GIXRD and UV-visible technique to observe the change in structural and optical properties due to thermal treatments.

**Experimental details:** NiO films were fabricated using DC magnetron sputtering in reactive sputtering mode in which two O<sub>2</sub> gas flows, 3sccm and 10sccm were used. These films were deposited at 100watt power for 15mins at Ar gas flow 20sccm. These films were named NiO2asdep and NiO6asdep respectively. NiO films obtained in these method were annealed in air as well as in vacuum of the order of 10<sup>-5</sup>mbar at 400°C for 1hour. NiO films annealed in air and vacuum were named as given NiO2aa, NiO2va, NiO6aa and NiO6va respectively. These films were deposited on silicon and glass substrates.

NiO thin films were characterized using GIXRD technique. Copper K<sub>α</sub> source having wavelength ( $\lambda$ ) 1.54 Å is used in this techniques to obtain diffraction pattern. The samples are recorded in a 2 $\theta$  range of 30° to 100°. Here parallel X-ray beam falls on a sample surface at the small angle of incidence so that the X-rays do not penetrate into the substrate and we get diffraction pattern of thin films only. Graph of intensity versus 2 $\theta$  was obtained at 0.5° grazing angle. For all the films, the crystallite size (*D*) was calculated from (FWHM) (*W*) of the applicable orientation diffraction peak by using the Debye-Scherrer's equation:

$$D = 0.9\lambda / B \cos\theta \quad (1)$$

Where,  $\lambda = 1.54\text{Å}$  is the X-ray wavelength,  $B = W\pi/180$ ,  $k = 0.94$  and  $\theta$  is the Bragg diffraction angle of the XRD peak. The microstrain ( $\epsilon$ ) in thin films were obtained employing the following equation:

$$\epsilon = B/4\tan\theta \quad (2)$$

UV-visible spectroscopy was performed on these films to study the band gap energy and transmission. Band gap energy was calculated by plotting the Tauc plot of the absorption spectra of the films.

**Result and Discussion:** GIXRD spectra of NiO<sub>2</sub> and NiO<sub>6</sub> films were shown Figure1(a) and (b). Films were characterized using pc pdf card 00-044-1159. In both as deposited samples NiO peaks were obtained at 43°(012) and 62°(110) 2 $\theta$  angle.

But in case of NiO6asdep NiO peak at 36° which is a little shifted from its original 37° peak was also obtained. When we calculated the crystallite size and micro-strain of the NiO peaks of both as deposited samples it was observed that crystallite size of the films have increased and strain decreased in case of NiO6asdep. This indicates lower oxygen flow gives better crystalline NiO formation in reactively sputtered thin films.

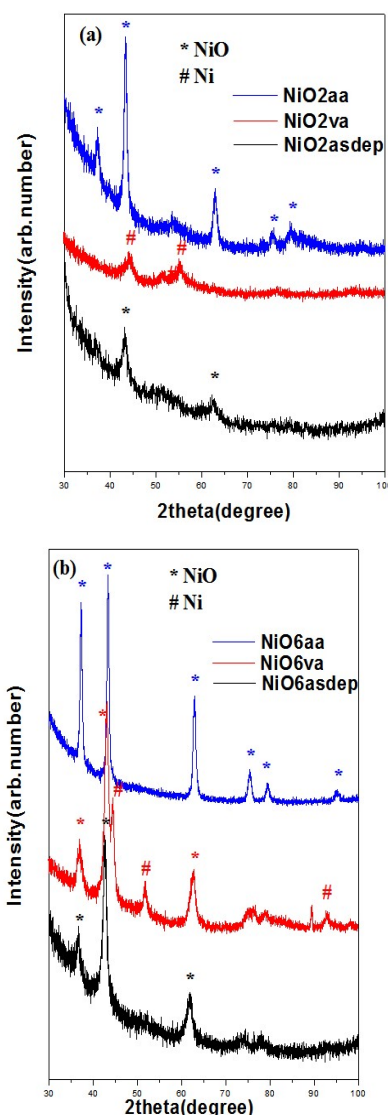


Figure 1: (a) GIXRD spectra of NiO<sub>2</sub>as-deposited, NiO<sub>2</sub> vacuum annealed and NiO<sub>2</sub> air annealed films. (b) GIXRD spectra of NiO<sub>6</sub>as-deposited, NiO<sub>6</sub> vacuum annealed and NiO<sub>6</sub> air annealed films.



In the figure 1(a) it is clearly seen that in case of NiO<sub>2</sub>, film was completely crystallized into Ni after vacuum annealing but in air annealing we get crystalline NiO. Crystallite size of NiO also increased after air annealing and strain decreased [5].

In case of NiO<sub>6</sub> films, vacuum annealing leads to dissociation, both Ni and NiO peaks were obtained which is evident from figure 2. But, in air annealing NiO peaks were obtained for which crystallite size was increased and strain decreased. Calculated crystallite size and strains were given in the table 1 below.

**Table 1.** Crystallite size (D) in Å and strain (ε) obtained from the GIXRD data for NiO<sub>2</sub>asdep, NiO<sub>2</sub>va, NiO<sub>2</sub>aa, NiO<sub>6</sub>asdep, NiO<sub>6</sub>va and NiO<sub>6</sub>aa films.

Film name	Crystallite Size (Å)	Micro-Strain
NiO <sub>2</sub> asdep (NiO)	85	0.0193
NiO <sub>2</sub> va (Ni)	83	0.0117
NiO <sub>2</sub> aa (NiO)	105	0.0073
NiO <sub>6</sub> asdep (NiO)	127	0.0235
NiO <sub>6</sub> va (Ni)	115	0.0065
NiO <sub>6</sub> va(NiO)	71	0.0142
NiO <sub>6</sub> aa(NiO)	148	0.0046

UV-visible spectroscopy obtained for both NiO<sub>2</sub> and NiO<sub>6</sub> samples were plotted for band gap energy measurement. NiO<sub>2</sub>asdep sample was showing band gap of 3.2eV and for NiO<sub>2</sub>aa sample it was 3.74eV. As in air annealing NiO<sub>2</sub>aa is giving increased crystallite size and decreased strain than the NiO<sub>2</sub>asdep film, band gap energy of the film also increased [6]. NiO<sub>6</sub>asdep film was showing band gap of 3.82eV which is greater than the band gap of NiO<sub>2</sub>asdep because of increased crystallite size in case of NiO<sub>6</sub>asdep film. There is a little increase in band gap energy of NiO<sub>6</sub>aa film than the NiO<sub>6</sub>asdep one because of oriented structure NiO formation in case of NiO<sub>6</sub>asdep. But, in case of vacuum annealing the band gap energy drops to 3.36eV because of Ni-NiO dissociation. Changes in band gap energy for NiO<sub>6</sub> films are shown in the figure 2.

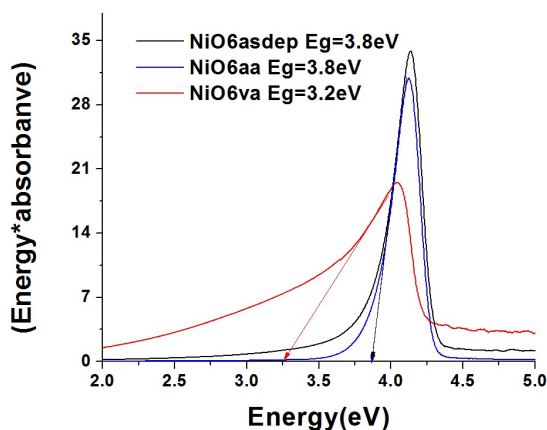


Figure 2: Band-gap energy of NiO<sub>6</sub>asdep, NiO<sub>6</sub>aa and NiO<sub>6</sub>va films.

Transmission spectra of the films were also recorded and shown in figure 3(a) and (b) below. NiO<sub>2</sub>asdep and NiO<sub>6</sub>asdep films had transmission of 80% and 65% at 500nm respectively. In case of air annealed samples both in NiO<sub>2</sub> and NiO<sub>6</sub> transmission increased as air annealing had developed visibly transparent films. After air annealing transmittance increased

from 80% to 86% in NiO<sub>2</sub>sample and in NiO<sub>6</sub> sample it increased from 65% to 100% for 500nm.

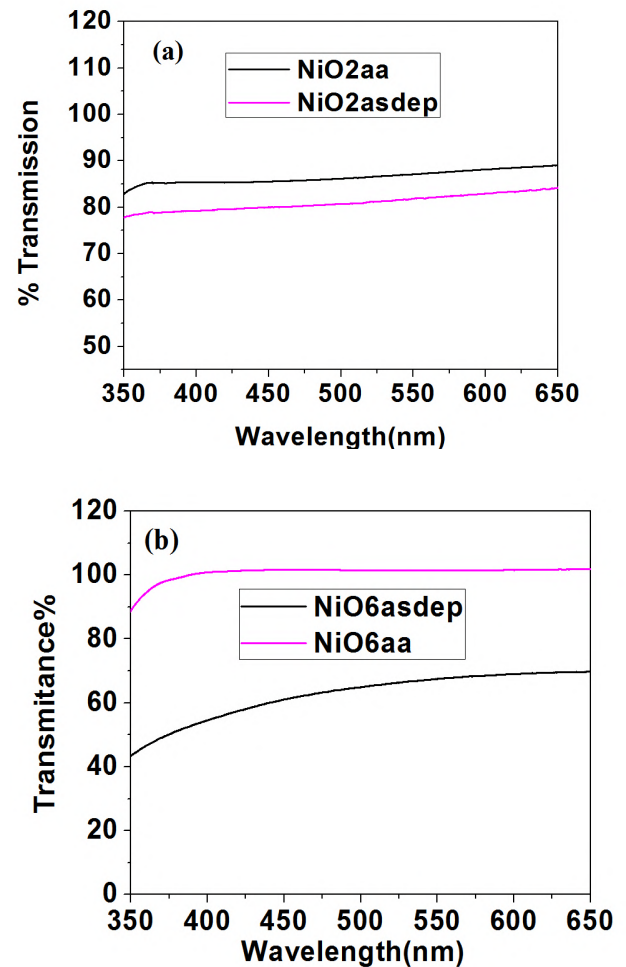


Figure 3:(a) Transmission spectra of NiO<sub>2</sub>asdep and NiO<sub>2</sub>aa film. (b) Transmission spectra of NiO<sub>6</sub>asdep and NiO<sub>6</sub>aa film.

**Conclusion:** NiO crystalline thin films were prepared using different gas flow rates of oxygen in DC magnetron sputtering system. These films were treated with different annealing conditions. Vacuum annealing shows dissociation and NiO to Ni transformation where in air annealing we obtained refined NiO structure. We had obtained increased crystallite size and decreased strain from GIXRD analysis in the case air annealing also increased band-gap energy value of air annealed samples which confirms relaxation and better orientation of structure in air annealing.

### References

1. I Hotový, J Huran , L Spiess , R Čapkovíc , Š Haščík, Vacuum, 300-307 (2000)
2. S. C. Bulakhe and R. J. Deokate, J Mater Sci: Mater Electron, 18180-18186 (2022)
3. A.K. Mahmud Hasan , K. Sobayel , Itaru Raifuku *et al*, Results in Physics, 103122 (2020)
4. Ashok Kumar Reddy, A. Mallikarjuna Reddy, A. Sivasankar Reddy, P. Sreedhara Reddy, Journal of Nano and Electronic Physics, 04002, (2012)
5. Parashurama Salunkhe and Dhananjaya Kekuda , J Mater Sci: Mater Electron, 21060–21074 (2022)
6. M.K. Beisembekov, G.I. Omarbekova, S.K. Tazhibayev, A.K. Aimukhanov, A.S. Baltabekov, A.Z. Ziyat and A.K. Zeinidenov, Optical Materials, 115398, (2024)

## Thermal Analysis – An Important Tool for Preparation and Qualification of CuCrO<sub>2</sub> towards Hydrogen Sensing Applications

Aleena Xavier<sup>a</sup>, Dipankar Kundu<sup>b</sup>, E. Prabhu<sup>b</sup>, Sajal Ghosh<sup>b</sup>, S. Muthuraja<sup>a\*</sup> & V. Jayaraman<sup>b</sup>

<sup>a</sup>Vellore Institute of Technology, Vellore – 632 104

<sup>b</sup>Materials Chemistry Division, Materials Chemistry and Metal Fuel Cycle Group

Indira Gandhi Centre for Atomic Research, Kalpakkam – 603 102

\* [muthurajas@vit.ac.in](mailto:muthurajas@vit.ac.in), +91 8667477039

### Abstract

Phase-pure hexagonal CuCrO<sub>2</sub>, a p-type conducting oxide synthesized by co-precipitation method in argon atmosphere by employing ascorbic acid as a reducing agent while solid state reaction method yielded CuO as an impurity in CuCrO<sub>2</sub>. Thermal analysis investigations elucidated the stability of CuCrO<sub>2</sub> up to 180°C in air. CuCrO<sub>2</sub> exhibits selective response towards H<sub>2</sub> at 180°C.

### Introduction

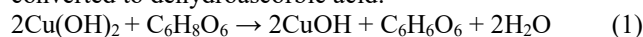
Hydrogen is a versatile gas and it has an excellent application in numerous industries and fields due to its unique properties. The key utilities of H<sub>2</sub> are in the field of energy, fuel, chemical industries, transportation etc. The demand for hydrogen is huge; hence any abnormal accidental leaks of H<sub>2</sub> in these places need surveillance. Technique like thermal conductivity detector (TCD), semiconducting metal oxide (SMO), electrochemical and pellistor based sensors are challenging sensing methods for hydrogen detection in air. Among these techniques TCD and SMO based sensors are most promising for online monitoring of H<sub>2</sub> in the ambient. Presently, development of gas sensors using conducting oxides in the family of SMOs is huge and especially developing sensing material for wide range detection for analytes are in more demand.

Conducting oxides exhibit excellent optical transparency and electrical conductivity. These oxides show wide band gap and excellent chemical and mechanical stability. The n-type conducting oxides show good electrical conductivity ( $\sigma$ : 10<sup>3</sup> – 10<sup>4</sup> S/cm), electronic charge carriers ( $n$ : 10<sup>18</sup> – 10<sup>20</sup> cm<sup>-3</sup>) and electron mobility ( $\mu_e$ : 10 – 300 cm<sup>2</sup>/Vs) when compared to p-type oxides ( $\sigma$ : 10<sup>-3</sup> – 10<sup>0</sup> S/cm,  $p$ : 10<sup>17</sup> – 10<sup>18</sup> cm<sup>-3</sup> &  $\mu_h$ : 0.1 – 10 cm<sup>2</sup>/Vs). The n-type conducting oxides are well known for the detection of low concentration of analytes. Its limitation is the basic sensor output of these oxides is very sensitive to the variation in ambient temperature and to changes in ambient humidity [1]. The p-type conducting oxides (PTCO) are chosen based on their inherent stability to thermal drift and humidity [2]. The thermal activation of holes from acceptor states in p-type oxides are less sensitive to small temperature changes, leading to reduced thermal drift. These oxides can be tailored for wide range detection. CuCrO<sub>2</sub> is a p-type conducting oxide, which belongs to the general family of A<sup>+</sup>B<sup>3+</sup>O<sub>2</sub> (A<sup>+</sup> = Cu<sup>+</sup>, B<sup>3+</sup> = Cr<sup>3+</sup>) and has a delafossite structure [3]. Present work discusses the preparation of phase-pure CuCrO<sub>2</sub> and its utility for sensing hydrogen.

### Experimental

Two synthetic routes, namely solid state reaction (SSR) and co-precipitation (CP) methods were adopted for the synthesis of CuCrO<sub>2</sub>. In the SSR, stoichiometric quantities of copper (II) acetate monohydrate (Alfa Aesar, 99.9%) and Cr<sub>2</sub>O<sub>3</sub> (Alfa Aesar, 99.9%) were mixed thoroughly and calcined the powder to 1000°C for 24 h and once again the calcined sample was ground and reheated to 1000°C in air. For CP, stoichiometric quantities of CrCl<sub>3</sub>.6H<sub>2</sub>O (Alfa Aesar, 99.9%) and

CuSO<sub>4</sub>.5H<sub>2</sub>O (Alfa Aesar, 99.9%) reactants were hydrolyzed to their respective hydroxides using 1M NaOH solution between the pH of 7 and 8 independently. The precipitates washed thoroughly to bring down the pH < 7. The hydroxides and L-(+)- ascorbic acid (99%) solution were taken inside argon glove box. Cupric hydroxide Cu(OH)<sub>2</sub> was reduced to cuprous hydroxide Cu(OH) using L-(+)- ascorbic acid (reducing agent) as shown in eqn. 1. During the reaction ascorbic acid was converted to dehydroascorbic acid.



Chromium hydroxide and cuprous hydroxide were mixed thoroughly inside the glove box. The solid state prepared compound and hydroxides were characterized by XRD (M/s. Explorer GNR, Italy). The as-prepared hydroxide analysed using thermogravimetry and differential thermal analysis (TG/DTA) in the temperature range of 27 – 800°C at a heating rate of 5°C/min in argon atmosphere. using Setsys Evolution 16/18 equipment, M/s Setaram Instrumentation, France. Similarly, the calcined CuCrO<sub>2</sub> from hydroxide characterized using TG/DTA up to 800°C in air. The sensing behavior of CuCrO<sub>2</sub> pellet was tested with H<sub>2</sub>, NH<sub>3</sub>, butane, NO<sub>2</sub> and CH<sub>4</sub> at 180°C in air.

### Results and Discussion

Figure 1 shows the powder XRD of CuCrO<sub>2</sub> synthesized by co-precipitation method exhibit the reflections of (006), (101), (012), (104), (018), (110), (0012), (116), (202) and (024) corresponding to the hexagonal structure of CuCrO<sub>2</sub> and agrees with the JCPDS card no. 0 – 077 – 9229 (Symmetry: R-3m(166), a = 2.97 Å, & c = 17.11 Å,  $\alpha = 90^\circ$ ,  $\beta = 90^\circ$ ,  $\gamma = 120^\circ$ ). The structural elucidation did not show any impurities of CuO or Cr<sub>2</sub>O<sub>3</sub>. XRD confirms the synthesized compound retain copper in +1 oxidation state. The oxide prepared by solid state reaction exhibited mixed phase of CuCrO<sub>2</sub> and CuO (XRD pattern not shown here).

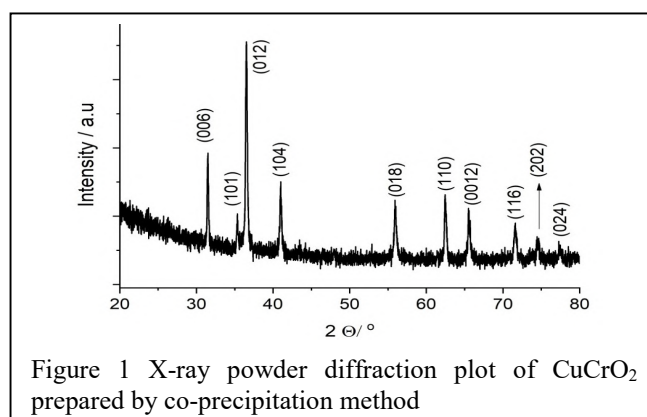


Figure 1 X-ray powder diffraction plot of CuCrO<sub>2</sub> prepared by co-precipitation method

Figure 2 shows TG/DTA plot of as prepared hydroxide phase of  $\text{CuCrO}_2$  in argon. The sample exhibits a gradual weight loss of physisorbed moisture (2%) between the temperature of 40 and 100°C without any thermal event in DTA. But, there is a broadened exothermic event was observed between the temperature of 103 and 145°C in DTA with a weight loss of about 3.5%. This weight loss is due to removal of chemisorbed moisture from the sample. There is a sharp exothermic peak at 609.5°C without any loss in the sample weight. This is probably due to structural rearrangement or relaxation to a stable crystalline oxide. There was no signature information noticed in the cooling cycle by the sample.

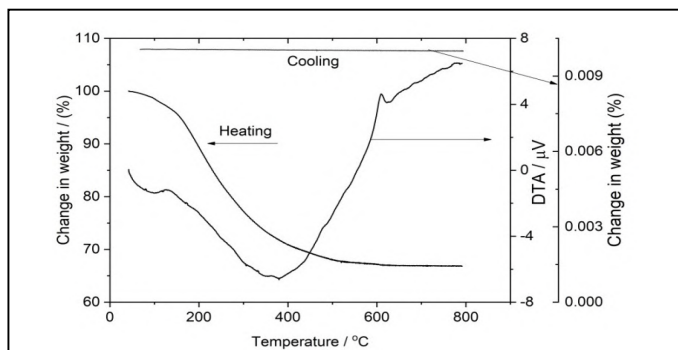


Figure 2 Thermal analysis traces by TG/DTA of hydroxide precursors of  $\text{CuCrO}_2$  in argon

The phase stability is a basic criterion for any sensing material to be operable at elevated temperature in the air ambient. Hence,  $\text{CuCrO}_2$  synthesized in argon ambient was tested for its phase stability by carrying out its TG/DTA profile in air. Figure 3 shows TG/DTA plot of  $\text{CuCrO}_2$  in air. As seen from the figure, there is a gradual uptake in sample weight from 185°C and the increase in weight was observed up to 700°C. Around 0.5% of total weight gain was observed at 800°C from the TG plot and there was no weight gain or loss was noticed in the cooling cycle of TG.

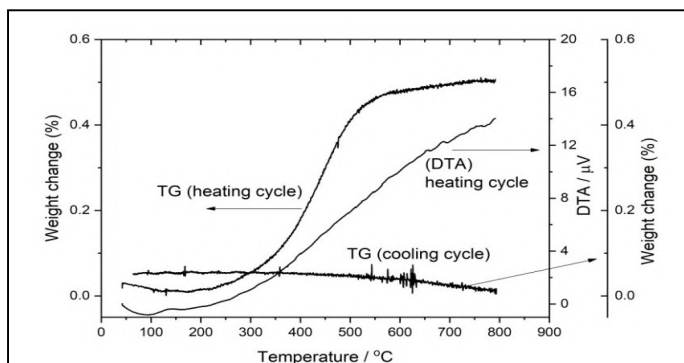


Figure 3 Thermal analysis traces by thermogravimetric and differential thermal analysis of  $\text{CuCrO}_2$  in air

$\text{CuCrO}_2$  to  $\text{Cu}^{2+}$  state resulting to  $\text{CuCrO}_{2.046}$ . From DTA spectrum, it is clear that the reaction is exothermic in nature. From the TG spectrum,  $\text{CuCrO}_2$  is stable up to 180°C. The sample did not exhibit any thermal event in the cooling cycle. The compound did not undergo oxidation between the temperature of 150 and 180°C in air. Thus, sensing characteristics of  $\text{CuCrO}_2$  was carried out at 180°C.

Figure 4 shows the typical response of bulk  $\text{CuCrO}_2$  for the concentration of 10 ppm of  $\text{H}_2$  at 180°C. The resistance of  $\text{CuCrO}_2$  gradually increases from 540Ω and gets stabilized at 558Ω. The increase in resistance is due to the interaction of  $\text{H}_2$

with chemisorbed oxygen ion on the surface as well as in the bulk. The reaction resulted in release of electrons.

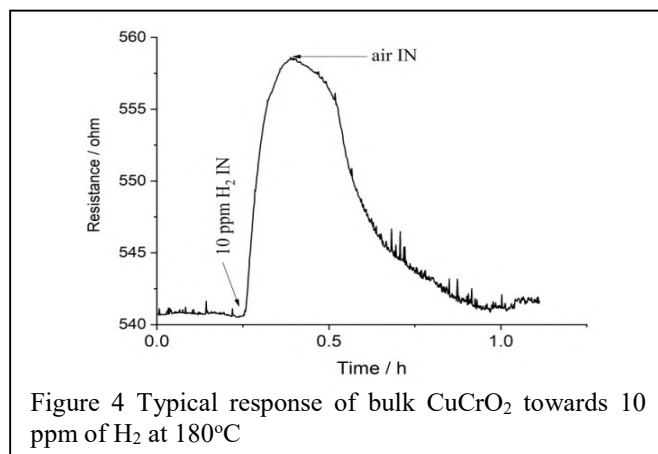


Figure 4 Typical response of bulk  $\text{CuCrO}_2$  towards 10 ppm of  $\text{H}_2$  at 180°C

During the process of sensing, oxygen from air abstracts electrons from the acceptor level, which resulted in hole creation in the valence band. The electrons released during the reaction of  $\text{H}_2$  with chemisorbed oxygen resulted in filling the electrons in the acceptor level. This resulted in increase in resistance of  $\text{CuCrO}_2$ . The response time ( $t_{90}$ ) is around 5 min. and the recovery time ( $t_{90}$ ) is around 45 min. The compound did not respond to  $\text{NH}_3$ ,  $\text{NO}_2$ , butane and  $\text{CH}_4$  at 180°C.

## Conclusion

Phase-pure  $\text{CuCrO}_2$  was synthesized by co-precipitation method. The reactant L-(+)- ascorbic acid act as reducing agent for converting  $\text{Cu}(\text{OH})_2$  from +2 state to +1 state to copper in  $\text{CuOH}$ . TG/DTA studies showed the compound is not getting oxidized in air between the temperature of 150 and 180°C. The thermal studies helped in studying the sensing characteristics of  $\text{CuCrO}_2$  towards different gases at 180°C in air. Preliminary studies show  $\text{CuCrO}_2$  as a promising compound for sensing hydrogen.

## References

1. G. Muller, G. Sberveglieri, Origin of baseline drift in metal oxide gas sensors: Effects of bulk equilibration, *Chemosensors*, 171 (2022)1 – 19
2. H. J. Kim, J.H. Lee, Highly sensitive and selective gas sensors using p-type oxide semiconductors: Overview, *Sensors and Actuators B*, 192(2014)607 – 627
3. A.N. Banerjee, K.K. Chattopadhyay, Recent developments in the emerging field of crystalline p-type transparent conducting oxide thin films, *Progress in Crystal Growth and Characterization of Materials*, 50(2005)52 – 105

## Structural and Thermal Investigation of Novel $\text{CaUW}_4\text{O}_{16}$

Geeta Patkare, Muhammed Shafeeq, Rohan Phatak, Sangit Dhara, Meera Keskar\*

Fuel Chemistry Division, Bhabha Atomic Research Centre

Trombay, Mumbai 40008, India.

Email: [mkeskar@barc.gov.in](mailto:mkeskar@barc.gov.in); Ph No. 022-25596333

### Abstract

A Novel quaternary tungstate compound  $\text{CaUW}_4\text{O}_{16}$  (CUW) was synthesized at  $950^\circ\text{C}$  using solid state method. Structure of the compound was derived from XRD data using Rietveld refinement method. Thermal stability and decomposition of CUW was investigated in air, argon and reduced atmosphere and products were identified by XRD technique. In air, CUW melts at  $1065^\circ\text{C}$  and finally decompose at  $1200^\circ\text{C}$  to  $\text{CaWO}_4$ . When heated in reduced atmosphere at  $800^\circ\text{C}$  for 2 h, the product was mixture of  $\text{CaWO}_4 + \text{UO}_2 + \text{WO}_2$ , indicating reduction of both U and W from (VI) to (IV) oxidation state.

### Introduction

Crystalline ceramics like phosphates, tungstates, zirconates have been studied as an alternative host matrices for immobilization of high level radioactive nuclear waste [1]. Scheelite mineral ( $\text{CaWO}_4$ ) can contain elements from 1+ to 6+ at calcium site and Mo, W, I, V in tungsten position. Structural study of  $\text{CaUMo}_4\text{O}_{16}$  has been carried out earlier [2]. Though, extensive studies have been carried out on uranium tungstates and calcium tungstate no compound is reported in Ca-U-W-O system. Synthesis of  $\text{CaUW}_4\text{O}_{16}$ , formula analog of molybdate was carried out first time and its structural and thermal properties were investigated.

### Experimental

$\text{CaCO}_3$ ,  $\text{UO}_{2.66}$  ( $\text{U}_3\text{O}_8$ ) and  $\text{WO}_3$  were mixed in 1:1:4 molar proportions, thoroughly ground in agate mortar and pestle and heated at different temperatures with intermittent grinding. Progress of reaction was checked by using X-ray diffraction (XRD) technique. XRD patterns of room temperature cooled products were recorded on X-ray diffractometer with  $\text{CuK}\alpha$  X-ray. Thermogravimetric (TG) curves of the compound were recorded in air, argon and reduced ( $\text{Ar}+7\% \text{H}_2$ ) atmosphere. ~50 mg sample was heated in alumina crucible with rate of  $10^\circ\text{C}/\text{min}$ . DTA curves during heating and cooling were recorded to check melting and decomposition of CUW.

### Result and Discussion

XRD pattern of  $950^\circ\text{C}$  heated product was similar to  $\text{CaUMo}_4\text{O}_{16}$ . Qualitative and quantitative elemental analysis of the product by EDXRF, confirmed the molecular formula. Structural parameters of CUW were obtained by refining XRD data of the compound using  $\text{CaUMo}_4\text{O}_{16}$  as model and are  $a=11.5446(3)$  Å,  $b=6.6718(1)$  Å,  $c=8.0818(2)$  Å,  $\beta=90.328(2)^\circ$  and  $\text{vol.}=620.86(3)$  Å<sup>3</sup>. XRD plot of CUW is shown in Fig. 1.

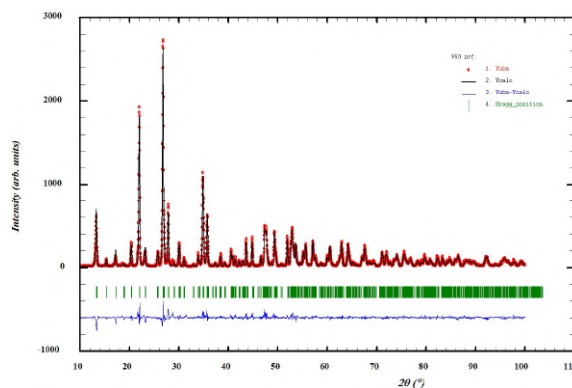


Fig. 1. Rietveld refinement plot for  $\text{CaUW}_4\text{O}_{16}$

To verify the thermal stability and understand decomposition mechanism, TG curves of CUW were recorded in different atmospheres and end products were characterized by using XRD technique. TG curve obtained during heating of CUW up to  $1200^\circ\text{C}$  in dynamic air is shown in Fig. 2.

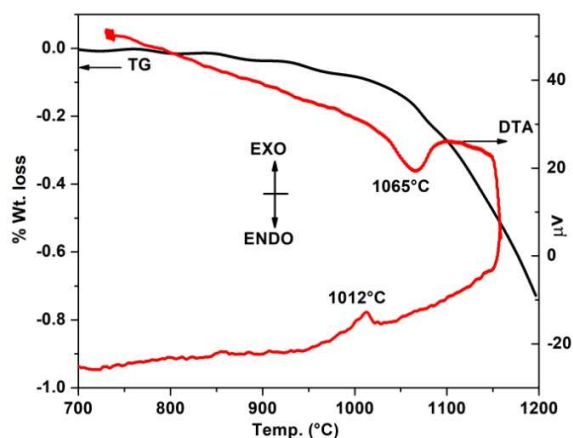
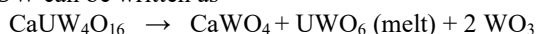


Fig. 2. TG and DTA curves of CUW in air.

TG curve showed slow weight loss above  $950^\circ\text{C}$  which is incomplete up to  $1200^\circ\text{C}$  (0.72%). DTA curve obtained during heating of CUW showed an endothermic peak at  $1065^\circ\text{C}$  whereas an exothermic peak was observed at  $1012^\circ\text{C}$  during cooling, suggested melting and re crystallization of CUW. End product after TG analysis, yellow colored melt, was scanned by XRD technique. The pattern showed broad hump between angle ( $2\theta$ ) 20 to  $30^\circ$  along with peaks which were identified for  $\text{CaWO}_4$  and  $\text{WO}_3$ .  $\text{UWO}_6$ , one of the decomposed product is

reported to melt at 1100°C and thus did not show any peaks in the XRD pattern. When heated at 1000°C in furnace, XRD confirmed formation of UWO<sub>6</sub>. Weight loss above 950°C can be due to slow evaporation of WO<sub>3</sub>. Thus, decomposition of CUW can be written as



To identify final product, CUW was heated in furnace at 1200°C for 10 h. XRD of melt showed peaks for only CaWO<sub>4</sub> and did not show presence of any uranium compounds. By using EDXRF technique presence of uranium remnant was confirmed in the 1200°C heated molten product.

TG recorded in argon atmosphere up to 1000°C was in molten state and XRD of the melt was similar to 1200 TG product confirming decomposition of CUW to CaWO<sub>4</sub> and WO<sub>3</sub>. TG curve of CUW recorded in reduced atmosphere did not show any weight change up to 800°C. Hence, TG curves of CUW were recorded in Ar+7% H<sub>2</sub> by holding isothermal at 800°C for 20, 60 and 120 min and are shown in Fig. 3.

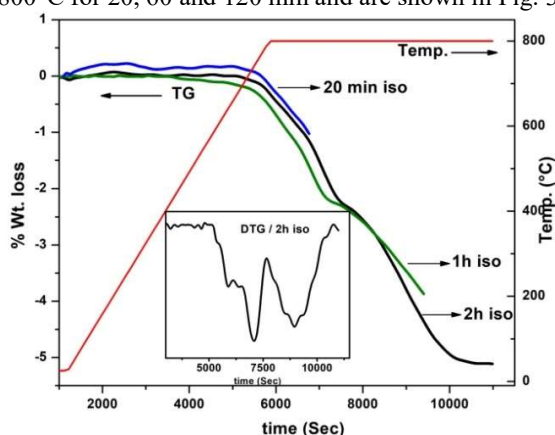


Fig. 3. TG recorded up to 800°C in reduced atmosphere for different time.

XRD of the end products are shown in Fig. 4 and products identified are listed in Table 1.

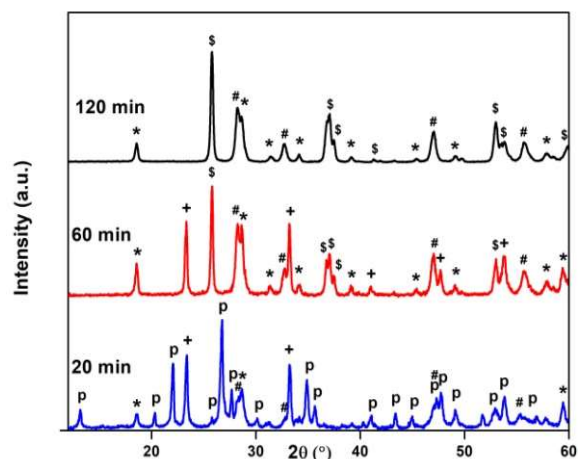


Fig.4. XRD of products obtained by reducing CUW at 800°C for different time. Peaks marked for; CUW(P), CaWO<sub>4</sub>(\*), WO<sub>2.83</sub>(+), UO<sub>2</sub>(#), WO<sub>2</sub>(\$)

TG curve of 120 min isothermal heated sample indicated complete weight loss. XRD of the product was a mixture of CaWO<sub>4</sub>+UO<sub>2</sub>+WO<sub>2</sub> and expected loss for formation of this mixture (5.04%) matches well with observed loss (4.92%). The lattice parameter calculated for UO<sub>2</sub> is 5.4703 Å. The derivative of 120 min TG curve (incept DTG curve Fig. 3.) clearly indicate reduction process in two steps. From TG data and XRD analysis of the heated products, given in table 1, it can be said CUW decomposes in reduced atmosphere and both uranium as well as tungsten get reduced from (VI) to (IV) state. It was also observed that uranium reduces first followed by reduction of tungsten. Earlier thermal studies on UWO<sub>6</sub> have also indicated reduction of uranium and then tungsten [3].

#### References

- [1] A. Gagalla, N. Mansour, Nucl Sci Eng 90 (1985) 320.
- [2] R. Marsh, J. Solid State Chem. 73 (1988) 577.
- [3] M. Keskar, K. Krishnan, R. Phatak, S. Dash, S.K. Sali, S. Kannan, J. Therm Anal Calorim 126 (2016) 659.

Table 1. TG and XRD data of CUW obtained during heating in different atmosphere

Atmosphere	Temp. range	Weight loss (%)		Product identified by XRD
		Exp.	Obs.	
Air	25-1200	-	-	CaWO <sub>4</sub> + 2WO <sub>3</sub> + UWO <sub>6</sub> (amorphous)
Ar	25-1000	-	-	CaWO <sub>4</sub> + 2WO <sub>3</sub> + UWO <sub>6</sub> (amorphous)
Ar+7%H <sub>2</sub>	25-800 (20 min iso)	0.95	1.20	0.5CUW + 0.5CaWO <sub>4</sub> + 0.5 UO <sub>2</sub> + 1.5WO <sub>2.83</sub>
	25-800 (60 min iso)	3.99	3.85	CaWO <sub>4</sub> + UO <sub>2</sub> + 2WO <sub>2</sub> + WO <sub>2.83</sub>
	25-800 (120 min iso)	5.04	4.99	CaWO <sub>4</sub> + UO <sub>2</sub> + 3WO <sub>2</sub>

## Thermodynamic Insights into the Design and Stability of High Entropy Oxides and their electrical behaviour

Jyoti Chahal<sup>\*a,b</sup>, Rimpi Dawar<sup>a,b</sup>, Rakesh Shukla<sup>a,b</sup>, Nitin Kumar<sup>c</sup> and V. Grover<sup>a,b</sup>

<sup>a</sup>Chemistry Division, Bhabha Atomic Research Centre, Mumbai- 400085, India

<sup>b</sup>Homi Bhabha National Institute, Anushaktinagar, Mumbai 400094, India

<sup>c</sup>UGC-DAE Consortium for Scientific Research Mumbai Centre, Mumbai, 400085, India

Corresponding Author: Phone: 0091-22-2559 2274; Fax: 0091-22-25505151

E-mail: vinita@barc.gov.in

### Abstract

This work demonstrates the synthesis of B-site maneuvered compositionally complex ABO<sub>3</sub>- type materials. Entropy-assisted synthesis approaches are utilized to synthesize single-phasic compound. The ability to stabilize single-phase perovskites with various cations on the B-sites offers possibilities for designing high-performance dielectric materials. Thermodynamic studies confirm the entropy stabilized nature of these high entropy compositions. The manifestation of this compositional complexity on electrical behaviour and its variation with temperature is also studied.

**Introduction:** The development of high entropy oxides (HEOs) attracts considerable interest in the materials science community due to the exceptional structural, electronic, and magnetic properties, which arise from the disorder and high configurational entropy associated with the incorporation of multiple metal cations on a single lattice site. In these materials, entropy contributions to the free energy, rather than the cohesive energy, promote thermodynamic stability. This compositional complexity can be used to create new materials with tunable properties. In this manuscript we focus on stabilization of B-site high entropy hexagonal perovskite-related structures of ABO<sub>3</sub>-type via non-equilibrium synthesis approach and the consequent effects of this compositional complexity.

**Experimental:** Various nominal compositions in YBO<sub>3</sub> (B: In, Mn, Fe, Ga, Al) system were synthesized by gel-combustion method in the fuel-deficient stoichiometry using glycine as fuel. The as-obtained powders were calcined followed by heating at various temperatures for phase stabilisation. Various trial and error of annealing temperatures were employed to stabilize the single-phase. The products were characterized by powder XRD on Proto A-XRD LPD. A high temperature Calvet calorimeter (HT-1000) supplied by M/s Setaram, France was employed for measurement of enthalpy of dissolution of the synthesized oxides. The dielectric properties of the HEO compounds were measured over a temperature range from 30 to 300 °C and a frequency range of 100 Hz to 5 MHz using a Novocontrol Alpha-AN impedance analyzer (Novocontrol Technologies GmbH, Germany) equipped with a Quatro nitrogen gas cooling/heating system.

**Results & Discussion:** The synthesized HEOs were characterized using XRD for phase purity and structural analysis. The thermal treatment of High entropy oxide (HEOs) at different temperatures leads to the formation of different phase. Typically, there is a temperature range that enables a multi-component metal oxide to achieve entropy stabilized-single phase, whereas outside this range, a multiphase mixture prevails. Fig. 1 shows the XRD patterns of the HEOs powders calcined at 900 °C. Upon heating, YInO<sub>3</sub>, YIn<sub>0.5</sub>Mn<sub>0.5</sub>O<sub>3</sub> form the single-phase but the composition YIn<sub>0.20</sub>Mn<sub>0.20</sub>Fe<sub>0.20</sub>Ga<sub>0.20</sub>Al<sub>0.20</sub>O<sub>3</sub> exhibits emergence of unidentifiable secondary phases. The systems studied the incorporation of multi-cations distributed randomly over the B-site, resulting in the most single-phasic solid solution.

For the composition and microstructural analysis of the samples, SEM+EDS techniques were utilized. The morphology of the samples is strongly affected by the number of ions present at B-site. SEM results of samples represent

agglomerated particles with uniform grain size distribution and irregular shape. The composition analysis by EDS show measured ratios were close to nominal, indicating no preferential loss of any component during synthesis. High-temperature XRD analysis shows the hexagonal structure splitting in peaks during heating within the 50-1000°C temperature range.

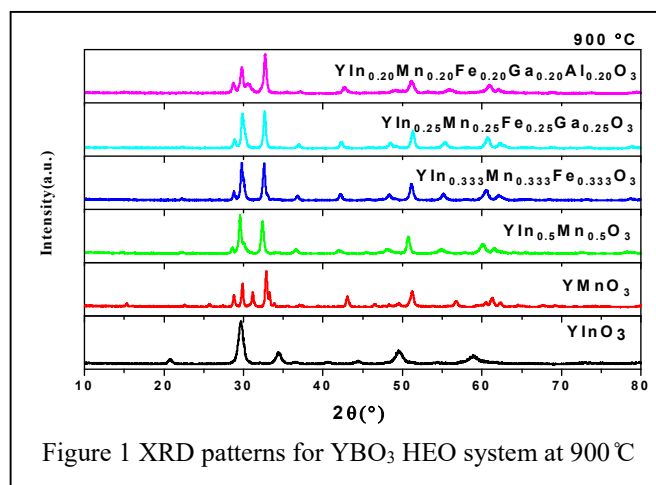


Figure 1 XRD patterns for YBO<sub>3</sub> HEO system at 900 °C

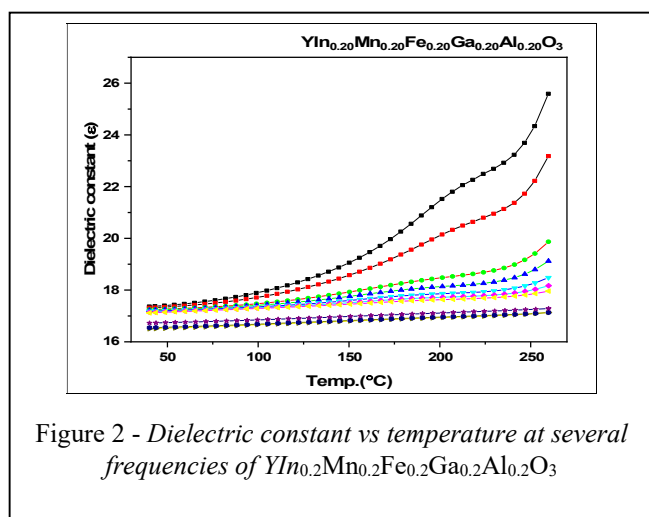
The standard molar enthalpy of formation of YInO<sub>3</sub>, YIn<sub>0.5</sub>Mn<sub>0.5</sub>O<sub>3</sub>, YIn<sub>0.33</sub>Mn<sub>0.33</sub>Fe<sub>0.33</sub>O<sub>3</sub>, YIn<sub>0.25</sub>Mn<sub>0.25</sub>Fe<sub>0.25</sub>Ga<sub>0.25</sub>O<sub>3</sub> and YIn<sub>0.20</sub>Mn<sub>0.20</sub>Fe<sub>0.20</sub>Ga<sub>0.20</sub>Al<sub>0.20</sub>O<sub>3</sub> oxides were obtained from high temperature dissolution experiments performed at 986 K in molten sodium molybdate (3Na<sub>2</sub>O.4MoO<sub>3</sub>) solvent. Using the experimental values of molar enthalpy of drop solution of binary and ternary oxides, the standard molar enthalpies of formation of YInO<sub>3</sub>, YIn<sub>0.5</sub>Mn<sub>0.5</sub>O<sub>3</sub>, YIn<sub>0.33</sub>Mn<sub>0.33</sub>Fe<sub>0.33</sub>O<sub>3</sub>, YIn<sub>0.25</sub>Mn<sub>0.25</sub>Fe<sub>0.25</sub>Ga<sub>0.25</sub>O<sub>3</sub> and YIn<sub>0.20</sub>Mn<sub>0.20</sub>Fe<sub>0.20</sub>Ga<sub>0.20</sub>Al<sub>0.20</sub>O<sub>3</sub> compounds from their respective oxides at 298.15 K were computed. For this, appropriate thermochemical equations based on Hess's law of thermodynamics were employed. The final values are given in Table 1.

The reaction enthalpies accomplished by high temperature calvet calorimeter show the enthalpy of formation ( $\Delta H_{f,ox}$ ) from binary oxides becomes endothermic with increase in the number of ions at B-site. The effect of this configurational entropy on dielectric behaviour and its variation with temperature has also been investigated.

**Table 1: Enthalpies of formation of HEOs from corresponding binary oxides at 298.15 K**

Compound	$\Delta_f H^\circ_{298.15}$
YInO <sub>3</sub> (s)	-1440.26 ± 22.47
YIn <sub>0.5</sub> Mn <sub>0.5</sub> O <sub>3</sub> (s)	-1425.51 ± 22.56
YIn <sub>0.33</sub> Mn <sub>0.33</sub> Fe <sub>0.33</sub> O <sub>3</sub> (s)	-1403.29 ± 22.38
YIn <sub>0.25</sub> Mn <sub>0.25</sub> Fe <sub>0.25</sub> Ga <sub>0.25</sub> O <sub>3</sub> (s)	-1422.76 ± 22.61
YIn <sub>0.20</sub> Mn <sub>0.20</sub> Fe <sub>0.20</sub> Ga <sub>0.20</sub> Al <sub>0.20</sub> O <sub>3</sub> (s)	-1492.86 ± 23.54

Temperature-dependent dielectric permittivity plot at different AC frequencies and shown in Figure 2 of a representative composition YIn<sub>0.2</sub>Mn<sub>0.2</sub>Fe<sub>0.2</sub>Ga<sub>0.2</sub>Al<sub>0.2</sub>O<sub>3</sub>. It is noteworthy that with increasing number of cations at B-site show a static behaviour of relative permittivity with gradual increase of temperature.



### Conclusion:

Our study implies that the deterministic creation of local configurational disorder could be an effective way to enhance functional responses in perovskite oxides and provide an approach to the design of new ferroelectrics.

### References

- [1]. Chahal, J.; Shukla, R.; Srinivasu, K.; Kumar, N.; Phapale, S.; Roy, A.; Grover, V., Mater. Chem. Phys. 2024, 317.
- [2]. Shukla, R.; Grover, V.; Deshpande, S. K.; Jain, D.; Tyagi, A. K., Inorg. Chem. 2013, 52 (22).
- [3] Giaquinta, D. M.; zur Loye, H.-C., Chem. Mater. 1994, 6 (4)
- [4] Grover, V.; Shukla, R.; Jain, D.; Deshpande, S. K.; Arya, A.; Pillai, C. G. S.; Tyagi, A. K. Chem. Mater. 2012, 24 (11),

## Kinetics of HI decomposition and Activation Energy Calculation

\*S.Phapale<sup>a,b</sup>, D.Tyagi<sup>a</sup>, A.N.Shirsat<sup>a</sup>, S.Varma<sup>a,b</sup>, A.K.Tyagi<sup>b</sup>

<sup>a</sup> Chemistry Division, Bhabha Atomic Research Centre, Trombay, Mumbai-400084

<sup>b</sup>Homi Bhabha National Institute, Anushaktinagar, Mumbai-400094.

\* Corresponding author: phapale@barc.gov.in, (022)25592282

### Abstract

This study examines how hydroiodic acid (HI) decomposes in the gas phase as part of the Sulphur-Iodine (S-I) cycle for hydrogen production, using nuclear or solar energy. We tested various metal catalysts, including both noble and non-noble metals, and characterized them with XRD and XPS techniques. Our results show that Bi-based catalysts achieve good conversion rates, reducing the reaction's activation energy. This makes them beneficial for sustainable hydrogen production. Future efforts will aim to enhance non-noble metal catalysts to make the process more economically viable.

### Introduction:

Energy generation is crucial for progress, but heavy reliance on fossil fuels has led to severe environmental, social, and economic issues, including climate change and health risks. This has prompted a shift toward sustainable energy sources like solar, wind, biomass, nuclear, tidal and hydrogen gas.

### Experimental Details:

Data for 3% Bi in C catalyst and calculated the activation energy graphically. The activation energy of a reaction can be calculated using the Arrhenius equation by graphically analyzing the rate constants of the reaction at different temperatures. For the decomposition of HI, the rate constants (k) are measured at various temperatures (T). By plotting the natural logarithm of k (ln k) against the inverse of T (1/T), a straight line is obtained, whose slope corresponds to the negative activation energy (E<sub>a</sub>) divided by the gas constant (R). From the slope, the activation energy can be calculated, providing valuable insights into the energy barrier of the reaction. For example, a steeper slope indicates higher activation energy, suggesting a more energy-demanding reaction. By analyzing the Arrhenius plot, we can determine the activation energy of the HI decomposition reaction and better understand the kinetic mechanisms involved.

### Result and Discussion:

We also studied the kinetics of the reaction for a particular catalyst at different temperatures and calculated the activation energy of the reaction in presence of the catalyst, which was found to be lesser than that in the absence of the catalyst

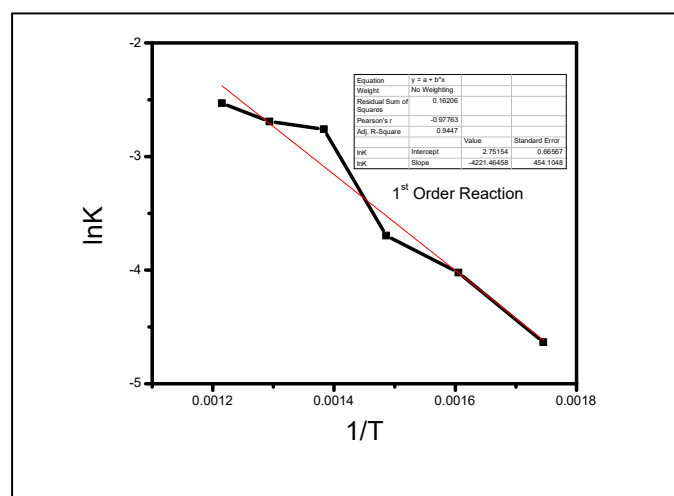


Fig.1. Plot of ln k vs 1/T

Table 1. Calculation for volume and conc. of HI

HI	0.42998345
H <sub>2</sub> O	6.383498379
HI calc. (μmoles)	18.12357361
H <sub>2</sub> O calc. (μmoles)	269.0610601
HI + H <sub>2</sub> O (μmoles)	287.1846337
gas vol (mL s <sup>-1</sup> )	6.432935796
total gas vol (mL s <sup>-1</sup> )	8.266269129
conc (mmol L <sup>-1</sup> s <sup>-1</sup> )	2.19247321
conc (mol L <sup>-1</sup> s <sup>-1</sup> )	0.002192473

Table 2: Data for the Arrhenius plot between ln k vs 1/T

T (K)	rate (mol L <sup>-1</sup> s <sup>-1</sup> )	k (s <sup>-1</sup> )	1/T	ln k
573	2.13132E-05	0.009721089	0.001745	-4.634
623	3.93062E-05	0.017927789	0.001605	-4.022
673	5.44363E-05	0.024828711	0.001485	-3.696
723	0.000138844	0.06332778	0.001383	-2.759
773	0.000148579	0.067767773	0.001293	-2.692
823	0.000174534	0.079605849	0.001215	-2.531

**Conclusion:** Developing catalysts for HI decomposition in the S-I thermo-chemical cycle is key for efficient H<sub>2</sub> production. The activation energy of the HI gas phase decomposition reaction using 3% Bi in C catalyst is found to be 35.1 KJ mol<sup>-1</sup>

### References

1. Turner J, Sverdrup G, Mann M.K, Maness P, Kroposki B, Ghirardi M, Evans RJ & Blake D, Renewable hydrogen Production. International Journal of Energy Research 92008), 32, 379-407.



## Ti<sub>2</sub>AlC MAX-Phase: Synthesis and its Oxidation

Rakesh Kumar\*, Mohammad Yunus and Bikas C. Maji

Mechanical Metallurgy Division, Bhabha Atomic Research Centre, Trombay, Mumbai-400085

\* [krakesh@barc.gov.in](mailto:krakesh@barc.gov.in)

### Abstract

High purity Ti<sub>2</sub>AlC MAX-phase was synthesized from 2Ti:1Al:1C stoichiometric elemental powder mixture through pressure less synthesis (PS) technique at 1470°C/1h under protective Argon atmosphere. The formation temperature of 1470°C was decided based on the differential scanning calorimetric analysis of the starting powder mixture heated up to 1550°C. Oxidation of Ti<sub>2</sub>AlC MAX-phase was carried out at 1200°C for 1h in static air. Phase identification and micro structural analysis of the PSed product as well as oxidized specimen were carried out using X-ray diffraction technique (XRD) and scanning electron microscopy and energy dispersive spectroscopy (SEM-EDS). Oxidized specimens showed an outer porous layer of TiO<sub>2</sub> and a dense inner layer comprising of Al<sub>2</sub>O<sub>3</sub>.

Keywords: High purity, Ti<sub>2</sub>AlC MAX-phase, SEM-EDS.

### Introduction

MAX-phases are a family of layered ternary compounds having a general formula of M<sub>n+1</sub>AX<sub>n</sub>, where M is an early transition metal, A is mainly group A element and X is either C or N. These materials possess a unique combination of properties ranging from metal to ceramics, such as high electrical and thermal conductivity, good machinability, excellent thermal shock resistance and damage tolerance, high elastic modulus, high temperature strength along with superior oxidation and corrosion resistances, which makes them a promising oxidation resistant coating material for high temperature applications. The Zr-based cladding materials currently in use in generation 2 & 3 nuclear power reactors suffer from excessive oxidation and hydrogen production during loss of coolant accident (LOCA), as occurred during Fukushima Daiichi nuclear accident in 2011. Al containing MAX-phases such as Ti<sub>2</sub>AlC, Ti<sub>3</sub>AlC<sub>2</sub> and Cr<sub>2</sub>AlC showed a propensity to form an adherent passive Al<sub>2</sub>O<sub>3</sub> layer while oxidation, which can prevent further inward mobility of oxygen at high temperature. Thus, these MAX-phases have been proposed as a potential coating material for Accident Tolerant Fuel (ATF) clad for the existing as well as next generation water cooled nuclear reactors [1-2].

The aim of the present work was to synthesize high-purity Ti<sub>2</sub>AlC MAX-phase ceramic using elemental powders as input material through pressure-less sintering technique and also evaluate the oxidation behaviour at 1200°C temperature.

### Experimental

Commercial purity elemental powders of Ti, Al and C were used as a starting material for synthesizing Ti<sub>2</sub>AlC MAX-phase. Elemental powders were ball milled for 2h to attain a homogeneous mixture and compacted into pellet by applying a load of 50 MPa using uniaxial hydraulic press. These pellets were pressure-less sintered at 1470°C for 1h in an alumina crucible using a high temperature tubular furnace. Sintering was carried out in flowing argon gas atmosphere. For oxidation study, few sintered pellets were kept at 1200°C in static air for different holding times varying from 1 to 10 h. Phase identification and microstructural characterization were carried out using XRD and SEM-EDS techniques.

### Results and Discussion

Figure 1 shows the HTDSC thermogram obtained from ball milled stoichiometric 2Ti:1Al:1C powder mixture. Apart from the initial endothermic peak at ~650°C associated with Al melting and followed by an exothermic peak at 675°C linked to Ti-Al intermetallic formation, two more exothermic peaks could be noticed at peak temperatures of 1450°C and 1510°C. These two peaks are mostly associated to MAX-phase formation. Guided by this HTDSC thermogram, pressure-less synthesis of the powder mixture was carried out at 1470°C for 1h and the corresponding XRD pattern obtained from the sintered product is shown in Fig. 2. XRD pattern clearly revealed the formation of single Ti<sub>2</sub>AlC MAX-phase without any traces of major secondary phases. Figure 3 shows the BSE image of the sintered specimen which shows a uniform contrast throughout the specimen with a compositional stoichiometry of Ti:Al similar to that of Ti<sub>2</sub>AlC MAX-phase as obtained from the EDS analysis. The fractured surface of this sintered specimen was also examined under SEM and Fig. 4 shows the characteristic layered structure of Ti<sub>2</sub>AlC MAX-phase. Ti<sub>2</sub>AlC specimens that were oxidized in static air at 1200°C were also examined by XRD as well as SEM.

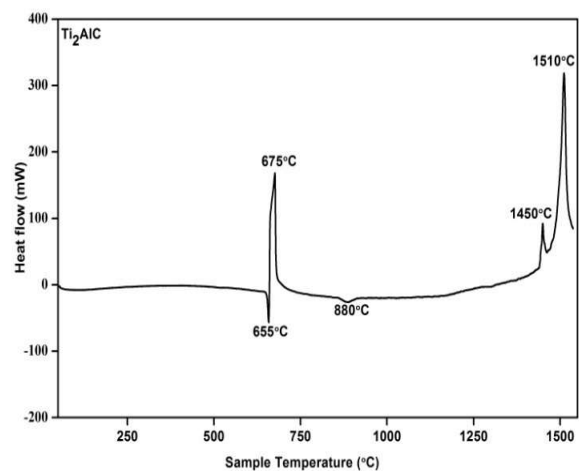


Fig. 1 HTDSC thermogram obtained from 2Ti:1Al:1C ball milled powder mixture.

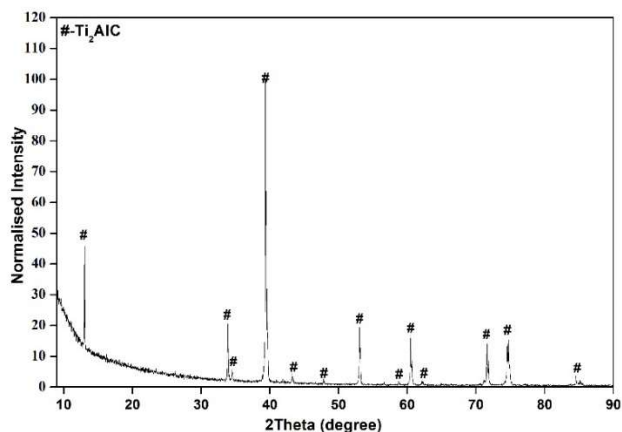


Fig. 2 XRD patterns obtained from the specimen pressureless sintered at 1470° C for 1h.

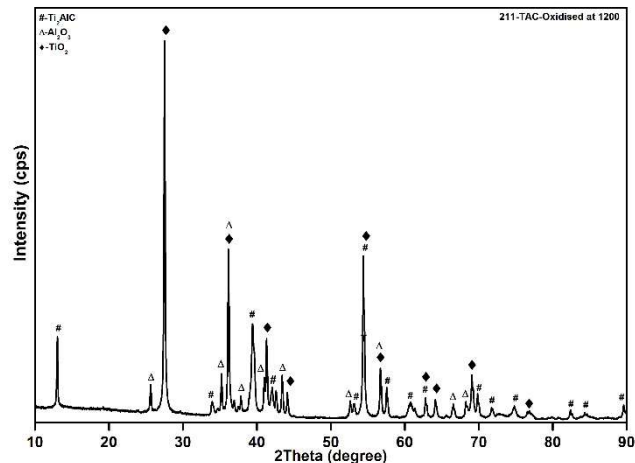


Fig. 5 showing XRD pattern obtained from Ti2AlC MAX-phase after oxidation at 1200°C for 1h in static air.

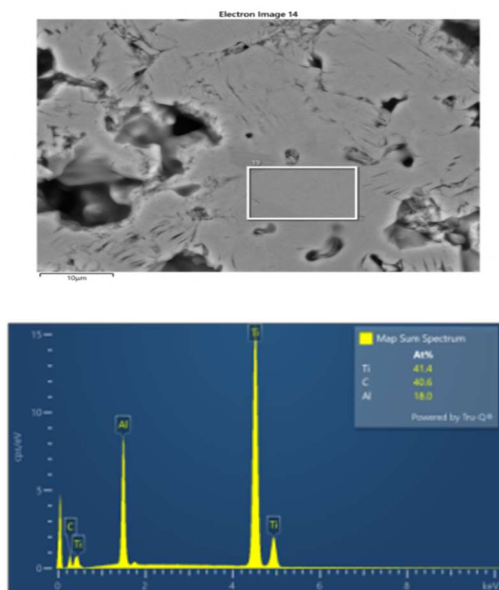


Fig. 3 BSE image of Pressure-less sintered Ti<sub>2</sub>AlC MAX-phase along with EDS spectra.

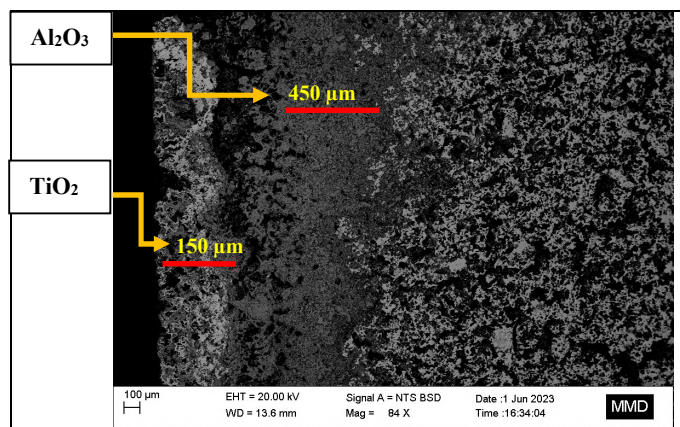


Fig. 6 Cross-sectional BSE image obtained from 1200°C/1h oxidized Ti<sub>2</sub>AlC MAX-phase.

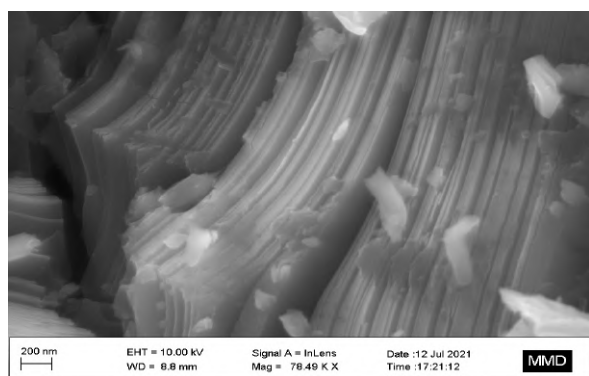


Fig. 4 SE image from fractured surface of Ti<sub>2</sub>AlC MAX-phase specimen.

Figure 5 shows the XRD pattern obtained from Ti<sub>2</sub>AlC MAX-phase specimen after air oxidation at 1200°C for 1h. The major oxide phases that could be clearly identified after oxidation were found to be TiO<sub>2</sub> and Al<sub>2</sub>O<sub>3</sub>. Figure 6 shows the cross-sectional SEM micrograph obtained from oxidized specimen. It was observed that a porous TiO<sub>2</sub> is present as outermost layer and a dense Al<sub>2</sub>O<sub>3</sub> layer exists under the sub-surface.

### Conclusion

Based on the results obtained from this study, the following conclusions can be arrived at:

1. High purity Ti<sub>2</sub>AlC MAX-phase can be synthesized from elemental powders of Ti, Al and C through pressure-less synthesis technique at 1470°C-1 h.
2. After oxidation at 1200°C for 1h, TiO<sub>2</sub> and Al<sub>2</sub>O<sub>3</sub> were the major oxidation products.
4. A porous TiO<sub>2</sub> layer at the outer surface followed by a dense inner Al<sub>2</sub>O<sub>3</sub> layer was noticed after oxidation at 1200°C for 1 h in static air environment.

### Acknowledgement

I would like to extend my heartfelt gratitude to Mr. V.C. Krishnamohan Nair, Mr. K.M. Bandal, Mr. Shubham Chakravorthy, and Mr. R.V. Hatwar for their invaluable technical support during the experiments. I also wish to express my sincere thanks to Ms. Nidhi for her assistance with XRD, Mr. Arjun Sarkar for providing access to the workshop facilities, and Dr. Amit Verma for facilitating the use of the SEM facility.

### References

- [1] Mohammad Yunus, Rakesh Kumar, Bikas C Maji, Madangopal Krishnan, Journal of the European Ceramic Society 42 (2) (2022) 354-363.
- [2] Bikas C. Maji, Mohammad Yunus, Rakesh Kumar, R.N. Singh and Madangopal Krishnan, BARC Report No. BARC/2020/I/014, Sept 2020.

## Solid-state synthesis, characterization and densification of aluminum borate ceramic

Jyothi Sharma<sup>\*1,2</sup>, Biranchi M Tripathi<sup>1</sup>, P.K. Patro<sup>1,2</sup>, Deep Prakash<sup>2</sup>, T. Mahata<sup>1,2</sup>

<sup>1</sup>Powder Metallurgy Division, Bhabha Atomic Research Centre, Vashi Complex, Navi Mumbai – 400703

<sup>2</sup>Homi Bhabha National Institute, Anushaktinagar, Mumbai-400084

Email Id: jyothis@barc.gov.in, Phone No. 022-2788-7184

### Abstract:

Aluminium Borate ceramic was synthesised by solid-state method using alumina and boric acid as starting materials. The formation mechanism was investigated by TG-DSC analysis which led to the optimization of calcination temperature of precursor to 1100°C, resulting in phase pure powder, as confirmed by XRD analysis. Dilatometry analysis was conducted to determine the appropriate sintering temperatures of synthesized powder. Sintering behaviour of the powder was investigated under argon and boron-rich atmospheres at 1500°C and 1600°C. Sintered pellets were characterised for phase stability, microstructures and density. As mitigating boron volatilization at temperature exceeding 1300°C is a critical issue for boron-containing materials, the present study establishes a novel processing technique to produce dense aluminium borate ceramic with negligible boron loss.

**Keywords:** Aluminium borate ceramic, Synthesis, Densification, Boron loss.

### 1. Introduction:

In  $\text{Al}_2\text{O}_3\text{-B}_2\text{O}_3$  binary system, two aluminium borates phases,  $\text{Al}_4\text{B}_2\text{O}_9$  and  $\text{Al}_{18}\text{B}_4\text{O}_{33}$  are stable. The second phase, owing to its favourable thermophysical and mechanical properties coupled with lightweight characteristics, is an excellent material for numerous applications, such as thermal insulation, reinforcement material in aluminium matrix, high-temperature structural components, and filtration in its porous form. In nuclear field, it can be utilised for neutron shielding application due to high neutron absorption capability of boron. However, for this application, controlling boron loss during high-temperature sintering of aluminium borate ceramic is a critical parameter that needs to be addressed, along with ensuring high density through optimisation of sintering conditions [1-3].

The present work focuses on synthesis of a phase-pure  $\text{Al}_{18}\text{B}_4\text{O}_{33}$  ceramic via solid state reaction, powder characterization, and optimisation of sintering parameters to achieve high-density with negligible boron loss.

### 2. Experimental, Result and Discussion:

Aluminium borate was synthesised by solid-state reaction employing commercial alumina and boric acid (99.8% purity) as starting material. The TG-DSC pattern of stoichiometric mixture of alumina and boric acid up to 1200°C in air atmosphere is depicted in Fig.1. The observed weight loss up to 350°C is due to successive endothermic decomposition of boric acid. The exothermic peak at ~880°C in DSC corresponds to crystallization of borate phase. For analysis of phase evolution, alumina and boric acid mixture was calcined at 1000°C, 1100°C and 1200°C and XRD patterns were recorded (Fig.2). Phase-pure  $\text{Al}_{18}\text{B}_4\text{O}_{33}$  was observed at 1100°C and above, and below this temperature mixture of both borate phases were observed.

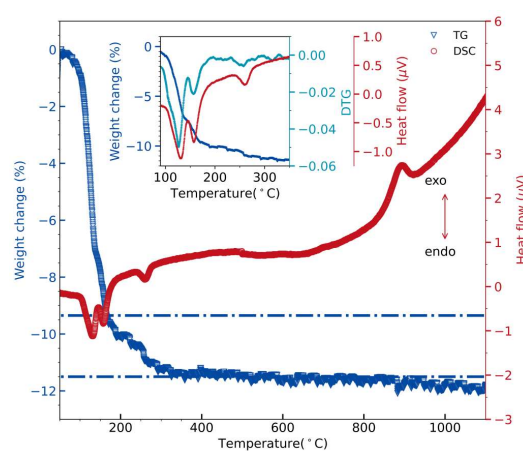


Fig1: TG-DSC of alumina-boric acid mixture

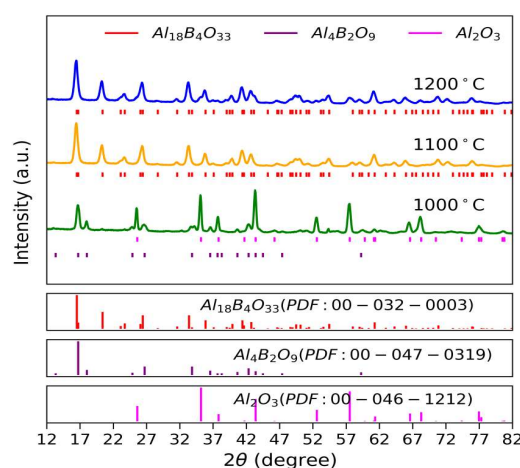


Fig2: XRD pattern of the Alumina- Boric acid mixture calcined at different temperatures.

The particle size of the synthesised powder, measured using laser diffraction particle size analyser, showed a median particle size of 12.68µm with 90% of particles being below 24.08µm.

The dilatometric linear shrinkage curve of aluminium borate disc, die-pressed uniaxially in a hydraulic press at 120MPa, was analysed up to 1600°C in an argon atmosphere, as shown in Fig 3. The onset of sintering occurs between 1100 - 1200°C, and cumulative linear shrinkage of about 5 – 5.5% is

observed up to 1500- 1600°C without attaining plateau, as shown in Fig.3. This suggests that a sintering temperature higher than 1500°C is required to achieve high-density aluminium borate. Therefore, aluminium borate pellets were sintered isothermally at 1500°C and 1600°C, both in an argon and in a powder bed of aluminium borate itself within a closed alumina crucible. It was observed that the weight loss in pellets sintered in the powder bed was drastically reduced in comparison to those sintered in the argon atmosphere, even at a sintering temperature of 1600°C. This confirms the effectiveness of powder bed method in preventing the loss of boron. This phenomenon can be explained by the fact that the powder bed within the closed alumina crucible, created a partial pressure of boron, which reduced the rate of boron volatilization. The phase stability of the aluminium borate sample was also investigated in an air atmosphere. It was observed that pellets sintered at 1400°C underwent about 12.5% weight loss, indicating nearly complete volatilization of boron. This result was confirmed through the XRD pattern, which showed only peaks corresponding to alumina.

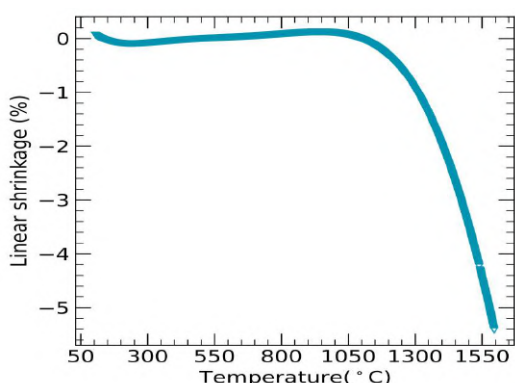


Fig 3: Dilatometric shrinkage curve of the aluminum borate ceramic in argon atmosphere

Sintered density of pellets, measured by water displacement method is given in Table 1. Aluminium borate sintered at 1600°C in powder bed achieved near theoretical density.

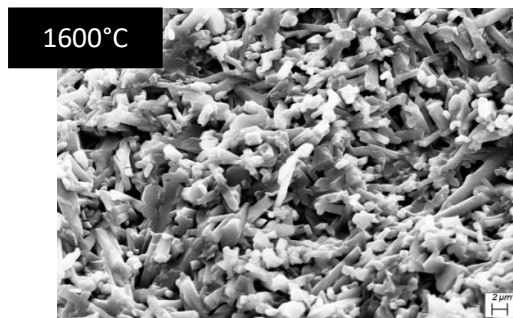
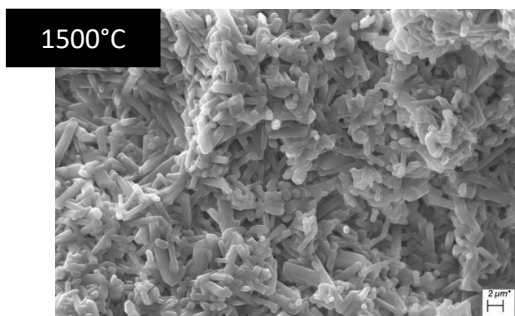


Fig 4: SEM microstructure of the aluminum borate powder sintered at 1600°C in powder bed of aluminum borate phase and argon atmosphere.

Table1: Density of Sintered Pellets

Temperature (°C)	Atmosphere	Density(g/cc)
1500	Argon	2.25(~82%ρ <sub>TH</sub> )
	Powder bed	2.36(~86%ρ <sub>TH</sub> )
1600	Argon	2.45(~89%ρ <sub>TH</sub> )
	Powder bed	2.768(~99.8%ρ <sub>TH</sub> )

The SEM images of fractured-surface microstructure of pellets sintered in powder bed at 1500°C as well as 1600°C shows nanorod- and needle- shape morphology of the aluminium borate phase (Fig.4). At higher sintering temperature, increase in size of needles with rounding of edges is observed. The nanorods showed no preferential direction and have tendency to overlap and sinter.

**3. Conclusion:** Solid-state method was used to synthesize aluminium borate ceramic, with formation mechanism revealed by TG-DSC and XRD analysis, and optimization of calcination temperature to 1100°C yielding phase-pure powder. A novel sintering method was developed to mitigate the loss of boron during sintering and achieve reasonably dense aluminium borate ceramic. Microstructural analysis revealed the presence of whisker / needle shaped grains after sintering.

**References:**

- 1.M.F. Hernandez, G. Suarez, C. Baudin, J. Asian Ceramic soc, 6 (2018), 374–383.
- 2.Preparation and characterization of aluminum borate, J. Am. Ceram. Soc,75 (1992) 2605–2609.
- 3.M.J.Readey, J. Am. Ceram. Soc,75[12] (1992) 345–56.

## Understanding the $\text{Na}_x\text{MnO}_2$ system: A Thermodynamics and XPS approach

Shubham Narang<sup>a,b</sup>, \*Rimpi Dawar<sup>a,b</sup>, Kaustava Bhattacharyya<sup>a,b</sup>, P. M. Aiswarya<sup>a,b</sup> and \*Ratikanta Mishra<sup>a,b</sup>

<sup>a</sup>Chemistry Division, Bhabha Atomic Research Centre, Trombay, Mumbai-400085

<sup>b</sup>Homi Bhabha National Institute, Anushaktinagar, Mumbai- 400094

\*Email id: [rimpid@barc.gov.in](mailto:rimpid@barc.gov.in), [mishrar@barc.gov.in](mailto:mishrar@barc.gov.in)

### Abstract

In this work, synthesis of  $\text{Na}_x\text{MnO}_2$  ( $x = 0.39, 0.44, 0.48, 0.66$  and  $0.70$ ) compounds and their characterization by powder X-ray diffraction (XRD), X-ray Photoelectron Spectroscopy (XPS), and Impedance Spectroscopy (IS) techniques was carried out. The change in the nature of bonding with increase in the Na-content and its effect on the material stability as well as on the electro-transport properties has been investigated. Detailed thermodynamic evaluation of these materials has been carried out employing calorimetric techniques and the data have been correlated with the change in chemical environment around Na-ion.

$\text{Na}_x\text{MnO}_2$  materials are being investigated for their wide range of applications as rechargeable batteries, super capacitors, catalysts, and gas sensors. In addition, the layered  $\text{Na}_x\text{MnO}_2$  compounds are considered as suitable cathode material for rechargeable sodium-ion battery due to their low cost, relatively facile synthesis, and high specific capacity [1].  $\text{Na}_x\text{MnO}_2$  system is also being studied for possible uses as super capacitor materials to store and deliver energy quickly [2]. In addition, Na-Mn-O based compounds are also investigated as magnetic storage material and as catalyst for various chemical processes like oxidation, reduction, hydrolysis, and for remediation and pollution control [3]. Although a large volume of data on structure, electrochemical, magnetic, catalytic properties of  $\text{Na}_x\text{MnO}_2$  compounds are available in the literature, the information on the thermodynamic stabilities of these compounds are scanty. These data are crucial to predict the stability of these compounds under reactive environments.

Synthesis of ternary sodium manganate compounds  $\text{Na}_x\text{MnO}_2$  ( $x = 0.39, 0.44, 0.48, 0.66$  and  $0.70$ ) was achieved by solid-state reactions. Compacted pellets made out of intimate mixtures of  $\text{Na}_2\text{CO}_3(\text{s})$  and  $\text{Mn}_3\text{O}_4(\text{s})$  in appropriate molar ratios were initially heated at 873 K for 5 h in platinum crucibles followed by final heating at 1223 K for 24 h under flowing oxygen atmosphere. The compositional analysis of  $\text{Na}_x\text{MnO}_2$  compounds was carried out employing ICP-OES and EDXRF techniques.

The synthesized products were characterized by powder XRD technique. The Fullprof-2k software was used to perform Rietveld refinement for structural analysis. Fig.1 shows the Rietveld refinement XRD patterns of representative  $\text{Na}_x\text{MnO}_2$  ( $x = 0.39, 0.48$  and  $0.66$ ) compounds.  $\text{Na}_x\text{MnO}_2$  ( $x = 0.39, 0.44, 0.48$ ) is isostructural with  $\text{Na}_4\text{Mn}_4\text{Ti}_5\text{O}_{18}$  and crystallizes in orthorhombic unit cell with  $Pbam$  space group. Manganese exists in two types of polyhedrons. First manganese is in octahedral site connected to other  $\text{MnO}_6$  octahedra by edge sharing while other manganese is in square pyramid site which is edge shared with other  $\text{MnO}_5$  square pyramid. The two polyhedrons are connected to each other via corner sharing resulting to the formation of two types of tunnels. There are three types of sodium sites in the structure of  $\text{Na}_{0.39}\text{MnO}_2$  and  $\text{Na}_{0.44}\text{MnO}_2$ . One sodium site (Na1) is located in the smaller pentagonal shaped tunnels and the other two sodium sites (Na2, Na3) are located in the larger S-shaped tunnels, as shown in Fig.2. The crystal structure of  $\text{Na}_{0.48}\text{MnO}_2$  consists of four types of sodium sites, with one sodium site (Na1) situated in the smaller pentagonal shaped tunnels while the other three sodium sites (Na2, Na3, Na4) are placed in the larger S-shaped tunnels, as illustrated in Fig.3. On the other hand,  $\text{Na}_x\text{MnO}_2$  ( $x = 0.66, 0.70$ ) has a  $\text{Na}_x\text{CoO}_2$ -type layered crystal structure and crystallizes in hexagonal crystal system with  $P6_3/mmc$  space group. Adjacent  $\text{MnO}_6$  octahedra are connected to each other via edge sharing. In this structure, there are two types of sodium ions (Na1 and Na2) both of which occupy trigonal prismatic sites. These sodium ions are sandwiched between the adjacent  $\text{MnO}_6$  layers as illustrated in Fig.4.

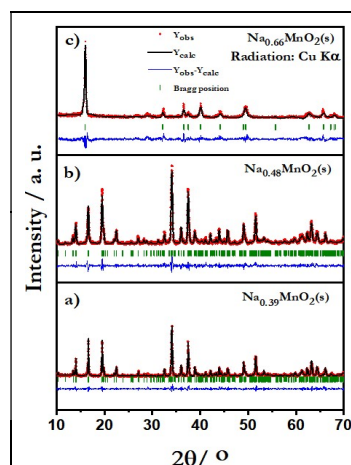


Fig. 1: Rietveld refinement patterns of (a)  $\text{Na}_{0.39}\text{MnO}_2$ , (b)  $\text{Na}_{0.48}\text{MnO}_2$  and (c)  $\text{Na}_{0.66}\text{MnO}_2$  compounds

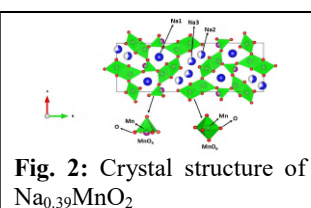


Fig. 2: Crystal structure of  $\text{Na}_{0.39}\text{MnO}_2$

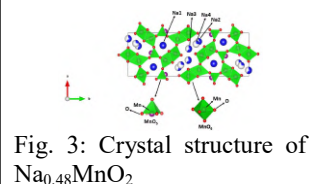


Fig. 3: Crystal structure of  $\text{Na}_{0.48}\text{MnO}_2$

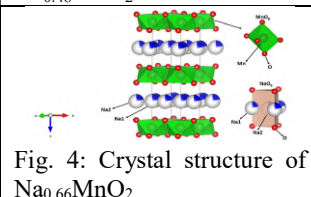


Fig. 4: Crystal structure of  $\text{Na}_{0.66}\text{MnO}_2$

The XPS studies for the  $\text{Na}_x\text{MnO}_2$  compounds were performed to determine the variation in the electronic density around Mn, Na and O as a function of Na-incorporation in  $\text{MnO}_2$  lattice. The XPS-spectra for Mn-2p peak of  $\text{MnO}_2$  and  $\text{Na}_x\text{MnO}_2$  ( $x = 0.39, 0.44, 0.48, 0.66$  and  $0.70$ ) compounds are shown in Fig.5. In all these samples, the Mn-2p peak splitted into Mn 2p<sub>3/2</sub> and Mn 2p<sub>1/2</sub> peaks with binding energy of 641.2 and 652.9 eV respectively, which indicates that Mn is present as  $\text{Mn}^{4+}$  as reported in the literature. It can be noticed that upon incorporation of Na in the  $\text{MnO}_2$  lattice, the Mn-2p<sub>3/2</sub> peaks could be de-convoluted into two peaks with binding energy of 641.4 and 639.4 eV. The later represents the  $\text{Mn}^{3+}$  state in  $\text{Na}_x\text{MnO}_2$  as seen in the  $\text{NaMnO}_2$  structure. The  $\text{Mn}^{3+}$  peak grows as a function of Na content in  $\text{Na}_x\text{MnO}_2$ . In  $\text{Na}_{0.7}\text{MnO}_2$ , Mn is mostly observed as  $\text{Mn}^{3+}$ . Further, for samples with Na content higher than  $\text{Na}_{0.48}\text{MnO}_2$ , a shift in the binding energy of Mn-2p by 0.7 eV was observed due to overall lowering in the electron density around Mn as the more electropositive  $\text{Na}^+$  is attracting the electron density towards itself in the Na-Mn-O bond. Fig. 6 shows the Na-1s XPS spectra for the different samples. There are two types of Na-peaks in the XPS spectra. In case of  $\text{Na}_x\text{MnO}_2$  ( $x = 0.39, 0.44, 0.48$ ) Na-1 located in the smaller pentagonal shaped tunnels is attached to a greater number of O atoms and has higher binding energy (1069.8 eV), whereas, Na2, Na3 and Na4 located in the larger S-shaped tunnels are linked to lower number of O-atoms and hence has lower binding energy (1068.4 eV). As there is more Na in  $\text{Na}_x\text{MnO}_2$  ( $x = 0.48$ ) compound compared to  $\text{Na}_{0.39}\text{MnO}_2$  and the intensity of the Na-1s peak 1068.4 eV increases indicating more Na in the larger S shaped tunnel. Again, as Na content increases, the number of bridging sites increases which leads to reduction of  $\text{Mn}^{4+}$  to  $\text{Mn}^{3+}$  and therefore, the bound Na will behave more as  $\text{Na}^+$  state resulting increase in their binding energy. In case of,  $\text{Na}_x\text{MnO}_2$  ( $x$

= 0.66, 0.70) due to formation of structural O-vacancy, which leads to formation of two types of sodium ions (Na1 and Na2). According to Kröger-Vink notation two types of Na attached to  $Mn^{3+}$  and  $Mn^{4+}$  can be represented as Na-O-Mn(III)-O-Mn(IV)-O-Na (state (I)). Similarly, with O-vacancies the Na can be represented as Na-O(Vac)-Mn(III)-O-Mn(IV)-O-Na (state (II)). The higher binding energy (1071.0 eV) is attributed to the Na1s with Na-O-Mn(III) state and the lower binding energy (1068.9 eV) to Na-O(Vac)-Mn(III) state. As evident from Fig. 6, the contribution of state (II) and thus oxygen vacant sites increase from  $Na_{0.66}MnO_2$  to  $Na_{0.7}MnO_2$ . The O-1s XPS spectra for  $Na_xMnO_2$  ( $x = 0.39, 0.44, 0.48, 0.66$  and  $0.70$ ) samples is shown in Fig. 7. It can be deconvoluted into four peaks (529.8, 530.4, 531.9 and 533.4) eV respectively. The initial peak at 529.8 eV corresponds to the lattice O-Mn peak whereas; the second peak at 530.4 eV is attributed to the lattice Na-O-Mn peak. The other peak at 531.9 eV corresponds to the O1s peak for the surface -OH group. The peak at 533.4 eV could be attributed to the O-vacancy. For  $Na_xMnO_2$  ( $x = 0.7$ ) sample, the O-1s peak for the O-vacancy is observed at slightly higher binding energy of 533.8 eV.

Impedance measurement for the  $Na_xMnO_2$  ( $x = 0.39, 0.48$  and  $0.70$ ) samples were carried out in the temperature range 300-600 K and frequency range 100 MHz to 1 Hz. Nyquist curves for these compounds at different temperatures are shown in Fig. 8. It was observed that the radius of the semicircles is quite small and decrease drastically with increase in sample temperature indicating that the samples have very good charge transfer properties and almost behave as a conductor above 450 K. The plots of  $\ln\sigma$  versus  $1/T$  for  $Na_{0.39}MnO_2$ ,  $Na_{0.48}MnO_2$  and  $Na_{0.66}MnO_2$  are shown in Fig. 9 (a) and (b) which clearly shows that among the three compounds,  $Na_{0.39}MnO_2$  has highest electrical conductivity. The appearance of two overlapping semi-circles in the Nyquist plots for  $Na_xMnO_2$  ( $x < 0.5$ ) samples indicates that there are two types of charge carriers i.e.,  $Na^+$  ions, which is in commensurate with crystal structure and XPS results. The first semi-circle in  $Na_{0.39}MnO_2$  corresponds to the transport of Na2 and Na3, whereas the second semicircle corresponds to transport of Na1. At a given temperature the higher conductivity of Na2 and Na3 compared to Na1 could be due to lower Na-binding energy, lower coordination number and larger tunnel size for Na2 and Na3 atoms compared to Na1 atom. The low conductivity of  $Na_{0.48}MnO_2$  compared to  $Na_{0.39}MnO_2$  due to higher average binding energy of Na and lower mean free path. The lowest ionic conductivity for  $Na_{0.70}MnO_2$  could be explained by the fact that in this compound each of the  $NaO_6$  polyhedra is bridged by two mutual O atom and the average binding energy (1068.9 and 1071.0 eV) of Na is higher compared to  $Na_{0.39}MnO_2$  and  $Na_{0.48}MnO_2$  (1068.4 and 1069.8 eV).

To further explain the nature of bonding in  $Na_xMnO_2$  compounds, their relative thermodynamic stability was determined employing calorimetric technique. The standard molar enthalpies of dissolution of  $Na_xMnO_2$  ( $x = 0.39, 0.44, 0.48, 0.66$  and  $0.70$ ) compounds and their components such as  $Mn_2O_3(s)$ ,  $MnO_2(s)$  and  $Na_2CO_3(s)$  measured employing a high temperature solution calorimeter in molten sodium molybdate ( $3Na_2O.4MoO_3$ ) solvent at 986 K. The average values of standard molar enthalpy of dissolution ( $\Delta_{sol}H_m^0$ ) for  $Na_2CO_3(s)$ ,  $Mn_2O_3(s)$ ,  $MnO_2(s)$  are found to be  $158.78 \pm 1.92$ ,  $149.12 \pm 1.69$ ,  $124.98 \pm 2.45$   $\text{kJ mol}^{-1}$ , respectively. While the corresponding values obtained for  $Na_{0.39}MnO_2(s)$ ,  $Na_{0.44}MnO_2(s)$ ,  $Na_{0.48}MnO_2(s)$ ,  $Na_{0.66}MnO_2(s)$  and  $Na_{0.70}MnO_2(s)$  are  $120.42 \pm 1.19$ ,  $126.47 \pm 0.75$ ,  $128.25 \pm 0.38$ ,  $118.79 \pm 0.43$  and  $127.88 \pm 2.29$   $\text{kJ mol}^{-1}$ , respectively. Using these values and other auxiliary data from the literature [4], the standard molar enthalpies of formation at 298K ( $\Delta_f H_{298}^0$ ) of was determined employing a suitable thermochemical cycle. The values of standard molar enthalpy of formation with respect to their elements and with respect to oxides  $\Delta_f H_{ox}^0$  for  $Na_xMnO_2$  ( $x=0.39, 0.44, 0.48, 0.66, 0.70$ ) are listed in Table 1.

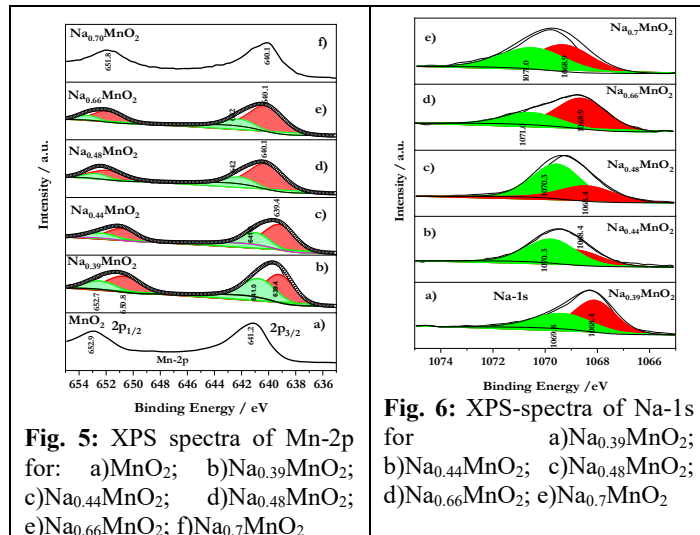


**Fig. 5:** XPS spectra of Mn-2p for: a)  $MnO_2$ ; b)  $Na_{0.39}MnO_2$ ; c)  $Na_{0.44}MnO_2$ ; d)  $Na_{0.48}MnO_2$ ; e)  $Na_{0.66}MnO_2$ ; f)  $Na_{0.7}MnO_2$

**Fig. 6:** XPS-spectra of Na-1s for a)  $Na_{0.39}MnO_2$ ; b)  $Na_{0.44}MnO_2$ ; c)  $Na_{0.48}MnO_2$ ; d)  $Na_{0.66}MnO_2$ ; e)  $Na_{0.7}MnO_2$

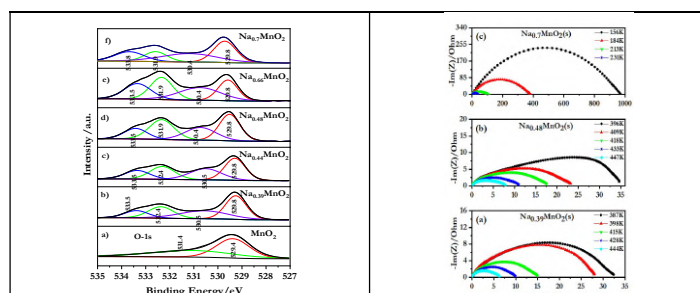


**Fig. 7:** XPS-spectra of O-1s for: a)  $MnO_2$ ; b)  $Na_{0.39}MnO_2$ ; c)  $Na_{0.44}MnO_2$ ; d)  $Na_{0.48}MnO_2$ ; e)  $Na_{0.66}MnO_2$ ; f)  $Na_{0.7}MnO_2$

**Fig. 8:** Temperature dependent Nyquist curves for a)  $Na_{0.39}MnO_2$ , b)  $Na_{0.48}MnO_2$  and c)  $Na_{0.7}MnO_2$  compounds

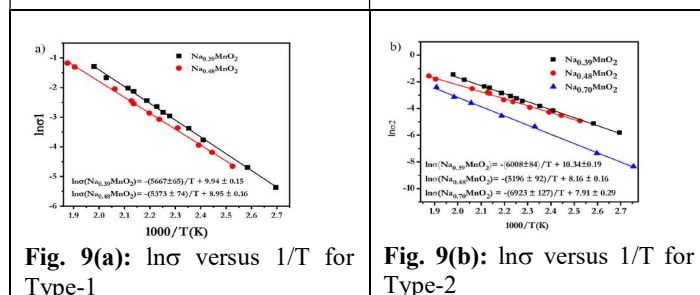


**Fig. 9(a):**  $\ln\sigma$  versus  $1/T$  for Type-1

**Fig. 9(b):**  $\ln\sigma$  versus  $1/T$  for Type-2

**Table-1:** Standard molar enthalpy of formation ( $\Delta_f H_{298}^0$ ) of  $Na_xMnO_2$  ( $x=0.39, 0.44, 0.48, 0.66, 0.70$ )

Compound	$\Delta_f H_{298}^0$ (kJ mol <sup>-1</sup> )	$\Delta_f H_{298,ox}^0$ (kJ mol <sup>-1</sup> )
$Na_{0.39}MnO_2$ (s)	$-639.54 \pm 2.06$	$-52.45 \pm 1.97$
$Na_{0.44}MnO_2$ (s)	$-661.32 \pm 1.75$	$-65.81 \pm 1.67$
$Na_{0.48}MnO_2$ (s)	$-675.68 \pm 1.56$	$-73.44 \pm 1.47$
$Na_{0.66}MnO_2$ (s)	$-722.83 \pm 1.34$	$-90.29 \pm 1.27$
$Na_{0.70}MnO_2$ (s)	$-744.50 \pm 2.61$	$-105.23 \pm 2.57$

The negative values of enthalpy of formation suggest that the  $Na_xMnO_2$  compounds are relatively stable with respect to their components and the stability increases with increase in sodium incorporation.

## References

1. F. Sauvage, L. Laffont, J. M. Tarascon and E. Baudrin, *Inorg. Chem.*, 46 (2007) 3289
2. Q. T. Qu, Y. Shi, S. Tian, Y. H. Chen, Y. P. Wu and R. Holze, *J. Power Sources*, 194 (2009) 1222
3. L. Kong, C. Tang, H. J. Peng, J. Q. Huang and Q. Zhang, *SmartMat.*, 1 (2020)
4. I. Barin, *Thermochemical data of pure substances*, third ed. (1995)

## Studies on Mg-Sb-Bi Alloy Towards Development of Uni-leg Thermoelectric Devices

Swadesh Mohanty<sup>a,b</sup>, Ajay Panthri<sup>c</sup>, Ajay Singh<sup>a,b</sup>, Ranita Basu<sup>\*1,2</sup>

<sup>a</sup>Technical Physics Division, Bhabha Atomic Research Centre, Mumbai-85

<sup>b</sup>Homi Bhabha National Institute, Anushaktinagar, Mumbai-85

<sup>c</sup>Raja Ramanna Centre for Advanced Technology, Indore, Madhya Pradesh 452013

\* [ranitab@barc.gov.in](mailto:ranitab@barc.gov.in); [ranitapaul@gmail.com](mailto:ranitapaul@gmail.com); 022-69293217

### Abstract

Economically viable Mg-based alloys are considered as an excellent alternative towards room temperature thermoelectric applications. Nevertheless, the persistent p type conduction due to inevitable Mg loss during the synthetic procedure with diminished electrical conductivity has been captivated to improvise the thermoelectric performance of p-type Mg<sub>3</sub>Sb<sub>2</sub> based alloys. But the glooming carrier concentration  $\sim 10^{17} \text{cm}^{-3}$ , conceals low figure-of-merit (ZT) value. This is attributed to the layered AB<sub>2</sub>X<sub>2</sub> type Zintl phase where covalently bonded anionic framework, (B<sub>2</sub>X<sub>2</sub>)<sup>2-</sup>, is the basis of the crystal structure & the electropositive cations contribute the electrons to appease the valence necessity. Thus, it can be visualized as a hybrid of ionic & covalent presence & are regarded as valence precise semiconductors. However, the recent studies unveil that n-type Mg<sub>3</sub>Sb<sub>2</sub> has more potential towards thermoelectric performance owing to the presence of multiple degenerate valleys in the conduction bands with added advantage of high mechanical strength. Alloying Mg<sub>3</sub>Sb<sub>2</sub> with Mg<sub>3</sub>Bi<sub>2</sub> has significant impact towards thermoelectric transport properties as the latter being semimetal, tunes the band gap such that the former exhibit high ZT in low as well as mid temperature range.

The composition dependent optimization of ZT in different temperature range of Mg-Sb-Bi alloys gives an opportunity to develop uni-leg devices operating at different temperature. In the present work, studies related to Mg-Sb-Bi alloy towards development of uni-leg thermoelectric devices will be presented. In addition the potential of Mg-Sb-Bi alloy for investigation of transverse thermoelectric effect i.e. the conversion of longitudinal heat current into transverse electric current will also be discussed.

### References

- [1] Zihang Liu, Hironori Oshima, Kazuo Nagase, Chul-Ho Lee and Takao Mori, Nature Communications, 13.1 (2022) 1120
- [2] Zhijia Han, Jing-Wei Li, Feng Jiang, Jiating Xia, Bo-Ping Zhang, Jing-Feng Li and Weishu Liu, Journal of Materiomics, Volume 8, 2022 Pages 427-436
- [3] Jiawei Zhang, Lirong Song, Steffen Hindborg Pedersen, Hao Yin, Le Thanh Hung and Bo Brummerstedt Iversen, Nature Communications, 8.1 (2017): 13901
- [4] Jing-Wei Li, Zhijia Han, Jincheng Yu, Hua-Lu Zhuang, Haihua Hu, Bin Su, Hezhang Li, Yilin Jiang, Lu Chen, Weishu Liu, Qiang Zheng and Jing-Feng Li, Nature Communications, 14.1 (2023) 7428
- [5] Qing Shi, Juan Li, Xuanwei Zhao, Yiyuan Chen, Fujie Zhang, Yan Zhong and Ran Ang, ACS Applied Materials & Interfaces, Vol 14 2022 49425-49445

Phase characterization and oxidation of  $M_2Zr_2O_7$  ( $M = Ce^{3+}$  and  $Pu^{3+}$ )

Chiranjit Nandi\*, Abhijeet Dadarya, K.M. Danny, Amrit Prakash\*

Radiometallurgy Division, Bhabha Atomic Research Centre, Mumbai-400 085, India

Email: cnandi@barc.gov.in/amritp@barc.gov.in

**Abstract**

In the context of inert matrix fuel applications,  $Ce_2Zr_2O_7$  and  $Pu_2Zr_2O_7$  were synthesized under reducing conditions and extensively characterized using X-ray Diffraction (XRD) and Raman spectroscopy. Both techniques confirmed the formation of pyrochlore-type phase. XRD studies demonstrated the retention of the pyrochlore structure upon oxidation of  $M_2Zr_2O_7$  pyrochlores at 1073 K in a thermogravimetric (TG) setup. However, Raman spectroscopy identified the oxidized  $Ce_2Zr_2O_8$  as the  $\kappa$ -type phase. Oxidation studies confirmed the exclusive presence of  $Ce^{3+}$  in  $Ce_2Zr_2O_7$ .

Zirconate pyrochlores have gained significant attention as potential inert matrix materials for transmutation of minor actinides and plutonium [1,2]. Studies on the phase behaviour of plutonium-based systems are typically conducted using cerium dioxide ( $CeO_2$ ) as a non-radioactive surrogate. This study investigates the phase evolution and lattice parameter variations in cerium- and plutonium-substituted zirconia ( $ZrO_2$ ) under reducing conditions. Additionally, it aims to characterize the oxidation products formed when the reduced phases are exposed to an oxidizing atmosphere.

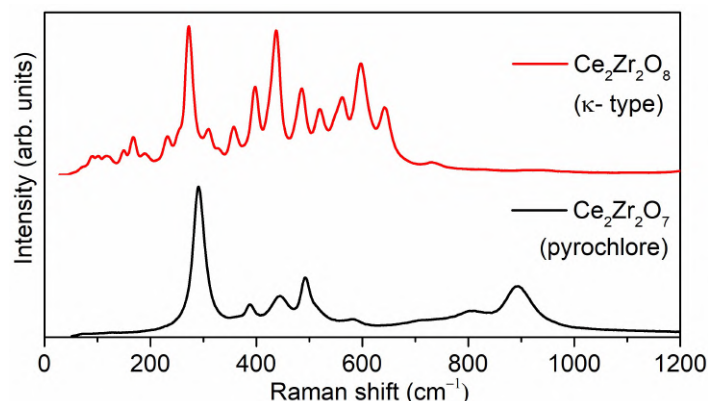
$Ce_2Zr_2O_7$  and  $Pu_2Zr_2O_7$  were synthesized using conventional solid-state reaction method in reducing atmosphere ( $Ar-H_2$ ) at 1973 K to stabilize Ce and Pu in their trivalent oxidation states.  $Ce_2Zr_2O_7$  was characterized using XRD, Raman spectroscopy and TG, while  $Pu_2Zr_2O_7$  was characterized by XRD only.

$Ce_2Zr_2O_7$  and  $Pu_2Zr_2O_7$  samples reveal the emergence of weak superstructure peaks alongside the characteristic reflections of the fluorite-type structure, classifying them as pyrochlore-type phases. Notably, the calculated radius ratios of 1.59 and 1.57 for  $Ce_2Zr_2O_7$  and  $Pu_2Zr_2O_7$ , respectively, are consistent with the formation of a pyrochlore-type phase. The lattice parameter of  $Ce_2Zr_2O_7$  was determined to be 10.7434(2) Å, which is in excellent agreement with previously reported values of 10.7414(3) Å [3]. For  $Pu_2Zr_2O_7$ , the lattice parameter was measured as 10.641(1) Å. Notably, Vaudez et al. [4] predicted a theoretical lattice parameter of 10.69 Å for the  $Pu_2Zr_2O_7$  phase, while their experimental measurements yielded a value of 10.62 Å. The observed reduction in lattice parameter may be attributed to potential aerial oxidation of the sample.

$ZrO_2$  is not redox-sensitive; thus, the weight gain upon oxidation of  $Ce_2Zr_2O_7$  is solely due to the conversion of  $Ce^{3+}$  to  $Ce^{4+}$ . A 2.76% weight gain recorded in TG confirms exclusive presence of  $Ce^{3+}$  in  $Ce_2Zr_2O_7$  (Fig. 1).

The pyrochlore-type phase observed for  $Ce_2Zr_2O_7$  and  $Pu_2Zr_2O_7$  samples under reducing conditions retains its structural identity upon oxidation. However, the diffraction patterns shift toward higher angles, indicating the conversion of the larger  $Ce^{3+}/Pu^{3+}$  to the smaller  $Ce^{4+}/Pu^{4+}$ . The lattice parameters for the oxidized phases i.e.  $Ce_2Zr_2O_8$  and  $Pu_2Zr_2O_8$  are determined to be 10.5288(1) Å and 10.523 (1) Å, respectively.

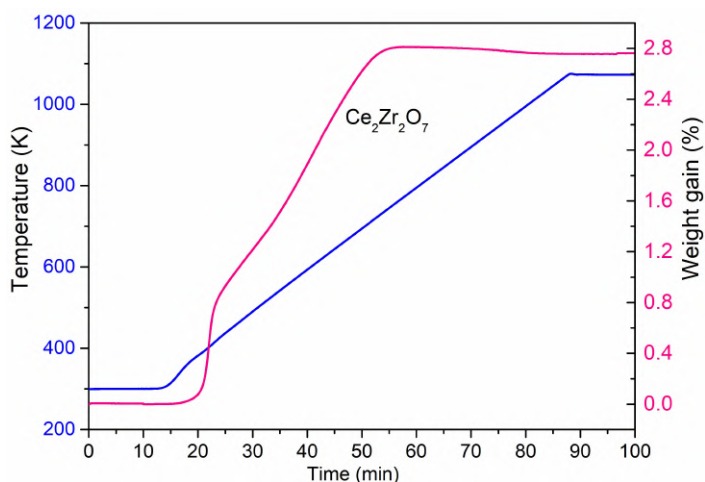
Raman spectra exhibit significant changes upon the oxidation of pyrochlore-type  $Ce_2Zr_2O_7$  to  $Ce_2Zr_2O_8$ , with numerous Raman bands emerging (Fig. 2). The appearance of these additional bands indicates that  $Ce_2Zr_2O_8$  adopts a crystal structure with lower symmetry compared to pyrochlore phase. The observed Raman spectrum for  $Ce_2Zr_2O_8$  is consistent with the  $\kappa$ - $Ce_2Zr_2O_8$  phase, which crystallizes in the P2<sub>1</sub>3 space group [3].

Figure 2. Raman spectra for  $Ce_2Zr_2O_7$  and  $Ce_2Zr_2O_8$ 

Pyrochlore-type  $Ce_2Zr_2O_7$  and  $Pu_2Zr_2O_7$  phases were successfully synthesized by conventional solid-state method. XRD studies also confirmed the retention of pyrochlore-type phase upon oxidation of  $M_2Zr_2O_7$  pyrochlores at 1073 K. However, Raman spectroscopy identified oxidized  $Ce_2Zr_2O_8$  as the  $\kappa$ -type phase. This observation underscores the importance of employing complementary techniques, such as the combined use of XRD and Raman spectroscopy, for accurate phase identification. TG study confirms the exclusive presence of  $Ce^{3+}$  in  $Ce_2Zr_2O_7$ , demonstrating that  $Ce^{4+}$  can be completely reduced to  $Ce^{3+}$  at high temperatures under reducing conditions. However, the reduced samples are susceptible to aerial oxidation. Furthermore,  $Ce_2Zr_2O_7$  and  $Pu_2Zr_2O_7$  exhibit similar structures, allowing  $Ce^{3+}$  to be considered as a suitable surrogate for  $Pu^{3+}$  and trivalent actinides for phase relation studies.

**References**

1. C. Nandi et al., *J. Nucl. Mater.*, 547 (2021) 152800
2. C. Nandi et al., *J. Nucl. Mater.*, 600 (2024) 155264
3. T. Omata et al. *J. Solid State Chem.*, 147 (1999) 573
4. S. Vaudez et al. INIS-FR-3041, (2004)

Figure 1. TG plot showing weight gain versus time during oxidation of  $Ce_2Zr_2O_7$  in oxygen atmosphere



## Tuning Thermal Properties of Zirconate Pyrochlore via Stoichiometric Alterations

Santosh K Sahu<sup>a</sup>, R. Shukla<sup>a,b</sup>, R. Dawar<sup>a,b</sup>, V. Grover<sup>a,b\*</sup>,

<sup>a</sup>Chemistry Division, Bhabha Atomic Research Centre, Mumbai- 400085, India

<sup>b</sup>Homi Bhabha National Institute, Anushaktinagar, Mumbai 400094, India

\* Corresponding author email ID- vinita@barc.gov.in

Telephone Number-02225592274

### Abstract

To investigate the thermal behavior of zirconate pyrochlore through stoichiometric variation, Zr-rich, non-stoichiometric  $\text{Nd}_{2-x}\text{Zr}_{2+x}\text{O}_{7+x/2}$  ( $x = 0, 0.2, 0.4$ ) samples were synthesized using a hybrid gel combustion method. X-ray diffraction confirmed a stable pyrochlore structure for all compositions, while Raman spectroscopy revealed disordered fluorite-like domains within the ordered matrix. High-temperature XRD established phase stability of the pyrochlore up to 1473 K, and non-stoichiometric samples showed increased heat capacities. This hybrid structure enhances thermal expansion and reduces thermal conductivity by lowering lattice energy and increasing phonon scattering, indicating potential for use in thermal barrier coatings.

### Introduction

The pyrochlore based materials, known for their unique crystal structures and versatile properties, are promising for applications like nuclear waste immobilization and solid oxide fuel cells. Non-stoichiometry plays a crucial role in altering their structural, electrical, and thermophysical properties by introducing defects and vacancies that influence lattice dynamics and ionic transport. Particularly in zirconate-based systems, excess cations or anions can create hybrid structures combining ordered pyrochlore and disordered fluorite-type domains, enhancing ionic conductivity [1] and thermal expansion while reducing thermal conductivity. Understanding these effects is essential for designing high-performance materials for high-temperature and radiation-resistant applications. This article investigates the synthesis and characterization of Zr-rich, non-stoichiometric  $\text{Nd}_{2-x}\text{Zr}_{2+x}\text{O}_{7+x/2}$  pyrochlores using a hybrid gel combustion method. Techniques like X-ray diffraction, Raman spectroscopy, and laser flash apparatus reveal a significant decrease in thermal conductivity for specific compositions, showcasing the potential of non-stoichiometric pyrochlores in advancing thermal barrier materials.

### Experimental section

AR-grade neodymium oxide ( $\text{Nd}_2\text{O}_3$ ), zirconium oxynitrate ( $\text{ZrO}(\text{NO}_3)_2 \cdot 4\text{H}_2\text{O}$ ), and glycine were employed as reactants for synthesis of various compositions in  $\text{Nd}_{2-x}\text{Zr}_{2+x}\text{O}_{7+x/2}$  ( $x = 0, 0.2, 0.4$ ) system. The appropriate amounts of  $\text{Nd}_2\text{O}_3$  were dissolved in dilute  $\text{HNO}_3$ , followed by the addition of  $\text{ZrO}(\text{NO}_3)_2 \cdot 4\text{H}_2\text{O}$  and glycine. The solution was evaporated at 353 K to form a viscous gel, which underwent auto-ignition at 573 K producing voluminous powders. The powders were calcined at 873 K, compacted into pellets and sintered at 1623 K for 24 hours to yield the final products. All the samples were thoroughly characterized by XRD, HT-XTRD, Raman spectroscopy, TMA, DSC and Laser flash studies.

### Result and discussion

The XRD patterns (Fig. 1a) of  $\text{Nd}_{2-x}\text{Zr}_{2+x}\text{O}_{7+x/2}$  ( $x = 0, 0.2, 0.4$ ) samples annealed at 1623 K show that all compositions exhibit weak superstructure peaks indicating a pyrochlore-type phase. Raman spectra (Fig. 1b) vary with composition:  $x = 0.0$  shows four distinct bands at 301, 399, 503, and 521  $\text{cm}^{-1}$ , and two weak peaks at 589 and 758  $\text{cm}^{-1}$ , consistent with pyrochlore-type modes.[2] Increasing  $\text{Zr}^{4+}$  content makes the 589  $\text{cm}^{-1}$  band more prominent, suggesting the presence of fluorite domains in the pyrochlore matrix.

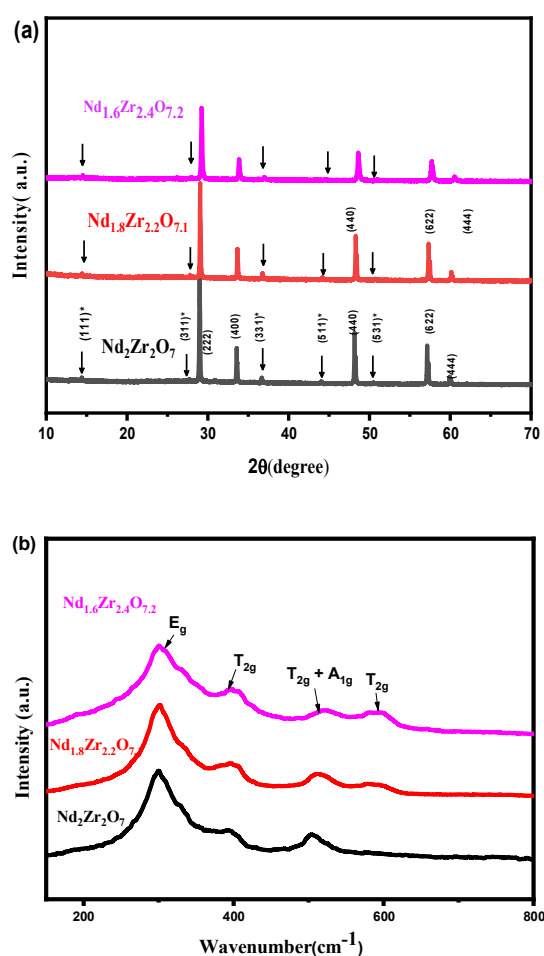
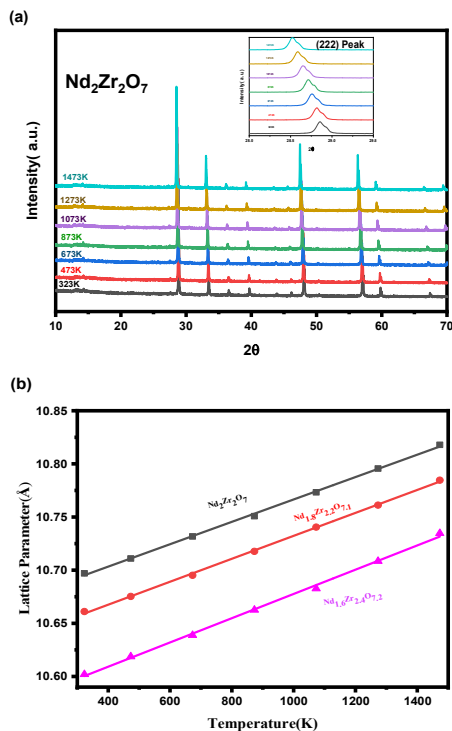


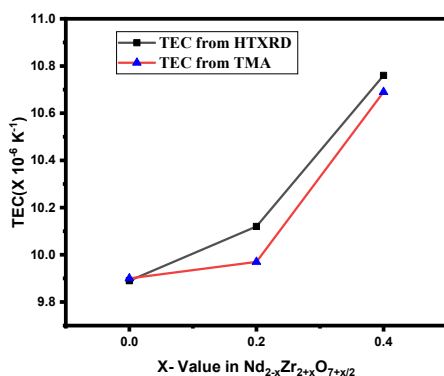
Fig. 1. (a) PXRD patterns, (b) Raman spectra of all nominal compositions  $\text{Nd}_{2-x}\text{Zr}_{2+x}\text{O}_{7+x/2}$  ( $x = 0, 0.2, 0.4$ )

Fig. 2(a) shows the temperature dependent XRD patterns for the stoichiometric pyrochlore  $\text{Nd}_2\text{Zr}_2\text{O}_7$ . It is evident that there is no visible phase change in the temperature range being explored and the peaks show shift towards lower  $2\theta$  on account of expansion of the lattice. No phase change is observed in any of the nominal compositions up to 1473K. For each sample, the variation of lattice parameters and absolute temperature is plotted and depicted in Fig2(b).



**Fig. 2.** (a) High temperature XRD pattern of  $\text{Nd}_2\text{Zr}_2\text{O}_7$ . Inset shows the zoomed XRD pattern from  $2\theta = 28$  to  $2\theta = 30$  at various temperatures (b) variation of lattice constant with temperature of all compositions  $\text{Nd}_{2-x}\text{Zr}_{2+x}\text{O}_{7+x/2}$  (i.e  $x = 0, 0.2, 0.4$ )

Lattice and bulk thermal expansion coefficient (TEC) were determined using HTXRD and Thermomechanical analyzer (TMA) shown in Fig. 3.



**Fig. 3.** Variation of TEC with compositions

The heat capacity values were measured over the temperature range 300K to 873K. The results of heat capacity measurements are shown in Fig.4. High temperature data results have been fitted to the equation  $a+b T-c/T^2$ , where T is Temperature in Kelvin. From 300K to 600K, on increasing  $\text{Zr}^{4+}$  content, heat capacity increases. This could be attributed to decrease in average inter-ionic distance that results in stronger bonds. Increase in bond strength requires more energy to increase the temperature of the material, hence causing an increase in heat capacity.

To understand the effect of non-stoichiometry on thermal conductivity, the samples were subjected to laser flash studies to determine the diffusivity. From the measured thermal diffusivity ( $D_{th}$ ), density ( $\rho$ ) and heat capacity ( $C_p$ ), the thermal conductivity ( $\lambda$ ) was calculated according to the equation.

$$\lambda = D_{th} \cdot \rho \cdot C_p$$

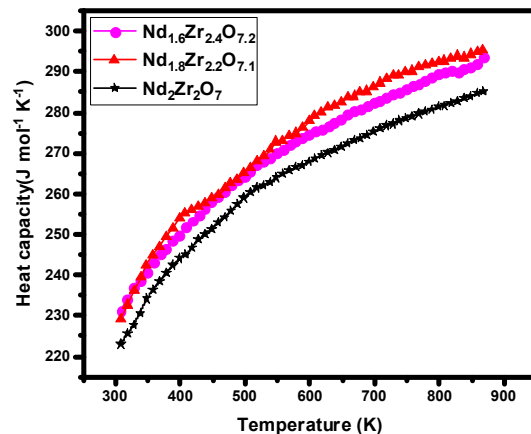


**Fig.4.** Heat capacity of all compositions

The thermal conductivities of all samples are shown in Fig 5. At 1023K, the thermal conductivities of  $\text{Nd}_2\text{Zr}_2\text{O}_7$ ,  $\text{Nd}_{1.8}\text{Zr}_{2.2}\text{O}_{7.1}$ , and  $\text{Nd}_{1.6}\text{Zr}_{2.4}\text{O}_{7.2}$  are 1.7, 1.55 and 1.56  $\text{W}/(\text{m}\cdot\text{K})$  respectively. It can be seen from Fig.5 that, the thermal conductivity values of nonstoichiometric  $\text{Nd}_{2-x}\text{Zr}_{2+x}\text{O}_{7+x/2}$  pyrochlore-type compositions are lower than the stoichiometric pyrochlore  $\text{Nd}_2\text{Zr}_2\text{O}_7$ . The thermal conductivity of oxide ceramics is mainly related to phonon scattering, which can be enhanced by loose bonding, introducing defect and distorted structure. According to Raman data analysis, increasing non-stoichiometry in  $\text{Nd}_{2-x}\text{Zr}_{2+x}\text{O}_{7+x/2}$  system, introduces local lattice distortion and forms local fluorite type microdomains in ordered pyrochlore. These micro-domains, due to different crystal structure than the parent lattice, act as phonon scatterer and decreases the thermal conductivity of material.

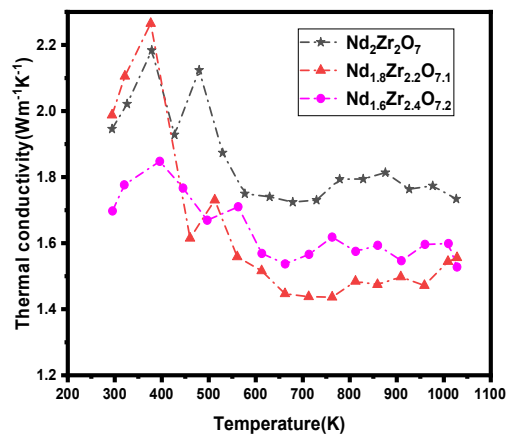


**Fig. 5.** Thermal conductivity of all compositions

## Conclusion

This study revealed that introducing non-stoichiometry in pyrochlore leads to the formation of defect fluorite microdomains. These microdomains significantly enhance phonon scattering, thereby reducing the material's thermal conductivity. This effect is achieved without the need for any hetero-valent substitution; simply altering the stoichiometry is sufficient to modify the thermal properties of the material.

## References

1. Anithakumari, P.; Grover, V.; Nandi, C.; Bhattacharyya, K.; Tyagi, A. K, RSC Adv. 2016, 6 (100), 97566–97579..
2. Glerup, M.; Nielsen, O. F.; Poulsen, F. W. *Journal of Solid State Chemistry* **2001**, 160 (1), 25–32.

## Investigating Thermal Expansion studies of Lithium Based $\gamma$ -LiAlO<sub>2</sub> compound

Jeetendra Dhanuskar<sup>a</sup>, K.B. Modi<sup>a</sup>, Shailesh Kumar<sup>a</sup>, Sheetal Raut<sup>a</sup>, Pratik Das<sup>a,b\*</sup>, Pradeep Samui<sup>a,b</sup>, Ram Avtar Jat<sup>a\*</sup> and S.C. Parida<sup>a,b</sup>

<sup>a</sup>Product Development Division, Bhabha Atomic Research Centre, Mumbai-85

<sup>b</sup>Homi Bhabha National Institute, Bhabha Atomic Research Centre, Mumbai-85

\* [pratikdas@barc.gov.in](mailto:pratikdas@barc.gov.in), \*[avtar@barc.gov.in](mailto:avtar@barc.gov.in)

### Abstract

Lithium based ceramics continue to demonstrate significant potential as breeder materials for International Thermonuclear Experimental Reactor (ITER). Research focused on the blanket design of ITER has brought to light specific aspects of the thermo-physical database concerning these lithium-based candidate materials that should be investigated more comprehensively. Considering its significance, thermal expansion studies were carried out on lithium-based  $\gamma$ -LiAlO<sub>2</sub> ceramic, which is viewed as a promising solid breeder material for fusion reactors. An in situ high-temperature X-ray diffraction (XRD) setup was employed in the present study, examining temperature ranges from 298 K to 1173 K in an argon atmosphere for investigation of thermal expansion studies. These findings from the high-temperature XRD patterns indicated that the compound retained its tetragonal structure up to 1173 K. The thermal expansion coefficients of the  $\gamma$ -LiAlO<sub>2</sub> compounds were calculated from the experimentally obtained HTXRD data.

### Introduction

The use of a deuterium (D) and tritium (T) mixture is under consideration as a fuel for first-generation fusion reactors, primarily due to its favorable fusion reaction cross-section at lower temperatures. Within the D-T fusion fuel cycle, deuterium will be obtained from naturally occurring sources, while the radioactive tritium will be produced artificially through the nuclear reactions:  ${}^6\text{Li} + n \rightarrow \text{T} + 4\text{He}$  and  ${}^7\text{Li} + n \rightarrow \text{T} + n + 4\text{He}$ . In situ tritium production in fusion reactors can be facilitated by Tritium Breeding Blanket Modules (TBM) that incorporate lithium based ceramics as solid breeders. It is imperative that these ceramics not only serve to breed tritium but also should provide adequate radiation stability, compatibility with blanket materials, and remarkable physical and chemical stability when subjected to high temperature operation. Ceramics containing lithium, such as Li<sub>2</sub>TiO<sub>3</sub>, Li<sub>2</sub>ZrO<sub>3</sub>, LiAlO<sub>2</sub>, and Li<sub>4</sub>SiO<sub>4</sub>, are recognized for these properties and hence considered as viable options for tritium breeding.[1] Therefore, it is essential to understand the thermo-physical studies of these materials to evaluate their compatibility under extreme operational conditions. Among these above mentioned explored materials, LiAlO<sub>2</sub> has been chosen for examination in this study. Six polymorphs of LiAlO<sub>2</sub> have been reported in scientific literature.[2] However, structural information is known for only four of these polymorphs ( $\alpha$ ,  $\beta$ ,  $\gamma$ , and  $\delta$ ). Importantly,  $\gamma$ -LiAlO<sub>2</sub> is recognized as the only stable phase under normal ambient conditions. [2]

### Experimental

Polycrystalline sample of  $\gamma$ -LiAlO<sub>2</sub> was produced via a solid-state reaction between Li<sub>2</sub>CO<sub>3</sub> and  $\gamma$ -Al<sub>2</sub>O<sub>3</sub>. Prior to its application,  $\gamma$ -Al<sub>2</sub>O<sub>3</sub> was subjected to heating at 973°C overnight. The appropriate quantities of Li<sub>2</sub>CO<sub>3</sub> and the preheated  $\gamma$ -Al<sub>2</sub>O<sub>3</sub>, in a molar ratio of 1.01:1.00, were thoroughly mixed and subsequently pressed into a pellet measuring 20 mm in diameter and 10 mm in height. A slight excess of Li<sub>2</sub>CO<sub>3</sub> was included to account for potential losses during high-temperature processing. The pellet was then heated at 873K for duration of 12hours, after which they were crushed into powder and reformed into pellets. These new pellets underwent a second heating at 1073K for 24 hours, followed by an increase in temperature to 1223K, maintained for an additional 24 hours. The resulting sintered pellets were crushed into powder and analyzed using powder X-ray

diffraction (XRD). The presence of phase-pure tetragonal  $\gamma$ -LiAlO<sub>2</sub> was verified by comparing the XRD results that matched with existing literature. The phase analysis of the synthesized compound was conducted utilizing the X-ray diffraction (XRD) technique. Both room temperature and elevated temperature X-ray diffraction measurements were performed with a diffractometer (theta–theta geometry) provided by GNR Analytical Instruments Group, Italy (Model: EXPLORER), employing Cu K $\alpha$  (1.5406Å) radiation at 40 kV and 40 mA.

### Results and discussion

Fig.1 illustrates the X-ray diffraction (XRD) profile of the  $\gamma$ -LiAlO<sub>2</sub> compound. Validation of the compound's formation has been achieved through X-ray diffraction patterns that match PCD database file no. {1502732}, associated with the literature phase of  $\gamma$ -LiAlO<sub>2</sub>, revealing no identifiable impurity phases. Lattice parameters were optimized by Rietveld refinement studies for each experimental temperature. The optimized crystal structure was provided in Fig.2. The substance crystallizes within the tetragonal space group P4<sub>1</sub>2<sub>1</sub>2, possessing a density of 2.62 g/cm<sup>3</sup>. The lattice framework is made up of AlO<sub>4</sub> and LiO<sub>4</sub> tetrahedra that are linked together. The optimized lattice parameters obtained from Rietveld refinement at ambient temperature were given in Table-1. Correspondingly, high-temperature XRD patterns were employed to calculate the lattice parameters at elevated temperatures. The calculated ratio of the high temperature lattice parameters and unit cell volumes relative to the ambient temperature values ( $T=298\text{K}$ ) are presented in Fig.3, depicted as a function of temperature. Evidence from the high-temperature XRD (HTXRD) study indicates that the compound preserves its tetragonal phase throughout the temperature range extending from ambient conditions to 1173K. The observed gradual shift of the XRD pattern towards lower  $2\theta$  values, in comparison to those recorded at ambient temperature can be attributed to lattice expansion. The different thermal expansion coefficients of the  $\gamma$ -LiAlO<sub>2</sub> compounds were calculated from the obtained HTXRD studies and detailed in Table-2.

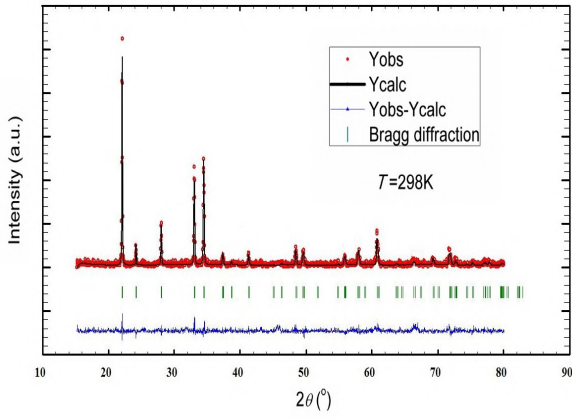


Fig.1. XRD pattern of  $\gamma$ -LiAlO<sub>2</sub> at ambient temperature.

Table-1: Fitting parameters of the synthesized  $\gamma$ -LiAlO<sub>2</sub> after Rietveld refinement

Parameters	$\gamma$ -LiAlO <sub>2</sub>
a= b (Å)	5.1721(1)
c (Å)	6.2651(1)
Rwp (%)	4.35
Rexp (%)	3.20
$\chi^2$ (%)	1.85

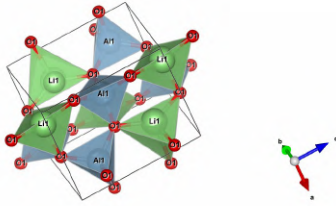


Fig.2. Optimized crystal structure of  $\gamma$ -LiAlO<sub>2</sub> at ambient temperature T=298K.

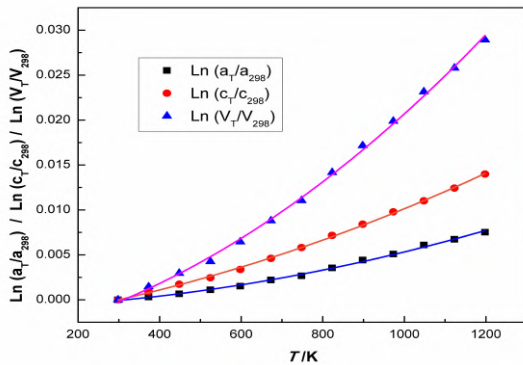


Fig.3. Variation of lattice parameters and unit cell volume of  $\gamma$ -LiAlO<sub>2</sub> with temperature.

From the definition of thermal expansivity of volume,  $\alpha_V = 1/V(dV/dT)_p$ , a volume at  $T$  ( $T > 298K$ ) can be derived as equation 1.

$$V_T = V_{298} \text{Exp}\left(\int_{298}^T \alpha_V dT\right) \quad \text{Eq.1.}$$

Where  $V_{298}$  is represented standard volume at  $T_{298}$ . If  $\alpha_V$  is considered as a linear function of  $T$ , ( $\alpha_V=A+BT$ ), then  $V_T$  can be rearranged and represented as equation 2.

$$\text{Ln}(V_T/V_{298}) = A_1(T-298) + B_1(T^2-298^2)/2 \quad \text{Eq.2.}$$

In this present study, we have plotted  $\text{Ln}(V_T/V_{298})$  against temperature ( $T$ ) and performed least squares fitting to derive the values of  $A$  and  $B$ , which correlate thermal expansivity with temperature. Consequently, thermal expansivity can be modeled as  $\alpha_V = A + BT$ . Similarly, we have fitted the lattice parameters  $a$  and  $c$  of the crystal structure using equations 3 and 4, as illustrated in Fig. 3 together with the volume data.

$$\text{Ln}(a_T/a_{298}) = A_2(T-298) + B_2(T^2-298^2)/2 \quad \text{Eq.3.}$$

$$\text{Ln}(c_T/c_{298}) = A_3(T-298) + B_3(T^2-298^2)/2 \quad \text{Eq.4.}$$

The values of  $A$  and  $B$  derived from the least squares fitting of equations 2, 3, and 4 are presented in Table-2.

Table-2. Obtained fitted parameters of different thermal expansion coefficients of  $\gamma$ -LiAlO<sub>2</sub> compound (fitted in  $A+B*T$  form).

Average thermal expansion coefficient [ $\times 10^{-6}$ ] K <sup>-1</sup>	$\alpha_a/\alpha_b / \alpha_c / \alpha_{vol} = A+B*T$	
	A	B
$(\alpha_a = \alpha_b)$	1.51243E-6 ( $\pm 0.80967E-6$ )	9.53954E-9 ( $\pm 0.10677E-9$ )
$\alpha_c$	6.75327E-6 ( $\pm 0.79674E-6$ )	11.86200E-9 ( $\pm 1.05064E-9$ )
$\alpha_v$	9.24448E-6 ( $\pm 0.23320E-6$ )	31.69420E-9 ( $\pm 3.07523E-9$ )

The values presented in Table-2 distinctly demonstrate the thermal anisotropy of the crystal structure. This anisotropic thermal expansion primarily arises from more significant lattice expansion along the  $c$ -axis in comparison to the  $a$  and  $b$  axes.

## References

- [1]. P. Samui, K. Modi, S. Phapale, S. Parida, R. Mishra, Calorimetric investigations on lithium based ceramics, The Journal of Chemical Thermodynamics, 163 (2021) 106590.
- [2]. M.K. Gupta, R. Mittal, B. Singh, O. Delaire, S.N. Achary, S. Rols, A.K. Tyagi, S.L. Chaplot, Phonons and lithium diffusion in LiAlO<sub>2</sub>, Physical Review B, 103 (2021) 174109.

## Pebble Bed Thermal Expansion and Sintering Investigation of Lithium Titanate for Fusion Blanket Application

Aroh Shrivastava<sup>a\*</sup>, Swapnil S. Lonare<sup>a</sup> and Paritosh Chaudhuri<sup>a</sup>

<sup>a</sup>Institute for Plasma Research, Bhat, Gandhinagar, Gujarat 382428

Email: aroh@ipr.res.in, Phone: +91-9586883329 Fax: 079-23962277

### Abstract

Lithium titanate ( $\text{Li}_2\text{TiO}_3$ ) is a candidate materials for tritium breeding application for the fusion reactor. The 14 MeV neutrons will react the lithium in the pebble bed and will produce tritium inside the reactor. In parallel, neutronic heating will also elevate the pebble bed temperature to  $\sim 900^\circ\text{C}$ . At high temperature the pebble bed will expand and shrink as a function of temperature and exposure duration. In this work, pebble bed thermal expansion of the  $\text{Li}_2\text{TiO}_3$  ceramic pebbles will be discussed with conventional dilatometry method. The pebble bed thermal expansion coefficients for non-isothermal as well as isothermal region and its effect on pebble bed sintering will also be discussed in this paper.

### 1. Introduction

Lithium-containing blankets are gaining wide attention for its capability in tritium breeding and energy extraction from the fusion reactor. Among various lithium-based ceramics such as  $\text{LiAlO}_2$ ,  $\text{Li}_2\text{ZrO}_3$ ,  $\text{Li}_2\text{TiO}_3$ , and  $\text{Li}_4\text{SiO}_4$ ;  $\text{Li}_2\text{TiO}_3$  (lithium titanate) is considered the candidate tritium breeder material for Indian breeding blanket concept. Typically,  $\sim 1$  mm sized spherical pebbles will be placed inside the breeding blanket, and collectively, they will form a pebble bed. During fusion reactor operation, high-energy neutrons (14 MeV) will interact with materials present inside the breeder and elevate its temperature to  $700$ - $900^\circ\text{C}$  depending on the location and distance of the materials from plasma. Due to the temperature distribution inside the blanket's structural and functional materials, thermal stresses arise from differential thermal expansion. This thermal expansion is the primary cause of thermo-mechanical stresses inside the breeding blanket. To simulate the thermo-mechanical behavior of the blanket, pebble bed thermal expansion needs to be studied under regulated temperatures and exposure duration. Several studies have been performed earlier on  $\text{Li}_2\text{TiO}_3$  thermal expansion in pellet[1][2][3] form however only few researcher have [4] focused on bed thermal expansion.

In this work, we have focused on the pebble bed thermal expansion in both isothermal and non-isothermal regions.

### 2. Materials & Experiments

$\text{Li}_2\text{TiO}_3$  powder was synthesized by the solid-state reaction process, and pebbles were fabricated using freeze granulation[5] method. A sample holder, as shown in Figure 1 was fabricated with recrystallized alumina to hold the pebble bed inside the dilatometer. The temperature of the pebble bed was raised from room temperature to desired temperature with  $10^\circ\text{C}/\text{min}$ ., and isothermal conditions were maintained for 300 minutes. The controlled cooling at  $10^\circ/\text{min}$  was maintained from high temperature to  $100^\circ\text{C}$ . A constant load of 1 N was applied to the sample equivalent to 0.015 MPa. The thermal programs of the experiments are shown in Figure 2.



Figure 1 Pebble bed arrangement and sintered pebbles after the experiment

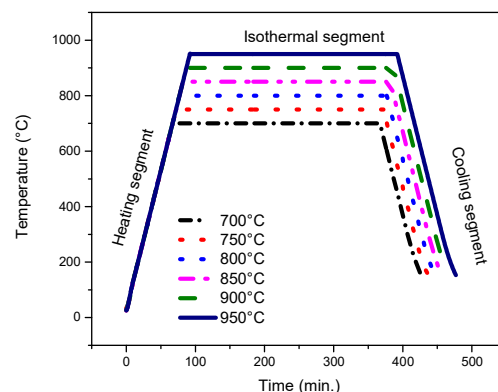


Figure 2 Temperature program for pebble bed thermal expansion experiments

### 3. Results

Figure 3 (a) shows the thermal expansion behavior of the  $\text{Li}_2\text{TiO}_3$  pebble bed for non-isothermal region of the experiment. The average thermal expansion from room temperature to  $700$ ,  $750$ ,  $800$ ,  $850$ ,  $900^\circ\text{C}$  is 1.1, 1.17, 1.25, 1.35, 1.43%. Above  $900^\circ\text{C}$  pebbles started to sinter with each other as well as sample holder material.

This phenomenon is also visible in the non-isothermal region of the experiments conducted at  $950^\circ\text{C}$ . Once the pebble bed reached the desired temperature, the isothermal conditions were maintained for 300 minutes followed by the cooling at  $10^\circ/\text{min}$ . Figure 3 (b) shows that the isothermal conditions at  $700$ - $800^\circ\text{C}$  do not show any major sintering effect. Two types of sintering reported here: one involving the sintering of the material itself and the other with the pebble-to-pebble sintering by a necking and growth mechanism.

The pebble-to-pebble sintering was not observed visually for isothermal region at temperature of  $700$ ,  $750$ ,  $800^\circ\text{C}$  and relative expansion data supported this with a shrinkage of

0.1%. The pebble heated at 850, 900°C shows slight shrinkage of ~0.5% over 300 minutes. The pebble bed heated at 950°C for 300 minutes duration shows a significant sintering behavior. After the experiments, pebble were visually sintered through necking and growth phenomenon. The materials also stuck to the alumina contained due to bonding of lithium and aluminum at high temperatures. The dilatometry data show a sintering of ~5% as shown in Figure 3 (b). The coefficients of thermal shrinkage for different temperature are also estimated. The pebble bed sintering mechanism are estimated and will also be discussed.

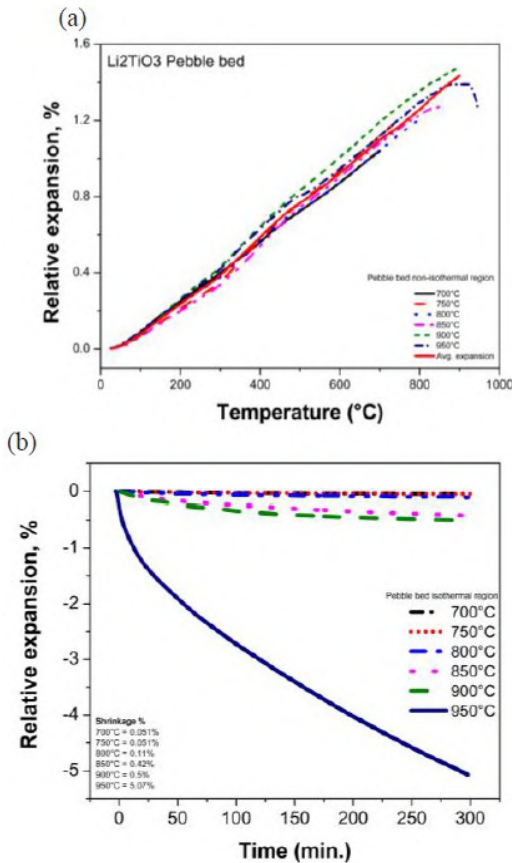


Figure 3 (a) relative expansion of pebble bed with temperature (b) relative expansion in isothermal region

Figure 4 shows the coefficient of thermal expansion of non-isothermal region for the green pellet, sintered pellet, and pebble bed along with their comparison to the literature data[1][2][3][4]. The green pellet started to shrink at 827°C, while the sintered pellet shows expansion till 1100°C. The CTE of the green pellet and sintered pellets is estimated to be  $19 \times 10^{-6}/^{\circ}\text{C}$  and  $19.5 \times 10^{-6}/^{\circ}\text{C}$ . These data are comparable to the literature values for non-isothermal region[1][2][3]. The pebble bed thermal expansion data was also compared with Tanigawa et al. [4] and data shows good agreement up to 300°C. Above this temperature, although it follows the same trend, the expansion values are higher than the literature value. There is a possibility that this experiment conducted at lower pressure of 0.015 MPa compared to the 0.1 MPa literature value have effect on the expansion data.

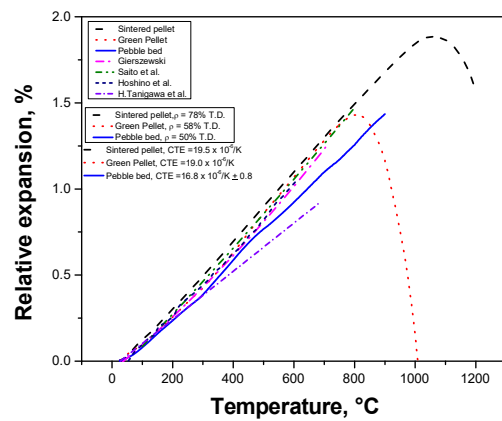


Figure 4 Relative thermal expansion comparison between sintered, green pellet and pebble bed

#### 4. Conclusion

In this work, a preliminary experiments were conducted to analyze the feasibility of pebble bed thermal expansion measurement using a conventional dilatometry technique. The CTE for non-isothermal region and CTS for isothermal region of the pebble bed were estimated under 0.015 MPa contact pressure. Future experiments are planned for higher pressure and variation in the pebble bed packing fraction.

#### References

- [1] S. Saito, K. Tsuchiya, H. Kawamura, T. Terai, S. Tanaka, Density dependence on thermal properties of Li<sub>2</sub>TiO<sub>3</sub> pellets, *J. Nucl. Mater.* 253 (1998) 213–218.
- [2] P. Gierszewski, Review of properties of lithium metatitanate, *Fusion Eng. Des.* 39–40 (1998) 739–743.
- [3] T. Hoshino, K. Tanaka, J. Makita, T. Hashimoto, Investigation of phase transition in Li<sub>2</sub>TiO<sub>3</sub> by high temperature X-ray diffraction, *J. Nucl. Mater.* 367-370 B (2007) 1052–1056.
- [4] H. Tanigawa, M. Enoeda, M. Akiba, Measurement of thermal expansion of Li<sub>2</sub>TiO<sub>3</sub> pebble beds, *Fusion Eng. Des.* 82 (2007) 2259–2263.
- [5] A. Shrivastava, T. Kumar, R. Shukla, P. Chaudhuri, Li<sub>2</sub>TiO<sub>3</sub> pebble fabrication by freeze granulation & freeze drying method, *Fusion Eng. Des.* 168 (2021) 112411.

Structural and Thermophysical Properties of Hf<sub>6</sub>Ta<sub>2</sub>O<sub>17</sub>Brij Mohan Singh<sup>a\*</sup>, Suryakant Nagar<sup>a</sup>, Pratik Das<sup>a,b\*</sup>, Pradeep Samui<sup>a,b\*</sup>, S.K. Rakshit<sup>a</sup> and S.C. Parida<sup>a,b</sup><sup>a</sup>Product Development Division, Bhabha Atomic Research Centre, Mumbai-85<sup>b</sup>Homi Bhabha National Institute, Bhabha Atomic Research Centre, Mumbai-85

\*brijms@barc.gov.in, \*pratikdas@barc.gov.in \*psamui@barc.gov.in

**Abstract**

Thermal barrier coating (TBC) plays an important role in high temperature application. Hf<sub>6</sub>Ta<sub>2</sub>O<sub>17</sub> is one of the TBC materials preferred over YSZ (Yttria Stabilized Zirconia). Structural and thermophysical properties of the super structured Hf<sub>6</sub>Ta<sub>2</sub>O<sub>17</sub> compound was explored using X-ray diffraction and heat capacity measurements, emphasizing its potential application as a thermal barrier coating material. Heat capacity as well as enthalpy increment of the compound was determined experimentally. The molar heat capacities of Hf<sub>6</sub>Ta<sub>2</sub>O<sub>17</sub> as a function of temperature has been least squares fitted and is expressed as  $C_{p,m}(T) (J \cdot K^{-1} \cdot mol^{-1})(\pm 3) = 551.1 + 0.0911 \cdot (T/K) - 6.577 \cdot 10^{-6} \cdot (K/T)^2$  ( $323 \leq T/K \leq 900$ ).

**Introduction**

High temperature material is most demanding as world is interested in energy generation and efficiency. Energy generation facility creates high temperature and stress for which material system rather than a particular material is required for optimal operation. Thermal barrier coatings (TBCs) are essential components of high temperature system for energy generation. The key material properties required for TBCs consist of: (i) adjustable thermal expansion coefficients, (ii) low thermal conductivity, and (iii) high chemical stability at elevated temperatures. Eutectic oxides have gathered significant interest and extensive research in recent years, primarily due to their remarkable thermochemical stability in corrosive environments and their distinctive eutectic structure. This structure allows for the simultaneous growth of two or three phases from the melt, which are seamlessly integrated at the interface. Notably, this configuration eliminates sliding or rotation at the grain boundary, and the presence of the interface inhibits dislocation movement, thereby enhancing mechanical properties at elevated temperatures. Advancement of Al<sub>2</sub>O<sub>3</sub>-based eutectic ceramics necessitates the investigation of additional eutectic systems derived from other oxides. The eutectic phenomenon is indeed present in numerous binary and ternary phase diagrams. McCormack et al. [1] have detailed the phase diagram of the HfO<sub>2</sub>-Ta<sub>2</sub>O<sub>5</sub> system up to 3000°C, utilizing a quadrupole lamp furnace and a conical nozzle levitator system that incorporates a CO<sub>2</sub> laser, alongside synchrotron X-ray diffraction techniques. Their findings indicate that at approximately 35% molar concentration of HfO<sub>2</sub>, both Hf<sub>6</sub>Ta<sub>2</sub>O<sub>17</sub> and Ta<sub>2</sub>O<sub>5</sub> coexist within the eutectic system. Ta<sub>2</sub>O<sub>5</sub> is characterized as an oxide material with a relatively high melting point of 1800°C, notable toughness, and resistance to corrosion [1, 2], making it suitable for use in anticorrosive coatings for silicon nitride and titanium alloys [1]. Hf<sub>6</sub>Ta<sub>2</sub>O<sub>17</sub>, on the other hand, serves as an exemplary high-temperature structural material, possessing a melting point around 2400°C, low thermal conductivity, minimal oxygen diffusion rate, and exceptional corrosion resistance, with no phase transitions occurring from room temperature to its melting point [1]. Consequently, Hf<sub>6</sub>Ta<sub>2</sub>O<sub>17</sub>/Ta<sub>2</sub>O<sub>5</sub> composite ceramics featuring a eutectic structure are poised to combine the inherent advantages of the materials with their unique structural properties, presenting significant potential for advancement in high-temperature structural applications. In light of this, it is important to analyze the structural and thermophysical properties of Hf<sub>6</sub>Ta<sub>2</sub>O<sub>17</sub> to facilitate better utilization of the material. Hence present studies mainly

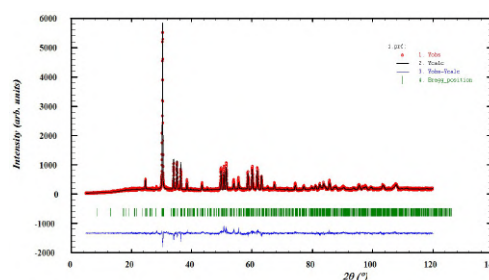
focused on synthesis, structural elucidation and thermophysical property measurement of Hf<sub>6</sub>Ta<sub>2</sub>O<sub>17</sub>(s).

**Experimental**

In this study, Hf<sub>6</sub>Ta<sub>2</sub>O<sub>17</sub>(s) was synthesized using solid-state method, involving stoichiometric amounts of HfO<sub>2</sub> (mass fraction 0.999) and Ta<sub>2</sub>O<sub>5</sub> (mass fraction 0.999). These materials were thoroughly mixed using a mortar and pestle and pelletized to pellet form. It was heated at 1073 K for 40 h. After cooling, the pellet was reground, repelletized, and subjected to further heating at 1723 K for 48 h. The successful formation of the compound was verified using X-ray diffraction (XRD) pattern derived from a Miniflex 600 diffractometer (Rigaku, Japan). Additionally, Rietveld analysis was performed to ascertain the purity of the material. The primary characterization of the compound was carried out by powder X-ray diffraction (XRD). Heat capacity of Hf<sub>6</sub>Ta<sub>2</sub>O<sub>17</sub>(s) was experimentally measured using Heat flux differential scanning calorimetry (DSC).

**Results and discussion**

Fig. 1 illustrates the Rietveld refinement pattern of the X-ray diffraction (XRD) data of the synthesized Hf<sub>6</sub>Ta<sub>2</sub>O<sub>17</sub>(s).

Figure 1. Rietveld refinement pattern of Hf<sub>6</sub>Ta<sub>2</sub>O<sub>17</sub>(s)

Hf<sub>6</sub>Ta<sub>2</sub>O<sub>17</sub>(s) can be indexed to orthorhombic superstructure and refined parameters are provided in Table 1.

Table 1: Fitting parameters of Hf<sub>6</sub>Ta<sub>2</sub>O<sub>17</sub>(s) after Rietveld refinement

Parameters	Hf <sub>6</sub> Ta <sub>2</sub> O <sub>17</sub>
Space group	I m a 2
a (Å)	40.826 (2)
b (Å)	4.935(2)
c (Å)	5.262(2)
Volume (Å <sup>3</sup> )	1060.21
R <sub>wp</sub> (%)	4.16
R <sub>exp</sub> (%)	3.20
χ <sup>2</sup> (%)	1.69

The elucidation of the crystal structure of  $\text{Hf}_6\text{Ta}_2\text{O}_{17}$  was accomplished recently by McCormack and Kriven [2]. They demonstrated that  $\text{Hf}_6\text{Ta}_2\text{O}_{17}$  features a superstructure with space group symmetry  $\text{Ima}2$  (S.G. 46) and room temperature lattice parameters of  $a = 8 \times 5.1038 = 40.837 \text{ \AA}$ ,  $b = 4.9434 \text{ \AA}$ , and  $c = 5.263 \text{ \AA}$ . The atomic structure is constructed from a series of asymmetric structural units centered on cations, which consist of: (i) one set of symmetry-equivalent, six-coordinated polyhedra, (ii) three sets of symmetry-equivalent, seven-coordinated polyhedra, and (iii) one set of symmetry-equivalent, eight-coordinated anti-polyhedra [2]. Table 1 illustrates an excellent agreement of our experimental structural data with previously reported findings of McCormack and Kriven [2]. Microstructural image of compound was also taken implying Scanning electron microscope and shown in Figure 2. Molar heat capacities of  $\text{Hf}_6\text{Ta}_2\text{O}_{17}(\text{s})$  as a function of temperature has been least squares analyzed and are expressed as -

$$C_{p,m}(T) (\text{J}\cdot\text{K}^{-1}\cdot\text{mol}^{-1}) \pm 3 = 551.1 + 0.091 \cdot (T/\text{K}) - 6.577 \cdot 10^6 \cdot (K/T)^2 \quad (306 \leq T/\text{K} \leq 900) \dots\dots\dots (1)$$

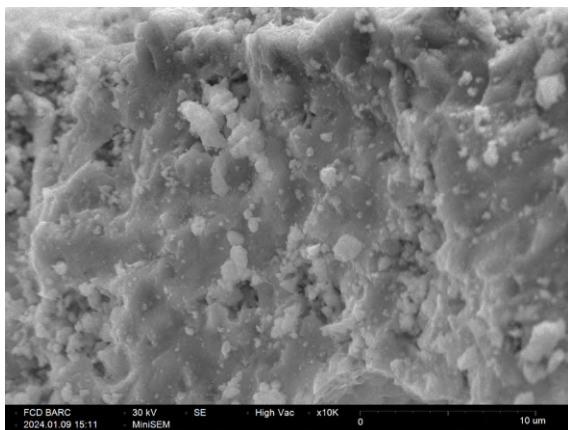


Figure 2: SEM image of compound

Figure 3 depicts experimentally measured heat capacity data of  $\text{Hf}_6\text{Ta}_2\text{O}_{17}(\text{s})$  from 323 K – 850 K using step method by employing a DSC (Setaram, France)

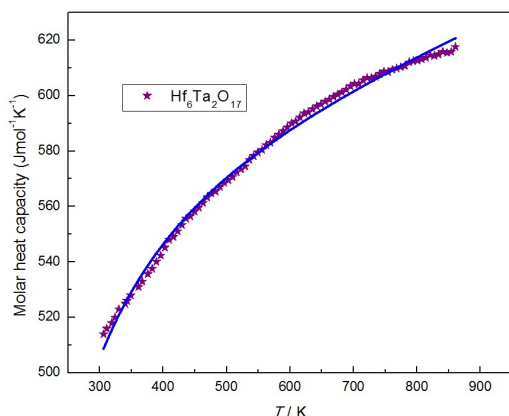


Figure 3. Heat capacity data of  $\text{Hf}_6\text{Ta}_2\text{O}_{17}(\text{s})$

Enthalpy increment was also determined employing high temperature calorimeter (ALEXSYS 1000) at 823 K, 873 K, 923 K, 973 K and 1023 K. This calorimeter was first calibrated by dropping alpha alumina (SRM 720) from ambient temperature to desired temperature and calibration factor was calculated at different temperature by comparing peak area. Enthalpy increment data at different temperature was calculated by dropping three solid samples at each temperature

and taking average of three values. Fitted equation is given below:

$$H(T) - H(298) (\text{J}\cdot\text{K}^{-1}\cdot\text{mol}^{-1}) = -101130.6 + 365.9 \cdot (T/\text{K}) - 0.1661 \cdot (K/T)^2 - 6745821.2 / (T/\text{K}) \quad (298 \leq T/\text{K} \leq 1100) \dots\dots\dots (2)$$

Table 2: Thermodynamic parameter

$T$ (K)	$C_p$ ( $\text{JK}^{-1}\text{mol}^{-1}$ )	$H_T - H_{298}$ ( $\text{Jmol}^{-1}$ )	$S_T - S_{298}$ ( $\text{JK}^{-1}\text{mol}^{-1}$ )
298	504.1	0	0
300	505.3	1009.4	2.2
350	529.3	26911.3	53.4
400	546.4	53823.6	96.2
450	559.6	81485.4	133.2
500	570.3	109740.1	166.1
550	579.4	138488.1	195.7
600	587.4	167662.8	222.8
650	594.7	197218.3	247.9
700	601.4	227121.8	271.2
750	607.6	257349.2	293.2
800	613.6	287882.4	313.9
950	630.3	381193.1	370.2
1000	635.5	412838.1	387.3
1050	640.7	444743.7	403.9

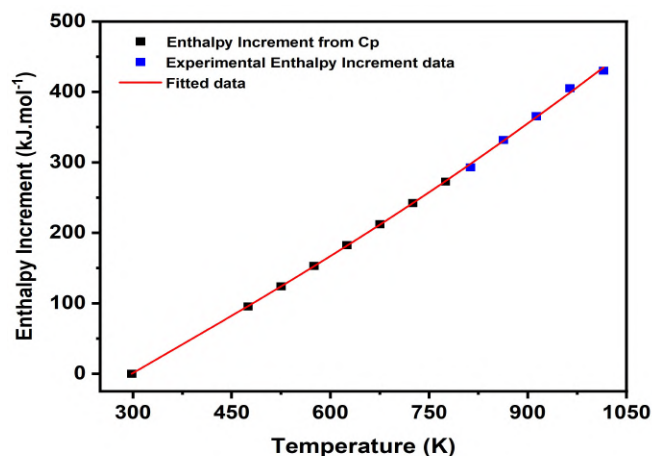


Figure 4. Enthalpy increment of  $\text{Hf}_6\text{Ta}_2\text{O}_{17}(\text{s})$

**Conclusion:**

Heat capacity of compound was determined first time as it is not available in literature. Using heat capacity data other thermodynamic parameters were calculated.

**References**

[1] S.J. McCormack, R.J. Weber, W.M. Kriven, In-situ investigation of  $\text{Hf}_6\text{Ta}_2\text{O}_{17}$  anisotropic thermal expansion and topotactic, peritectic transformation, *Acta Materialia*, 161 (2018) 127-137.  
 [2] S.J. McCormack, W.M. Kriven, Crystal structure solution for the  $\text{A}_6\text{B}_2\text{O}_{17}$  (A= Zr, Hf; B= Nb, Ta) superstructure, *Acta Crystallographica Section B: Structural Science, Crystal Engineering and Materials*, 75 (2019) 227-234.



# Synthesis, Characterization and Properties of Nanosized Nickel Cobalt Ferrites Synthesized by the Thermolysis of an Hexahydrazine Nickel Cobalt Ferrous Succinate Precursor

Daniel M. Coutinho<sup>a,\*</sup> and V.M.S.Verenkar<sup>b</sup>

<sup>a</sup>Department of Chemistry, Carmel College of Arts, Science and Commerce for Women, Nuvem

<sup>b</sup>School of Chemical Science, Goa University, Taleigao Plateau, Goa-403206, India

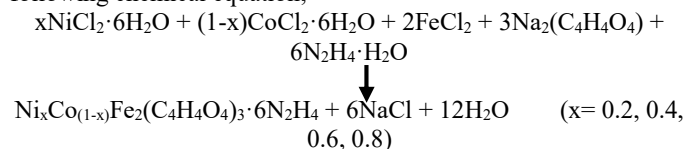
\*Email: [danielcoutinho@carmelcollegegoa.org](mailto:danielcoutinho@carmelcollegegoa.org), 9823806686

## Abstract

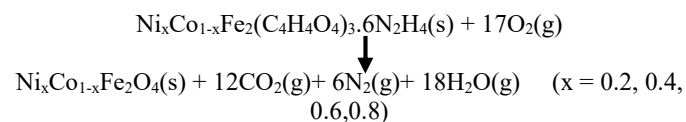
Pure and single-phase nickel cobalt ferrites, having particles of nanosize dimensions were synthesized by the thermal decomposition of a precursor having the molecular formula  $Ni_xCo_{1-x}Fe_2(C_4H_4O_4)_3 \cdot 6N_2H_4$  ( $x = 0.2, 0.4, 0.6, 0.8$ ). Thermal analysis explained the step involved in the decomposition of the precursors. A combination of TG, DTA, isothermal mass loss and total mass loss studies was used. The formation of cubic spinel phase was determined by powder X-ray diffraction analysis. The coercivity and magnetic moment of the ferrite decreasing with increase in Ni concentration. The Curie temperature increased with Ni doping.

**Introduction:** The metal oxide nano crystals (MONCs) have been extensively studied over the last decade as they have potential for magnetic, electronic and optical applications as well as for their unique and tuneable properties. The ability to alter the properties of these MONC's from their bulk counterparts by rational design and nano scale synthesis techniques can lead to new and interesting phenomena's [1]. A class of these MONCs are the magnetic nano particles (MNPs) have applications in different fields such as data storage, permanent magnets, optics, catalysis, nanomedicine, etc [2]. The nano particles of ferrites having spinel structure form an important class of these MNPs not only because of their applications in various technological fields but also because they can be fundamental to understanding basic properties.

**Synthesis:** The precursor combustion synthesis route was employed to prepare the nanoparticles [3]. In this method, solid Sodium succinate was dissolved to make an aqueous solution. To this solution, hydrazine monohydrate was added, with the two solutions in the molar ratio of 1:2. The mixture was stirred in a three neck round bottom flask that was maintained under an inert atmosphere of Nitrogen gas. After two hours, a homogenous mixture was obtained. The required amounts of Nickel Chloride, Cobaltous Chloride and Ferrous chloride (freshly prepared) were taken and dissolved in minimum amounts of distilled water. This aqueous solution was added in a drop wise manner to the flask with constant stirring. A light brown coloured precipitate of the precursor formed that was filtered, washed first with ethanol and then with diethyl ether. The dried precipitate of hexa-hydrazine Nickel Cobalt Ferrous Succinate obtained was stored in a vacuum desiccator. The formation of the precursor can be given by the following chemical equation,



A lit match was used to ignite the powder precursor. The powder sparks and catches fire burning with the emission of a red glow. This then spreads over the entire powder in a slow and controlled manner ultimately giving the auto combusted nano-sized ferrite. Some amount of carbon may remain during the combustion process; hence the powder was calcined at 500°C for 5h in a muffle furnace to remove this residual carbon if any present in the decomposed product.



Finally, the grinding of the calcined powder was done to give the 'as-prepared' ferrite having the chemical formula  $Ni_xCo_{1-x}Fe_2O_4$  ( $x = 0.2, 0.4, 0.6, 0.8$ ).

**Characterization:** In-order to determine the mode by which the different ligand complex to the metal ions, Fourier transform Infrared spectra analysis was performed (Fig. 1). The  $\nu_{strec}$  (N-H) was observed in the region of 3176-3362  $cm^{-1}$ . The hydrazine molecule has lone pairs on both the N-atoms and hence can link to the metal in different ways. From the position of the N-N stretching band at 965  $cm^{-1}$  and 967  $cm^{-1}$  in the two precursors, it points to a bridging bidentate linkage of the hydrazine molecule. The  $\nu_{sym}$  (C-H) and  $\nu_{asym}$  (C-H) bands were observed at 2957  $cm^{-1}$  and ~2919  $cm^{-1}$  in both the precursors while the  $\nu_{asym}$  (C-C) band was observed at ~1217  $cm^{-1}$ . The succinate group can bind to the metal in different ways. In the present study, the  $\nu_{asym}$  (COO) and  $\nu_{sym}$  (COO<sup>-</sup>) were observed at ~1621 and ~1408  $cm^{-1}$ , respectively, which gives a difference of ~213  $cm^{-1}$  indicating that the succinate groups are bound in a monodentate fashion [4].

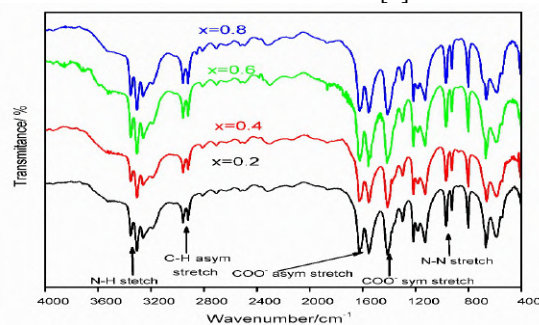
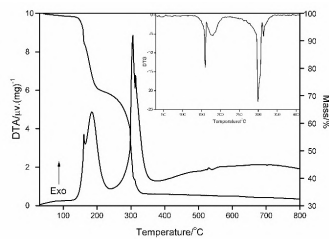


Fig. 1: Infrared Spectra of  $Ni_xCo_{1-x}Fe_2(C_4H_4O_4)_3 \cdot 6N_2H_4$  ( $x = 0.2, 0.4, 0.6, 0.8$ ) precursors.

The precursors undergo a thermal decomposition on ignition to give stable ferrite phase. In order to analyze the way, the precursor changes with increase in temperature the TG-DTA analysis was performed. In all the precursors the loss of hydrazine takes place first and only after complete dehydration does the decomposition of the succinate ligand start. For the precursor  $Ni_{0.2}Co_{0.8}Fe_2(C_4H_4O_4)_3 \cdot 6N_2H_4$  the loss of hydrazine takes place in two steps (Fig. 2). In the temperature range of 130°C to 160°C two molecules of hydrazine are lost and the remaining four hydrazine molecules decompose in the range of 170°C to 235°C. Two peaks observed in the DTA in this region collaborate this two-step dehydrazination. The three succinate groups are also lost in two steps, two molecules are lost between 235°C to 310°C and the third molecule decomposed in the temperature range of 310°C to 400°C.

To get a better understanding of the decomposition pattern isothermal mass loss studies were performed. The precursor  $Ni_{0.2}Co_{0.8}Fe_2(C_4H_4O_4)_3 \cdot 6N_2H_4$  losses hydrazine in a step wise

manner. Two molecules are lost between 100°C and 130°C. The final four molecules are lost between 130°C to 150°C. The hydrazine analysis in this region decreases with increase in temperature and becomes zero at 150 °C further confirming that complete dehydrazination is achieved at 150°C. From the mass loss obtained after 200°C, it matched with the decomposition of the succinate group, two group between 200-250 °C while the third group is lost between 250-300 °C.



**Fig. 2:** TG-DTA curves of  $\text{Ni}_{0.6}\text{Co}_{0.4}\text{Fe}_2(\text{C}_4\text{H}_4\text{O}_4)_3 \cdot 6\text{N}_2\text{H}_4$  precursor

The ‘as-prepared’ ferrite was then characterized. The diffractogram of the ferrites showed peaks that have a broad nature which is due to the nano size of the ‘as-prepared’ ferrites. The seven peaks obtained in the diffractogram are observed at 2θ positions that correspond to a spinel cubic crystal structure (Fig. 3) [5]. There are no others peaks in the diffractogram which confirms the formation of pure spinel ferrite phase.

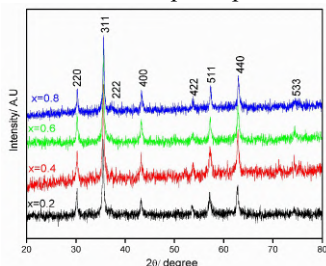


**Fig. 3:** X-ray diffractogram of ‘as-prepared’  $\text{Ni}_x\text{Co}_{1-x}\text{Fe}_2\text{O}_4$  ( $x=0.2, 0.4, 0.6, 0.8$ ) ferrites.

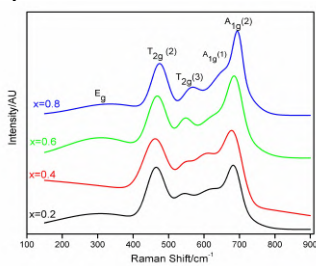


**Fig. 4:** Raman spectra of ‘as-prepared’  $\text{Ni}_x\text{Co}_{1-x}\text{Fe}_2\text{O}_4$  ( $x=0.2, 0.4, 0.6, 0.8$ ) ferrites.

The Raman spectra, recorded at room temperature are shown in Fig 4. The spectra reveal four prominent peaks that have a sharp and intense nature. This is another indication of the crystalline nature of the ferrites. The intense band at  $690\text{ cm}^{-1}$  is due to the stretch between the metal ion and oxygen at the tetrahedral site and is assigned the notation  $A_{1g}$ . The bands at  $308\text{-}320\text{ cm}^{-1}$ ,  $536\text{-}555\text{ cm}^{-1}$  and  $462\text{-}475\text{ cm}^{-1}$  arise due to the symmetric bending and asymmetric bending of the M-O bond at the octahedral site and are assigned the notations  $E_g$ ,  $T_{2g}(3)$  and  $T_{2g}(2)$ , respectively [6]. All the five band positions shift to higher wavenumber (blue shift) with increase in Ni concentration.

The XPS spectrum of Co 2p is observed as a doublet with a separation of  $\sim 16\text{ eV}$  between the  $2p_{3/2}$  and  $2p_{1/2}$ . The separation between the two peaks confirms the +2 oxidation state of cobalt. The Ni 2p peaks can also be resolved into a doublet, separated by a distance of  $18\text{ eV}$ . The two peaks are the  $2p_{3/2}$  and  $2p_{1/2}$ . The absence of shoulders in the peaks indicates the +2 oxidation state of Ni cation. The Fe 2p doublet due to the  $2p_{3/2}$  and  $2p_{1/2}$  peaks have a separation of  $\sim 14\text{ eV}$ . The  $2p_{3/2}$  peaks has a split into two due to iron at the two crystallographic sites. The  $\text{Fe}^{3+}$  cation is in a high spin state. A satellite peak with B.E  $\sim 8\text{ eV}$  higher than the main peak was also observed in all the ferrite samples. The position of this satellite peaks confirms that iron is in +3 oxidation state and also the high spin configuration of  $\text{Fe}^{3+}$ .

The room temperature MH curves show hysteresis behavior which indicates that the ferrites have ferromagnetic alignment of the magnetic spins (Fig. 5). The curve however has a smaller width for the ferrites with higher Ni content. This means that there is a decrease in the hardness of the ferrites as we replace Co for Ni in the ferrites. The saturation magnetization also showed a decreasing trend with increase in Ni concentration. The Remanent

magnetization at room temperature are less than 0.5 times the  $M_s$  value. This points to the anisotropy in the ferrites is of uniaxial. Also, there is magnetostatic interaction between the ferrite particles [7]. The MH curve at 50K have a much larger width than the room temperature curves. The large increase in coercivity is due to the fact that  $\text{Co}^{2+}$  ions have the ability to move to the octahedral sites at a low temperature.

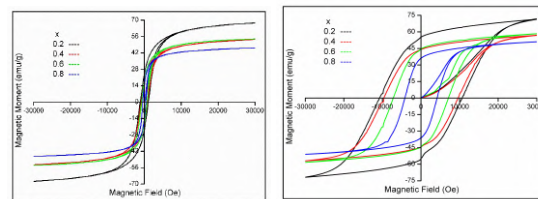


**Fig. 5:** M-H curves of ‘as-prepared’  $\text{Ni}_x\text{Co}_{1-x}\text{Fe}_2\text{O}_4$  ( $x=0.2, 0.4, 0.6, 0.8$ ) ferrites at room temperature and 50K.

The variation of the magnetic moment with increase in temperature (MT) at different static applied field are shown in Fig. 6. The ZFC curve has the lowest value to 50K and the magnetization increases with increase in temperature. The thermal fluctuation on the spins at room temperature prevent them for adopting a perfect anti-parallel alignment. At low temperatures the magneto crystalline energy is stronger than the thermal effects and the spins take up an antiparallel alignment. As the temperature is increased, the spins will start to deviate from this alignment causing the magnetic moment to increase. The FC curve is independent of temperature over from 50K to 400K. The magnetocrystalline energy blocks the spins from rotating. This gives a high magnetic moment that remains constant. The thermal energy is not sufficient to overcome the magnetocrystalline energy. But again, there is small decrease in the curve above 300K for the Ni rich samples. There is a decrease in magnetocrystalline energy with increase in Ni content. The ZFC and FC curves do not intersect over the temperature range.

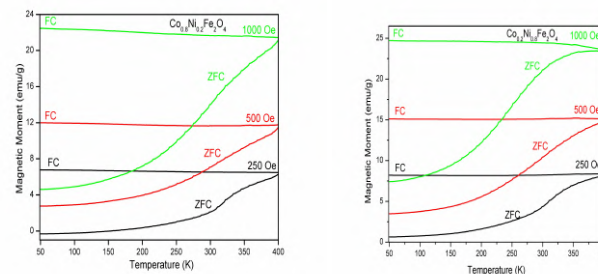


**Fig. 6:** MT curves of prepared’  $\text{Ni}_x\text{Co}_{1-x}\text{Fe}_2\text{O}_4$  ( $x=0.2, 0.8$ ) at 250Oe, 500Oe and 1000Oe.

## References:

1. J. Kim, H. R. Cho, H. Jeon, D. Kim, C. Song, N. Lee, S. H. Choi, T. Hyeon, *J Am Chem Soc.* 139 (2017) 10992-95.
2. I. S. Lyubutin, C. R. Lin, S. S. Starchikov, A. O. Baskakov, N. E. Gervits, K. O. Funtov, Y. Tseng, W. Lee, K. Shih, J. Lee, 56 (2017) 12469-75.
3. D. M. Coutinho, V. M. S. Verenkar, *J. Therm. Anal. Calorim.* 128 (2017) 807-17.
4. L. R. Gonsalves, V. M. S. Verenkar, *J Therm. Anal. Calorim.* 108 (2012) 877-80.
5. D. M. Coutinho, V. M. S. Verenkar, *J. Alloys Comp.* 782 (2019) 392-403.
6. F. L. Deepak, M. Bañobre-López, E. Carbó-Agribay, M. F. Cerqueira, Y. Piñeiro-Redondo, J. Rivas, C. M. Thompson, S. Kamali, C. R. Abreu, K. Konvir, Y. V. Kolen'ko, *J. Phys. Chem. C.* 19 (2015) 11947-57.
7. R. Topkaya, A. Baykal, A. Demir, *J Nanopart Res.* 15 (2013) 1359-76.

## Effect of Nb Substitution on the Thermal Stability and Glass-Forming Ability of Zr-Based Bulk Metallic Glasses

Sanjay Saini<sup>a,\*</sup>, A.P.Srivastava<sup>a</sup> and Suman Neogy<sup>a</sup>

<sup>a</sup>Materials Science Division, Bhabha Atomic Research Centre, Trombay, Mumbai, 400085

\* ssaini@barc.gov.in

### Abstract

In present study, Zr-based bulk metallic glasses (BMGs) with two compositions,  $Zr_{60}Ti_5Cu_{20}Fe_5Al_{10}$  and  $Zr_{60}Nb_5Cu_{20}Fe_5Al_{10}$  were prepared using the suction casting technique. X-ray diffraction and transmission electron microscopy confirmed that both alloys exhibit a fully amorphous structure. Differential scanning calorimetry was employed to investigate the thermal stability and crystallization kinetics under non-isothermal conditions. The Kissinger analysis revealed that the glass transition activation energy is higher than the crystallization activation energy for both as cast BMGs. The results showed that the addition of Nb enhances the glass-forming ability (GFA) and thermal stability compared to Ti, as indicated by higher  $T_{rg}$ ,  $\gamma$ , and PHSS parameters.

Bulk metallic glasses (BMGs) are materials with a disordered atomic structure, giving them unique properties like high strength, hardness, and resistance to corrosion [1-4]. These properties make BMGs useful for many applications. However, due to their instability, BMGs tend to crystallize upon heating, altering their structure and properties. Understanding this crystallization process is important to improve their thermal stability and improving the glass forming ability (GFA). The GFA measures a material's tendency to form an amorphous structure rather than a crystalline. The crystallization behavior and GFA of BMGs have been extensively studied across various alloy systems, including Fe-based, Zr-based, Ti-based, and Cu-based alloys. Among the methods used, differential scanning calorimetry (DSC) is one of the most effective techniques. Non-isothermal DSC experiments are especially useful for analyzing parameters such as activation energy, crystallized volume fraction, and nucleation and growth mechanisms [5]. Methods such as Kissinger's and Ozawa–Flynn–Wall are often used to calculate these kinetic parameters [4]. Further, thermodynamic parameters such as PHS (Product of  $\Delta H_{chem}$  with  $S_{\sigma}/k_B$ ) and PHSS (Product of PHS with  $S_{\sigma}/R$ ) are widely used to predict GFA. These parameters incorporate enthalpy of mixing ( $\Delta H_{chem}$ ), mismatch entropy ( $S_{\sigma}$  normalized by Boltzmann's constant), and configurational entropy ( $S_c$  normalized by the universal gas constant). These parameters are calculated theoretically, making them effective tools for understanding and optimizing GFA in metallic glasses.

Zr-based bulk metallic glasses (BMGs) have gathered significant attention due to their excellent glass-forming ability (GFA), high mechanical strength, and superior corrosion resistance [1-4]. These materials, particularly those containing elements such as Cu, Ti, Ni, and Al, are widely studied for their promising structural and functional applications. The GFA of Zr-based BMGs is influenced by factors such as atomic size distribution, enthalpy of mixing, and entropy, with careful alloying playing a crucial role in optimizing these properties. Research has shown that minor additions of elements like yttrium can improve the GFA. Niobium (Nb), an intermediate transition metal, has been widely used as an alloying element in various metallic glass systems to alter their structure and properties. Nb improves the passivation ability of the material, enhancing its corrosion resistance. In systems such as Ti-Nb and Zr-Nb alloys, Nb is known for its ability to form solid solutions with transition metals and increase atomic disorder, which can enhance the stability of the amorphous phase.

The present study focuses on understanding the thermal stability and GFA of two Zr-based BMGs:  $Zr_{60}Ti_5Cu_{20}Fe_5Al_{10}$  (referred to as ZrTi) and  $Zr_{60}Nb_5Cu_{20}Fe_5Al_{10}$  (referred to as ZrNb) using the non-isothermal crystallization

kinetics. By comparing the two alloy systems, the study provides insights into how the substitution of Ti with Nb affects the thermal stability and crystallization behavior of these BMGs. The results contribute to a better understanding of Zr-based BMGs and their potential for advanced material applications.

In the present study the master alloy ingots were prepared by arc melting of high-purity constituent elements (Zr, Ti or Nb, Cu, Fe, and Al) under a high-purity Ti-gettered argon atmosphere. The ingots were re-melted five times to ensure compositional homogeneity. After melting, the molten alloys were suction-cast into water-cooled copper molds, forming cylindrical rods with a diameter of 5 mm and a length of 5 cm. The as-cast microstructure of the BMGs was characterized by X-ray diffraction (XRD) using a Bruker D8 Discover X-ray diffractometer with Mo  $K\alpha$  radiation. For further structural characterization at the atomic scale, transmission electron microscopy (TEM) analysis was carried out using a LIBRA 200 FE TEM. Samples for TEM observations were prepared by cutting thin sections from the as-cast rods and polishing them using a Tenupol-2 twin-jet electropolisher with a solution of 15% nitric acid in methanol at  $-40^{\circ}C$  and a voltage of 20 V. Thermal behavior was studied using differential scanning calorimetry (DSC) with a Mettler Toledo DSC system under an argon atmosphere. The DSC system was calibrated using pure indium. Specimens with a thickness of 1 mm were cut from the as-cast rods and placed in  $Al_2O_3$  pans for the DSC experiments. The samples were heated at continuous rates of 5, 10, 20, and 40 K/min to study their crystallization and glass transition behaviors.

The XRD patterns obtained from the as-cast ZrTi and ZrNb BMGs are shown in Fig. 1. Both alloy systems exhibit broad humps around  $12^{\circ}$  and  $18^{\circ}$ , which are characteristic of an amorphous structure. This broad feature in the XRD patterns is typically observed in BMGs, indicating a lack of long-range atomic order.

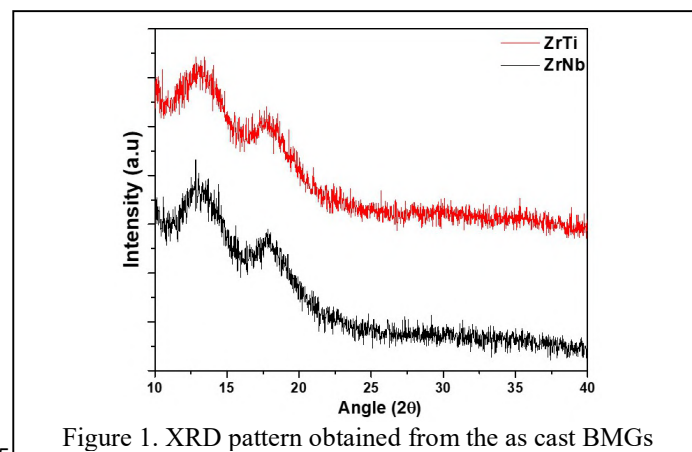


Figure 1. XRD pattern obtained from the as cast BMGs

Fig. 2 displays a representative of the bright field TEM micrograph and the selected area electron diffraction (SAED) pattern obtained from both as cast samples. The TEM images reveal a homogeneous microstructure with no signs of crystalline regions, suggesting a well-developed amorphous phase. Additionally, the SAED patterns exhibit broad halo rings, further confirming the absence of long-range order and the amorphous nature of the as-cast BMGs. These combined, RD and TEM results provide strong evidence that both the ZrTi and ZrNb alloys are fully amorphous in their as-cast state.

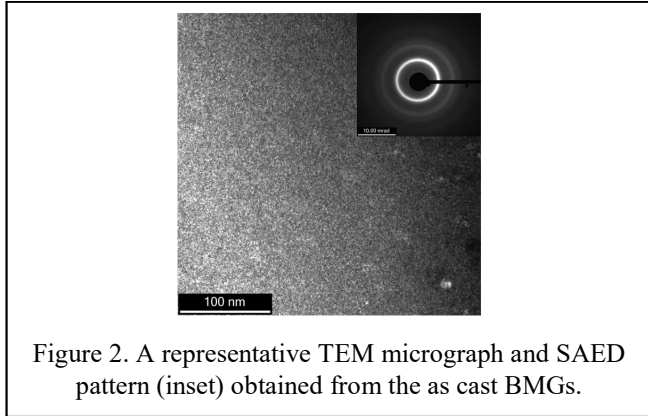


Figure 2. A representative TEM micrograph and SAED pattern (inset) obtained from the as cast BMGs.

Fig. 3(a) and 3(b) presents the non-isothermal DSC scans at various heating rates of 5, 10, 20, and 40 K/min for the as-cast ZrTi and ZrNb BMG alloys. The DSC curves for both alloys show a distinct endothermic event characteristic of the glass transition and supercooled liquid region, followed by exothermic peaks associated with multiple crystallization events.

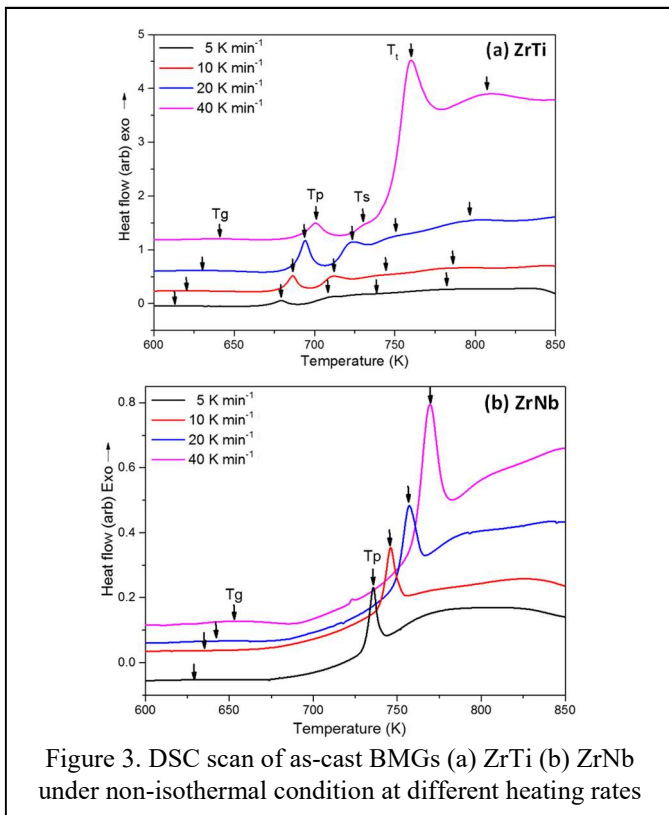


Figure 3. DSC scan of as-cast BMGs (a) ZrTi (b) ZrNb under non-isothermal condition at different heating rates

The glass transition temperature ( $T_g$ ), primary crystallization temperature ( $T_c$ ), and, in the case of ZrTi, the secondary crystallization temperature ( $T_s$ ), are marked by arrows in the respective DSC scans. Table 1 shows the thermal parameters namely  $T_g$ , and  $T_c$ , obtained from DSC curves for both samples at the commonly reported heating rate of 20 K/min. It is

observed that as the heating rate increases from 5 to 40 K/min, all the characteristic temperatures ( $T_g$  and  $T_c$ ) shift to higher values for both alloys. This behavior confirms that the crystallization and glass transition processes in both BMGs are thermally activated in nature. The rate dependence of these events was analyzed to study the detailed kinetics using the Kissinger model [6]. According to this model, a linear fit of the plot of  $\ln(\beta/T_x^2)$  vs.  $(1/T_x)$  where  $x$ , stands for either crystallization temperature or glass transition temperature, is used to determine the activation energy. The activation energy values for both cases are listed in Table 1. The Kissinger method indicates nearly identical  $E_g$  values within the error margin, while  $E_g$  is higher than  $E_c$  for both samples. Since glass transition occurs at a lower temperature than crystallization, the reduced atomic mobility results in a higher energy barrier, leading to higher  $E_g$  values. It is observed that the value of  $E_c$  increased after Nb-addition. Therefore, it is concluded that Nb-addition modifies the amorphous matrix in a way that increases its resistance to crystallization.

**Table 1. Different thermal parameters for both BMGs. Characteristics temperature at heating rate of 20 K/min.**

Alloy	$T_g$ (K)	$T_p$ (K)	$E_g$ (kJ/mol)	$E_c$ (kJ/mol)	$\gamma$	$Trg$
ZrTi	635	694	378	315	0.4215	0.631
ZrNb	642	757	385	342	0.4352	0.642

The glass-forming parameters, namely  $Trg$  ( $=T_g/T_l$ ) and  $\gamma$  ( $=T_x/(T_g+T_l)$ ), for both as-cast BMG alloys were evaluated and are presented in Table 1 [7]. It was observed that the  $Trg$  and  $\gamma$  values are higher for the ZrNb BMG system, indicating improved glass-forming ability (GFA) and thermal stability compared to the ZrTi system. The PHSS parameter for both BMGs was calculated as -3.084 for ZrTi and -3.101 for ZrNb [8]. The more negative value of this parameter indicates the superior GFA of the ZrNb alloy. The enhancement in thermal stability and GFA with Nb addition can be attributed to several factors. In the ZrTi and ZrNb metallic glass systems, the atomic radii of Ti and Nb are 0.147 nm and 0.207 nm, respectively [9]. According to Inoue's criteria, a larger overall atomic size difference ( $R_{Nb/XX} > R_{Ti/XX}$ ) increases atomic size mismatch between Nb and the other constituent elements. This mismatch restricts long-range atomic diffusion and promotes dense random packing in the supercooled liquid. Additionally, the mixing enthalpy increases from -15.5434 kJ/mol to -15.8594 kJ/mol after Nb addition. This suggests that Nb atoms have a stronger affinity to pair with Zr, Cu, Fe, and Al, thereby enhancing resistance to the formation of major crystalline phases. As a result, the Nb-containing BMG alloy exhibits better GFA and thermal stability.

## References

- [1] S. Cheng, C. Wang, M. Ma, D. Shan, B. Guo, J. Alloys Compd. 676 (2016) 299-304.
- [2] J.J. Fan, Y.F. Yan, S.H. Chen, C.-H. Ng, F.F. Wu, K.C. Chan, Intermetallics, 74 (2016) 25-30.
- [3] N.W. Khun, H. Yu, Z.Z. Chong, P. Tian, Y. Tian, S.B. Ror, E. Liu, Mater. Des. 92 (2016) 667-673.
- [4] A.P. Srivastava, T. Stefanov, D. Srivastava, D.J. Browne, Mater. Sci. Eng. A 651 (2016) 69-74.
- [5] Z.F. Yao, J.C. Qiao, C. Zhang, J.M. Pelletier, Y. Yao, J. Non-Cryst. Solids 415 (2015) 42-50.
- [6] H.E. Kissinger, Analytical Chemistry 29 (11) (1957) 1702-1706.
- [7] S. Guo, Z.P. Lu, C.T. Liu, Intermetallics 18 (2010) 883-888.
- [8] C. Suryanarayana, A. Inoue, Int. Mater. Rev. 58 (2013) 131.
- [9] G. Sheng, C.T. Liu, Prog. Nat. Sci. Mater. Int. 21 (2011) 433.

# Thermolysis of Coordination Polymer of Copper(II) of 4,4'-dipyridyldiselenide and its Conversion to Copper Selenide Nanostructures

Manoj K. Pal<sup>a</sup>, Gourab Karmakar<sup>a</sup>, Alpa Y. Shah<sup>a</sup>, Adish Tyagi<sup>a</sup>, Nattamai Bhuvanesh<sup>b</sup> and Sandip Dey<sup>a,\*</sup>

<sup>a</sup>Chemistry Division, Bhabha Atomic Research Centre, Mumbai-400 085, India

<sup>b</sup>Department of Chemistry, Texas A&M University, College Station, TX 77842-3012, USA.

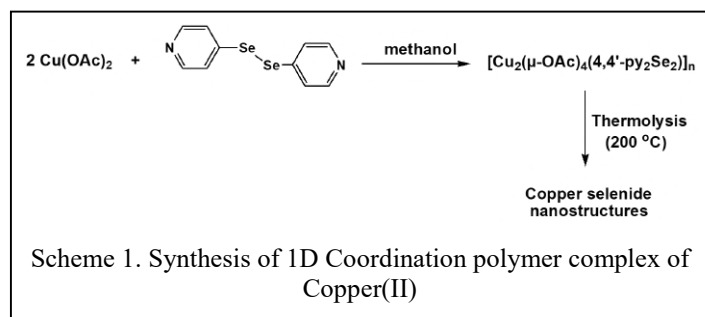
\* E-mail: dsandip@barc.gov.in

## Abstract

A new one dimensional copper(II) coordination polymer was constructed from  $\text{Cu}(\text{OAc})_2$  and 4,4'-dipyridyldiselenide ligand. The molecular structure of the complex elucidated from single crystal XRD revealed the formation of a one-dimensional zig-zag chain of the  $[\text{Cu}_2(\mu\text{-OAc})_4(4,4'\text{-py}_2\text{Se}_2)]$  repeating unit. Thermal studies of the polymeric complex have been carried out in a furnace or high boiling solvents to give copper selenide nanostructures. The synthesized copper selenide nanostructures have been thoroughly characterized by p-XRD, EDS and electron microscopy.

There is great interest in developing metal chalcogenide nanostructures owing to their significant and promising applications in the area of material science. Copper selenide nanostructures have attracted growing attention due to their potential application in sustainable solar cells and photo catalysis. The designing and synthesizing coordination polymer based single source precursors for metal chalcogenide nanostructures have always been a research hotspot for coordination chemists [1]. Here, we present a new 1D coordination polymer of Cu(II) derived from a 4,4'-dipyridyldiselenide  $[(4,4'\text{-py}_2\text{Se}_2)]$  ligand wherein the Cu(II) is coordinated to pyridyl nitrogen instead of the selenide group [2].

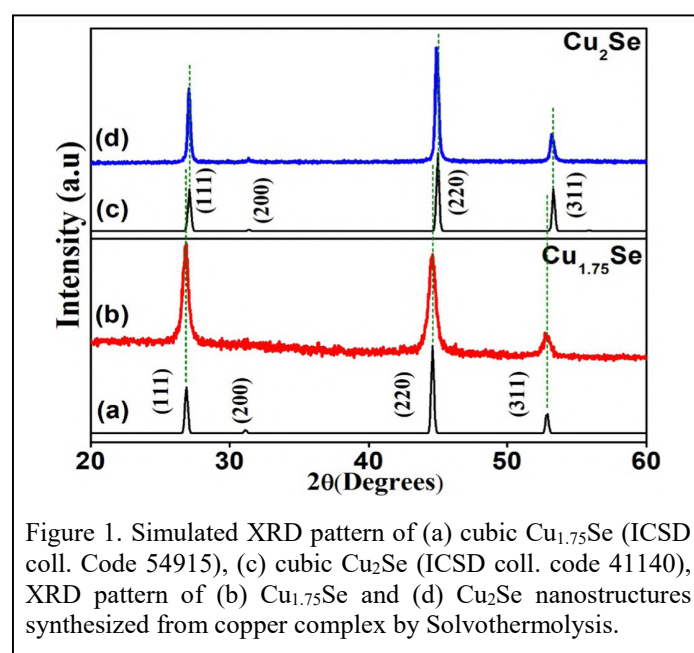
A solution of  $\text{Cu}(\text{OAc})_2$  in methanol (20 ml) was layered onto a solution of 4,4'-dipyridyl diselenide in the same solvent (10 ml). The solution was allowed to stand for one day to give insoluble green coloured crystals of the desired complex in good yield (Scheme 1).



The solid-state structure of the complex  $[\text{Cu}_2(\mu\text{-OAc})_4(4,4'\text{-py}_2\text{Se}_2)]_n$  shows zig-zag chain structure with copper atom in five coordination environment. The structure consists of a one-dimensional polymeric chain of the repeating unit  $[\text{Cu}_2(\mu\text{-OAc})_4(4,4'\text{-py}_2\text{Se}_2)]$  bonding via the Cu–N bond of the dipyridyldiselenide ligand. The copper atom acquires a square-pyramidal geometry with Cu–O bond lengths (~1.97 Å) and Cu–N bond length (2.17 Å) and Cu–Cu distances (2.62 Å).

To evaluate information about the thermal stability of the complex, thermogravimetric (TGA) analysis was carried out up to the temperature 700 °C under a flowing argon atmosphere. TG curve revealed that the complex remains thermally stable up to ~190 °C. Beyond this point, it undergoes two step decomposition up to ~320 °C and total weight loss observed in the TG curve was ~60.9%. In order to study the state of the residue, the complex was heated in a furnace at a rate of 10 °C min<sup>-1</sup> under flowing Ar up to 400 °C for 1 h. The powder X-ray diffraction pattern (p-XRD) of the black residue

obtained after solid state decomposition of the complex revealed the formation of cubic phase  $\text{Cu}_{1.8}\text{Se}$  material.



The solvothermolysis of the complex in different solvents have been carried out to prepare colloidal copper selenide nanostructures. The p-XRD pattern of the nanostructures synthesized from copper complex is presented in Fig. 1. The complex on thermolysis in octadecene at 200 °C gave cubic phase of  $\text{Cu}_{1.75}\text{Se}$  material which was confirmed by p-XRD (ICSD coll. Code 54915). Interestingly, the p-XRD pattern for materials obtained in oleylamine showed exactly a similar pattern to that of the material synthesized in octadecene but at a slightly higher  $2\theta$ , i.e., at 27.1, 45, 53.3 and 65.41. These peaks can be well indexed to the reflections emerging from the (111), (200), (220) and (311) planes of the cubic  $\text{Cu}_2\text{Se}$  material (ICSD coll. code 41140). The average crystallite size calculated using the Scherrer formula was found to be ~17 and ~36 nm for  $\text{Cu}_{1.75}\text{Se}$  and  $\text{Cu}_2\text{Se}$  synthesized in octadecene and oleylamine respectively.

## References

1. M. Y. Masoomi and A. Morsali, *Coord. Chem. Rev.*, 256 (2012) 2921.
2. M. K. Pal, G. Karmakar, A. Y. Shah, A. Tyagi, N. Bhuvanesh and S. Dey, *New J. Chem.*, 47 (2023) 16954.

## Methyl indium 4,6-dimethyl-2-pyrimidyl selenolate as molecular precursor for the synthesis of $\beta$ - $\text{In}_2\text{Se}_3$ and $\gamma$ - $\text{In}_2\text{Se}_3$ nanoparticles

Nisha Kushwah<sup>\*a</sup>, G. Kedarnath<sup>a,b</sup>, A. Wadawale<sup>a</sup>, Gourab Karmakar<sup>a</sup>, Sanjay Kumar<sup>c</sup> and Amit P. Srivastava<sup>c</sup>

<sup>a</sup>Chemistry Division, Bhabha Atomic Research Centre, Mumbai- 400 085 (India),

<sup>b</sup>Homi Bhabha National Institute, Anushaktinagar, Mumbai- 400 094 (India)

<sup>c</sup>Materials Science Division, Bhabha Atomic Research Centre, Mumbai- 400 085 (India).

Email: [knisha@barc.gov.in](mailto:knisha@barc.gov.in), 022-25591660

### **Abstract**

Air and moisture stable organoindium complex, methyl indium 4,6-dimethyl-2-pyrimidyl selenolate [ $\text{MeIn}\{\text{SeC}_4\text{H}(\text{Me-4,6})_2\text{N}_2\}_2$ ] was synthesized and characterized by elemental analyses and NMR ( $^1\text{H}$ ,  $^{13}\text{C}$ ,  $^{77}\text{Se}$ ) spectroscopy. The complex has been employed as molecular precursor for the synthesis of indium selenide nanostructures by thermolysis and the deposition of indium selenide ( $\beta$ - $\text{In}_2\text{Se}_3$  and monoclinic  $\text{InSe}$ ) thin films by aerosol assisted chemical vapor deposition (AACVD) on glass and silicon substrates at 400 and 450°C. Thermolysis in oleylamine (OAm)/1-octadecene (ODE) yielded hexagonal  $\beta$ - $\text{In}_2\text{Se}_3$  nanosheets and in OAm/oleic acid (OA) resulted  $\gamma$ - $\text{In}_2\text{Se}_3$  nanobullets.

## Air Processed Asymmetric Squaraine Dyes for Photovoltaic Application

Vilko Mandić <sup>a,\*</sup><sup>a</sup> University of Zagreb Faculty of Chemical Engineering and Technology, Trg Marka Marulića 19, 10000 Zagreb, Croatia  
\* [vmandic@fkit.unizg.hr](mailto:vmandic@fkit.unizg.hr), Tel: +385 1 4597 226, Fax: +385 1 4597 260**Abstract**

Recently, organic photovoltaics (OPV) have been heavily researched as alternatives to silicon and significant progress in terms of power conversion efficiency (PCE) and stability has been made. The comparative advantages of OPV are mainly their low cost, flexibility, transparency, and bending durability. To obtain good performance, the electron donor absorbers are used in a bulk heterojunction (BHJ) configuration (maximizing the specific surface of the interface) with fullerene-based electron donors. One of the most promising ways to boost the PCE of the OPV was found through the incorporation of non-fullerene and small molecule donors and acceptors, which exhibit high absorption spectra, resulting in high photocurrents, with PCEs above 18% in state-of-the-art solar cells, bringing them closer to the market. The most important factors affecting OPV performance are traps and recombination, charge carrier mobility, charge carrier density, and parasitic resistances. Therefore, a few essential steps in the design of the improved SC devices are: the determination of appropriate processing and molecule design. In this work, we follow a structure modification strategy. We developed new small molecule photoabsorbers that are based on squaraines (SQ). Even though squaraines have been previously applied as xerographic photoreceptors, an optical recording medium, electro-light-emitting diodes, and nonlinear optical devices on behalf of their unique electronic structures and optical properties, their application in a group of organic photovoltaic devices (OPV) and related devices is still scarce in the literature. SQs advantages, when considering applications as donor materials in OPVs, are high absorption coefficients, where bandwidths can be adjusted in the visible and NIR range, as well as high photochemical and thermal stability. The seemingly straightforward synthetic pathways are also a nominal advantage. Namely, a variety of SQs can be prepared through the modification of the SQ structure. Replacement of the side groups allows for some adjusting of the physicochemical behaviour and optoelectrical properties, as well as the morphological and organizational properties of the SQs when processed into thin films, which can be used as a valuable tool to optimize the photovoltaic properties of squaraine based bulk heterojunction absorber layers. We assembled the solar cells on a laboratory scale and characterized them thoroughly (J/V, EQE, LID testing). Recombination mechanisms pointed out to differences in nanomorphology, which were later identified via structural methods (WAXS) and microscopy (FIB-SEM, AFM). The results gave new insight into the influence of processing parameters and molecule design on device performance and stability.

**Aim and Approach**

The aim of the research is to explore air stable complex squaraine structures for photovoltaic application while retaining their ease of synthesis following the principles of green chemistry. We try to understand the structure-property relationship by utilizing an extensive set of characterization techniques. Through morphology and structure analysis, we hope to better understand the processes that govern charge carrier transfer whose behaviour is obtained through electrical measurements.

**Scientific Innovation and Relevance**

Innovation in our work is best recognized when considering the easy synthesis and air stable conditions in which these solar cells can function application wise. However, during this research, a plethora of information has been collected which helps further understand energy losses in all organic photovoltaic systems.

**Results**

The potential of the synthesized squaraines for photovoltaic application was tested through the most important property, UV-Vis absorption and bandgap.

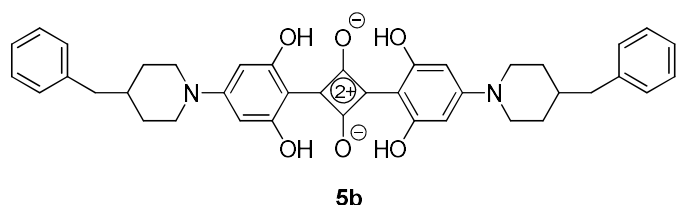


**Figure 1.** An example of the molecular structure of designed compounds.

The bandgap was estimated to be around 1.6 – 1.7 eV for all synthesized compounds (from the onset). The assembled devices are shown on Figure 3.

Where the device architecture can be observed: ITO(cathode)/ZnO (30 nm, electron transport layer)/BHJ (active layer, SQ:PC<sub>70</sub>BM)/MoO<sub>3</sub> (8 nm, hole transport layer)/Ag (100 nm, anode, current collector).

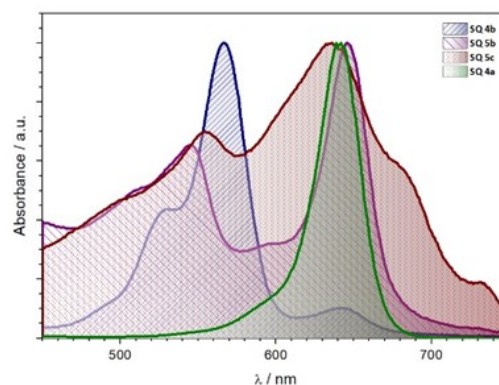


**Figure 2.** UV-Vis absorption spectra of the compounds in ethanol.

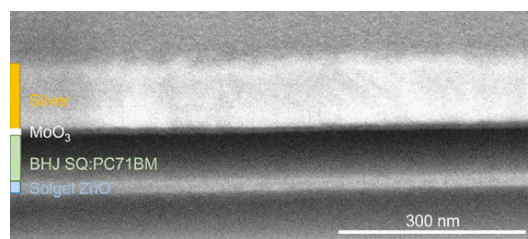


**Figure 3.** Cross-section of the assembled thin film device.

**Conclusion**

Research results point out to good photovoltaic properties of the synthesized squaraines as well as a good interface during solar cell assembly, which implies that these compounds have good potential to be studied further.

**Acknowledgement**

This work has been funded by the project UIP-2019-04-2367 SLIPPERY SLOPE by CSF.

## Water-Soluble Pd Metallacycles catalyst as a reservoir for Pd Nanoparticle in Suzuki Coupling Reaction

K. R. Chaudhari, A. P. Wadawale and S. Dey\*

Chemistry Division, Bhabha Atomic Research Centre, Mumbai-400085, India

\*E-mail: dsandip@barc.gov.in; Telephone: +91 22 25592589

### Abstract

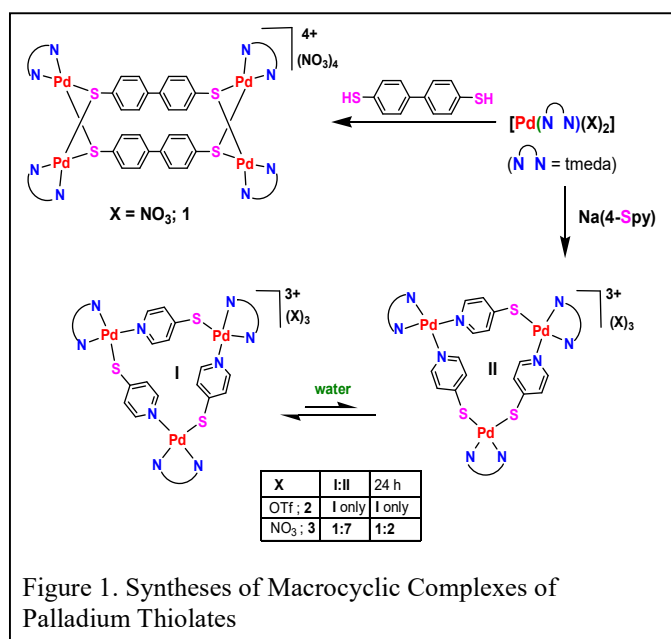
The water-soluble stable Pd metallacycles  $[Pd(tmeda)(4-Spy)]_3(X)_3$  (*tmeda* = tetramethylethylenediamine,  $X = OTf$ , 2;  $NO_3$ , 3) have been constructed from ambidentate ligand 4-pyridylthiolate. They show catalytic activity with high turnover numbers in aqueous Suzuki cross-coupling reactions using phenyl boronic acid and a number of aryl halides. The black residue obtained after catalytic reaction has been characterized by PXRD, SEM and EDAX spectroscopy.

### Introduction

The development of a water-soluble and stable Pd complex of less toxic ligand as recyclable catalyst has received increasing attention from industry and academia from the green chemistry and economic viewpoints. The manufacturing of fine chemicals and pharmaceuticals using cross-coupling reactions in water can greatly contribute to the field of sustainable organic synthesis.

### Experimental Detail

Starting material  $[Pd(tmeda)(X)_2]$  ( $X = NO_3, OTf$ ) was reacted with freshly synthesized Na(4-Spy) to produce a yellow coloured solid, when recrystallized from acetone, yielded yellow crystals of  $[Pd(tmeda)(4-Spy)]_n(OTf)_n$  (2) and  $[Pd(tmeda)(4-Spy)]_n(NO_3)_n$  (3) in good yield.



### Result and Discussion

The integration in  $^1H$  NMR spectrum of 2 in  $D_2O$  shows that *tmeda* and pyridyl groups are in 1:1 ratio, suggesting the formula of  $[Pd(tmeda)(4-Spy)]_n(OTf)_n$ . The  $^1H$  NMR spectrum of 2 shows two sharp doublets at  $\delta$  8.20 and 7.58 ppm for the  $\alpha$  and  $\beta$  protons of py group, one singlet for ethylene group and two singlets of methyl groups (Figures 2). The  $^1H$  NMR spectrum of 3 displays six distinct doublets in the range of 7.42-8.32 ppm, assignable to three sets for  $\alpha$  and  $\beta$  protons of the pyridyl groups signifying the presence of three unlike pyridylthiolate ligands different from 2 (Figures 2). In addition to the above six prominent doublets, one doublet at  $\delta$  7.55 ppm

and another peak merged in the base of the peak at  $\delta$  8.17 ppm have been identified. These resonances have been attributed to the more symmetric structure I of 3 as observed exclusively in case of 2. Crystal structure of 2 & 3 were unambiguously determined by X-ray crystallography. ORTEP drawings with atomic numbering schemes are shown in Figures 3 & 4. The cationic part of 2 and 3 are triangular shaped molecules  $[Pd(tmeda)(4-Spy)]_3^{3+}$  containing three *tmeda*-capped Pd centers as corners, which are bridged by 4-pyridylthiolate ligand.

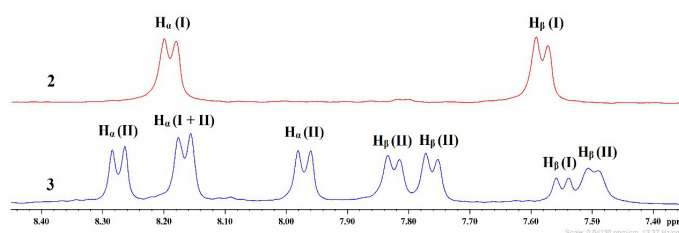


Figure 2. Pyridyl region of  $^1H$  NMR (300 MHz,  $D_2O$ ) spectra of 2 (above) and 3 (below).

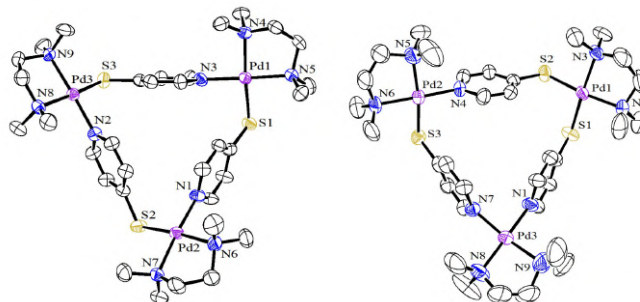


Figure 3. ORTEP diagram of  $[Pd(tmeda)(Spy)]_3(OTf)_3$ ;  $[Pd(tmeda)(Spy)]_3(NO_3)_3$  (3) ellipsoids drawn at 50% probability. Hydrogen atoms and nitrate ions are omitted for clarity.

The coupling reactions of phenylboronic acid with various aryl bromides were investigated using 0.3 mol % of Pd of the catalyst 3 under the above optimized reaction conditions. The arylbromides containing electron withdrawing groups such as cyano, fluoro, aldehyde, nitro and acetyl groups gave the coupling products in excellent to quantitative yields of 83-92%. The reaction of deactivated substrates 4-bromotoluene



and 4-bromoanisole afforded 79 and 81% yield of the desired products, respectively. The hetero-aryl bromide, 2-bromopyridine successfully showed also moderate yield (56%) of the corresponding coupling product. Furthermore, the coupling reactions with the difficult coupling partner aryl chlorides containing electron-withdrawing group resulted moderate yield of 55%, in the presence of TBAB (tetrabutylammonium bromide) as a promoter. The thermal stability of **3** was evaluated by thermogravimetric (TG) analyses. The TG curves of **3** display the two step decomposition starting after 194 °C (Figure 4) which indicates the solid compounds are stable enough for catalysis reactions. The Pd complexes show excellent catalytic activity with high turnover number in Suzuki coupling reaction. The powder X-ray diffraction pattern (PXRD) of the black residue obtained after zero and third cycle showed the broad peaks at  $2\theta \sim 39.9^\circ$ ,  $46.2^\circ$  and  $67.6^\circ$  (Figure 5). These reflection peaks may be attributed to the formation of palladium nanoparticles (PdNPs), (JCPDS File no. 46-1043, 1993). The average size of the particles was calculated as 4 nm from Debye-Scherrer formula considering the broadening of the highest peak. The reusability of the Pd catalyst in the coupling reaction of 4-bromoacetophenone and phenylboronic acid for eight consecutive cycles.

Cycle	0	1	2	3	4	5	6	7	8
% yield	92	91	89	87	85	82	80	77	75

### Conclusion

Water-soluble Pd metallacycles from the 4-pyridylthiolate ligand without attaching any hydrophilic group have been synthesized. These Pd complexes show excellent catalytic activity with high turnover numbers ( $7 \times 10^6$ ) in aqueous Suzuki coupling reactions and can be reused at least eight times without loss of significant activity.

The catalytic activity has been attributed to the formation of heterogeneous PdNPs. We believe such combinations of ligands can generate potential water-soluble functional materials that can contribute to the field of green and sustainable chemistry.

### References

- [1.] K. P. Chaudhari, A. P. Wadawale, A.K. Pathak and S. Dey, *Inorg. Chem.*, 63 (2024) 1427 - 1438.
- [2.] K. V. Vivekananda, S. Dey, D. K. Maity, N. Bhuvanesh, V. K. Jain, *Inorg. Chem.*, 54 (2015) 10153 – 10162.

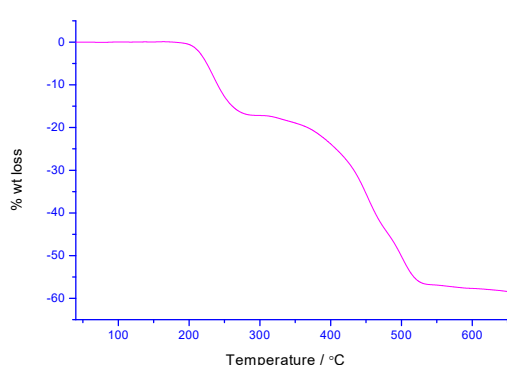


Figure 4. TG curve of  $[\text{Pd}(\text{temda})(\text{Spy})]_3(\text{NO}_3)_3$  (**3**).

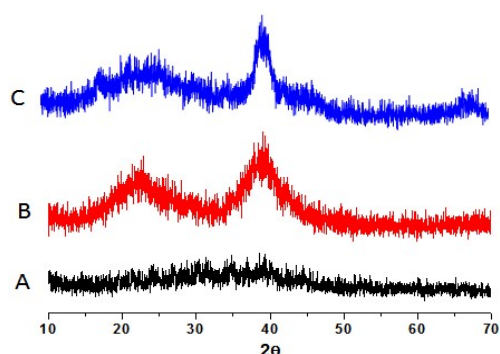


Figure 5. PXRD of (A) Complex **3** (B) After 0 cycle (C) After 3 cycle of catalysis reaction.

We have examined the reusability of the Pd catalyst **3** in the coupling reaction of 4-bromoacetophenone and phenylboronic acid for eight consecutive cycles. After the completion of zero cycle, hexane was added to extract the organic part containing the product, then fresh reactants in required quantities were added to the remaining aqueous layer containing the catalyst, for the next round of reaction. The yields maintained very high from 92 to 75%, even after eight successive cycles, which suggests the catalyst is still very active.

## Development of Biocompatible Ag<sub>2</sub>S Quantum Dots for Receptor-mediated Photothermal Therapy

Sonali Gupta <sup>a,b</sup>, Mansi Murkar <sup>c</sup>, Bijaideep Dutta <sup>a,b</sup>, S. B. Shelar <sup>a</sup>, K. C. Barick <sup>a,b,\*</sup>  
<sup>a</sup>Chemistry Division, Bhabha Atomic Research Centre, Trombay, Mumbai-400085, India  
<sup>b</sup>Homi Bhabha National Institute, Anushaktinagar, Mumbai-400094, India  
<sup>c</sup>K. J. Somaiya College of Science and Commerce, Vidyanagar, Vidyavihar (E)  
 \*Email: kcbarick@barc.gov.in, Tel.: + 91 22-6929 0284

### Abstract

Photothermal therapy (PTT) is a new treatment modality that has been gaining significant attention for cancer therapy due to its low invasiveness and ability to provide localized treatment. However, the development of multifunctional photothermal agents (PTAs) is essential for improving their biocompatibility and photothermal efficiency. In this aspect, we have developed water dispersible cysteine functionalized Ag<sub>2</sub>S quantum dots (Cy-Ag<sub>2</sub>S QDs). These QDs exhibited good photothermal heating efficacy under near infrared (NIR) light (808 nm). Furthermore, folic acid conjugated Cy-Ag<sub>2</sub>S QDs (FA@Cy-Ag<sub>2</sub>S QDs) exhibited enhanced toxicity toward folate receptor overexpressed cancer cells (KB cells).

### Introduction

Over the years, photothermal therapy (PTT) has gained much attention in the field of cancer therapy. Photothermal agents (PTA), upon exposure to NIR light, generate localized hyperthermia, leading to protein denaturation or cell membrane disruption, ultimately causing cancer cell death [1]. PTT has gained prominence due to its high specificity, minimal side effects, potent anti-cancer efficacy, and non-invasive nature [2]. These advantages have sparked significant interest in development of various PTAs. However, the development of efficient PTAs for PTT remains a major challenge.

Various nanoparticles-based PTAs, such as Ag NPs, Au NPs, carbon-based NPs, Cu-Based NPs, and others, have been reported for antibacterial treatment [2]. However, the development of PTA with low biotoxicity, good colloidal stability and efficient thermal conversion still possess a challenge. Among others, Ag<sub>2</sub>S QDs have shown promising results in PTT due to their low bio-toxicity, low solubility product and strong absorption in the NIR region [3]. Various reports have demonstrated the use of organic solvent and high-temperature synthetic route for development of Ag<sub>2</sub>S QDs [4]. Furthermore, the obtained QDs often require modification to enhance their water dispersibility for application in biomedical field. In recent years, several water-dispersible Ag<sub>2</sub>S QDs have been synthesized at higher temperature [5]. However, the low-temperature synthesis and development of tumor-specific nano formulation for targeted therapy remain significant challenges.

Herein, we report synthesis of the aqueous stabilized cysteine functionalized Ag<sub>2</sub>S (Cy-Ag<sub>2</sub>S) QDs using cysteine as surface passivating agent. The synthesized Cy-Ag<sub>2</sub>S QDs have shown good water-dispersibility, strong NIR absorption and good photothermal heating ability under 808 nm laser irradiation. Further, folic acid (FA) was introduced onto the surface of these Cy-Ag<sub>2</sub>S QDs (FA@Cy-Ag<sub>2</sub>S QDs) for receptor mediated targeting of cancer cells. The successful conjugation of FA has been confirmed by UV visible absorbance and FTIR spectra. These FA@Cy-Ag<sub>2</sub>S QDs have shown enhanced toxicity towards folate receptor enriched cancer (KB) cells than folate negative (A549) cancer cells.

### Experimental

Cy-Ag<sub>2</sub>S QDs were prepared by simple soft-chemical approach. Briefly, AgNO<sub>3</sub> (0.25 mmol) and L-cysteine (0.6 mmol) was dissolved in 75 ml Milli Q water by stirring for 20 minutes at 30°C under argon condition. Further NaOH (1M) was added dropwise to maintain pH 10 and stirring was continued for another 10 minutes. In a beaker, Na<sub>2</sub>S (0.125 mmol) was

dissolved in 25 ml Milli Q water under argon condition. This solution was added to the reaction mixture and the reaction was kept for 2 h with continuous stirring at 30°C to prepared Cy-Ag<sub>2</sub>S QDs. The obtained brownish black solution was dialyzed for 24 h against Milli Q water for removal of unreacted species. Further, folic acid was conjugated to the developed Cy-Ag<sub>2</sub>S QDs through EDC-NHS coupling.

The structural/ microstructural analysis of Cy-Ag<sub>2</sub>S QDs was investigated using various characterization techniques such as XRD, TEM, FTIR, DLS and zeta-potential measurements. Photothermal studies were performed using irradiation of NIR light (808 nm) on 1 ml aqueous suspension of Cy-Ag<sub>2</sub>S QDs (Ag concentration: 50-200 µg/ml) at different power density (0.69-0.95 W). The change in temperature of dispersion medium was measured using an optical fiber-based temperature sensor (accuracy = ± 0.1°C) at every 10 s. Further, the conjugation of FA has been confirmed by UV visible absorption and FTIR spectra. The *in-vitro* cytotoxicity of Cy-Ag<sub>2</sub>S QDs were evaluated in normal (WI26VA4) as well as cancerous cell lines (A549, MCF-7 and KB cells) by MTT assay. The cell lines were seeded in 96 well plate (1 × 10<sup>4</sup> cells per well) in complete culture medium at 37°C and 5% CO<sub>2</sub> for 24 h. After 24 h, culture medium was replaced by fresh media containing different concentrations Cy-Ag<sub>2</sub>S QDs and incubated for 24 h at 37°C and 5% CO<sub>2</sub>. The relative cell viabilities were determined by MTT assay as reported earlier [5]. Each experiment was accomplished in triplicates and the standard deviation was specified in the plot.

### Result and discussion

Cysteine was chosen as a surface passivating agent for development of water-dispersible Ag<sub>2</sub>S QDs due to its good biocompatibility and availability of multiple functional moieties such as amine, carboxyl and thiol on its backbone. The appearance of characteristic diffraction peaks corresponding to (111), (-112), (120), (-121), (022) and (121) lattice planes of Ag<sub>2</sub>S (JCPDS card no.: 14-0072) suggested the formation of single-phase monoclinic Ag<sub>2</sub>S phase (Fig. 1a). In addition, several peaks are broadened due to the smaller size of QDs. TEM micrograph revealed the formation of roughly spherical shaped Ag<sub>2</sub>S QDs with an average size of 5 nm (Fig. 1b). The surface modification of the Ag<sub>2</sub>S QDs were confirmed by FTIR spectroscopy where we have compared the characteristic IR peaks of pure cysteine with that of the Cy-Ag<sub>2</sub>S QDs (Fig. 1c). The characteristic S-H vibration of cysteine at 2562 cm<sup>-1</sup> has disappeared in the Cy-Ag<sub>2</sub>S QDs suggesting the binding of cysteine molecules onto the surface of Ag<sub>2</sub>S via thiol groups. In addition, the presence of vibration bands corresponding to the

characteristic  $\text{-C=O}$  vibration at  $1635\text{ cm}^{-1}$  and  $\text{-CH}_2$  vibration at  $1390\text{ cm}^{-1}$  of pure cysteine on Cy- $\text{Ag}_2\text{S}$  QDs further confirmed their successful surface modification by cysteine molecule.

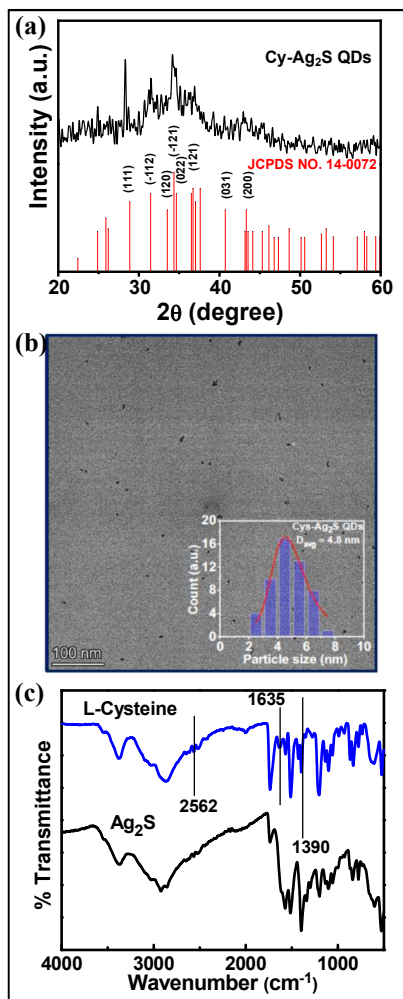


Fig. 1. (a) XRD pattern, (b) TEM micrograph (inset: particle size distribution plot) and (c) FTIR spectra of cysteine and Cy- $\text{Ag}_2\text{S}$  QDs.

In order to assess the colloidal stability of the prepared QDs and determination of their surface charge, zeta potential analysis of Cy- $\text{Ag}_2\text{S}$  QDs have been performed. The pH dependent zeta potential of Cys- $\text{Ag}_2\text{S}$  have shown a steady variation of surface charge from  $5.9\text{ mV}$  to  $-40.3\text{ mV}$ . This pH dependent charge reversal of developed QDs is mainly due to the ionizable carboxyl and amine groups present on their surface. To determine the dynamic behavior of the particle DLS measurement was recorded. The hydrodynamic diameter ( $H_D$ ) of particle was found to be  $116\text{ nm}$ . The observed higher average size by DLS over TEM is possibly due to the presence of hydrated organic coating on the surface of  $\text{Ag}_2\text{S}$  QDs. The highly negative zeta potential at  $-16.6\text{ mV}$  at physiological insignificant change in  $H_D$  even after 72 h makes them colloidal stable and ideal for therapeutic application.

Fig. 2a displays the time dependent temperature elevation study of an aqueous solution of Cys- $\text{Ag}_2\text{S}$  QDs as a function of NIR laser power (continuous wavelength laser,  $808\text{ nm}$ ,  $0.95$ ,  $0.817$  and  $0.685\text{ W/cm}^2$ ). The time required to reach  $43\text{ }^\circ\text{C}$  in  $0.9$ ,  $0.817$  and  $0.68$  watt are  $340$ ,  $564$  and  $890$  seconds respectively for Cys- $\text{Ag}_2\text{S}$  QDs dispersion containing  $0.2\text{ mg/ml}$  of Ag showing the power dependent heating of the QDs whereas the water is only heated up to  $35.1\text{ }^\circ\text{C}$  even after 600 seconds. The concentration dependent heating profile was also investigated in three different concentrations  $200$ ,  $150$  and  $100\text{ }\mu\text{g/ml}$  at a particular laser power density of  $0.95\text{ W/cm}^2$ . In this

case the time required to reach  $43\text{ }^\circ\text{C}$  in  $200$  and  $150\text{ }\mu\text{g/ml}$  are  $340$  and  $442$  seconds respectively. However, in case of  $100\text{ }\mu\text{g/ml}$  even after 1200 seconds the temperature did not raise beyond  $40\text{ }^\circ\text{C}$ .

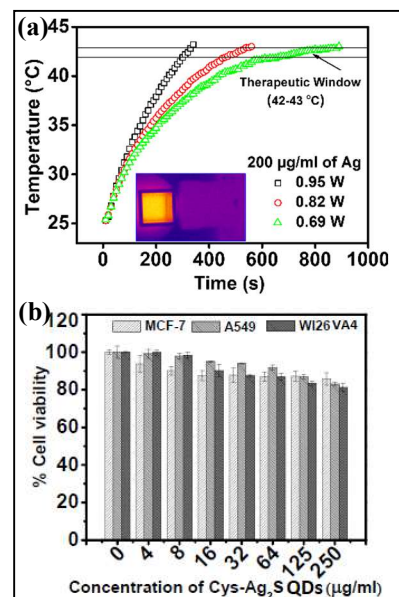


Fig. 2. (a) Power dependent photothermal heating of 1ml of aqueous suspension of Cy- $\text{Ag}_2\text{S}$  QDs containing  $200\text{ }\mu\text{g/ml}$  of Ag by irradiating  $808\text{ nm}$  NIR laser and (b) biocompatibility study via MTT assay by incubating different conc. of synthesized Cys- $\text{Ag}_2\text{S}$  QDs for 24h under culture condition at  $37\text{ }^\circ\text{C}$ .

The photothermal stability and reusability of the QDs was observed up to five cycle (heating-cooling curve) which has shown extreme stability along with pertinent heating efficacy. In order to explore the application of the synthesized Cys- $\text{Ag}_2\text{S}$  QDs in photothermal cell killing module, the biocompatibility needs to be checked and for that purpose we have done the MTT measurements with three different cell lines for 24 h (Fig. 2b). The experimental investigation showed that the Cys- $\text{Ag}_2\text{S}$  QDs are almost 90% viable at  $250\text{ }\mu\text{g/ml}$  concentration in lung normal (WI26VA4) cell line. In case of the cancer cell line (A549 and MCF-7) they are found to be nontoxic with the range of 90 % viability in the same concentration range. Thus, it can be asserted that the particles are highly biocompatible for their application as the photothermal heating source for photothermal therapy assisted cancer cell killing.

Further, it has been observed that the developed FA@Cy- $\text{Ag}_2\text{S}$  QDs retained aqueous colloidal stability and exhibited good photothermal heating efficacy under NIR light. Moreover, the *in-vitro* photothermal study using FA@ Cy- $\text{Ag}_2\text{S}$  QDs revealed higher toxicity towards KB cell line (overexpressed folate receptor) than to folate negative A549 cell line. Specifically, the present study demonstrated the development of biocompatible, aqueous stabilized Cy- $\text{Ag}_2\text{S}$  QDs and investigation of their potential applications in photothermal therapy.

## References

1. L. Cheng, C. Wang, L. Feng, K. Yang and Z. Liu, Chem Rev. 114 (2014) 10869.
2. X. Liu, Q. Ren, F. Fu, R. Zou, Q. Wang, G. Xin, Z. Xiao, X. Huang, Q. Liu and J. Hu, Dalton Trans. 44, (2015) 10343.
3. X. Zhang, Z. Liu, W. Shen, S. Gurunathan, Int. J. Mol. Sci. 17 (2016) 1534.
4. L. M. Nieves, K. Mossburg, J. C. Hsu, A. D. A. Maidment, D. P. Cormode, Nanoscale 13 (2021) 19306.
5. Q. Ren, Y. Ma, S. Zhang, L. Ga, J. Ai, ACS Omega 6 (2021) 636.

## Thermal Studies of highly monodispersed $\gamma$ -Fe<sub>2</sub>O<sub>3</sub>, ZnO, $\gamma$ -Fe<sub>2-2x</sub>Zn<sub>2x</sub>O<sub>3</sub> and $\gamma$ -Fe<sub>2</sub>O<sub>3</sub>@ZnO nanostructures

Ruchi Agrawal<sup>a,b</sup>, Ratikant Mishra<sup>a,b</sup> and Raghmani Singh Ningthoujam<sup>a,b\*</sup>

<sup>a</sup>Chemistry Division, Bhabha Atomic Research Centre, Mumbai 400085, India

<sup>b</sup>Homi Bhabha National Institute, Anushaktinagar, Mumbai 400094, India

\* rsn@barc.gov.in, Phone: +91-22-25592321

### Abstract

The thermal behavior of  $\gamma$ -Fe<sub>2</sub>O<sub>3</sub>, ZnO,  $\gamma$ -Fe<sub>2-2x</sub>Zn<sub>2x</sub>O<sub>3</sub> and  $\gamma$ -Fe<sub>2</sub>O<sub>3</sub>@ZnO nanostructures are discussed in this paper. All the nanoparticles were characterized by XRD, TEM and FT-IR studies. Due to the presence of capping ligands, it is difficult to determine the exact amount of the materials with respect to oleic acid. Also, it is difficult to identify the specific properties per mass of the materials prepared by thermolysis method. To solve this problem, the thermal behavior of all these nanoparticles is discussed. Depending upon the oleic acid content in the nanoparticles, the mass loss of capping agents per mass sample is different.

### 1. Introduction:

Thermolysis is a method for preparation of highly crystalline and monodispersed inorganic nanoparticles with desired shape and size in the presence of high boiling point solvents and capping ligands. Here, metal precursors get converted to metal oxide or fluoride or sulphides by the decomposition of precursors at high temperature  $\sim 300$  °C [1]. The substitution, core@shell and epitaxial growth of materials can be performed. The organic solvents having high boiling point like 1-octadecene (b.p. 315°C) have been used. Also, different capping ligands having high boiling points such as oleic acid (b.p. 360°C), oleyl amine (b.p. 364°C), linolenic acid (b.p. 443.4 °C), TOPO (b.p. 408.8°C), etc. have been used. All these capping ligands are the long chain fatty acids or surfactants. Due to which, the prepared nanoparticles are hydrophobic in nature. A lot of luminescent and magnetic nanoparticles can be prepared from the thermolysis method on heating at 300°C and were already reported in literature [1-3].

Also, due to the presence of organic capping ligands, it is difficult to determine the exact amount of materials with respect to oleic acid. Magnitude of property of any material depends on amount of samples. So, it is important to study the thermal behavior of such materials. That is why, in this paper, the thermal behavior of  $\gamma$ -Fe<sub>2</sub>O<sub>3</sub>, ZnO,  $\gamma$ -Fe<sub>2-2x</sub>Zn<sub>2x</sub>O<sub>3</sub> (Substitution, SUB in the form of spinel structure) and  $\gamma$ -Fe<sub>2</sub>O<sub>3</sub>@ZnO (core@shell, CS) nanoparticles are studied.

### 2. Experimental Details:

Highly monodispersed  $\gamma$ -Fe<sub>2</sub>O<sub>3</sub>, ZnO,  $\gamma$ -Fe<sub>2-2x</sub>Zn<sub>2x</sub>O<sub>3</sub> (Substitution, SUB) and  $\gamma$ -Fe<sub>2</sub>O<sub>3</sub>@ZnO (core@shell, CS) nanostructures are synthesized by thermolysis method [4].

### 3. Characterizations:

All the nanoparticles were characterized by XRD, TEM and FT-IR studies in our previous work [4]. Thermal analysis of as-prepared samples was performed using a thermogravimetric-differential thermal analysis (TG DTA) instrument (SETARAM 92-16.18). The sample under examination was heated at a rate of 5 °C/ min under N<sub>2</sub> atmosphere.

### 4. Results and Discussion:

From the thermo-gravimetric analysis (TGA) of all these nanostructures (Figure 1), it was found that ZnO decomposes completely ( $\sim 90$  %) at 400-450°C due to the presence of excess amount of oleic acid. At this temperature range, the  $\gamma$ -Fe<sub>2</sub>O<sub>3</sub>@ZnO (CS) decomposes slowly upto  $\sim 40$ %;  $\gamma$ -Fe<sub>2</sub>O<sub>3</sub> shows decomposition upto  $\sim 40$ % and  $\gamma$ -Fe<sub>2-2x</sub>Zn<sub>2x</sub>O<sub>3</sub> (SUB)

decomposes upto 30%. These results suggest that ZnO sample has the highest content of oleate. SUB material shows the continue loss of mass with temperature.

### 5. Conclusions:

Depending upon the oleic acid content in the nanoparticles, their mass losses are different. The ZnO nanoparticles have 90% oleic acid content. Then, each sample of  $\gamma$ -Fe<sub>2</sub>O<sub>3</sub> and  $\gamma$ -Fe<sub>2</sub>O<sub>3</sub>@ZnO (CS) has 40% oleic acid content while  $\gamma$ -Fe<sub>2-2x</sub>Zn<sub>2x</sub>O<sub>3</sub> (SUB) has 30% oleic acid content up to 600 °C.

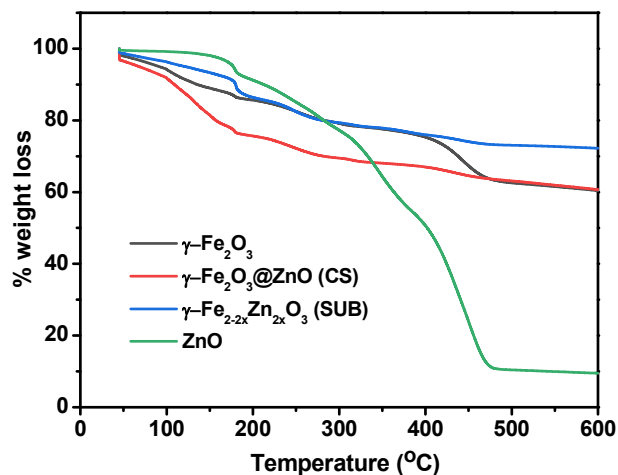


Figure 1. TGA curves of  $\gamma$ -Fe<sub>2</sub>O<sub>3</sub>, ZnO,  $\gamma$ -Fe<sub>2-2x</sub>Zn<sub>2x</sub>O<sub>3</sub> (SUB) and  $\gamma$ -Fe<sub>2</sub>O<sub>3</sub>@ZnO (CS).

### 6. References:

1. Fereshteh, Z; Niasari, M.S., *Advances in Colloid and Interface Science*, 243, 2017, 86-104.
2. Li, Z.; Ding, X.; Cong, H.; Wang, S.; Yu, B.; Shen, Y., *Journal of Luminescence*, 228, 2020, 117627.
3. Joshi, R.; Singh, B. P.; Prajapat, C. L.; Kashyap, Y.; Nayak, C.; Bhattacharyya, D.; Ningthoujam, R. S., *J. Phys. Chem. C*, 17971- 17982
4. Agrawal, R. and Ningthoujam, R. S. (unpublished work).

**Acknowledgement:** Authors thank Dr. Niharendu Choudhury, Head, Chemistry Division, BARC for his support.

# Metal-Organic-Framework Based Aerogel: A Novel Thermally Stable Adsorbent for the Efficient Removal of Heavy Metal Ions from Aqueous Solution

Hiral Ukani<sup>a</sup>, Nildhara Parsana<sup>a</sup>, Naved Malek<sup>a,b\*</sup>

<sup>a</sup>*Ionic Liquids Research Laboratory, Department of Chemistry, Sardar Vallabhbhai National Institute of Technology, Surat-395007, Gujarat, India*

Corresponding Author: [navedmalek@chem.svnit.ac.in](mailto:navedmalek@chem.svnit.ac.in)

## Abstract

We present a novel MOF/biopolymer composite aerogel based on ZIF-8 and iota-carrageenan (iCG) for the removal of heavy metal ions from contaminated water. The ZIF-8@iCG aerogel exhibits excellent thermal stability, mechanical strength, and flame retardancy. Adsorption thermodynamics follow the Langmuir isotherm model, confirming the endothermic nature of the process. This cost-effective, eco-friendly material efficiently removes Pb<sup>2+</sup>, Cd<sup>2+</sup>, and Cr<sup>6+</sup> ions. Ion leaching tests confirm negligible zinc release, making it ideal for water purification and industrial applications.

## Introduction:

Industrialization has led to significant wastewater pollution, containing heavy metal ions that pose serious risks to human health and aquatic ecosystems. Traditional methods like sorbents and separation membranes are often costly, inefficient, and produce secondary pollutants such as chemical sludge. Heavy metal ions, once introduced into the environment, accumulate in organisms and drinking water, leading to long-term health issues such as organ damage and cancer. Thus, there is a pressing need for more efficient, affordable, and sustainable water purification methods.

Metal-organic frameworks (MOFs), particularly ZIF-8, have emerged as promising materials due to their large surface area, thermal stability, and high adsorption efficiency for heavy metal ions. However, the powder form of ZIF-8 poses challenges in recovery and can cause secondary contamination. To address these issues, we developed a ZIF-8/iota-carrageenan aerogel. This composite offers enhanced mechanical strength, is easily recoverable, and provides efficient removal of heavy metal ions from water. The aerogel is cost-effective, recyclable, and demonstrates excellent adsorption performance with minimal leaching.

## Methods

### Preparation of ZIF-8

ZIF-8 was synthesized by dissolving 0.6672 g of Zn(NO<sub>3</sub>)<sub>2</sub>·6H<sub>2</sub>O and 12.89 g of 2-methylimidazole (2-MeIm) in 8 mL and 42 mL of deionized water, respectively. After stirring for 5 hours at 30°C, the turbid solution was centrifuged and washed with deionized water and methanol. The final product was dried in a convection oven at 80°C for 12 hours.

### Preparation of ZIF-8@iCG

ZIF-8 powder (100 mg) was mixed in 25 mL of ultrapure water with ultrasound. Iota-carrageenan (100 mg) was added, and the solution was stirred at 60-65°C. ZIF-8@iCG hydrogel was formed upon cooling, and the aerogel was obtained via freeze-drying for 24 hours.

## Characterization

### Morphology & Structure Analysis

The microstructure was analyzed via SEM and EDX. FTIR was used to confirm functional groups, and XRD analyzed crystal structures. Mechanical properties were assessed by rheometer and a universal testing machine.

### Stability

Thermal stability was examined using thermogravimetric

analysis (TGA), and pH stability was evaluated by weight loss in buffer solutions over 10 days.

## Pollutant Adsorption

The aerogel's adsorption capacity for Pb<sup>2+</sup>, Cd<sup>2+</sup>, Cr<sup>6+</sup>, and CV was assessed using UV-vis spectroscopy. The adsorption capacity (q<sub>e</sub>) and removal efficiency (%) were calculated using:

- $q_e = (C_0 - C_e) \times v / m$
- Removal efficiency =  $(C_0 - C_e) / C_0 \times 100$

Where C<sub>0</sub> and C<sub>e</sub> represent initial and equilibrium concentrations, v is the solution volume, and m is the mass of aerogel.

Enough scientific information about the work should be 3.

## Results and Discussions

ZIF-8, a well-known metal-organic framework (MOF), consists of Zn<sup>2+</sup> ions coordinated by 2-methylimidazole and is recognized for its non-toxic character and high adsorption capacity. However, its water insolubility and difficulty in separating from solution after contaminant removal limit its application in wastewater treatment. To address this, the current study combines ZIF-8 with the biopolymer iota-carrageenan (iCG), forming a ZIF-8@iCG composite aerogel through a freeze-drying method. iCG, a low-cost, biodegradable, and biocompatible material, enhances ZIF-8's mechanical strength and adsorption capacity while facilitating easier recovery. The resulting ZIF-8@iCG aerogel demonstrates the combined properties of its constituents, showing excellent structural flexibility, adsorption properties, and stability. Characterization techniques such as X-ray diffraction (XRD), scanning electron microscopy (SEM), energy dispersive X-ray (EDX), and Fourier-transform infrared (FTIR) spectroscopy confirmed the successful integration of ZIF-8 and iCG, retaining ZIF-8's crystalline structure and porosity. Mechanical tests revealed strong flexibility and load-bearing capacity, with the aerogel showing excellent recovery after compression. Stability studies demonstrated that the ZIF-8@iCG aerogel remained relatively stable under alkaline conditions, although degradation increased in neutral and acidic environments. This novel aerogel is highly promising for selective removal of heavy metal ions and positively charged toxic dyes from wastewater, offering improved mechanical properties, recoverability, and environmental compatibility compared to ZIF-8 alone.

Thermo-gravimetric analysis (TGA) was used to assess the thermal stability of the ZIF-8@iCG aerogel. The TGA curves showed that ZIF-8@iCG exhibited greater thermal stability compared to iCG alone. While iCG began decomposing

rapidly between 35 °C and 100 °C, ZIF-8@iCG maintained its stability up to 192 °C, with slower degradation occurring between 192 °C and 300 °C, attributed to the protective effect of ZIF-8. The decomposition of the composite occurred at higher temperatures (400–600 °C), confirming the improved stability provided by ZIF-8. This increased thermal stability enhances the longevity of iCG in practical applications. Additionally, flame retardancy tests demonstrated that ZIF-8@iCG could quickly self-extinguish upon exposure to flame, with most of the aerogel remaining intact, highlighting the composite's enhanced flame resistance.

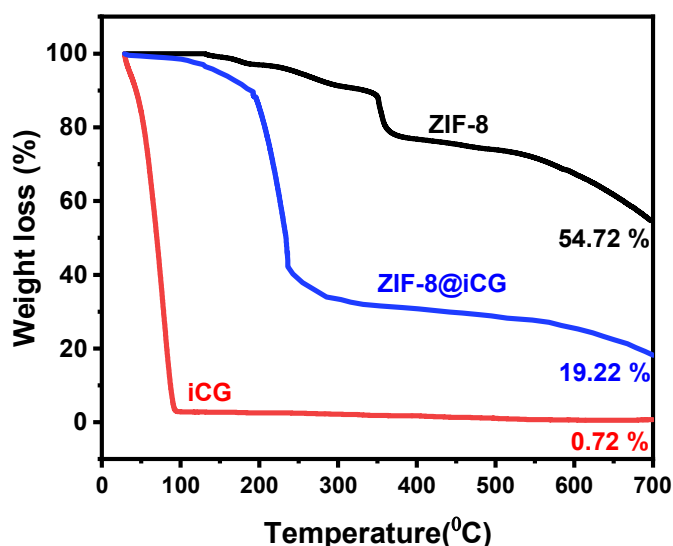


Figure 1: TGA graph of the iCG, ZIF-8 and ZIF-8@iCG aerogel.

In summary, the ZIF-8@iCG aerogel, prepared via freeze drying, combines the adsorption properties of ZIF-8 with the flexibility and biodegradability of iCG. The aerogel exhibited excellent mechanical strength, structural integrity, and recoverability, along with enhanced thermal and flame resistance. Its stability in various pH environments and under mechanical stress makes it a promising material for applications such as heavy metal ion and dye removal from wastewater.

ZIF-8@iCG aerogels show great promise for heavy metal adsorption, offering improved capacity and recyclability compared to pristine ZIF-8. The combination of ZIF-8 with iCG introduces functional groups like OH and SO<sub>3</sub>H, enhancing interactions with pollutants and boosting adsorption performance. Experimental results demonstrate high adsorption capacities for metals like Pb<sup>2+</sup>, Cd<sup>2+</sup>, and Cr<sup>6+</sup> at neutral pH, with capacities reaching 1277.4 mg/g for Pb<sup>2+</sup>. The aerogel shows stability over multiple adsorption-desorption cycles, maintaining significant capacity after three cycles. Adsorption efficiency is influenced by pH, with optimal performance at pH 7.4 due to reduced competition with H<sup>+</sup> ions at higher pH levels. Regeneration using EDTA allows for repeated use, and the material shows low zinc leaching, supporting its long-term viability. Additionally, adsorption kinetics align with pseudo-second-order models, and thermodynamic studies confirm the spontaneity and endothermic nature of the adsorption process. This aerogel offers a cost-effective, stable, and efficient method for removing heavy metals from wastewater, including lead, which is reduced to safe drinking levels in treated water. However, the aerogel lacks selectivity in multi-ion solutions, which may limit its application for targeted metal removal.

## Conclusion

In this work, ZIF-8@iCG aerogel was successfully fabricated and characterized using PXRD, FTIR, SEM, and EDX analyses, confirming the preservation of ZIF-8 within the composite. The aerogel demonstrated high adsorption capacities for heavy metals, with maximum values of 1277.4 mg/g for Pb<sup>2+</sup>, 466 mg/g for Cd<sup>2+</sup>, and 706.1 mg/g for Cr<sup>6+</sup> after three cycles. It effectively removed 92.03% of Pb<sup>2+</sup> from spiked drinking water. The aerogel performed best at pH levels between 5 and 7, showed minimal zinc ion leaching, and retained efficiency after four regeneration cycles. Despite the cost of ZIF-8, the aerogel's recyclability, stability, and scalability make it a promising candidate for large-scale industrial applications in removing heavy metals from contaminated water.

## References

1. Wang, M.; Wang, Z.; Zhou, X.; Li, S. Efficient Removal of Heavy Metal Ions in Wastewater by Using a Novel Alginate-EDTA Hybrid Aerogel. *Appl. Sci.* 2019, 9 (3), 547.
2. Mahdavinia, G. R.; Bazmizaynabad, F.; Seyyedi, B. Kappa-Carrageenan Beads as New Adsorbent to Remove Crystal Violet Dye from Water: Adsorption Kinetics and Isotherm. *Desalin. Water Treat.* 2015, 53 (9), 2529–2539.
3. Zhang, Z.; Liu, J.; Wang, Z.; Zhang, J. Bimetallic Fe–Cu-Based Metal–Organic Frameworks as Efficient Adsorbents for Gaseous Elemental Mercury Removal. *Ind. Eng. Chem. Res.* 2021, 60 (1), 781–789.
4. Mo, Z.; Tai, D.; Zhang, H.; Shahab, A. A Comprehensive Review on the Adsorption of Heavy Metals by Zeolite Imidazole Framework (ZIF-8) Based Nanocomposite in Water. *Chem. Eng. J.* 2022, 443, 136320.
5. Peng, H.; Xiong, W.; Yang, Z.; Xu, Z.; Cao, J.; Jia, M.; Xiang, Y. Advanced MOFs@aerogel Composites: Construction and Application towards Environmental Remediation. *J. Hazard. Mater.* 2022, 432, 128684.

## Sequential and Synergistic Ageing Assessment of XLPE used in I&C Cables of NPPs

Rohit Ranjan<sup>a</sup>, NB Shrestha<sup>b</sup>, AK Ahirwar<sup>b</sup>, TV Santhosh<sup>b\*</sup>,  
PK Ramteke<sup>b</sup>, KA Dubey<sup>a,c</sup>, Gopika Vinod<sup>a,b</sup>, J Chattopadhyay<sup>a,b</sup>

<sup>a</sup>Homi Bhabha National Institute, Mumbai, India.

<sup>b</sup>Reactor Safety Division, Bhabha Atomic Research Centre, Mumbai, India.

<sup>c</sup>Radiation Technology Development Division, Bhabha Atomic Research Centre, Mumbai, India.

[santutv@barc.gov.in](mailto:santutv@barc.gov.in); Ph: 25590985

### Abstract

Instrumentation and control (I&C) cables used in nuclear power plants for control and monitoring applications are subjected to ageing mechanisms causing the degradation of cable components over time. The ageing assessment of I&C cables with individual stressors is a well understood topic and the effect of such ageing assessment has been extensively studied through equipment qualification and remaining useful life estimation studies. However, the studies on understanding the effect of sequential and synergistic ageing are limited due to difficulty in setting up of synergistic ageing test facilities, and establishing the correlation with the field ageing. In view of this, cross-linked polyethylene (XLPE) used as insulation in I&C cables of nuclear power plants (NPP) has been simulated under sequential and synergistic ageing environment consisting of thermal and radiation stressors. The elongation at break (EAB) measurement has been carried out to assess the aging effect under various ageing scenarios. Scanning electron microscopy (SEM) has also been performed to study the ageing effect in XLPE insulation.

The polymeric insulation materials used for insulation and sheath in instrumentation and control (I&C) cables are susceptible to ageing and degradation mechanisms caused by exposure to high temperature, humidity and radiation in nuclear power plants (NPP). Ageing of components is a serious concern since degradation can impact the performance of connecting equipment/system. This is of particular concern for safety-related equipment since the failure due to ageing can compromise the continued safe operation of NPP. Ageing assessment of I&C cables with individual stressors has been well understood and several studies exist [1]. However, understanding the effect of sequential and synergistic ageing has been challenging to researchers due to the requirement of combined ageing environment with two or more stressors acting simultaneously. Conducting life tests on cables under normal operating conditions is usually time-consuming. Hence, accelerated life tests (ALT) are commonly employed [2]. This study aims at investigating the sequential and synergistic ageing effect in cross-linked polyethylene (XLPE) insulation by subjecting to accelerated ageing comprising of thermal and radiation stressors and comparing with individual stressors.

In order to identify the correct stressor causing ageing in insulation materials, and to study the effect of specific ageing sequence, the ageing scenarios, as shown in Table 1, have been considered in this study. The samples were prepared from XLPE sheet as per ASTM D638 and D418 standards. Test matrix showing the cumulative dose at different temperature is shown in Table 2. Minimum of 5 samples were placed under each test condition including baseline reading, and accelerated laboratory ageing has been carried out at constant temperature of 90°C, 100°C, and 110°C with radiation dose upto 100 MRad at a dose rate in the range from 0.136 to 0.14MRad/hr. The samples were taken out regularly to measure the performance parameters.

Table-1: Ageing scenarios

Sequence code	Ageing scenario
T	Thermal ageing scenario
R	Radiation ageing scenario
T→R	Sequential ageing scenario 1 (thermal

	followed by radiation ageing)
R→T	Sequential ageing scenario 2 (radiation followed by thermal ageing)
Syn	Synergistic ageing (simultaneous ageing by thermal and radiation stressors)

Table-2: Test matrix for ageing assessment

Test duration (hr)	Cumulative dose (MRad)	90°C	100°C	110°C
48	5.03	5	5	5
96	10.07	5	5	5
168	17.62	5	5	5
270	28.32	5	5	5
504	52.86	5	5	5
720	75.52	5	5	5
960	100.70	5	5	5

Elongation at break (EAB) measurement was performed using Tinius Olsen Universal Testing Machine (UTM) with a load cell of 10kN. Tests were performed with an initial jaw separation of 25mm at a strain rate of 25mm/min. Data analysis has been carried out and the mean EAB as a function of dose for various ageing scenarios is shown in Figure 1. Refer Table 1 for legends in Figure 1.

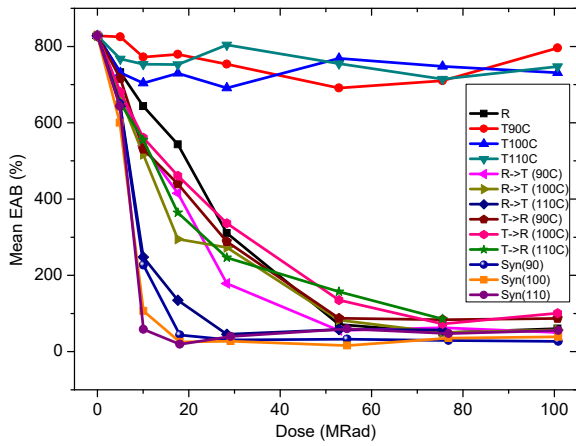


Figure 1: Mean EAB vs. accumulated dose for all ageing sequences

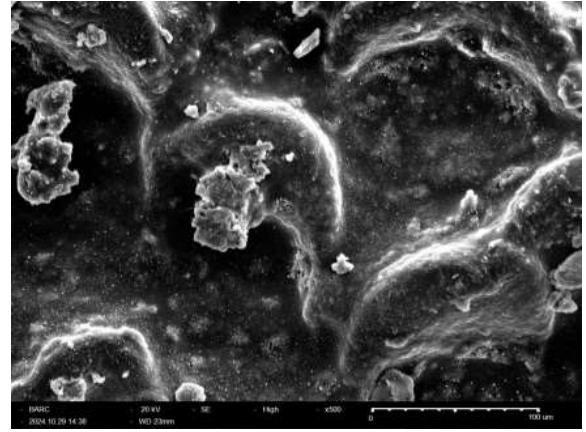


Figure 3: SEM micrograph of XLPE sample aged at 110°C upto 100 MRad

It is observed from Figure 1 that synergistic ageing effect in XLPE is more severe than other form of ageing. The EAB reduced to below acceptable value of 50% in case of synergistic ageing after subjecting to a cumulative dose of 17 MRad at all temperatures. However, XLPE insulation is not much affected by the thermal ageing even after 960 hours of ageing at all temperatures. It is evident that the ageing in XLPE insulation is dominated by radiation ageing; however, when it is coupled with simultaneous thermal ageing the resultant ageing effect is quite significant compared to ageing effect in all other sequences. The drastic reduction in EAB from initial value of 828 to 19 under synergistic ageing is attributed to permanent chain scission in XLPE caused primarily by radiation damage. It is also apparent from the findings that the order of sequential ageing (i.e. thermal followed by radiation or radiation followed by thermal) has no noticeable effect except one scenario which is being further investigated.

In order to support the findings obtained from tensile testing for various ageing scenarios, the fresh and aged samples were subjected to scanning electron microscopy (SEM). The micrographs of fresh and aged sample of XLPE are shown in Figure 2 and 3 respectively. As can be seen from SEM micrographs, the XLPE material has become brittle after thermal and radiation ageing which is also evident from EAB findings. Both fresh and aged samples were obtained at same resolution under same voltage level for comparison. The presence of detectable voids in the aged XLPE sample is a result of chain scission mechanism under high temperature and at high radiation dose. Similar morphological changes have been observed in other ageing scenarios also excepting in thermal ageing case where material didn't exhibit noticeable features under SEM which therefore is in good agreement with EAB findings.

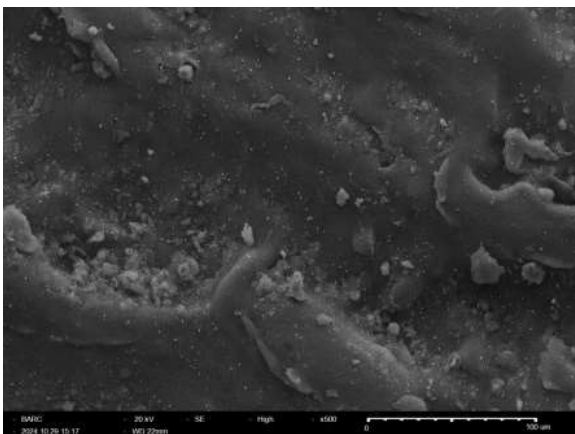


Figure 2: SEM micrograph of fresh XLPE sample

### Acknowledgements

We are thankful to Dr. MK Samal and Mr. Syed Ather, Reactor Safety Division, BARC for providing us the facility and helping us in carrying out SEM experiments at their laboratory.

### References

- [1] TV Santhosh, V Gopika, AK Ghosh, BG Fernandes and KA Dubey, Reliability Prediction of I&C cable insulation materials by DSC and Weibull theory for probabilistic safety assessment of NPPs, Nuclear Engineering and Design, No. 296, pp. 51-61, (2015).
- [2] K Anandakumaran, W Seidl, PV Castaldo, Condition assessment of cable insulation systems in operating nuclear power plants, IEEE transactions on dielectrics and electrical insulation, vol. 6, no. 3, pp. 376-384, 1999.
- [3] ASTM D638, Standard test method for tensile properties of plastics, ASTM International, 2002.
- [4] ASTM D412, Test methods for vulcanized rubber and thermoplastic rubbers and thermoplastic elastomers-tension, ASTM International, 2006.



## Studies of the effect of high energy $\gamma$ -radiation on the extensional viscosity of Ethylene-Vinyl Acetate copolymer

K. Varshney<sup>a,b</sup>, J. Rana<sup>c</sup>, T. Shokeen<sup>c</sup>, R. K. Mondal<sup>a,b\*</sup>, K. A. Dubey<sup>a,b</sup> and Y. K. Bhardwaj<sup>a,b</sup>

<sup>a</sup>Homi Bhabha National Institute, Mumbai

<sup>b</sup>Radiation Technology Development Division

Bhabha Atomic Research Centre, Trombay, Mumbai-400 085, India

<sup>c</sup>Thapar Institute of Engineering and Technology, Patiala

\* Email: rkmondal@barc.gov.in

Tel.: +91-022-2559 0179; Fax: +91 22 2550 5151

### Abstract

The study reports the studies of extensional viscosity of high energy gamma radiation modified EVA copolymers in lower dose limit. The strain hardening factor was assessed and found that SHF increases with radiation dose, maximize at 10 kGy and decrease at high dose range. An effort was made to correlate the SHF with long chain branching of radiation modified EVA copolymers. The extensional viscosity measurement helps to understand the molecular architecture at lower dose limit particularly before gelling dose.

Extensional viscosity of polymer melts is a crucial rheological property that measures resistance to deformation under tensile stress. The extensional viscosity measurements of polymer melts are particularly important for process operations involving stretching or elongational flows like blow molding, injection molding and foaming. Measurement of extensional viscosity also yielded strain hardening of branched polymer melts that helps to understand the molecular architecture particularly for high energy radiation treated polymers [1]. Ethylene-vinyl acetate (EVA) consisting of ethylene and vinyl acetate moiety to form the copolymer macromolecular structure. Although, high energy  $\gamma$ -radiation is known to impart crosslinked network in polymers like EVA at sufficiently high radiation dose but the effect of lower dose on molecular architecture in the light of flow behaviour particularly before gelling dose is still under-explored. Extensional viscosity measurement and strain hardening factor (SHF) may be helpful to understand the effect of lower radiation dose on molecular entanglement of radiation modified EVA. This study particularly focused on the studies of extensional viscosity and SHF of high energy  $\gamma$ -radiation treated EVA and made an effort to understand the long chain branching of EVA macromolecule under radiation treatment. The so-called strain hardening coefficient is defined as

$SHF = \eta_e(t)/\eta_e^0(t)$ , where,  $\eta_e(t)$  is the extensional viscosity and  $\eta_e^0(t)$  is extensional viscosity at lower strain rate.

The EVA sheets were made by compression molding at 100 °C and irradiated with Co-60 gamma rays. The extensional viscosities were measured at different extensional strain rates (0.05, 0.3, 1.0, 3.0 and 5 s<sup>-1</sup>) at 100 °C with a universal extension fixture.

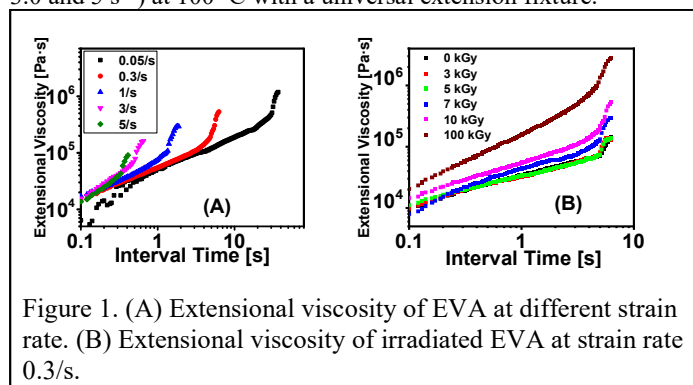


Figure 1. (A) Extensional viscosity of EVA at different strain rate. (B) Extensional viscosity of irradiated EVA at strain rate 0.3/s.

Figure 1A shows the extensional viscosity of EVA with 10 kGy radiation dose for strain rate of 0.05-5 s<sup>-1</sup>. It was evident that with increase in strain rate the corresponding time of failure decrease, however, the viscosity curve overlays each other's. The viscosity curve matching with three times of steady shear viscosity envelope. There was overshoot of viscosity curve from

linear elongational viscosity for all strain rate corroborated strain hardening behaviour. Strain hardening increases with increasing in strain rate due to chain alignment. As a polymer melt is stretched, its polymer chains align in the direction of the applied stress and this alignment increases the resistance to further deformation.

Effect of radiation dose on extensional viscosity of EVA copolymers were represented in figure 1B. It was observed that the extensional viscosity value increase with radiation dose. The increase in viscosity primarily due to the formation of crosslinking and or long chain branching. The long chain branching formation can be probed by monitoring the SHF. The values of SHF have been tabulated in table 1 as a function of radiation dose.

**Table 1.** Effect of radiation dose on SHF of EVA copolymers

Radiation dose (kGy)	Strain hardening ratio
0	1.90
3	1.77
5	1.83
7	2.25
10	4.08
100	3.04

It can be observed that SHF was around 1.8 to 1.9 for pristine EVA and irradiated to small dose upto 5 kGy. It is worth noting that, for linear polymer, the SHF should be close to unity due to unrestricted flow of untangled polymeric chain. However, SHF of 1.9 for pristine EVA confirmed the presence of entanglement due to the copolymer architecture. The EVA used in current study have vinyl acetate content of 28wt% imparts sufficient amount of amorphous region which is mainly responsible for entanglement of polymer chain. With radiation dose the SHF increases, maximize at 10 kGy and decrease thereafter. At 7kGy the SHF was 2.25 which was significantly higher than the SHF at 5kGy. This significant enhancement of SHF clearly evident the formation of interlinking of polymeric chain eventually formed the crosslinked structure. The decrease in SHF at higher dose of 100 kGy is evident of chain scission.

### References

- Schußmann, Max G, Wilhelm, Manfred, Hirschberg, Valerian, *Nature Communications*, 15 (2023) 3545

## Studies of the thermal stability of radiation synthesised glycidyl methacrylate-based copolymer

B. N. Kaul<sup>a,b,†</sup>, Annapurna Chandane<sup>a,b,†</sup>, R. K. Mondal<sup>a,b</sup>, C. V. Chaudhari<sup>a,b\*</sup>, K. A. Dubey<sup>a,b</sup>, Y. K. Bhardwaj<sup>a,b</sup>

<sup>a</sup>Homi Bhabha National Institute, Mumbai

<sup>b</sup>Radiation Technology Development Division

Bhabha Atomic Research Centre, Trombay, Mumbai-400 085, India

\* Email: cvchau@barc.gov.in

Tel.: +91-022-2559 0179; Fax: +91 22 2550 5151

[† both authors contributed equally]

### Abstract

The study reports the studies of thermal properties of poly(GMA-co-TMPTMA) copolymers. Copolymeric poly(GMA-co-TMPTMA) porous network were prepared via radiation polymerization followed by solvent removal. The synthesized poly(GMA-co-TMPTMA) porous copolymer exhibited rather high thermal stability in inert atmosphere. The thermal degradation steps of poly(GMA-co-TMPTMA) copolymer runs mainly according to the depolymerization mechanism.

Thermal stability of copolymers plays significant role in predicting long term usability of them as functional adsorbent at harsh environment [1]. Multifunctional acrylate-based monomers are very reactive and particularly useful for imparts mechanical and thermal stability when used them with some other functional monomer for making copolymers. High energy radiation like gamma radiation is an additive free modality for synthesis of copolymers for various applications like, functional adsorbent, drug delivery system, separation membrane etc. Internal porous structure is a prerequisite for many of these applications. Porosity often incorporates by adapting the copolymerization of two monomer in presence of a solvent and subsequently removing them. However, removing of solvent and incorporation of porosity comes with a cost of mechanical integrity and thus thermal stability of copolymers. Hence it is important to assess the thermal stability of copolymers which could predict the mechanical stability specially in harsh condition. Another important aspect is that often thermal stability improves hand on hand with molecular weight of polymer system. This study focused on the thermal stability assessment of radiation synthesised poly(GMA-co-TMPTMA) copolymer and predicts the different copolymer moiety formed by closely examine the thermal degradation behaviour of copolymers.

The series of poly(GMA-co-TMPTMA) copolymers were synthesized by radiation polymerization of different ratio of monomers. DMF was used as a solvent in the ratio of 80:20 with total monomer. A radiation dose of 20 kGy was sufficient to complete the polymerization reaction. After polymerization the copolymers were extracted in water for removing the solvent and subsequently freeze dried for retaining the porous structure. Thermal stability of the as synthesized copolymers was studied by thermogravimetry analysis.

Figure 1(A-B) shows TGA and DTG graph of radiation synthesized GMA-TMPTMA copolymers. The initial decrease in weight at ~10-20% at about 100 °C was due to the removal of the remaining water from the porous structure of copolymers. As the porous structure of copolymers were recovered from solvent removing method by putting them into water, some water remains in the porous structure even after drying. As can be seen from the graph that the G0 and G20 contains highest amount of water and water content decrease as GMA ratio increase in copolymer system. This observation corroborates the fact that higher GMA copolymers may form a rigid crosslinked network hence the porosity may be very low compare to the low GMA fraction.

**Table 1.** TG and DTG data of GMA-TMPTMA copolymers.

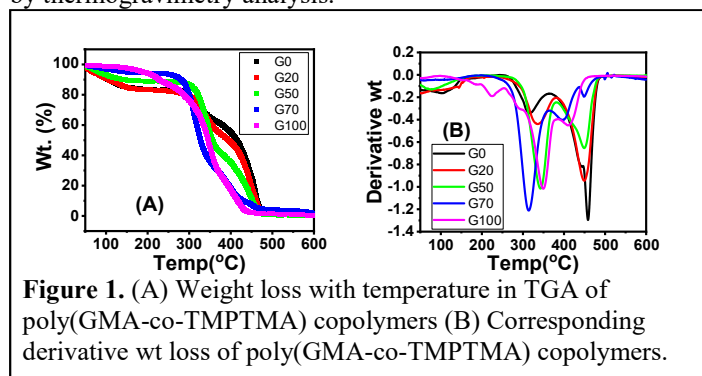
Copolymer	T <sub>50%</sub> wt loss	T <sub>80%</sub> wt loss	T <sub>max1</sub>	T <sub>max2</sub>
G0	416.8°C	457°C	314°C	456°C
G20	395.6°C	450°C	335°C	450°C
G50	356°C	435°C	341°C	448°C
G70	345°C	393°C	311°C	396°C
G100	327.2°C	395°C	350°C	410°C

Table 1 tabulated the corresponding temperature of copolymers for 50% (T<sub>50</sub>) and 80% (T<sub>80</sub>) weight loss. It was observed that the T<sub>50</sub> was 416.8 °C for G0 and decreases as GMA content increase, and that for G100 it reaches to 327.2 °C. Same observation was for T<sub>80</sub>; it decreases from, 457 °C to 395 °C as GMA content increase from 0 to 100%. The thermal stability increases for the copolymers having higher percentage of TMPTMA. It is well understood that higher molecular weight of polymer chain gives more thermal stability. As TMPTMA has three acrylate group, it is expected that it forms more interlinked networks in relatively lower radiation dose, hence can achieve higher molecular weight compare to GMA which has only one acrylate group.

Furthermore, DTG graph reveals that the GMA copolymer decomposes in two major steps, one at around 310 °C to 350 °C and another at ~450 °C. The major degradation peak depends upon the composition of copolymers. The degradation peak in lower temperature can be attributed as the depolymerization of copolymers and is accompanied by the isomerization reaction in the gaseous phase. Degradation at higher temperature is mainly due to random chain scission.

### References

- Grochowicz, Marta Pączkowski, Przemysław Gawdzik, Barbara, *Journal of Thermal Analysis and Calorimetry*, 133 (2018) 499-508.



**Figure 1.** (A) Weight loss with temperature in TGA of poly(GMA-co-TMPTMA) copolymers (B) Corresponding derivative wt loss of poly(GMA-co-TMPTMA) copolymers.

## Studies of thermal stability of radiation crosslinked polyolefin-multifunctional acrylate rubber blends

Pratap Singh<sup>a,c</sup>, Arijit Ghoshal<sup>a,b</sup>, R. K. Mondal<sup>a,b\*</sup>, K. A. Dubey<sup>a,b</sup>, Y. K. Bhardwaj<sup>a,b</sup><sup>a</sup>Homi Bhabha National Institute, Mumbai<sup>b</sup>Radiation Technology Development Division<sup>c</sup>Health Physics Division, Bhabha Atomic Research Centre, Trombay, Mumbai-400 085, India

\* Email: rkmondal@barc.gov.in

Tel.: +91-022-2559 0179; Fax: +91 22 2550 5151

**Abstract**

The radiation stability of ethylene propylene diene monomer (EPDM) terpolymer is of interest due to the use of that particular rubber in nuclear industry as insulation of cables. In this study the isothermal and non-isothermal oxidative degradation behaviour of radiation crosslinked EPDM-multifunctional acrylate blends has been evaluated. Isothermal oxidative induction time found to decrease with temperature and was observed to follow Arrhenius equation, the activation energy estimated by fitting the data in Arrhenius equation found on par with literature value. Non-isothermal degradation of EPDM found to follow the decreasing trend with radiation dose corroborates the critical role of crosslinked network formed by radiation induced crosslinking of EPDM macromolecule.

Ethylene propylene diene rubber (EPDM) has attracted a lot of interest because of its outstanding heat, ozone and weather resistance. It exhibits good resistance to polar solvent substances and steam condition too making an attractive component for used in radiation field. Additionally, EPDM exhibits excellent electrical properties, good mechanical properties, resistance to various aggressive chemicals (acids, alkalies, phosphate esters or ketones), good adhesion characteristics and good low-temperature properties due to its saturated and stable polymer backbone structure. Radiation crosslinked EPDM rubber offers excellent thermal stability, making it suitable for a wide range of applications in demanding environments [1, 2].

Even when crosslinked by high energy radiation oxidative degradation of EPDM is a major factor limiting the long-term performance of it. Oxidative degradation process involves a chain reaction initiated by free radicals, which attack the polymer chain, leading to chain scission and crosslinking. Over time, this degradation can significantly deteriorate the mechanical properties of the rubber, such as tensile strength, modulus, elongation, and hardness of materials. This study reports non-isothermal oxidative degradation behaviour of radiation crosslinked EPDM-multifunctional acrylate blends. An effort has been made to correlate the radiation dose with onset degradation temperature of EPDM-MFA blends. Also, the isothermal degradation of EPDM found to obey the Arrhenius equation which is a primary postulate for estimation of the activation energy for oxidative degradation.

EPDM/MFA blends were prepared by mixing the components homogeneously in Brabender plasticordar at 100°C, 30rpm for 20 min. Cutting the homogeneous mix into small pieces, it was then compressed at 150 kg/cm<sup>2</sup> for 30 minutes at 90°C into sheets of size 10 x 10 cm<sup>2</sup>. The composites were irradiated using a Co-60 gamma source (GC-5000, M/s BRIT, India) under inert atmosphere. Both the isothermal and non-isothermal oxidative degradation studies were conducted in DSC setup in presence of high purity oxygen gas.

The isothermal degradation at different temperature of pristine EPDM was conducted and the data has been presented in fig 1A. The time taken for isothermal degradation was found to decrease with increase in temperature. The reciprocal of the degradation time was plotted against reciprocal of absolute temperature and found to vary linearly which gives activation energy from the negative slope of it. The Arrhenius equation given by,  $\ln k = \ln A - E_a/RT$ , where k is reciprocal of oxidation time,  $E_a$  is activation energy, R is universal gas constant. The linear fitting

yielded the activation energy value of 135.6 kJ/mol which is in agreement with literature value. Non isothermal oxidative degradation study was conducted with a heating rate of 10 °C/min in oxygen environment and data has been presented in fig 1B for different radiation dose. It can be observed that for unirradiated EPDM, the onset of oxidation was 214 °C and gradually decrease the onset temperature as radiation dose increase. For 5 kGy irradiated sample onset was 202 °C and that for 100 kGy sample onset was 196 °C. This decrease in onset of oxidative degradation was due to the formation of highly crosslinked structure which does not allow the formation of C-O-C bonds which could lead to participation in crosslinking reaction. Also absence of any antioxidant and stabilizer may be another reason for decrease in oxidation stability of irradiated samples. However, by understanding the mechanisms of oxidative degradation and implementing effective mitigation strategies, the long-term performance of radiation crosslinked EPDM rubber can be significantly improved.

**References**

1. K. Dubey, S. Sinha, Y. Bhardwaj, L. Panicker, L. Varshney, Polymer-Plastics Technology and Engineering, 53 (2014) 442-450.
2. R. Mondal, J. Kumar, K. Dubey, Y. Bhardwaj, J. Melo, L. Varshney, Sensors and Actuators B: Chemical, 265 (2018) 193-203.

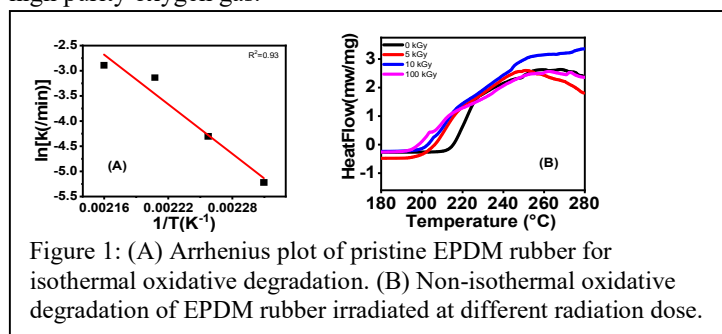


Figure 1: (A) Arrhenius plot of pristine EPDM rubber for isothermal oxidative degradation. (B) Non-isothermal oxidative degradation of EPDM rubber irradiated at different radiation dose.

## Studies of the effect of high energy $\gamma$ -radiation on the oxidative stability of Ethylene-Vinyl Acetate copolymer

Arijit Ghoshal<sup>a,b</sup>, R. K. Mondal<sup>a,b\*</sup>, K. A. Dubey<sup>a,b</sup>, Y. K. Bhardwaj<sup>a,b</sup>

<sup>a</sup>Homi Bhabha National Institute, Mumbai

<sup>b</sup>Radiation Technology Development Division

Bhabha Atomic Research Centre, Trombay, Mumbai-400 085, India

\* Email: rkmondal@barc.gov.in

Tel.: +91-022-2559 0179; Fax: +91 22 2550 5151

### Abstract

This study reports non-isothermal oxidative degradation of radiation treated ethylene vinyl acetate (EVA) elastomers. Radiation crosslinked EVA exhibited distinct oxidative onset temperature (OOT) when subjected to degradation. Based on the OOT degradation mechanism has been accessed. It can be postulated that the deacetylation of acetate group and formation of many peroxides and hydroperoxides are primary reason for oxidative degradation of EVA.

Ethylene vinyl acetate elastomers (EVA) have several industrial applications, such as corrosion protection, electrical insulation, protection of solar panel and manufacture of adhesives, including hot melts etc. Many of these applications demands high thermal stability. Oxidative degradation specially at elevated temperature is a major hinderance for realization in such applications [1,2]. Radiation induced crosslinking is one of the key process for improve mechanical stability, due to its additive free crosslinking process. Crosslinking of EVA imparts physical barrier for diffusion of oxygen, hence the thermal stability towards oxidation improves with radiation doses. Conversely sometimes too high radiation dose increases the possibility of formation of oxygen centered radical which helps degradation process. Hence there has to be an optimized radiation dose. However, the oxidative stability of EVA based copolymer still possesses challenges due to the alteration occurs in molecular structure during the process of degradation. This study reports the non-isothermal oxidative degradation of EVA copolymers treated with different amount of radiation dose. An effort was also made to understand the mechanism behind the degradation process. High energy radiation plays a significant role to improve the oxidative stability.

The EVA sheets were made by compression molding at 100 °C and irradiated with Co-60 gamma rays. The oxidative degradation was studied by differential scanning calorimetry under high purity oxygen environment.

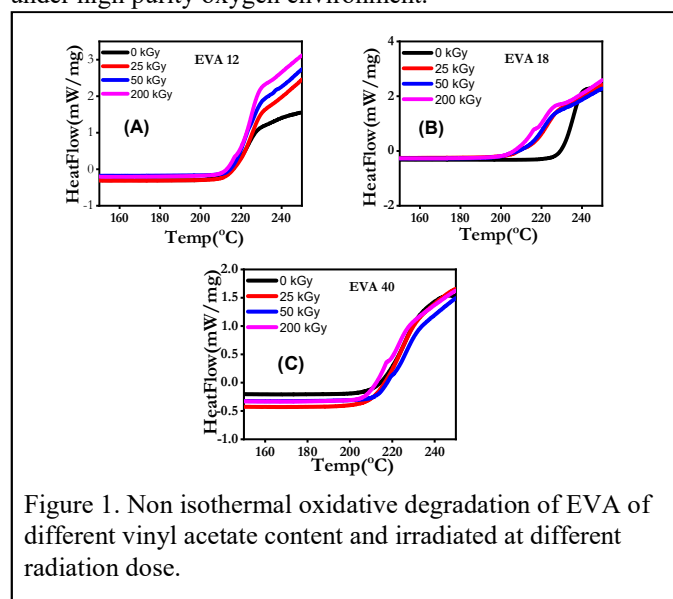


Figure 1. Non isothermal oxidative degradation of EVA of different vinyl acetate content and irradiated at different radiation dose.

Figure 1 shows the onset DSC curve of EVA12, EVA18 and EVA40 under non-isothermal oxidative condition. The

oxidative degradation can be identified from exothermal heat flow in DSC curve. All EVA shows good oxidative stability upto 200 °C. The oxidative degradation of EVA copolymer is mainly due to the deacetylation of acetate group at elevated temperature. Also, formation of peroxide and hydroperoxides plays important role in degradation mechanism. During oxidative degradation samples turns yellow is an indication of formation of carbonyl group as lactone, aldehydes and ketones.

**Table 1.** Oxidative onset temperature of EVA of different vinyl acetate content irradiated at different radiation dose.

Dose (kGy)	0	25	50	200
EVA 12	204°C	211°C	213°C	210°C
EVA 18	223°C	205°C	201°C	202°C
EVA 40	211°C	209°C	210°C	206°C

The onset of oxidative degradation of all EVA samples have been tabulated in table 1. It can be seen that for unirradiated EVA, onset temperature was highest for EVA18. With irradiation OOT increase for EVA12; for instance, OOT was 211 °C for 25 kGy irradiated EVA12 and that was 213 °C for 50 kGy. Due to the crosslinking nature of EVA, there was a formation of barrier with crosslinking for diffusion of oxygen which might push OOT to higher temperature. Conversely, OOT was found to decrease for other two EVA sample with radiation dose. EVA18 exhibited highest decrease in OOT compare to EVA40. Presence of vinyl acetate plays crucial role for OOT of EVA as its contribution to the generation of free radicals. Also, absence of any antioxidant and stabilizer may be another reason for decrease in oxidation stability of irradiated samples. However, by understanding the mechanisms of oxidative degradation and implementing effective mitigation strategies, the long-term performance of radiation crosslinked EVA rubber can be significantly improved

### References

- R.K. Mondal, J. Kumar, K. Dubey, Y. Bhardwaj, J. Melo, L. Varshney, *Sensors and Actuators B: Chemical*, 265 (2018) 193-203.
- Giurginca, Maria Popa, Livia Zaharescu, Traian, *Polymer Degradation and Stability*, 82 (2003) 463-466.

## Studies on PBI Based Amperometric Hydrogen Sensor for Sodium Cleaning Application of Fast Reactor Components

Sukumaran<sup>V1,2\*</sup>, N.Murugesan<sup>1</sup>, P.Manikandan<sup>1</sup>, Hrudananda Jena<sup>1,2</sup>

<sup>1</sup>Materials Chemistry & Metal Fuel cycle, IGCAR, Kalpakkam

<sup>2</sup>Homi Bhabha National Institute, Mumbai

\*vsuku@igcar.gov.in

### Abstract

Sodium is used as coolant in fast reactors and the used components removed from the reactor need to be cleaned free of sodium prior to their repair, maintenance or reprocessing. The sodium cleaning process releases hydrogen and to maintain the hydrogen under lower explosion limit during the process, hydrogen sensor is required. For this, the proton conducting electrolyte was prepared by doping phosphoric acid into Polybenzimidazole (AD-PBI) and it was used in developing an electrochemical amperometric sensor. The temperature dependent conductivity of electrolyte was studied and activation energy was determined. The assembled sensor was studied for hydrogen sensing characteristics in the range of 0-4% in argon.

### Introduction

Sodium is used as coolant in fast reactors due its favourable heat transfer and nuclear properties. The components (primary sodium pump, intermediate heat exchangers and spent fuel sub-assemblies) taken out from the reactors for various purposes like repair, maintenance and reprocessing need to be cleaned of the sodium adhering to them. Sodium cleaning of reusable components is carried out by water vapour- CO<sub>2</sub>- (WV-CO<sub>2</sub>) process and the fuel sub-assemblies by steam nitrogen process [1]. During the cleaning, the sodium reacts with water vapour or steam and releases hydrogen. In the sodium-cooled fast reactors (SFR), cold traps are employed to maintain the hydrogen and oxygen impurities within allowed levels. The secondary sodium cold trap (SCT) is mainly loaded with hydrogen impurity due to steam generator corrosion. SCT gets saturated with its continued usage in the reactor and it needs to be regenerated. In the regeneration process, the sodium hydride decomposes at 400° C under vacuum, a large quantity of hydrogen [2]. To maintain the hydrogen below 50% of the lower limit, hydrogen sensor is required to monitor and manage it.

In our laboratory, Nafion and PVA-based polymer electrolyte membrane (PEM) hydrogen sensors were developed and used in sodium cleaning experiments for hydrogen sensing [1].

PBI based hydrogen sensor have been reported in potentiometric mode [3]. The H<sub>3</sub>PO<sub>4</sub> doped PBI (AD-PBI) electrolyte is operational at moderate temperatures (150°C) and it does not require humidification and avoids Pt poisoning by CO. In the present study, AD-PBI based hydrogen sensor is developed and is investigated for its hydrogen sensing capability.

### Experimental

**Phosphoric acid doping on PBI membrane:** PBI membrane (M/S PBI Performance Products, Inc. USA) having 55 micron thickness was soaked in 60% Phosphoric acid for 24 hours. The membrane before and after soaking in phosphoric acid was characterized by Fourier Transform Infrared Spectroscopy (FTIR) to confirm the doping of the acid.

### Catalyst Ink preparation

The catalyst ink was prepared by mixing 100mg of 37% Platinum-Carbon (Pt-C) catalyst with 1mL of distilled water and 1.5 mL of iso propyl alcohol. The mixture was sonicated for 15 minutes. Then 0.2 mL of PBI solution (1% PBI powder in N, N Dimethyl Acetamide) and 1 mL of distilled water were added to the above solution and sonicated until the solution turned into the slurry.

The catalyst ink thus prepared above was coated on the micro porous carbon paper (Gas Diffusion Layer [GDL]). The amount of catalyst loading on the anode and the cathode was 0.5 mg/cm<sup>2</sup> and 0.9 mg/cm<sup>2</sup>, respectively. The GDL thus coated was dried at 190°C in vacuum oven. The electrolyte membrane with the dimensions 2.5 cm × 2.5 cm was sandwiched between the anode and cathode and hot pressed at 160°C for 90 seconds using high pressure hydraulic press. The above assembly was sandwiched between the grooved graphite plates which were used for the flow of gases over the anode and the cathode. Two insulated end plates were provided on the graphite plates and the entire set up was fastened with bolts and nuts to achieve the leak tightness. The carbon cloth of 0.1mm thickness was used as the current collector. 0.1 mm thick Teflon membrane was kept between the anode and the graphite plate to regulate the amount of H<sub>2</sub> reaching the anode. Two rod heaters fixed to the end plates were used for heating the sensor to 150°C and the temperature was controlled using PID controller.

### Conductivity measurement

The conductivity of the cell thus assembled was studied as a function of temperature in the range RT-180°C by the electrochemical impedance spectroscopy technique using the Potentiostat/Galvansat of Autolab, Netherlands. The impedance of the cell was measured in the frequency range of 100 KHz to 1Hz with the perturbation potential of 10 mV. The impedances data were converted to the specific conductivity. The conductivity data were plotted against the temperature to obtain the activation energy for proton conduction in the electrolyte.

### Hydrogen sensing studies

The sensor thus assembled was calibrated at the temperature 150°C for hydrogen sensing by passing known concentrations of H<sub>2</sub>/Ar mixture having H<sub>2</sub> in the range 1-4% and air through the anode and the cathode, respectively. The sensor current as a function of time was recorded using Agilent data acquisition on system. Repeatability test (t<sub>90</sub>) was done by passing 1% H<sub>2</sub>/Ar mixture.

### Results and discussion

FTIR spectra of fresh and H<sub>3</sub>PO<sub>4</sub> doped PBI are shown in Fig. 1. Once the PBI material is doped with phosphoric acid, a very broad absorption band appears in the wave number range between 2400 and 3000 cm<sup>-1</sup> which is consistent with protonation of the N-sites on the imidazole groups of PBI. The adsorption bands of the acid anion (H<sub>2</sub>PO<sub>4</sub><sup>-</sup>) between 400 and 1300 cm<sup>-1</sup> in the IR-spectrum can also be used as markers for the degree of protonation of PBI. Specifically, the area of the

peak at  $1630\text{ cm}^{-1}$  is sensitive to the acid content in the membrane.

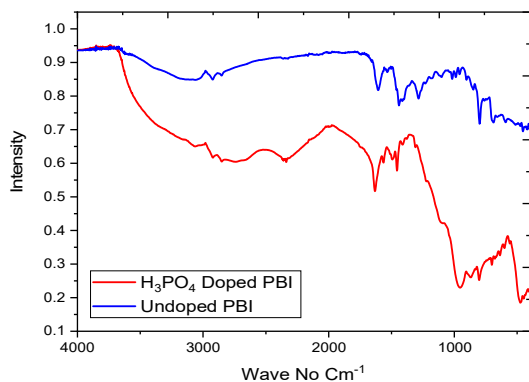


Fig.1. FTIR of undoped and doped PBI

Fig.2 shows the EIS spectra in Nyquist plot for the acid doped PBI membrane as function of temperature. The plot shows the electrolyte resistance of the membrane with Warburg impedance. The plot clearly shows a decrease in the membrane resistance with an increase in the temperature. The specific conductivity was calculated using resistance and cell constant. The Arrhenius plot was constructed as shown in Fig.3. The conductivity at  $150^\circ\text{C}$  is  $4 \times 10^{-3}\text{ S/cm}$ , which is one order less compared to the literature value ( $0.01\text{ S/cm}$ ) and it is sufficient for  $\text{H}_2$  sensor applications.

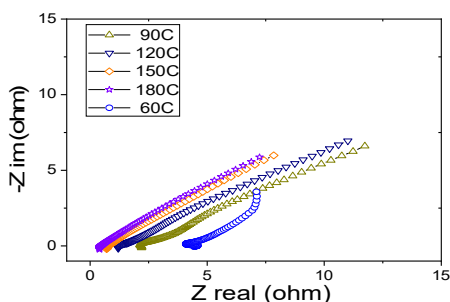


Fig. 2 EIS spectra of the acid-doped PBI as a function of temperature

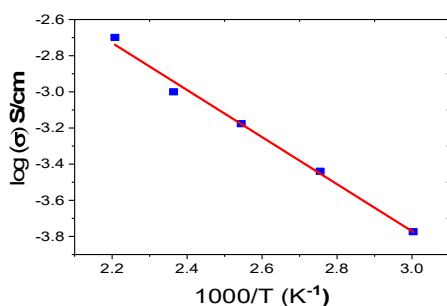


Fig.3 Arrhenius plot of acid-doped PBI as a function of temperature.

From the slope of the Arrhenius fit, the activation energy was derived to be  $10.8\text{ kJ/mole}$  which is low compared to the literature value. This may be attributed due to the contribution of free acid in the membrane. Fig.4 & 5 show the response curve and calibration of the sensor. The calibration plot shows that the current varies linearly with  $\text{H}_2$  concentration in the above range. The sensitivity (the slope) of the sensor is quite high with the value of  $6.45\text{ mA}/\%$ . The sensor has very sharp response time ( $t_{90}$ ) is  $\sim 4$  seconds.

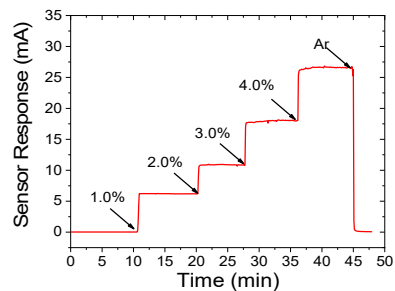


Fig.4 Response curve of the sensor

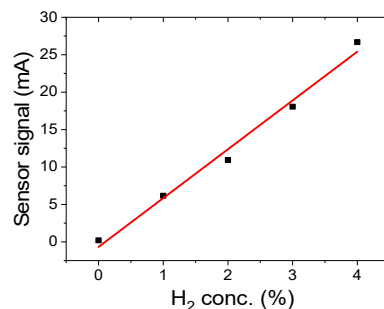


Fig.5 Calibration plot of the sensor

This fast response is due to the higher; electrode kinetics, electrolyte conductivity and the operating temperature of the sensor. The repeated value of sensing at  $1\% \text{ H}_2/\text{Ar}$  is shown in Fig.6.

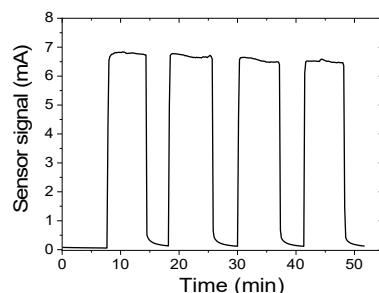


Fig.6 Repeatability of the sensor

Repeatability was observed to be within  $\pm 6\%$ . The retrace time was  $\sim 7$  seconds.

### Conclusion

The phosphoric acid doped PBI membrane was prepared and characterised by FTIR. Electrical conductivity was measured to be  $10^{-3}\text{ S/cm}$ . Which is adequate for the sensor application. The assembled sensors has good sensitivity, repeatability with satisfactory response and retrace time.

### References

1. Proton exchange membrane base hydrogen sensor for sodium cleaning application by N. Murugesan, C. Ramesh, N. Sanil, M.V. Krishnaiah, S.I. Sundar Raj, V. Ganesan, Sensors and Actuators B: Chemical, 182 (2013) 598– 604
2. Studies on in-situ regeneration of cold trap of a bench-top Sodium loop, N. Murugesan, Faizal V. A., Prabhu E., Shyam Kumar S., Sajal Ghosh, Sree Rama Murthy A., Sudha R., Hrudananda Jena, Rajesh Ganesan, Jayaraman V. Nucl. Eng. Des. 403 (2023) 112156.
3. Acid Doped Polybenzimidazole as the Membrane of Electrochemical Hydrogen Sensors, R. Bouchet et al 1997 J. Electrochem. Soc. 144 L95

## Development of Radiolytically Functionalized Amine Dense Biodegradable Adsorbent for CO<sub>2</sub> capture: Thermogravimetric Characterization and Adsorption Analysis

Nilanjali Misra<sup>a,b\*</sup>, Swarnima Rawat<sup>a,b</sup>, Shubhangi A. Shelkar<sup>a</sup> and Virendra Kumar<sup>a,b\*</sup>

<sup>a</sup>Radiation Technology Development Division, Bhabha Atomic Research Centre, Mumbai-400085

<sup>b</sup>Homi Bhabha National Institute, Anushaktinagar, Mumbai-400085

\* Email ID: vkumar@barc.gov.in, Tel: 022-69295683

[nilanjali@barc.gov.in](mailto:nilanjali@barc.gov.in), Tel: 022-69295681

### Abstract

This work reports a facile radiation mediated two step fabrication of an amine dense, cellulose based biodegradable adsorbent for selective sequestration of CO<sub>2</sub>. <sup>60</sup>Co gamma radiation induced graft polymerization (C-RIGP) process was employed to introduce amine rich group tetraethylene pentaamine (TP5) onto a cellulose matrix. Samples were characterized by FTIR and TGA analysis. CO<sub>2</sub> adsorption behavior of the samples were isothermally analyzed by recording increase in weight of the samples in the presence of CO<sub>2</sub>. Parameters such as CO<sub>2</sub>/N<sub>2</sub> ratio and N<sub>2</sub> flow rate were varied. Preliminary investigations have revealed the samples to be capable of rapid CO<sub>2</sub> uptake with a maximum uptake capacity recorded at 31.5 mg/g adsorbent.

### Introduction

The emission of greenhouse gases into atmosphere, especially carbon dioxide (CO<sub>2</sub>), is a worldwide acknowledged problem. In this respect, CO<sub>2</sub> emitted from point sources, such as fossil fuel-based power plants, has to be captured, utilised and stored (CCUS). The four general ways of handling CO<sub>2</sub> in large scale are oxy-fuel-, pre-, and post-combustion captures and the capture associated with industrial process streams [1]. Common CO<sub>2</sub> capture techniques include (i) gas-liquid absorption, (ii) gas-solid adsorption and (iii) separation by a membrane. In addition, direct air capture (DAC) is also an attractive proposition for harvesting CO<sub>2</sub> from the environment for potential catalytic methanation applications [2].

### Experimental

<sup>60</sup>Co gamma radiation mediated Radiation Induced Graft Polymerization (RIGP) technique was employed to incorporate polyacrylonitrile groups (PAN) onto the cellulose fabric surface. Grafting parameters- radiation dose, monomer concentration, solvent polarity etc. were optimized to arrive at a desired grafting yield of ~30 %. These samples (PAN-g-cotton) were then subjected to amination by dipping in a mixture of 40 % tetraethylene pentaamine (TP5) in 60 % glycerol and subjected to stirring for ~3 hours at 80°C. The covalent attachment of the amine functional groups was indicated by the transition of the grafted fabric to a bright orange color, a result of the formation of N-N chains. This was also confirmed by FTIR and TGA analysis of the control and functionalized samples.

For thermogravimetrically estimating the CO<sub>2</sub> uptake capacity of the sample, a known weight of the sample (~5 mg) was taken and initially heated to a temperature of 80°C in N<sub>2</sub> atmosphere (50 ml/min) for ~1 hour to ensure complete degassing. Subsequently, sample was cooled to 25°C and then isothermally introduced to CO<sub>2</sub> at a flow rate of 50 ml/min while keeping the N<sub>2</sub> flow constant at 50 ml/min. Thereafter, experiments were also carried out by varying the N<sub>2</sub> flow rate between 25-100 ml/min while keeping CO<sub>2</sub> flow rate constant at 50 ml/min.

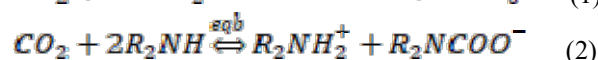
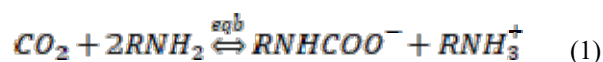
### Results and Discussion

The TGA analysis of control cotton, PAN-g-cotton and TP5 functionalized PAN-g-cotton are presented in Fig. 1. PAN-g-cotton, in addition to the major degradation step arising from the cellulose backbone (due to pyrolysis of the β-1,4 glycosidic bond) in the range 300-400 °C, showed an additional small degradation platform between 270 and 320 °C. This

Adsorbents for CO<sub>2</sub> capture consist of a support to which functional groups are attached by different techniques. There are several possibilities for the support, including mesoporous silica, amine-based functionalization (or amination) etc., since CO<sub>2</sub> is a Lewis acid [3]. In this work, we report the development of a novel radiation mediated functionalization process to tailor an amine dense, biodegradable cellulose-based adsorbent for CO<sub>2</sub> capture. The adsorbent was tested in the column flow operation mode for CO<sub>2</sub> uptake at different flow rates and also by using the thermogravimetric route wherein the weight gain of the adsorbent upon exposure to CO<sub>2</sub> is monitored with respect to time.

decomposition platform probably originates from the cyclization of the pendant –CN groups [4]. However, complete degradation of the PAN chains occurs at much higher temperatures and the substantial char yield of PAN-g-cotton (~27 %) even at 800 °C could be assigned to the presence of these chains rather than any enhancement in the thermal stability of the grafted cellulose matrix. For the TP5 functionalized sample, an additional small degradation step between 380 and 480 °C was obtained. The appearance of this step confirms the introduction of TP5 moiety on to PAN-g-cotton matrix. From the FTIR analysis (Fig. 2), the grafting of PAN groups onto cellulose could be confirmed by the appearance of CN stretching peak at 2239 cm<sup>-1</sup>. Functionalization of TP5 led to disappearance of the CN stretching peak and the emergence of a broad CH<sub>2</sub> asymmetric and symmetric stretching band in the region of 2700-3000 cm<sup>-1</sup>, as well as an NH deformation band at ~1500-1660 cm<sup>-1</sup>. In addition, the broad NH/OH stretching band was also visible at ~3300 cm<sup>-1</sup>.

The adsorption of CO<sub>2</sub> by amine functionalized adsorbents occurs as per the following chemisorption reaction mechanism:



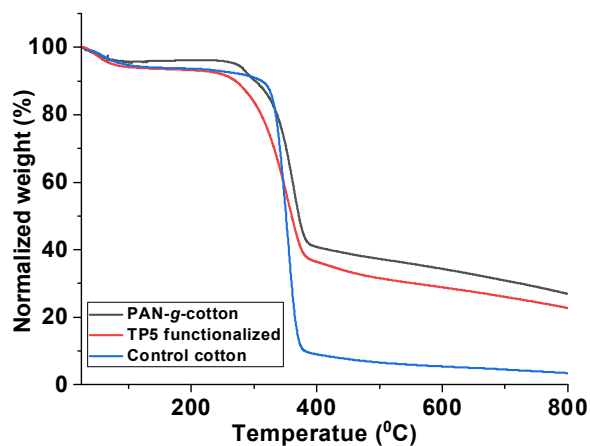


Fig. 1: TGA of control cotton, PAN-g-cotton and TP5 functionalized PAN-g-cotton

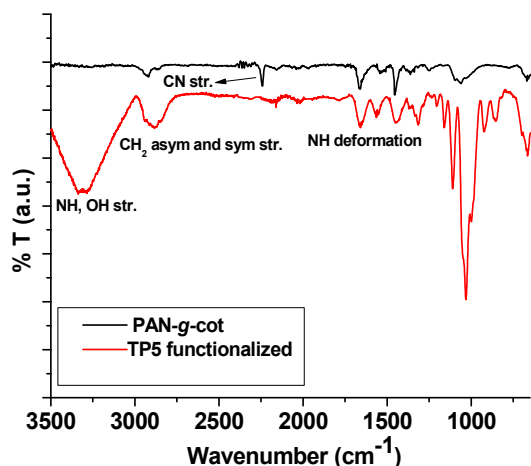


Fig. 2: FTIR spectra of PAN-g-cotton and TP5 functionalized adsorbent

The preliminary CO<sub>2</sub> adsorption behavior of the adsorbent was investigated under isothermal conditions by monitoring the increase in weight with time at a constant temperature (25 °C). The adsorption capacity was calculated at 31.5 mg/g at a CO<sub>2</sub> flow rate of 50 ml/min, while keeping the N<sub>2</sub> flow rate constant at 50 ml/min. Variation of N<sub>2</sub> purge gas flow rate seemed to affect the adsorption capacity, albeit at high flow rates. As can be seen from Fig. 3, the adsorption capacity remained almost unchanged for N<sub>2</sub> flow rates of 25 and 50 ml/min (CO<sub>2</sub> flow rate: 50 ml/min). However, further increase up to 100 ml/min led to an almost 30 % drop in adsorption efficiency. This behavior may be attributed to the dilution of the analyte gas i.e. CO<sub>2</sub> in the presence of excess N<sub>2</sub>, resulting in lower availability of reactants for the amine groups on the adsorbent surface.

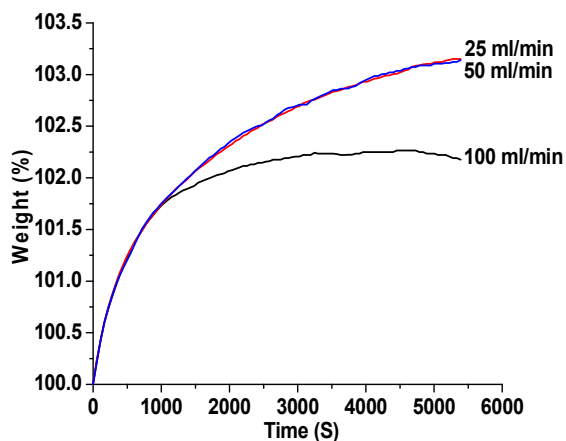


Fig. 3: CO<sub>2</sub> adsorption characteristics of TP5 functionalized PAN-g-cotton at different N<sub>2</sub> flow rates and CO<sub>2</sub> flow rate of 50 ml/min

## Conclusion

We have successfully employed the radiation functionalization approach to fabricate amine dense cellulose based biodegradable adsorbents for CO<sub>2</sub> uptake. Reaction parameters were optimized to achieve desired level of functionalization using tetraethylene pentaamine (TP5) as the amine dense moiety. Samples were characterized by FTIR and TGA analysis. Preliminary uptake studies carried out under CO<sub>2</sub>/N<sub>2</sub> gas mixture using a TGA set up revealed the TP5 functionalized adsorbent to possess an uptake capacity of 31.5 mg/g under optimized flow rate conditions.

## References

1. B. Metz, O. Davidson, H. Coninck, M. Loos and L. Meyer, Carbon Dioxide Capture and Storage, Cambridge University Press, Newyork, **2005**.
2. R. Socolow and M. Desmond, "Direct air capture of CO<sub>2</sub> with chemicals, A Technology Assessment for the APS Panel on Public Affairs," **2011**
3. A.M. Varghese and G.N. Karanikolos, G.N., *Int. J. Greenh. Gas Control* (**2020**) 96, 103005
4. W. Duan, J. Wang, L. Chang, L. Zhao, Z. Tian, Z. Huang and W. Huang, *RSC Adv.* (**2018**) 8:38259–3



## Thermal analysis of radiation-synthesized super porous polymer using Thermogravimetric Analysis (TGA) and Differential Scanning Calorimetry (DSC)

Sanju Francis\* and N. K. Goel

Advanced Materials Section, Radiation Technology Development Division,  
Bhabha Atomic Research Centre, Mumbai 400085

Email ID: sanju@barc.gov.in, Telephone Number: 022-25595639

### Abstract

This study investigates the thermal properties of radiation-synthesized super porous hydrogel (SPH) of Poly(hydroxyethylmethacrylate) (PHEMA) and Poly([2-(methacryloyloxy)ethyl] trimethylammonium chloride) PMAETC-grafted-PHEMA. PHEMA was found to be an ideal matrix for grafting PMAETC for increasing water adsorption capacity many folds and addition of antibacterial properties due to presence of quaternary groups in PMAETC. TGA studies showed the incorporation of the PMAETC moiety in the PHEMA hydrogel which was further confirmed by DSC studies. The DSC and TGA/DTGA curves show a strong correlation in the temperature range of analysis, from 35°C to 500°C. The porosity of the hydrogel was confirmed by SEM.

PHEMA is a well-known biocompatible, transparent, and non-toxic polymer that's used in many medical devices particularly in making contact lenses. Many investigators have tried to convert PHEMA matrix with high surface area due its various inherent properties. In the present study, Radiation assisted SPH PHEMA have been synthesized using single step radiation induced cross linking in presence of PMAETC as a porogen, a degrading polymer in nature. It has high hydrodynamic volume in aqueous solution which helps in phase separation of PHEMA. In this study a green route of synthesis has been adopted to synthesize PHEMA as no toxic cross-linker or initiators was used for its synthesis.

PMAETC is a notable polymer with unique cationic properties, derived from the quaternary ammonium groups in its structure. These properties give it a wide range of applications, especially in areas requiring antimicrobial activity and interaction with negatively charged entities. SPH PHEMA which was synthesized in the first step was further grafted with PMAETC using gamma radiation to incorporate antibacterial property with high water adsorption capacity. Mutual radiation grafting method was adopted.

The SPH PHEMA and PMAETC-g-SPH PHEMA samples were characterized using SEM and Mettler-Toledo DSC 823 and TGA/DSC1 for their morphology and thermal properties respectively. Average pore size of ~300µm was found using SEM as shown in Fig. 1. Thermal properties of the hydrogels were determined in an inert atmosphere of N<sub>2</sub> at a heating rate of 10°C/min for all the experiments. TGA and DSC data was evaluated using the STAR<sup>®</sup> software. TGA and DSC are sophisticated and versatile tools for evaluating and extracting unique information about the thermal behavior of materials, particularly polymers.

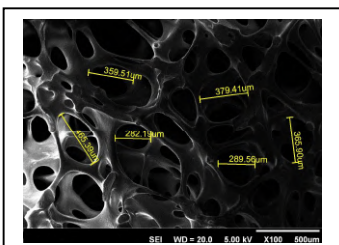


Fig.1. SEM of the PHEMA

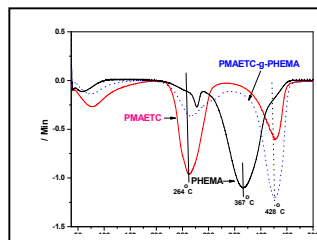


Fig.2. DTGA of samples

Figure 2. shows the DTGA plot of the SPH PHEMA, PMAETC-g- SPH PHEMA and PMAETC. Peak around 75°C correspond to loss of water in PMAETC and PMAETC-g- SPH PHEMA due to hygroscopic nature of quaternary ammonium group in PMAETC but loss is not significant in case of control hydrogel because of its diminished hydrophilicity and hygroscopicity. Thermal stability of all the samples was found

intact up to about 225°C, after which decomposition was observed. Pure PMAETC undergoes two-step decomposition with peaks at around 280°C and 420°C. PMAETC-g-SPH PHEMA hydrogel also reveals peaks at about 280°C and 420 °C corresponding to decomposition of PMAETC component in the porous PHEMA hydrogel and hence confirming the minute incorporation of PMAETC. Incorporation of PMAETC was found responsible for addition of amphiphilic properties to porous HEMA and convert it to versatile matrix suitable for surface modifications with all kinds of monomers (ionic, nonionic, polar and nonpolar monomers).

Various thermal transitions were further recorded and analyzed using differential scanning calorimetry (DSC). Figure 3 confirmed loss of water at ~75°C as depicted in TGA analysis.

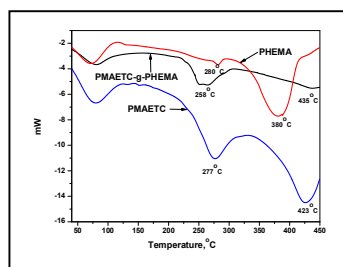


Fig.3. DSC analysis of samples

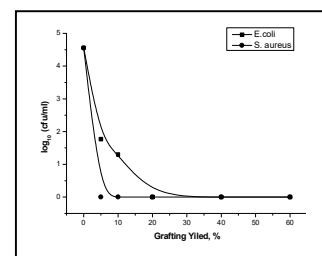


Fig. 4. Antibacterial study

Peaks at about 280°C 420°C again confirmed the incorporation of PMAETC in the PHEMA matrix during radiation assisted cross-linking synthesis of it. All three decompositions have been recorded in DSC as were depicted in TGA analysis.

SPH PHEMA was grafted with PMAETC using mutual irradiation grafting method. Grafting was found as a function of monomer concentration. Water adsorption capacity of the grafted Porous PHEMA was found as function of the grafting yield and 8500% water adsorption was obtained at grafting yield of ~50%. Grafted porous PHEMA was investigated for antibacterial activity for gram positive and gram negative bacterial as *S.aureus* and *E.coli* respectively. 4.5 log cycle and 2.5 log cycles reduction was found for *S.aureus* and *E.coli* after 4hrs of treatment with grafting yield of ~50% grafting yield while it is 4.5 log cycle reduction for both bacteria after 24hrs treatment.

### References

1. A. First, B. Second and C. Third, *Journal*, 12 (2007) 345
2. A. Glavan, D. C. Christodouleas, B. Mosadegh, H-D. Yu, B. S. Smith, J. Lessing, M.T. Fernandez-Abedul, and G. M. Whitesides, *Analytical Chemistry*, 86 (2014)
3. P. Aggarwal, D. Dollimore and K. Heon, *Journal of Thermal Analysis*, 50 (1997)
4. J. J. Maurer, D. J. Eustace and C. T. Ratcliffe, *Macromolecules* (1987)

## Synthesis and Characterization of Polymeric Composite for Fire Retardant Application

Darshana K. Ghonge<sup>a</sup>, Naina Raje<sup>\*a</sup>, Meena Mahipal<sup>b</sup>, C.V. Choudhary<sup>c</sup> and K.A. Dubey<sup>c</sup>

<sup>a</sup>Analytical Chemistry Division, Bhabha Atomic Research Centre, Mumbai – 400094, India

<sup>b</sup>Centre for Fire, Explosive and Environment Safety, DRDO, Delhi – 110054, India

<sup>c</sup>Radiation Technology Development Division, Bhabha Atomic Research Centre, Mumbai – 400094, India

\* Email: [nraje@barc.gov.in](mailto:nraje@barc.gov.in), Ph. No. :022 69293291

### Abstract

EVA and Bentonite based polymeric sheets were synthesized by varying bentonite content from 0 – 80% and using melt extrusion method. Effect of crosslinking on thermophysical properties was studied using chemical / radiation crosslinking by varying the TMPTA concentration (1-10%) or radiation dose (25 – 500 KGy). Based on their thermochemical properties, EVA – Bent 60% composition was selected to study the fire-retardant properties through UL94 test and limiting oxidation Index (LOI) measurements. These studies confirmed that EVA – Bentonite 60%-100KGy composite achieved a V0 rating in UL94 and LOI of 24, indicating excellent fire safety properties. These findings demonstrate the potential of EVA-Bentonite composites for applications requiring enhanced mechanical strength and fire resistance.

The study of polymers and polymeric composite materials is one of the most important and focus areas in chemical and material research with respect to the preparation of advanced functional materials. New nanomaterials with improved properties with respect to the pristine clay minerals may be obtained by surface modification by covalent linkages. According to their ability to entrap and release inorganic/organic moieties, they have found applications in several fields, such as, support for catalyst, environmental remediation and filler for polymeric matrices. Although particulate-filled polymer composites are mature materials with a long history of applications, their structure–property correlations are more complicated than usually assumed. Due to the inherent structural properties of clay minerals, these have been used as filler material for the formation of polymeric composites[1-2].

The experimental work has been carried out to make polymeric composites using EVA 25 as copolymer and Bentonite as filler material in different weight ratios and homogenization through melt mixing method. And, the obtained composite materials were converted into sheets of suitable size for further characterization. It has been observed that mechanical properties like tensile strength increases with increase in bentonite content in the polymer matrix. Also, it was noted that thermal stability of EVA 25 reduces in the presence of higher concentration of Bentonite. These studies suggest that EVA25 – Bentonite composites are better for the applications upto 280 °C in comparison to EVA25 due to the better mechanical properties.

To see the effect of cross linker, radiation and filler material on thermal, mechanical and fire-retardant properties of synthesized polymeric composites, the work involved the preparation of polymeric composites, their characterization with respect to mechanical and thermal properties, radiation effect studies on the properties of synthesized polymeric composites and their fire-retardant behavior in irradiated / unirradiated form.

The experimental work was carried out to prepare polymeric composites using EVA 25 as copolymer and Bentonite as filler material in different weight ratios, with or without addition of crosslinker and homogenization through melt mixing method at 100°C. Thus, obtained composite materials were converted into thin sheets of suitable dimensions for further characterization. Trimethyl propanol triacrylate (TMPTA) was used as a chemical crosslinker while making polymeric composites. It is found that TMPTA crosslinking enhances the mechanical strength of the synthesized polymeric composites. It was found that presence of bentonite is reducing the thermal stability by around 100°C. Probably, under irradiation, bentonite particles may change in their distribution within the polymer matrix due to release of bound water and leading to reduced thermal stability. It was found that mechanical properties of EVA – Bentonite composites were improving on increasing the

bentonite concentration but at 80%, the composite becomes brittle and breaks. Also, on increasing the cross linker TMPTA concentration from 1% to 10%, mechanical properties were found best for EVA – 60%Bent -5%TMPTA polymeric composite, and so, it was used for all other studies.

Gamma irradiation effects on polymeric composite sheets were studied for various mechanical and thermal properties by irradiating the synthesized composites from 25KGy to 500 KGy radiation dose using Co-60 source, and, it was observed that thermal stability reduces on irradiation. Also, it was noted that presence of Bentonite, enhances the thermal conductivity of polymeric composite in unirradiated/ irradiated form.

Fire retardant and flammability tests were performed using UL94 and limiting oxygen index (LOI) tests [3]. It was observed that irradiation improves the fire- retardant properties. EVA – Bentonite 60%-100KGy irradiated composite had V0 rating in UL94 test and LOI as 24. Therefore, this material is suitable to be applied where crucial fire safety concerns exist.

**Conclusion:** The present study highlights the successful development and characterization of EVA-Bentonite polymeric composites with enhanced mechanical, thermal, and fire-retardant properties. The incorporation of Bentonite as a filler improved the tensile strength of the composites, while its higher concentrations reduced thermal stability, likely due to the release of bound water. Crosslinking with TMPTA significantly enhanced mechanical properties, with EVA-60%Bentonite-5%TMPTA identified as the optimal composition. Gamma irradiation further improved fire resistance, with the EVA-60%Bentonite-100kGy composite achieving a V0 rating in UL94 and LOI of 24. These composites demonstrate significant potential for applications demanding superior mechanical strength, thermal conductivity, and fire safety performance.

### References:

1. Bajracharya R. M., Jeelani S., & Rangari V. K., "Influence of clay content on mechanical and thermal properties of polymer nanocomposites." *Composites Part B: Engineering*, 60 (2014) 517-523.
2. Zhang, H., Zhang, Z., & Friedrich, K., "Effect of micro- and nanoparticles on mechanical and tribological properties of polymer composites." *Wear*, 256(11-12) (2004), 1172-1178
3. Maiti, S., & De, P. P., "Fire retardant ethylene-vinyl acetate copolymer compositions." *Polymer Degradation and Stability*, 9(4) (1984), 249-257

### Acknowledgements:

Authors sincerely thank to Dr. Prasun Roy, CFEES, DRDO, Dr. C. N. Patra, Head, Analytical Chemistry Division and Dr. Y. K. Bhardwaj, Associate Director, RC & IG for their continuous support.

## Evaluation of thermal stability and polymorphism in dihydroxy selenolane: a pharmacological agent in cancer management

Prasad P. Phadnis<sup>a,b\*</sup>, Shubham Narang<sup>a</sup>, Ratikant Mishra<sup>a,b\*</sup>

<sup>a</sup>Chemistry Division, Bhabha Atomic Research Centre (BARC), Trombay, Mumbai 400 085, India

<sup>b</sup>Homi Bhabha National Institute (HBNI), Anushaktinagar, Mumbai 400 094, India

\*Email: phadnisp@barc.gov.in, mishrar@barc.gov.in

### Abstract

Thermal studies of organo-selenium compounds and their platinum complexes having potent pharmacological properties in cancer management have been performed. TG-DTA and DSC analyses of dihydroxyselenolane (DHS) were carried out to evaluate the stability and also to check the existence of polymorphism in these compounds, especially in the normal storage temperature range. We observed that some of our selected compounds have exhibited polymorphic forms and while others do not. The compounds with absence of polymorphic forms and stable at room storage conditions have been considered as better choice for their further evaluations in pharmacological studies, which is an important step for future drug development.

In developments of pharmacological agents of diverse organic or organometallic compounds, the existence of polymorphism plays a crucial role, as some individual polymorphous structures have been found to differ in their physicochemical and pharmacological properties. Hence, identification of polymorphism has been considered as one of the important aspects in drug development [1]. It is important to identify the polymorphic forms in the compounds being projected as drugs. The appropriate synthesis procedures hold importance of comprehensive control over the polymorphs at different stages of product development [2]. Among the diverse chemical compounds, the organo-selenium compounds or their metal complexes have emerged with highly potential medicinal properties. The organoselenium compounds have exhibited potent pharmacological properties like antioxidant, anti-inflammatory, radioprotection and most importantly anticancer and radiosensitizers during radiotherapy. Hence, in analogy with other chemical drugs, the existence of polymorphism and its effects were studied in case of selenium compounds also [3]. In our efforts to develop anticancer drugs, we have designed and synthesized diverse organoselenium-based compounds. Some of them with potent cyto-toxicities were evaluated for their physico-chemical properties. In this effort, we have evaluated these compounds for their thermal stability and existence of polymorphism. Additionally, isolation of different polymorphic forms was achieved by recrystallizing the compounds by different appropriate solvents [4].

In the present work, we have synthesized the dihydroxy selenolane (DHS) (an organoselenium compound) [5] and its complex with Pt(II) as a cisplatin analogue. We found the potential pharmacological properties of DHS as an antioxidant, glutathione peroxidase (GPx) enzyme mimic, useful for ulcer curation and its Pt(II) complexes in cancer management. The results of this work are discussed here.

### Synthesis

**Dihydroxy selenolanes (DHS):** The DHS was synthesized by slight modifications in literature reports [5, 6] via the reaction of an aqueous NaHSe with 1,3-butadiene diepoxide (1:1) at 0-5 °C followed by extraction with diethyl ether and recrystallization from the same extract.

**Platinum(II) complexes with DHS:** Reaction of DHS with Pt(II) precursors and aquated cisplatin have afforded the Pt(II)-DHS complexes.

### Results and discussion

These compounds were characterized by microanalyses, NMR (<sup>1</sup>H, <sup>13</sup>C{<sup>1</sup>H}, <sup>77</sup>Se{<sup>1</sup>H}, <sup>195</sup>Pt{<sup>1</sup>H}), FT-IR spectroscopy as well as the crystal and molecular structural elucidations for DHS derivative and DHS-Pt complexes were performed by single crystal XRD analyses. The thermal stability and evaluation for existence of polymorphism in these compounds were evaluated by TG-DTA and DSC analyses, prior to studies of their biological and/or anticancer activities. The cytotoxicity of these compounds against cancer cell lines were evaluated by MTT assays which revealed their utility in cancer management. At this point, we will focus on the results pertaining to thermal studies.

#### Thermal Studies by TG-DTA and DSC analyses

Before considering dihydroxy selenolanes for any pharmacological application, its thermal stability was assessed by TG-DTA and DSC measurements. The mass loss and heat effects (TG-DTA) were plotted as a function of temperature to assess the thermal stability of test compounds. The test samples taken in a platinum crucible was heated at a heating rate of 5 K/min under a flow of argon on a Setaram SETSYS evo TG-DTA instrument. In DSC measurements, temperature and the enthalpy change involved in phase transition of the samples were determined. In this case the sample sealed in an aluminium (Al) crucible was subjected to thermal cycle at a heating/cooling rate of 5 K/min under a flow of argon employing a Mettler DSC1 instrument and data were analyzed by STAR<sup>c</sup> software.

Figure 1 shows the TG-DTA plot of dihydroxy selenolane compound. The TG plot of the compound shows complete mass loss (100%) of the sample in the temperature range 120 to 225 °C. The DTA plot shows a broad endothermic peak in the temperature range 68-100 °C which is attributed to the melting of DHS. This endothermic peak was followed by another broad endothermic peak in the temperature range 175-225 °C attributable to thermal decomposition of DHS.

Although, it is expected that the expected mass loss due to thermal decomposition of about 50%; we observed the complete mass loss which could be due to the vaporization loss of elemental Se formed during thermolysis in a single step. This complete single step mass loss was reflected in the second DTA endotherm. The thermogram indicated the thermal stability of DHS in the temperature range of 25-175 °C which satisfies the usual room storage conditions (25-45 °C).

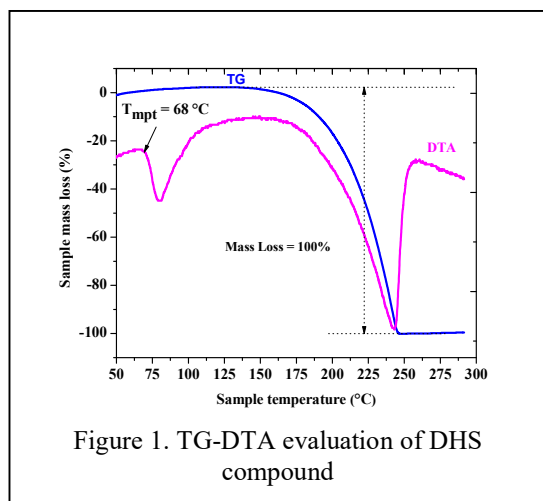


Figure 1. TG-DTA evaluation of DHS compound

To assess any phase transformation, DSC analysis of DHS was performed in the temperature range 25 to 125 °C (Figure 2). As is evident from Figure 2, the endothermic peak with an onset temperature of 79.98 °C involving a small energy of 104 J/g was observed which is attributable for a phase change leading to melting of DHS which is in good agreement with experimental detection of melting point. Most importantly, no other endotherm in a range of 25-45 °C was observed, which is the common storage temperature range across the Globe. Further, it confirms the absence of any minor crystallographic modification in the molecule *i.e.*, absence of polymorphism.

From the thermal studies it is clear that DHS stable in the temperature window 25 to 125 °C. In this temperature window it retains the same crystal lattice arrangement and can therefore be used for biological applications, without any further recrystallization within specific organic solvents to isolate stable polymorphic forms.

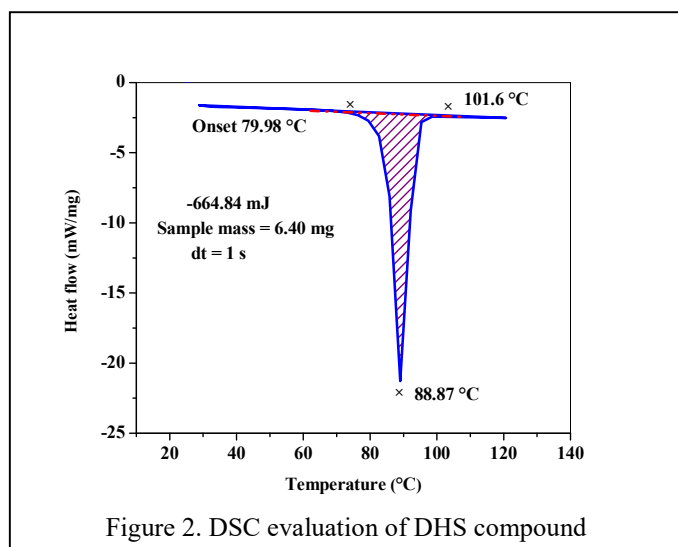


Figure 2. DSC evaluation of DHS compound

## References

1. R. Hilfiker In: Polymorphism: In the Pharmaceutical Industry, R. Hilfiker (Ed.), (2006) Wiley-VCH Verlag GmbH & Co. KGaA; Weinheim, Germany.
2. S. Byrn, R. Pfeiffer, M. Ganey, C. Hoiberg and G. Poochikian, *Pharm. Res.*, 12 (1995) 945-954.
3. D. Plano, E. Lizarraga, J. A. Palop and C. Sanmartín, *J. Therm. Anal. Calorim.*, 105 (2011) 1007-1013.
4. P. P. Phadnis, A. Kunwar, M. Kumar, R. Mishra, A. Wadawale, K. I. Priyadarsini, V. K. Jain, *J. Organomet. Chem.*, 852 (2017) 1-7.
5. P. P. Phadnis, A. Wadawale, K. I. Priyadarsini, V. K. Jain and M. Iwaoka, *Tetrahedron Lett.*, 56 (18) (2015) 2293-2296.
6. M. Iwaoka, T. Takahashi, S. Tomoda, *Heteroat. Chem.*, 12 (2001) 293-299.

## Conclusions

The presented studies by TG-DTA revealed the thermal stability of DHS compound at usual storage room conditions. Additionally, the DSC analyses revealed that the DHS is existing exclusively in only one form at room storage conditions (25-45 °C). This reveals the appropriate uniform synthesis or production strategy of a DHS molecule to be evaluated for further pharmacological applications.

## Acknowledgements

The authors are thankful to the Director, Chemistry Group and Head, Chemistry Division, BARC for encouragement and support for this work.

## Exploring Potential of Pluronics Induced Protein Fibrils as Drug Delivery Agents: Mechanistic Understanding via Biophysical Approach

Anu Jain<sup>a</sup>, and Nand Kishore<sup>a\*</sup>

<sup>a</sup>Department of Chemistry, Indian Institute of Technology Bombay, Powai, Mumbai – 400076, India

\* Corresponding author's email- [nandk@chem.iitb.ac.in](mailto:nandk@chem.iitb.ac.in)

### Abstract

The impact of pluronics (F68 and F127) on the fibrillation process of protein lysozyme has been investigated. This was carried out to determine whether pluronics may either encourage or prevent the fibrillation process. Additionally, the use of fibrils for drug delivery has been investigated. Mechanistic insights into protein fibrillation and its applications are obtained through the combination of calorimetric and spectroscopic techniques.

Understanding misfolding and aggregation of proteins is important in disciplines of proteins, pharmaceutical, and biomedical fields. Protein misfolding and assembly results in formation of amyloid fibrils leading to crippling conditions referred to as "amyloidosis" [1,2]. They are fundamentally robust and insoluble nanofibres with considerable potential as nanotechnology and bionanotechnology materials. This work examines lysozyme fibrillation in the presence of pluronics (F68 and F127).

In an A-B-A conformation, pluronic copolymers consist of three blocks: two hydrophilic poly(ethylene oxide) blocks (PEO, part A) and a hydrophobic poly(propylene oxide) block (PPO, part B). When pluronic copolymers are present in an aqueous solution, they self-assemble to form polymeric micelles, or micellar-type nanostructures, at concentrations higher than critical micellar concentration. Compared to micelles based on surfactants, these micelles are substantially more stable because they consist of a hydrophobic core and a hydrophilic surface [3,4].

A combination of calorimetry and spectroscopy has been used to obtain mechanistic insights into effect of pluronics on the protein aggregation/ fibrillation. Isothermal titration calorimetry results suggest that interaction of protein with F68 is exothermic while with F127 it is endothermic due to more hydrophobicity of the latter pluronic. The conformation of protein fibrils formation was examined by TEM images and ThT binding assay, which demonstrated that pluronics promoted fibrillation process rather than inhibiting it. The pre- and post-micellar concentrations of pluronics on interaction with protein (at varying fibrillation stages) exhibit a reduction in  $\Delta H_m^o$  value as the incubation time increases. This indicates formation of amorphous aggregates due to which endothermic enthalpy is observed. AGGREGSCAN program was used to identify aggregation-prone regions of protein. According to analysis, pluronics interact with the areas that are not prone to aggregation, exposing hotspot areas to the solvent and triggering formation of fibrils.

The knowledge of these fascinating macromolecular assemblies has been progressively expanding and deepening, from identifying the role of protein amyloid fibrils in neurodegenerative diseases to their recent uses in high-performance materials [5]. Consequently, the potential use of these formed aggregates for drug delivery was explored. Interaction of anticancer drugs (5-fluorouracil and cytarabine) with the protein fibril systems was studied using calorimetry and spectroscopy.

The results suggest one less order of binding for 5-fluorouracil with protein fibril systems than with cytarabine.

Consecutively, static fluorescence quenching was observed in presence of these drugs. Moreover, cytotoxicity of the protein fibril system was examined with and without these anticancer drugs. UV-visible spectroscopy was used for adsorption studies.

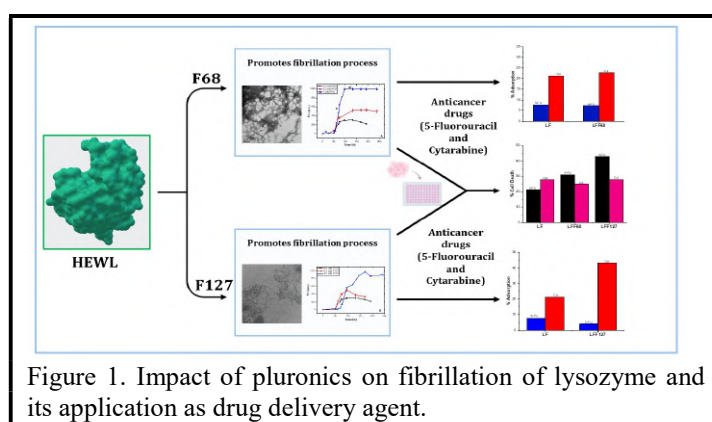


Figure 1. Impact of pluronics on fibrillation of lysozyme and its application as drug delivery agent.

When cytarabine is used with protein fibrils, the hydrophobic interaction predominates, according to endothermic enthalpy of interaction, but the electrostatic interaction predominates with 5-fluorouracil. On the other hand, the former drug exhibited more adsorption on the surface of protein fibrils compared to the latter. Therefore, it is concluded that cytarabine has weak adsorption on fibril surfaces and is readily desorbed in cells, whereas 5-fluorouracil has relatively strong adsorption; as a result, the complex of LFF127 and 5-FU is fatal to malignant cells.

These results are beneficial for exploring numerous applications of the formed protein fibrils/aggregates and in providing suitable strategies for the design and development of drug delivery agents.

### References

1. P. Ghosh, P. De, ACS Appl Bio Mater 3 (2020) 6598–6625.
2. J.D. Sipe, M.D. Benson, J.N. Buxbaum, S. Ikeda, G. Merlini, M.J.M. Saraiva, P. Westermark, Amyloid 23 (2016) 209–213.
3. Y. Yamamoto, K. Yasugi, A. Harada, Y. Nagasaki, K. Kataoka, Journal of Controlled Release 82 (2002) 359–371.
4. G. Pérez-Sánchez, N. Schaeffer, A.M. Lopes, J.F.B. Pereira, J.A.P. Coutinho, Physical Chemistry Chemical Physics 23 (2021) 5824–5833.
5. M. Zaman, A.N. Khan, Wahiduzzaman, S.M. Zakariya, R.H. Khan, Int J Biol Macromol 134 (2019) 1022–103

## Quantitative Calorimetric and Spectroscopic Analysis of Protein Interactions with Solid Lipid Nanoparticles (SLNs)

Jyoti Rathee<sup>a</sup>, and Nand Kishore\*

<sup>a</sup> Department of Chemistry, Indian Institute of Technology Bombay, Powai, Mumbai, India.

\* nandk@chem.iitb.ac.in, 0-22-25767157

### Abstract

This study elucidates the quantitative analysis of the thermodynamic properties governing the interactions between Bovine Serum Albumin (BSA) and lipid nanoparticles, employing a combination of calorimetric and spectroscopic techniques. The size of prepared SLNs after incubation with the BSA is almost similar to pristine SLNs, suggesting no significant adsorption of the protein on SLNs' surface. The energetics of thermodynamic interactions highlight the dominant role of hydrophobic interactions between BSA and lipid nanoparticles. Overall, the results demonstrate less possibility of weak protein corona formation on the surface of the lipid nanoparticles.

With the booming development of nano-medicines, significant attention has been paid to biocompatible solid lipid nanoparticles (SLNs) owing to their desired nano-assembly properties such as long-term stability, longer circulation time, higher drug loading, and encapsulation efficiency [1]. SLNs are lipid-based nano-assemblies that consist of core-shell structures having a hydrophobic lipid core surrounded by a hydrophilic surfactant shell.

When the lipid nanoparticles are administered in in-vivo, their bio-distribution, metabolism, and cellular internalization are significantly affected by the diversified biological fluids having different pH and abundant biomolecules (amino acids and peptides) [3-5]. After administration of NPs, a diverse range of biomolecules like proteins can adsorb on their surface leading to protein corona formation. With few exceptions, protein corona formation takes place with almost all known NPs. Interaction of a variety of molecules with protein corona leads to changes in size, surface potential, and conformational changes in the protein.

Therefore, the study of the binding interactions of the SLNs with the serum albumins will pave the way to understanding the bimolecular recognition process essential for the rational drug design process. The current investigation delineates the quantitative analysis of the thermodynamic signatures associated with Bovine Serum Albumin (BSA) interactions with lipid nanoparticles using a combination of calorimetric and spectroscopic techniques.

The particle size of the prepared SLNs is  $(100 \pm 3)$  nm which after incubation with SLNs increases to  $(120 \pm 5)$  nm. The energetics of the interactions of the BSA with the lipid nanoparticles were examined using fluorescence and isothermal calorimetry. The thermodynamic parameters accompanying the interactions ( $\Delta H_{\text{int}}^{\circ} = + (9.8 \pm 0.2)$  kJ/mol and  $\Delta S_{\text{int}}^{\circ} = + (13.96 \pm 3.0)$  kJ/mol suggests the association is hydrophobic.

The interactions between the hydrophobic part of the lipid nanoparticles and hydrophobic patches of the BSA molecule are indicated. SLNs showed binding affinity of the order of  $10^2$  which suggests the weak interactions accompanied by the blue shift in the fluorescence spectra. UV-visible spectra also confirmed the change in the microenvironment of the tryptophan towards a more nonpolar environment with an affinity of the order of  $10^3$ .

Differential scanning calorimetry results suggest the stabilization of the BSA in the presence of the SLNs. Further, CD spectroscopic signatures reveal a small increase in the  $\alpha$ -helicity of the secondary structure, while the tertiary structure of protein is maintained. It is known that the development of the protein corona on the surface of the nanoparticles poses a significant challenge to the bench-to-bedside approach of the targeted drug delivery systems both in terms of unfavorable distribution and by interfering with the targeting of the desired site. To design a targeted drug delivery system, the present work will provide new insights into the mechanical aspects of comprehending the interactions of lipid nanoparticles with protein.

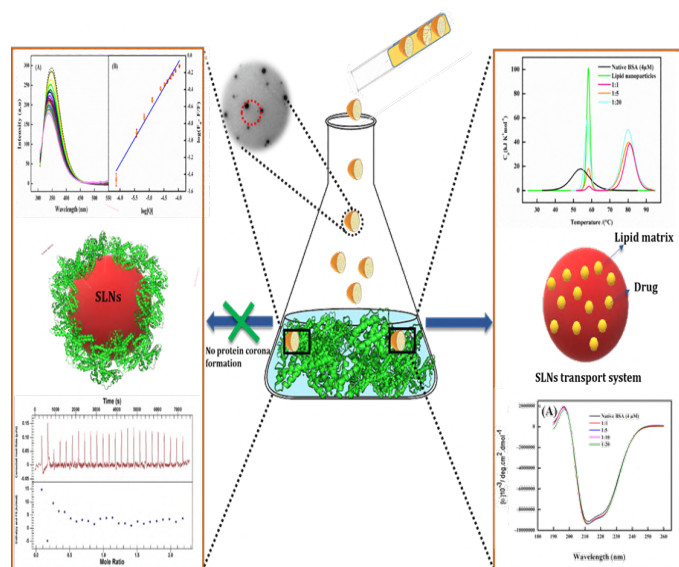


Figure 1: Schematic representation of the interaction of the SLNs with the BSA

### References

- [1] H. Moss, P. Popova, S.R. Hadrup, K. Astakhova and M. Taskova, *Mol. Pharm.* 16 (2019) 2265–2277.
- [2] W. Wang, Z. Huang, Y. Li, W. Wang, J. Shi, F. Fu, Y. Huang, X. Pana and C. Wu, *Acta Pharm. Sin. B.* 11 (2021) 1030–1046
- [3] S. Das, W.K. Ng and R.B.H. Tan, *Eur. J. Pharm. Sci.* 47 (2012) 139–151.
- [4] J. Wolfram, Y. Yang, J. Shen, A. Moten, C. Chen, H. Shen, M. Ferrari and Y. Zhao, *Acta Pharm. Sin. B.* 124 (2014) 17–24.
- [5] P. Del Pino, B. Pelaz, Q. Zhang, P. Maffre, G.U. Nienhaus and W.J. Parak, *Mater. Horizons.* 1 (2014) 301–308

## Temperature and Solvent Dependent Aggregation Characteristics of Biocompatible Ionic and Non-ionic Surfactants

M. Basu<sup>a\*</sup><sup>a</sup>Chemistry Division Bhabha Atomic Research Centre, MumbaiEmail: [deepa@barc.gov.in](mailto:deepa@barc.gov.in)**Abstract**

Self-assembly of bile salt sodium deoxycholate is significantly influenced by solvent polarity and the enthalpy changes involved in the self-assembly process are exothermic. For non-ionic surfactant Brij 35 both solute concentration and temperature play significant roles in modulating the self-assembly behavior and structural changes of the formed aggregates since the aggregation process in Brij 35 is strongly dependent on hydration pattern that get affected with increase of solute concentration and temperature

Salt of bile acids, namely sodium deoxycholate (NaDC) is a well known biocompatible surfactant having high potential in solubilization of poorly water soluble drugs and acts as an efficient permeation enhancer in pharmaceutical formulations [1]. Amongst biocompatible nonionic surfactants, Brij 35 is well known as an efficient solubilizer and emulsifier and is widely used in drug formulations [2]. Hence it is important to know their self-assembly behaviour in different biocompatible low-melting solvents and as function of temperature.

In view of this aggregation behavior of NaDC was studied in different biocompatible solvents and water at 25°C and 37°C using isothermal titration calorimetry with an initial 100 mM stock solution. Aggregation behavior of Brij 35 was studied in water at different temperature using density, sound velocity and isothermal calorimetry (ITC) measurements. For the ITC measurements a stock solution of 5.4 mM was used. The calorimetric studies were done using Microcal VPITC. Density and sound velocity measurements were carried out using DSA-5000M.

**Table 1.** Critical micellization constant (CMC) and enthalpy of micellization of NaDC in different solvents at room (25°C) and physiological temperature (37°C)

Micellization medium	CMC (mM)	Micellization Enthalpy (cal/mole)
Water at 25°C	10.3	-210
Water at 37°C	9.9	-651
50 wt% Glucose-urea at 25°C	25	-404
50 wt% Glucose-urea at 37°C	24	-820
50 wt% Glucose-fructose at 25°C	7.6	-2041
50 wt% Glucose-fructose at 37°C	7.8	-1965

Aggregation characteristics of NaDC, as obtained from calorimetry data are presented in Table 1. The CMC values of NaDC in these solvents are seen to be negligibly dependent on temperature. However, they are very sensitive to the polarity of the medium. Among the three medium, glucose-fructose is seen to have lowest polarity since the polarity directly affects the CMC values. Glucose-urea solvent is found to exhibit highest polarity, even higher than water. Glucose, fructose and urea are all known to be structure breakers for water. The large variations in CMC values give an indication about the subtle changes in hydration pattern of these organic molecules when present in combination in aqueous medium. Enthalpy of micellization is exothermic at all temperatures and in all three solvents since micelle formation involves liberation of counterions which get extensively hydrated thereby releasing heat. A noteworthy feature is significantly higher enthalpy of micellization for NaDC in hydrated glucose-fructose as compared to the other two. A probable reason is extensive hydration of glucose-fructose moiety as compared to pure water or glucose-urea on release of water molecules from monomers as they form aggregates. This also supports the overall lower polarity of the medium that is reflected in low CMC values.

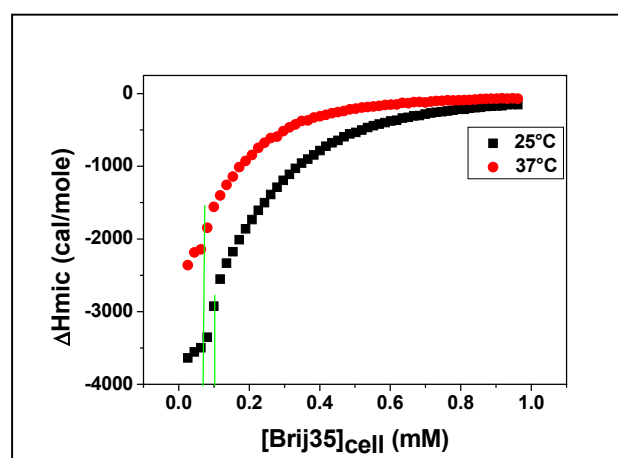


Figure 1 Micellization in Brij 35 at room and physiological temperature using ITC (Enthalpy change plotted as a function of cell concentration of the surfactant)

ITC studies for 5.4 mM aqueous solutions were carried out between 10–40 °C and showed an increase in CMC from 0.092 mM at 10°C to a maximum of 0.1 mM at 25°C with a steady decrease at higher temperature. Decrease in CMC with increase in temperature is shown in Figure 1 above, indicated by the green line. Enthalpy of micellization showed a minimum of 2580 cal/mole at 25°C. Unlike NaDC, self-assembly of Brij 35 is highly sensitive to temperature. And both CMC and micellization enthalpy are strongly dependent on the hydration pattern of the oxyethylene chains and the ether groups that vary significantly with temperature. The hydration patterns of oxyethylene chains also affect other thermo-physical properties like apparent molar volume, isentropic compressibility etc that reflect the compactness of packing of the polyoxyethylene chains and their variations with temperature.

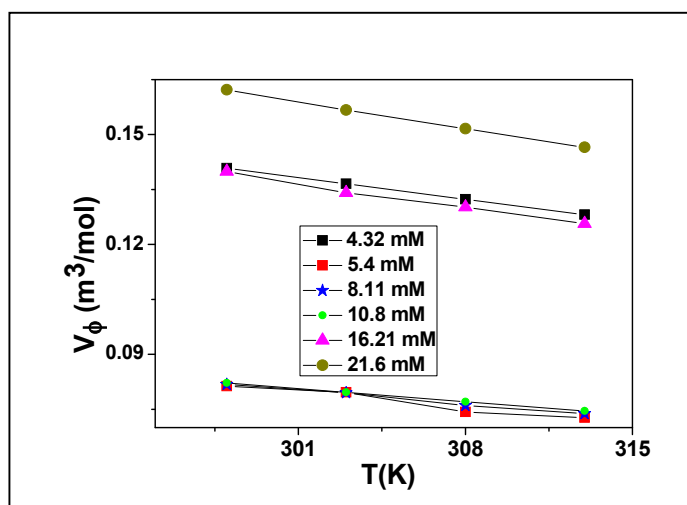


Figure 2 Variation of apparent molar volume of Brij 35 in aqueous solution at different concentrations as function of temperature

As seen in Fig 2 the apparent molar volume decreased with increase of temperature and this is a direct effect of increased dehydration.

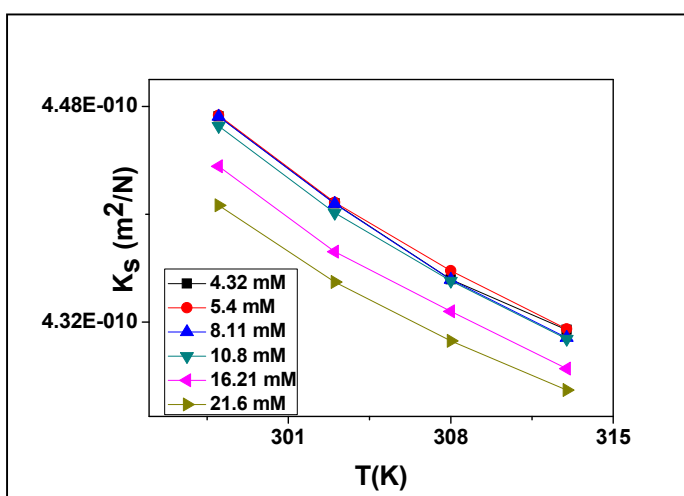


Figure 3 Variation of isentropic compressibility of Brij 35 in aqueous solution at different concentrations as function of temperature

Isentropic compressibility reflects the variation of volume change with pressure of dissolved solutes and reflects the rigidity of solute-solvent structure since it is directly dependent on the density of the solution and is related to transmission of sound velocity through the medium. Hence this thermodynamic parameter is very sensitive to changes of solute concentration and temperature.

From Figure 3 it is evident that at any particular temperature compressibility decreases with increased concentration of the surfactant indicating an increase in rigidity of the oxyethylene chains that signifies increase hydration around the chains. The same effect, namely a decrease in its value is observed for a particular concentration with increase in temperature which could be due to released water molecules that form their own H-bonded rigid network around the surfactant assemblies.

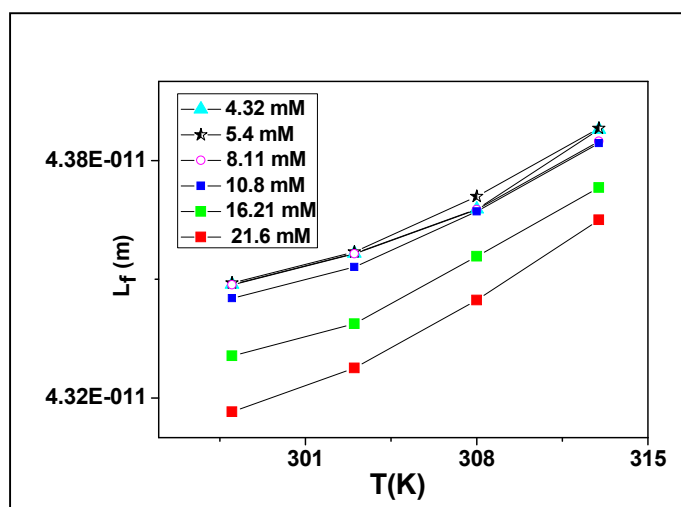


Figure 4 Variation of intermolecular free length of Brij 35 aggregates or monomers in aqueous solution at different concentrations as function of temperature

Trend of intermolecular free length variation with temperature indicates formation of water structures around the micelles that separate the aggregates from each other thereby increasing the value. All these properties showed an abrupt jump above 10 mM concentration, at any particular temperature, indicating an increased rigidity of the self-assembled structures above this concentration that signifies a conformation change of polyoxyethylene chains within the micelles.

#### References

1. T. R. Bjerck, P. Severinno, S. Jain, C. Marques, A. M. Silva, T. Pashinova and E. B. Souto, *Bioengineering*, 8 (2021) 115
2. C. Feng-Hung, C. Lang Fang, M. Hui Liao, J. You Fang, *Int. J. Pharm.*, 335 (2007) 193



## Evaluation polymorphism in a cytotoxic 2,2'-dipyridyl diselenide (Py<sub>2</sub>Se<sub>2</sub>): a step A Step closer to development of anticancer drug

Prasad P. Phadnis<sup>a,b\*</sup>, Shubham Narang<sup>a</sup>, Ratikant Mishra<sup>a,b\*</sup>

<sup>a</sup>Chemistry Division, Bhabha Atomic Research Centre (BARC), Trombay, Mumbai 400 085, India

<sup>b</sup>Homi Bhabha National Institute (HBNI), Anushaktinagar, Mumbai 400 094, India

\*Email: phadnisp@barc.gov.in, mishrar@barc.gov.in

### Abstract

The thermal evaluations of 2,2'-dipyridyl diselenide (Py<sub>2</sub>Se<sub>2</sub>), a potent cytotoxic compound have been performed with TG-DTA and DSC analyses to access the stability and to check the existence of polymorphism in the titled compound, especially in the normal storage temperature ranging from room temperature till its melting. We observed absence of polymorphic forms and the compound was stable at room storage conditions, which is an important step for future drug development. The results have indicated that the Py<sub>2</sub>Se<sub>2</sub> compound may be considered as better choice for its further evaluations in pharmacological studies.

Evaluation of thermal stability at room storage conditions and finding an existence of polymorphism plays a crucial role in the developments of pharmacological agents of diverse organic or organometallic compounds. Since, it has been evidenced that some individual polymorphous structures have been found to differ considerably in physicochemical and pharmacological properties. Hence, finding the existence of polymorphism has been thought as an important aspect in drug development [1], along with diverse physico-chemical properties need to fulfilled. Hence, identification of polymorphic forms in the compounds being projected as drugs, is an important task. It was found that the appropriate strategies of synthesis govern the importance of comprehensive control for existence of polymorphic forms at different stages of product development [2]. In the Global efforts for anticancer drug development, diverse chemicals-based compounds like organo-selenium compounds as well as their metal complexes have been emerged as highly potential pharmacological agents. The organoselenium compounds have exhibited potent pharmacological properties like anti-inflammatory, radioprotective, antioxidant, and most importantly anticancer and radio-sensitizing agents during cancer treatments by radiotherapy. In view of this, similar to other chemical drugs, the existence of polymorphism and its effects were studied in case of selenium compounds also [3]. In our program of developing anticancer drugs, we have designed and synthesized organoselenium-based compounds by using diverse heterocyclic organic moieties like pyridyl, pyrimidyl substituted rings which are known to constitute the diverse biomolecules, and hence are biocompatible. Some of them with potent cyto-toxicities were evaluated for their physico-chemical properties. In this effort, we have evaluated these compounds for their thermal stability and existence of polymorphism. Additionally, isolation of different polymorphic forms was achieved by recrystallizing the compounds by different appropriate solvents [4].

In efforts, we have synthesized the 2,2'-dipyridyl diselenide (Py<sub>2</sub>Se<sub>2</sub>) which has exhibited antioxidant [5] as well as cytotoxic activity against human non-small cell lung carcinoma (A549) and human normal lung fibroblast (WI38) cells [6]. We found that the Py<sub>2</sub>Se<sub>2</sub> caused significant DNA damage *via* apoptosis. Hence, before further pharmacological studies leading to drug development, it was necessary to evaluate thermal effect on Py<sub>2</sub>Se<sub>2</sub>. The results of this work are discussed here.

### Synthesis

**2,2'-dipyridyl diselenide (Py<sub>2</sub>Se<sub>2</sub>):** The Py<sub>2</sub>Se<sub>2</sub> was synthesized by slight modifications in literature reports. In a round bottom flask with an inert atmosphere of argon, the 2-bromopyridine (7.5 g, 47.25 mmol) was added to an aqueous brownish solution of Na<sub>2</sub>Se<sub>2</sub> (prepared from selenium powder

(3.75 g, 47.5 mmol) in deoxygenated water and sodium borohydride (1.8 g, 47.25 mmol) at 0 °C with stirring. The resulted reaction mixture was refluxed for 3 h till the solution became yellow containing a small amount of suspended selenium. The hot reaction mixture was filtered and allowed to cool to room temperature, whereupon dipyridyl diselenide (3.0 g, 42%) crystallized out as yellow crystals and was filtered using a Buchner funnel and dried *in-vacuo*.

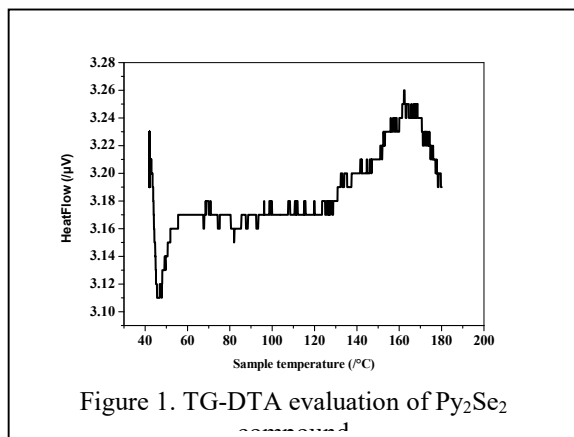
### Results and discussion

The titled compound was characterized by microanalyses, NMR (<sup>1</sup>H, <sup>13</sup>C{<sup>1</sup>H}, <sup>77</sup>Se{<sup>1</sup>H}), FT-IR spectroscopy. The thermal stability and evaluation for existence of polymorphism in this compound was evaluated by TG-DTA and DSC analyses, prior to escalate its biological and/or anticancer activities. The cytotoxicity of these compounds against cancer cell lines were evaluated by MTT assays which revealed their utility in cancer management. At this point, we will focus on the results pertaining to thermal studies.

### Thermal Studies by TG-DTA and DSC analyses

Before considering dihydroxy selenolanes for any pharmacological application, its thermal stability was assessed by TG-DTA and DSC measurements. The mass loss and heat effects (TG-DTA) were plotted as a function of temperature to assess the thermal stability of test compounds. The test samples taken in a platinum crucible was heated at a heating rate of 5 K/min under a flow of argon on a Setaram SETSYS evo TG-DTA instrument. In DSC measurements, temperature and the enthalpy change involved in phase transition of the samples were determined. In this case the sample sealed in an aluminium (Al) crucible was subjected to thermal cycle at a heating/cooling rate of 5 K/min under a flow of argon employing a Mettler DSC1 instrument and data were analyzed by STAR<sup>c</sup> software.

Figure 1 shows the TG-DTA plot of Py<sub>2</sub>Se<sub>2</sub>. The TG plot of the compound shows clear melting at ~ 50 °C. The DTA plot shows a broad endothermic peak in the temperature range 65-70 °C which is attributed to the melting of Py<sub>2</sub>Se<sub>2</sub>. This endothermic peak was followed without any change in heat flow, attributable to thermal stability of Py<sub>2</sub>Se<sub>2</sub> which has indicated that although the compound has melted, it does not decompose till 200 °C. Hence, it was found that there was no mass loss since no thermal decomposition was observed. The thermogram indicated the thermal stability of Py<sub>2</sub>Se<sub>2</sub> in the temperature range of 25-200 °C which satisfies the usual room storage conditions which are possible in 25-45 °C range for storage.

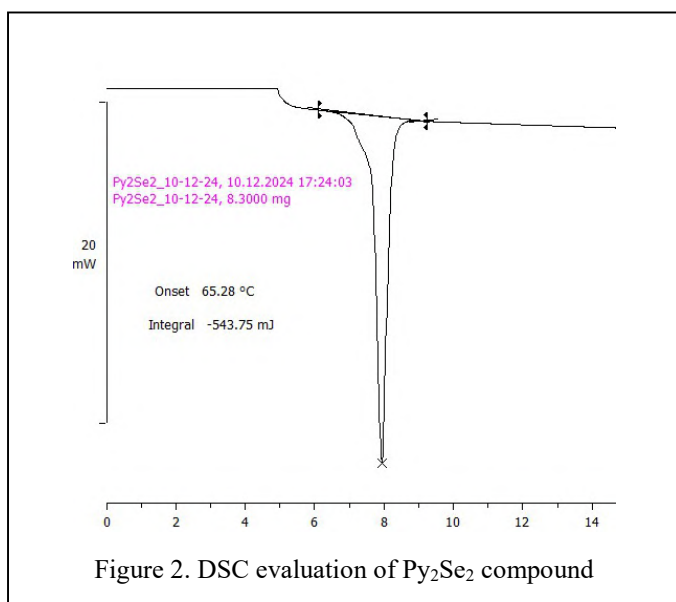


To assess any phase transformation, DSC analysis of  $\text{Py}_2\text{Se}_2$  was performed in the temperature range 25 to 125 °C (Figure 2). As is evident from Figure 2, the endothermic peak with an onset temperature of 62.28 °C involving a small energy of 65.1 J/g was observed which is attributable for a phase change leading to melting of  $\text{Py}_2\text{Se}_2$  which is in good agreement with experimental detection of melting point. Most importantly, no other endotherm in a range of 25-45 °C was observed, which is the common storage temperature range across the Globe. Further, it confirms the absence of any minor crystallographic modification in the molecule *i.e.*, absence of polymorphism.

From the thermal studies it is clear that  $\text{Py}_2\text{Se}_2$  stable in the temperature window 25 to 125 °C. In this temperature window it retains the same crystal lattice arrangement and can therefore be used for biological applications, without any further recrystallization within specific organic solvents to isolate stable polymorphic forms.

## References

1. R. Hilfiker In: Polymorphism: In the Pharmaceutical Industry, R. Hilfiker (Ed.), (2006) Wiley-VCH Verlag GmbH & Co. KGaA; Weinheim, Germany.
2. S. Byrn, R. Pfeiffer, M. Ganey, C. Hoiberg and G. Poochikian, *Pharm. Res.*, 12 (1995) 945-954.
3. D. Plano, E. Lizarraga, J. A. Palop and C. Sanmartín, *J. Therm. Anal. Calorim.*, 105 (2011) 1007-1013.
4. P. P. Phadnis, A. Kunwar, M. Kumar, R. Mishra, A. Wadawale, K. I. Priyadarsini, V. K. Jain, *J. Organomet. Chem.*, 852 (2017) 1-7.
5. A. S. Hodage, C. P. Prabhu, P. P. Phadnis, A. Wadawale, K. I. Priyadarsini and V. K. Jain, *J. Organomet. Chem.*, 720 (2012) 19-25.
6. V. V. Gandhi, P. P. Phadnis and A. Kunwar, *Metallomics*, 12 (2020) 1253-1266.



## Conclusions

The presented studies by TG-DTA revealed the thermal stability of  $\text{Py}_2\text{Se}_2$  compound at usual storage room conditions. Additionally, the DSC analyses revealed that the  $\text{Py}_2\text{Se}_2$  is existing exclusively in only one form at room storage conditions (25-45 °C). This reveals the appropriate uniform synthesis or production strategy of a  $\text{Py}_2\text{Se}_2$  molecule to be evaluated for further pharmacological applications.

## Acknowledgements

The authors are thankful to the Director, Chemistry Group and Head, Chemistry Division, BARC for encouragement and support for this work.

## Thermal Study of *Bombyx Mori* Silk Fibroin Film obtained through Degumming Process for Biomaterial Applications

Sanasam Yaiphabi<sup>a, b</sup>, Sanjenbam Kabita<sup>a</sup>, Sorokhaibam Jibankumar Singh<sup>a</sup>, Shamjetshabam Babeeta Chanu<sup>a</sup>, Langlen Meinam<sup>a</sup>, Thota Manoj Kumar<sup>d</sup>, R. Mishra<sup>b, c</sup>, Senjam Sunil Singh<sup>a</sup>, Laishram Rupachandra Singh<sup>a</sup>, Sanjenbam Kunjeshwori Devi<sup>a</sup>, Raghumani Singh Ningthoujam<sup>b, c, \*</sup>

a. Department of Biochemistry, Manipur University, Canchipur, Imphal - 795003, India

b. Chemistry Division, Bhabha Atomic Research Centre, Mumbai – 400085, India

c. Homi Bhabha National Institute, Mumbai – 400094, India

d. Mechanical Metallurgy Division, Bhabha Atomic Research Centre, Mumbai – 400085, India

\*Corresponding author: [rsn@barc.gov.in](mailto:rsn@barc.gov.in), 25592321

In the present study, silk fibroin films are successfully fabricated from the regenerated silk fibroin solution prepared from the dissolution of degummed silk fiber in calcium nitrate solution. The thermal stability of silk fibroin film is characterized by Fourier-transform infrared spectroscopy, thermogravimetric analysis, and differential scanning calorimetry. Silk fibroin film is thermally stable upto 225 °C. Therefore, this study supports the potential utilization of silk fibroin film as biomaterial for various biomedical applications.

### 1. Introduction

Silk fibroin, derived from the cocoons of *Bombyx mori*, is a promising biomaterial for biomedical applications due to its biocompatibility, biodegradability, mechanical strength, and thermal stability [1]. It can be processed into films, hydrogels, sponges, and nanoparticles using regenerated silk fibroin solutions. Previous studies dissolved degummed silk fibroin fibers in lithium bromide and lithium thiocyanate, but improved dissolution methods are needed to enhance biomaterial properties. In this study, calcium nitrate tetrahydrate was used as a solvent to prepare regenerated fibroin solutions for film fabrication. The films were characterized using FTIR, TGA, and DSC to assess functional groups and thermal stability.

### 2. Experimental Section

#### 2.1 Materials

*Bombyx mori* cocoon used in this study was provided by RSRS (Regional Sericulture Research Stations), Imphal, Manipur. Ethylenediaminetetraacetic acid (EDTA), Sodium carbonate ( $\text{Na}_2\text{CO}_3$ ), Sodium hydroxide ( $\text{NaOH}$ ), were purchased from HiMedia and Calcium nitrate tetrahydrate ( $\text{Ca}(\text{NO}_3)_2 \cdot 4\text{H}_2\text{O}$ ) was purchased from Merck. Deionized (DI) water (Milipore, USA) was used in this study.

#### 2.2 Methods:

##### 2.2.1 Preparation of regenerated silk fibroin film

Briefly, following the slight modified protocol [2], *Bombyx mori* cocoons were washed, dried, and cut into small pieces. 5 g of cocoon pieces were demineralized in 200 mL of 1 M ethylenediaminetetraacetic acid (EDTA) at 40 °C for 72 h to remove minerals. The demineralized cocoons were extensively washed with DI  $\text{H}_2\text{O}$  and air-dried overnight. To remove sericin, 1 g of demineralized cocoon was boiled with 0.02 M sodium carbonate ( $\text{Na}_2\text{CO}_3$ ) for 1 hour at 100 °C, rinsed with DI water, and dried overnight at 40 °C (process known as degumming). 1 g dried degummed silk fibers were dissolved in 50 mL 7 M calcium nitrate tetrahydrate at 120 °C for 5 h. The dissolved solution was dialyzed against deionized (DI) water using HiMedia dialysis membrane cellulose tubing for 48 h at room temperature and then centrifuged at 22,000Xg for 30 min at 4 °C to remove calcium nitrate ions.

In order to fabricate the silk fibroin film, 800  $\mu\text{L}$  of the regenerated solution was cast on the surface of autoclavable plastic sheet placed in a petri plate and dried at 40°C for 10-12 h under an incubator. Figure 1 represents the schematic diagram of sequential steps of fabrication of silk fibroin film.

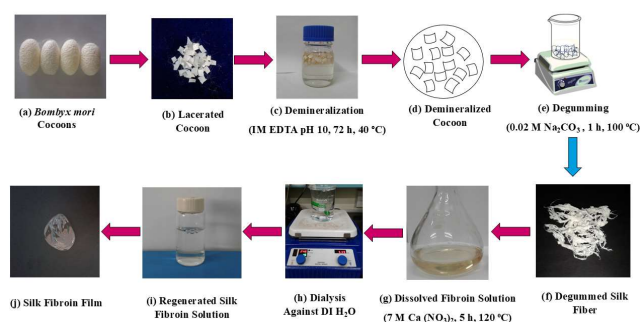


Figure 1: Schematic diagram illustrating sequential steps of fabrication of silk fibroin film.

#### 2.3 Characterization:

Materials from raw cocoon to fabricated silk fibroin film were characterized using Fourier-transform infrared spectroscopy (FTIR), Thermogravimetric Analysis (TGA), and Differential Scanning Calorimetry (DSC).

### 3. Results and Discussion

#### 3.1 FT-IR study

Figure 2 shows FTIR spectra of raw cocoon, demineralized cocoon, degummed silk fiber and silk fibroin film. Amide I ( $1614, 1614, 1613 \text{ cm}^{-1}$ , corresponding to the  $\beta$  sheet structure ( $\text{C}=\text{O}$ ) and  $1641 \text{ cm}^{-1}$  to the random coil structure or bending vibration of O-H, amide II ( $1513, 1513, 1512, 1530 \text{ cm}^{-1}$ ) corresponding to N-H bending and amide III at ( $1231, 1233, 1231, 1236$ ), corresponding to C-N are observed [1,3]. This is suggested that the silk fibroin film consist of  $\beta$  sheet structure as well as water. Details are given in Table 1.

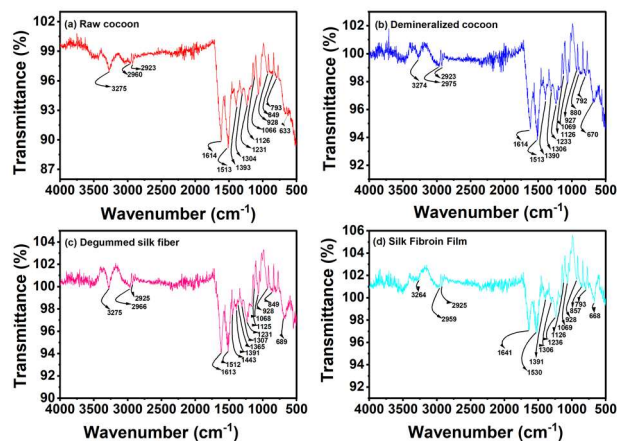


Figure 2: FTIR spectra of (a) raw cocoon, (b) demineralized cocoon, (c) degummed silk fiber, and (d) silk fibroin film.

Table 1: Peaks assignments to FTIR peaks of raw cocoon (R-C), demineralized cocoon (D-C), Degummed silk fiber (D-S-F) and Silk Fibroin Film (S-F-F) [1, 3].

R-C	D-C	D-S-F	S-F-F	Assignment
3450	3450	3450	3450	O-H stretch
3275	3274	3275	3264	N-H stretch
2960	2975	2966	2959	CH <sub>2</sub> stretch
2923	2923	2925	2925	CH <sub>2</sub> stretch
1614	1614	1613	1641	C=O (Amide I)
1513	1513	1512	1530	N-H (Amide II)
1393	1390	1391	1391	CH <sub>2</sub> bending
1304	1306	1307	1307	C-N (Amide III)
1231	1223	1231	1236	N-H def
1066	1069	1068	1069	C-O stretching
928	927	928	928	CH <sub>2</sub> bending

### 3.2 TGA study

To study the thermal stability of the samples, TGA was performed (Figure 3). The initial mass losses of raw cocoon, demineralized cocoon, degummed silk fiber and silk fibroin film occurred at 70 °C, 69 °C, 58 °C and 83 °C, respectively due to the loss of bound water molecules [4, 5]. The higher temperature for water loss in silk fibroin film as compared to others indicates strong binding of water molecules in film. It is supported by FTIR study, in which presence of water in film is observed at 1641 cm<sup>-1</sup>. Film has more hydrophilic nature as compared to others, which is good for wound healing and dressing applications. The second mass losses of all occurs at 265 °C, 245 °C, 265 °C and 246 °C, which are related to starting of decomposition of NH<sub>2</sub>-COOH groups in protein [4, 5]. Sharper transition occurs in raw cocoon, demineralized cocoon, degummed silk fiber than silk fibroin film. This is indicated that secondary structure of proteins is disturbed by presence of water in film. The final loss at ~ 350 °C, is due to decomposition of protein which is the highest loss in mass in TGA curve [4, 5].

### 3.3 DSC study

DSC curves of raw cocoon, demineralized cocoon, degummed silk fiber and silk fibroin film are shown in Figure 4. Endothermic peaks of raw cocoon, demineralized cocoon, degummed silk fiber and silk fibroin film are observed at 81.66 °C, 92.60 °C, 70.69 °C, and 81.89 °C, which are related to removal of water in materials [4, 5]. There is another distinct endothermic peak at 290 – 323 °C, which is related to association of protein decomposition [4, 5]. The sharpness of peak decreases from raw cocoon, demineralized cocoon, degummed silk fiber to silk fibroin film.

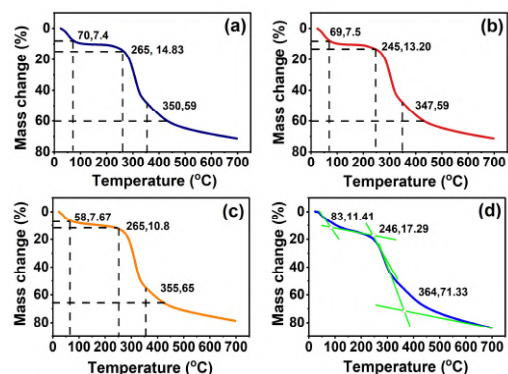


Figure 3: TGA curve of (a) raw cocoon, (b) demineralized cocoon, (c) degummed silk fiber, and (d) silk fibroin film.

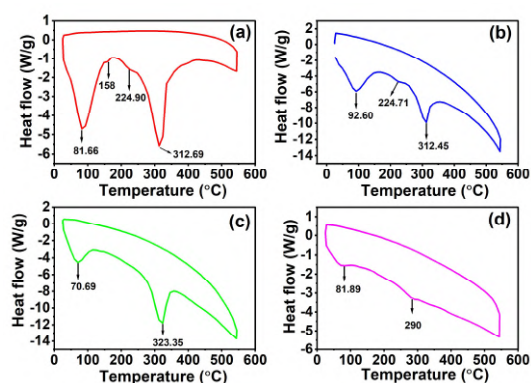


Figure 4: DSC curves of (a) raw cocoon, (b) demineralized cocoon, (c) degummed silk fiber, and (d) silk fibroin film.

This is suggested that structure of proteins is affected during the film formation from demineralized cocoon and degummed silk fiber. In addition, there are endothermic peaks at 158 °C and 225 °C in case of raw cocoon and 225 °C in case of demineralized cocoon. The former one at 158 °C in raw cocoon may be related to removal of compounds of metals (Ca/Mg/Na) as minerals. The second one at 225 °C is rearrangement of secondary proteins (conformational changes accompanying silk's transition from random coil/ $\alpha$ -helix to  $\beta$  sheet) [4, 5].

## 4. Conclusions

*Bombyx mori* cocoon has been used to prepare silk fibroin film through steps of demineralization, degumming, and dissolution. The protein structure (amide I, II and III) is obtained in all samples. The hydrophilicity is more in this film as compared to other precursors, which is important in fabrication of biomaterials for wound healing and dressing applications. The secondary protein structure is maintained upto 225 °C.

## 5. References

- [1] M.-J. Lin, *et al*, *Pharmaceutics* (2021), 13, 1459.
- [2] Shuko Suzuki, Traian V. Chirila, Grant A. Edwards, *Prog Biomater.* (2016) 5:193-198.
- [3] T.-C. Hou, S.-C. Jeng, *ACS Appl. Bio Mater.* (2020), 3, 8575.
- [4] N. Agarwal, D. A. Hoagland, R. J. Farris, *J. Appl. Poly.* (1997), 63, 401.
- [5] B. Aksakal, *et al*, *Mater. Res. Express* (2019), 6, 125356.

**Acknowledgement:** Authors thank Dr. Niharendu Choudhury, Head, Chemistry Division, BARC for his

## Effect of Thermalization of Cobalt based Metal Organic Frameworks (MOFs) in supercapacitor application

Srikant Sahoo\*, and Ashis Kumar Satpati\*

Analytical Chemistry Division, Bhabha Atomic Research Centre, Trombay, Mumbai, India

Email id: srikants@barc.gov.in/ asatpati@barc.gov.in

### Abstract.

In the present study the effect of thermalization on the electrochemical performance of a cobalt-based MOF in supercapacitor applications has been investigated. Cobalt based Metal Organic Frameworks (MOFs) was synthesized by co-precipitation method. The MOFs were subjected to thermalization at different temperatures (e.g., 300°C, 500°C, and 900°C) under an inert atmosphere to prevent oxidation. The samples thus obtained were labeled as MOF-300, MOF-500, and MOF-900. X-ray diffraction (XRD) was carried out to observe the crystalline structure of the material and Scanning Electron Microscopy (SEM) and Atomic force Microscopy (AFM) were used to study the structural morphology. Cycle voltammetric experiment was carried out to check the reversibility of the electrode in the potential range from 0V to 0.8. The sample MOF-300 exhibited the highest specific capacitance of 370 F/g at a current density of 1A/g, outperforming MOF-500 and MOF-900.

### Introduction:

Metal-Organic Frameworks (MOFs) are a class of porous crystalline materials composed of metal ions or clusters coordinated to organic ligands. The MOFs have garnered significant attention in energy storage systems due to their high surface area, tunable porosity, and introduction of diverse metal centers. Supercapacitors also known as electrochemical capacitors are energy storage devices characterized by their high-power density, rapid charge-discharge rates, and long cycle life. However, the relatively low energy density of supercapacitors compared to batteries has driven the exploration of novel materials like MOFs to enhance their performance

### Result and Discussion:

The cyclic Voltammetric (CV) experiment was carried out in 1M KOH solution and it is shown in Fig (1). The CV curve of MOF-300 indicated that the material is pseudo capacitive in nature and highly stable up to the 500cycle.

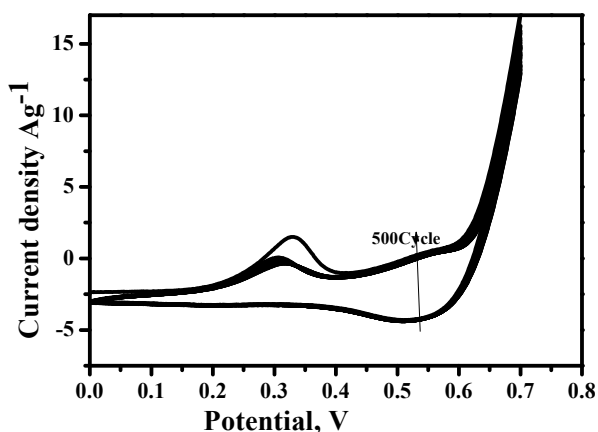


Fig.1. Cyclic voltammetry plot MOF-300 in 1M KOH solution

Fig (2) shows the cyclic voltammetry plot of the MOFs annealed at different temperature such as MOF-300, MOF-500, and MOF-900. The sample MOF-300 exhibited the highest current as compared to sample MOF-500 and MOF-900. Thermalization significantly impacts the electrochemical properties of cobalt-based MOFs. With increase in temperature from MOF-300 to MOF-900, the performance has been reduced, initially redox capacitance and later the electrostatic capacitance. Optimal thermalization at 300°C produces a balance between structural

integrity and conductivity, resulting in superior performance in super capacitor applications.

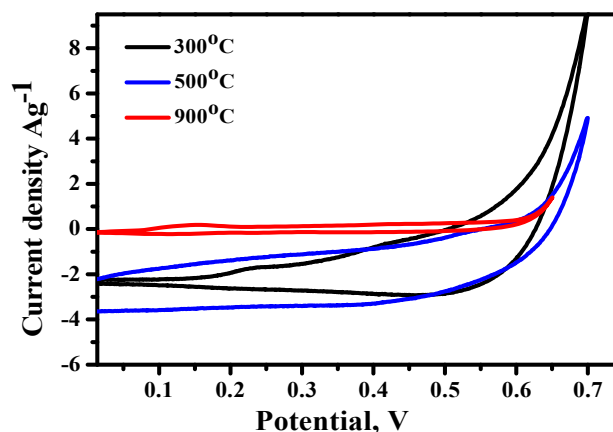


Fig.2. Cyclic voltammetry plot MOF annealed at different temperature in 1M KOH solution

### Conclusion:

The Cobalt based Metal Organic Frameworks (MOFs) were successfully synthesized by co-precipitation method and samples were characterized using various techniques such as XRD, SEM, AFM and FTIR etc. The MOF-300 sample exhibited a specific capacitance of 370 F/g at a current density of 1 A/g, exceeding the performance levels of both MOF-500 and MOF-900. Thermalization significantly impacts the electrochemical properties of cobalt-based metal-organic frameworks (MOFs). Optimizing thermalization at 300°C strikes a balance between preserving structural integrity and enhancing electrical conductivity, thereby improving their performance in supercapacitor applications

### References

- [1] S. Sahoo, A. K. Satpati, P. K Sahoo, P. D. Naik, ACS Omega, 3(2018)17936-17946
- [2] S. Sahoo, A. K. Satpati, J. Electroanal Chem., 801 (2017) 416–424.
- [3] P. Zhang, F. Wang, M. Yu, X. Zhuang, X. Feng, Chem. Soc. Rev. 2018,17, 7426
- [4]. Shen, L.; Yu, Le.; Wu, H-B.; Yu, X-Y.; Zhang, X. Lou, X-W (David), NATURE COMMUNICATIONS, | 6:6694 | DOI: 10.1038/ncomms.7694.

## Thermal Analysis of Zirconium loaded Iron Phosphate Glass

Akhilesh C Joshi<sup>a\*</sup>, R K Mishra<sup>b</sup>, Dimple P Dutta<sup>c</sup> and S.N.Achary<sup>a</sup>

<sup>a</sup>Chemistry Division, BARC, Mumbai ; <sup>b</sup>WMD, BARC, Mumbai ; <sup>c</sup>HRDD, BARC, Mumbai

\* [acjoshi@barc.gov.in](mailto:acjoshi@barc.gov.in); Phone: 91-22-25599276 and Fax: 91-22-25505151

### Abstract

Iron phosphate glass is considered a viable option for vitrification of nuclear waste generated from the operation of nuclear power plant. IPG has several advantages over the commercially used Borosilicate glass especially for heavy elements which have low solubility in BSG. The critical concentration of Zirconium which can form iron phosphate glass is found to be 15 mol% of Zirconium. TG/DTA of the Zr loaded glass showed improved thermal properties over the pristine IPG.

Nuclear waste disposal in a safe way is a critical part for successful operation of any nuclear power plant. The immobilization of nuclear waste generated inside the glass matrix is considered one of the safest way for disposal of nuclear waste. The Iron phosphate glass (IPG) doped with different mole percent of Zirconium was prepared by melt quench technique. XRD pattern of the prepared samples showed that up to approximately 15 mol% Zirconium, a broad amorphous peak with  $2\theta$  ranging from  $20^\circ$  to  $30^\circ$  was obtained supporting the formation of glass without any significant crystalline phases. With further increase in concentration of Zirconium to 20mol%, sharp peaks appeared corresponding to the crystalline phase. 15 mol% Zirconium loaded IPG was irradiated by proton beam in FOTIA with three different doses of 12 MGy, 25MGy and 50 MGy at two different energy of 3 MeV and 5MeV. Irradiated samples did not show any significant change in structure of IPG. The limiting concentration of Zirconium which can be loaded inside IPG without formation of any crystalline phases was found to be approx. 15 mol% Zirconium.

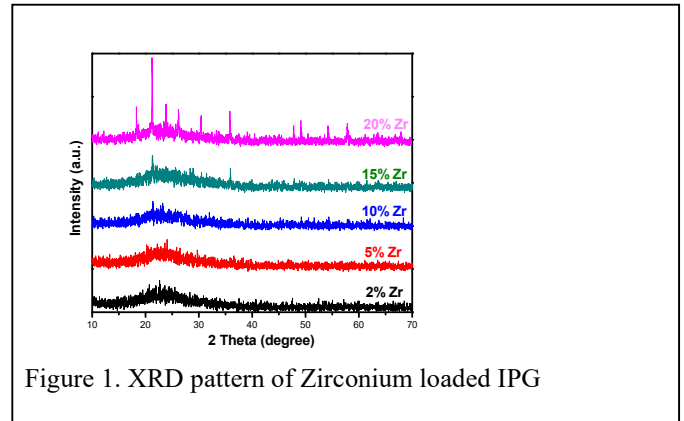


Figure 1. XRD pattern of Zirconium loaded IPG

### References

1. Akhilesh C Joshi, M. Roy, Dimple P Dutta, R K Mishra, S S Meena, R Kumar International Journal of Applied Glass Science (2024) 15:292-306.

## Engineered Ionic Liquid based Hydrogel: A Multifunctional, Thermally Stable Platform for the Breast Cancer Treatment

Raviraj Pansuriya<sup>a</sup>, Tapas Patel<sup>a</sup>, Sugam Kumar<sup>b</sup>, Vinod K Aswal<sup>b</sup>, Naina Raje<sup>c</sup>, Suresh Kumar Kailasa<sup>a</sup>, Naved I. Malek<sup>a\*</sup>

<sup>a</sup>*Ionic Liquids Research Laboratory, Department of Chemistry, Sardar Vallabhbhai National Institute of Technology, Surat-395007, Gujarat, India*

<sup>b</sup>*Solid State Physics Division, Bhabha Atomic Research Centre, Trombay, Mumbai-400085, India*

<sup>c</sup>*Analytical Chemistry Division, Bhabha Atomic Research Centre, Trombay, Mumbai-400085, India*

\* Corresponding Author email: [navedmalek@chem.svnit.ac.in](mailto:navedmalek@chem.svnit.ac.in)

### Abstract

Transdermal drug delivery systems (TDDS) are a promising approach for breast cancer treatment, offering advantages such as non-invasiveness, potential for localized and prolonged drug delivery while minimizing side effects through avoiding first-pass metabolism. The present work we prepared ionic hydrogels through synergistic interaction between ionic liquids (ILs), Choline Alanine ([Cho][Ala]) and Choline Proline ([Cho][Pro]) with oleic acid (OA). Ionic hydrogel was characterized by various analytical techniques including SANS, FTIR, and rheological analysis. Further, effect of temperature and thermal stability of hydrogel was investigated by DSC and TGA analysis. The *in vitro* skin permeation, biocompatibility and cytotoxicity of hydrogel was studied in detail. These results indicate that the investigated biocompatible hydrogels enable the transdermal delivery of hydrophilic drugs, making them a viable option for effectively treating breast cancer.

### Introduction

Breast cancer is a widespread issue in various regions of the world.[1,2] The standard approaches including chemotherapy or radiation therapy are available to treat breast cancer. However, in certain cases where surgery is not possible or recommended, chemotherapy could be a more suitable option; however, some side effects are observed after treatment.[3] Transdermal drug delivery systems (TDDS) offer several key benefits in comparison to traditional treatments as well as injectable and oral methods.[4] These advantages include circumventing the ability to bypass enzymatic degradation, the initial metabolic impact from the liver and diaphragm, ensuring extended therapeutic presence, and enhancing patient adherence to treatment.[5]

TDDSs have certain complications in drug delivery, specifically when it comes to hydrophilic and high-molecular-weight substances such as proteins and peptides.[6] Predominantly due to the formidable barrier imposed by the skin's robust hydrophobic outer layer, known as the stratum corneum (SC). To overcome this drawback, various approaches have been reported, which encompass the implementation of chemical agents that enhance permeation and physical methods such as microneedles or electroporation ablation to diminish the barrier.[7] Fatty acids based Chemical permeation enhancers (CPEs) are studied in recent times because of its low toxicity and negligible skin irritation.[8] Apart from these, solubility of the drugs in pharmaceutically approved solvent also limit their application as the TDD. To resolve these limitations, ionic liquid (IL) based drug delivery systems have been investigated thoroughly. Basically, ILs are liquid at room temperature and/or melt below 100 °C because cations and anions are arranged in an asymmetric manner and possess several unique physico-chemical properties.[9]

### Materials and Methods

#### Preparation of SAIL-based polymeric patch

The ionic hydrogels were prepared through interacting ILs with OA. Briefly, 0.80 M solution of both ILs were kept at room temperature (25°C), followed by the dropwise addition of OA keeping in vortex in order to get homogeneity. Once the OA concentration reached 0.70 M and 0.75 M, the [Cho][Ala] and [Cho][Pro] based ionic hydrogel were formed, respectively.

#### Thermogravimetric analysis (TGA)

Thermal stability of investigated patch was tested by SDTQ600 TGA instrument. The analysis is done at temperature range 20-500 °C with temperature ramp 10°C/min. Aluminum pan is used as a sample holder and the sample purge flow of nitrogen gas is set to 100 mL/min.

#### Differential scanning calorimetry (DSC)

the Mettler-Toledo DSC (Model DSC3/700/761) apparatus was used to observe the temperature effect on both hydrogels. For this purpose, we used an aluminum pan and samples were heated from 25 to 150 °C with a 5 °C/min heating rate under a nitrogen atmosphere.

#### Drug Loading

The physical entrapment method was used for drug loading in ionic hydrogels. In this method, we dissolved 5-FU at its saturated concentration in an aqueous solution of ILs (0.8 M) followed by adding an OA to form hydrogels. The amount of 5-FU in hydrogels was measured through UV spectroscopy

#### Results and discussion

In our efforts to prepare smart TDDs, in the present investigation we have designed biocompatible, stimuli-responsive, adhesive, and self-healable ionic hydrogels as the new age TDDSs. ILs used in the study have choline as the cation and alanine and proline as the anions and are denoted as [Cho][Ala] and [Cho][Pro] respectively. Both ILs are synthesized from natural origins and are biocompatible. Although these ILs increase the solubility of the chemotherapeutic drug 5-Fluorouracil (5-FU), they could not efficiently penetrate through the skin with the drug because of their hydrophilic nature and inability to form hydrogel itself. To overcome this limitation, we introduced oleic acid (OA) as a skin penetration enhancer. Additionally, OA plays a multifaceted role in biocompatibility, self-healing and adhesive properties of the hydrogel, as it has ability to form various nano-aggregates including ionic hydrogel through synergistic interaction with ILs. These aggregates within the hydrogel can contribute to the self-healing properties of the hydrogel by promoting molecular rearrangement and reformation of the gel structure upon mechanical damage. Further, these aggregates also enhance adhesiveness by interactions with the substrate surface including hydrogen bonding or hydrophobic interactions. Furthermore, OA exhibit biocompatibility and do not pose harmful effect on healthy tissues. We have characterized the hydrogels and their mechanical properties using various state of the art analytical techniques including SANS, FE-SEM, FTIR, and rheological analysis in detail. To assess the skin permeation of 5-FU utilizing these ionic hydrogels and their impact on skin barrier function, we conducted experiments on goat skin through the Franz diffusion cell. Additionally, we evaluated the *in vitro* biocompatibility of ionic hydrogels using normal cell lines (M132 cells) as well as cancerous cell lines (MCF-7 and HeLa cells). Further, the effectiveness and IC<sub>50</sub> of 5-FU loaded ionic hydrogels were

assessed through performing *in vitro* cytotoxicity study on MCF-7 and HeLa cell lines.

### Thermal Analysis of Hydrogel

We applied DSC analysis to find the temperature ( $T_g$ ) for gel to sol conversion. In the DSC graph, a distinct and sharp endothermic peak was arrived at 90 °C, and 110 °C for [Cho][Pro] and [Cho][Ala] based ionic hydrogel, respectively (Figure 1a). These gel to sol conversion observed due to larger size aggregates that are converted in to small size aggregates at high temperature value. Notably,  $T_g$  of [Cho][Ala] based ionic hydrogel is higher than that of [Cho][Pro] based ionic hydrogel. The reasons for above result are, unlike the alanine-based IL, the bulkiness of proline-based IL, and the stronger interaction of OA with [Cho][Ala] compared to [Cho][Pro], leading to a lower temperature threshold for gel-to-sol conversion. Remarkably, this conversion process exhibits complete reversibility; when the temperature decreases, the ionic hydrogel reverts back to its initial gel form.

Additionally, we have investigated the thermal stability of both ionic hydrogels, oleic acid as well as ILs through TGA analysis. A gradual degradation was observed in the TGA graph (Figure S4 f). ILs and oleic acid are starting to degrade in the 150–160 °C and 200–220 °C temperature ranges, respectively. Furthermore, multi-step degradation observed in ionic hydrogels, in which the initial mass loss was observed at 100–110 °C, attributed to the evaporation of water. Subsequently, a second mass loss occurred at 200–250 °C, attributed to the degradation of IL and OA.

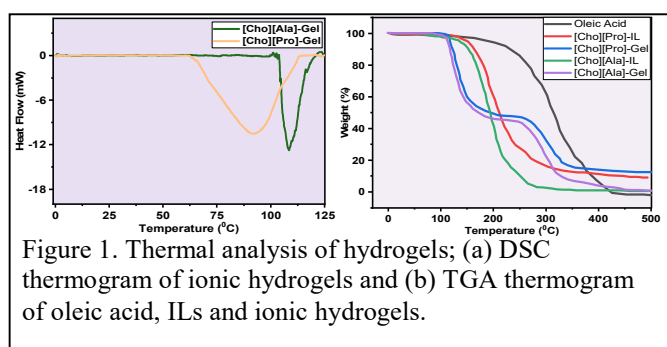


Figure 1. Thermal analysis of hydrogels; (a) DSC thermogram of ionic hydrogels and (b) TGA thermogram of oleic acid, ILs and ionic hydrogels.

### Drug Loading

The primary objective of this study is to develop a hydrogel with capability of encapsulating higher amount of anticancer drug. To achieve this, we started to dissolve 5-FU in an aqueous solution of ILs (0.84 M) to its saturation point, which is 156 mg/mL and 149 mg/mL for [Cho][Ala] and [Cho][Pro], respectively. After reaching the saturation point of 5-FU in ILs, OA was introduced for the formation of a drug loaded ionic hydrogels. This 3-D network of the ionic hydrogels contains the maximum possible amount of 5-FU drug. Subsequently, the drug concentration was determined using the UV spectroscopy. The encapsulated amount of 5-FU was 155 mg/mL and 147 mg/mL in [Cho][Ala] and [Cho][Pro] based ionic hydrogel, respectively, which is significantly higher than the water (12.2 mg/mL) and other organic solvents (5.5 mg/mL in 95 % ethanol, 8 mg/mL in pH-7.2 PBS and 53 mg/mL in DMSO).

### Skin Permeation of Drug

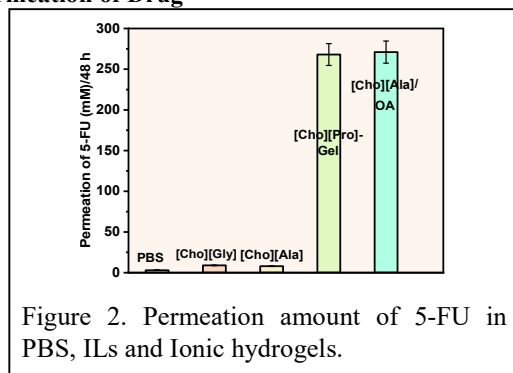


Figure 2. Permeation amount of 5-FU in PBS, ILs and Ionic hydrogels.

It is necessary to surmount the SC barrier in order to permeate drug molecules through skin effectively. The essential requirements for permeation of drug through skin are; a drug molecular weight should be less than 500 Da, it must have significant lipophilicity (log octanol-water partition coefficient between 1-3) and melting must be less than 200 °C.[60] As 5-FU is having a log octanol-water coefficient of -0.89, which makes it difficult in penetration.[61] We overcome this difficulty by encapsulating 5-FU within ionic hydrogels. We investigated the *in vitro* skin permeation of 5-FU using goat skin through the Franz diffusion cell at 32 °C and 48 h. The reason for using the goat skin is the similarity between biological characteristics with human skin.[62] Here, we investigated the permeation of 5-FU in ionic hydrogels, and PBS used as control system. As shown in Table 3, the permeated amount of 5-FU is 255 μM, 250 μM, and 0.001 μM for [Cho][Ala], [Cho][Pro] based ionic hydrogel and PBS, respectively (Figure 2). Without OA, the permeated amount of 5-FU is 9 μM and 8 μM in [Cho][Ala] and [Cho][Pro], respectively.

### Conclusion

In this research, we have prepared successfully two different ionic hydrogels through synergistically interacting [Cho][Ala] and [Cho][Pro] with OA and analysed them using SANS, FTIR, FE-SEM, EDX, DSC and TGA techniques. The mechanism of formation, morphology, mechanical properties, physical and thermal stability of the ionic hydrogels are also investigated. The hydrogels exhibited excellent *in vitro* biocompatibility. As results shows, when cells were treated with different concentrations of hydrogel, the viability of normal and cancerous cells was above 92% after 48 h. The ionic hydrogels were found to enhance the permeability of the hydrophilic drug 5-FU through the skin by making the intracellular lipid of the SC layer more fluid. Interestingly, the both ionic hydrogels showed significantly greater permeation of 5-FU compare to PBS and other conventional chemical enhancer. Among both, [Cho][Ala] based ionic hydrogel show greater skin permeability compared to [Cho][Pro] based ionic hydrogel. That can potentially overcome the challenges of delivering hydrophilic drug through the skin. *In vitro* cytotoxicity results revealed the synergistic anticancer impact of 5-FU-loaded ionic hydrogels on MCF-7 and HeLa cell lines with lower dosage values. These findings suggest that newly introduced ionic hydrogels hold a promising approach for the treatment of breast cancer in a transdermal way. Nevertheless, further research still requires *in vivo* clinical behaviour study before considering the use of ionic hydrogels in breast cancer treatment.

### References

- Chen, S.; Liu, Y.; Fong, D. Y. T.; Zhou, J.; Chen, H.; Wan, C. *Sci. Rep.* **13** (2023), 15176.
- Bray, F.; Ferlay, J.; Soerjomataram, I.; Siegel, R. L.; Torre, L. A.; Jemal, A. CA. *Cancer J. Clin.* **68** (2018), 394–424.
- Chakraborty, S.; Rahman, T. *Ecancermedicallscience* **6** (2012), ed16.
- Prasnitz, M. R.; Langer, R. *Nat. Biotechnol.* **26** (2008), 1261–1268.
- Alkilani, A.; McCrudden, M. T.; Donnelly, R. *Pharmaceutics* **7** (2015), 438–470.
- Paudel, K. S.; Milewski, M.; Swadley, C. L.; Brogden, N. K.; Ghosh, P.; Stinchcomb, A. L. *Ther. Deliv.* **1** (2010), 109–131.
- Ramadan, D.; McCrudden, M. T. C.; Courtenay, A. J.; Donnelly, R. F. *Drug Deliv. Transl. Res.* **12** (2022), 12 (4), 758–791.
- Ibrahim, S. A.; Li, S. K. *Pharm. Res.* **27** (2010), 115–125.
- Lei, Z.; Chen, B.; Koo, Y.-M.; MacFarlane, D. R. *Chem. Rev.* **117** (2017), 6633–6635.



# Metal-Organic Framework-Integrated Polymeric Hydrogel: A promising Drug Delivery Platform for Breast Cancer Treatment

Ishani Pandya<sup>a</sup>, Sugam Kumar<sup>b</sup>, Vinod K. Aswal<sup>b</sup>, Naved Malek<sup>a,c\*</sup>

<sup>a</sup>Ionic Liquids Research Laboratory, Department of Chemistry, Sardar Vallabhbhai National Institute of Technology, Surat-395007, Gujarat, India

<sup>b</sup>Solid State Physics Division, Bhabha Atomic Research Centre, Trombay, Mumbai 400085, India

<sup>c</sup>Institute of Chemistry, University of São Paulo, 05508-000 São Paulo, SP, Brazil

Corresponding Author e-mail: navedmalek@chem.svnit.ac.in

## Abstract

Current limitations in cancer treatments have driven researchers to develop more precise and safe drug delivery systems that enhance therapeutic efficacy, protect healthy cells, and reduce cancer recurrence. This study presents a self-healing, injectable hybrid hydrogel, created by combining the metal-organic framework CuBTC with poly(vinyl alcohol) (PVA), designed for targeted cancer therapy. This biocompatible hydrogel, crosslinked with borax, forms a stable 3D network ideal for encapsulating 5-Fluorouracil (5-FU). Responsive to physiological pH, it releases 5-FU at targeted sites, and *in vitro* tests confirm its effectiveness against MCF-7 and HeLa cells, demonstrating its potential for sustained, localized cancer treatment.

## Introduction

The development of advanced drug delivery systems (DDS) is essential to overcome the drawbacks of traditional cancer therapies, including systemic toxicity and non-specific targeting. [1] Among emerging DDS options, metal-organic frameworks (MOFs) show promises due to their high surface area, tunable pore sizes, and exceptional drug-loading efficiency, making them ideal carriers for targeted drug release in cancer treatment. However, MOF-based DDS face challenges like burst release and limited biocompatibility. To address these limitations, integrating MOFs with polymers has shown potential, forming stable, multifunctional hydrogels with adjustable mechanical and chemical properties suitable for biomedical applications.

This study introduces a CuBTC-based hybrid hydrogel, synergistically integrated with poly(vinyl alcohol) (PVA) and crosslinked using biocompatible borax. This innovative DDS combines the pH-responsive behavior of MOFs with PVA's stability, creating an injectable hydrogel that selectively releases the anticancer drug 5-Fluorouracil (5-FU) in acidic tumor environments. The hydrogel exhibits high drug-loading capacity, self-healing properties, and enhanced mechanical strength. Its efficacy was confirmed *in vitro* against MCF-7 and HeLa cancer cell lines. The results highlight the hybrid hydrogel's potential as a localized, biocompatible DDS, offering a controlled, sustained release of anticancer drugs and promising advancements in cancer therapy applications.

## Experimental section

### Preparation of CuBTC and Hybrid hydrogel

CuBTC was synthesized using a solvothermal process, with minor alterations to the synthesis process described earlier. [2] First  $\text{Cu}(\text{NO}_3)_2 \cdot 3\text{H}_2\text{O}$  (1.94 g) and BTC (benzene 1,3,5-tricarboxylic acid, 0.84 g) were dissolved in 24 mL deionized water and ethanol respectively in separate beaker. The two aforementioned solutions were combined and mixed until a suspension formed at room temperature. Second, the mixture was transferred into a Teflon-lined stainless-steel reactor and heated to 110 °C for 28 h. The reactor was then given time to spontaneously cool to normal temperature. The main result was a dark blue solid, which was separated and washed with ethanol, DMF, and chloroform. Lastly, the solid was collected and dried in a vacuum oven for 12 h at 120 °C to produce a fine CuBTC powder.

To prepare the Hybrid Hydrogel, the initial step involves preparing a uniform suspension of CuBTC in the deionized water. In 5 mL of deionized water, 0.5 wt% CuBTC was added and thoroughly mixed on a magnetic stirrer to achieve uniform dispersion of CuBTC particles. After adding 5 wt% PVA into above mixture, heat the solution at 60 °C to mixture and stirred well at room temperature and it formed hydrogel. Figure 1 shows a schematic illustration of CuBTC and Hybrid hydrogel preparation.

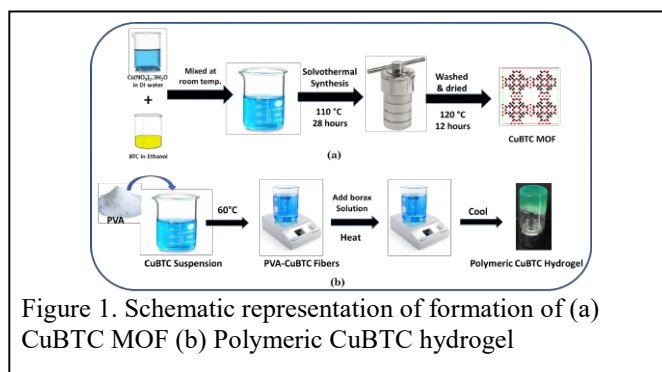


Figure 1. Schematic representation of formation of (a) CuBTC MOF (b) Polymeric CuBTC hydrogel

## Result and Discussion

This study focuses on creating a polymeric MOF-based hydrogel designed to encapsulate and release the chemotherapy drug 5-Fluorouracil (5-FU) in response to physiological triggers, like pH variations. Metal-organic frameworks (MOFs) have gained attention for drug delivery due to their unique properties: high surface area, chemical stability, and significant pore volume, making them ideal for targeted drug release. Among MOFs, CuBTC stands out for its high 5-FU loading capacity, stability, and low toxicity, positioning it as an appealing choice for drug carriers. While CuBTC can induce cancer cell death by releasing 5-FU, its delivery limitations—such as burst release—pose challenges for sustained drug administration.

To address these challenges, we developed a hybrid hydrogel that integrates CuBTC with poly(vinyl alcohol) (PVA) and borax. In this system, CuBTC interacts with PVA's hydroxyl groups, while borax acts as a biocompatible crosslinker, forming reversible boronate connections that give the hydrogel self-healing and shape-memory properties. Introducing borax solution crosslinks PVA chains, resulting in a stable 3-D hydrogel network.

### Thermal stability of CuBTC and Hybrid hydrogel

Figure 2a illustrates the TGA curves of CuBTC and Hybrid hydrogel. CuBTC exhibits three weight loss stages: 10.8% (40–140 °C) due to solvent volatilization, 24.1% (140–320 °C) from the elimination of water molecules bound to  $\text{Cu}^{2+}$ , and a sharp loss above 320 °C from organic ligand decomposition, leaving 22.8% residue as copper oxide. [3] In contrast, the Hybrid hydrogel demonstrates greater thermal stability, with minimal mass loss up to 100 °C. The mass loss of gel at 150 °C, 350 °C, and 460 °C is 8.2%, 48.3%, and 74.75%, respectively, attributed to strong hydrogen bonding between CuBTC and PVA.

In Figure 2b CuBTC shows a crystallization peak at -110 °C during the cooling process, and a melting peak is shown at -60 °C in the process of heating. This indicates that CuBTC retains its structural integrity up to -110 °C without going through a phase transition or structural changes. PVA is a well-known and well-recognized antifreeze substance that successfully lowers the

freezing point. Zhang et al. reported sharp peaks at  $-15.1\text{ }^{\circ}\text{C}$  in PVA/Borax hydrogel. [4] In the case of Hybrid Hydrogel, sharp exothermic peak was observed at  $-106\text{ }^{\circ}\text{C}$  (Figure 2c). This outcome can be attributed to the incorporation of CuBTC, which effectively restrained water crystallization and consequently led to a pronounced reduction in the freezing point of this hydrogel. The strong hydrogen bonding within the gel disrupts the arrangement of water molecules, which is necessary for the growth of ice crystals. This characteristic allows the patch to keep its fluid state even at sub-zero temperatures.

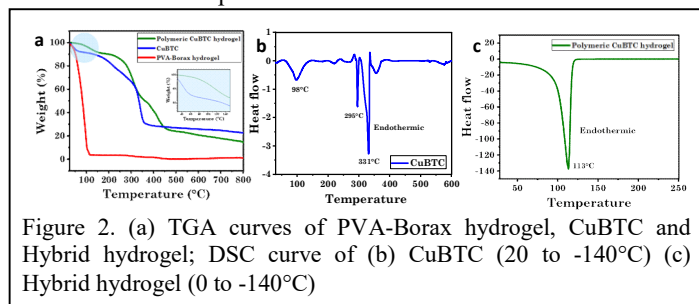


Figure 2. (a) TGA curves of PVA-Borax hydrogel, CuBTC and Hybrid hydrogel; DSC curve of (b) CuBTC (20 to  $-140\text{ }^{\circ}\text{C}$ ) (c) Hybrid hydrogel (0 to  $-140\text{ }^{\circ}\text{C}$ )

### Structural Characterization through SANS

We conducted SANS analysis both before and after the addition of borax. We determined the differential scattering cross-section ( $d\Sigma/d\Omega$ ) per unit volume as a function of the wave vector transfer ( $q$ ) during the SANS experiment (Table 1). We used the mass fractal structure model with a ( $q^{-1}$ ) relation to fit all of the data, as shown in Figure 3. Before adding borax, the solution exhibited a viscous nature with a matrix resembling a Gaussian coil, as illustrated in Figure 3a. These SANS data confirm that the Gaussian coil of PVA is cross-linked with borax to form the hybrid hydrogel (Figure 3b). The radius of gyration in the Gaussian coil-like model was found to be 5.2 nm. Following the addition of borax, the mass fractal model exhibited measurements of 15.5 Å for building block radius and  $>1000\text{ \AA}$  for Correlation length. The parameter Dm can be used to quantify the openness in fractal dimensions. It takes on a value of 1 for loosely connected aggregates and a value of 3 for tightly packed aggregates. [5] In the polymeric CuBTC hydrogel, when we add the concentration of borax increased from 0.1 ml to 0.2 ml, Dm value increased from 1.5 to 1.8, suggesting that gel becomes tough with no change in the structures. We made injectable hydrogel for this study; thus, we took 0.2 ml of borax for further studies.

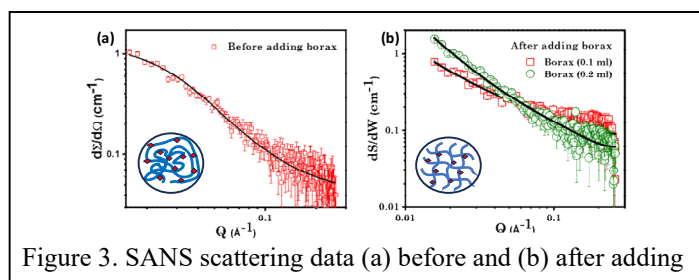


Figure 3. SANS scattering data (a) before and (b) after adding

### Drug loading and release behavior in hydrogel

The injectable hydrogel developed here effectively delivers 5-Fluorouracil (5-FU) for cancer treatment, achieving a high encapsulation efficiency of 261.4 mM, over 300 times its solubility in water. This efficiency is due to the inclusion of CuBTC, which enhances 5-FU loading through strong interactions with the drug, unlike PVA-only hydrogels.

Designed for sustained, pH-responsive release, the hydrogel releases more 5-FU at pH 5.2 (tumor-like conditions), achieving 84.4% release, while releasing less at pH 7.4 (normal tissue conditions), with 64.1% over 48 hours. This targeted, controlled release ensures consistent drug delivery to tumor sites, reducing side effects on healthy tissues.

Table 1. Fitted SANS scattering data

System	Analysis			Model
Before adding borax (CuBTC + PVA)	Radius of gyration $R_g$ (nm) = 5.2			Gaussian coil
	Building block radius (Å)	Fractal dimension Dm	Correlation length ( $\zeta$ )	
After adding borax CuBTC+PVA + Borax (0.1 ml)	16.2	1.5	$>1000\text{ \AA}$	Mass fractal structure
CuBTC+PVA + Borax (0.2 ml)	15.5	1.8		

### Conclusions

In summary, the pH responsive an injectable Hybrid Hydrogel demonstrated high efficiency as a carrier for delivering anticancer drugs has been successfully produced in this study using a simple approach. SANS data confirmed the formation of hydrogel by cross-linking the Gaussian coil-like matrix of PVA-CuBTC using borax. The injectable properties of the hydrogel were examined by conducting a thixotropic rheology study. FT-IR, XRD and SEM analyses provided confirmation of the formation of Hybrid Hydrogel, with the CuBTC structure preserved. The biocompatibility of the hydrogel was assessed using the HaCaT cell line. The designed Hybrid Hydrogel exhibited exceptional thermomechanical properties, flexibility, biocompatibility, self-healable and adhesiveness, and thus, collectively showcasing its multifaceted functionality. The anti-freezing property of the Hybrid Hydrogel was confirmed through DSC analysis, where a distinct sharp exothermic peak was observed at  $-106\text{ }^{\circ}\text{C}$ , indicating its capability to function effectively even in sub-zero temperatures. The Hybrid Hydrogel doped with 5-FU demonstrated increased drug absorption, cytotoxicity, and encapsulation efficiency with a targeting on the MCF-7 and HeLa cell lines. This research provides insight into the development of a new Hybrid Hydrogel with several potential uses, such as smart drug delivery for sustained release and environmental protection.

### References

- Parsana, N., Kumar, S., Aswal, V. K., Seoud, O. El., Malek, N. I. *ACS Appl. Eng. Mater.* (2023), 1 (1), 380–393.
- Gautam, S., Singhal, J., Lee, H. K., Chae, K. H. *Mater. Today Chem.* (2022), 23, 100647.
- Yang, C.-F., Tian, D., He, J.-H. *Therm. Sci.* (2021), 25, 1469–1475.
- Zhang, W., Wen, J. Y., Ma, M. G., Li, M. F., Peng, F., Bian, J., *J. Mater. Res. Technol.* (2021), 14, 555–566.
- Agrawal, S.K., Sanabria-DeLong, N., Jemian, P.R., Tew, G.N., Bhatia, S.R., *Langmuir* (2007) 23, 5039–5044.



Photo Credit: Dr. Mayuresh Mukadam, SSPD, BARC

Supported by  
**Board of Research in Nuclear Sciences**  
**Department of Atomic Energy, Government of India, Mumbai**